

ALMA MATER STUDIORUM  
UNIVERSITÀ DI BOLOGNA

---

---

DOTTORATO DI RICERCA IN  
ASTROFISICA

Ciclo XXXIV

Tesi di Dottorato

## Quasars at the dawn of cosmic time

Presentata da:  
**Antonio Pensabene**

Supervisore:  
**Dr. Roberto Decarli**

Coordinatore di Dottorato:  
**Prof. Francesco Rosario Ferraro**

Esame finale anno 2022

---

Settore Concorsuale: 02/C1 - Astronomia, Astrofisica, Fisica della Terra e dei Pianeti  
Settore Scientifico Disciplinare: FIS/05 - Astronomia e Astrofisica





INAF - Astrophysics and Space Science Observatory  
of Bologna

Ph.D. Thesis

# **Quasars at the dawn of cosmic time**

Antonio Pensabene

*Supervisor:*  
Dr. Roberto Decarli

*Academic Advisor:*  
Prof. Marcella Brusa

October 29, 2021

This Thesis has been devoted to a research project selected and funded by INAF (the Italian National Institute for Astrophysics) within the framework of the formal agreement between INAF and the University of Bologna for the PhD program in Astrophysics.

**Antonio Pensabene**

*Quasars at the dawn of cosmic time*

Ph.D. Thesis, October 29, 2021

Supervisors: Dr. Roberto Decarli

Academic Advisor: Prof. Marcella Brusa

**Alma Mater Studiorum University of Bologna**

Department of Physics and Astronomy

Via Piero Gobetti 93/2

40129, Bologna (Italy)

**INAF - Astrophysics and Space Science Observatory of Bologna**

Via Piero Gobetti 93/3

40129, Bologna (Italy)





*To my family,  
To Francesca,  
To all my true friends.*

---



# Acknowledgements

I am immensely grateful to Dr. Roberto Decarli without whom this research would not have been possible. All along the years of my Ph.D. course, Roberto taught me how to do Science, he has constantly employed enormous efforts to convey to me his scientific experience to correctly interpret the problems, by viewing them from multiple perspectives, and by facing them with increasingly proficient approaches. I am also grateful to him for leading my way into the scientific community by involving me in international collaborations to get in touch with prestigious scientists all around the world. This gave me the chance to have unforgettable experiences as visiting astronomer in some of the most important institutes and observatories of the world. I am particularly grateful to Roberto for all the time he spent working right along with me, for his patience, for being available at any time, for our long chats, for all the time we have shared, and for his enormous passion for Astronomy. It was a privilege to work with him and his group.

I am really thankful to the whole high- $z$  quasar community, particularly to Dr. Fabian Walter, and Dr. Eduardo Bañados for including me in their collaborations and being extremely supportive to my work. They made me feel totally part of their group, since the first time we met. I really hope to pursue our collaboration in the future.

During the last year of my Ph.D. course I was lucky enough to collaborate with Prof. Paul van der Werf and his group at Leiden Observatory. I am extremely glad to have had the opportunity to work with them, and I really want to thank Paul for his kindness and for his enlightening explanations of concepts and ideas.

I wish to acknowledge all the people that have contributed to my work over the years by providing invaluable insights and precious help: in alphabetic order, Prof. Frank Bertoldi, Prof. Marcella Brusa, Prof. Xiaohui Fan, Dr. Emanuele Paolo Farina, Dr. Jianan Li, Prof. Roberto Maiolino, Dr. Chiara Mazzucchelli, Dr. Romain A. Meyer, Dr. Mladen Novak, Prof. Dominik Riechers, Prof. Hans-Walter Rix, Prof. Michael A. Strauss, Dr. Bram Venemans, Prof. Ran Wang, Dr. Axel Weiß, Dr. Jinyi Yang, Dr. Yujin Yang.

I wish to thank all the researchers working at INAF – Astrophysics and Space Science Observatory and at the Department of Physics and Astronomy of University of Bologna together with whom I spent my research activity. They are part of an exciting environment in which I hugely grown scientifically and by which I benefited a lot.

I am also sincerely grateful to researchers with whom I collaborated in the past whose efforts are included in an important part of this thesis. Specifically, I want to greatly thank Prof. Alessandro Marconi for his inspiring guidance during my first steps in the astrophysical research and for having laid the foundation of my future career during my years at University of Florence when I was an undergraduate student. He is still a key reference point for my scientific research. I would also like to explicitly thank Dr. Stefano Carniani, Dr. Michele Perna, Dr. Giovanni Cresci for their great support, and all the researcher community at INAF – Arcetri Astrophysical Observatory in Florence where I spent part of my research activity.

I wish to thank all the Ph.D. students with whom I shared this exciting path. Profound thanks go to Dr. Carlo Cannarozzo, and Dr. Francesco Salvestrini for the amazing time we spent in Bologna together. A special thank goes to my office mates Dr. Elena Lacchin and Dr. Maria Giulia Campitiello for being always supportive and for her patience during the Ph.D. course and, particularly, during the writing of this thesis.

An immense thanks finally goes to my family, to Francesca, and to all my best friends that are always close to me in this journey and whose love gave me the strength to get here.

# Abstract

Quasars beyond redshift  $z \sim 6$  (age of the Universe  $< 1$  Gyr) are the most luminous non-transient sources in the Universe and are believed to be the progenitors of present-day early-type massive galaxies. The immense luminosities ( $L_{\text{bol}} > 10^{13} L_{\odot}$ ) from their active nuclei are powered by rapid accretion of matter (at rates  $> 10 M_{\odot} \text{yr}^{-1}$ ) onto a central supermassive black hole ( $M_{\text{BH}} > 10^8 M_{\odot}$ ) such that quasars outshine the starlight emission of their host galaxies. The fast growth of the black hole in these quasars pairs with the rapid consumption of huge gas reservoirs through vigorous episodes of star formation ( $\text{SFR} > 100 M_{\odot} \text{yr}^{-1}$ ). Such active galactic nuclei are able to regulate the star formation activity in the host by expelling gas from galaxy via large-scale outflows, thus constraining both the final stellar mass and dynamical properties of the host. This and other feedback mechanisms set a closely linked evolution between growing black holes and the assembling galaxies across the cosmic time, giving place to the black hole–galaxy scaling relations observed in the local Universe ( $z < 1$ ). The host galaxies of  $z > 6$  quasars are therefore ideal laboratories to characterize the physical properties of the interstellar medium (ISM) in extreme conditions, and they provide an insight of the interplay between star formation and black hole accretion in massive galaxies emerging from cosmic dawn. The redshift  $z \sim 6$  range is of particular interest because it coincides with the last phase transition of the Universe, from neutral state at  $z > 10$  to a mostly ionized phase at  $z < 6$ . Hence,  $z > 6$  quasars can be used as beacons to shed new light on the properties of intergalactic medium at the end of the Epoch of Reionization. Models and numerical simulations of massive black hole formation at early epochs predict that  $z > 6$  quasars reside at the extreme peak of the large-scale density structure such that they can be used to pinpoint the first galaxy overdensities.

The discovery and characterization of quasars beyond  $z \sim 6$  therefore opens a unique window to study the formation and the early evolution of black holes and galaxies. To date, thanks to increasingly deep wide-field surveys in conjunction with the refinement of the selection techniques,  $\sim 200$  quasars have been discovered at  $z > 6$ . The very presence of such supermassive black holes at these early epochs requires rapid build-up of black hole and galaxy,

thus challenging our understanding of how black holes form in the first place. The advent of powerful telescopes such as the Atacama Large Millimeter Array (ALMA), and the Northern Extended Millimeter Array (NOEMA) have marked a rapid change of gear for the study of galaxies at (sub-)mm wavelengths at the earliest cosmic times. Thanks to the great capabilities of such facilities, high-resolution observation of bright emission lines of the ISM, such as the fine-structure transition  $[\text{CII}]_{158\mu\text{m}}$  of CO rotational lines, allow us to map the cold gas kinematics in galaxies at the largest redshifts with unprecedented details. By surveying multiple ISM tracers, we can infer first quantitative constraints on the physical properties (density, temperature, excitation mechanism) of the star-forming medium and the local radiation field.

In this thesis, we capitalize on multiple approaches to study the early evolution of quasars and their host galaxies at high redshift. We infer dynamical masses for a sample of  $z > 4$  quasar host galaxies observed at high angular resolution in  $[\text{CII}]_{158\mu\text{m}}$ , and we compare them with the central black hole masses to test the onset of the black hole–host galaxy relations. We then study the impact of the luminous accreting black hole on the ISM properties of the host, by comparing the emission of various gas tracers (CO,  $[\text{CI}]$ ,  $[\text{NII}]$ , OH,  $\text{H}_2\text{O}$ ) in pairs of galaxies with and without a luminous quasar at  $z > 6$ . Finally, through a systematic study of water vapor ( $\text{H}_2\text{O}$ ) emission in bright primordial quasars, we shed light on the properties of the warm and dense phase of the ISM that is still largely unknown at these high redshifts. In this thesis we also report the discovery and characterization of new  $z > 6$  quasars to which I contributed by performing optical/NIR photometric observations using 2- and 4-m class ground-based telescopes. We discuss how our results fit within the context of the interplay between black hole activity and galaxy formation and we highlight their impact for our understanding of the early evolution of massive galaxies.

# Contents

|          |   |           |
|----------|---|-----------|
| <b>1</b> | <b>The violent Universe</b>   | <b>1</b>  |
| 1.1      | A short history of AGN  | 2         |
| 1.2      | Fundamental properties of AGN   | 5         |
| 1.3      | Census of AGN   | 16        |
| 1.4      | BH mass measurements for AGN  | 17        |
| 1.5      | The host galaxies of growing BHs  | 22        |
| 1.6      | Thesis aims & structure   | 26        |
| <b>2</b> | <b>The rise of the giants</b>   | <b>29</b> |
| 2.1      | Formation and evolution of the first supermassive black holes   | 31        |
| 2.2      | The population of high- $z$ quasars   | 36        |
| 2.3      | Contribution to the identification of new $z > 6$ quasars in the sky  | 44        |
| 2.4      | The discovery of two quasars at $z > 6$   | 44        |
| 2.5      | The discovery of the most distant radio-loud quasar at $z = 6.82$   | 49        |
| <b>3</b> | <b>The early black hole–galaxy coevolution</b>  | <b>55</b> |
| 3.1      | An overview of the galaxy population  | 56        |
| 3.2      | The luminosity and stellar mass function of galaxies  | 58        |
| 3.3      | BH–galaxy scaling relations   | 61        |
| 3.4      | BH-to-galaxy mass ratio at high redshift  | 62        |
| 3.5      | AGN feedback  | 66        |
| 3.6      | Evolutionary sequence   | 71        |
| <b>4</b> | <b>The ALMA view of the high-redshift relation between supermassive black holes and their host galaxies</b> | <b>75</b> |
| 4.1      | Introduction  | 75        |
| 4.2      | ALMA data selection and reduction   | 78        |
| 4.3      | Methods of data analysis  | 79        |
| 4.4      | Kinematical modeling  | 87        |
| 4.5      | Determination of the BH masses  | 96        |

|          |   |            |
|----------|---|------------|
| 4.6      | Summary of sample subselections   | 98         |
| 4.7      | Comparison of results and uncertainties on dynamical mass estimates   | 100        |
| 4.8      | The $M_{\text{BH}} - M_{\text{dyn}}$ relation at high redshift  | 107        |
| 4.9      | Discussion  | 110        |
| 4.10     | Conclusions   | 116        |
| <b>5</b> | <b>The interstellar medium of galaxies at high redshift</b>   | <b>119</b> |
| 5.1      | Characteristics of the ISM  | 120        |
| 5.2      | Tracers of the ISM  | 123        |
| 5.3      | The role of the CMB on high- $z$ ISM observations   | 136        |
| 5.4      | Modeling the line emission  | 137        |
| <b>6</b> | <b>Characterizing the interstellar medium in <math>z &gt; 6</math> quasar host galaxies with a multiline survey</b> | <b>141</b> |
| 6.1      | Introduction  | 141        |
| 6.2      | Observations and data reduction   | 144        |
| 6.3      | Line and continuum measurements   | 147        |
| 6.4      | CLOUDY models of photo- and X-ray dissociation regions  | 149        |
| 6.5      | Dust properties: FIR continuum  | 158        |
| 6.6      | Ionized medium  | 163        |
| 6.7      | Atomic medium   | 169        |
| 6.8      | Molecular medium  | 173        |
| 6.9      | Mass budgets  | 190        |
| 6.10     | Summary and conclusions   | 193        |
| <b>7</b> | <b>Unveiling the warm dense gas in <math>z &gt; 6</math> quasars via water vapor emission</b>                       | <b>199</b> |
| 7.1      | Introduction  | 199        |
| 7.2      | Observations and data reduction   | 201        |
| 7.3      | Overview on the $\text{H}_2\text{O}$ emission lines   | 203        |
| 7.4      | Line and continuum measurements   | 205        |
| 7.5      | Dust properties from FIR continuum  | 206        |
| 7.6      | Radiative transfer analysis   | 213        |
| 7.7      | Results and discussion  | 216        |
| 7.8      | Summary and conclusions   | 231        |
| <b>8</b> | <b>Summary &amp; Concluding remarks</b>   | <b>235</b> |

|   |            |
|---|------------|
| <b>References</b>   | <b>243</b> |
| <b>A Appendix</b>   | <b>265</b> |
| A.1 Integrated spectra: line properties and derived quantities                    | 265        |
| A.2 Mass support from random motions  | 266        |
| A.3 Comparison between dynamical masses and the spectroastrometric mass estimates | 269        |
| A.4 LBT observations and NIR spectra  | 273        |
| A.5 Maps, integrated spectra, and the results of the kinematical modelling        | 275        |



# 1

## The violent Universe

“ *There is nothing permanent except change.*

— **Heraclitus of Ephesus**

Black holes (BHs) are among the most unfathomable objects in Nature. A BH is defined as a *region in spacetime where the gravitational field is strong enough to prevent the escape of any particle or electromagnetic radiation*. As a direct consequence, an event horizon is set beyond which no information can be retrieved. The existence of such exotic objects was first predicted in 1916 by Karl Schwarzschild as a particular solution of the field equations of Albert Einstein’s theory of general relativity. It would take several years however before BHs started to be considered a bona fide class of astrophysical sources, and not just a theoretical oddity. Theory of stellar evolution predicts the creation of stellar-mass (few to several tens of solar masses) BHs as the final stage of a massive star that undergoes gravitational collapse. The existence of such BHs has been first deduced from the study of X-ray binary systems in which a BH accretes material from a companion star in its immediate vicinity (see, e.g., McClintock & Remillard, [2006](#), for a review). In 2016, the first detection of gravitational waves (GWs) by the LIGO (Laser Interferometer Gravitational-Wave Observatory) and Virgo collaboration opened a new window on the Universe. The analysis of the observed space-time perturbations unambiguously showed that such GWs were produced by a binary stellar-mass BH merger event occurred in our Galaxy (Abbott et al., [2016](#)). To date,  $\sim 20$  BH coalescence events have been detected from LIGO and Virgo thus showing that stellar-mass BHs are relatively common objects (Abbott et al., [2019](#)).

Besides stellar-mass BHs, astronomers have identified another class of BHs, this time with masses  $M_{\text{BH}} > 10^6 M_{\odot}$  that are believed to reside at the center of every galaxy. One of the first – although indirect – observational evidence of the existence of such BHs, relies on the study of the proper motion of stars in the central region of the Milky Way galaxy. By mapping the star motions since the early 1990s with increasingly high precision, two groups led by R. Genzel and A. M. Ghez inferred that the observed stars perform Keplerian orbits around an invisible object, referred to as Sagittarius A\* (Sgr A\*), with an estimated mass of  $\simeq 4.3 \times 10^6 M_{\odot}$  (Ghez et al., 1998; Gillessen et al., 2009). These measurements, in conjunction with radio/mm observations toward Sgr A\* (e.g., Doeleman et al., 2008), represent one of the most indisputable evidence of the existence of a very massive compact object in the center of our galaxy, possibly associated with a supermassive BH. Thanks to these efforts, the two group leaders were recently honored with the Nobel prize (2020), together with R. Penrose for his theoretical investigation on BHs.

In more recent years, thanks to the unparalleled technology advancements in (sub-)mm and radio observations, the Event Horizon Telescope Collaboration (2019) imaged the light “shadow” caused by the massive compact object at the center of the nearby giant elliptical galaxy Messier 87 (M87, see Fig. 1.1). This breakthrough result provided, for the very first time, a direct evidence of the existence of a supermassive BH at the center of a galaxy. These BHs are likely the relics of a past activity as active galactic nuclei (AGN), occurred during the galaxy evolution, and they are thought to be determinant in shaping the galaxies during their assembly at early epochs.

## 1.1 A short history of AGN

Active galactic nuclei were already identified in the early 1900’s in some spiral galaxies as extraordinary bright core central regions. However, a first systematic study was only reported in 1943 by Carl Seyfert. The observed spectra of these regions typically show broad emission lines associated to highly excited ions and moderately dense gas. According to the Doppler shift ( $\Delta\lambda/\lambda = v/c$ ), the line width can be produced by gas moving at speeds  $\sim 2000 - 10\,000 \text{ km s}^{-1}$ . This velocity is much higher than that of stellar orbits around the galaxy center. Furthermore, the strong excitation of the

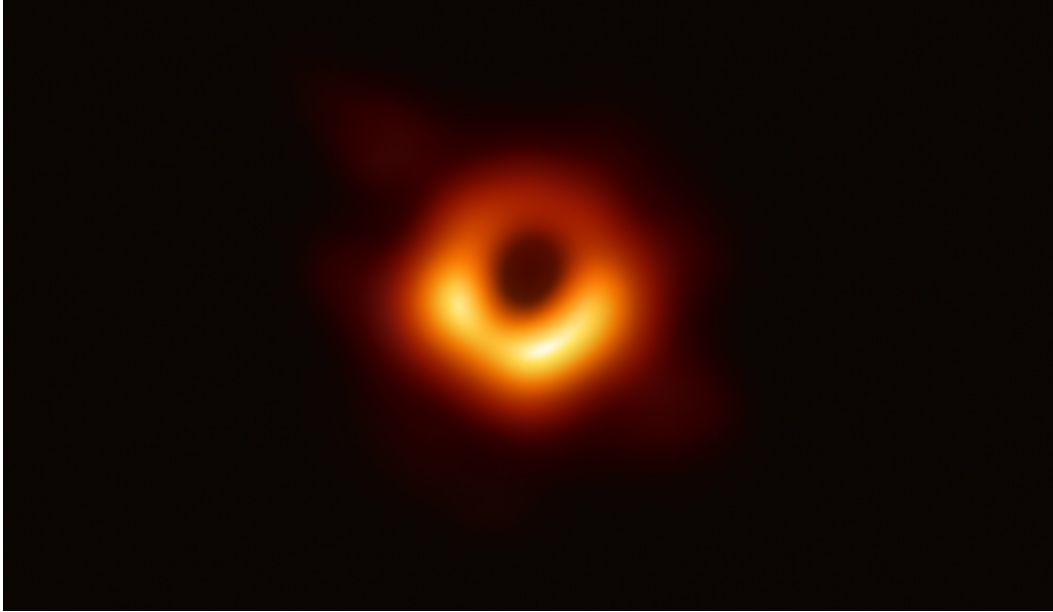


**Figure 1.1**

The light “shadow” of the supermassive black hole at the center of the galaxy M87. Surrounding the shadow is a bright ring of emitting gas swirling around and falling onto the central black hole. This image was captured in April 2017 involving eight ground-based telescopes around the globe operating together as a planet-scale telescope. Credits: Event Horizon Telescope Collaboration.

line-emitting gas can be produced only by ionizing photons that are much more energetic than those present in typical ionized regions (HII regions) surrounding the young stars. These *Seyfert* galaxies were therefore classified in Type 1 and Type 2 based on the properties of their spectrum. *Seyfert*-1 galaxies show very broad emission lines and strong core continuum emission at UV/X-ray wavelengths relative to the rest-frame of the galaxy, while *Seyfert* 2 appear less luminous showing only relatively narrow lines ( $< 1000 \text{ km s}^{-1}$ ). In 1959, Lodewijk Woltjier argued that the core of *Seyfert* galaxies appeared spatially unresolved (point-like) in optical images thus posing an upper limit on the core dimension of  $r \sim 100 \text{ pc}$ . In this case, if the line emitting gas is gravitationally bound  $GM/r \simeq v^2$ , the estimated mass budget within the central region would be of the order of

$$M(< r) \sim 2 \times 10^{10} \left( \frac{r}{100 \text{ pc}} \right) M_{\odot}, \quad (1.1)$$

assuming  $v \sim 1000 \text{ km s}^{-1}$ . This means that, unless  $r$  is much smaller than the estimated upper limit, an enormous concentration of mass and energy must

be present inside the AGN. Moreover, the rapid variability (a few days/weeks) observed in Seyfert galaxies has placed tighter constraints on the physical dimension of their luminous cores (we return on this in the next section). These arguments suggested that a supermassive compact object could be therefore associated with the central engine of Seyfert galaxies.

In the following years, as radio astronomy blossomed, strong radio emission was found associated to elliptical galaxies, thereafter named *radio galaxies*. First radio catalogs 3C (158 MHz) and 3CR (178 MHz) were compiled in the 1960s. Remarkably, many of these radio sources were observed associated with radio-bright lobe pairs located symmetrically at  $\sim 1$  Mpc away from the galaxy and extending over  $> 100$  kpc. Follow-up radio observations revealed in many cases the presence of linear jets connecting the central compact radio core with the outer lobes. Based on a systematic study at 1.4 GHz carried out by Bernard L. Fanoff and Julia M. Riley in 1974, these sources were then classified into two classes: FR-I, and FR-II, the first having luminosity of  $L_{1.4\text{GHz}} \lesssim 10^{32} \text{ erg s}^{-1} \text{ Hz}^{-1}$  with a surface brightness peaked at the core and decreasing outward, while the second class were characterized by the opposite properties,  $L_{1.4\text{GHz}} \gtrsim 10^{32} \text{ erg s}^{-1} \text{ Hz}^{-1}$ , and brighter outer radio lobes.

In those years, astronomers found optical nearby counterpart for many of the radio-detected sources. However, for a large number of these objects, the relatively low angular resolutions achieved with radio telescopes of that time, resulted in large positional uncertainty thus hindering the identification of a counterpart. An important milestone in the history of AGN was made by Thomas Matthews, Allan Sandage and Marteen Schmidt in 1963 when they showed that the optical counterparts of 3C48 and 3C273 appeared as “stellar-like” (point-like) sources exhibiting complex spectra with blue continuum and broad emission lines centered at unusual wavelengths. These “radio galaxies with no galaxy” were therefore called *quasar* (i.e., quasi-stellar radio source). In the same year, Marteen Schimdt and John Beverley Oke identified the emission lines in 3C273 as the hydrogen Balmer series redshifted at  $z = 0.158$ , thus placing this object a few billion light-years away  $D \approx zc/H_0 \sim 500 h^{-1} \text{ Mpc}^1$ , and pushing the frontiers of the Universe known until then considerably farther. Following this breakthrough result, a peculiar common characteristic of quasars emerged. Their strong blue color index

<sup>1</sup>Here we expressed the Hubble constant as  $H_0 = h 100 \text{ km s}^{-1} \text{ Mpc}^{-1}$

$U - B = m_U - m_B < -0.3$ , where  $m_U$  and  $m_B$  are the apparent magnitude in ultraviolet (UV), and optical “blue” band, respectively, pushed astronomers to search for relative strong emitters at UV wavelengths appearing stellar. The results of such surveys revealed a huge amount of so-called “radio-quiet” (RQ) quasi-stellar objects (or QSOs), exceeding the number of quasars by at least a factor of  $\sim 10$ . Nowadays, the different nomenclatures of “quasars” and “QSOs” are deprecated since the two families are not sharply separated. RQ quasars show radio emission if observed at sufficient high sensitivity and both RQ and radio-loud (RL) quasars (or QSO) are now regarded as more powerful versions of Seyfert nuclei. In this thesis we therefore employ the term QSO and quasar indifferently.

In the '90s, the advent of Hubble Space Telescope (HST) marked a huge change of gear for our understating of the nature of quasars. Thanks to its unmatched capabilities, the host galaxies of quasars were identified and spatially resolved in optical/UV wavelengths revealing their underlying starlight emission. Such observations revealed that quasar host galaxies appeared to be fairly normal galaxies with an immense nuclear activity able to easily outshine the emission of any galaxy (see **Fig. 1.2**). As a result, quasars have started to be considered as a fundamental part in the evolution of galaxies rather than a rare extreme phenomenon.

## 1.2 Fundamental properties of AGN

### 1.2.1 An accreting supermassive black hole

As we have seen in the previous section, the observed properties of AGN imply an enormous amount of energy confined in a relatively compact region. This is also required to explain the observed linewidth of the broad emission lines. However, additional lines of evidence point to the presence of a supermassive BH as a driver of AGN activity. Radio emission in radio galaxies have been observed to be extended over  $\gtrsim 1$  Mpc. Therefore, assuming that the emitting material is relativistically expanding, a minimum lifetime for the nuclear activity can be derived of  $\tau \gtrsim 10^7$  Mpc. Furthermore, assuming a constant quasar bolometric luminosity of  $L_{\text{bol}} \sim 10^{14} - 10^{15} L_{\odot}$  through its life, the total emitted energy must be  $E \gtrsim 3 \times 10^{61}$  erg. Moreover, AGN are

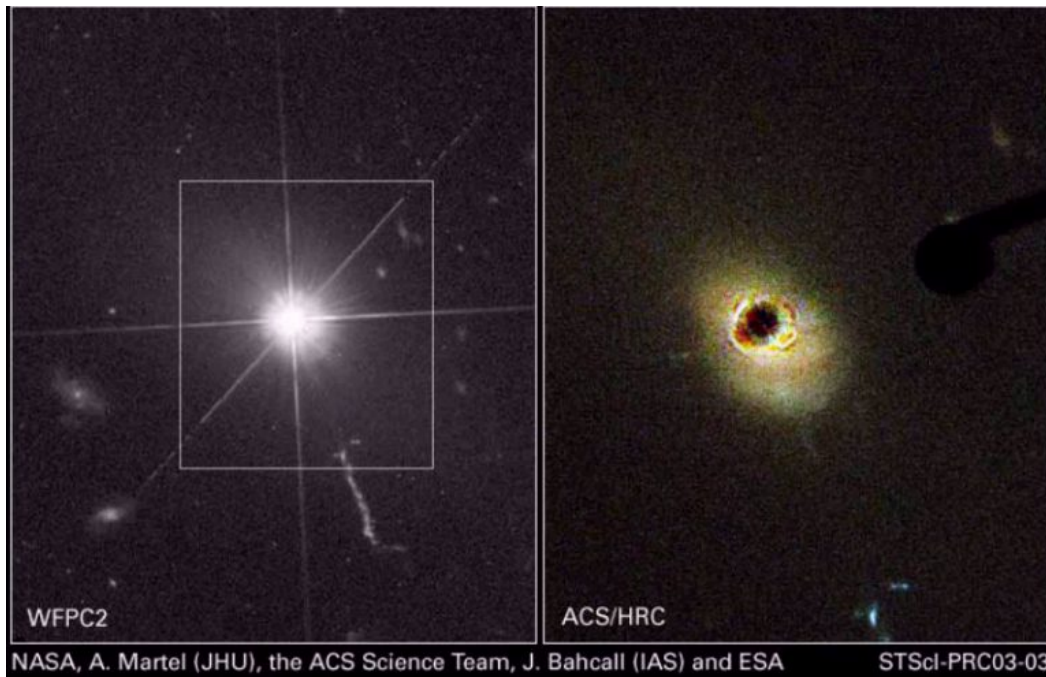


**Figure 1.2**

HST images of the first identified quasar 3C273. *Left panel:* snapshot of the quasar with the Wide Field and Planetary Camera (WFPC2) in optical bands. The white square indicates the sky region reported in the right image. Credits: NASA and J. Bahcall (IAS). *Right panel:* the emission of the host galaxy revealed by using the coronagraph on the Advance Camera for Surveys (ACS) to block the light from the central quasar. Jet clumps blasted by the quasar are visible in both images on the bottom right part. Credits: NASA, M. Clampin (STScI), H. Ford (JHU), G. Illingworth (UCO/Lick Observatory), J. Krist (STScI), D. Ardila (JHU), D. Golimowski (JHU), the ACS Science Team, J. Bahcall (IAS) and ESA.

observed to vary their luminosity by more than 50% over time-scales of days or weeks. This is possible only if (at least) a large part of the emitting region is causally connected. This yields to an upper limit on the physical dimension of  $r \lesssim 3 \times 10^{15}$  cm. Hypothetically, if the energy output is caused by the hydrogen-burning thermonuclear reaction of stars inside the AGN, the mass required to produce such energy would be  $M = E/\epsilon c^2 \sim 2 \times 10^9 M_{\odot}$ , with the characteristic mass-energy conversion efficiency of  $\epsilon \sim 0.8\%$ . However, the Schwarzschild radius<sup>2</sup> associated to this mass is  $R_s = 2GM/c^2 \sim 6 \times 10^{14}$  cm, that is comparable with the estimated extension of the AGN. This simple estimate suggests that the gravitational force must play a key role within

<sup>2</sup>The Schwarzschild radius is defined as the last stable orbit for a spherical non-rotating black hole as  $R_s = 2GM_{\text{BH}}/c^2$ .

the AGN. As a consequence, any (putative) star cluster inside such compact region would be highly unstable. In contrast, the accretion of matter onto a massive compact object can ease the match between theory and observations. Indeed, BH accretion is the only known process having a high mass-energy conversion efficiency, especially in the case of accretion onto rotating BH (i.e., Kerr BH), where the efficiency attains its maximum value ( $\epsilon \sim 29\%$ ; see, Kerr 1963; Bardeen 1970).

Now, the collected experimental evidence alongside with the comprehensive theoretical frameworks has led to a general consensus on the nature of AGN. A supermassive BH is believed to reside at the center of every galaxy and it is thought to be responsible for the nuclear luminosity in active galaxies through accretion of matter. In this scenario, gas orbiting around the BH settles into an accretion disk. The viscosity among gas particles reduces their angular momentum and converts their kinetic energy into thermal energy that is then radiated away. This causes gas to drift inward converting its potential energy into kinetic energy. As a result, the gas moves on a smaller orbit. Finally, this mechanism allows the gas to settle within the last stable orbit and to ultimately accrete onto the BH. The physics of accretion allows the disk to emit as a superposition of blackbodies with a radial temperature gradient peaking in the far-UV (FUV) range and extending from optical to the X-ray wavelengths (see, e.g., Shakura & Sunyaev, 1973; Soltan, 1982; Rees, 1984). An observational evidence of a dusty disk feeding BH were reported by Ferrarese et al. (1996) and Jaffe et al. (1996) toward the core region of the elliptical galaxy NGC 4161 (see Fig. 1.3).

## 1.2.2 A unified view of AGN types

In the mid 1980s, Antonucci & Miller (1985) reported for the first time the discovery of broad emission lines in the polarized spectrum of an archetypal Seyfert 2 galaxy, NGC 1068, which properties revealed a very close similarity with those expected in Seyfert 1 galaxies. In their seminal paper, Antonucci & Miller (1985) proposed that the gas clouds in the broad line region (BLR), where broad ( $> 2000 \text{ km s}^{-1}$ ) emission lines arise, are located in a thick disk, which is hidden from our line of sight. Material distributed over a larger scale therefore reflects broad line photons toward the observer and imprints a polarized pattern. This intuition opened the so-called “Unification Era”.

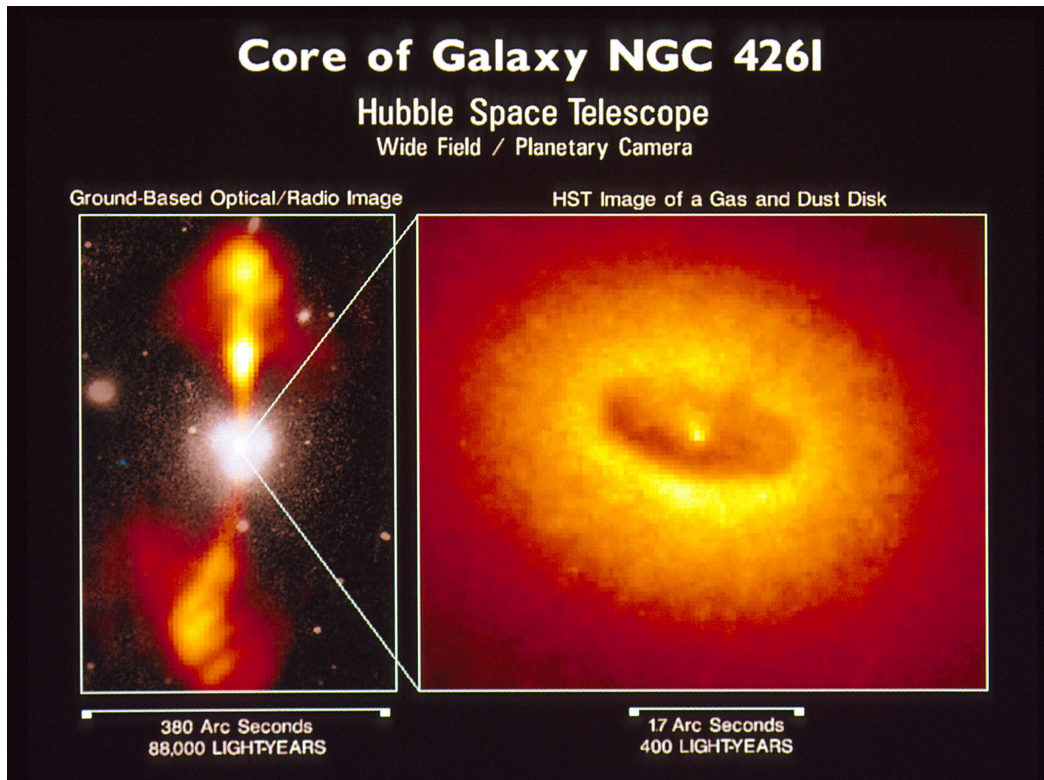


**Figure 1.3**

Images of the elliptical galaxy NGC 4261. *Left panel:* Composite optical/radio view of the galaxy. White colors map the visible light emission, showing a fuzzy disk of stars, while the orange color shows the radio emission from jets blasted by the nucleus. *Right panel:* HST image of the core central region. A dark, dusty spiral-shaped disk represents the outer region of a disk likely feeding a central supermassive black hole. Credits: National Radio Astronomy Observatory, California Institute of Technology; Walter Jaffe/Leiden Observatory, Holland Ford/JHU/STScI, and NASA.

In this scenario, Type-2 and Type-1 AGN are intrinsically the same objects that are observed from different orientation angles relative to the absorbing material (e.g., Antonucci 1993; Urry & Padovani 1995, see also Netzer 2015 for a review). The geometry of the absorbing structure has been inferred from indirect arguments based on the fraction of Type-1 and Type-2 AGN in the local Universe. Such analysis suggests a “toroidal” axisymmetric geometry of the absorber surrounding the BLR and the BH accretion disk. However, many years of observations and multiwavelength monitoring of AGN have shown that this “old” unification scheme is unable to naturally explain the observed differences between AGN subgroups (e.g., the lack of BLR in some systems), the transition from one type to another, or the

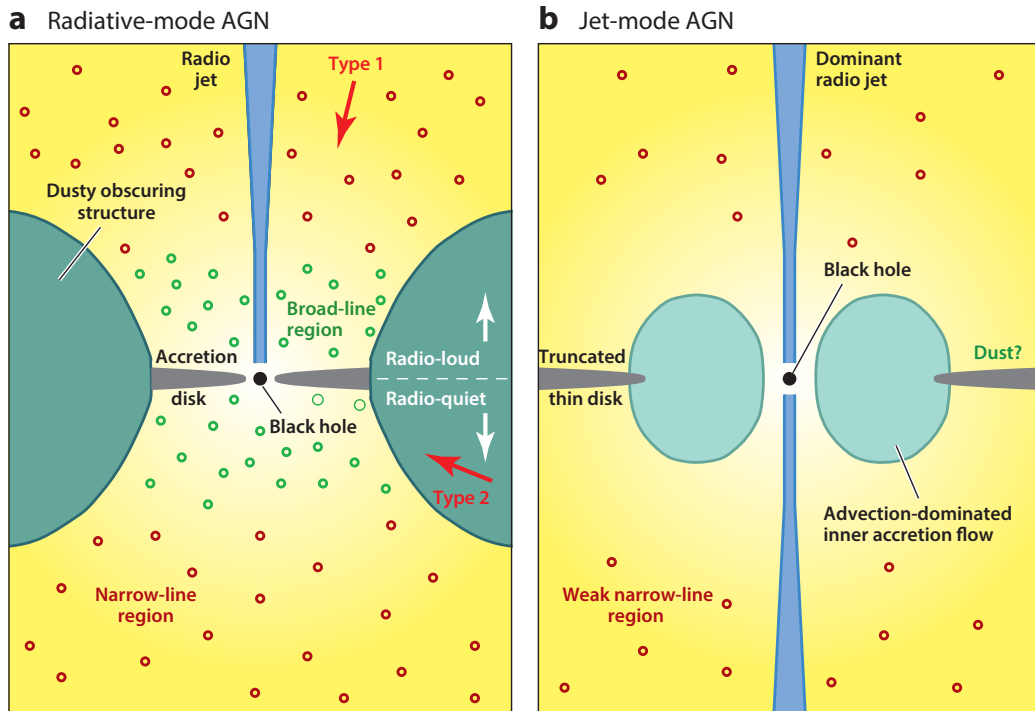


**Figure 1.4**

Schematic illustration of the central region of a “radiative-mode” (a) and “jet-mode” AGN (b) (not to scale). *Left panel:* a geometrically thin accretion disk feeds the central supermassive BH, the ionized radiation excites the dense gas clouds in the closer BLR. The central engine is surrounded by an obscuring toroidal-shaped structure which hides the inner region in the case of Type 2 AGN (red arrow on the right). Over a larger scale, the less dense quiescent gas of NLR is impinged by the radiation escaping along polar directions. In some cases (radio-loud) two radio jets can be launched by the AGN. *Right panel:* an advection-dominated geometrically thick accretion flow is the mechanism of BH accretion, eventually accompanied by an outer truncated thin disk. The majority of energy is realised via powerful radio jets launched by the AGN. Radiative emission from accretion, although less powerful, produces a low-ionization narrow-line region over larger scale. Figure from Heckman & Best (2014).

complex observed phenomenology of the torus obscuration (e.g., Bianchi et al., 2012; Netzer, 2015; Spinoglio & Fernández-Ontiveros, 2021). Variations and expansions on the model focus on the properties of the torus (the clumpiness, or the connection with the accretion disk and the BLR), the physics and modes of accretion (e.g., slim disk, advection-dominated flows), the presence of jets and the impact of magnetic fields, and the repercussions on the host galaxies (e.g., “radiative-” and “jet-mode”; see Fig. 1.4). In particular, the “jet-mode” of AGN is characterized by a distinct mode of BH

accretion in which the gravitational energy lost by the infalling particles is not efficiently radiated away (i.e., the inflow time scale is much shorter than the radiative cooling time). This process is referred to as “Advection-Dominated” or “Radiatively Inefficient Accretion Flows” (ADAFs/RIAFs). Current models predict the presence of a geometrically thick structure in the inner region of AGN, possibly accompanied with a truncated disk. The jet-mode AGN is characterized by powerful radio jets that are launched by the central AGN, and travelling at relativistic speed. The interaction of jets with the circumgalactic (CGM) or intergalactic medium (IGM) generates the radio lobes observed in FR galaxies. The FR classification fits in this framework depending on the radio luminosity of galaxy which determines the survival or disruption of the jets. A coherent picture of AGN *zoo* is presented in the review by Heckman & Best (2014). Recently, Padovani (2016, 2017) argued that the two classes of RQ and RL AGN are misleading and obsolete since the major difference between the two categories is the presence or not of strong relativistic jets. The energy output of “jetted” AGN is primarily radiated in form of non-thermal emission, while thermal energy dominates the emission of “non-jetted” AGN, thus suggesting that they could be intrinsically different objects.

### 1.2.3 The multiwavelength emission

Observationally, AGN are recognized by the properties of their spectrum. The latter significantly differs from that of a “normal” galaxy. Beside their huge luminosity (up to  $L_{\text{bol}} \approx 10^{15} L_{\odot}$ ), AGN are detectable over the whole electromagnetic spectrum. In **Fig. 1.5** we report a schematic representation of AGN spectral energy distribution (SED). The relative contribution of the different components that are thought to make up the overall SED, can however vary dramatically for different types of AGN. In the AGN model framework discussed above, the supermassive BH is surrounded by an accretion disk. Models of geometrically-thin, optically-thick accretion disk (e.g., Shakura & Sunyaev, 1973), predict a temperature in the disk that increases inwards proportionally to the disk radius as  $T(r) \propto r^{-3/4}$ . The resulting spectrum has a broad energy distribution due to the superposition of different blackbodies consisting of rings at different radii and temperatures. This component peaks in the UV ( $\approx 10 - 400$  nm). Unfortunately, in the UV range at (observed-frame) wavelengths  $\lambda \leq 912 \text{ \AA}$ , the observation of AGN spectrum from the

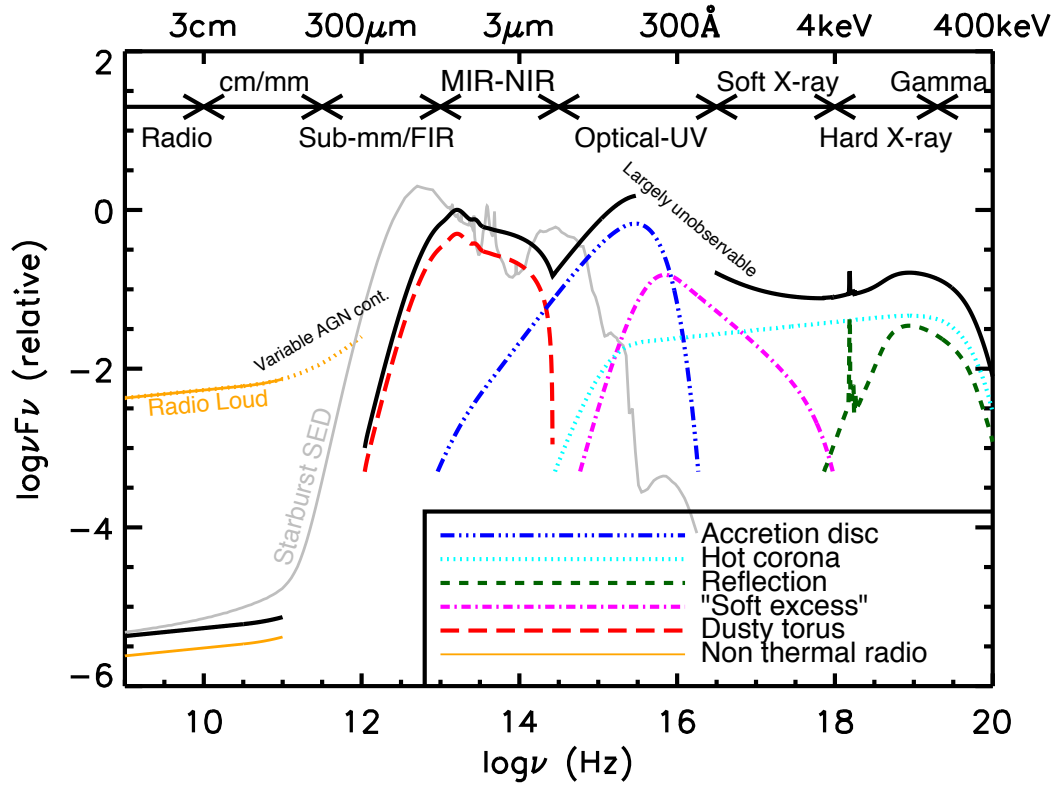


**Figure 1.5**

Schematic representation of an AGN SED (based on, e.g., Elvis et al., 1994; Richards et al., 2006). Individual components are reported by colored lines (see the main text), while the total SED is the black curve in arbitrary units. Radio-loud AGN have radio emission that can be several order of magnitudes brighter than radio-quiet AGN. The gray curve is the SED of the local starburst galaxy M82 (from Silva et al., 1998). The AGN SED over the (sub-)mm band is highly uncertain and likely represents a minor contribution to the galaxy SED, except for highly luminosity quasars and/or powerful radio-loud AGN. Figure from Harrison (2014).

Earth is very difficult due to the photoelectric absorption by the neutral hydrogen in our Galaxy. Only at considerable higher frequencies, in the soft X-ray band (at photon energies  $\gtrsim 0.2\text{keV}$ ), the extragalactic sky becomes observable again.

The BH accretion disk is thought to be surrounded by a “corona” made of hot plasma, generally depicted as an atmosphere above the inner accretion disk. This corona is responsible for the continuum emission observed in the X-rays via inverse Compton scattering of the photons emitted by the disk. The resulting observed flux density is therefore a power-law in the form  $S_\nu \propto \nu^{-\alpha}$ , with  $\alpha \sim 0.7 - 1.2$ , together with a “excess” in the soft X-rays,

whose origin is still debated (see, e.g., Crummy et al., 2006; Sobolewska & Done, 2007; Boissay et al., 2016). The photons emitted by the corona can return on the accretion disk and/or reprocessed by the intervening torus or distant material in BLR, producing a “reflection” component. The latter is composed by a Compton “hump” peaking at  $\sim 30$  keV and fluorescence lines, the most important of which is the Fe  $K\alpha$  line at 6.4 keV. In some cases, the X-ray emission can be significantly absorbed by the obscuring torus (the so-called Compton-thick case), whose inferred column density along the line of sight can reach  $N_{\text{H}} \sim 10^{23} - 10^{25} \text{ cm}^{-2}$ . Also, the interstellar medium (ISM) of the host galaxy can significantly contribute to AGN obscuration up to the soft X-rays, particularly when the host galaxy’s disk is projected along the line of sight with high inclination angle (see, e.g., Gelbord, 2003; Lagos et al., 2011).

The UV/optical radiation from BH accretion disk is partially absorbed and re-emitted by the dust dominating the IR AGN SED from  $1 \mu\text{m}$  to a few  $10 \mu\text{m}$  (e.g., Rowan-Robinson, 1995; Polletta et al., 2000). The exact form of the IR spectrum varies from different sources peaking at  $\lambda \approx 20 - 50 \mu\text{m}$ , and steeply falls at longer wavelengths (e.g., Schartmann et al., 2008; Mullaney et al., 2011). At sub-mm/FIR wavelengths, the AGN SED is dominated by the emission of cooler dust heated by the star formation in the host galaxy (see review by Lutz, 2014). However, AGN can significantly contribute to the dust heating in the most luminous quasars at  $\lesssim 70 \mu\text{m}$  (but see also, Symeonidis et al., 2016; Symeonidis, 2017). In addition the non-thermal emission from radio-luminous AGN could also affect the observed SED in this range (e.g., Tadhunter et al., 2007; Dicken et al., 2009, 2010; Hill & Shanks, 2011).

Finally, in the “jet-mode” AGN, a large fraction of energy is also released in the radio band with two-sided jets emitting non-thermal synchrotron radiation due to relativistic charged particles gyrating around magnetic fields. The resulting spectrum is the superposition of multiple synchrotron spectra produced by particles at different energies, and it is usually parametrized as a power-law whose spectral index is used to classify radio galaxies in flat- ( $\alpha < 0.5$ ) and steep-spectrum sources ( $\alpha \geq 0.5$ ).

## 1.2.4 AGN UV/optical emission-line regions

The UV and optical spectra of AGN feature strong emission lines. These are lines of the hydrogen Balmer series, the Ly- $\alpha$  transition, and metal lines of ions like MgII, CIII], CIV, NIV]. These lines are thought to arise from dense gas clouds (electron density  $n_e \gtrsim 10^8 \text{ cm}^{-3}$ ; Osterbrock & Ferland 2006) excited by UV photons produced by the BH accretion disk. These clouds move at high velocity under the gravitational influence of the BH producing extremely Doppler-broadened emission lines (full-width-at-half-maximum, FWHM  $\approx 1000 - 10\,000 \text{ km s}^{-1}$ ). The estimated size of BLR ranges from light-days to light-months (e.g., Peterson et al., 2004).

At circumnuclear scales, gas can be photoionized by radiation escaping along polar directions. This region is populated by more quiescent gas likely responsible for narrow (i.e., FWHM  $\lesssim 2000 \text{ km s}^{-1}$ ) UV-/optical-/IR-permitted and forbidden emission lines (e.g., [OII], [OIII]). This region is therefore dubbed as “narrow-line region” (NLR). The existence of forbidden lines implies that the gas (electron) density in the NLR is lower than the line critical densities<sup>3</sup>, that is  $n_e < 10^6 \text{ cm}^{-3}$  (Osterbrock & Ferland, 2006). The size of NLR is estimated to be few 100 – 1000 pc based on maps of the gas photoionization conditions (e.g., Bennert et al., 2002; Veilleux et al., 2003) which is consistent with the narrow width and modest variability of the emission lines.

## 1.2.5 Quasar absorption lines

The rest-frame optical/UV quasar spectra may contain a plethora of absorption lines. These features can have an intrinsic origin, either due to absorption material within the AGN or its host galaxy, or may be caused by intervening gas located between the source and the observer along the line of sight. In the latter case, one can expect that the absorption lines are due to metal-poor gas mainly composed by hydrogen and helium. However, absorptions from metals such as those of MgII ( $\lambda = 2795 \text{ \AA}$ ,  $2802 \text{ \AA}$ ), and CIV ( $\lambda = 1548 \text{ \AA}$ ,  $1551 \text{ \AA}$ ) are also observed typically in association with the disk or the halo around some intervening galaxy. Thanks to their immense

---

<sup>3</sup>The density at which the rate of collisional depopulation of a quantum level equals the spontaneous radiative decay rate. Above the critical density, collisional de-excitation quenches the emission of forbidden lines, relative to the permitted ones.

luminosity, quasars can therefore be used as beacons to shed light on the properties of the foreground medium.

The absorption associated with the Ly- $\alpha$  transition of neutral hydrogen (rest-frame wavelength 1216 Å) is particularly important as it allows astronomers to gauge the ionization state of the IGM across the cosmic epochs. The emission from a quasar suffers from strong absorption by the damping wings of the resonance Ly- $\alpha$  absorption of the intervening neutral IGM (Miralda-Escudé 1998; see also, Wolfe et al. 2005 for a review). As a result, Ly- $\alpha$  photons are absorbed and reemitted multiple times in the IGM, resulting in an extended, low surface brightness line, which is difficult to observe (Loeb & Rybicki, 1999). Patches of neutral gas in the sightline of bright quasars imprint absorption lines blueward to the Ly- $\alpha$  emission of quasar. This effect is exacerbated in the spectra of very high redshift quasars due to the large neutral hydrogen column density (Gunn & Peterson, 1965). In addition, photons with wavelengths shorter than  $\lambda \lesssim 921$  Å (i.e., the Lyman limit) are able to photoionize the neutral hydrogen. The combination of such effects gives rise to an almost complete suppression of the quasar spectrum blueward to the quasar Ly- $\alpha$  emission line (see Fig. 1.6). This characteristic is crucial to select high- $z$  quasars from wide-field multiwavelength surveys (see Sect. 2.2.1).

The observed Ly- $\alpha$  profile in the spectra of quasars allows us to estimate the quasar lifetime ( $t_Q$ ). The continuum radiation from the BH accretion disk ionizes the surrounding IGM. In this situation Ly- $\alpha$  photons can escape absorption, provided they redshift out of resonance before they reach the boundary of the ionized medium. This translates in wavelength range of enhanced transmission immediately blueward of the Ly- $\alpha$  line before the onset of Gunn-Peterson absorption. This is called *quasar proximity zone* (or *near zone*; Cen & Haiman, 2000; Madau & Rees, 2000; Haiman & Cen, 2001; Wyithe et al., 2005; Bolton & Haehnelt, 2007a,b; Lidz et al., 2007; Bolton et al., 2011; Keating et al., 2015; Eilers et al., 2017, 2018b). The hydrogen recombination time in the IGM is longer than the Hubble time at  $z \lesssim 10$ . This means that the equilibrium is never reached and the size of the ionized region by the quasar radiation depends on the quasar lifetime. Under very simplistic assumptions – similarly to the definition of the Strömgen sphere around



## 1.3 Census of AGN

Since the discovery of the first quasar almost 60 years ago (Schmidt, 1963), astronomers have developed different techniques to efficiently identify AGN across all environments and redshifts. In the nearby Universe, large-scale spectroscopic surveys in the optical band, particularly 2dFGRS (Two-degree-Field Galaxy Redshift Survey; Colless et al. 2001), and SDSS (Sloan Digital Sky Survey; York et al. 2000; Strauss et al. 2002), have enabled the most extensive studies of AGN by providing high-quality spectra for millions of galaxies (see, Ho 2008, for a review, and references therein). Thanks to this huge amount of data, (radiative-mode) Type-1 AGN have been identified through the unambiguous presence of the broad emission lines and the strong non-stellar blue continuum. On the other hand, optical spectroscopy has also allowed us to inventory Type-2 and jet-mode AGN through the identification of narrow emission lines. In this case, since also young stars in star-forming galaxies produce such narrow emission lines, AGN can be identified through the study of the relative intensities of the strong-forbidden and permitted lines via the BPT diagnostic diagrams (Baldwin et al., 1981a,b; Veilleux & Osterbrock, 1987).

Sensitive mid-IR ( $\sim 3$ - to  $30$ - $\mu\text{m}$ ) observations with *Infrared Astronomical Satellite* (IRAS) and *Spitzer Space Telescope*, have extended our understanding and census of nearby AGN activity by targeting the strong warm dust emission due to the AGN's obscuring structure (see, e.g., Miley et al., 1985; Spinoglio & Malkan, 1989), and allowed IR-color selection techniques to sample the local AGN population (e.g. Richards et al., 2006; Donley et al., 2008). The situation has been then revolutionized with the NASA's mission *Wide-Field Infrared Survey Explorer* (WISE; Wright et al. 2010) which detected tens of thousands AGN including many of the optically-selected AGN by the SDSS survey (e.g., Donoso et al., 2012; Shao et al., 2013).

However, one the most unambiguous techniques to identify AGN is via X-ray observations which can select AGN even in the presence of heavy dust obscuration. In this case, one of the advantages is that X-ray emission from stars is typically weak thus minimizing the contamination from the host galaxy. The *Rosat* all-sky survey (Voges et al., 1999) in the soft-X band, in the years 2000s, the *Chandra* and *XMM-Newton* surveys in multiwavelength extragalactic fields (Brandt & Alexander, 2015) have significantly contributed to achieve a complete census of AGN activity. However, Compton-thick AGN

could remain undetected in these surveys and are recovered at least in the local Universe with surveys at  $E > 10$  keV (e.g., *Swift/Burst Alert Telescope* (BAT) survey; Baumgartner et al. 2013).

Finally, radio continuum surveys are particularly effective in detecting (especially the jet-mode) AGN. The National Radio Astronomy Observatory (NRAO) Karl G. Jansky Very Large Telescope (VLA) Sky Survey (NVSS; Condon et al. 1998), the Faint Images of the Radio Sky at Twenty centimeters (FIRST; Becker et al. 1995), the Westerbork Northern Sky Survey (WENSS; Rengelink et al. 1997), and the Sydney University Molonglo Sky Survey (SUMSS; Bock et al. 1999) have covered large sky area with sufficient high sensitivity to unveil the majority of radio-AGN in the local Universe.

The increasingly large multiwavelength surveys over the past decades have systematically identified a large number of quasars at different redshifts thus allowing us to map out their volume density across the cosmic time (above a certain flux threshold; Fig. 1.7, see, e.g., Boyle et al. 2000; Richards et al. 2006). These studies have revealed that quasar activity significantly evolves with redshift, rising from early times, peaking at  $z \approx 2$  (“The quasar epoch”), and steadily declines afterwards until the present day. Since quasars are powered by accretion of matter onto the supermassive BH, the aforementioned result is expected to be related to the BH triggering mechanism. Indeed, AGN are often found in the vicinity of other galaxies, with clear signatures of interactions, or undergoing galaxy merging (see, e.g., Koss et al., 2010; Comerford et al., 2009). If interactions with neighboring galaxies are determinant to allow the galaxy gas to flow toward the center and feeds the BH, the observed evolution of quasar density with time is easily interpreted: at earlier times, galaxies have experienced many more interactions than today. More recently, the availability of sensitive, wide-field optical/near-IR surveys, allowed us to identify an increasingly population of  $z > 6$  quasars. The mere existence of these massive BHs at such early epochs, suggests that BH must have formed very early on.

## 1.4 BH mass measurements for AGN

The BH mass measurements in the Milky Way briefly discussed in the introduction of this chapter are based on direct observations of star kinematics

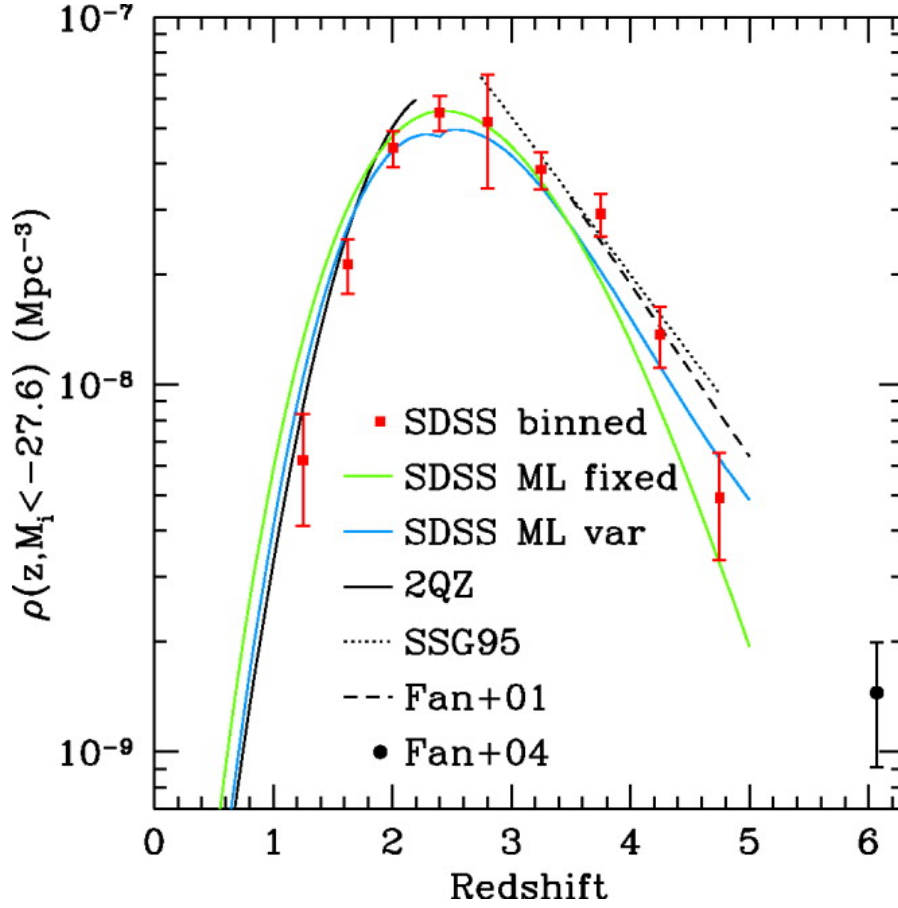


**Figure 1.7**

Number of quasars per unit of comoving volume obtained by integrating luminosity function in the  $i$ -band with a limiting absolute magnitude  $M_i(z = 2) < -27.2$ . The black solid line is from 2QZ (Boyle et al., 2000). The red squares are the binned data from the SDSS survey (Data Released 3). The green and blue lines are model from different parametrization. The dotted and dashed lines are from Schmidt et al. (1995, SSG+95), and Fan et al. (2001b, Fan+01), respectively. The  $z \sim 6$  point is from Fan et al. (2004, Fan+04). Figure from Richards et al. (2006).

orbiting around the BH. This was possible thanks to high-resolution observations that spatially resolved the region in the proximity of the singularity, where the BH dominates the gravitational potential field. This region is defined as the BH *sphere of influence*. The radius of this sphere is defined by comparing the characteristic velocity dispersion of stars (or gas,  $\sigma$ ) in galactic bulge, with the Keplerian rotational velocity around the BH,  $\sqrt{GM_{\text{BH}}/r}$ :

$$r_{\text{inf}} = \frac{GM_{\text{BH}}}{\sigma^2} \sim 0.4 \left( \frac{M_{\text{BH}}}{10^6 M_{\odot}} \right) \left( \frac{\sigma}{100 \text{ km s}^{-1}} \right)^{-2} \text{ pc.} \quad (1.3)$$

For a galaxy at distance  $D$ , this corresponds to an angular scale projected onto the sky plane of

$$\theta_{\text{inf}} = \frac{r_{\text{inf}}}{D} \sim 0''.1 \left( \frac{M_{\text{BH}}}{10^6 M_{\odot}} \right) \left( \frac{\sigma}{100 \text{ km s}^{-1}} \right)^{-2} \left( \frac{D}{1 \text{ Mpc}} \right)^{-1}. \quad (1.4)$$

The Eq. (1.4) implies that the direct detection of BH signatures through the tracking of the star and gas motion in galaxies, heavily depends on the achieved angular resolution. Indeed, despite HST has enabled tremendous progresses in this sense, such direct method remains still limited to relatively nearby galaxies (see, e.g., Ferrarese & Ford, 2005; Kormendy & Ho, 2013, and references therein). Most AGN are so distant that any attempt to resolve  $r_{\text{inf}}$  is impossible with the current facilities. Even worse, their immense luminosity outshines the starlight features in the host galaxy spectra. On the other hand, the kinematics of the circumnuclear ionized gas might be used to trace the potential well in the center of AGN, but non gravitational or non circular motions might bias or completely invalidates the result (see, e.g. Marconi et al., 2008).

In order to overcome such limitations, two different methods have been developed to estimate the BH mass in (distant) AGN host galaxies.

### 1.4.1 Reverberation Mapping

The reverberation mapping (RM) method traces back to Bahcall et al. (1972), Lyutyi & Cherepashchuk (1972), and Cherepashchuk & Lyutyi (1973), which reported the observed lag between broad emission lines and continuum variation in several local Seyfert galaxies. Since broad emission lines in AGN are excited by the UV photons emitted by the inner BH accretion disk, the observed lag reflects the light travel time from the ionizing source to the BLR,  $\tau = R/c$ . The original name was coined by Blandford & McKee (1982) who argued that by tracing the “reverberation” of broad emission lines in response to a continuum variation, one can in principle reconstruct the structure and kinematics of the BLR. Therefore, by “temporally” resolving the emission from the BH sphere of influence, the RM technique overcomes the angular resolution limitations and has become a powerful tool to investigate the BLR (see e.g. Netzer & Peterson, 1997; Pancoast et al., 2014). By capitalizing on this method, it is possible to estimate the BLR size and the BH mass by

assuming that the broad-line-emitting clouds are virialized within the BH sphere of influence (Ho, 1999; Wandel et al., 1999):

$$M_{\text{BH}} = f \frac{W^2 R}{G}, \quad (1.5)$$

where  $W$  is an indicator of the virial velocity. The latter can be estimated from the width of the broad emission lines, assuming a Doppler broadening due to the virial motion of the emitting clouds. The factor  $f$  in Eq. (1.5) encloses the unknown parameters related to the BLR structure and the viewing angle affecting the observed line profiles. This factor is either determined under a number of simplified assumptions and approximations (Netzer, 1990), or it is empirically determined from the comparison of BH mass estimates obtained with other methods (e.g., Onken et al., 2004). The systematic uncertainty related to this method ranges  $\sim 0.4 - 0.5$  dex (see, Shen 2013, for further discussion).

The application of RM led to the remarkable finding of a tight correlation between the BLR size (obtained from RM) and the optical continuum luminosity ( $L$ ), conventionally measured at  $5100 \text{ \AA}$ , ( $R \propto L^\alpha$ ; Kaspi et al., 2000, 2005; Bentz et al., 2006). A reference result by Bentz et al. (2009) is based on  $\text{H}\beta$  line RM measurements and reports  $\alpha \approx 0.5$  after correcting for the host galaxy starlight contamination:

$$\log\left(\frac{R}{\text{light days}}\right) = -21.3 + 0.519 \log\left(\frac{\lambda L_\lambda(5100 \text{ \AA})}{\text{erg s}^{-1}}\right). \quad (1.6)$$

This relation extends over  $\sim 4$  orders of magnitude in luminosity with an intrinsic scatter of  $\sim 0.15$  dex.

One of the main limitation of RM method is that it is very expensive in terms of observing time and it is almost impracticable for high redshift quasars due to the cosmological time dilation and the intrinsic low variability of these sources.

## 1.4.2 Single-Epoch spectroscopy

From the Eq. (1.5), and (1.6), the combination of continuum luminosity and emission-line width provides us with a much less expensive method to estimate  $M_{\text{BH}}$  via the Single-Epoch (SE) virial BH mass estimate. This tech-

nique was first pioneered by Dibai (1977, 1987), and is therefore sometimes referred to as “Dibai method” (Bochkarev & Gaskell, 2009; Gaskell, 2009). The SE estimator takes the following form:

$$\log\left(\frac{M_{\text{BH}}}{M_{\odot}}\right) = a + b \log\left(\frac{L}{10^{44} \text{ erg s}^{-1}}\right) + c \log\left(\frac{W}{\text{km s}^{-1}}\right), \quad (1.7)$$

where  $L$  and  $W$  are the quasar continuum (or line; see, Greene & Ho 2005) luminosity, and the width of a specific line, respectively. The coefficients  $a$ ,  $b$ , and  $c$  are determined by a calibration of the relation. Typical assumption is  $c = 2$  as expected from the virial theorem (see Eq. 1.5). To date, thanks to the efforts of various groups (e.g., McLure & Jarvis, 2002; McLure & Dunlop, 2004; Vestergaard & Peterson, 2006; McGill et al., 2008; Wang et al., 2009; Shen et al., 2011; Denney, 2012; Park et al., 2013; Coatman et al., 2017), many virial relations have been calibrated by employing different broad lines. However, all calibrations are based on the implicit assumption that the BH mass estimated via SE method must agree with that obtained from the RM technique, which in turn, is calibrated against the local BH-galaxy scaling relations for normal galaxies (Onken et al., 2004). The most widely used SE estimator is based on  $\text{H}\beta$  line, but different alternatives have been developed. In particular, for high-redshift quasars, the atomic transitions of MgII 2800 Å and CIV 1549 Å are widely employed in conjunction with the continuum luminosities conventionally measured respectively at 3000 Å for MgII, and 1550 Å in the case of CIV line. Indeed, such lines are the most common and brightest BLR lines that are observed in the optical (rest-frame UV) spectra of quasars. The MgII line is considered an unbiased and reliable surrogate for the Balmer lines as the line is not self-absorbed and has a similar ionization energy to the hydrogen. On the other hand, the reliability of CIV line is still strongly debated. Firstly, the CIV virial relation is based on very few measurements (Kaspi et al., 2007; Saturni et al., 2016; Park et al., 2017); secondly the CIV line is often detected with broad and blueshifted wings likely associated with outflowing gas (e.g., Richards et al., 2011; Denney, 2012). These effects may bias the BH mass measurements.

The SE method is more indirect than RM, for this reason the resulting intrinsic uncertainty on  $M_{\text{BH}}$  is not smaller compared to BH masses estimated via the RM technique ( $\sim 0.4 - 0.5$  dex; e.g., Vestergaard & Peterson 2006; Denney 2012; Park et al. 2017). In addition, it worth to stress that SE method

is rooted on BH masses estimated via RM. The application of the latter is limited to relatively nearby AGN ( $z < 0.3$ ) that poorly sample the high-luminosity regime of quasars observed at high redshifts. Only recently, first RM measurements at intermediate redshift appeared in the literature (Shen et al., 2019b,c).

## 1.5 The host galaxies of growing BHs

According to the “unified” model, in Type-1 AGN the central BH and its associated continuum and broad emission-line region are viewed directly. In this case, the optical/UV continuum is dominated by non-thermal emission. In such cases, the study of AGN host galaxy is hindered. Even harder is the investigation of quasar host galaxies where the galaxy’s stellar emission is completely overwhelmed by the continuum radiation from the compact central region (see Fig. 1.2). HST in the ’90s was successful in facing these challenges as it showed, for the first time, the diversity in morphology among quasar host galaxies. Such observations unveiled fairly normal galaxies, or in some cases heavily disturbed systems due to the tidal interaction with other galaxies or mergers in progress (see Fig. 1.8). Subsequent large systematic surveys revealed that the representative population of AGN in the contemporary Universe is predominately hosted in moderately-massive disk galaxy (stellar mass  $M_{\star} \gtrsim 10^{10} M_{\odot}$ ), showing high stellar mass surface densities ( $> 10^{8.5} M_{\odot} \text{ kpc}^{-2}$ ), and with a significant amount of ongoing star formation and young stellar populations similar to those of normal “late-type” galaxies (see, e.g., Kauffmann et al., 2003b). Most AGN host galaxies are not mergers in progress with the fraction of merger remnants that increases with increasing mass (see, Kormendy & Ho, 2013). The most massive AGN host galaxies, and in particular radio galaxies, are massive ellipticals ( $M_{\star} \sim 10^{11} - 10^{12} M_{\odot}$ ), with no evidence of recent star formation activity. Further studies suggest that a similar situation is still in place up to  $z \sim 2$  (see, Kormendy & Ho, 2013). To first approximation, the representative population of AGN at these redshifts seems like a scaled-up version of the local Universe counterparts, with: larger luminosity, more massive BHs, and higher star-formation rate (SFR, see, e.g., Aird et al., 2012; Mainieri et al., 2011; Schawinski et al., 2012).

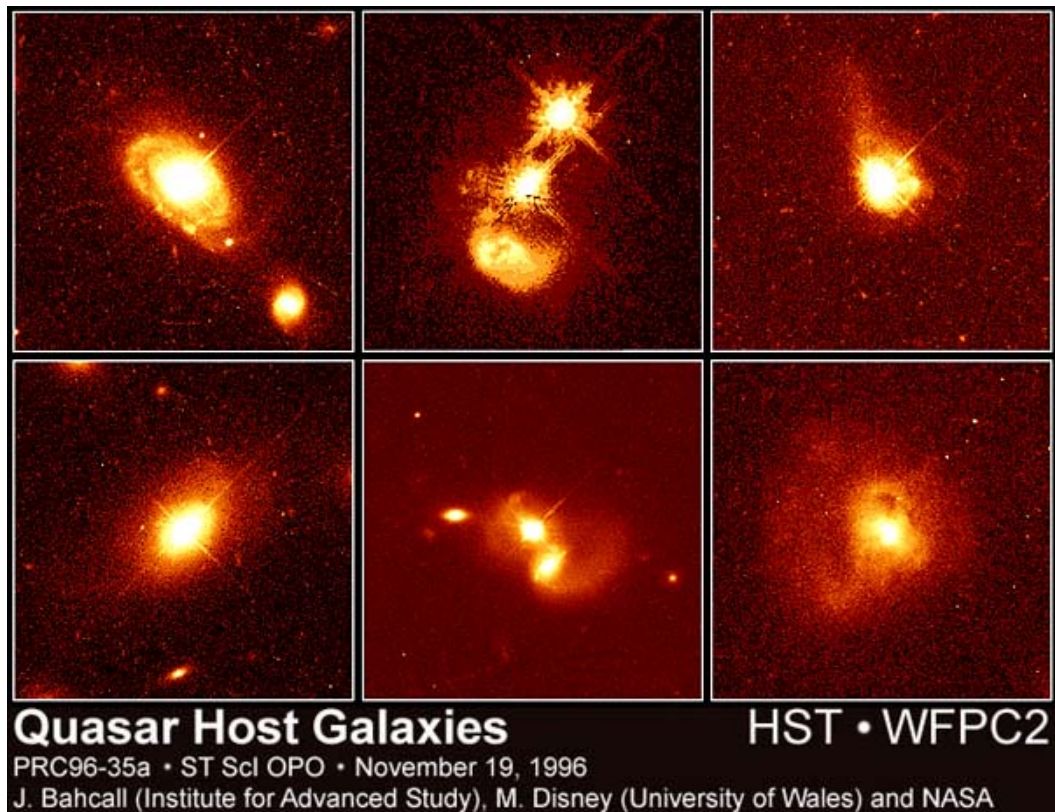


**Figure 1.8**

HST images of local quasars. *Top left panel:* PG 0052+251 quasar hosted by an undisturbed normal spiral galaxy. *Lower left panel:* PHL 909 quasar host is a normal elliptical galaxy. *Top central panel:* IRAS 04505-2958 quasar (at the center) is part of a merging system with a spiral galaxy (at the bottom). A bright foreground star is located just at the top of the central quasar. *Bottom central panel:* PG 1012+008 quasar at the centre is part of a collision with another galaxy (just below) as evidence by the swirling wisps of dust and gas surrounding the system. *Top right panel:* The tidal tail of QSO 0316-346 host galaxies is likely the result of an interaction with a passing galaxies (not in the image). *Lower right panel:* The IRAS 13218+0552 quasar host galaxies is just went through a merger process. The system is surrounded by loops of glowing gas possibly produced by the interacting galaxies that have orbited each other several times before merging. Credits: John Bahcall (Institute for Advanced Study, Princeton), Mike Disney (University of Wales), and NASA.

At higher redshifts, the classification of quasar host galaxies is hard. However, a consensus picture is recently emerging. The majority of distant AGN are hosted in massive disk galaxy, even when they are optically obscured (e.g., Cisternas et al., 2011a,b; Schawinski et al., 2011, 2012; Kocevski et al., 2012; Treister et al., 2012; Böhm et al., 2013; Schramm & Silverman, 2013), with the highest-luminosity quasars that are often found in dust-enshrouded

mergers in progress (e.g., Urrutia et al., 2008; Treister et al., 2010; Treister et al., 2012). However, the selection of distant quasars is naturally biased toward more massive and luminous BHs, and this bias becomes more severe at increasing redshift thus further disfavoring the “contrast” between galaxy’s stellar emission and quasar continuum. In addition, the  $\propto (1+z)^4$  dimming in the surface brightness strongly limits the detection of the galaxy’s starlight emission with the current facilities. In this sense, the forthcoming commissioning of the James Webb Space Telescope (JWST) promises to revolutionize the study of the stellar population of high- $z$  quasars (see, e.g., Marshall et al., 2020a,b, 2021). However, at the moment, the best way to probe the host galaxies of luminous high- $z$  quasars is via the gas line emission and cool dust continuum at FIR/(sub-)mm wavelengths, where the contribution of the AGN is not dominant. Interferometric observations with high-sensitivity facilities such as the IRAM/NOEMA (Institute de Radio Astronomie Millimétrique/Northern Extended Millimeter Array) and ALMA (Atacama Large (sub-)Millimeter Array) have transformed this field. Thanks to their exquisite capabilities, we can now unravel, and even spatially resolve the host galaxies of  $z > 6$  quasars (see, e.g., Venemans et al., 2019; Walter et al., 2022, for extremely high-resolution observations). By capitalizing on this approach, various observational campaigns (e.g., Decarli et al., 2017, 2018; Neeleman et al., 2019, 2021; Venemans et al., 2020) revealed that  $z > 6$  quasars are characterized by high FIR luminosities ( $\sim 10^{12-13} L_{\odot}$ , typical of the brightest nearby ultra-luminous infrared galaxies; ULIRGs, such, e.g., Arp 220) and large gas and dust reservoirs ( $\sim 10^{9-10} M_{\odot}$ , and  $\sim 10^{7-8} M_{\odot}$ , respectively; see, e.g., Carilli & Walter 2013) which fuel intense episodes of star-formation ( $\text{SFR} \sim 100 - 1000 M_{\odot} \text{yr}^{-1}$ ). These recent studies also highlight that the cold gas kinematics of quasar host galaxies show a diverse range, including compact dispersion-dominated systems and rotationally supported disks. Remarkably,  $z > 6$  quasars are often found accompanied by or interacting with other galaxies in the close environments suggesting that external processes might play a key role in triggering the AGN activity in such primordial galaxies (see, e.g., Fig. 1.9, Decarli et al. 2019a). This evidence is in line with the expectations from models and numerical simulations of massive BH formation showing that  $z > 6$  quasars reside at the extreme peak ( $\sim 5 - 6\sigma$ ) of the cosmic large-scale density structure (e.g., Begelman et al., 2006; Overzier et al., 2009; Bonoli et al., 2009, 2014; Angulo et al., 2012;

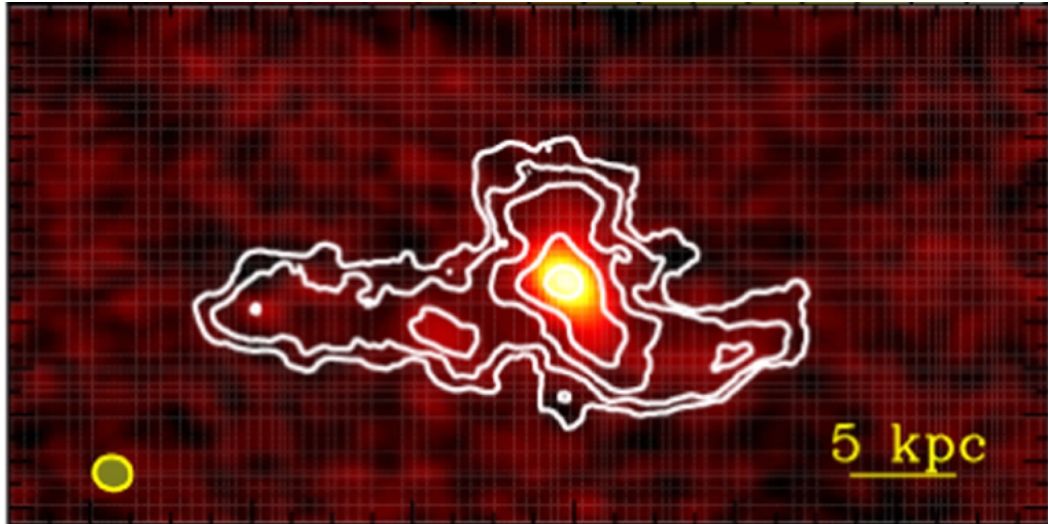


**Figure 1.9**

Interferometric high-angular resolution ( $\sim 0''.3$ ,  $\approx 1.7$  kpc at the redshift of the source) ALMA observation of PJ308-21 quasar at  $z = 6.23$ . The map shows the dust continuum emission with superimposed contours of the singly-ionized carbon  $[\text{CII}]_{158\mu\text{m}}$  line emission. Line emission is stretched over about 25 kpc and  $> 1500 \text{ km s}^{-1}$  toward and beyond the central quasar host suggesting that the satellite galaxy is tidally stripped by the interaction with the central quasar. Figure adapted from Decarli et al. (2019a).

Costa et al., 2014b). However, the question of whether there are in fact overdensities of galaxies around  $z \sim 6$  quasars is still open (e.g., Overzier et al., 2009; Morselli et al., 2014; Balmaverde et al., 2017; Farina et al., 2017; Mazzucchelli et al., 2017a; Decarli et al., 2019b). On a smaller scale ( $\sim 100$  pkpc), ALMA has allowed us to image the dust and cold-gas reservoir of galaxies in the early Universe, leading to strong evidence of overdensities around  $z > 5 - 6$  quasars (e.g., Decarli et al., 2017; Trakhtenbrot et al., 2017; Willott et al., 2017; Neeleman et al., 2019; Venemans et al., 2019). Such observations are also supported by the intriguingly serendipitous discoveries of starburst and submillimeter galaxies (SMGs) in the close environment of the quasars, which have high star formation rates ( $\text{SFR} > 500 - 1000 M_{\odot} \text{ yr}^{-1}$ ), and show no evidence of BH accretion (Decarli et al. 2017; Mazzucchelli et al. 2019; but see also Connor et al. 2019, 2020; Vito et al. 2019 for tentative evidence of X-ray emission from these companions).

## 1.6 Thesis aims & structure

This Ph.D. thesis is aimed at characterizing the quasar host galaxies at  $z > 6$  (age of the Universe  $< 1$  Gyr) through the study of their ISM properties and the cold gas kinematics. To this purpose, we capitalize on observations carried out with ALMA and NOEMA that allowed us to image with unprecedented details the ISM of high- $z$  quasar host galaxies at (sub-)mm wavelengths. Our approach is multifaceted, aiming to put quantitative constraints on the gas and dust physical properties, and to study the complex interplay between BH growth and star-formation in shaping the first massive galaxies during their evolution from the earliest epochs to the contemporary Universe.

In the following, the structure of this thesis is summarized.

- **The rise of the giants**

In **Chap. 2**, we briefly discuss the theories on the formation of the first black holes and the tensions with the current observations of the most massive quasars at early epochs. We therefore illustrate the main techniques adopted to identify high- $z$  quasars starting from wide-field optical/NIR surveys, and what is currently known about the general population of quasars at  $z > 6$ . Finally, we report the discovery and characterization of three new  $z > 6$  quasars to which I contributed by carrying out several optical/NIR photometric observations using telescopes based in La Silla Observatory (Chile) and in the Roque the Los Muchachos Observatory (La Palma, Canary Islands).

- **The early black hole–galaxy coevolution**

The **Chap. 3** is dedicated to the general properties of the galaxy population and the black hole–galaxy scaling relations in the local Universe, and their evolution with the redshift. We then review theories on AGN feedback and its role on the evolution of galaxies.

- **The ALMA view of the high-redshift relation between supermassive black holes and their host galaxies**

In **Chap. 4**, we present our study that investigates the onset of the black hole-to-host galaxy mass relation at high- $z$ . In this chapter, we measure the dynamical mass of a large sample of  $z > 4$  quasar host galaxies by the analysis of the cold gas kinematics traced by bright emission lines. We then discuss how biases can affect such kind of studies and

how our results provide us with key insights on the early formation and evolution of the first massive galaxies.

- **The interstellar medium of galaxies at high redshift**

In **Chap. 5**, we review the general properties of the interstellar medium in galaxies. We focus on the tracers of atomic, ionized, and neutral interstellar medium. We also examine the molecular gas at high redshift, and the properties of the observed FIR dust continuum. We then discuss the current methods for modeling the observed emission to retrieve quantitative constraints on the physical properties of the gas and dust.

- **Characterizing the interstellar medium in  $z > 6$  quasar host galaxies with a multiline survey**

In **Chap. 6**, we present our original work in which we explore the impact of star formation and BH growth in two quasar host–companion galaxy pairs at  $z > 6$ . In this work, we capitalize on ALMA observations targeting multiple probes of the ISM as well as FIR continuum. By combining various diagnostics, we dissect the physical properties of the manifold interstellar medium in galaxies with and without a luminous quasar.

- **Unveiling the warm dense gas in  $z > 6$  quasars via water vapor emission**

In **Chap. 7**, we study a sample of IR-bright  $z > 6$  quasars through their multiple  $\text{H}_2\text{O}$  emission lines targeted with NOEMA. This approach allows us to investigate the properties of the warm dense gas, the local IR dust radiation field, and water vapor excitation mechanisms in massive galaxies at cosmic dawn. This work sheds a first light on properties of the interstellar medium a largely uncharted at such early cosmic epochs.

- **Concluding remarks**

In the final **Chap. 8**, we summarize the results derived in this thesis and we discuss the main implications of our studies into a broader context. Finally, we discuss the future perspectives to further our investigations via new campaigns.



# 2

## The rise of the giants

“*The history of astronomy is a history of receding horizons.*”

— Edwin P. Hubble

The most challenging goal of the extragalactic astronomy is to provide a coherent picture of the history of the Universe and the formation and evolution of structures. The first observable light in the Universe is the permeating radiation of the Cosmic Microwave Background (CMB) released when baryons and radiation decoupled at  $z \sim 1200$ , roughly 400,000 years after the Big Bang. This event marks the beginning of the cosmic “dark ages” where neutral hydrogen fills most of the Universe. At  $z \sim 20 - 50$  baryons starts to assemble into the center of dark matter (DM) proto-halos ( $\sim 10^6 M_{\odot}$ ) forming the first generation of protogalaxies. The ignition of thermonuclear reactions in the first stars marked the birth of the “luminous” Universe. Young stars started to release abundant UV radiation that photoionized the diffuse inter-galactic medium (IGM), and to pollute their surroundings with heavy elements (metals) via stellar winds and supernova (SN) explosions. The first massive stars are thought to collapse forming the first BHs, that settle at the centers of galaxies and seed the first supermassive BHs and quasars. The primeval galaxies began to ionize again the neutral hydrogen in the IGM, starting to the “Epoch of Reionization” (EoR) at  $z \sim 10$ , which lasted until about  $z \simeq 6$ . **Fig. 2.1** schematizes the history of the Universe across the different epochs.

Searching for and studying the most distant quasars and galaxies at the dawn of cosmic time is key to test our theoretical picture of the evolution

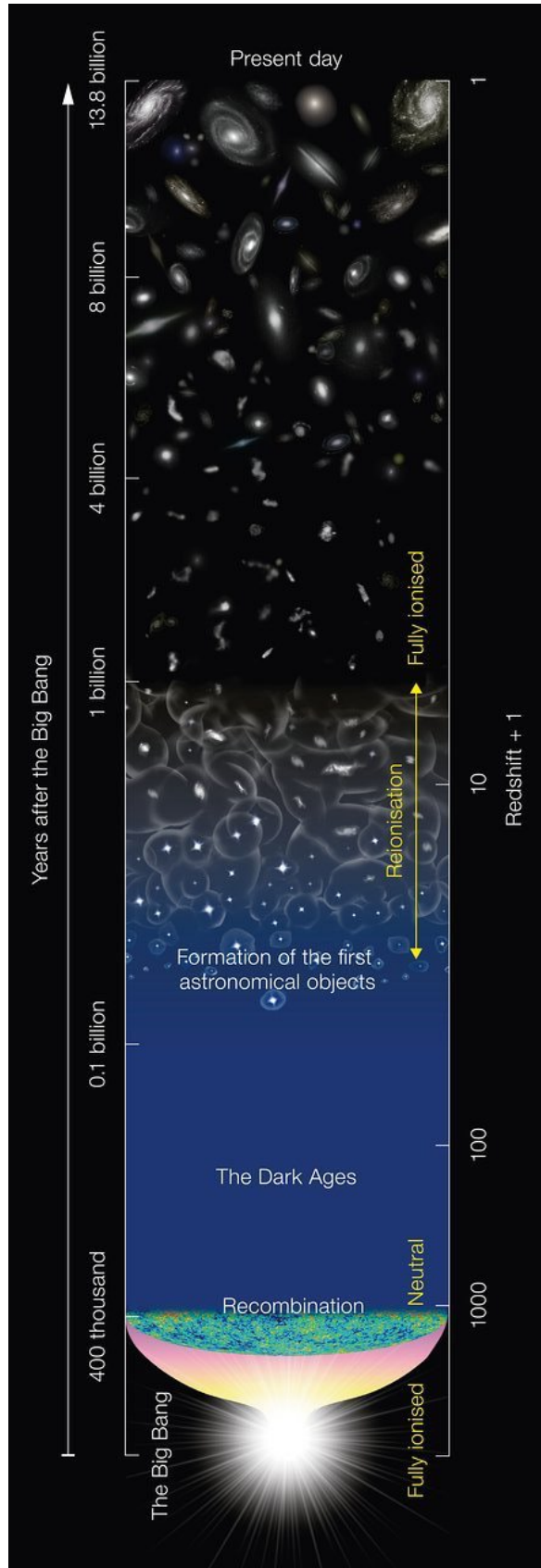


**Figure 2.1**

Schematic diagram of the history of the Universe. The most important epochs are reported. The first generation of astronomical objects are expected to form at  $z > 20$  marking the end of the Dark Ages. The first galaxies started the Reionization down to  $z \sim 6$  where we found the most luminous and distant quasars known to date. Credits: NAOJ

of the Universe, and to understand how the first galaxies and BHs formed and evolved. Pushing our redshift frontier further away has always put our technical capability to the limit. The last few years have witnessed a rapid progress in this field. The refinement of selection techniques and the advent of increasingly sensitive telescopes and wide-field surveys led to the discovery of a large number of galaxies and quasars down to the EoR ( $z > 6$ ), when the Universe is less than 1 Gyr old. At these epochs star-forming galaxies are abundant and have already assembled up to  $10^{10} M_{\odot}$  in their stellar mass. Primeval massive galaxies host luminous quasars which are powered by a rapid accretion of matter onto massive BHs ( $> 10^9 M_{\odot}$ ). The mere existence of such supermassive BHs at these early epochs challenges our understating of the early assembly of BHs and galaxies.

In this chapter, we briefly review the models of formation and growth of the first supermassive BHs. Then, we outline the main techniques to identify new high- $z$  quasars starting from survey catalogs. Finally, we present two recent works in which I contributed as a co-author that led to the discovery of three new  $z > 6$  quasars, including the most distant radio-loud quasar known to date.

## 2.1 Formation and evolution of the first supermassive black holes

The development of the SE technique has enabled astronomers to quickly estimate the BH mass provided the quasar rest-frame optical/UV spectrum. This method, in conjunction with the ample dataset provided by large-scale spectroscopic surveys (e.g., SDSS), together with optical and near-IR dedicated follow-up campaigns, allowed us to obtain BH mass estimates up to  $z \sim 7$  (e.g., McLure & Dunlop, 2004; Labita et al., 2009a,b; Jiang et al., 2007a; Mortlock et al., 2011; Shen et al., 2019a). Despite the limitations related to the reliability of the SE virial method (see Sect. 1.4.2), these studies show that massive BHs ( $\gtrsim 10^9 M_{\odot}$ ) must be already in place by  $z \sim 7$ . *How have these massive black holes grown given the limited time available at that epoch?*

## 2.1.1 The Eddington limit

As a BH accretes mass, a huge amount of radiation is released. The outward-directed radiation interacts with the infalling plasma that therefore experiences a radiation pressure. Considering a fully ionized plasma, the interaction between the radiation and the matter is primarily due to Thomson scattering of photons by free electrons. Given the Thomson cross-section  $\sigma_T$  and the source luminosity  $L$ , the radiation force on an electron at distance  $r$  from the source is

$$F_{\text{rad}} = \sigma_T \frac{L}{4\pi r^2 c}, \quad (2.1)$$

in a spherical symmetry configuration. In order for matter to accrete onto the BH, the radiation pressure must be smaller than the gravitational force per electron-proton pair, that is  $F_{\text{rad}} < F_{\text{grav}}$ . The luminosity at which the two forces are equal sets the definition of the *Eddington luminosity* ( $L_{\text{Edd}}$ ):

$$L_{\text{Edd}} = \frac{4\pi G c m_p}{\sigma_T} M_{\text{BH}} \approx 1.3 \times 10^{38} \left( \frac{M_{\text{BH}}}{M_{\odot}} \right) \text{erg s}^{-1}. \quad (2.2)$$

The **Eq. (2.2)** can be also used to estimate (a lower limit on) the BH mass by assuming that the observed bolometric luminosity is equal (or less) to the Eddington luminosity (e.g., Wang et al., 2013). In principle, since the Eddington luminosity is derived assuming isotropic emission, this limit can be exceeded in case of a large fraction of radiation is emitted along specific directions. The energy released by the accretion disk is a fraction of the accreted mass  $M_{\text{acc}}$ , depending on the mass-energy conversion efficiency  $\epsilon$  via  $L = \epsilon \dot{M}_{\text{acc}} c^2$ . Therefore, the BH mass growth rate is  $\dot{M}_{\text{BH}} = (1 - \epsilon) \dot{M}_{\text{acc}}$ , or

$$\dot{M}_{\text{BH}} = \lambda L_{\text{Edd}} \frac{1 - \epsilon}{\epsilon c^2}, \quad (2.3)$$

where  $\lambda = L/L_{\text{Edd}}$  is and the Eddington ratio. The Eddington limit for the mass growth rate ( $\dot{M}_{\text{Edd}}$ ) is obtained from **Eq. (2.3)** by imposing  $\lambda = 1$ . If both  $\lambda$  and  $\epsilon$  are non-evolving, the BH mass increases by one  $e$ -fold on a characteristic time scale

$$t_e = \frac{M_{\text{BH}}}{\dot{M}_{\text{BH}}} = \frac{\epsilon c^2}{(1 - \epsilon) \lambda L} \approx 4.5 \times 10^8 \frac{\epsilon}{\lambda(1 - \epsilon)} \text{yr}, \quad (2.4)$$

where  $l = L_{\text{Edd}}/M_{\text{BH}}$ . This is also known as *Salpeter time* or *e-folding time*. The accretion of mass at the Eddington rate ( $\lambda = 1$ ) causes BH mass to increase in time as:

$$M_{\text{BH}}(t) = M_{\text{BH}}(0) \exp\left(\frac{1 - \epsilon}{\epsilon} \frac{t}{t_{\text{Edd}}}\right), \quad (2.5)$$

where  $t_{\text{Edd}} = 0.45 \text{ Gyr}$ . For a typical efficiency of  $\epsilon \approx 0.1$ , and a seed mass  $M_{\text{BH}}(0) = 10^2 - 10^5 M_{\odot}$ , a BH takes at least 0.5 Gyr to grow to  $\simeq 10^9 M_{\odot}$ .

## 2.1.2 The first BH seeds

Various scenarios have been proposed in order to explain how the most massive BHs that we observe in the distant Universe were put together at early times. The first stars formed in primeval environments are predicted to be very massive ( $> 100 M_{\odot}$ ). They eventually collapsed and seeded the first BHs. However, the resulting remnants cannot exceed  $\sim 1000 M_{\odot}$ , thus posing severe challenges to the BH formation theories. Other scenarios involving more massive BH seeds, super-Eddington accretion, or low radiative efficiency are adduced in order to explain the assembly of supermassive BHs during the first Gyr of the Universe. In this section we briefly review the main theories of the formation and the evolution of the first BHs.

### Population III star remnants

One of the most popular scenario for the early growth of BH is that they have assembled by accretion on remnants of the first generation of stars (Pop III stars). These stars are expected to form within the  $\sim 10^{5-6} M_{\odot}$  DM minihalos at  $z \sim 20 - 50$ . Simulations of primordial metal-free gas predict inefficient fragmentation of collapsing clouds, making the Pop III unusually massive  $10 \lesssim M_{\star} / M_{\odot} \lesssim 10^3$  (e.g., Abel et al., 2000; Yoshida et al., 2006; Gao et al., 2007). The first stars will then die after a short time scale (of a few Myr). However, the fate of these stars depends on their exact mass. Direct BH formation is predicted for stars with low-metallicity and masses between approximately 25 and  $140 M_{\odot}$ , or higher than  $260 M_{\odot}$ . In these cases, the BH remnant is about half of the mass of the progenitor star (see, Volonteri, 2010, and references therein). However, light BHs produced in the first range of masses, are expected to wander within their host rather than settling at the center of galaxy's gravitational potential. For this reason they are not believed to seed the first supermassive BHs. On the other hand,

Pop III  $\gtrsim 150 M_{\odot}$  BH relics are predicted to cluster in the galaxy center. In this case the mass accretion is significantly increased by subsequent mergers and it could lead to the onset of supermassive BHs (Madau & Rees, 2001). While, this seems a possible and natural scenario for the early growth of the first supermassive BHs, the predicted masses of the putative Pop III stars are actually highly uncertain.

### The timescale (open) problem

In Fig. 2.2 we report SE virial BH masses from different samples of quasars across the cosmic time. Assuming a radiative efficiency of  $\epsilon \approx 10\%$ , the figure shows three different BH accretion paths under the hypothesis that massive BHs were seeded by  $M_{\text{seed}} = 10, 20, 100 M_{\odot}$  starting from  $z = 20$  with  $\lambda = 1$  (black solid lines),  $z = 30$  with  $\lambda = 1$  (green dashed lines), and  $z = 20$  assuming slightly super-Eddington accretion at  $\lambda = 1.5$  (blue dotted lines). These simple calculations show that, despite the uncertainties and biases affecting the SE BH mass estimates, the Eddington-limited accretion hardly allows to achieve  $\gtrsim 10^9 M_{\odot}$  BHs at  $z \sim 6$  starting from a Pop III star remnant seeds at  $z \sim 20 - 30$ . In order to match the observed BH masses at  $z \sim 7$ , one needs to either boost the accretion rate (e.g., super-Eddington accretion), or increase the mass of BH seed, and/or lower the radiative efficiency. Further tension comes from the lingering assumption that the mass accretion on BH seeds is effective at near-Eddington limit all over  $\approx 0.8 \text{ Gyr}$  (which is comparable with the age of the Universe at  $z \approx 6$ ), and over eight orders of magnitude in mass (see, e.g., Inayoshi et al., 2020, for a recent review). In any case, the observed  $z > 6$  quasars must reside in rare highly-biased environments characterized by extreme conditions that have, to some extent, boosted their early growth.

### Alternative scenarios for the early BH growth

Beyond the scenario of Pop III stars, different models try to ease the match between theoretical predictions and the observed BH masses at  $z \sim 6 - 7$ . Here we briefly report the main proposed possibilities.

One possibility is that of a super-critical accretion greatly exceeding the Eddington limit with a canonical radiation efficiency of  $\epsilon \approx 10\%$  (Volonteri & Rees, 2005). This is explained by invoking radiation trapping in the accretion flow significantly lowering the radiation efficiency, and therefore the

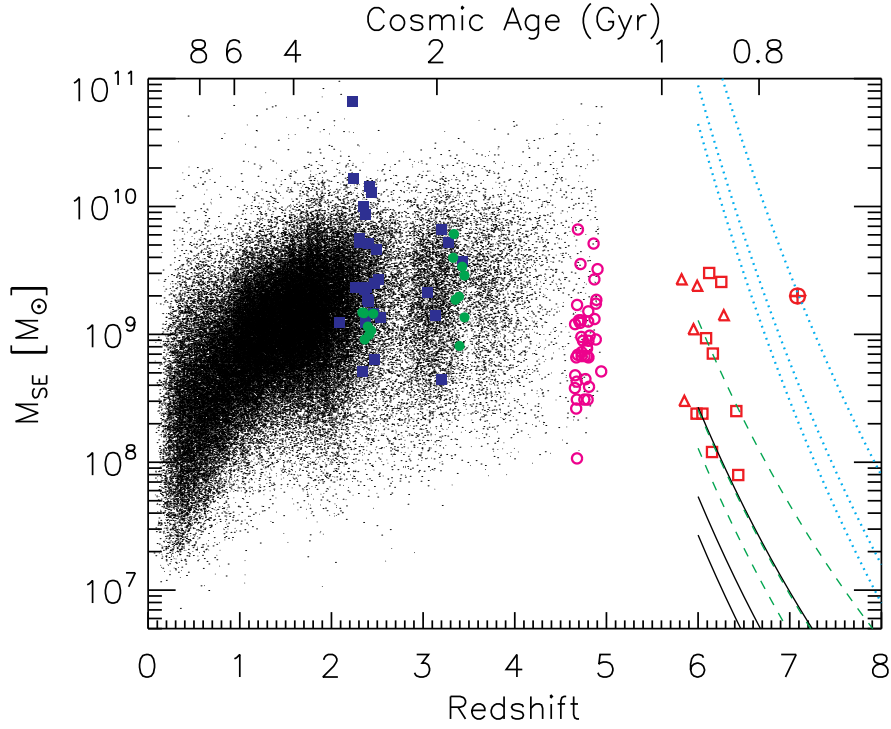


**Figure 2.2**

Sample of BH masses measured from SE methods at various redshifts. The black dots are BH masses of SDSS quasars estimated by employing different emission lines:  $H\beta$  (at  $z < 0.7$ ),  $MgII$  (at  $0.7 < z < 1.9$ ), and  $CIV$  ( $z > 1.9$ ). The colored filled symbols are SE masses estimated via  $H\beta$ , while empty ones are those from  $MgII$  lines (see, Shen 2013, for references). The lines show different growth histories assuming constant Eddington ratio  $\lambda$  and a radiative efficiency  $\epsilon = 0.1$ , starting at different redshifts. The black solid lines report Eddington-limited accretion ( $\lambda = 1$ ) from BH seeds at  $z = 20$ ; green dashed lines are  $\lambda = 1$  accretions from  $z = 30$ ; the blue dotted lines are mildly super-Eddington growths ( $\lambda = 1.5$ ) from  $z = 20$  BH seeds. Each models are reported for three different seed masses of  $M_{seed} = 10, 20, 100 M_{\odot}$ , according to the theoretical expectations for the Pop III stars. Figure from Shen (2013).

$e$ -folding time (Wyithe & Loeb, 2012).

Another popular scenario relies on the rapid formation of massive ( $\sim 10^3 - 10^5 M_{\odot}$ ) BH seeds from direct collapse of primordial gas cloud (DCBH; e.g., Begelman et al., 2006; Agarwal et al., 2012), or the formation of a super-massive star (or “quasi-star”) than promptly collapses in a massive BH (e.g. Shibata & Shapiro, 2002; Begelman et al., 2008; Johnson et al., 2012). For some of these models super-/hyper-Eddington accretion is also predicted to enable these “massive seeds” to grow to the final BH mass.

Alternatively, intermediate mass BH (IMBH) seeds ( $M_{seed} \approx 10^3 - 10^4 M_{\odot}$ ) are

hypothesized to rapidly form in metal-poor protogalaxies in a runaway collisional growth via merging of stars in ultra dense clusters (e.g., Devecchi & Volonteri, 2009). Recently, Kroupa et al. (2020) suggested that supermassive-BH seeds with masses up to a few times of  $10^6 M_{\odot}$  might emerge within a few hundred Myr of the first star formation via BH-BH coalescences in a central extremely massive ( $> 10^8 M_{\odot}$ ) starburst star cluster.

Finally, more exotic possibilities include primordial BHs (PBHs) formed in the early Universe after the Big Bang (see, e.g., Carr, 2003; Cappelluti et al., 2021), and massive ( $500 - 1000 M_{\odot}$ ) “Dark Star” BH seed supported by dark matter annihilation, collapsing into a massive BH (e.g., Freese et al., 2008).

In **Fig. 2.3** we report accretion tracks of known  $z \geq 7$  supermassive BHs in different scenarios of BH formation at  $z \sim 15 - 30$  assuming constant Eddington accretion, and a radiative efficiency of  $\epsilon = 10\%$ . DCBH is the favoured scenario for the formation of the most distant quasars observed in the early Universe (Wang et al., 2021a). However, future sensitive surveys (e.g. in the X-rays with *Athena*; see Aird et al. 2013) will push farther the current redshift frontiers thus expanding the sample of  $z > 7$  quasars toward lower luminosities and BH masses. These studies will therefore help us to better understand the formation of the first BHs.

## 2.2 The population of high- $z$ quasars

### 2.2.1 Identification of $z > 6$ quasars

The main technique to identify a high-redshift quasar (or galaxy) goes back to several decades (e.g. Meier, 1976a; Meier, 1976b). The basic idea is to exploit the strong absorption in the quasar’s spectrum at wavelength shorter than Ly- $\alpha$ , caused by the intervening neutral hydrogen in the ISM and/or IGM along the line of sight (see **Sect. 1.2.5**). By employing this method, high redshift quasars are identified by an extreme observed-frame red optical color: the quasar is visible only in the longer wavelength images and nearly absent in the bluer bands where the spectrum is nearly completely absorbed (see, e.g., **Fig. 2.5**). Objects selected with this technique are dubbed as “dropout” galaxies. As the redshift increases, the spectral “break” moves

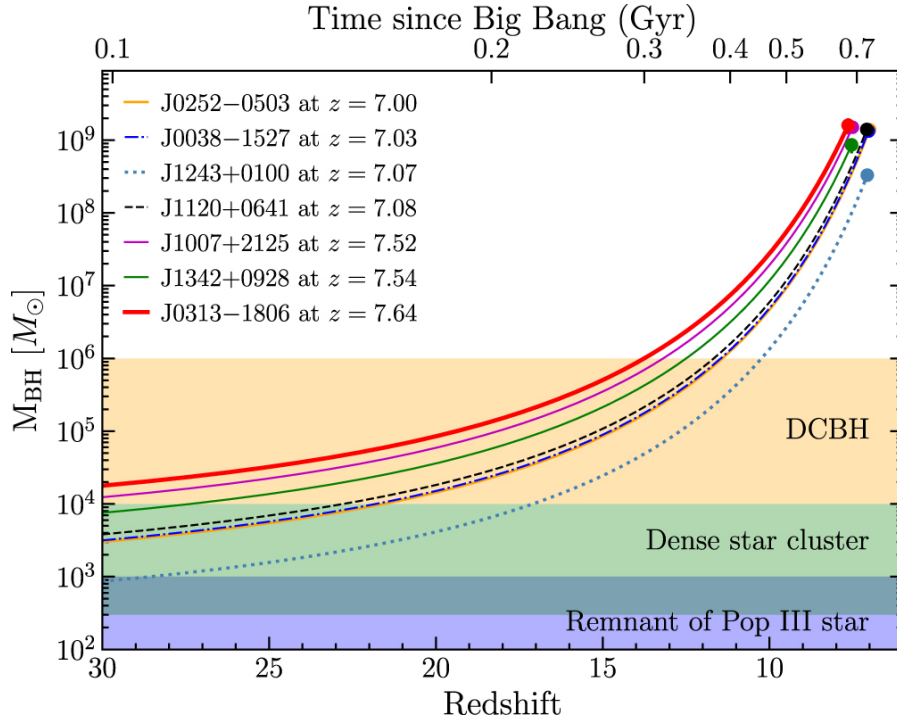


**Figure 2.3**

Black hole growth tracks of  $z \geq 7$  quasars assuming Eddington accretion and radiative efficiency of  $\epsilon = 0.1$ . The BH masses in these quasars are taken from Wang et al. (2018a, 2020, 2021b), Matsuoka et al. (2019b), and Yang et al. (2020b). The blue, green, and yellow shaded regions define the approximate ranges of BH seed masses predicted by Pop III stars, dense star clusters, and direct-collapse black holes (DCBHs), respectively. Figure from Wang et al. (2021a).

toward longer wavelength enabling to select quasar candidates in different redshift ranges via deep broad-band imaging. As an example, at  $z \sim 6$  the spectral break is shifted to the observed wavelength  $\lambda = 0.8 \mu\text{m}$ , between the  $i$ - and  $z$ -band filters (see, Bessell, 2005). Objects identified by this color are called  $i$ -dropouts. Observations in both  $i$ - and  $z$ -band are required to identify the sharp Ly- $\alpha$  break while additional near-IR imaging is necessary to ensure the presence of the strong rest-frame UV continuum. Then, spectroscopic follow-up observation is essential for a proper assessment of the nature of the source, and for a precise determination of the redshift.

The “Lyman-Break” technique enables to efficiently separate the quasar candidates from possible contaminants (e.g., low-redshift interlopers) in the field, using only photometric information. The first class of contaminants that affect the color-selection of  $z > 6$  quasars comprises cool Galactic stars, in particular the M-, L-, and T-type (MLT) brown dwarfs which are characterized

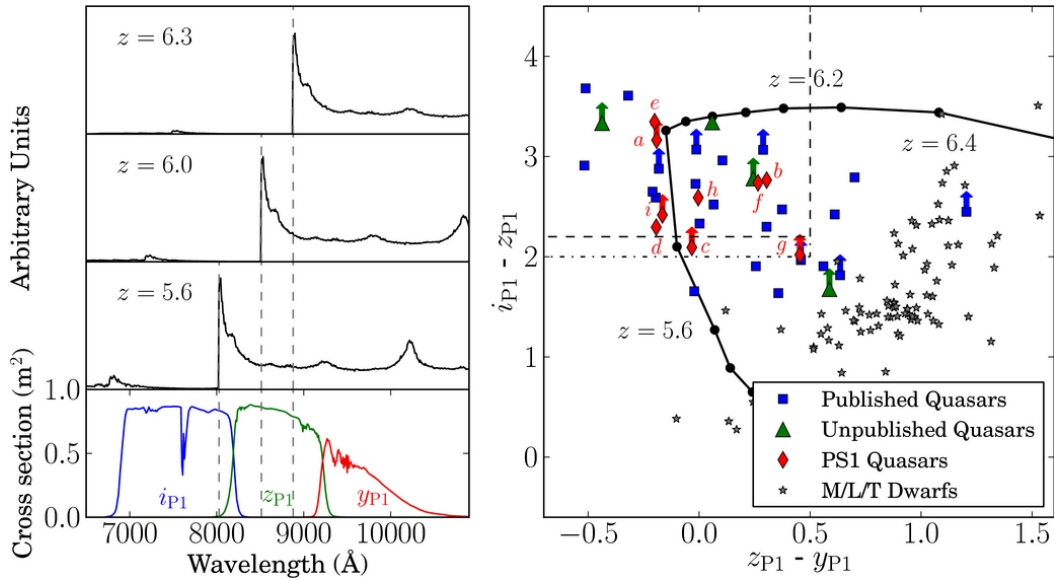


**Figure 2.4**

The Lyman-Break technique to select  $z > 6$  quasar candidates. *Left panel*: composite quasar spectrum (see Decarli et al., 2010) redshifted to  $z = 5.6, 6.0, 6.3$  (from the bottom to the top), the vertical dashed lines show the Ly- $\alpha$  line wavelength at each redshift. The bottom panel reports the filter responses of different Pan-STARRS1 (PS1, see text) bandpasses (in unit of  $\text{m}^2 e^{-1} \text{photons}^{-1}$ ). *Right panel*: color-color diagram showing  $i - z$  and  $z - y$  indices used to select quasar candidates. The black thick line shows the expected color of the quasar template at different redshifts in step of  $\Delta z = 0.1$ . Black stars indicate color values of some MLT dwarfs with PS1 counterparts. Blue squares, green triangles and red diamonds are the observed colors of known quasars. Upward arrows are upper limits. Black dashed line defines the criterium adopted to select quasar candidates. Figure from Bañados et al. (2014).

by very red  $i - z$  color index and point-like appearance. The second class is composed by red galaxies at  $z \sim 1$ , for which the Lyman Break could be confused with the intrinsically strong rest-frame  $4000 \text{ \AA}$  break. This is associated to the blanket absorption of high energy radiation from metals in the stellar atmospheres of old stellar population in galaxy. The third class includes faint  $z > 6$  Lyman-Break galaxies which are also affected by IGM absorption (see, Dunlop, 2013, for a review). The efficiency in selecting quasars varies depending on the dropout band. As an example, at  $z \sim 6.5$ , the quasar Ly- $\alpha$  line drops out from the  $z$  band. In this case, the  $i - z$  color is uninformative and  $z$ -dropout quasar candidates become more difficult to be distinguished from contaminants. In **Fig. 2.4** we illustrate the principle of color-color selection of  $z > 6$  quasar candidates.

## 2.2.2 High-redshift quasar surveys

The dropout selection is the main tool used in the exploration of high- $z$  quasar population. This method was first applied by Warren et al. (1987) in  $z > 4$  quasar surveys in 1980s, and it revolutionized the study of high-redshift galaxies. Fan et al. (2000) employed such selection criteria discovering the first handful of  $z \gtrsim 6$  quasars in the SDSS, out to  $z \lesssim 6.5$  (Jiang et al. 2016; see, e.g., Fig. 2.5). Additional efforts were accomplished with the Canada-France High-redshift Quasar Survey (CFHQS; Willott et al. 2007), and the Panoramic Survey Telescope & Rapid Response System 1 (Pan-STARRS1; Morganson et al. 2012; Chambers et al. 2016), bringing well over 100 the number of known quasars at  $z \gtrsim 6$  (Bañados et al., 2016). More recently, this number was doubled by the Hyper Suprime-Cam (HSC) Subaru Strategic Program (HSC-SSP) Survey (Aihara et al., 2018), and the Subaru High- $z$  Exploration of Low-Luminosity Quasars (SHELLQs) survey, that expanded the known sample toward fainter quasars (Matsuoka et al., 2018c). At increasing redshift, the Lyman Break shifts more and more into optical reddest bands ( $z$ ,  $y$ ), and the IR bands ( $J$ ,  $H$ ,  $K$ ). The highest-redshift sources ( $z > 6.5 - 7$ ) have indeed been identified combining optical surveys, such as Pan-STARRS1 (Bañados et al., 2016; Koptelova et al., 2017; Mazzucchelli et al., 2017b; Tang et al., 2017), the SHELLQs survey (Matsuoka et al., 2016, 2018b,a, 2019a), the Dark Energy Survey (DES; Reed et al. 2015, 2017, 2019; Yang et al. 2019b), the Dark Energy Spectroscopic Instrument (DESI) Legacy Imaging Surveys (DELS; Wang et al. 2018b, 2019a; Yang et al. 2019b; including the Dark Energy Camera Legacy Survey, DECaLS; Dey et al. 2019), and IR surveys such as the UKIRT (United Kingdom Infrared Telescope) Infrared Deep Sky Survey (UKIDSS; Lawrence et al. 2007; Mortlock et al. 2011), the UKIRT Hemisphere Survey (UHS; Wang et al. 2018b), the VISTA (Visible and Infrared Survey Telescope for Astronomy) Kilo-degree Infrared Galaxy Survey (VIKING; Edge et al. 2013; Venemans et al. 2013), the VLT (Very large Telescope) Survey Telescope ATLAS (VST ATLAS; Carnall et al. 2015; Chehade et al. 2018), and the VISTA Hemisphere Survey (VHS; McMahon et al. 2013; Venemans et al. 2015; Pons et al. 2019).

All these studies, have contributed to push toward a complete census of supermassive BHs at increasingly high-redshift over the time (see Fig. 2.6). As a result, to date astronomers discovered  $\sim 400$  quasars at  $z > 5.5$ , of which  $\gtrsim 200$  at  $z > 6.0$ ,  $\gtrsim 50$  at  $z > 6.5$ , and 8 quasars at  $z > 7.0$  (Mortlock

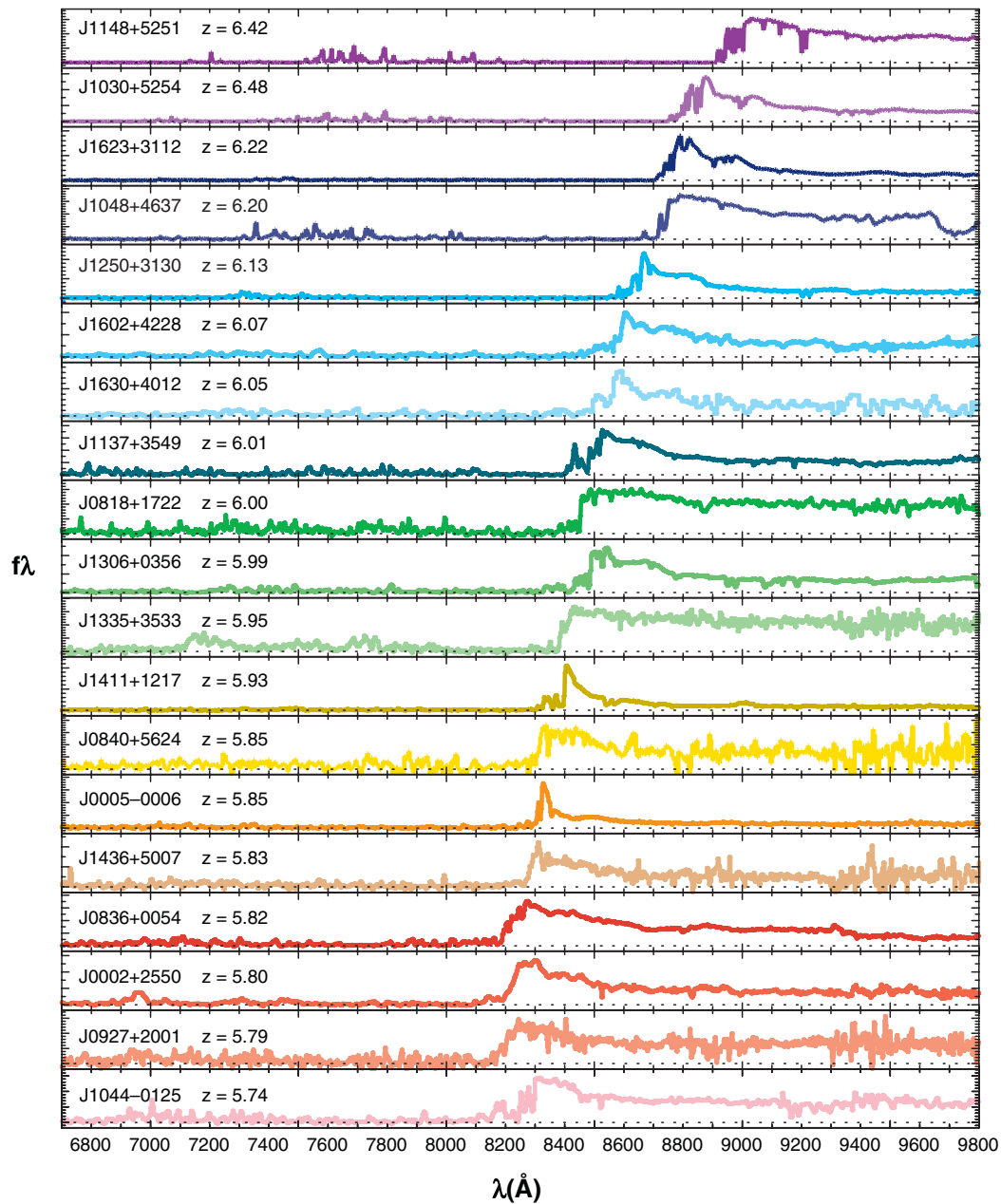


**Figure 2.5**

Spectra of nineteen SDSS quasars at  $5.74 < z < 6.42$  showing significant absorption feature at wavelength shorter than observed Ly- $\alpha$  emission. Figure from Fan et al. (2006).

et al., 2011; Wang et al., 2018a; Matsuoka et al., 2019a,b; Bañados et al., 2018; Yang et al., 2019b, 2020b) including the most distant quasar known to date at  $z = 7.642$  (Wang et al., 2021a).

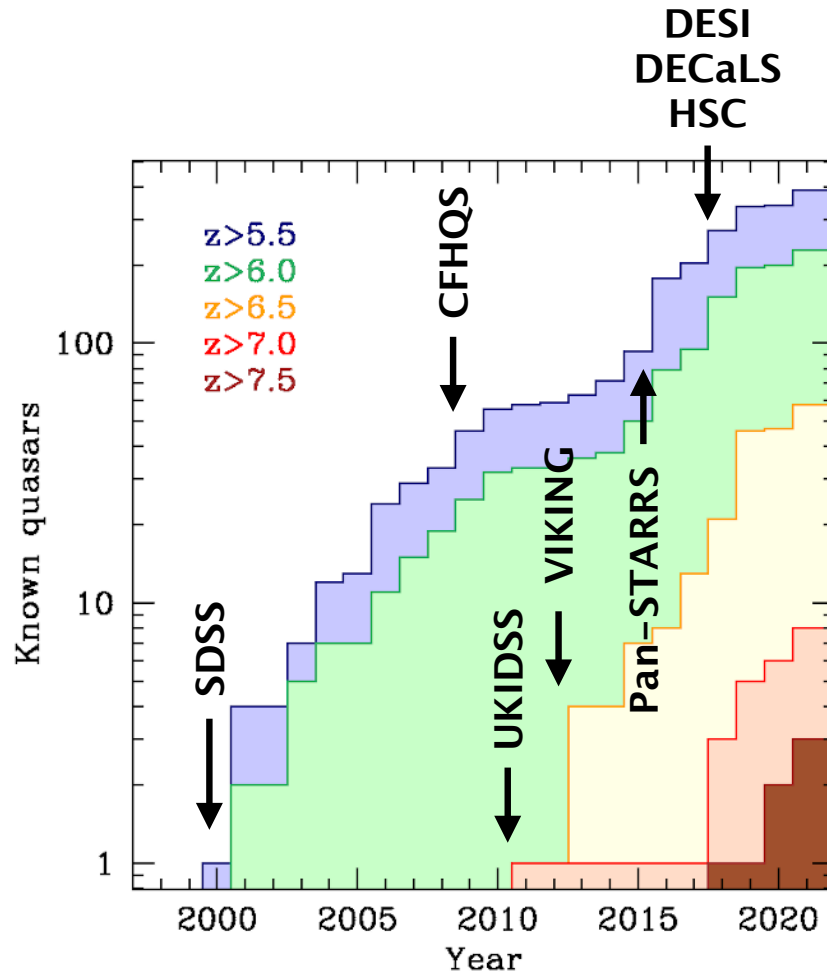


**Figure 2.6**

Cumulative number of quasars discovered over the time color-coded by redshift bin (see the upper-left corner). Various surveys that significantly contributed to increase the number of identified high- $z$  quasars are indicated at the year of advent. Courtesy of R. Decarli.

### **Selection biases**

It is important to note that the detection of distant quasars with the current surveys is not devoid of selection effects. The optically-selected quasars at high- $z$  could possibly be unrepresentative of the typical population of BHs at early epochs. Indeed, the shallow all-sky maps reveal quasars that host unusually massive BHs that accrete near to the Eddington limit. In addition, many early BHs can remain undetected due to the heavy obscuration from either material in the surrounding of the BH and/or dust and gas in the host galaxy (e.g., Buchner & Bauer, 2017). As a consequence, the population of

Type-2 quasars at high- $z$  remains still uncharted. In this regard, Vito et al. (2018) suggest that  $\sim 80 - 90\%$  of all  $z > 6$  quasars may be obscured and thus missed by optical surveys.

### 2.2.3 The luminosity function of $z \sim 6$ quasars

By counting the number of quasars (with a flux larger than a given threshold), in conjunction with the determination of the redshift, it is possible to obtain the quasars' *luminosity function* (LF),  $\Phi(L, z)$ . This function is defined such that  $\Phi(L, z)dL$  is the number density of quasars in a comoving volume element of the Universe at redshift  $z$ , with a luminosity between  $L$  and  $L + dL$ . This function is usually parametrized as a double power law of the form

$$\Phi(L, z) = \frac{\Phi^*}{L^*(z)} \left[ \left( \frac{L}{L^*(z)} \right)^\alpha + \left( \frac{L}{L^*(z)} \right)^\beta \right]^{-1}, \quad (2.6)$$

where  $\Phi^*$  is the normalization, and  $L^*(z)$  represents a characteristic luminosity where the two power-law components join.  $L^*(z)$  strongly depends on redshift (e.g., at  $z \lesssim 2$ ,  $L^*(z) = L_0^*(1+z)^k$ , with  $k \approx 3.45$ ; Schneider 2006), indicating a rapid evolution of the LF across the cosmic time. At  $z \sim 6$ , the quasar LF has been measured extensively (Willott et al., 2010a; Jiang et al., 2016; Matsuoka et al., 2018c, see Fig. 2.7). These results highlight that at  $z = 6$  the LF is roughly consistent with an extrapolation from lower redshifts (i.e., the shape remains self-similar), with the normalization that drops dramatically at increasing redshift. This implies that, at given luminosity,  $z \sim 6$  quasars are about  $\sim 100$  times less abundant than that at  $z \approx 4$  (see also Sect. 1.3).

In the last decade, significant efforts have been invested to collect a substantial sample of high- $z$  quasars to better sample the quasar LF at high redshifts. Recent works (e.g., Wang et al., 2019c) show that the exponential decline in the number density of  $z > 3$  quasars accelerates by a factor of  $\sim 6$  per unit redshift at  $z = 5 - 7$  as also suggested by previous works (e.g., Fan et al., 2001a; Willott et al., 2010a; Kashikawa et al., 2015; Jiang et al., 2016). This implies that the density of typical quasars detected in the SDSS (UV continuum absolute magnitude of  $M_{AB} \sim -26$ , corresponding to  $M_{BH} \sim 10^9 M_\odot$  assuming Eddington accretion) drops to  $< 1 \text{ Gpc}^{-3}$  at  $z > 6$ . This makes  $z > 6$  quasars the rarest objects currently known in the early Universe. As a

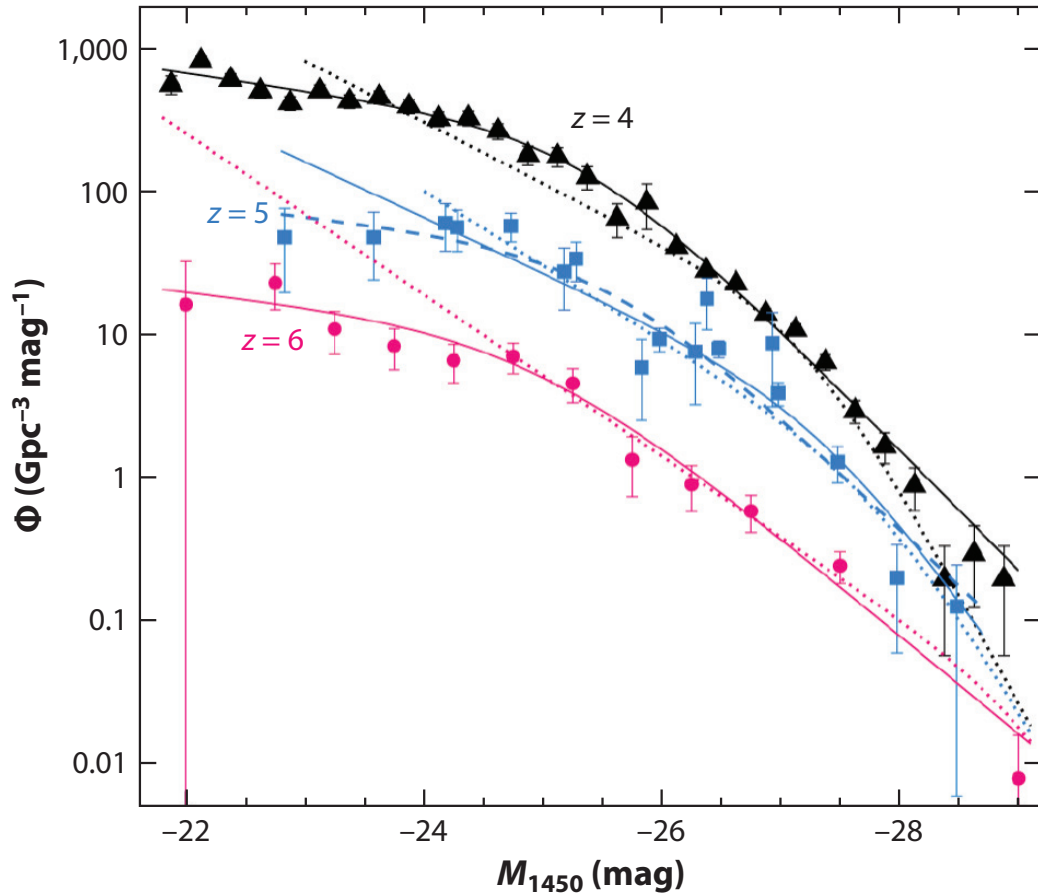


**Figure 2.7**

Quasar luminosity function at different redshifts. From SHELLQs at  $z = 6$  (red circle; Matsuoka et al., 2018c), CFHTLS (Canada-France-Hawaii Telescope Legacy Survey) at  $z = 5$  (blue squares; McGreer et al., 2018), and combination of SDSS and HSC Wide survey at  $z = 4$  (black triangles; Akiyama et al., 2018). The dotted lines are the best fit models to the data. Note that the LFs are parametrized as a function of the absolute magnitude at 1450 Å. Figure from Inayoshi et al. (2020).

result, the extrapolation of the observed density evolution to higher redshifts, predicts that only about one quasar at  $z \sim 9$  with  $M_{\text{AB}} < -26$  exists in the entire observable Universe. The  $z = 9 - 10$  could be therefore the epoch when the very first luminous quasars emerge from the cosmic dawn. In this sense, the limiting magnitude and the survey volume are the main limitations for the discovery of  $z > 9$  quasars. Ambitious projects such as the *Vera C. Rubin Observatory*, the *Euclid Space Telescope*, and the *Roman Space Telescope*, promise to push the boundaries of our discovery space toward the very first supermassive BHs at the earliest epochs.

## 2.3 Contribution to the identification of new $z > 6$ quasars in the sky

During my Ph.D. I took part to a long-term project led by an international team aiming at the discovery and characterization of new quasars at  $z > 6$  through extensive, multiwavelength (from optical/NIR to sub-mm) observational campaigns using state-of-the-art facilities. To this purpose, I performed optical/NIR photometric observations of ample samples of quasar candidates. I executed various observing runs as visiting astronomer at the ESO (European Southern Observatory) La Silla Observatory (Chile) with the *New Technology Telescope* (NTT) during the period December 20-26, 2018, and July 18-27, 2019 within the project “*Identification of new  $z > 6$  quasars in the Southern Sky*” (PI: R. Decarli); and at the Roque de Los Muchachos Observatory (La Palma, Canary Islands) using the *Northern Optical Telescope* (NOT), during the period November 9-13, 2019 within the project “*Identification of new  $z > 6$  quasars in the Northern Sky*” (PI: R. Decarli). Some of these observations have been at the base of spectroscopic follow-up observations that led to the unambiguous identification of new quasars (Andika et al., 2020), including the discovery of the most distant radio-loud quasar known to date (Bañados et al., 2021). In the following sections, I summarize the main results from these recent works to which I contributed as a co-author.

## 2.4 The discovery of two quasars at $z > 6$

In this section we present the discovery and characterization of the quasars PSO J083.8371+11.8482 (hereafter PJ083+11) at  $z = 6.3401$ , and PSO J344.1442-02.7664 (hereafter PJ344-02) at  $z \approx 6.5$ , reported in Andika et al. (2020, hereafter AI20) to which we refer for full details.

PJ083+11 and PJ344-02 were initially selected as point-like dropout sources in the Pan-STARRS1 (PS1) survey among a few million candidates following and expanding the selection via the Lyman-Break technique (see Sect. 2.2.1) by Mazzucchelli et al. (2017b) to focus on the redshift range  $6.3 \leq z \leq 7.1$ . A cross-match among various catalogs allowed us to clear out contaminants (MLT dwarfs, and elliptical galaxies at  $z \approx 1 - 2$ ) and already known quasars from the candidate list. Secondly, AI20 collected publicly-available NIR/MIR photometric data from the DELS, UKIDSS, UHS, VHS surveys, and unWISE

catalog (Schlafly et al., 2019). This information were complemented with NIR photometric observations that I obtained using the SofI infrared spectrograph and imaging camera (Moorwood et al., 1998), and EFOSC2 (ESO Faint Object Spectrograph and Camera v.2; Buzzoni et al., 1984) mounted on the ESO/NTT at the La Silla Observatory. By combining all the photometric data, AI20 modeled the SEDs of the candidates. In Fig. 2.8 we show SED fit results suggesting the quasar nature of these sources (see, AI20 for full details on the data reduction and analysis). As a result, PJ083+11 and PJ344-02 were included in the final quasar candidate list that comprises a hundred of objects. In order to finally assess the quasar nature and to determine the precise redshift of the objects, we performed several spectroscopic campaigns by using the Folded-port Infrared Echellette (FIRE Simcoe et al., 2013) on the 6.5-m *Magellan BADE Telescope* located at the Las Campanas Observatory (Chile), and the Gemini NIR Spectrograph (GNIRS) at the 8.1-m *Gemini North Telescope* during 2019. In Fig. 2.9 we report the spectra of the sources. The current low-S/N spectrum of PJ344-02 is not sufficient to study the emission line and BH properties and the detailed analysis of this object will be report in a future paper (Andika et al., in prep.). In the following we therefore briefly discuss the characteristics of PJ083+11 only.

Fig. 2.9 immediately shows that the spectrum of PJ083+11 is deprived of strong emission lines, with the only exception of the MgII line. The Ly- $\alpha$  appears weak while CIV line is not detected at all. From MgII, AI20 inferred a SE virial BH mass (Vestergaard & Osmer, 2009) of  $\log(M_{\text{BH}}/M_{\odot}) = 9.30^{+0.16}_{-0.10}$ , and a Eddington ratio of  $L_{\text{bol}}/L_{\text{Edd}} = 0.51^{+0.13}_{-0.17}$ , where  $L_{\text{bol}}$  is the bolometric luminosity estimated via the bolometric correction  $L_{\text{bol}} = 5.15 \lambda L_{\lambda}(3000 \text{ \AA}) \text{ erg s}^{-1}$  (Richards et al., 2006). These values place PJ083+11 in the typical parameter space of other  $z > 5.7$  quasars at similar luminosity (see Fig. 2.10).

The properties of the broad emission lines in the spectrum of PJ083+11 suggest that this quasar can be classified as weak emission line quasar (WLQ). These are rare quasars that were originally investigated by Diamond-Stanic et al. (2009) in the SDSS survey. WLQs are characterized by exceptionally weak UV broad emission line relative to typical Type-1 AGN, on the basis of their equivalent width  $\text{EW}(\text{Ly}\alpha 1216 \text{ \AA} + \text{NV} 1240 \text{ \AA})_{\text{rest}} < 15.4 \text{ \AA}$ , and/or  $\text{EW}(\text{CIV} 1549 \text{ \AA})_{\text{rest}} < 10 \text{ \AA}$ . However, the nature of WLQs are still debated. Plotkin et al. (2015) proposed that the BLR of WLQs could be less photoionized either due to extremely high accretion rate (Leighly et al., 2007a,b),

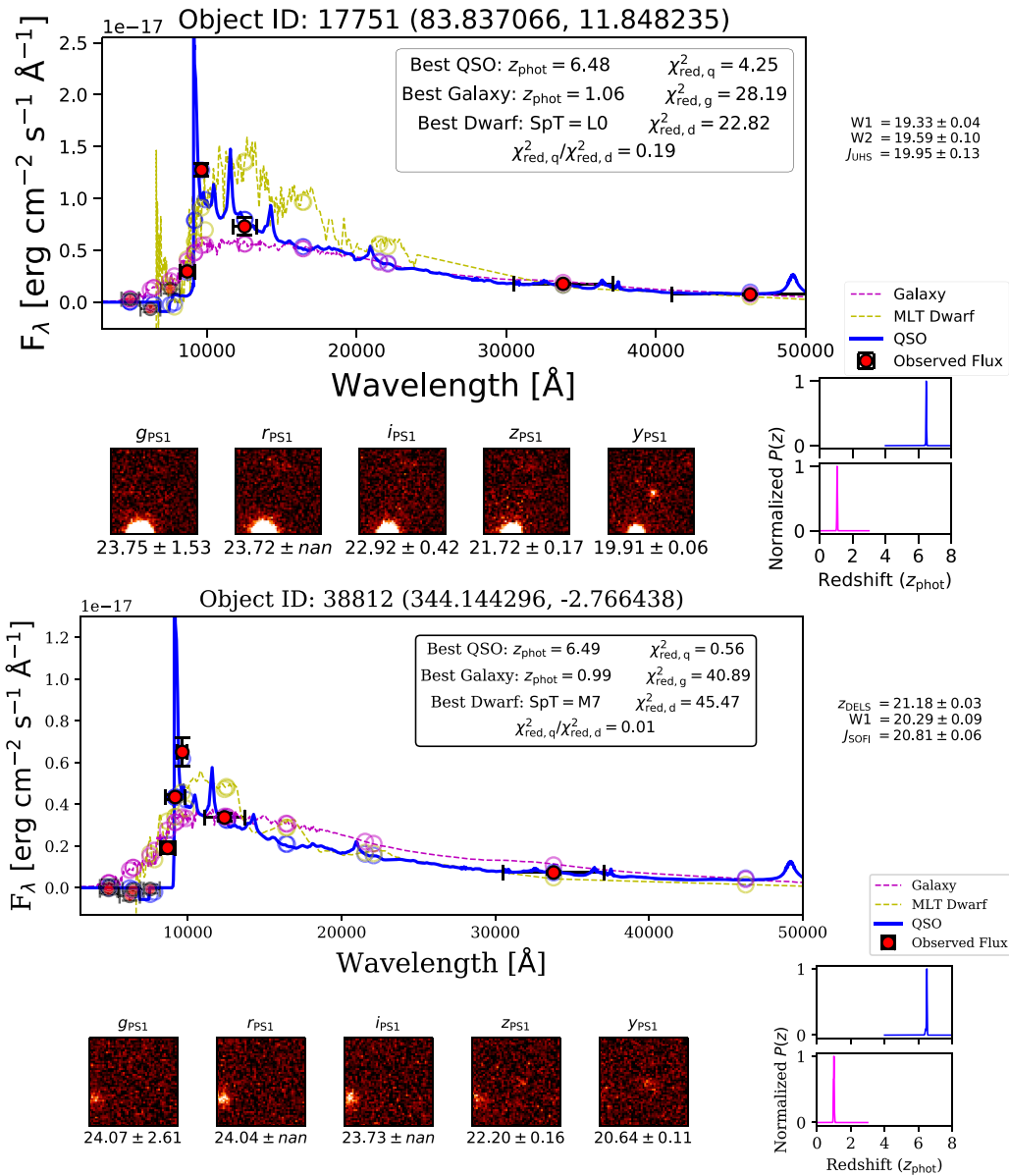


**Figure 2.8**

SED fitting results for PJ083+11 (*top panel*) and PJ344-02 (*bottom panel*). Photometric data are shown with red filled circles. The colored lines show the best fit spectral templates: the blue line for quasar, the magenta line for galaxy, and the yellow line for MLT dwarf model (see Andika et al., 2020, for details). Fit statistics are also reported. Bottom panels of each figure show 12'' postage stamps in five PS1 bands and source AB magnitudes. Other magnitude values from different surveys are also reported on the right. Bottom right panels show the probability density function of the photometric redshift ( $z_{\text{phot}}$ ) for quasar (in blue) and galaxy model (in magenta). Figure adapted from Andika et al. (2020).

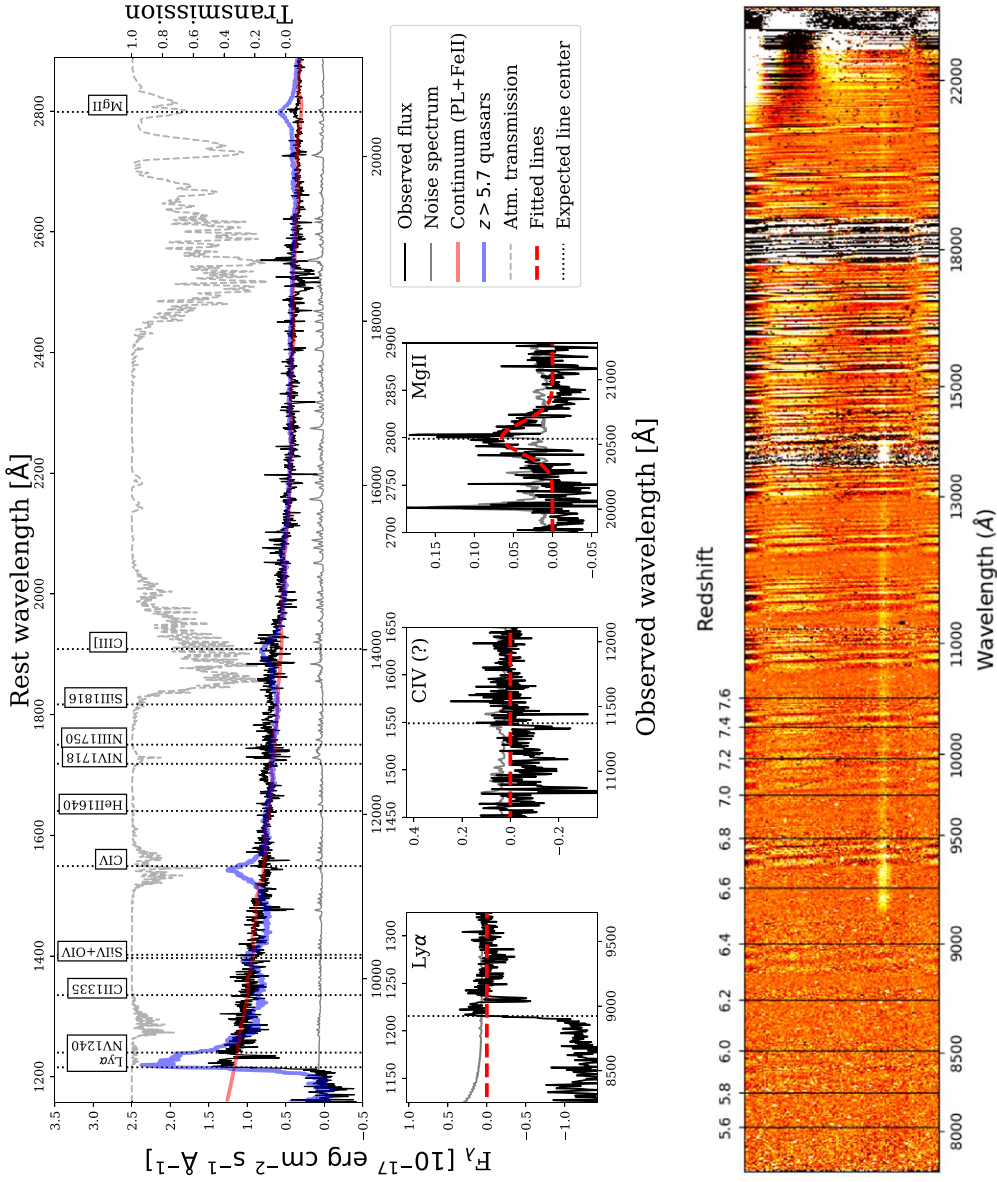


**Figure 2.9**

*Top panel:* spectrum of PJ083+11 obtained with Gemini/GNIRS. The observed flux is the black line while the noise is reported in gray. The gray dashed line shows the scaled atmospheric transmission (right axis). The red line is the best-fit continuum model consisting of a power law plus a FeII emission line. Vertical lines report the expected wavelength of various emission lines. The blue line shows the median continuum-subtracted spectrum around the Ly- $\alpha$ , CIV and MgII line. The line best-fit models are also reported in red. *Bottom panel:* two-dimensional spectrum of PJ344-02 taken with Magellan/FIRE. A strong Ly- $\alpha$  break is evident around 9100  $\text{\AA}$  (observed-frame). This places this object approximately at  $z \approx 6.5$ . Figure adapted from Andika et al. (2020).

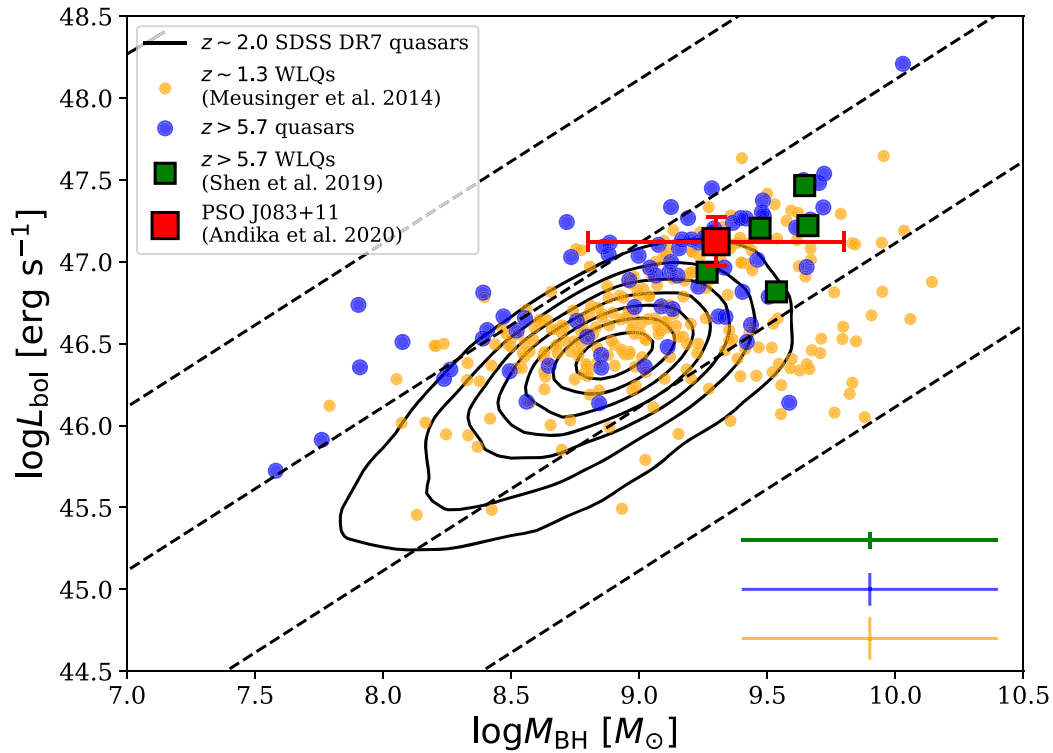


**Figure 2.10**

BH mass-bolometric luminosity plane of quasars. The magenta circles are  $z \sim 1.3$  WLQs from Meusinger & Balafkan (2014), the green squares are  $z > 5.7$  WLQs from Shen et al. (2019a), and the blue circles are other  $z > 5.7$  from the literature (see Andika et al., 2020, and references therein). The black contours show the distribution of SDSS  $z \sim 2$  quasars (Shen et al., 2011). The typical uncertainties for each samples are shown in the bottom right corner. The red square is the measurement for PJ083+11. The black dashed lines indicate different Eddington ratio, respectively of 10, 1, 0.1, and 0.01 (from top left to bottom right). Figure from Andika et al. (2020).

or due to radiatively inefficient cold accretion disk with low accretion rate in very massive BH (Laor & Davis, 2011). Alternatively, the BLR in WLQs could be screened from high-energy photons due to a shielding component of the optically- and geometrically-thick inner accretion disk (the so-called “slim disk” model) in quasars with significantly high Eddington ratio (Wu et al., 2011; Luo et al., 2015; Ni et al., 2018). In the first scenario, the accretion mode leads to a less efficient production of high-energy photons possibly due to a quenched X-ray corona, or caused by the X-ray photons being trapped and advected directly into the BH thus preventing their diffusion out of the innermost region of the quasar. In this case, the continuum

source cannot significantly excite high-ionization potential lines such as CIV. However, PJ083+11 does not exhibit significantly higher Eddington ratio and luminosity with respect to other high- $z$  quasars (within the limitations related to SE virial BH mass estimate; see **Sect. 1.4.2**). This fact also disfavors the “slim disk” scenario. However, we cannot completely rule out the presence of a screening material due to the lack of X-ray spectroscopy for this source (Wu et al., 2011, 2012). Finally, the radiatively inefficient accretion scenario requires a critical mass of BH that is at least a factor of  $\sim 2$  higher than the measured BH mass in PJ083+11.

A different theory suggests that WLQs may have an “anemic” BLR with low amount of gas and/or with small covering factor (Shemmer et al., 2010; Nikołajuk & Walter, 2012), possibly because WLQs are in an early phase of accretion in which BLR has not yet fully formed (Hryniewicz et al., 2010; Meusinger & Balafkan, 2014). The time needed to form the BLR is estimated around  $\sim 10^3$  Myr (Hryniewicz et al., 2010). To test this scenario, AI20 inferred the lifetime of the quasar PJ083+11 from the size of its proximity zone (see **Sect. 1.2.5**). From the observed spectrum of PJ083+11 AI20 inferred a proximity zone size of  $R_p = 1.17 \pm 0.32$  pMpc, corresponding to a quasar lifetime of  $t_Q = 10^{3.4 \pm 0.7}$  yr. This value is consistent with the BLR formation time. As a comparison, the proximity zone sizes of quasars with  $-27.5 \lesssim M_{1450} \lesssim -26.5$  are  $R_p = 3 - 7$  pMpc, corresponding to typical lifetimes of  $t_Q = 10^{5-6}$  yr (Eilers et al., 2017). However, as pointed out by Eilers et al. (2018a), the estimation of  $t_Q$  from the proximity zone size, should be considered a lower limit of the quasar lifetime. Quasars could have experienced an initial phase of heavily dust-enshrouded BH accretion in which UV radiation was significantly attenuated by the obscuring material for a period of  $\sim 10^3 - 10^4$  yr (see also, Hopkins et al. 2005; DiPompeo et al. 2017; Mitra et al. 2018; we return to this point in **Sect. 3.6**).

## 2.5 The discovery of the most distant radio-loud quasar at $z = 6.82$

In this section we report the discovery and characterization of PSO J172.3556+18.7734 (hereafter PJ172+18) at  $z = 6.82$ , the most distant RL (“jetted”) quasar currently known. The following discussion is drawn from Bañados

et al. (2021, hereafter BE21), to which we refer for full details.

RL quasars appear to be a rare phenomenon or at least, associated with short-lived phase of galaxy evolution. To date, the number of known quasars that are powerful radio emitters is estimated to be  $\sim 10\%$  of all quasars. This fraction is almost invariant with the redshift up to  $z \sim 6$  (e.g., Bañados et al. 2015b; Yang et al. 2016b; Shen et al. 2019a; but see also, Jiang et al. 2007b; Kratzer & Richards 2015). Among the currently  $\sim 200$  known quasars at  $z > 6$ , only three have been classified as RL (see, McGreer et al., 2006; Stern et al., 2007; Belladitta et al., 2020; Willott et al., 2010b), while the highest redshift radio galaxy is at  $z = 5.7$  (Saxena et al., 2018), with the previous redshift record at  $z = 5.2$  (van Breugel et al., 1999).

PJ172+18 was initially selected as  $z$ -dropout RL candidates in Bañados et al. (2015b). This source was selected by searching for red ( $z_{P1} - y_{P1} > 1.4$ ) objects in the PS1 catalog with a counterpart in the radio survey FIRST, thus avoiding most of the L- and T-dwarfs contaminants (see, Bañados et al., 2015b, for full details). PJ172+18 was also independently selected by cross-matching the PS1 and DECaLS catalogs as a promising  $z \gtrsim 6.5$  quasar candidate. MIR photometric data for this object were also retrieved from WISE DECaLS matched photometry. We finally spectroscopically confirmed PJ172+18 as  $z \sim 6.82$  quasar on 2019 January 12 using FIRE spectrograph at the *Magellan BADE Telescope*. However, the poor S/N of the spectrum did not allow us to unequivocally identify PJ172+18 as the *most* distant RL quasar known to date. For this reason, a number of follow-up observations were executed. We obtained *JHK* photometry using the NOTCam instrument mounted at the *Nordic Optical Telescope* (Djupvik & Andersen, 2010) at the Roque de Los Muchachos Observatory. We also obtained three follow-up spectra of PJ172+18 using the Near-Infrared Echellette Spectrometer (NIREs; Wilson et al., 2004) at the *Keck Telescope* on 2019 February 18. We also targeted the object with the VLT/X-Shooter spectrograph (Vernet et al., 2011), and with the *Large Binocular Telescope* (LBT) using the Multi-Object Double Spectrographs (MODS; Pogge et al., 2010) in March to June 2019. **Fig. 2.11** shows the final spectrum of the source (see, Bañados et al. 2021 for full details on the data processing). Finally, on 2019 March 5 and 11 we carried out radio-frequency observations with the NRAO/VLA in bands S (2–4 GHz) and L (1–2 GHz). In **Fig. 2.12** we show radio VLA observations and optical NIR images. Follow-up VLA observations reveal PJ172+18 as

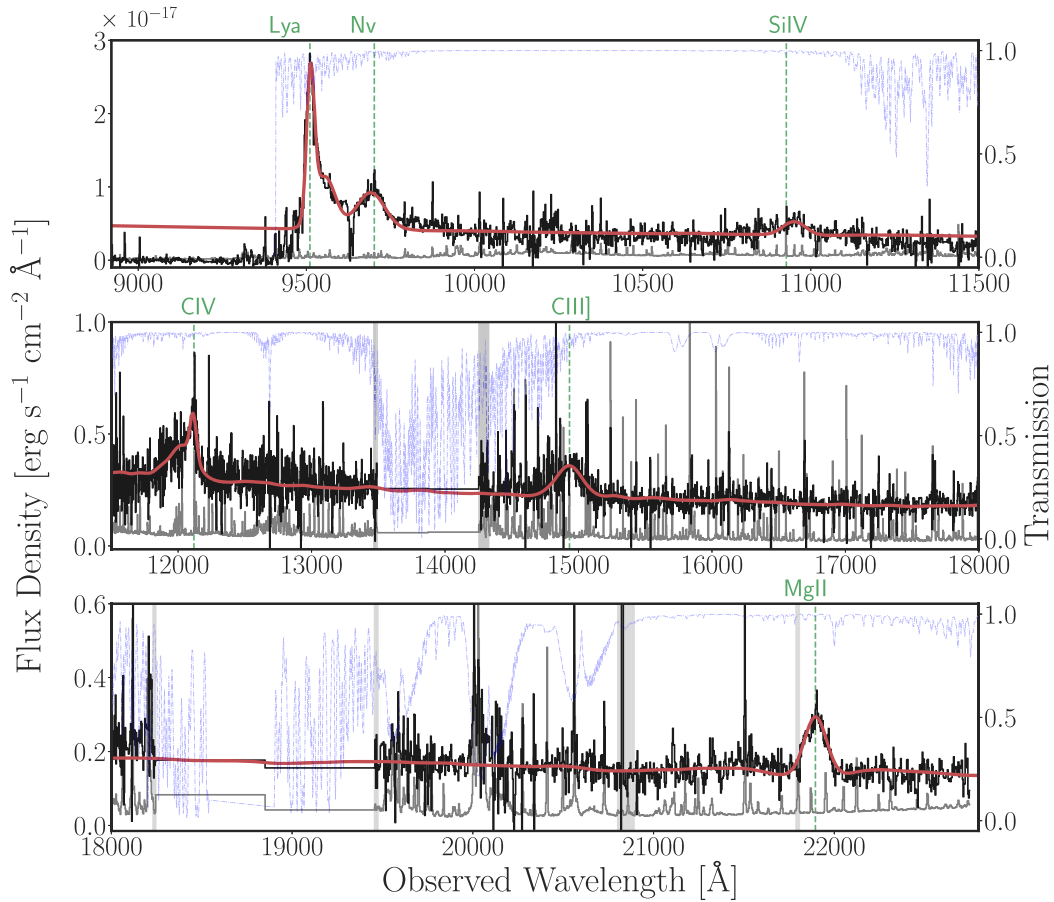


**Figure 2.11**

The combined *Keck*/NIRES, *VLT*/X-Shooter, and *LBT*/MODS optical/NIR spectrum of PJ172+18. The black line is the observed signal, the red line is the total spectral fit consisting in a power law continuum plus a Balmer and FeII pseudo-continua. Emission lines were modeled with multiple Gaussians (see, Bañados et al., 2021, and references therein). Vertical green lines indicate the location of the main emission lines. The noise is reported with the gray line, while atmospheric transmission (right axis) is the purple dashed line. The gray vertical bands are regions with high noise and/or absorption features, and were excluded in the fit. Figure from Bañados et al. (2021).

a point-like source (smaller than  $1''.9 \times 0''.87$ ) with  $S/N > 20$  in both the L- and S-band. Noticeably, the L-band flux density in the follow-up observations is a factor  $\sim 2$  smaller than that reported in the previous FIRST detection. In addition these radio observations revealed the presence of a secondary source at north-west with respect to the position of the quasar. Interestingly, despite this serendipitous source is slightly brighter than the quasar at 1.4 GHz, it was not revealed in the previous FIRST image. BE21 exclude that this source

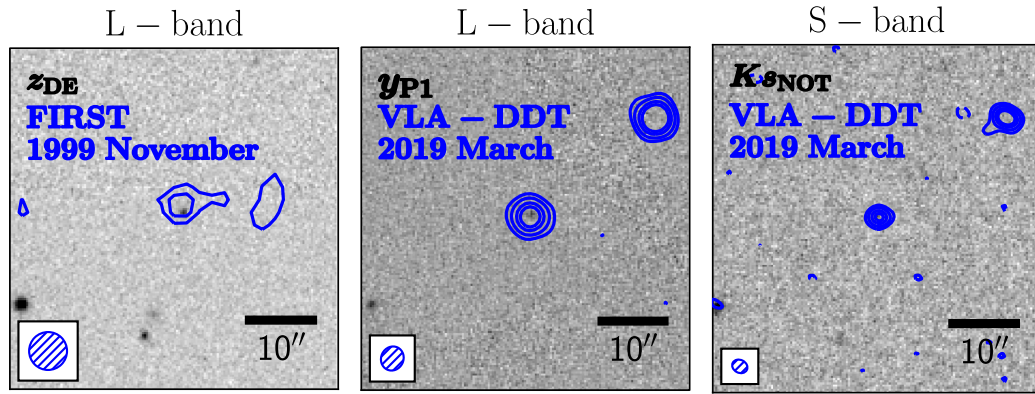


**Figure 2.12**

Radio VLA L- and S-band observations (blue contours) of PJ172+18 overlaid to optical/NIR images from DECaLS ( $z$ -band, *left panel*), PS1 ( $y$ -band, *central panel*), and NOT observations ( $K_s$ -band, *right panel*). Contours are  $[3, 5]\sigma$  for FIRST archival image (*left panel*), and  $[3, 7, 14, 21]\sigma$  for VLA-DDT (Director’s Discretionary Time) images. Negative contours are reported with dashed lines. Follow-up observations reveal the presence of a secondary source at north-west with respect to the position of the quasar undetected in the previous FIRST image. Figure from Bañados et al. (2021).

could be a hot spot of the radio jet expanding over the last  $\sim 20$  yr between the two observations, and therefore they suggest that the source can be a dust-obscured radio-AGN companion to the quasar. However, the second radio source could lie at different redshift than that of the quasar. More follow-up observations are needed to establish the nature of such object.

The MgII-based redshift of PJ172+18 is  $z = 6.823$ . Its spectrum is characterized by strong and narrow Ly- $\alpha$  and NV emission lines. The derived EW of Ly- $\alpha$  + NV is  $\sim 56 \text{ \AA}$  is consistent with the mean EW(Ly- $\alpha$  + NV) distribution of  $3 < z < 5$ , and  $z > 5.6$  quasars (Diamond-Stanic et al., 2009; Bañados et al., 2016). The CIV equivalent width is  $\text{EW}(\text{CIV}) = 21.3^{+2.4}_{-2.0}$ , and is blueshifted with respect to the MgII line of  $\Delta v_{\text{MgII-CIV}} = 195 \pm 225 \text{ km s}^{-1}$ . These values are in line with the SDSS RL quasars at  $z \sim 2$ . These objects occupy a specific region of CIV EW–blueshift parameter ( $\lesssim 1000 \text{ km s}^{-1}$ ). However, further investigations are needed in order to understand if these properties are informative of (e.g.) the physical properties of the BLR and/or the BH accretion mode of the RL quasars.

BE21 estimated for PJ172+18 a BH mass (via SE relation of Vestergaard & Osmer, 2009) of  $M_{\text{BH}} = 2.9^{+0.7}_{-0.6} \times 10^8 M_{\odot}$ , and an Eddington ratio of

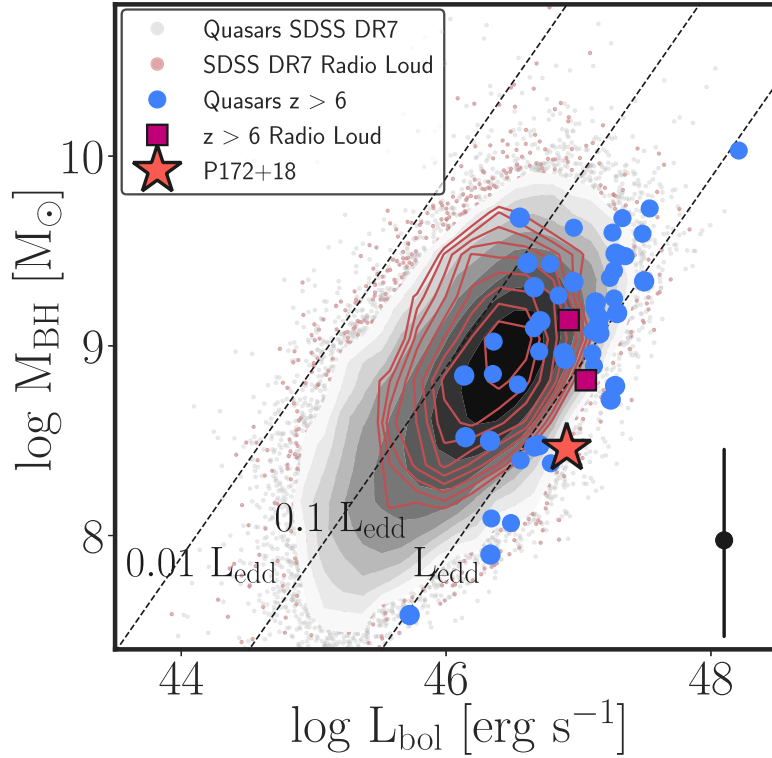


**Figure 2.13**

BH mass-bolometric luminosity plane. The gray points and the black contours show the distribution of SDSS DR7 (Data Release 7) quasars at  $0.35 < z < 2.25$ . The red points and contours are the RL quasars. The blue circles and the red squares are, respectively, RQ and RL  $z > 6$  quasars from literature (see, Bañados et al., 2021, and references therein). PJ172+18 (red star) is consistent with a BH accreting at super-Eddington rate. The typical uncertainty on BH measurements is reported with a bar at the bottom right corner. The latter is dominated by systematic bias on SE virial relation. Figure from Bañados et al. (2021).

$L_{\text{bol}}/L_{\text{Edd}} = 2.2^{+0.6}_{-0.4}$  using the bolometric correction from Richards et al. (2006). In Fig. 2.13 we report  $M_{\text{BH}} - L_{\text{bol}}$  distribution for PJ172+18 as well as other  $z > 6$ , and  $0.35 < z < 2.25$  quasars from SDSS for which BE21 estimated BH masses and bolometric luminosities in a consistent way. The measurements for PJ172+18 are consistent with super-Eddington accretion mode placing this object among the fastest accreting BHs at any redshift.

The estimation of the PJ172+18 proximity zone size of  $R_p = 6.31 \pm 0.76$  pMpc places this object within the top quintile of the distribution of quasar proximity zones at  $z \gtrsim 6$  (Eilers et al., 2017). The resulting quasar lifetime exceeds the average time during which the high- $z$  quasars are luminous in

the UV ( $\langle t_Q \rangle \sim 10^6$  yr, Eilers et al. 2020). In addition, the proximity zone size of PJ172+18 is considerably larger than the expected value at  $z = 6.8$  predicted from the redshift evolution of  $R_p$  studied by Venemans et al. (2015,  $\langle R_p \rangle_{z=6.8} \approx 2.2$  pMpc), and Eilers et al. (2017,  $\langle R_p \rangle_{z=6.8} \approx 4.2$  pMpc). The large proximity zone observed in PJ172+18 could be explained if PJ172+18 was more luminous in a recent past and it is currently observed to be in a receding phase.

The aforementioned scenario is further supported by the significant ( $\geq 3\sigma$ ) discrepancy between the observed flux density  $f_{1.52\text{GHz}} = 510 \pm 15 \mu\text{Jy}$  in the L-band VLA follow-up observations, and the previous detection reported in the FIRST catalog. This difference suggests that PJ172+18 could have experienced a variability over the last  $\sim 20$  yr ( $\sim 2.5$  yr rest frame, see also Nyland et al. 2020). However, since the observed  $f_{1.52\text{GHz}}$  is just below the faint limit of the FIRST survey, the observed variation could also be ascribable to noise fluctuations in the FIRST data. Assuming a power law radio SED ( $f_\nu \propto \nu^\alpha$ ), our L- and S-band measurements correspond to a power-law slope of  $\alpha_L^S = -1.31 \pm 0.08$ , steeper than  $\alpha = -0.75$ , typically assumed in high-redshift studies (e.g., Wang et al., 2007; Momjian et al., 2014; Bañados et al., 2015a). BE21 estimated the radio-loudness parameter (that is the radio-to-optical flux density ratio,  $R_{4400} = f_{5\text{GHz}}/f_{4400\text{\AA}}$ ; see, Kellermann et al. 1989) by extrapolating the rest-frame 5-GHz radio emission using the measured spectral index  $\alpha_L^S$ , and the rest-frame 4400 Å flux density using the power-law fit to the NIR spectrum. This yields a  $R_{4400} = 70 \pm 7$ , thus classifying PJ172+18 as RL quasar (see, e.g., Bañados et al., 2015a).

# 3

## The early black hole–galaxy coevolution

” *The evolution of the Universe can be likened to a display of fireworks that has just ended: some few red wisps, ashes, and smoke. Standing on a well-chilled cinder, we see the fading of the suns and try to recall the vanished brilliance of the origin of the worlds.*

— **Georges Lemaître**

The discovery of the first AGN and quasars in the seminal works by Seyfert (1943), Schmidt (1963), and Sandage (1965) dates back to more than half century ago. However, the true relevance of AGN in galaxy evolution became evident only several decades later. The extensive multiwavelength surveys of the subsequent years revealed that powerful AGN represents only the tip of the iceberg. Low activity is ubiquitously found in local early-type galaxies, revealing that AGN can be considered not just a dramatic rare phenomenon, but rather a fundamental part of the lifecycle of a typical galaxy. Observations over the past decades suggest that supermassive BHs reside at the center of virtually all massive galaxies. The growth of such massive BHs pairs with the star formation in the hosts, thus constraining their final stellar mass. This interplay is thought to drives a closely linked (co-)evolution between BHs and galaxies across the cosmic time.

## 3.1 An overview of the galaxy population

Since the beginning, astronomers studied various galaxy properties in the hope to shed light on their origin. While a complete review of this topic is beyond the scope of this thesis, I will highlight here a few observational milestones for our understanding of galaxy evolution.

The first galaxy classification was made in the late 1936 by Edwin Hubble (the so-called “Hubble Tuning Fork”). His diagram was originally thought as an evolutionary sequence from “early-type” galaxies (ellipticals and lenticular) to “late-type” galaxies (normal and barred spirals). Thanks to the tremendous advances in observational and theoretical astronomy over the last century, today we know that the Hubble sequence is not correct (albeit the early- and late-type terms are still used) and it merely relies on galaxy morphology. Results from the SDSS survey in the first decade of 2000s, have provided homogeneous spectroscopy of millions of galaxies in the local Universe, revealing that galaxies define a bimodal distribution in the color-magnitude diagram (Strateva et al., 2001; Kauffmann et al., 2003a; Blanton et al., 2003; Baldry et al., 2004). A “blue-cloud” is populated by disk-dominated late-Hubble-type galaxies with significant ongoing star formation (blue colors), low stellar mass density, which tend to show small stellar mass ( $M_{\star}$ ). In addition, a “red-sequence” in the color-magnitude plane consists of bulge-dominated early-Hubble-type galaxies with little star-formation activity (red colors), high stellar mass density, which generally exhibit larger  $M_{\star}$ . However, the two population are not sharply separated. By capitalizing on the progresses in multiwavelength observations, subsequent works have then showed that the SFR of star-forming galaxies strongly depends on  $M_{\star}$  (e.g., Brinchmann & Ellis, 2000; Brinchmann et al., 2004; Bell et al., 2005; Juneau et al., 2005; Schiminovich et al., 2007, see Fig. 3.1). This correlation is known as “star-forming main sequence”. Galaxies with significantly high star-formation activity at given stellar mass lie above the main sequence and are dubbed as *starburst galaxies*. In addition, red “passive” galaxies with low star-formation activity populate the SFR– $M_{\star}$  diagram below the main sequence.

Over the past few years, substantial efforts have been invested in characterizing the galaxy populations out to the contemporary Universe. These studies have established that the qualitative distribution shown in Fig. 3.1 also characterizes galaxies out to at least  $z \lesssim 2$  (e.g., Daddi et al., 2007;

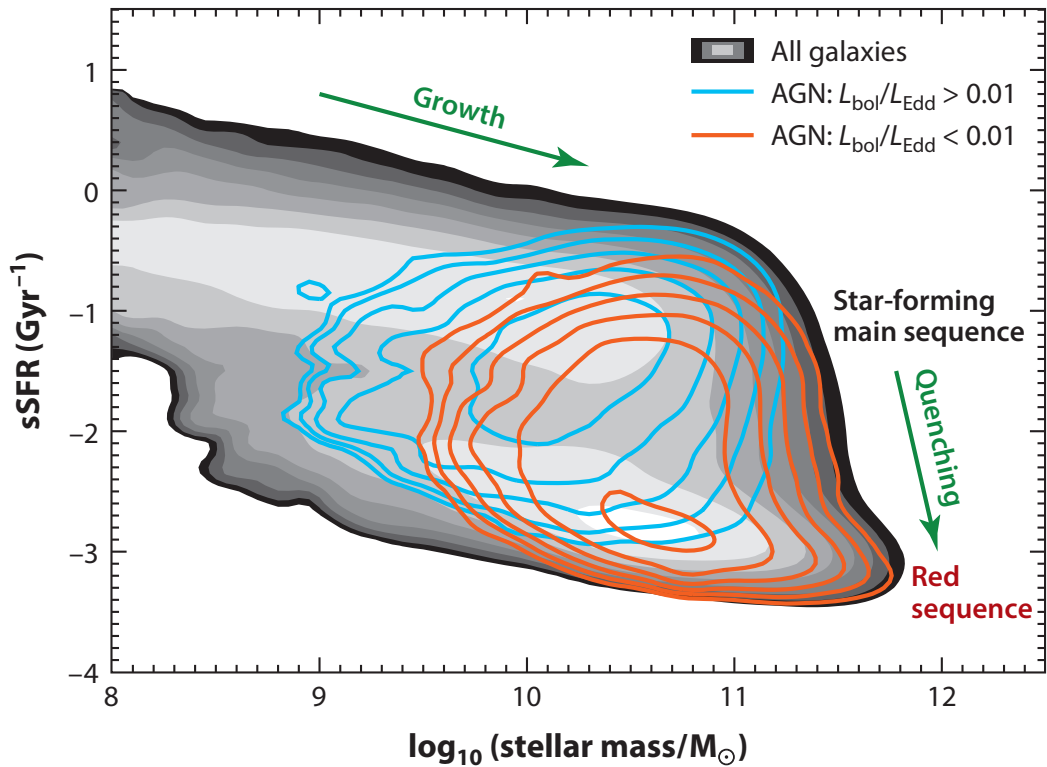


**Figure 3.1**

Distribution of galaxies of the SDSS sample in the  $s\text{SFR} - M_*$  plane. The gray area shows the volume-weighted distribution of all galaxies. Blue and red contours are the volume-weighted distribution of AGN with high ( $> 1\%$ ; mostly radiative-mode), and low ( $< 1\%$ ; mostly jet-mode) Eddington ratio, respectively. The scale gray colors and contours are increasingly spaced by a factor of two. Figure from Heckman & Best (2014).

Rodighiero et al., 2010, 2011; Whitaker et al., 2012), with the specific star-formation rate ( $s\text{SFR} = \text{SFR}/M_*$ ) that strongly evolves with time (Elbaz et al., 2011). In particular, for the galaxies on the main sequence at a given  $M_*$ , the  $s\text{SFR}$  increases by a factor  $\approx 20$  from  $z = 0$ , to  $z \simeq 2$  (Rodighiero et al., 2011; Sargent et al., 2012). According to a rough picture of the galaxy evolutionary scenario (e.g., Faber et al., 2007; Lilly et al., 2013), steady star-formation can carry a galaxy along the main sequence increasing its mass primarily via the accretion of cold gas from the cosmic web and secondarily through mergers with other galaxies. As a galaxy approaches a critical mass, various mechanisms are able to halt the star formation and to push galaxies off from the main sequence leading to the migration from the “blue” to the “red” population. However, the physical process(es) responsible for

the galaxy quenching are still debated. A possibility is that the suppression of the star-formation may involve a change in the nature of accretion (e.g., Dekel et al., 2009): as galaxies build up their mass, they form a halo of hot ( $> 10^6$  K) plasma against which cold streams of infalling material are shock-heated thus further accreting the halo instead of reaching the cold ISM where stars form. However, numerical and semianalytic models need to include additional processes in order to reproduce the observed properties of massive galaxies (see, Somerville & Davé, 2015, for a review). A popular idea is that AGN are able to profoundly affect the evolution of massive galaxies by heating and/or ejecting the surrounding gas, thus preventing galaxies from forming a significant amount of stars. These processes are dubbed as “AGN feedback” (see Sect. 3.5). In the hope of studying how galaxies halt their star formation, astronomers have focused on the so-called “green valley”, the region where the tails of the red sequence and the blue cloud overlap. This part of the diagram is composed by a relatively fast transitional population of galaxies as implied by their lower number – otherwise a bimodality would not be observed (e.g., Faber et al., 2007; Schawinski et al., 2010; Mendez et al., 2011; Gonçalves et al., 2012). Remarkably, these studies revealed that the AGN fraction of the green valley population is statistically higher compared to galaxies placed in the other populations.

## 3.2 The luminosity and stellar mass function of galaxies

As seen for quasars (see Sect. 2.2.3), the galaxy LF describes how galaxies are distributed depending on their luminosity. Specifically, observations in the local and high- $z$  Universe (e.g., Trentham & Tully 2002; Trentham & Hodgkin 2002; Trentham et al. 2005; Reddy & Steidel 2009; Cucciati et al. 2012; Gruppioni et al. 2013; Bouwens et al. 2015; see also Madau & Dickinson 2014, for a review) show that the number density of galaxies with luminosity between  $L$  and  $L + dL$ , within a comoving volume element of the Universe,  $\Phi(L) dL$ , is globally described by a Schechter function (Schechter, 1976; Binggeli et al., 1988):

$$\Phi(L) = \left(\frac{\Phi^*}{L^*}\right) \left(\frac{L}{L^*}\right)^\alpha \exp(-L/L^*), \quad (3.1)$$

where  $\Phi^*$  is a normalization factor,  $\alpha$  is the slope at the faint end, and  $L^*$  determines the luminosity cut-off over which the LF drops exponentially. This means that, at a given redshift, low-luminosity galaxies are more numerous than brighter ones, and the extremely bright galaxies are rare. Since the total luminosity of a galaxy is proportional to the stellar mass, from the knowledge of the galaxy LF one can derive the galaxy stellar mass function (MF). The MF is typically described by one or two Schechter functions (see, e.g., Baldry et al., 2012; Madau & Dickinson, 2014; Weigel et al., 2016). Explaining Eq. (3.1) from a theoretical standpoint is far from trivial. DM halos are predicted to form hierarchically: small halos form earlier and then they aggregate into progressively larger system (Press & Schechter, 1974; Sheth & Tormen, 1999). Within the halos, the baryonic matter collapses leading to the formation of a rotationally-supported-disk protogalaxy. Massive ellipticals then form as subsequent (major) mergers of disk galaxies. Since the baryonic matter is coupled with the DM, one would expect some similarities between the theoretical prediction of the DM halo MF from simulations and that observed for galaxies in the local Universe. In particular, if baryonic matter behaves as DM, the galaxy MF would be that of the DM halos scaled by the universal baryon fraction ( $f_b = 0.163$ ; Hinshaw et al., 2013). However, contrary to the DM, the baryonic gas is strongly affected by radiative cooling during its collapse, and this process has different effects depending on the mass (e.g., Cole, 1991). Furthermore, baryonic matter is susceptible to interactions with radiation in the form of radiative pressure or winds. For these reasons, the shape of the two MFs differs, especially at the low- and high-mass end (see Fig. 3.2).

Simulations have shown that without any form of energy input, the (cold) gas accretion (Kereš et al., 2005; Dekel et al., 2009) can be very efficient, thus leading to the formation of galaxies with an unrealistic high baryon fraction (e.g., Rees & Ostriker, 1977; Dekel & Birnboim, 2006; Behroozi et al., 2013). The lack of low-mass galaxies (i.e., the *missing satellites problem*; see, e.g., Kauffmann et al. 1993; Klypin et al. 1999), and the steep decline of the high-mass end of the galaxy MF require efficient process(es) that are able to slowdown or completely cease the accretion flow and quench the star formation in the majority of the smaller and bigger DM halos. Theoretical models suggest that SNe can be efficient in heating and ejecting gas and dust away from low-mass galaxies in their shallow DM gravitational potential.

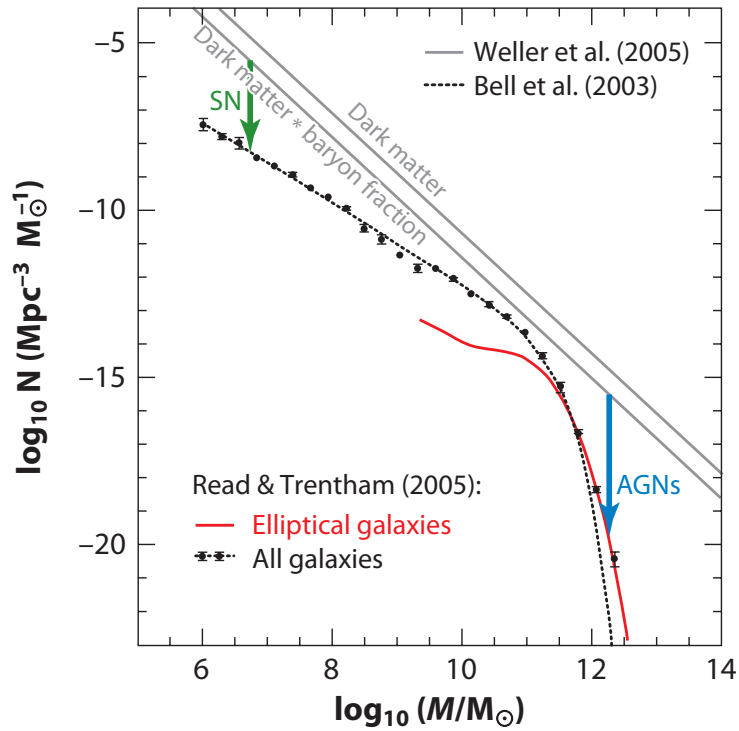


**Figure 3.2**

Comparison between the observed galaxy MF in the local Universe (Bell et al., 2005), and the DM halos MF predicted by simulations (Weller et al., 2005). The latter, multiplied by the universal baryonic fraction determines the maximum possible galaxy stellar mass content as function of the halo mass (see main text). SNe (green arrow), and AGN feedback (blue arrow) are able to reduce the star-formation efficiency in galaxies, thus giving rise to the observed discrepancies at the low- and high-mass end of the MFs. Figure from Kormendy & Ho (2013), adapted from Read & Trentham (2005).

In addition, young stars can also reduce the star-formation efficiency by photoionizing the surrounding IGM, and by photodissociating molecular gas in star-forming regions (see, e.g., Dekel & Silk, 1986; Benson et al., 2002a,b, and references therein). However, quenching star formation in massive halos requires a much more powerful mechanisms than the star-formation feedback. In this context, AGN feedback appears to provide the required energetic input (see Sect. 3.5). Indeed, it is now ubiquitously incorporated in (semi-)analytical models and hydrodynamical simulations of galaxy formation.

Other evidence suggest that the feedback mechanism play a key role during the galaxy evolution. Further studies of the galaxy MF (or LF) at different redshifts highlight that massive galaxies are in place earlier than the smaller

ones (e.g., Ilbert et al., 2010, 2013; Tomczak et al., 2014)<sup>1</sup>. This observational evidence, referred as *galaxy downsizing* (e.g., Cowie et al., 1996; Cattaneo et al., 2008), appears in contrast with the hierarchical build-up of galaxies. However, if SNe are effective in heating and sweeping out the gas in low-mass galaxies, they will also retard the growth of the BH in these galaxies with respect to the massive ones. Therefore, AGN feedback starts to be efficient earlier in more massive galaxies rapidly quenching their star formation. As a result, galaxies in the contemporary Universe have increasingly older stellar population and metallicity increasing the mass (i.e., they quickly move toward the “red sequence”; see Sect. 3.1), while low-mass galaxies show younger stellar populations due to the slowed star-formation caused by feedback from SNe (thus these galaxies linger in the “blue cloud”; see, e.g., Thomas et al. 2005).

### 3.3 BH–galaxy scaling relations

Correlations between the mass of central BHs and the properties of their host galaxies have first highlighted by Dressler (1989), Kormendy (1993), Kormendy & Richstone (1995), and Magorrian et al. (1998) using the earliest BH demographics. These studies revealed that  $M_{\text{BH}}$  is directly proportional to the luminosity of the bulge component of the host galaxy ( $L_{\text{bulge}}$ ). In the subsequent years, the  $M_{\text{BH}} - L_{\text{bulge}}$  correlation was further studied by using heterogeneous samples of galaxies (e.g., Ho, 1999; Laor, 2001; McLure & Jarvis, 2002; Marconi & Hunt, 2003; Häring & Rix, 2004; Ferrarese & Ford, 2005; Graham, 2007; Gültekin et al., 2009; Sani et al., 2011; Beifiori et al., 2012; McConnell & Ma, 2013). Since the  $L_{\text{bulge}}$  is proportional to the bulge stellar mass ( $M_{\text{bulge}}$ ), the  $M_{\text{BH}} - L_{\text{bulge}}$  relation implies a correlation between  $M_{\text{BH}}$  and  $M_{\text{bulge}}$ . Independent measurements of  $M_{\text{bulge}}$  are obtained using the virial theorem  $M_{\text{bulge}} \propto R_{50} \sigma_{\star}^2$  (where  $\sigma_{\star}$  is the bulge stellar velocity dispersion; see, e.g., Marconi & Hunt 2003), or from dynamical modeling (Magorrian et al., 1998; Häring & Rix, 2004). These studies consistently find an average BH-to-bulge mass ratio of  $\langle M_{\text{BH}}/M_{\text{bulge}} \rangle \approx 0.1 - 0.2\%$ , and a slope of  $M_{\text{BH}} - M_{\text{bulge}}$  relation varying from linear to steeper than linear ( $\simeq 1.5$ , e.g.,

<sup>1</sup>This evidence is also supported by studies on the redshift evolution of the mass-metallicity relation and the cosmic star formation history (see, e.g., Juneau et al., 2005; Mannucci et al., 2009; Thomas et al., 2010; Behroozi et al., 2013).

Häring & Rix 2004; Laor 2001). Alongside with the aforementioned results, a very tight correlation between  $M_{\text{BH}}$  and the velocity dispersion of stars within the galaxy bulge  $\sigma_{\star}$  ( $M_{\text{BH}} \propto \sigma_{\star}^{4-4.5}$ ) was independently found in the same years by Ferrarese & Merritt (2000) and Gebhardt et al. (2000). Remarkably, the scatter of such relation appeared to be primarily driven by observational errors only, thus revealing itself as a fundamental relationship between BHs and galaxies. Many other studies including a growing sample of BHs showed that the BH–galaxy correlations are also in place in other kind of objects such as AGN and global clusters (see, e.g., Merritt & Ferrarese 2001; Tremaine et al. 2002; Marconi & Hunt 2003; Ferrarese & Ford 2005; Wyithe 2006a,b; Hu 2008; Greene et al. 2010; Woo et al. 2010, 2013, 2015; Bennert et al. 2011a, 2015; Graham & Scott 2013; Ho & Kim 2014; Reines & Volonteri 2015; Läsker et al. 2016; Bentz & Manne-Nicholas 2018; Baron & Ménard 2019; Schutte et al. 2019), albeit with some controversies (see, Kormendy & Ho 2013, for a comprehensive review). **Fig. 3.3** shows the  $M_{\text{BH}} - M_{\text{bulge}}$  and  $M_{\text{BH}} - \sigma_{\star}$  correlations found respectively by Bennert et al. (2011a, left panel), and Woo et al. (2010, right panel) including samples of local inactive galaxies and AGN.

The discovery of BH–galaxy correlations in the local Universe currently represents one of most fundamental findings of the last two decades for the astrophysics of galaxies. These relations cannot be thought as the mere result of the gravitational balance between BH and galaxy given that the volume under the influence of BH is a small fraction of the total volume of the galaxy bulge ( $V_{\text{BH}} \sim 10^{-7} V_{\text{bulge}}$ ). Therefore, BH–galaxy correlations must be established by more complex mechanisms allowing BHs to communicate with their host galaxies at large scale (see **Sect. 3.5**).

## 3.4 BH-to-galaxy mass ratio at high redshift

The study of the BH–galaxy correlations beyond the local Universe is challenging due to large uncertainties affecting the measurements of BH and galaxy (bulge) stellar mass. As seen in **Sect. 1.4**, the BH mass estimate for AGN at high- $z$  relies on SE virial relations. In addition, in powerful AGN the huge luminosity from the central region severely affects the observation of

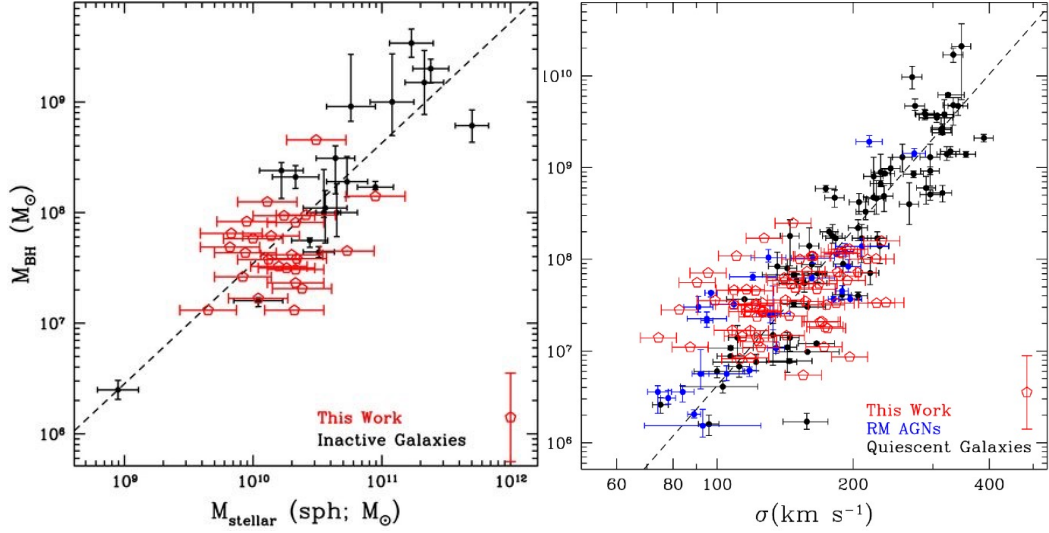


**Figure 3.3**

BH–galaxy scaling relations for local quiescent galaxies and AGN. *Left panel:*  $M_{\text{BH}} - M_{\text{bulge}}$  correlation. The red points are a sample of active galaxies from Bennert et al. (2011a), the black circles are data of inactive galaxies from Gültekin et al. (2009). The dashed line is the best-fit relation. *Right panel:*  $M_{\text{BH}} - \sigma_*$  relation. The red points are local active galaxies from Bennert et al. (2015), blue circles are reverberation-mapped AGN from Woo et al. (2015), and black points are quiescent galaxies from McConnell & Ma (2013). The black dashed line is the best-fit correlation. Figure adapted from Bennert et al. (2011a, left panel), and Bennert et al. (2015, right panel).

the starlight emission from the host galaxy. As a result, the measurements of galaxy stellar mass in high- $z$  AGN is very difficult with the current facilities. Deblending the starlight host galaxy emission from the AGN contribution is possible only for relatively nearby sources with low AGN-to-host galaxy brightness contrast (e.g., Kim et al., 2008; Bennert et al., 2010). At high redshifts only a handful of works attempted to perform instrumental point-spread function (PSF) decomposition by making use of either HST, or deep images from ground-based 8-m-class telescopes (e.g., Kukulka et al., 2001; Ridgway et al., 2001; McLeod & Bechtold, 2009; Targett et al., 2012; Marshall et al., 2020a). Alternatively, galaxy stellar masses at relatively high redshift have been measured by employing SED fitting decompositions taking into account the AGN and the galaxy component (e.g., Merloni et al., 2010; Bongiorno et al., 2014). However, this approach requires a number of assumptions on the galaxy SED template which depends on a large number of parameters that are difficult to be measured at high- $z$ . At the highest

redshifts the detection of the extended starlight emission around quasars is practically impossible (e.g., Mechtley et al., 2012; Decarli et al., 2019a; Marshall et al., 2020a), except for particular cases in which the quasar host galaxy is magnified due to gravitational lensing (e.g., Peng et al., 2006a), or the AGN obscuration along the line of sight creates a natural coronagraph (e.g., McLure et al., 2006; Sarria et al., 2010). However, even if the host galaxy is detected either from imaging or SED fitting, then the starlight luminosity has to be converted in mass. This requires some assumptions on the mass-to-light ratio, or the star-formation history (see, e.g., Jahnke et al., 2009; Bennert et al., 2010, 2011b; Decarli et al., 2010; Merloni et al., 2010; Sarria et al., 2010; Cisternas et al., 2011a; Schramm & Silverman, 2013). Notwithstanding the above limitations on  $M_{\text{BH}}$  and  $M_{\text{bulge}}$  measurements, several studies suggest that the zero point, and possibly the intrinsic scatter of the BH–galaxy relations may evolve with the redshift (Treu et al., 2004, 2007; Walter et al., 2004; McLure et al., 2006; Peng et al., 2006a,b; Shields et al., 2006; Woo et al., 2006, 2008; Ho, 2007; Bennert et al., 2010, 2011b; Decarli et al., 2010; Merloni et al., 2010; Wang et al., 2010; Canalizo et al., 2012; Targett et al., 2012; Bongiorno et al., 2014). In particular, at high- $z$ , galaxies appear to host more massive BHs than their local counterparts with similar stellar mass. This is shown in Fig. 3.4, where a collection of  $M_{\text{BH}}$  and  $M_{\text{bulge}}$  measurements of AGN up to  $z \simeq 7$  is compared to the local BH–galaxy relation. Published works introduced a parametrization of the BH-to-galaxy mass ratio in the form  $\Gamma = M_{\text{BH}}/M_{\text{bulge}} \propto (1+z)^\beta$ , with  $\beta$  in the range  $\beta \approx 0.7 - 2$ . These results suggest an “excess” in the BH mass by a factor of  $\gtrsim 4$  at  $z \approx 4 - 6$ . At face value, this trend suggests a scenario in which, during the competitive accretion of matter from the galactic halo that occurred at early epochs, the BH growth preceded that of the host galaxy (e.g., Decarli et al., 2010; Bongiorno et al., 2014; Wang et al., 2016). Based on results showed in Fig. 3.4, various considerations are worthy of note. At intermediate redshifts, the representative population of galaxies is composed by spiral disk galaxies (see Sect. 1.5) with lower-mass BHs ( $M_{\text{BH}} \approx 10^7 - 10^8 M_\odot$ ; e.g., Cisternas et al. 2011a,b; Schawinski et al. 2011; Kocevski et al. 2012; Treister et al. 2012; Böhm et al. 2013; Schramm & Silverman 2013). Some galaxies lie above the local  $M_{\text{BH}} - M_{\text{bulge}}$  relation if only the bulge is considered, but they align with the relation if one takes into account the *total* stellar mass. This suggests that galaxies might have

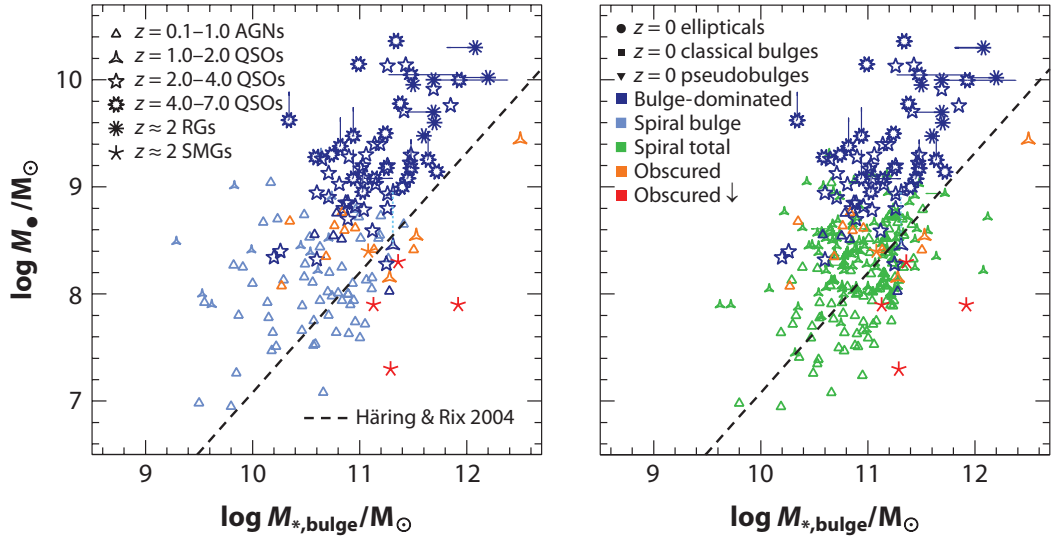


**Figure 3.4**

Correlations between  $M_{\text{BH}}$  and galaxy stellar mass of AGN at  $z \sim 0.1 - 7$ , for the bulge component only (*left panel*), and for the total galaxy mass (*right panel*). The dashed line shows the reference relation for local quiescent galaxies (Haring & Rix, 2004). The dark blue symbols are elliptical galaxies or object that are massive enough to be the progenitors of bulge-dominated galaxies by  $z \sim 0$ . The orange and the red symbols are dust-reddened or obscured quasars and AGN. They appeared to host undermassive BHs, with the most extreme cases represented by the SMGs. Less massive hosts are  $z \lesssim 2$  disk-like or spiral galaxies. Figure adapted from Kormendy & Ho (2013).

redistributed stars from the disk to the bulge, possibly via mergers or violent disk instabilities. In addition, the undermassive BHs in **Fig. 3.4** correspond to SMGs at  $z \approx 2$ . They are, similar to the ULIRGs, dusty gas-rich merger-in-progress galaxies, with a significant amount of star-formation activity, and host heavily obscured AGN (e.g., Tacconi et al., 2008). SMGs are not just run-of-the-mill, high- $z$  star-forming galaxies. The median stellar mass of these  $z \sim 2$  galaxies is  $\sim 2 \times 10^{11} M_{\odot}$  (e.g., Borys et al., 2005), reasonably compatible with being the precursors of the most  $z \sim 2$  quasars and likely of the present-day early-type massive galaxies (see, e.g., Alexander et al., 2008; Coppin et al., 2008; Carrera et al., 2011). Given the already substantial stellar masses observed in the SMGs, BHs in these galaxies have to find a mechanism to ends up with the reference  $M_{\text{BH}}/M_{\text{bulge}}$  value a  $z \sim 0$ . Such considerations warn against a simple interpretation of the  $M_{\text{BH}} - M_{\text{bulge}}$ . Critically, the aforementioned results might be affected by observational biases and instrumental limitations. The selection of host galaxies revealed

at high redshift is driven by the AGN luminosity, so that more massive black holes are preferably selected (Lauer et al., 2007; Vestergaard et al., 2008; Volonteri & Stark, 2011; Portinari et al., 2012; Schulze & Wisotzki, 2014; Volonteri & Reines, 2016). This could naturally lead to an oversampling of BHs that are too massive for their host galaxies, especially at increasing redshift. Another caveat to consider is that when the *total* galaxy mass is considered instead of just the bulge component, the observed evolution of  $M_{\text{BH}}/M_{\star}$  is significantly reduced (Fig. 3.4, right panel). However, whatever is the initial  $M_{\text{BH}}/M_{\star}$  distribution, there is evidence of the existence of a BH–galaxy correlation already at  $z \sim 6$ . Investigating the early BH–galaxy relation is therefore fundamental to explore the interplay between BH accretion and star formation activity, and to constrain, accordingly, galaxy formation and evolution models. Moreover, constraining the value of BH-to-galaxy mass ratio at early epochs is key to put constraints on models of the formation of the first supermassive BHs. In particular if DCBH is the primary mechanism of BH formation, as suggested by previous findings (see Sect. 2.1.2), one would expect an enhanced value of  $M_{\text{BH}}/M_{\star}$  at high- $z$ . The recent discovery of RL AGN at high- $z$  has paved the way to the study of the activation mechanism of AGN jets and their effect on the host galaxy at early epochs. Future studies will provide us with new key insights on the onset of BH–galaxy relation. The next chapter addresses the topic of the  $M_{\text{BH}}$ -host galaxy relation at high- $z$  by presenting our original work (Pensabene et al., 2020).

## 3.5 AGN feedback

As discussed in previous sections, AGN feedback is invoked as a mechanism to constrain the final stellar mass of galaxies and to explain the observed properties of galaxy populations. Moreover, the mere existence of the BH–galaxy correlations suggest that BHs evolve in close connection with their host galaxies. The various observational arguments presented so far naturally suggest that AGN feedback may play a key role during the galaxy evolution. The strict similarity of the history of BH growth and galaxy SFR (see Fig. 3.5) further supports this idea. These rates show a steep rise from  $z = 0$  to  $z \sim 1$ , and a maximum at  $z \sim 2 - 3$  where the quasar activity peaks and galaxies are most gas rich. Then, they decline relatively rapidly at higher redshifts. Remarkably, the ratio between the volume-averaged rates of BH

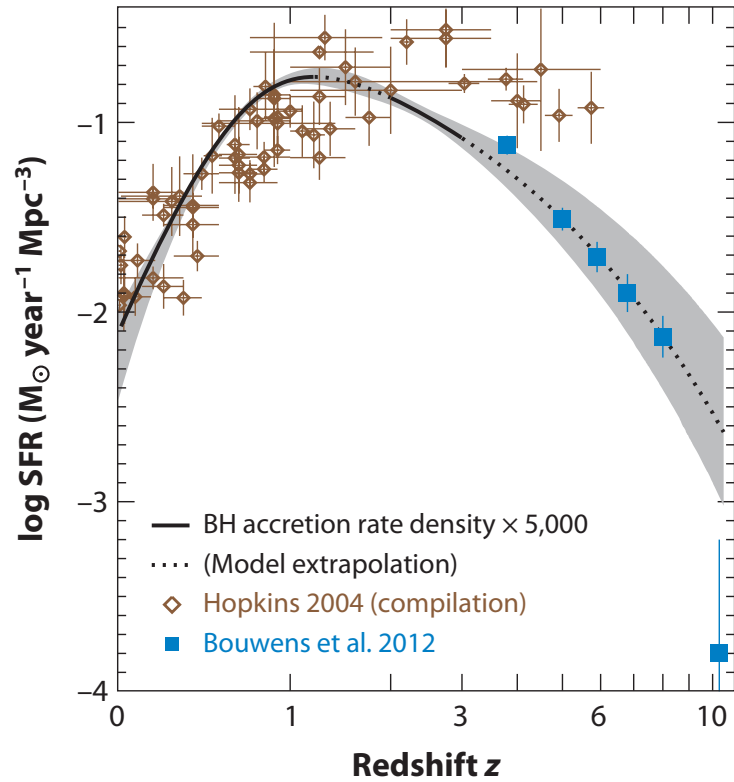


**Figure 3.5**

The volume density of BH accretion (black line and grey shaded area), and the star-formation rate (brown diamonds, Hopkins 2004; and blue squares from Bouwens et al. 2012). The BH accretion rate is scaled-up by a factor of 5000. This closely tracks the cosmic star-formation history. Figure from Kormendy & Ho (2013). Adapted and updated from Aird et al. (2010).

accretion and star formation seems to have remained always constantly close to the local reference value  $M_{\text{BH}}/M_{\text{bulge}} \sim 10^{-3}$ . This implies that: at least in a cosmological volume-averaged sense, the growth of galaxies and BHs is tightly linked. This paradigm is typically referred to as *BH-galaxy coevolution*.

Some implementations of AGN feedback are now routinely featured in models of galaxy formation and evolution (see, e.g., Granato et al. 2004; Di Matteo et al. 2005; Croton et al. 2006a,b; Hopkins et al. 2006, 2008; Sijacki et al. 2007; Menci et al. 2008; Ciotti et al. 2010; Lamastra et al. 2010; Cattaneo et al. 2011; Costa et al. 2014b,a; Schaye et al. 2015; Sijacki et al. 2015; see, also, Silk & Mamon 2012; Somerville & Davé 2015; for reviews). A detailed discussion of this topic is beyond the scope of this thesis. However, here we

briefly summarize some basic concepts of AGN feedback phenomenon. Given the low fraction of BH-to-galaxy mass ratio of  $\sim 0.1\%$ , the BH gravitational force cannot significantly affect the galaxy assembly over a large spatial scales merely through gravity. On the other hand, the energy released during the accretion flow onto the BH,  $E_{\text{grow}} = \epsilon M_{\text{BH}} c^2 / (1 - \epsilon)$ , can be much larger than the bulge gravitational binding energy,  $E_{\text{grav}} \approx M_{\text{bulge}} \sigma_{\star}^2$ :

$$\frac{E_{\text{grow}}}{E_{\text{grav}}} \approx \frac{\epsilon}{1 - \epsilon} \left( \frac{M_{\text{BH}}}{M_{\text{bulge}}} \right) \left( \frac{\sigma_{\star}}{c} \right)^{-2} = 250 \left( \frac{\sigma_{\star}}{200 \text{ km s}^{-1}} \right)^{-2}, \quad (3.2)$$

assuming  $M_{\text{BH}} = 10^{-3} M_{\text{bulge}}$ , and  $\epsilon = 0.1$ . In principle, if the energy injected by BH couples with the bulge gas, AGN can clear out a significant fraction of gas from the galaxy gravitational potential (e.g., Silk & Rees 1998; Ostriker & Ciotti 2005; see also Zubovas & King 2012; Nayakshin 2014; King & Pounds 2015; for a review on the physics of outflows). AGN feedback can operate via different physical mechanisms, such as radiation pressure, jets, and winds. As we saw in Sect. 1.2.2, in terms of energetics, (at least) two AGN regimes have been identified: the “radiative mode” (also known as quasar or wind mode) and the “radio-jet mode” (kinetic or maintenance mode). The first class is associated with high-luminosity AGN where the BH accretes near to the Eddington limit. In this regime, most of the energy is released in form of radiation (or a wind) by the accretion disk, pushing the cold gas reservoir out of galaxy bulge via massive outflows. Radio-jets could also play a role in this regime. In the second class, powerful radio jets are launched from the vicinity of the BH. The ejected plasma provides the main source of energy in mechanical form, preventing the gaseous atmosphere from cooling back into galaxy (see, e.g., Cattaneo et al., 2009; Alexander & Hickox, 2012; Fabian, 2012; Morganti, 2017; Harrison, 2017). Silk & Rees (1998), King (2010), and King & Pounds (2015) provided a simple theoretical model of radiative-mode feedback that predicts the observed  $M_{\text{BH}} - \sigma_{\star}$  correlation. In this model, AGN-driven wind interacts with the host galaxies ISM creating a bubble which expands and sweeps the gas away. At the interface between the outflow and the surrounding ISM a shock front propagates outward. If the shocked material efficiently cools (primarily via inverse Compton effect; Ciotti & Ostriker 1997), the wind may transfer to the gas only its momentum (ram pressure) while the thermal pressure remains negligible. This regime is dubbed as *momentum-driven outflow*. In the opposite case, the shocked

gas does not significantly cool and the wind may transfer its energy to the swept gas. As a result, the thermal pressure dominates over the ram pressure originating an *energy-driven outflow*. In the first case, the momentum of the swept ISM is equal to the total momentum of AGN photons. If we assume that the AGN shines at the Eddington luminosity (see **Sect. 2.1.1**), the following equation holds:

$$\dot{M}_{\text{gas}} v_{\text{gas}} = \frac{L_{\text{Edd}}}{c} = \epsilon \dot{M}_{\text{Edd}} c, \quad (3.3)$$

where  $\dot{M}_{\text{gas}}$  is the mass outflow rate, and  $v_{\text{gas}}$  is the velocity of the gas outflow. If the mass flow rate is equal to the Eddington mass accretion rate ( $\dot{M}_{\text{gas}} = \dot{M}_{\text{Edd}}$ ), the outflow achieves velocity that can be comparable to the speed of light  $v_{\text{gas}} \approx 0.1c$ , for a typical radiative efficiency of  $\epsilon \approx 0.1$ . Assuming that the mass in the galaxy's spheroid is distributed according to a singular isothermal sphere (the density profile and escape velocity of which are  $\rho(r) = \sigma_{\star}^2 / 2\pi G r^2$ ,  $v_{\text{esc}}(r) = 2\sigma_{\star}$ , respectively), and that the gas mass is a fraction  $f_{\text{gas}}$  of the total galaxy mass including DM ( $M_{\text{gas}}(r) = f_{\text{gas}} M(r)$ ), we get

$$\dot{M}_{\text{gas}} = 4\pi r^2 \rho_{\text{gas}}(r) v_{\text{gas}} = 4\pi r^2 f_{\text{gas}} \frac{\sigma_{\star}^2}{2\pi G r^2} v_{\text{gas}}. \quad (3.4)$$

For the swept material to escape from the galaxy gravitational potential well, the outflow velocity must be equal (or larger) than the escape velocity at each  $r$ . By inserting the **Eq. (3.4)** into **Eq. (3.3)**, and by using the definition of the Eddington Luminosity (see **Eq. 2.2**)

$$v_{\text{gas}}^2 = \frac{2\pi G^2 M_{\text{BH}} m_{\text{p}}}{\sigma_{\text{T}} f_{\text{gas}} \sigma_{\star}^2} = v_{\text{esc}}^2 = 4\sigma_{\star}^2, \quad (3.5)$$

from which we obtain  $M_{\text{BH}} \propto \sigma_{\star}^4$ , in agreement with the observed  $M_{\text{BH}} - \sigma_{\star}$  relation in the local Universe. A similar calculation can be applied to the energy-driven case, leading to  $M_{\text{BH}} \propto \sigma_{\star}^5$  thus resulting in a far smaller BH mass than actually observed at a given galaxy stellar mass.

Although many efforts have been devoted to the study of AGN feedback from both theoretical and observational point of view, the physics of AGN outflows and their properties are still debated. King & Pounds (2015) suggest that, when the BH mass reaches the value predicted by **Eq. (3.5)**, AGN outflow changes its regime from momentum-driven – acting on small spatial scale near the BH – to energy-driven – acting on the whole galaxy bulge and

producing a high-energy clear-out of its gas preventing further accretion (“feedback cut-off”). The turning point is therefore determined by

$$M_\sigma = \frac{f_{\text{gas}} \sigma_T}{2\pi G^2 m_p} \sigma_\star^4 \simeq 4 \times 10^8 \left( \frac{\sigma_\star}{200 \text{ km s}^{-1}} \right)^4 M_\odot. \quad (3.6)$$

This value is obtained for  $f_{\text{gas}} = 0.16$  fixed to the cosmological value (Hinshaw et al., 2013) which is expected for a protogalaxies forming at high redshift. However, galaxy forming at later times may have either larger  $f_{\text{gas}}$  if it gained a lot of gas, or smaller  $f_{\text{gas}}$  if its gas has been largely cleared out or turned into stars. However, at this point the BH can eventually grow through episodes of minor accretion with low gas fraction. The phenomenology of such BH history might comprise fossil outflow in galaxy with little ongoing AGN activity.

Direct evidence of AGN feedback in action has been revealed as X-ray cavities inflated by AGN jets (e.g., McNamara & Nulsen, 2007, 2012; Cattaneo et al., 2009; Fabian, 2012), Ultra Fast Outflows (UFOs) detected via blueshifted X-ray absorption lines (e.g., Pounds & Page, 2006; Reeves et al., 2009; Tombesi et al., 2010a,b, 2012; Bertola et al., 2020; Chartas et al., 2021), and non-relativistic ionized or molecular gas outflow with mass outflow rate up to hundreds-thousands of Solar masses per year (Nesvadba et al., 2006, 2008, 2010; Cano-Díaz et al., 2012; Maiolino et al., 2012; Brusa et al., 2015a,b, 2016, 2018; Ciccone et al., 2015; Cresci et al., 2015; Bischetti et al., 2017, 2019a,b; Carniani et al., 2017a; Feruglio et al., 2017; Herrera-Camus et al., 2019, 2020a,b, 2021; Spilker et al., 2020).

So far, we mainly focused on the “negative” effect of AGN feedback on the assembly of a galaxy. However, some theoretical models suggest that feedback process can eventually boost the star formation in galaxy through the compression of the interstellar and circumgalactic medium, thus favoring the fragmentation and the gravitational collapse of the gas clouds. This is typically referred as *positive* feedback (see, e.g., Rees, 1989; Nayakshin & Zubovas, 2012; Bieri et al., 2016; Zubovas & King, 2016). This theoretical prediction is indirectly supported by the discovery of the positive correlation between AGN and starburst activity in the nuclear regions of local AGN host galaxies (e.g., Imanishi, 2002; Imanishi & Wada, 2004; Imanishi et al., 2011; Rodríguez-Ardila & Viegas, 2003). Furthermore, a few works report possible observational evidence of star forming clumps triggered by outflows (e.g.,

Cresci et al., 2015; Carniani et al., 2016). More recently, different authors suggested that star formation could also be triggered within the outflowing gas (e.g., Gaibler et al., 2012; Ishibashi & Fabian, 2012, 2014; Ishibashi et al., 2013; Silk, 2013; Zubovas et al., 2013; Zubovas & King, 2014; Dugan et al., 2014; Mukherjee et al., 2018), with an exciting direct observational evidence reported by Maiolino et al. (2017).

*Are thus AGN the fundamental ingredient that regulates the life of massive galaxies? Or is nuclear activity just an accidental phase amongst a plethora of astrophysical processes at play?* Definitively, AGN feedback provides a convincing mechanism for the central BH to communicate with its host galaxy and it allows to explain a large number of galaxy properties. However, although important, AGN might not be the primarily responsible in regulating the star formation activity in the hosts during their evolution; starburst-driven feedback cooperate with AGN energy feedback (e.g., Weiner et al., 2009; Genzel et al., 2011; Rupke & Veilleux, 2011; Sturm et al., 2011; Newman et al., 2012; Spilker et al., 2020), and statistical mass averaging in mergers may significantly contribute to the onset of the BH–galaxy correlations (e.g., Croton, 2006; Peng, 2007; Gaskell, 2010, 2011; Hirschmann et al., 2010; Jahnke & Macciò, 2011).

## 3.6 Evolutionary sequence

It is tempting to synthesize the evidence described so far in a single, comprehensive evolutionary sequence of galaxies across the cosmic time. This was first proposed by Sanders et al. (1988), and then rearranged by other (e.g., Hopkins et al., 2008, see Fig. 3.6). At early epochs, gas-rich galaxy disks grow in quiescence. They are rotationally-supported with a supermassive BH at their center. In this phase (Fig. 3.6a) secular-driven processes can occur (e.g., formation of a bar or a pseudobulge). A significant fraction of Seyferts or low-luminosity quasars with a low-mass BH may arise from this secular evolution. However, in this phase the BH mass is insufficient to activate any substantial feedback mechanism (e.g., Silk & Rees, 1998), and galaxies continue to grow via cold-gas accretion or minor mergers (Hopkins et al., 2009). In the meanwhile, the surrounding dark matter halo accretes similar-mass companions according to the hierarchical growth of structure

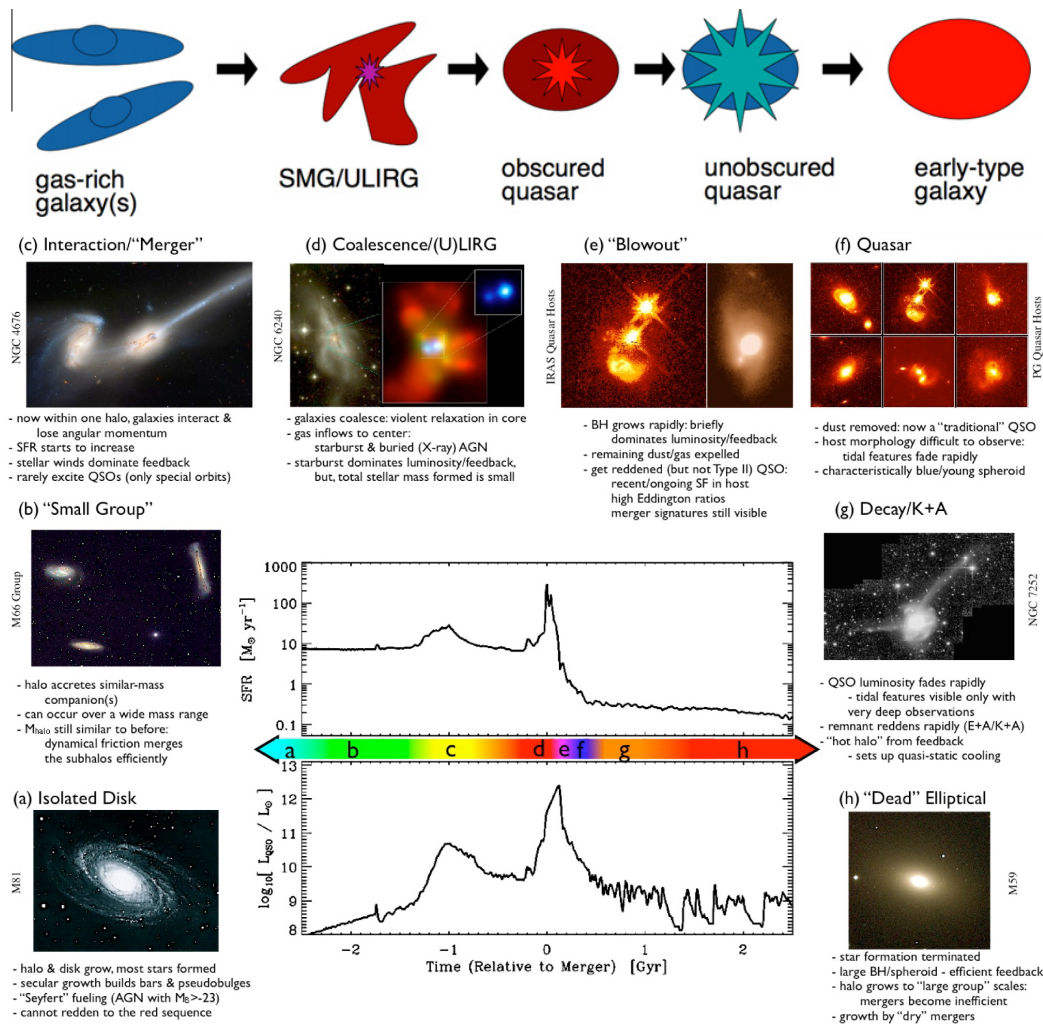


**Figure 3.6**

*Top panel:* the major-merger evolutionary sequence scenario first proposed by Sanders et al. (1988). *Bottom panel:* Schematic outline of the different phases of galaxy evolution undergoing gas-rich major merger (see the main text). Pictures show observations of archetypal system along the evolutionary track. The Central plot shows the SFR in galaxy and the AGN luminosity as a function of time relative to the merger event. Figure from Alexander & Hickox (2012, top panel), and Hopkins et al. (2008, bottom panel).

(Fig. 3.6b). Any quasar trigger mechanism requires relatively massive systems with large supplies of cold gas. Such massive objects reside in dark matter halos with mass of  $\sim 10^{12} - 10^{13} M_{\odot}$  (e.g., Croton, 2009). As the halo mass grows, gas-rich galaxy mergers (wet major-mergers) exert tidal torques on gas, depleting its angular momentum and driving inflows toward the nucleus of the remnants. This powerful mechanism significantly enhances

the star-formation activity and triggers a rapid BH accretion enshrouded by gas and dust (**Fig. 3.6c, d**). UV radiation by the AGN and the young stars is reprocessed by dust at longer wavelengths, thus boosting the FIR luminosity and reddening the colors (ULIRG, or SMG phase). A large fraction of gas is then consumed by the starburst, the galaxy reaches its peak of star-formation activity, and BH feedback starts to blow out the residual gas via powerful outflows (**Fig. 3.6e**). This rapid transitional “blow-out” phase is typical of luminous and dust-reddened quasars (e.g., Gregg et al., 2002; Richards et al., 2003; Hopkins et al., 2004; Urrutia et al., 2009; Brusa et al., 2010; Banerji et al., 2012; Ross et al., 2015; Zakamska et al., 2016). As the gas is swept away, the radiation from the BH accretion disk becomes visible as a traditional Type-I or -II quasar depending on the inclination angle of the obscuring torus (**Fig. 3.6f**). Then, the consumption and dispersion of gas due to the star formation and the quasar activity lead to a quick evolution from a blue to a red galaxy and a remnant spheroid is produced (**Fig. 3.6g, h**). Finally, the exhaust red-and-dead galaxy will ultimately passively evolve along the red sequence largely by dry mergers.



# 4

## The ALMA view of the high-redshift relation between supermassive black holes and their host galaxies

“If man loses the sense of adventure, of knowing, of measuring himself, it is all over.

— Walter Bonatti

This chapter is drawn from “*The ALMA view of the high-redshift relation between supermassive black holes and their host galaxies*”, Pensabene A., Carniani S., Perna M., Cresci G., Decarli R., Maiolino R., and Marconi A., 2020, *A&A*, 637, A84.

### 4.1 Introduction

The discovery of the strong correlations (in the local Universe) between the mass of the central BH and the physical properties of host galaxies (e.g., stellar velocity dispersion of the bulge stars, mass of the bulge, etc.; see **Sect. 3.3**) has been one of the most significant breakthroughs of the past decades and represents a key building block for our understanding of galaxy formation and evolution across the cosmic time. In the framework of coevolution between BHs and their host galaxies, the observed local

relations are believed to arise from the balance between the energy released by the AGN, which generates galactic-scale outflows expelling gas from the galaxy (see **Sect. 3.5**), and the gravitational potential that keeps the galactic system bound. According to current galaxy evolution models (see, e.g., Lemastra et al., 2010; Sijacki et al., 2015), AGN are able to regulate the star formation activity in the host and constrain both the final stellar mass and dynamical properties of the galaxy (e.g., Di Matteo et al., 2005; Menci et al., 2008; Hopkins et al., 2008; Kormendy & Ho, 2013). Therefore, investigating the onset of BH–galaxy relations at high redshift is fundamental to exploring the interplay between BH accretion and star formation activity in the host galaxies, and to constrain, accordingly, galaxy formation and evolution models.

In this chapter, we focus on the relation between BH mass and that of the host galaxy ( $M_{\text{BH}}-M_{\text{gal}}$  relation). The latter has been widely sampled for active and quiescent galaxies in the local Universe ( $z < 1$ ), indicating that the BH mass is a fixed fraction of the bulge stellar mass ( $M_{\text{BH}} \sim 10^{-3} M_{\text{bulge}}$ ; see, **Sect. 3.3** and references therein). Several groups have attempted to sample this relation beyond the local Universe, showing that there are indications for a possible evolution with redshift (see, **Sect. 3.4**; and references therein). Although these results may be affected by observational biases and instrumental limits, this fact possibly implies that during the competitive accretion of matter from the galactic halo that occurred at early epochs, BH growth may have preceded that of the host galaxy.

The recent advent of ALMA opened a new era for the observations of the most distant quasars enabling to study the ISM in the first galaxies with unprecedented details. At FIR/(sub-)mm wavelengths the host galaxies of (at least) RQ quasars are unveiled via their cold gas and dust emission that dominate the SED of galaxy. Thanks to the unparalleled capability of ALMA in terms of sensitivity, signal-to-noise ratio (S/N), and angular resolution, it is now possible to spatially resolve the cold gas kinematics in quasar host galaxies up to the higher redshifts targeting the brightest line emission of the cold gas, such as  $[\text{CII}]_{158\mu\text{m}}$  or CO rotational line transitions with sub-mm spectroscopic observations (see **Sect. 5**). Therefore, thanks to the efforts of many groups, ALMA has made it possible to trace the BH–galaxy relation at very high redshift using dynamical mass ( $M_{\text{dyn}}$ ) estimations of host galaxies

(e.g., Wang et al., 2013, 2016; Willott et al., 2013, 2015b; Venemans et al., 2012, 2016, 2017c; Decarli et al., 2017; Trakhtenbrot et al., 2017; Feruglio et al., 2018). The dynamical masses provided in these works are estimated assuming rotating disk geometry and by simply combining the FWHM of the observed line emission, the observed size of the emitting region, and the inclination angle of the galaxy disk with respect to the sky plane. However, it is hard to test the basic assumption that the cold atomic/molecular gas of the galaxy is a rotating disk. Furthermore, the disk inclination is calculated from the observed morphology by using the axial ratio of the flux map, and is thus affected by significant uncertainties.

In this chapter, we study a large sample ( $\sim 70$ ) of  $2 < z < 7$  quasars observed by ALMA targeting the  $[\text{CII}]_{158\mu\text{m}}$  atomic fine-structure line or the CO rotational line emission, which we exploited in order to trace the morphology and kinematics of quasar host galaxies. Overall, we identified ordered rotational motion in a sample of ten quasars (for which high S/N allowed a spatially resolved analysis). By carefully modeling the kinematics with rotating disks, we were able to measure their host galaxy dynamical mass, thus improving on the rough estimates presented so far. Our dynamical mass measurements, combined with  $M_{\text{BH}}$  estimates obtained from the literature allowed us to trace the evolution of the  $M_{\text{BH}} - M_{\text{gal}}$  relation and to study the trend of  $\Gamma = M_{\text{BH}}/M_{\text{gal}}$  across the cosmic time.

This chapter is organized as follows: in **Sect. 4.2**, we outline our starting sample and the data reduction performed on the raw data. In **Sect. 4.3**, we illustrate the methods of data analysis to retrieve the information on the morphology and kinematics of the host galaxies. In **Sect. 4.4**, we present the kinematical model used to measure the galaxy dynamical mass. In **Sect. 4.5**, we obtain the BH masses from the literature and from our LBT (Large Binocular Telescope) observations. In **Sect. 4.6**, we recap the different sub-selections of the starting sample that occurred during this work. In **Sect. 4.7**, we compare our dynamical mass estimates with previous similar studies and discuss the uncertainties on our measurements. Then, we investigate limits of validity of the assumptions. In **Sect. 4.8**, the  $M_{\text{BH}} - M_{\text{dyn}}$  relation and the trend of  $M_{\text{BH}}/M_{\text{dyn}}$  ratio across cosmic time are presented. Then, in **Sect. 4.9**, we discuss our results and compare them with previous works. We also examine how possible additional uncertainties and biases could affect

the results both from observational and theoretical points of view. Then, we compute the virial masses of our final sample, and we compare them with our dynamical mass estimates. Finally, in **Sect. 4.10**, we draw our conclusions.

Throughout this chapter, we assume a standard  $\Lambda$ CDM cosmology with  $H_0 = 69.3 \text{ km s}^{-1} \text{ Mpc}^{-1}$ ,  $\Omega_m = 0.287$ ,  $\Omega_\Lambda = 1 - \Omega_m$  from Hinshaw et al. (2013).

## 4.2 ALMA data selection and reduction

We started by collecting all  $[\text{CII}]_{158\mu\text{m}}$  and  $\text{CO}(J \rightarrow J-1)$  (rotational quantum number  $J = 4, 3$ ) observations of  $z > 1.5$  quasars on the ALMA data archive public as of June 2017 for a total of 72 quasars in the redshift range  $1.5 < z < 7.1$ . Different ALMA bands were involved according to the targeted atomic/molecular transition and the redshift of the sources. The collected data were calibrated using the ALMA pipeline in the Common Astronomy Software Applications, CASA (McMullin et al., 2007), by executing the appropriate ALMA calibration scripts corresponding to each specific observation. Continuum images were produced for each quasar from the calibrated visibilities, by combining the line-free channels from all spectral windows in multifrequency synthesis mode using the CASA task `tclean` and `briggs` weighting scheme (with robustness parameter  $R = 0.5$ ) to maximize both the signal-to-noise ratio and angular resolution. The line-free channels were determined by inspecting the visibilities in all the frequency sidebands. For those quasars in which the FIR line was not detected, we selected the line-free channel by adopting a line width of  $300 \text{ km s}^{-1}$  and the redshift from literature.

These same channels were also used to produce a UV plane model by fitting the continuum emission with a zeroth order polynomial<sup>1</sup> that was then subtracted from the spectral windows containing the line using the CASA task `uvcontsub`. The continuum-subtracted line visibilities were then imaged using `tclean`. In order to recover all the information within the resolution element, the pixel size was commonly set to  $\sim B_{\text{min}}/7$ , where  $B_{\text{min}}$  is the minor FWHM of ALMA's synthesized beam. Therefore, we obtained cubes with a typical pixel size of  $0.025'' - 0.05''$  and with a spectral bin width set to  $40 - 70 \text{ km s}^{-1}$ . Self-calibration was attempted but showed no additional

<sup>1</sup>For a typical  $S/N \sim 60 - 100$  over a bandwidth of 4 GHz in ALMA band 3, the continuum emission is well-described by a zeroth-order polynomial within the uncertainties.

improvement for almost all observations and was not used for the final cubes. Finally, both continuum images and the line cubes were corrected for the primary beam response.

Among these observations, we selected the cubes in which the line detection was significant ( $\geq 3\sigma$ ). This first selection reduced the sample to 32 quasars at  $2.2 < z < 7.1$  on which we performed all of the analysis described in the following sections. Different sub-selections occurred at each step of the analysis (see **Sect. 4.6**) and the final sample is composed of only ten sources, for which we obtained constraints on the host galaxy's dynamical mass. We thus picked deeper observations from the archive for this final subsample of sources that became public while the work was in progress (by the end of February 2018). In **Tab. 4.1**, we list the starting sample of 32 objects and the characteristics of the observations, including the aforementioned deeper observations for the final sub-sample. The distribution of redshifts of our quasars is illustrated in **Fig. 4.1**.

### 4.3 Methods of data analysis

Our goal is to measure the dynamical mass of our sample of host galaxies (listed in **Tab. 4.1**) by modeling the gas kinematics as traced by  $[\text{CII}]_{158\mu\text{m}}$  or CO line emission with rotating disks. Therefore, in order to obtain the kinematical maps, we performed a spaxel-by-spaxel fit of the emission line profile by adopting a single Gaussian model with three free parameters: the amplitude  $A$ , the central frequency  $\nu_{\text{obs}}$ , and the standard deviation  $\sigma$ . For this purpose, we designed an algorithm to achieve a robust residual minimization in each pixel. Since the beam smearing affects the observed emission, we expect the spatial shape of the line to change smoothly from one pixel to the adjacent one, and the signal-to-noise ratio to decrease as a function of the distance from the center of the galaxy. The underlying idea of the procedure is the subsequent performance of the line fit in all spaxels starting from the central pixel and moving away following a spiral-like path. The basic operations are: (1) performing a 2D Gaussian fit on the continuum image and defining the central spaxel; (2) extracting the spectrum from the central spaxel and computing a 1D Gaussian line fit in which the starting points are properly chosen by inspecting the line shape; (3) following a spiral-like path to select the next spaxel, extracting the spectrum, and performing a 1D

**Table 4.1:** List of 32 quasars revealed with emission line detection significant at  $\geq 3\sigma$  and related information about the ALMA observing project.

| No. | Object ID             | R.A. (J2000.0)                                      | DEC. (J2000.0) | $z_{\text{cat}}^{(1)}$ | Observed line                                | Flags [rot, $\beta$ , $M_{\text{BH}}]^{(2)}$ |
|-----|-----------------------|---|----------------|------------------------|--|--|
| 1   | CXOCDFS J0332-2746    | 03 <sup>h</sup> 32 <sup>m</sup> 31 <sup>s</sup> .46 | -27°46'23".18  | 2.2234                 | CO(4-3)                                      | r, u, -                                      |
| 2   | VHS J2101-5943        | 21 <sup>h</sup> 01 <sup>m</sup> 19 <sup>s</sup> .5  | -59°43'45"     | 2.313                  | CO(3-2)                                      | r, b, a                                      |
| 3   | ULAS J1234+0907       | 12 <sup>h</sup> 34 <sup>m</sup> 27 <sup>s</sup> .52 | +09°07'54".2   | 2.503                  | CO(3-2)                                      | u, -, -                                      |
| 4   | ULAS J2315+0143       | 23 <sup>h</sup> 15 <sup>m</sup> 56 <sup>s</sup> .23 | +01°43'50".38  | 2.560                  | CO(3-2)                                      | r, u, -                                      |
| 5   | ULAS J0123+1525       | 01 <sup>h</sup> 23 <sup>m</sup> 12 <sup>s</sup> .52 | +15°25'22".52  | 2.629                  | CO(3-2)                                      | u, -, -                                      |
| 6   | SDSS J1328-0224       | 13 <sup>h</sup> 28 <sup>m</sup> 53 <sup>s</sup> .65 | -02°24'41".79  | 4.62271                | [CH] <sub>158 <math>\mu\text{m}</math></sub> | r, c, e                                      |
| 7   | SDSS J0923+0247       | 09 <sup>h</sup> 23 <sup>m</sup> 03 <sup>s</sup> .52 | +02°47'39".68  | 4.66307                | [CH] <sub>158 <math>\mu\text{m}</math></sub> | r, c, e                                      |
| 8   | SDSS J0331-0741       | 03 <sup>h</sup> 31 <sup>m</sup> 19 <sup>s</sup> .66 | -07°41'43".16  | 4.72426                | [CH] <sub>158 <math>\mu\text{m}</math></sub> | r, u, -                                      |
| 9   | SDSS J0129-0035       | 01 <sup>h</sup> 29 <sup>m</sup> 58 <sup>s</sup> .5  | -00°35'39"     | 5.780                  | [CH] <sub>158 <math>\mu\text{m}</math></sub> | r, l, a                                      |
| 10  | SDSS J1044-0125       | 10 <sup>h</sup> 44 <sup>m</sup> 33 <sup>s</sup> .04 | -01°25'02".07  | 5.800                  | [CH] <sub>158 <math>\mu\text{m}</math></sub> | r, c, a                                      |
| 11  | SDSS J1306+0356       | 13 <sup>h</sup> 06 <sup>m</sup> 08 <sup>s</sup> .25 | +03°56'26".33  | 6.016                  | [CH] <sub>158 <math>\mu\text{m}</math></sub> | r, c, e                                      |
| 12  | SDSS J2310+1855       | 23 <sup>h</sup> 10 <sup>m</sup> 38 <sup>s</sup> .88 | +18°55'19".72  | 6.040                  | [CH] <sub>158 <math>\mu\text{m}</math></sub> | r, c, e                                      |
| 13  | SDSS J0842+1218       | 08 <sup>h</sup> 42 <sup>m</sup> 29 <sup>s</sup> .43 | +12°18'50".48  | 6.055                  | [CH] <sub>158 <math>\mu\text{m}</math></sub> | u, -, -                                      |
| 14  | SDSS J2054-0005       | 20 <sup>h</sup> 54 <sup>m</sup> 06 <sup>s</sup> .49 | -00°05'14".57  | 6.062                  | [CH] <sub>158 <math>\mu\text{m}</math></sub> | r, c, a                                      |
| 15  | [WMH2013] 05          | 02 <sup>h</sup> 26 <sup>m</sup> 27 <sup>s</sup> .03 | -04°52'38".3   | 6.068                  | [CH] <sub>158 <math>\mu\text{m}</math></sub> | u, -, -                                      |
| 16  | CFHQS J2100-1715      | 21 <sup>h</sup> 00 <sup>m</sup> 54 <sup>s</sup> .62 | -17°15'22".5   | 6.09                   | [CH] <sub>158 <math>\mu\text{m}</math></sub> | u, -, -                                      |
| 17  | DES J0454-4448        | 04 <sup>h</sup> 54 <sup>m</sup> 01 <sup>s</sup> .79 | -44°48'31".1   | 6.100                  | [CH] <sub>158 <math>\mu\text{m}</math></sub> | u, -, -                                      |
| 18  | CFHQS J1509-1749      | 15 <sup>h</sup> 09 <sup>m</sup> 41 <sup>s</sup> .8  | -17°49'27"     | 6.120                  | [CH] <sub>158 <math>\mu\text{m}</math></sub> | u, -, -                                      |
| 19  | ULAS J1319+0950       | 13 <sup>h</sup> 19 <sup>m</sup> 11 <sup>s</sup> .29 | +09°50'51".34  | 6.130                  | [CH] <sub>158 <math>\mu\text{m}</math></sub> | r, l, e                                      |
| 20  | PSO J065-26           | 04 <sup>h</sup> 21 <sup>m</sup> 38 <sup>s</sup> .05 | -26°57'15".60  | 6.14                   | [CH] <sub>158 <math>\mu\text{m}</math></sub> | u, -, -                                      |
| 21  | [CLM2003] J0228-04161 | 02 <sup>h</sup> 28 <sup>m</sup> 02 <sup>s</sup> .97 | -04°16'18".3   | 6.17                   | [CH] <sub>158 <math>\mu\text{m}</math></sub> | u, -, -                                      |
| 22  | PSO J308-21           | 20 <sup>h</sup> 32 <sup>m</sup> 10 <sup>s</sup> .00 | -21°14'02".4   | 6.2342                 | [CH] <sub>158 <math>\mu\text{m}</math></sub> | r, b, u                                      |
| 23  | VIKING J1152+0055     | 11 <sup>h</sup> 52 <sup>m</sup> 21 <sup>s</sup> .27 | +00°55'36".6   | 6.37                   | [CH] <sub>158 <math>\mu\text{m}</math></sub> | u, -, -                                      |
| 24  | PSO J159-02           | 10 <sup>h</sup> 36 <sup>m</sup> 54 <sup>s</sup> .19 | -02°32'37".94  | 6.38                   | [CH] <sub>158 <math>\mu\text{m}</math></sub> | u, -, -                                      |
| 25  | PSO J183+05           | 12 <sup>h</sup> 12 <sup>m</sup> 26 <sup>s</sup> .98 | +05°05'33".49  | 6.4386                 | [CH] <sub>158 <math>\mu\text{m}</math></sub> | r, l, u                                      |
| 26  | PSO J167-13           | 11 <sup>h</sup> 10 <sup>m</sup> 33 <sup>s</sup> .98 | -13°29'45".6   | 6.508                  | [CH] <sub>158 <math>\mu\text{m}</math></sub> | r, c, e                                      |
| 27  | PSO J231-20           | 15 <sup>h</sup> 26 <sup>m</sup> 37 <sup>s</sup> .84 | -20°50'00".8   | 6.58651                | [CH] <sub>158 <math>\mu\text{m}</math></sub> | r, u, -                                      |
| 28  | VIKING J0305-3150     | 03 <sup>h</sup> 05 <sup>m</sup> 16 <sup>s</sup> .92 | -31°50'56".0   | 6.605                  | [CH] <sub>158 <math>\mu\text{m}</math></sub> | r, c, e                                      |
| 29  | VIKING J1048-0109     | 10 <sup>h</sup> 48 <sup>m</sup> 19 <sup>s</sup> .08 | -01°09'40".29  | 6.661                  | [CH] <sub>158 <math>\mu\text{m}</math></sub> | u, -, -                                      |
| 30  | VIKING J0109-3047     | 01 <sup>h</sup> 09 <sup>m</sup> 53 <sup>s</sup> .13 | -30°47'26".3   | 6.750                  | [CH] <sub>158 <math>\mu\text{m}</math></sub> | r, u, -                                      |
| 31  | VIKING J2348-3054     | 23 <sup>h</sup> 48 <sup>m</sup> 33 <sup>s</sup> .34 | -30°54'10".0   | 6.890                  | [CH] <sub>158 <math>\mu\text{m}</math></sub> | u, -, -                                      |
| 32  | ULAS J1120+0641       | 11 <sup>h</sup> 20 <sup>m</sup> 01 <sup>s</sup> .48 | +06°41'24".3   | 7.080                  | [CH] <sub>158 <math>\mu\text{m}</math></sub> | u, -, -                                      |

**Table 4.1:** (continued)

| No. <sup>(3)</sup> | ALMA ID        | P.I. <sup>(4)</sup> | $\sigma_{\text{line}}^{(5)}$<br>(mJy/beam) | $\theta_{\text{beam}}^{(6)}$<br>( $''$ ) | Ref. <sup>(7)</sup> | No. <sup>(3)</sup> | ALMA ID        | P.I. <sup>(4)</sup><br>(mJy/beam) | $\sigma_{\text{line}}^{(5)}$<br>( $''$ ) | $\theta_{\text{beam}}^{(6)}$ | Ref. <sup>(7)</sup> |
|--------------------|----------------|---------------------|--|--|---------------------|--------------------|----------------|-----------------------------------|--|------------------------------|---------------------|
| 1                  | 2015.1.00228.S | GP                  | 0.60                                       | 1.66                                     | P17                 | 2                  | 2015.1.01115.S | FW                                | 1.25                                     | 1.24                         | V18                 |
| 3                  | 2015.1.01247.S | MB                  | 0.68                                       | 5.39                                     | B17                 | 4                  | 2015.1.01115.S | FW                                | 1.10                                     | 1.04                         | D18                 |
| 5                  | 2015.1.01247.S | MB                  | 1.20                                       | 2.65                                     | B17                 | 6                  | 2012.1.00240.S | RW                                | 0.62                                     | 0.22                         | J17                 |
| 7                  | 2015.1.01247.S | MB                  | 0.73                                       | 2.22                                     | B17                 | 8                  | 2015.1.01115.S | FW                                | 1.28                                     | 0.82                         | D18                 |
| 9                  | 2015.1.01247.S | MB                  | 0.74                                       | 2.58                                     | B17                 | 10                 | 2013.1.00815.S | CW                                | 0.60                                     | 0.39                         | W15                 |
| 11                 | 2013.1.01153.S | PL                  | 0.71                                       | 0.44                                     | T17                 | 12                 | 2016.A.00018.S | RD                                | 0.54                                     | 0.27                         | D17                 |
| 13                 | 2013.1.01153.S | PL                  | 0.69                                       | 0.45                                     | T17                 | 14                 | 2015.1.01115.S | FW                                | 1.21                                     | 0.92                         | D18                 |
| 15                 | 2013.1.01153.S | PL                  | 1.60                                       | 0.34                                     | T17                 | 16                 | 2015.1.01115.S | FW                                | 1.20                                     | 0.89                         | D18                 |
| 17                 | 2012.1.00240.S | RW                  | 0.66                                       | 0.17                                     | –                   | 18                 | 2016.1.00544.S | EB                                | 0.64                                     | 0.25                         | –                   |
| 19                 | 2011.0.00206.S | RW                  | 1.84                                       | 0.48                                     | W13                 | 20                 | 2015.1.00606.S | CW                                | 0.58                                     | 0.63                         | W17                 |
| 21                 | 2015.1.01115.S | FW                  | 1.35                                       | 0.83                                     | D18                 | 22                 | 2015.1.01115.S | FW                                | 1.37                                     | 0.97                         | D17                 |
| 23                 | 2011.0.00206.S | RW                  | 1.39                                       | 0.57                                     | W13                 | 24                 | 2015.1.00399.S | BV                                | 0.51                                     | 0.19                         | –                   |
| 25                 | 2015.1.01115.S | FW                  | 1.35                                       | 0.93                                     | D17                 | 26                 | 2015.1.01115.S | FW                                | 1.01                                     | 0.98                         | D18                 |
| 27                 | 2011.0.00206.S | RW                  | 1.81                                       | 0.45                                     | W13                 | 28                 | 2012.1.00882.S | BV                                | 1.45                                     | 0.36                         | V16                 |
| 29                 | 2013.1.00815.S | CW                  | 0.58                                       | 0.37                                     | W15                 | 30                 | 2012.1.00882.S | BV                                | 1.88                                     | 0.42                         | V16                 |
| 31                 | 2015.1.01115.S | FW                  | 1.30                                       | 0.62                                     | D17                 | 32                 | 2012.1.00882.S | BV                                | 0.67                                     | 0.20                         | V17                 |

**Notes.** *Top table:* <sup>(1)</sup>Redshift values retrieved from SIMBAD Astronomical Database (<http://simbad.u-strasbg.fr/simbad/>). <sup>(2)</sup>The flags provide information on kinematics (rot), disk inclination angle ( $\beta$ ) as resulting from our kinematical modeling, and BH mass ( $M_{\text{BH}}$ ) as follows: [rot]: unresolved (u) or resolved (r) kinematics. [ $\beta$ ]: unconstrained (u) or constrained (c) disk inclination angle, lower limit (l), bimodal distribution (b). [ $M_{\text{BH}}$ ]: unavailable in the literature (u), single-epoch virial mass estimated in this work (e) or value retrieved the literature (a). *Bottom table:* <sup>(3)</sup>Identification numbers (No.) refer to those of the top table. <sup>(4)</sup>Principal investigator of the project: BV (Venemans, B.), CW (Willott, C.), EB (Bañados, E.), FW (Walter, F.), GP (Popping, G.), MB (Banerji, M.), PL (Lira, P.), RD (Decarli, R.), RW (Wang, R.). <sup>(5)</sup>Line sensitivity over  $10 \text{ km s}^{-1}$ . <sup>(6)</sup>Angular resolution. <sup>(7)</sup>References: B17 (Banerji et al., 2017), D17, D18 (Decarli et al., 2017, 2018), J17 (Jones et al., 2017) P17 (Popping et al., 2017), T17 (Trakhtenbrot et al., 2017), V16, V17, V18 (Venemans et al., 2016, 2017c, 2018), W13 (Wang et al., 2013), W15, W17 (Willott et al., 2015a, 2017).

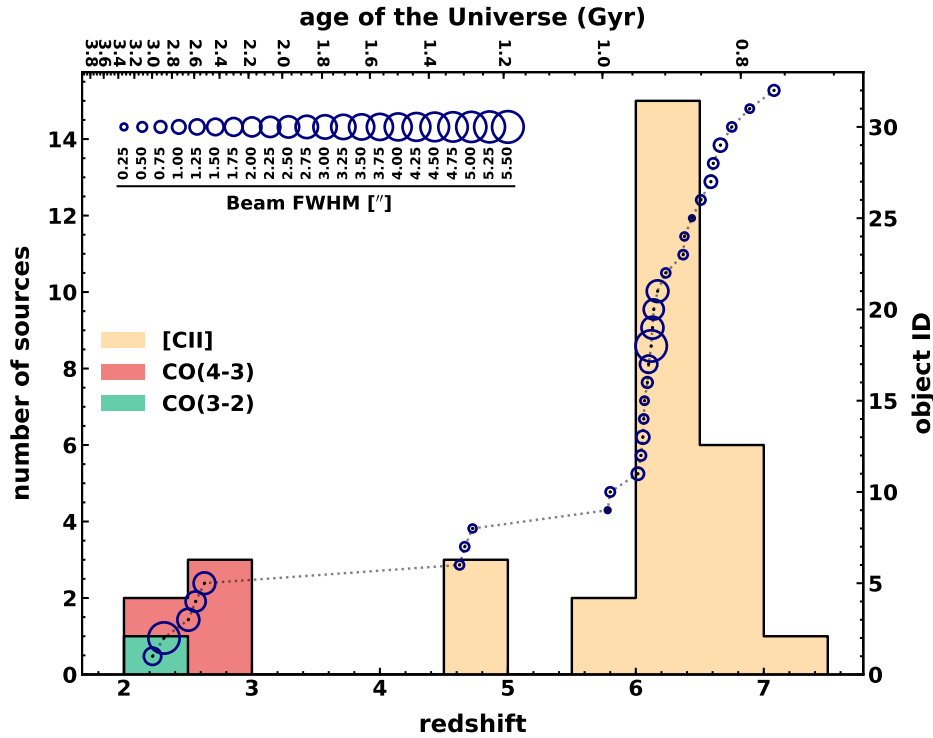


**Figure 4.1**

Redshift distribution of 32 quasars listed in **Tab. 4.1**. The histogram colors indicate the emission line detected in the ALMA data. The figure also shows the sample cumulative redshift distribution (dotted line and right axis). Individual sources are marked with blue circles (sizes are proportional to the ALMA synthesized beam FWHM).

Gaussian line fit by using the best-fitting results from the neighbor spaxels as starting points for the spectral fit; (4) continuously repeating step 3 for the consecutive spaxel until the end of the spiral-like path. We used the minimum chi-square method to estimate the best-fitting parameters.

The result of the fit in each pixel is accepted or rejected on the basis of criteria illustrated in **Sect. 4.3.2**, while the stopping criteria to break the entire fitting procedure can be fixed by setting the dimension  $d$  of the spiral path, that is the distance from the central pixel. In the case of our datacubes, a typical value of  $d \sim 20 - 25$  pixels ( $\sim 0.5'' - 1.25''$  depending on the pixel size; see, **Sect. 4.2**) turned out to be adequate to fit the line throughout the emitting region with a total of  $\sim 1200 - 2000$  pixels analyzed for each source. This fitting strategy enables a more robust minimization compared with using a unique set of initial guess parameters for all the pixels, thus avoiding numerical problems arising from incorrectly-chosen starting-points.

Finally, we retrieved the information regarding the line together with the uncertainties on each spectral channel of the cube by measuring the RMS of the noise ( $r_\nu$ ) over a wide spatial region where no emission is detected.

### 4.3.1 Integrated spectra and derived quantities

We obtained the integrated spectra of all the sources by adding all the fitted spectra in spaxels selected based on criteria illustrated in **Sect. 4.3.2** (e.g., **Fig. 4.2**; see also, **Appx. A.5**). Then, the resulting integrated spectrum was fitted using a Monte Carlo method in order to estimate the redshift uncertainty. Firstly, we collected a large number (e.g., 2000) of different integrated spectra obtained by adding a random value extracted from a normal distribution defined by a zero mean, and a standard deviation equal to the corresponding RMS in that channel ( $r_\nu$ ) to each channel of the original spectrum. Then, we performed the fit of each spectrum with a single Gaussian, and we estimated the redshift of the line as  $\nu_{\text{obs}} = \nu_{\text{rest}}/(1+z)$ , where  $\nu_{\text{obs}}$  is the mean of the Gaussian model and  $\nu_{\text{rest}}$  is the line rest-frame frequency. Finally, all the estimates of  $z$  obtained with this method were histogrammed and its distribution was fitted with a Gaussian model. We finally assumed the mean and the standard deviation of the best-fit model as the best value of redshift and its uncertainty, respectively. In addition, the fit of integrated spectra allowed us to determine the line FWHM and flux. In **Appx. A.1**, we use these quantities to derive the line luminosity, the [CII] mass ( $M_{[\text{CII}]}$ ), the total gas mass ( $M_{\text{gas}}$ ) and the SFR of the quasar host galaxies.

### 4.3.2 Flux, velocity, and velocity-dispersion maps

The cube fitting procedure provides the best-fit values of the Gaussian parameters ( $A, \nu_{\text{obs}}, \sigma$ ) in each pixel. We used these values to obtain the line-integrated velocity and the velocity-dispersion maps along the line of sight (LOS).

In order to produce the maps, among all the spaxels in which we performed the line fit, we selected those satisfying the following conditions: (1) the peak of the best-fitting Gaussian is  $\geq 1.5 \times \text{RMS}$  in the corresponding channel;

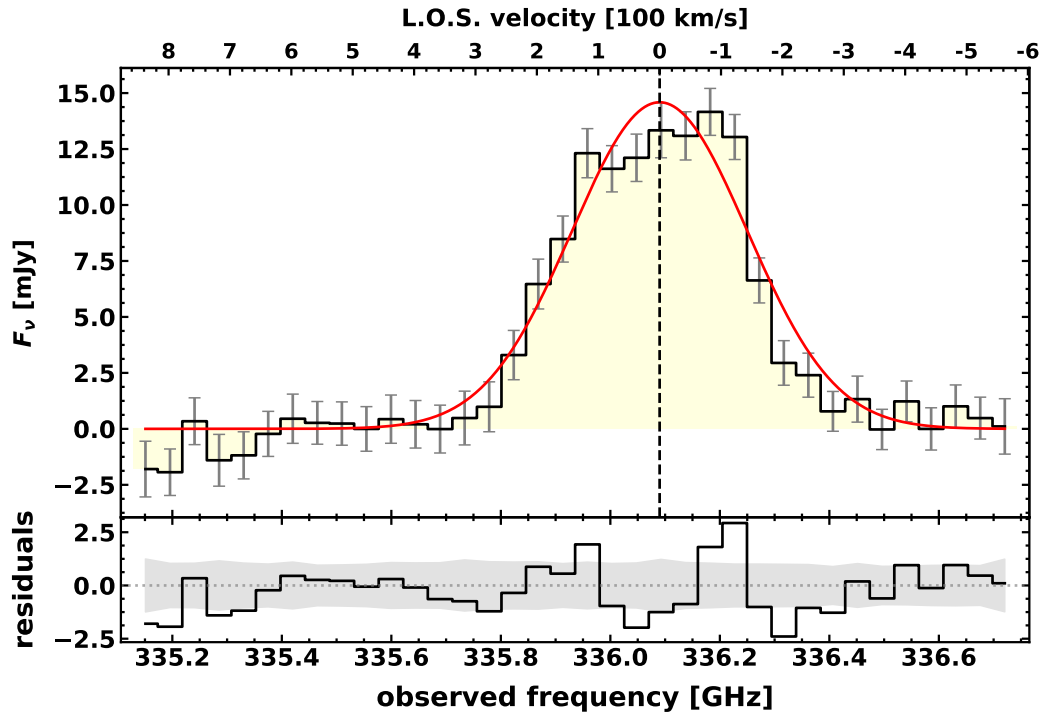


**Figure 4.2**

Integrated spectrum of source SDSS J0923+0247. *Top panel:* the observed data is shown in light yellow with error bars in gray (RMS in each channel). The red solid curve is the best-fit Gaussian model. The velocity scale (top axis) has as its reference the central frequency of the best fit. *Bottom panel:* the fit residuals ( $model - data$ ), the gray filled area shows the RMS along the spectral axis.

(2) the percentage relative error on the flux value is  $\leq 50\%$ .

Condition 1 represents the signal-to-noise cut-off we used to reject pixels in which the line emission is not clearly detected. However, in case of poor signal-to-noise ratio, the fit process possibly fails, resulting in a bad Gaussian model for which condition 1 could be still satisfied. Therefore, we also imposed condition 2 in order to avoid this kind of effect and to consequently reject the corresponding pixels when producing the maps.

We also manually masked bad pixels far away from the galaxy center, which are clearly associated with spikes of noise. Finally, we obtained error maps using the uncertainties on the best-fit Gaussian model parameters of each pixel. As an example, in **Fig. 4.3**, we report the maps obtained from the continuum-subtracted cube of SDSS J0923+0247 (see also, **Appx. A.5**).

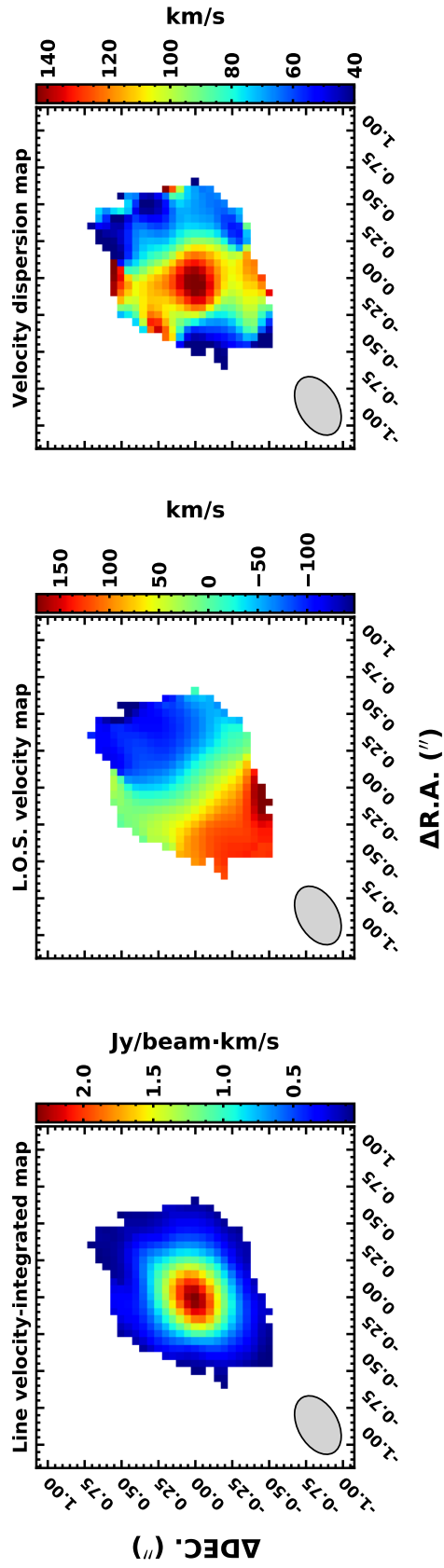


**Figure 4.3**

Observed maps of SDSS J0923+0247. From left panel to right we report, respectively, flux map, velocity map, and velocity-dispersion map along the LOS. At the bottom-left corner of each panel, we report the ALMA synthesized beam FWHM. The coordinates indicate offsets with respect to the map center.

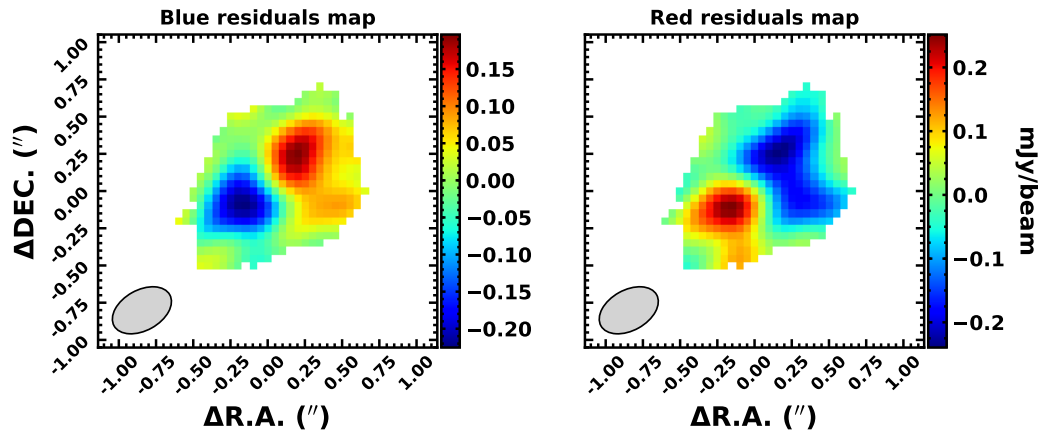


**Figure 4.4**

Red and blue residual maps of SDSS J0923+0247. This test reveals spatially resolved kinematics consistent with what we would expect from a rotating disk.

### 4.3.3 Red and blue residual maps

The angular resolution may not be high enough to spatially resolve the rotation of the emitting gas in host galaxies. In order to assess if the kinematics are spatially resolved or not, we performed the same analysis computed by Carniani et al. (2013) for ALMA [CII] observations of a quasar at  $z = 4.7$ . We replicated the spaxel-by-spaxel fit of continuum-subtracted cubes with a single Gaussian component, using the amplitude ( $A$ ) as the only free parameter, and by fixing the values of  $\nu_{\text{obs}}$  and  $\sigma$  to the best values obtained from the fit of the integrated spectrum (see Sect. 4.3.1). Then, we computed the residuals of fits in each channel, which is the *data - model*, and we obtained two maps by collapsing all channels in the blue-shifted and red-shifted (with respect to the central frequency) side of the residual spectrum. If the kinematics are consistent with a spatially resolved rotating disk, we expect the blue and red residual maps to show two symmetric lobes: a positive and negative lobe at the opposite side with respect to the map center (e.g., as shown in Fig. 4.4). Otherwise, if rotation is not resolved then we expect a random distribution of negative and positive residuals on both the maps. After performing this test on the 32 objects listed in Tab. 4.1, we conclude that 14 of them ( $\sim 45\%$ ) show no evidence of spatially resolved kinematics. We therefore excluded them from the final sample (see, Sect. 4.6 for a summary of sample subselections). In Sect. 4.7.4, we investigate biases possibly occurring while excluding these objects.

## 4.4 Kinematical modeling

In **Sect. 4.3**, we obtained all the necessary information about galaxy morphology (line-integrated maps) and kinematics (velocity and velocity-dispersion maps). In order to measure the dynamical masses of the host galaxies, we designed a kinematical model to perform a 2D fit of the maps. Therefore, we assumed that:

1. The observed line emission (i.e.,  $[\text{CII}]_{158\mu\text{m}}$  or CO transition) traces cold gas distributed in a rotating thin disk.
2. The gas mass surface density  $\Sigma(r)$ , is an exponential distribution that also tracks the distribution of surface brightness  $I(r)$ , that is:

$$\Sigma(r) \propto I(r) = I_0 \exp(-r/R_D), \quad (4.1)$$

where  $I_0$  is a normalization constant and  $R_D$  is the scale radius.

3. The galaxy stellar mass is distributed as the gas mass component (see **Eq. 4.1**).
4. The contribution of the dark matter is negligible.

Under these assumptions, Freeman (1970) showed that the corresponding circular velocity is given as:

$$V^2(r) = 4\pi G \Sigma_0 R_D y^2 [\mathcal{I}_0(y) \mathcal{K}_0(y) - \mathcal{I}_1(y) \mathcal{K}_1(y)], \quad (4.2)$$

where  $\mathcal{I}$  and  $\mathcal{K}$  are the modified Bessel functions evaluated at  $y = r/2R_D$ , and  $\Sigma_0$  is the normalization constant of the mass distribution that accounts for both gas and stars contribution. The total mass of the disk, which is the dynamical mass of the galaxy ( $M_{\text{dyn}}$ ), is thus obtained by integrating the mass surface density over all the radii;  $M_{\text{dyn}} = 2\pi R_D^2 \Sigma_0$ . By inserting this expression in **Eq. (4.2)**, we can relate the total dynamical mass with the velocity curve:  $V^2(r) = 2(M_{\text{dyn}}/R_D) G y^2 [\mathcal{I}_0(y) \mathcal{K}_0(y) - \mathcal{I}_1(y) \mathcal{K}_1(y)]$ . Therefore, by estimating  $R_D$  from the flux map, we can infer the galaxy dynamical mass by performing a 2D fit of the velocity field.

## 4.4.1 Details on the kinematical model and the strategy of the analysis

The kinematical model is calculated using Monte Carlo methods. At first, the 3D space is randomly filled with  $N \gg 1$  point-like sources uniformly distributed in a thin disk. Each source represents a “cloud” that contributes with a unit of flux in the computation of the total observed flux. Then, the 3D disk model is projected on the sky plane and convolved with the appropriate instrumental PSF and line spread function (LSF) of the observation. Thus, the flux map, the flux-weighted velocity map and the velocity-dispersion map are obtained through 2D-weighted histograms by using the pixel size of the corresponding observed map as the bin width. By properly choosing the weights, we can set the flux contribution of each cloud forming the model in order to reproduce any brightness (density) and velocity profiles. We set the weights in order to create an exponential thin disk defined by **Eq. (4.1)** and **Eq. (4.2)**. As an example, in **Fig. 4.5**, we show the simulated flux, velocity and velocity-dispersion maps obtained with our kinematical model in three different geometrical configurations. In order to recover the galaxies dynamical masses, we basically adopted the same method used in Cresci et al. (2009) and Carniani et al. (2013). We first performed a 2D fit of the observed flux map using a thin disk model with an exponential brightness profile, and we recovered the best value of scale radius  $R_D$  (see **Eq. 4.1**); then, by using the resulting  $R_D$  value, we computed the velocity field of our disk model accordingly with **Eq. (4.2)**, and we performed a 2D fit of the LOS velocity map, thus recovering the best estimate of  $M_{\text{dyn}}$ .

## 4.4.2 Estimation of $R_D$ : 2D fit of the flux maps

Following the method illustrated in the previous section, we first estimated the scale radius  $R_D$  on the 18 flux maps of the sources with spatially-resolved kinematics. The typical angular extension of the observed maps is  $\sim 1''$ , with a pixel size depending on the beam size of the observation (see **Sect. 4.2**) resulting in a typical map size of  $\sim 15 - 20$  pixels in linear diameter. We thus generated simulated maps using a 3D disk model with radius of  $R = 20$  pixels filled by  $N_p = 5 \times 10^6$  clouds. These values turned out to be the best compromise to smooth the stochastic oscillations of the cloud’s numerical density and to avoid spurious numerical effects at the boundary of the model,

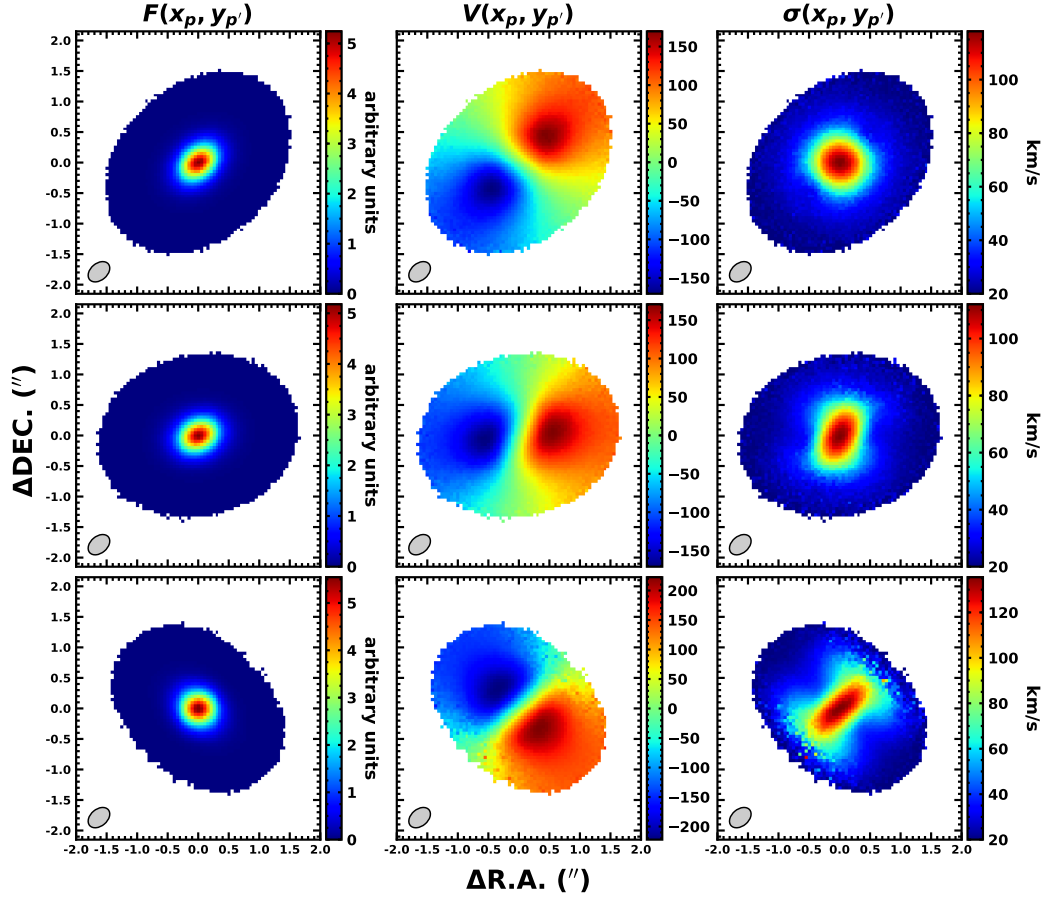


**Figure 4.5**

Simulated maps obtained with the kinematical model for a galaxy thin disk with an exponential brightness profile defined by a scale radius  $R_D = 0.125''$  and dynamical mass  $M_{\text{dyn}} = 5.0 \times 10^{10} M_{\odot}$ . The flux, velocity, and velocity-dispersion maps along the LOS are indicated by  $F(x_p, y_p)$ ,  $V(x_p, y_p)$ , and  $\sigma(x_p, y_p)$ , respectively. From the top to the bottom panel disk inclination and the position angle ( $\beta, \gamma$ ) are, respectively, equal to  $(40, -45)$  deg,  $(40, 0)$  deg, and  $(60, 45)$  deg. The other parameters defining the model are: the FWHM of the synthesized beam ( $0.4'' \times 0.275''$ ), the position angle of the beam ( $B_{\text{PA}} = -50$  deg), the FWHM of the LSF ( $\sigma_{\text{LSF}} = 20 \text{ km s}^{-1}$ ), the bin size ( $0.05'' \times 0.05''$ ), and the angular radius of the disk ( $R = 1.25''$ ). The number of clouds used in this model is  $N_p = 7.5 \times 10^6$ .

while simultaneously keeping the computational time relatively short. The 3D disk model is then projected on the sky plane, and, according to Eq. (4.1), the observed image of the simulated flux map depends on the normalization constant  $I_0$ , the scale radius  $R_D$ , and on the geometrical parameters: the coordinates of the map center  $(x_0, y_0)$ , the inclination with respect to the sky plane ( $\beta$ ) and the position angle of the line of nodes ( $\gamma$ ) measured clockwise

with respect to the east. We note that, for the purposes of this work, we were not interested in the physical value of  $I_0$ .

The aforementioned parameters were variable during the fit procedure. Thus, to retrieve their best estimations, we carried out the 2D map fit using the `cap-mpfit` PYTHON procedure part of the `pPXF` package by Cappellari & Emsellem (2004) based on `minpack-1` (Moré et al., 1980), performing a Levenberg-Marquardt least-squares minimization between the data and the model. For each map, the best model minimized the following function:

$$\chi^2 = \sum_{p,p'} \left[ \frac{\tilde{F}(x_p, y_{p'}) - F(x_p, y_{p'}; [I_0, R_D, \beta, \gamma, x_0, y_0])}{\sigma_F(x_p, y_{p'})} \right]^2 + \mathcal{P}, \quad (4.3)$$

where  $\tilde{F}$ ,  $F$  and  $\sigma_F$  are, respectively, the observed flux map, the flux model map, and the flux error map. We note that, in addition to the standard  $\chi^2$  function, we inserted a penalty term  $\mathcal{P} = 5 \times N_{\text{out}}$  in Eq. (4.3), where  $N_{\text{out}}$  is the number of pixels defined in the data but not in the model. Indeed, the sum in Eq. (4.3) is computed only taking into account the pixels  $(x_p, y_{p'})$  on the observed map in which the model is defined. Therefore, unless the model is defined in all the pixels in which the observed data are present, during the minimization process, the penalty term  $\mathcal{P}$  ensures the adequate penalization of configurations for which the model cannot reproduce the data in all the points (e.g., since the disk model is thin, completely edge-on disk configurations are highly unlikely unless the PSF is large enough).

In order to obtain a robust  $\chi^2$  minimization avoiding the convergence to a possible local minimum, the 2D flux map fit is performed multiple times by fixing the disk inclination angle ( $\beta$ ) to 5 deg and up to 90 deg with a step size  $\Delta\beta = 5$  deg. For each value of  $\beta$ , the  $\chi^2$  function in Eq. (4.3) is minimized with respect to the free parameters  $[I_0, R_D, \gamma, x_0, y_0]$ . At the end of each step, we retrieve the minimum of  $\chi^2(\beta)$  function and the corresponding set of best values of free parameters. We then used them as starting points for the next step. Once the minimization is performed for all the inclination values in the range  $[5, 90]$  deg, we sampled the curve of the minima as a function of the disk inclination angle, which is  $\chi_m^2(\beta)$ . Finally, by finding the absolute minimum of  $\chi_m^2(\beta)$ , we retrieved the best set of  $[I_0, R_D, \beta, \gamma, x_0, y_0]$ . Following the method illustrated above, we estimated the best value of  $R_D$  measured in arcseconds for all 18 objects indicated in Tab. 4.1 with flag

**Table 4.2:** Key parameters estimated from integrated spectra and kinematical modeling.

| No. <sup>(1)</sup> | Object ID                     | $z_{[\text{CII}]}$ <sup>(2)</sup> | $R_D$ <sup>(3)</sup><br>(kpc) | $M_{\text{dyn}}$ <sup>(4)</sup><br>( $10^{10} M_{\odot}$ ) | $\sin \beta$           |
|--------------------|-------------------------------|-----------------------------------|-------------------------------|--|------------------------|
| 2                  | VHS J2101-5943 <sup>(†)</sup> | $2.307262 \pm 0.000007$           | $2.95 \pm 0.11$               | $2.6^{+1.5}_{-0.9}$  | $0.73^{+0.17}_{-0.15}$ |
| 6                  | SDSS J1328-0224               | $4.64616 \pm 0.00002$             | $0.776 \pm 0.015$             | $0.26^{+0.03}_{-0.02}$                                     | $0.84^{+0.02}_{-0.03}$ |
| 7                  | SDSS J0923+0247               | $4.654876 \pm 0.000015$           | $0.850 \pm 0.008$             | $0.6^{+1.6}_{-0.3} \times 10^1$                            | $0.48^{+0.18}_{-0.23}$ |
| 9                  | SDSS J0129-0035               | $5.778883 \pm 0.000010$           | $0.626 \pm 0.006$             | $> 0.78 \times 10^1$                                       | $< 0.16$               |
| 10                 | SDSS J1044-0125               | $5.78440 \pm 0.00006$             | $1.14 \pm 0.07$               | $3.7^{+3.2}_{-0.3}$  | $0.90^{+0.03}_{-0.26}$ |
| 11                 | SDSS J1306+0356               | $6.03332 \pm 0.00003$             | $3.21 \pm 0.09$               | $1.8^{+0.3}_{-0.4}$  | $0.70^{+0.08}_{-0.13}$ |
| 12                 | SDSS J2310+1855               | $6.002841 \pm 0.000011$           | $0.876 \pm 0.006$             | $3.3^{+0.9}_{-0.9}$  | $0.58^{+0.11}_{-0.06}$ |
| 14                 | SDSS J2054-0005               | $6.038828 \pm 0.000009$           | $0.595 \pm 0.007$             | $0.7^{+4.5}_{-0.3}$  | $0.64^{+0.21}_{-0.42}$ |
| 19                 | ULAS J1319+0950               | $6.13334 \pm 0.00004$             | $1.50 \pm 0.03$               | $> 4 \times 10^2$  | $< 0.12$               |
| 22                 | PSO J308-21                   | $6.23265 \pm 0.00004$             | $0.9 \pm 0.02$                | bimodal distributions                                      |                        |
| 25                 | PSO J183+05                   | $6.43835 \pm 0.00002$             | $1.30 \pm 0.01$               | $> 2 \times 10^1$  | $< 0.24$               |
| 26                 | PSO J167-13                   | $6.514770 \pm 0.000015$           | $4.28 \pm 0.08$               | $1.69^{+0.14}_{-0.11} \times 10^1$                         | $0.83^{+0.03}_{-0.04}$ |
| 28                 | VIKING J0305-3150             | $6.61434 \pm 0.00002$             | $1.231 \pm 0.019$             | bimodal distributions                                      |                        |

**Notes.** <sup>(1)</sup>Source identification numbers in agreement with those listed in the first column of **Tab. 4.1**. <sup>(2)</sup>Redshift estimates obtained from the line integrated spectra. <sup>(†)</sup>This source is observed in CO(3–2), therefore the redshift estimate refers to this line. <sup>(3)</sup>Uncertainties on scale radius are statistical errors provided from  $\chi^2$ -minimization algorithm (see **Sect. 4.4.2**). <sup>(4)</sup>Uncertainties on dynamical masses are statistical errors computed using the posterior probability distributions of  $M_{\text{dyn}}$ , ignoring any possible systematic biases: lower limits, nominal values and the upper limits correspond to 16th, 50th, and 84th percentiles, respectively. Bimodal posterior probability distributions of the inclination angle (and dynamical mass) are explicitly indicated. In the case of bimodal distributions, no values are provided and the corresponding object was rejected from the final sample.

[rot]=“r”. Finally, we computed  $R_D$  values in physical length, using the redshift estimates obtained in **Sect. 4.3.1**.

In the next section, we use the  $R_D$  estimates to compute the kinematical model in order to perform the 2D fit of the velocity fields. For this purpose, we use the  $\chi_m^2(\beta)$  curve as a prior knowledge on disk inclination angle. As an example, in **Fig. 4.6**, we show flux map modeling results and the correspondent  $\chi_m^2(\beta)$  curve for SDSS J0923+0247. The  $R_D$  values are listed in **Tab. 4.2** for those objects with constraints on dynamical mass (see also, **Appx. A.5**).

### 4.4.3 Estimation of $M_{\text{dyn}}$ : 2D fit of the velocity maps

In order to estimate the dynamical masses of the quasars sample, we performed the 2D fit of LOS velocity maps. At high- $z$ , uncertainties on the

**Figure 4.6**

Figure shows the kinematical modeling performed on SDSS J0923+0247. The upper panels ([a.1]& [a.2]) show the fit result of the flux map, while the bottom panels ([b.1] & [b.2]) show the result of the 2D velocity field fit. [a.1]: the curve of  $\chi^2$  minima as a function of the disk inclination (see, Sect. 4.4.2 for details). The magenta hexagon indicates the absolute minimum ( $= 35$  deg) of  $\chi_m(\beta)$ . The green area (see, Sect. 4.4.3 for the definition) indicates the allowed inclination values used as a prior in performing a 2D velocity field fit. [a.2]: 2D best-fit model of the flux map. From left to right, we report the observed map, the model, and the residuals ([data-model]/error). Residuals values are color-coded according to the horizontal colorbar displayed at the bottom-left corner of the panel. [b.1]: the posterior probability distributions of the free parameters in 2D velocity field fits retrieved with the MCMC algorithm with the best values and their uncertainties. [b.2]: 2D best-fit model of the kinematical map. From left to right, we report the observed velocity map, the model, and the velocity curves extracted from a long-slit of two pixels in width aligned with the line of nodes. The slit is superimposed on maps; red circles and solid black lines in the right panel indicate the observed flux-weighted velocity values in each bin of the slit and the model, respectively.



dynamical mass estimates are mainly driven by the poor angular resolution of observations. As the integrated flux map of line emission, even the velocity maps are affected by beam smearing, thus introducing additional uncertainties in the fitting parameters (as also pointed out by other authors, see, e.g., Bosma, 1978; Begeman, 1987; de Blok & McGaugh, 1997; O'Brien et al., 2010; Swaters et al., 2000; Epinat et al., 2009, 2010; Swaters et al., 2009; Carniani et al., 2013; Kamphuis et al., 2015). This effect leads to the disk inclination angle and the dynamical mass becoming almost degenerate parameters, meaning the observed velocity field can be similarly reproduced by different couples  $(\beta, M_{\text{dyn}})$  with similar  $M_{\text{dyn}} \sin^2 \beta$  (which determines the LOS velocity field), thus providing very near values of  $\chi^2$  function (see also, e.g., Epinat et al., 2010). In **Fig. 4.7**, we show the effect of the beam smearing on the isovelocity curves of simulated velocity fields.

Consistently with the method illustrated in **Sect. 4.4.1**, we performed fits of velocity maps using thin rotating disk models defined by exponential mass distributions with the  $R_D$  values estimated in **Sect. 4.4.2**. In order to retrieve the best-fitting model and to estimate the parameter uncertainties, we used the PYTHON affine invariant Markov chain Monte Carlo (MCMC) ensemble sampler emcee (Foreman-Mackey et al., 2013). For this purpose, we defined the likelihood function of a model, given the data, as:

$$\begin{aligned} \ln p = & -\frac{1}{2} \left( \frac{\bar{x}_0 - x_0}{\Delta x_0} \right)^2 - \frac{1}{2} \left( \frac{\bar{y}_0 - y_0}{\Delta y_0} \right)^2 + \\ & -\frac{1}{2} \sum_{p,p'} \left\{ \frac{[\tilde{V}(x_p, y_{p'}) - V(x_p, y_{p'}; [\mu, \gamma, \sin \beta, x_0, y_0]) - V_{\text{sys}}]^2}{\sigma_V^2(x_p, y_{p'})} \right\} + \\ & + \ln \left[ 2\pi(\sigma_V^2(x_p, y_{p'})) \right] \Bigg\} - \frac{1}{2} \mathcal{D}, \end{aligned} \quad (4.4)$$

where  $\tilde{V}$ ,  $V$ , and  $\sigma_V$  are the observed velocity map, simulated velocity map, and velocity error map, respectively. The simulated field depends on geometrical parameters, the scale radius, and the dynamical mass (see **Eq. 4.2**). However, instead of  $M_{\text{dyn}}$ , we used  $\mu = \log(M_{\text{dyn}} \sin^2 \beta)$  as free parameter, since it is decoupled from disk inclination, thus it uniquely determines the intrinsic velocity field. Here, we also took into account the systemic velocity of the galaxy, which is  $V_{\text{sys}}$ , as an additional free parameter. Furthermore, defining the likelihood function in **Eq. (4.4)**, we assumed Gaussian priors

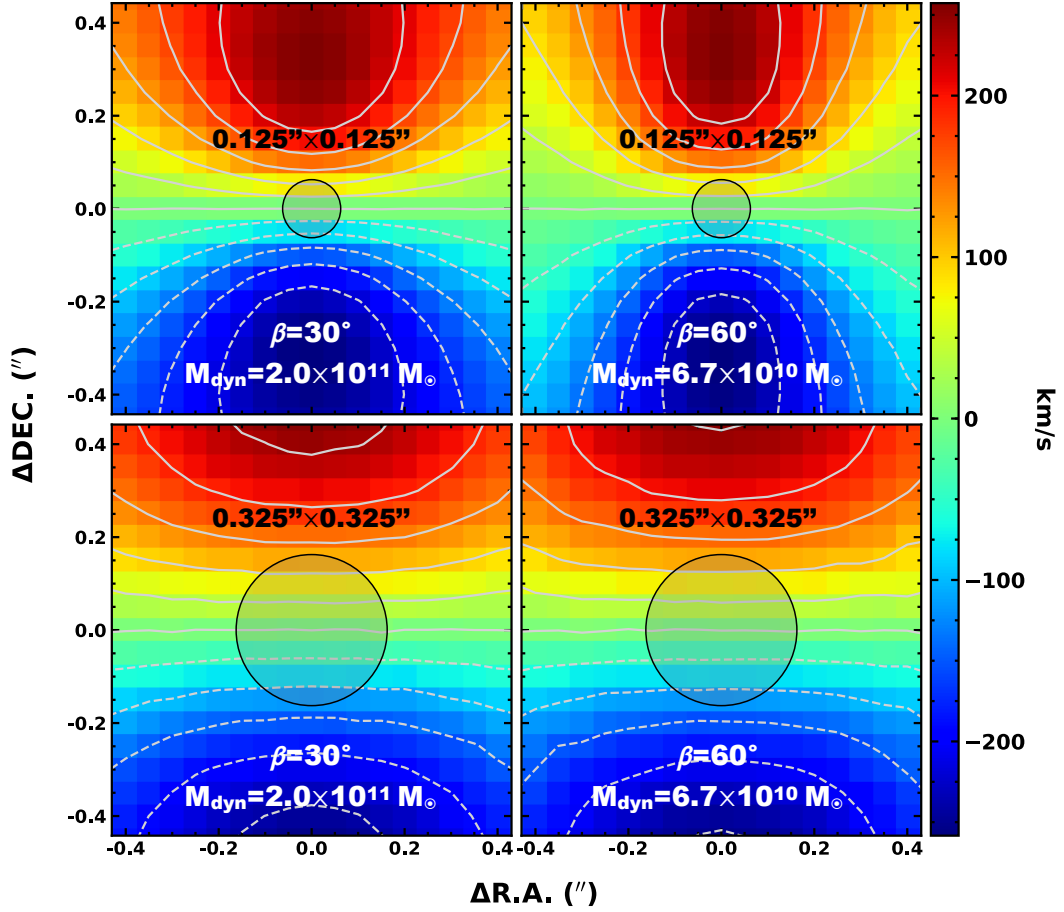


**Figure 4.7**

Simulated velocity field corresponding to four different couples of inclination angle  $\beta$  and dynamical mass  $M_{\text{dyn}} = 5.0 \times 10^{10} / \sin^2 \beta$ . Increasing the dimension of the beam FWHM (shaded area), the isovelocity curves are increasingly smoothed, and different configurations of the disk appear almost indistinguishable. The simulated maps are obtained with the kinematical model for a galaxy thin disk with  $R_D = 0.125''$ ,  $\gamma = -90$  deg. The other parameters defining the model are set as equal to the model in Fig. 4.5.

for the coordinates of the galaxy center with maximum probability corresponding to  $(x_0, y_0)$  obtained from the flux map modeling, as illustrated in Sect. 4.4.2. Here,  $\Delta x_0$  and  $\Delta y_0$  are the standard deviations assumed equal to 0.1 pixel. In addition, we assumed a box-like prior on the position angle of the disk ( $-180 \leq \gamma(\text{deg}) \leq 180$ ) and on the dynamical mass ( $M_{\text{dyn}} > 0$ ). Finally, we accounted for prior knowledge on disk inclination from morphology by imposing that, during the fitting process,  $\Delta \chi_m^2(\beta) < \max\{\Delta \chi_m^2(\beta)\}/2$ ; where  $\Delta \chi_m^2(\beta) = \chi_m^2(\beta) - \chi_M^2$  with  $\chi_M^2$  the absolute minimum of  $\chi_m^2(\beta)$  curve resulting from the fit of the flux map (see Sect. 4.4.2). We thus maximized

**Eq. (4.4)** using  $[V_{\text{sys}}, \mu, \gamma, \sin \beta, x_0, y_0]$  as free parameters, and we recovered their posterior probability distributions<sup>2</sup>. Finally, the best values of parameters and related uncertainties were estimated by computing the 16th, 50th, and 84th percentile of the distributions. As an example, **Fig. 4.6** shows the kinematical modelling of SDSS J0923+0247 (see also, **Appx. A.5**).

Due to the poor spatial resolution of some observations, we successfully constrained the disk inclination and the dynamical mass for only 13 objects of the sample (see **Tab. 4.2**). We note that for two of them we find bimodal distributions for  $\sin \beta$  and  $\mu$ , thus not permitting us to define unique values.

## 4.5 Determination of the BH masses

Currently, as we seen in **Sect. 1.4**, the only possible technique to carry out BH mass estimates at high- $z$  is the use of SE virial relation, which combines the FWHM or the line emission that originated in the BLR of quasar, with the continuum luminosity emitted from the BH accretion disk (e.g., McLure & Dunlop 2004; Vestergaard & Peterson 2006; Vestergaard & Osmer 2009; but see also, e.g., Trevese et al. 2014; Grier et al. 2019).

### 4.5.1 BH masses from the literature

In this work, we adopted a unique SE virial relation to estimate the BH masses of our sample homogeneously. In detail, we used the relation by Bongiorno et al. (2014), which was calibrated by assuming the BH–galaxy scaling relations by Sani et al. (2011). The latter is consistent with the relation used as a  $z = 0$  reference for studying the redshift evolution (e.g. Kormendy & Ho, 2013; de Nicola et al., 2019):

$$\log\left(\frac{M_{\text{BH}}}{M_{\odot}}\right) = 6.6 + 2 \log\left(\frac{\text{FWHM}(\text{MgII})}{10^3 \text{km s}^{-1}}\right) + 0.5 \log\left(\frac{\lambda L_{\lambda}(3000 \text{\AA})}{10^{44} \text{erg s}^{-1}}\right). \quad (4.5)$$

Thus, where available, we retrieved MgII FWHM and the continuum luminosity estimates from the literature and, if they were unavailable, we assumed  $M_{\text{BH}}$  estimates as provided in the literature.

<sup>2</sup>We set up the MCMC procedure with 50 walkers performing 1000 steps each for a total of  $5 \times 10^4$  evaluations of the log-likelihood function.

**Table 4.3:** Black hole masses retrieved from literature and spectroscopic data used to estimate  $M_{\text{BH}}$  through MgII-based virial relation.

| No. <sup>(1)</sup> | Object ID         | FWHM(MgII)<br>(km s <sup>-1</sup> ) | $\lambda L_{\lambda}(3000 \text{ \AA})$<br>(10 <sup>46</sup> erg s <sup>-1</sup> ) | $M_{\text{BH}}$ <sup>(2)</sup><br>( $M_{\odot}$ ) | References <sup>(3)</sup> |
|--------------------|-------------------|-------------------------------------|--|---|---------------------------|
| 2                  | VHS J2101-5943    | -                                   | -  | $3.2 \pm 0.7 \times 10^{10}$                      | Ban2015                   |
| 6                  | SDSS J1328-0224   | $3815 \pm 954$                      | $1.9 \pm 0.4$  | $8 \pm 4 \times 10^8$                             | Tra2011                   |
| 7                  | SDSS J0923+0247   | $2636 \pm 264$                      | $1.4 \pm 0.3$  | $3.3 \pm 1.0 \times 10^8$                         | Tra2011                   |
| 9                  | SDSS J0129-0035   | -                                   | -  | $1.7^{+3.1}_{-1.1} \times 10^8$                   | Wan2013                   |
| 10                 | SDSS J1044-0125   | -                                   | -  | $5.6 \pm 0.5 \times 10^9$                         | She2019                   |
| 11                 | SDSS J1306+0356   | $3158 \pm 145$                      | $2.45 \pm 0.06$  | $6.3 \pm 1.5 \times 10^8$                         | DeR2011                   |
| 12                 | SDSS J2310+1855   | $4497 \pm 352$                      | $6.027 \pm 0.018$  | $2.0 \pm 0.6 \times 10^9$                         | She2019                   |
| 14                 | SDSS J2054-0005   | -                                   | -  | $0.9^{+1.6}_{-0.6} \times 10^9$                   | Wan2013                   |
| 19                 | ULAS J1319+0950   | $3675 \pm 17$                       | $3.8 \pm 1.0$  | $1.1 \pm 0.2 \times 10^9$                         | Sha2017                   |
| 26                 | PSO J167-13       | $2350 \pm 470$                      | $1.5 \pm 0.7$  | $2.7 \pm 1.4 \times 10^8$                         | Ven2015                   |
| 28                 | VIKING J0305-3150 | $3189 \pm 85$                       | $1.66 \pm 0.02$  | $5.2 \pm 1.2 \times 10^8$                         | DeR2014                   |

**Notes.** <sup>(1)</sup>Source identification numbers in agreement with those listed in the first column of **Tab. 4.1**. <sup>(2)</sup>BH mass estimated using SE virial relation in **Eq. (4.5)** when possible, otherwise, the value provided here is the one available in literature (see references for full details). The uncertainties we report do not include the systematic uncertainties intrinsic to the  $M_{\text{BH}}$  estimators. <sup>(3)</sup>References: Ban2015 - Banerji et al. (2015); DeR2011, DeR2014 - De Rosa et al. (2011) and De Rosa et al. (2014); Sha2017 - Shao et al. (2017); She2019 - Shen et al. (2019a); Tra2011 - Trakhtenbrot et al. (2011); Ven2015 - Venemans et al. (2015); Wan2013 - Wang et al. (2013).

In summary, we recover BH masses from the literature for everything except PSO J308-21 and PSO J183+05, using  $H\beta$ , MgII, and CIV BLR lines. For SDSS J0129-0035 and SDSS J2054-0005, the BH masses were estimated from the bolometric luminosity ( $L_{\text{bol}}$ ) assuming Eddington accretion ( $L_{\text{bol}}/L_{\text{Edd}} = 1$ ). We note that this assumption is supported by some evidences showing that BHs at  $z \gtrsim 6$  accrete matter at a rate comparable to the Eddington limit (De Rosa et al., 2014; Mazzucchelli et al., 2017b). The data are listed in **Tab. 4.3**. The BH masses computed in this work using Bongiorno et al. (2014) calibrations are a factor  $\sim 2$  smaller than those reported in literature using different calibrations (see references in **Tab. 4.3**, for full details). However, both estimates are consistent within the typical uncertainties ( $\sim 0.4$  dex).

## 4.5.2 BH mass from LBT data

The study of the redshift evolution of  $M_{\text{BH}} - M_{\text{dyn}}$  relation can be severely affected by reliability of  $M_{\text{BH}}$  estimates; in particular, the available spectroscopic information for our sample did not allow us to derive  $M_{\text{BH}}$  measurements with a unique method. We therefore started an observational campaign with

the LBT (Large Binocular Telescope), of those sources with estimated  $M_{\text{BH}}$  assuming  $L_{\text{bol}}/L_{\text{Edd}} = 1$  (SDSS J0129-0035, SDSS J2054-0005, and SDSS J2310+1855), and of two additional targets without previous  $M_{\text{BH}}$  estimates from the literature (PSO J308-21 and PSO J138+05; even though dynamical masses of these two sources are tentative). We thus obtained NIR spectra of the quasars with LUCI (LBT Utility Camera in the Infrared) targeting the CIV line and the adjacent continuum, which are redshifted into the  $zJ$  filter (central  $\lambda = 1.17 \mu\text{m}$ ), for everything except PSO J183+05. In fact, for all these sources, the MgII line falls in a spectral region with a very low atmospheric transmission. For PSO J183+05, instead, we targeted the BLR MgII line, which is redshifted at  $\approx 2.0817 \mu\text{m}$  and can be observed with the  $HK$  filter (central  $\lambda = 1.93 \mu\text{m}$ ).

Unfortunately, due to poor weather conditions, we did not achieve the requested sensitivities. No BLR emission lines have been detected in any of the quasars except J2310+1855, from which we derived a CIV-based  $M_{\text{BH}}$  estimate of  $6 \times 10^9 M_{\odot}$  (see, **Appx. A.4** for full details of the observations). Our estimation is consistent, within the error, with that reported by Feruglio et al. (2018) and Shen et al. (2019a). We note that Shen et al. (2019a), who published NIR spectra of a large sample of  $z \sim 5.7$  quasars, also provide a  $M_{\text{BH}}$  measurement for J2310+1855 through virial relation based on MgII as well. In the following, we refer to the MgII estimate from Shen et al. (2019a), because of the issues related to CIV-based measurements (see **Sect. 1.4.2**).

## 4.6 Summary of sample subselections

The data analysis described in **Sects. 4.3** and **4.4** was performed on the 32 continuum-subtracted cubes of the sources listed in **Tab. 4.1**. Each step of the analysis has led to the rejection of a number of objects that turned out not to be suitable for the method adopted in this work. Here, we briefly summarize the different subselections used throughout this work:

1. By inspecting the velocity maps and red/blue residuals maps (see, **Sect. 4.3.3** for details), we found that 14 out of 32 objects ( $\sim 45\%$ , flagged with [rot]=“u” in **Tab. 4.1**) do not show spatially resolved kinematics or rotating disk kinematics. This is possibly due to the presence of outflows or merging events, or of a companion located

in proximity (projected on the sky plane) of the quasar. For this purpose, velocity-dispersion maps provide additional information on the kinematics. However, a comprehensive interpretation of the complex velocity fields observed in these sources is beyond the scope of this thesis. As a result of this analysis, the sample has been reduced from 32 to 18 objects. On the other hand, excluding these objects from the final sample may introduce bias in the final results (see **Sect. 4.7.4**).

2. We then performed the fits of the flux and velocity maps (see, **Sects. 4.4.2** and **4.4.3** for details) on the remaining 18 objects selected in the previous step. As a result, for five objects ( $\sim 30\%$ ), the kinematical modeling has not enabled us to constrain the disk inclination, and consequently the dynamical mass. It is possible that incorrect assumptions on the mass distribution (see **Eq. 4.1**) and/or the poor angular resolution of the observations making inclination and dynamical mass almost degenerate parameters (see **Sect. 4.4.3**) have prevented the determination of the mass in these host galaxies. In addition, the isovelocity curves of the kinematical fields are typically distorted, suggesting the presence of non-circular motion. In particular, for two objects (PSO J308-21, VIKING J0305-3150), the posterior probability distributions of the inclination angle  $\beta$  and  $\mu$  are bimodal, preventing us from constraining these parameters. For three objects (PSO J183+05, SDSS J0129-0035, ULAS J1319+0950), we derived an upper limit on the disk inclination, which is a lower limit on mass  $M_{\text{dyn}}$ . In summary, we obtained 8 constrained, 2 bimodal, and 3 lower limit measurements of the dynamical mass (see **Tab. 4.2**).
3. The final step is to relate our dynamical mass estimates with  $M_{\text{BH}}$  retrieved from the literature. We illustrate this step in **Sects. 4.5** and **4.8**. Despite several studies performed in this field aiming to estimate  $M_{\text{BH}}$  even for high-redshift quasars, for two objects ( $\sim 15\%$  of the remaining 13 resulted from the previous step), BH mass estimates were not available at the time this work was written. Therefore, we rejected these objects from the final sample (see **Tab. 4.3**). These quasars are flagged with  $[M_{\text{BH}}] = \text{“u”}$  in **Tab. 4.1**.

These selection steps are shown in the scheme drawn in **Fig. 4.8**. Overall, we were able to obtain a measurement of galaxy dynamical mass and retrieve

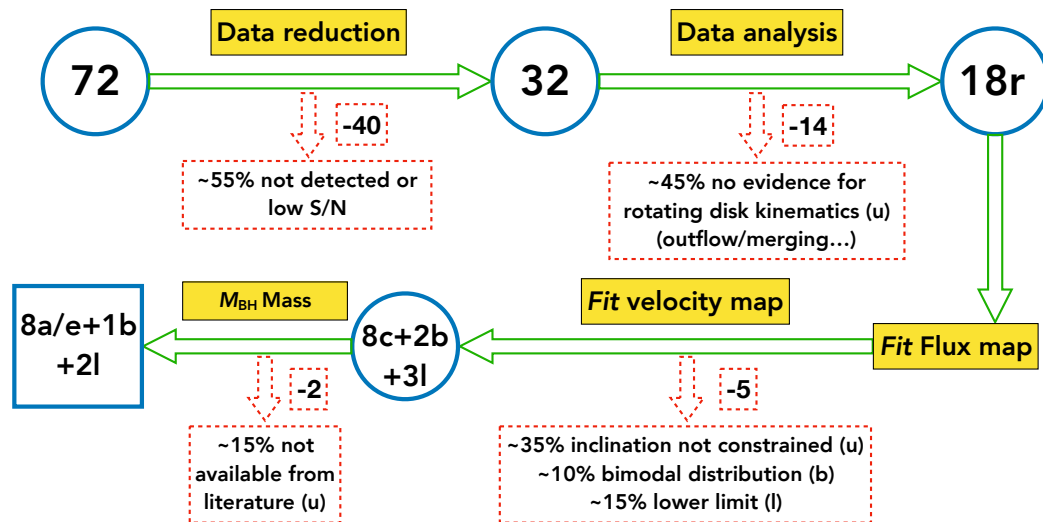


**Figure 4.8**

Scheme summarizes the different sub-selections used throughout this work. Starting from an initial sample of 72 quasar host galaxy observations extracted from the ALMA data archive, the final sample is composed of ten high- $z$  objects for which we study the BH–galaxy relation. The characters indicating the selection type are in accordance with **Tab. 4.1**. The number of objects rejected from the sample is also indicated at each step.

BH mass only for eight sources, that is  $\sim 10\%$  of the initial sample of 72 quasars.

## 4.7 Comparison of results and uncertainties on dynamical mass estimates

In **Sect. 4.7.1**, we compare our results with those obtained by other authors who attempted to perform a full kinematical modeling of individual sources that belong to our sample. Other works highlighted the presence of companion sources in the close environment of a few quasars analyzed in this work. Such satellite galaxies can disturb the gas kinematics of the host through tidal interaction, thus introducing additional uncertainties in measuring the galaxy dynamical mass. We discuss this point in **Sect. 4.7.2**. In **Sect. 4.7.3**, we discuss the limit of validity of the assumption of a rotating disk model and the possible mass contribution arising from random motions through-

out the galaxy (see also, **Appx. A.2**). Finally, in **Sect. 4.7.4**, we investigate observational biases possibly arising from the sub-selection of the sample.

### 4.7.1 Comparison of results from other kinematical modeling in the literature

In the following sections, we discuss the results obtained from the kinematical modeling of J1319+0950, J0305-3150, J1044-0125, and J0129-0035, making a comparison between our results and those obtained in previous works.

#### **ULAS J1319+0950**

Jones et al. (2017) and Shao et al. (2017) performed a kinematical characterization of [CII] emission of J1319+0950 by using a tilted rings warpleless model and assuming purely circular rotation. They inferred, respectively, a dynamical mass of  $15.8 \times 10^{10} M_{\odot}$  and  $13.4 \times 10^{10} M_{\odot}$  and an inclination angle of 29 deg and 33 deg (which are roughly consistent with the value estimated by Wang et al. 2013) by using the axial ratio of the [CII] flux map to estimate the disk inclination and the [CII] FWHM as estimate of maximum circular velocity. Furthermore, by fitting the dust continuum emission in UV plane, Carniani et al. (2019) inferred an inclination angle of  $\sim 15$  deg. In contrast, we are not able to constrain the disk inclination angle from our kinematical modeling, resulting in a lower limit on dynamical mass ( $> 4 \times 10^{12} M_{\odot}$ ). The disagreement between our result and the previous ones may arise from the beam smearing effect that is not taken into account in the model used by Jones et al. (2017) and Shao et al. (2017). As discussed in **Sect. 4.4.3**, beam smearing strongly affects the observed velocity gradients and introduces additional uncertainties in the fitting parameters. In addition, Shao et al. (2017) mentioned that current data cannot fully rule out the presence of a bidirectional outflow, which introduces additional uncertainty regarding the dynamical mass. In such a case, the strong deviation of the ratio  $M_{\text{BH}}/M_{\text{dyn}}$  could be associated with an incorrect kinematical modeling of the observed data, for which we also assume rotating disk kinematics, like in Jones et al. (2017) and Shao et al. (2017).

## VIKING J0305-3150

High angular resolution ( $0.076'' \times 0.071''$ ) ALMA [CII] observations of J0305-3150 were recently presented and analyzed by Venemans et al. (2019). The resulting analysis highlights that the distribution and kinematics, as traced by the [CII] emission, are highly complex and include the presence of cavities and blobs. Venemans et al. (2019) attempted to model the kinematics adopting different 3D models (thin rotating disk with constant velocity, Keplerian disk, truncated disk, and a simple AGN model embedded in a uniform rotating spherical gas) taking into account beam smearing effects and pixel correlation within the beam with a Bayesian approach. The results show that the gas kinematics in J0305-3150 appear to be dispersion-dominated, with some overall rotation in the central kiloparsecs, and cannot easily be reproduced by a simple rotating disk model with the implication that most of the gas has not settled in a disk yet. In addition, authors point out that energy injection into the ISM produced by AGN feedback processes, and the presence of a companion in the close environment, may play an important role in producing the observed [CII] cavities and in perturbing the gas kinematics. In conclusion, a simple model of a rotating disk is not sufficient to match the [CII] observations of J0305-3150 also derived by our analysis, where  $M_{\text{dyn}}$  is unconstrained by the simple model assumed.

## SDSS J1044-0125 & SDSS J0129-0035

In the work by Wang et al. (2019c), authors carried out observations of J1044-0125 and J0129-0035 through the ALMA program 2012.1.00240.S (the same dataset used in this thesis for the latter source) with angular resolution of  $\sim 0.2''$ . The authors show that gas in J1044-0125, as traced by [CII] emission, does not show a clear sign of rotation, suggesting a very turbulent gas velocity field. Furthermore, the [CII] spectrum reveals offset components that could be associated with a node of outflowing gas or the dense core of a satellite galaxy, which contribute to increasing the velocity-dispersion component of the gas in the host galaxy. On the other hand, the lower angular resolution data used in our work ( $\sim 0.6'' \times 0.5''$ , ALMA program 2011.0.00206.S; see, Wang et al. 2013) reveal the presence of a velocity gradient. This could be the result of beam smearing effects producing a smoothing of the rapidly changing velocity gradients. In the case of J1044-0125, we find that the observed velocity field is roughly consistent with a nearly edge-on rotating

disk model. Therefore, we conclude that our dynamical mass estimate is tentative. We also note that Wang et al. (2019c) show that [CII] and dust emissions in the nuclear region of J1044-0125 and J0129-0035 follow an exponential light profile, in accordance with the hypothesis at the base of our model.

In the case of J0129-0035, the observations analyzed in Wang et al. (2019c) reveal that [CII]-emitting gas shows clear velocity gradients likely associated with a rotating disk with additional gas clumps, thus suggesting complex kinematics in the nuclear region. They attempted to constrain the host galaxy dynamics adopting the same method as in the works of Jones et al. (2017) and Shao et al. (2017). The results show that the kinematics are consistent with a nearly face-on rotating disk with an inclination angle of  $\beta = (16 \pm 20)$  deg and a lower limit on the dynamical mass equal to  $M_{\text{dyn}} = 2.6 \times 10^{10} M_{\odot}$ . The results are consistent with what we found in this thesis. The BH mass of J0129-0035 is estimated as in Wang et al. (2013), assuming Eddington accretion, and is the same one that we used in this thesis. Hence, Wang et al. (2019c) estimated a BH-to-host-galaxy dynamical mass ratio of  $M_{\text{BH}}/M_{\text{dyn}} = 0.0066$  to be compared with  $M_{\text{BH}}/M_{\text{dyn}} = 0.0022$ , which is roughly consistent with the local ratio predicted in Decarli et al. (2010), unlike the most luminous quasars with massive BHs ( $10^9 - 10^{10} M_{\odot}$ ) at this redshift that show ratios from a few to  $\gtrsim 10$  times higher (Venemans et al., 2016; Decarli et al., 2018). Therefore, as pointed out by Wang et al. (2019c), this result may suggest that the BH–galaxy coevolution of a less massive system ( $M_{\text{BH}} \sim 10^7 - 10^8 M_{\odot}$ ) in the early Universe is closer to the trend of local galaxies (see also, Willott et al. 2010a, 2015b, 2017; Izumi et al. 2018, 2019).

#### 4.7.2 Possible contamination due to the presence of companion sources in the quasar’s local environment

Decarli et al. (2017) serendipitously discovered companion galaxies in the ALMA field of SDSS J0842+1218, CFHQS J2100-1715, PSO J231-20, and PSO J308-21. Such companions appear similar to the host galaxies of quasars in terms of [CII] brightness and implied dynamical mass, but do not show ev-

idence of AGN activity. In our work, we analyzed the same dataset as Decarli et al. (2017) (ALMA program 2015.1.01115.S), concluding that the kinematics are unresolved (flag [rot]=“u”; see, **Tab. 4.1**) in the case of J0842+1218 and J2100-1715 (beam size of  $\sim 1.0'' \times 0.9''$  and  $\sim 0.7'' \times 0.6''$ , respectively); and marginally resolved (disk inclination angle is unconstrained; flag  $[\beta]$ =“u”; see, **Tab. 4.1**) in the case of J231-20 (beam size of  $\sim 1.0'' \times 0.8''$ ). This last source together with J308-21 has a [CII]-bright companion at small projected separation of  $\sim 10$  kpc, suggesting a strong gravitational interaction between quasar and companion able to alter the disk kinematics increasing the velocity-dispersion component of the gas. In particular, Decarli et al. (2017) show that the [CII] emission of J308-21 stretches over about  $4''$  ( $\approx 25$  kpc) and more than  $1000 \text{ km s}^{-1}$  connecting the companion source suggesting that is undergoing a tidal disruption due to the interaction or merger with the quasar host. This scenario is successively supported by higher angular resolution ( $\sim 0.3''$ ; ALMA program 2016.A.00018.S) follow-up observation of J308-21 presented in Decarli et al. (2019a); the same dataset analyzed in this thesis. However, the bulk of [CII] emission of the quasar host galaxy shows a spatially resolved velocity gradient, which, in this thesis we attempt to model with a rotating disk by excluding pixels that are clearly not associated with the quasar host. Nevertheless, our analysis leads to a bimodal posterior probability distribution of disk inclination angle and dynamical mass parameters of J308-21. We can thus conclude that the complex kinematics of this system highlighted in the previous analysis presented in Decarli et al. (2017, 2019a), cannot be easily interpreted with a simple rotating disk, likely due to the perturbed kinematics caused by the strong interaction with the satellite galaxy. In **Chap. 6**, we will further focus on J231-20 and J308-21 and their companions by studying in details their ISM physical properties.

Willott et al. (2017) analyzed the source PSO J167-13 observed in ALMA Cycle 3 project 2015.1.00606.S; the same dataset analyzed in this thesis. This source shows an asymmetric continuum emission that is more extended to the south–east than north–west of the peak. This excess is located at  $\approx 0.9''$  (projected distance  $\approx 5.0$  kpc), and it is associated with a companion galaxy whose [CII] blueshifted ( $270 \text{ km s}^{-1}$ ) emission corresponds to about 20% of the quasar [CII] luminosity. The P-V diagram of the source shows a positive velocity gradient, suggesting a rotating disk geometry. With this assumption,

Willott et al. (2017) infer the dynamical mass of  $M_{\text{dyn}} = 2.3 \times 10^{11} M_{\odot}$  using the axial ratio of the quasar (excluding the companion source) [CII] flux map as an estimate of the disk inclination angle. The BH mass of J167-13,  $M_{\text{BH}} = (4.0 \pm 2.0) \times 10^8 M_{\odot}$ , is estimated in Venemans et al. (2015) using calibration based on MgII broad emission line (Vestergaard & Osmer, 2009). By comparison, we measure a dynamical mass of  $1.67^{+0.14}_{-0.11} \times 10^{11} M_{\odot}$  and a BH mass of  $M_{\text{BH}} = (2.7 \pm 1.4) \times 10^8 M_{\odot}$  (see, Sect. 4.5 for details) resulting in a ratio of  $M_{\text{BH}}/M_{\text{dyn}} = 0.0016$ , which is completely consistent with the value found by Willott et al. (2017) ( $M_{\text{BH}}/M_{\text{dyn}} = 0.0017$ ) and with the prediction of the local relation (Decarli et al., 2010; Kormendy & Ho, 2013).

Neeleman et al. (2019) further investigated the aforementioned four quasar host-companion galaxy pairs of J0842+1218, J2100-1715, J231-20, J167-13 by analyzing high angular resolution ( $\sim 0.4'' \times 0.3''$ ) ALMA observations of [CII] emission. They observe tidal interactions disturbing the gas in these high- $z$  galaxies making the ISM turbulent and thus confirming previous results of Decarli et al. (2018, 2019a) and Willott et al. (2017). Furthermore, these high angular resolution observations reveal that [CII] emission of SDSS J1306+0356 arises from two spatially and spectrally distinct sources with a physical separation of 5.4 kpc that are interacting tidally. Neeleman et al. (2019) modeled the [CII] kinematics of the galaxy pairs with a rotating thin disk model, taking into account the beam smearing and the correlation between pixels. They obtained upper limits on dynamical masses for all the sources except J167-13 and J2100-1715. In particular, they measured a dynamical mass of  $(3.5 \pm 0.4) \times 10^{10} M_{\odot}$  for the J167-13 quasar. This value is about one order of magnitude lower than the result of Willott et al. (2017) and our work. In our estimate, we also take into account the emission from the companion galaxy, thus possibly overestimating the quantities derived from the total integrated spectrum ( $\text{FWHM}_{[\text{CII}]}$ , [CII] flux, luminosity, etc.; see, Tab. A.1 in Appx. A.1), the scale radius of the mass profile and the total mass content of the quasar host galaxy. This could explain the inconsistency in our dynamical mass measurements of J167-13 compared to the works of Willott et al. (2017) and Neeleman et al. (2019).

### 4.7.3 Limit on the assumption of thin rotating disk

The comparison of our results discussed in **Sects. 4.7.1** and **4.7.2** highlights that, at least in some cases, the assumption of a thin rotating disk is too simplified to properly describe the observed complex kinematic field. Furthermore, from the analysis of the velocity maps, we find extreme cases in which the disk inclination with respect to the sky plane is very low (e.g., ULAS J1319+0950), compatible with a face-on configuration. However, for these objects, the observed velocity dispersions are still high ( $\sim 100\text{--}200\text{ km s}^{-1}$ , as is clear from the figures in **Appx. A.5**), which is not expected for thin face-on disks. The observed velocity dispersion can be produced both by instrumental effect and random motions throughout the galaxy (see, e.g., Flores et al., 2006; Weiner et al., 2006; Epinat et al., 2010). Different authors (e.g. Cresci et al., 2009; Epinat et al., 2009; Taylor et al., 2010) pointed out that random motions can support part of the mass. In this case, modeling the kinematics with a rotating disk could result in underestimating the galaxy’s dynamical mass. In **Appx. A.2**, we investigate the contribution of random motions to the dynamical mass and find that, in our sample, the mass supported by non-rotational motions is negligible, meaning it is included within the dynamical mass uncertainties. Therefore, we conclude that the rotating gas disk model provides an overall good description for the gas kinematics of our quasar host galaxies.

### 4.7.4 Potential observational biases in excluding the unresolved objects

In **Sect. 4.3.3**, we investigated whether the observed kinematics are spatially resolved. Out of 32 objects with a line detection, 14 ( $\geq 40\%$ ) were rejected from the final sample (see also, **Sect. 4.6**). Excluding those objects that are spatially unresolved could result in an observational bias. In fact, if these sources were significantly less massive than the others, the final results might therefore be biased towards more massive host galaxies.

The observed size of the line emitting region may depend on both the achieved sensitivity and the angular resolution. Therefore, in the case of spatially unresolved emission, it is difficult to assess if this is due to the

intrinsic compact size of the galaxy or to the low sensitivity level of the observations. For this purpose, deeper observations of these objects with similar observational setups could help us to make a fair comparison of the observed size. However, we do not observe a strong correlation between the spatial size of the FIR line emission and the dynamical mass of the galaxy (see **Tab. 4.2**). Therefore, we conclude that we cannot safely argue that a possible bias is introduced in rejecting the spatially unresolved objects.

## 4.8 The $M_{\text{BH}} - M_{\text{dyn}}$ relation at high redshift

In order to trace the relation between BH mass and dynamical mass for the final high- $z$  quasar sample, we compared the  $M_{\text{dyn}}$  measurements obtained through kinematical modeling illustrated in **Sect. 4.4** (see **Tab. 4.2**), with the BH masses obtained from literature as we explained in **Sect. 4.5** (see **Tab. 4.3**). The relation is shown in the plot of **Fig. 4.9**. We also report two reference relations obtained with samples of local quiescent galaxies (Kormendy & Ho, 2013; de Nicola et al., 2019) and AGN (Reines & Volonteri, 2015). In order to infer the average redshift evolution of the  $M_{\text{BH}} - M_{\text{dyn}}$ , we adopted the relation  $\log M_{\text{BH}} = \alpha + \beta (\log M_{\text{dyn}} - 10.8)$ , and we performed the fit assuming fixed slope  $\beta = 1.01 \pm 0.07$  as found by de Nicola et al. (2019), and the normalization  $\alpha$  as the only free parameter. Furthermore, to reduce the impact of any possible outliers, we executed the fit adopting the bootstrap method on the standard  $\chi^2$  minimization. Using  $10^4$  bootstrap iterations, we obtained the best value of  $\alpha$  and its uncertainties by computing the 16th, 50th, and 84th percentiles, respectively:

$$\alpha = 9.4 \pm 0.3. \quad (4.6)$$

Our result is in agreement with those reported by other high- $z$  works (e.g. Decarli et al., 2010, 2018; Trakhtenbrot et al., 2015, 2017; Venemans et al., 2016, 2017c) suggesting that the  $M_{\text{BH}} - M_{\text{dyn}}$  relation evolves with redshift. It should be noted that the local reference relation (e.g. Kormendy & Ho, 2013; de Nicola et al., 2019) is obtained using bulge stellar mass in spiral and elliptical galaxies (where, in the latter case, bulge stellar mass corresponds to the total stellar mass). As a result, the galaxy dynamical masses estimated in this work should be treated as an upper limit of the total stellar mass. By

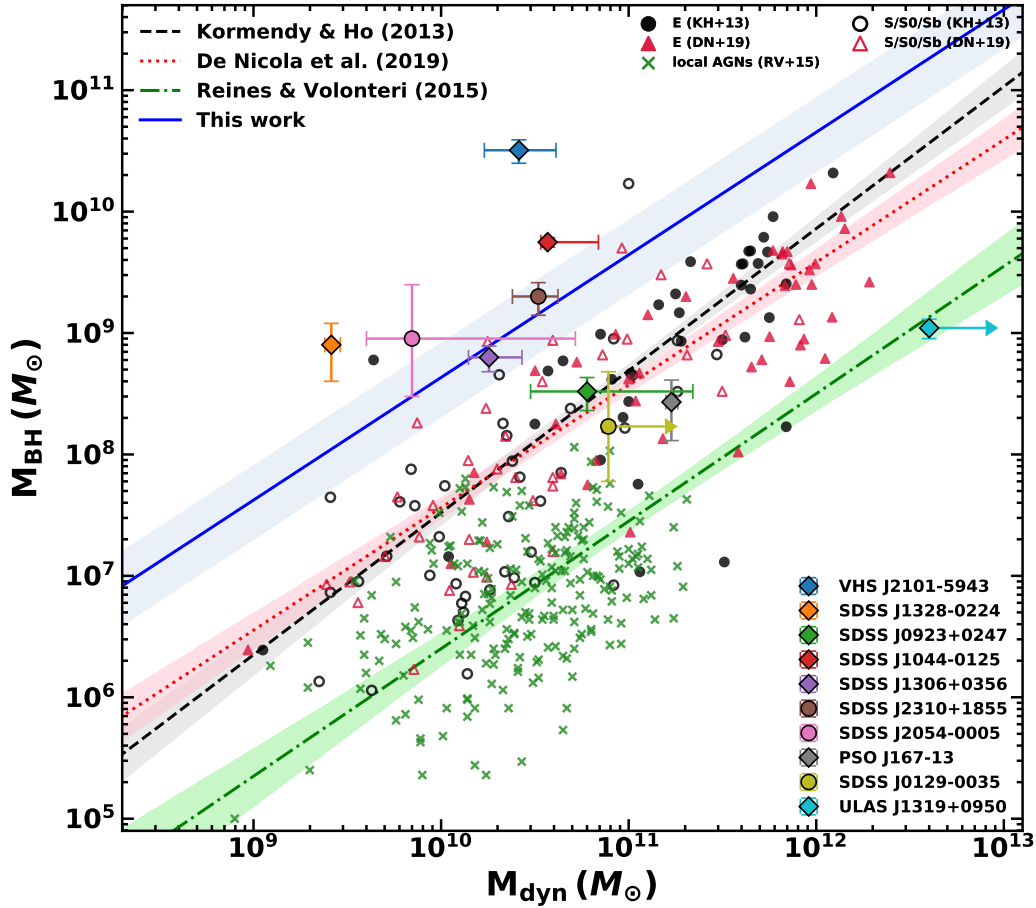


**Figure 4.9**

High-redshift relation between the BH mass ( $M_{\text{BH}}$ ) and the dynamical mass of the host galaxy ( $M_{\text{dyn}}$ ). The dashed black line and the dotted red line represent the reference local relation inferred using samples of local galaxies (E=ellipticals, S/S0/Sb=spirals) shown as black dots (Kormendy & Ho, 2013, also indicated as KH+13) and red triangles (de Nicola et al., 2019, or DN+19). The green line is the relation found by Reines & Volonteri (2015, or RV+15) by measuring the total stellar mass in a sample of the local AGN (green crosses). The solid blue line is the best fit to our data. The shadowed areas show the  $1\sigma$  uncertainty. In the case of SDSS J0129-0035 and ULAS J1319+0950, we inferred a lower limit on the dynamical mass. We do not take these data into account in the fit. The circles of our data points indicate the sources for which the BH masses are estimated from bolometric luminosity assuming Eddington accretion.

comparing our results with the relation by Reines & Volonteri (2015), who adopted the total stellar mass of the AGN host galaxy (green line in Fig. 4.9), we find an even stronger evolution with redshift.

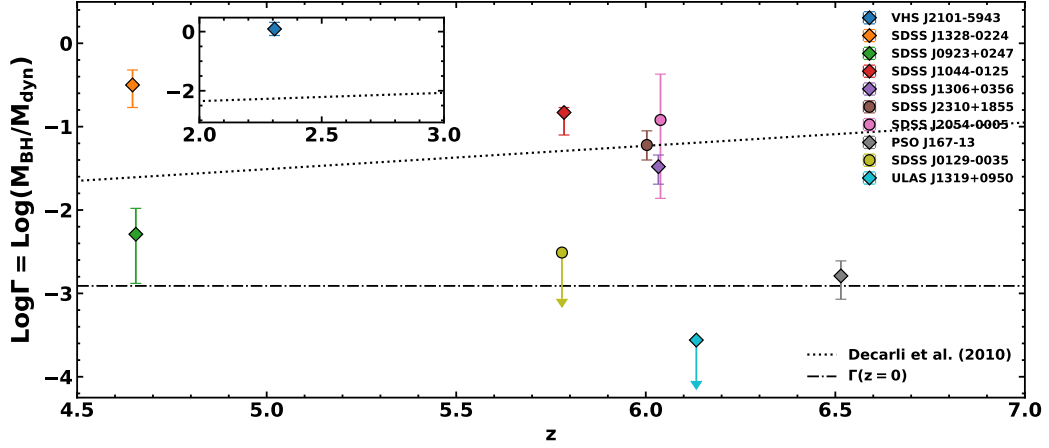


**Figure 4.10**

Evolution of  $\Gamma = M_{\text{BH}}/M_{\text{dyn}}$  as a function of redshift  $z$ . The black dotted and dash-dotted lines represent, respectively, the relation found by Decarli et al. (2010) at  $z \lesssim 3$ , and the corresponding ratio at  $z = 0$ . The inset panel shows the same plot at  $2 < z < 3$ . In the case of SDSS J0129-0035 and ULAS J1319+0950 we inferred lower limits on dynamical masses (i.e. an upper limit on the ratio  $\Gamma$ ). The circles indicate those sources which BH masses are estimated from bolometric luminosity assuming Eddington accretion.

### 4.8.1 The evolution of $M_{\text{BH}}/M_{\text{dyn}}$ across the cosmic time

The evolution of the ratio  $\Gamma = M_{\text{BH}}/M_{\text{dyn}}$  as a function of redshift provides key information about the relative time scale between BH growth and galaxy mass assembly. For this purpose, we show the  $M_{\text{BH}}/M_{\text{dyn}}$  ratios as a function of  $z$  estimates obtained from the integrated spectra of the lines provided in Tab. 4.2. The final result is shown in Fig. 4.10, where we also overplot the relation found by Decarli et al. (2010) using galaxy stellar masses of a sample of quasars at  $z \lesssim 3$ , extrapolated up to  $z = 7$ :

$$\log \Gamma(z) = (0.28 \pm 0.06)z - (2.91 \pm 0.06). \quad (4.7)$$

We conclude that the trend of  $\Gamma$  that we inferred at high redshift is roughly consistent with that of Eq. (4.7), and therefore this result confirms the evidence that  $M_{\text{BH}} - M_{\text{dyn}}$  appears to evolve with the redshift, as has been highlighted in previous works (Walter et al., 2004; Decarli et al., 2010, 2018; Merloni et al., 2010; Venemans et al., 2012, 2017c). The ratio  $\Gamma$  appears to be  $\sim 10\times$  the local value  $\log \Gamma(z = 0) = 0.28$  at  $z \sim 4 - 6$ . However, from

**Fig. 4.10**, we can infer that for SDSS J0923+0247, SDSS J0129-0035, ULAS J1319+0950, and PSO J167-13 at redshift  $4.6 \lesssim z \lesssim 6.6$ , the  $M_{\text{BH}}/M_{\text{dyn}}$  is consistent with the value observed in galaxies in the local Universe. Although a very preliminary result, this possibly suggests a decreasing of  $\Gamma$  at  $z \gtrsim 6$ .

The discussions reported in **Sects. 4.7.1** and **4.7.2** point out that at least some of the galaxy masses estimated in this thesis could suffer from large uncertainties associated with the simple assumptions that are the basis of the fitting method. Therefore, although  $M_{\text{BH}}$  estimates are strongly affected by the large (systematic) uncertainties associated with  $M_{\text{BH}}$  measurements at high- $z$  (up to  $\sim 0.4$  dex; see, **Sect. 4.5**), we conclude that the observed  $M_{\text{BH}}/M_{\text{dyn}}$  values are also likely affected by uncertainties in  $M_{\text{dyn}}$ . Our method did, however, allow us to obtain accurate galaxy dynamical mass estimates at such high redshift. We find that the spread in  $M_{\text{BH}}/M_{\text{dyn}}$  values at  $z \sim 4-7$  is much greater compared with that of local galaxies. This suggests that the observed spread could not arise from the large uncertainties associated with rough galaxy (virial) mass estimates at high- $z$  usually adopted, but it could have a physical reason.

## 4.9 Discussion

In order to extend the context of our work, we compare our results with both observational and theoretical predictions of the BH–galaxy relation obtained in other works. Then, we investigate observational biases possibly affecting the results, and we test the reliability of galaxy virial mass estimates.

In **Sect. 4.9.1**, we compare the  $M_{\text{BH}}-M_{\text{dyn}}$  and  $\Gamma-z$  relation presented in this work with other results on the high- $z$  BH–galaxy relation and we discuss the effect of observational biases. In **Sect. 4.9.2**, we compare the BH–galaxy relation prediction from recent simulations of galaxy evolution, and we discuss potential issues on dynamical mass estimates at high redshift outlined from theoretical models. Finally, in **Sect. 4.9.3**, we test the reliability of virial mass estimates by comparing them with the dynamical mass measurements.

### 4.9.1 Observational biases: comparison with other results on the early BH–galaxy relation

Previous works that aimed to study the BH–host galaxy coevolution in the early epochs show that  $z \gtrsim 6$  luminous quasars have BH-to-host-galaxy-mass ratios  $\sim 10$  times larger than the typical value observed in the local Universe, implying that these BHs formed significantly earlier than their hosts (e.g. Walter et al., 2004; Maiolino et al., 2009; Merloni et al., 2010; Decarli et al., 2010, 2018; Venemans et al., 2012, 2016; Wang et al., 2013, 2016; Trakhtenbrot et al., 2015). However, these results may be affected by observational biases. As we mentioned in Sect. 3.4, because most luminous quasars are powered by the most massive BHs at high redshift, if there is a scatter in BH–host galaxy mass relation, for a given  $M_{\text{BH}}$ , the selection of objects with low galaxy mass is favored due to the steepness of the galaxy MF at its high-mass end (see, e.g., Grazian et al., 2015; Song et al., 2016), thus producing an artificially high average  $M_{\text{BH}}/M_{\text{dyn}}$  (Lauer et al., 2007; Schulze & Wisotzki, 2014). In order to investigate this selection bias effect, in Fig. 4.11, we compare the distribution of our dynamical mass estimates, with the galaxy stellar MF at different redshift. For this purpose, our dynamical mass measurements represent upper limits on galaxy stellar masses ( $M_{\star}$ ). Most of the quasars are at the knee of the quasar luminosity function (Song et al., 2016), indicating that they represent the bulk of the quasar population at such high redshifts. On the other hand, J183+05, J167-13, and the most extreme J1319+0950 are at the massive end of the  $M_{\star}$ -function, and they may be more affected by the ‘Lauer’ bias. Notwithstanding all considerations of the reliability of dynamical mass estimates of the aforementioned objects, we can conclude that these three quasars may be considered the most evolved system known at  $z \sim 6$  in terms of galaxy mass. Interestingly, J167-13 together with J0923+0247 and J0129-0035 in our sample have a BH mass  $M_{\text{BH}} < 5.0 \times 10^8 M_{\odot}$  (see Tab. 4.3), and all of them are consistent with the local BH–galaxy relation at  $z \sim 0$ . As discussed in Venemans et al. (2016), Wang et al. (2016), and Willott et al. (2015b, 2017), this may suggest that, while the  $z \sim 6$  quasars with BH masses to the order of  $10^8 M_{\odot}$  are close to the relation valid for their local counterpart, the most massive BHs ( $M_{\text{BH}} > 10^9 M_{\odot}$ ) at the earliest epochs grow faster than the quasar host galaxy

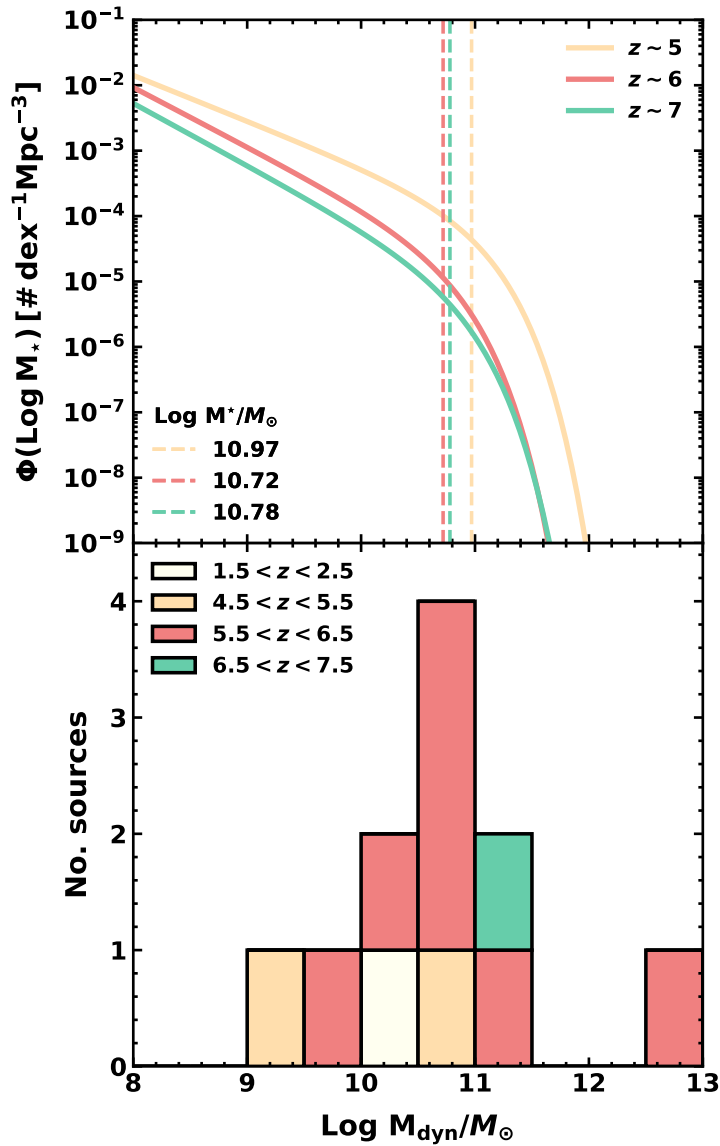


**Figure 4.11**

Comparison between our dynamical mass measurement distribution and galaxy stellar mass function. *Upper panel:* Galaxy stellar mass function at different redshifts (Song et al., 2016). The dashed vertical lines show the position of the  $M^*$  values that represent the 'knee' of the mass function. *Lower panel:* Stacked histogram of our dynamical mass estimates.

and tend to be above the trend of local galaxies. This may imply that actually, there is no strong correlation between the two properties in high-redshift quasars, but that the scatter was much larger in the early Universe than today. However, to confirm this conclusion, a wide range of BH masses and larger sample are required to overcome the observational bias due to

the intrinsic scatter of the BH–galaxy relation. In this context, Izumi et al. (2018, 2019) studied the  $M_{\text{BH}} - M_{\text{dyn}}$  using a sample of seven  $z \gtrsim 6$  low-luminosity quasars (absolute magnitude at  $1450 \text{ \AA}$ ,  $M_{1450} > -25$ ) targeted in  $[\text{CII}]_{158 \mu\text{m}}$  by ALMA. They derived the quasar host galaxy dynamical (virial) masses assuming rotating disk geometry, and the axial ratio of  $[\text{CII}]$  flux map as a proxy of the disk inclination angle. Furthermore, they estimated  $M_{\text{BH}}$  through a SE virial relation or assuming Eddington-limited accretion. Izumi et al. (2018, 2019)’s results show that while the luminous quasars ( $M_{1450} < -25$ ) typically lie above the local relation (Kormendy & Ho, 2013) with BHs overmassive compared to local AGNs, the discrepancy becomes less evident at  $M_{\text{dyn}} \gtrsim 10^{11} M_{\odot}$  (see also, e.g., Trakhtenbrot et al., 2017). On the other hand, most of the low-luminosity quasars show comparable or even lower ratios than the local one, particularly at a range of  $M_{\text{dyn}} \gtrsim 4 \times 10^{10} M_{\odot}$ . Therefore, Izumi et al. (2018, 2019) show that, at least in this high  $M_{\text{dyn}}$  range, previous works based on sample of luminous quasars might have been biased toward more massive BHs. If these results were confirmed with future follow-up observations, the observed evolution of  $M_{\text{BH}}/M_{\text{dyn}}$  ratio out to  $z \sim 2 - 3$  could be explained as the result of sample selection bias only. However, Izumi et al. (2018, 2019) could be biased, due to the use of virial masses. As we illustrate in **Sect. 4.9.3**, the galaxy masses estimated in this work through a full kinematical model, are not correlated with those estimated through virial theorem. This fact suggests that the use of galaxy virial mass in studying the BH–galaxy relation, could be reflected in an increasing scatter in the observed relation.

## 4.9.2 Comparison with recent theoretical models and simulations

The benchmark correlation in local galaxies is based on bulge stellar masses (Kormendy & Ho, 2013). In high-redshift quasars, the host galaxies are completely outshone by the central emission, and the limited angular resolution of the current UV-based observations does not allow us to easily decouple the quasar from its host (see **Sect. 3.4**). Therefore, estimating the stellar mass content in a galaxy out to  $z \sim 2 - 3$  is very challenging. However, at such high redshifts, the galaxies’ bulges may not have formed yet, or they cannot be detected. Therefore, in the high redshift studies, the dynamical

mass of the host galaxy is estimated from the gas properties in the sub-mm observations, and it is usually used as a proxy of bulge stellar mass.

Beyond the observational biases affecting these studies (see **Sect. 4.9.1**), Lupi et al. (2019) recently pointed out that the high- $z$  deviation from the local  $M_{\text{BH}}-M_{\text{dyn}}$  relation might be due to the different tracers used to estimate the mass of galaxies at high redshift, namely gas-based dynamical mass and the stellar mass. Lupi et al. (2019) performed a high-resolution cosmological zoom-in simulation in order to investigate the evolution of quasar hosts by properly resolving both the distribution of the cold gas phase ( $30\text{ K} < T < 3000\text{ K}$ ) traced by  $[\text{CII}]_{158\mu\text{m}}$  line emission, and stars traced by FUV flux. Their results show that the gas settles in a well-defined dense thin disk extending out to  $\sim 1\text{ kpc}$  already at  $z \sim 7$ . Adopting the techniques used in observational studies, they derived dynamical mass estimates through the virial theorem under the assumption of rotationally supported systems. Comparing these dynamical (virial) mass estimates with the masses of the central BHs, they obtained an average BH-dynamical mass ratio of  $M_{\text{BH}}/M_{\text{dyn}} \sim 0.017$ , which is  $\sim 15$  times greater than local values (Decarli et al., 2010; Kormendy & Ho, 2013; Reines & Volonteri, 2015), in agreement with previous high- $z$  observations and simulations (see, e.g., Walter et al., 2004; Venemans et al., 2017a; Barai et al., 2018; Decarli et al., 2018), and roughly consistent with our results. Additionally, they also compared galaxy stellar masses with BH masses, showing no sign of clear deviation with the local relation (Reines & Volonteri, 2015). This result implies that dynamical mass estimated using the virial theorem underestimates the dynamical mass of the system. A similar discussion was recently reported by Kohandel et al. (2019), who analyzed the kinematical properties of a simulated star forming galaxy at  $z \sim 7$ . They show that using the virial theorem in a rotationally supported system, the dynamical mass estimates suffer from large uncertainties depending on the disk inclination.

The approach proposed in this thesis, in which we perform a kinematical modeling of observed velocity fields, allows us to infer both disk inclination and dynamical mass, thus reducing the uncertainties and biases on our estimates. However, larger samples with higher angular resolution observations are required to finally assess whether a deviation from the local relation exists or not.

### 4.9.3 Comparison between virial masses and dynamical mass estimates

We tested the reliability of virial mass estimates by comparing them with our dynamical mass measurements. For this purpose, we made rough dynamical (virial) mass ( $M_{\text{vir}}$ ) measurements of our galaxy sample following; e.g., Wang et al. (2013), Willott et al. (2015b), Decarli et al. (2018), and Neeleman et al. (2021):

$$M_{\text{vir}} = G^{-1} R_{\text{em}} (0.75 \text{FWHM}_{\text{line}} / \sin \beta)^2, \quad (4.8)$$

where  $R_{\text{em}}$  is the radius of the emitting region, and  $\text{FWHM}_{\text{line}}$  is the full width at half maximum of the line emission. We performed 2D Gaussian fits, within CASA, of the flux maps obtained in **Sect. 4.3**, and we estimated the deconvolved major ( $a_{\text{maj}}$ ) and minor axes ( $b_{\text{min}}$ ) of the best model. Then, we computed  $R_{\text{em}}$  as  $a_{\text{maj}}/2$  in physical length using the redshift estimates obtained in **Sect. 4.3.1** and the disk inclination angle as  $\sin^2 \beta = 1 - (b_{\text{min}}/a_{\text{maj}})^2$ . Finally, we retrieved the  $\text{FWHM}_{\text{line}}$  from the Gaussian fit of the line spectra (see **Tab. A.1**). The results of the 2D Gaussian fits, the  $R_{\text{em}}$  values, and virial masses are listed in **Tab. A.2**. In **Fig. 4.12**, we compare dynamical virial masses estimated through **Eq. (4.8)** with the dynamical mass measurements obtained in this work through a full kinematical modeling (see **Tab. 4.2**).

We conclude that  $M_{\text{vir}}$  and  $M_{\text{dyn}}$  are roughly in good agreement, but they appear not to be correlated, confirming that virial mass is not a reliable dynamical mass estimate of the host galaxy. We note that the errors on virial mass measurements are statistical errors, ignoring any intrinsic uncertainties and systematic biases associated to the virial assumption.

In order to improve the galaxy virial mass estimate, we can use the spectroastrometry method by Gnerucci et al. (2011). With this method, it is possible to probe spatial scales smaller than the angular resolution, thus allowing a more accurate measurement of the dimension of the line-emitting region. On the other hand, the mass estimates are affected by uncertainties associated with the measurement of the galaxy disk inclination angle, for which it is possible to use the axial ratio from galaxy morphology. In **Appx. A.3**, we compare the mass factor  $M_{\text{dyn}} \sin^2 \beta$  obtained through the full kinematical model, the virial formula, and the spectroastrometry method. The results show that spectroastrometry is a robust proxy for the galaxy dynamical mass in contrast with the 'classical' virial estimates usually adopted.

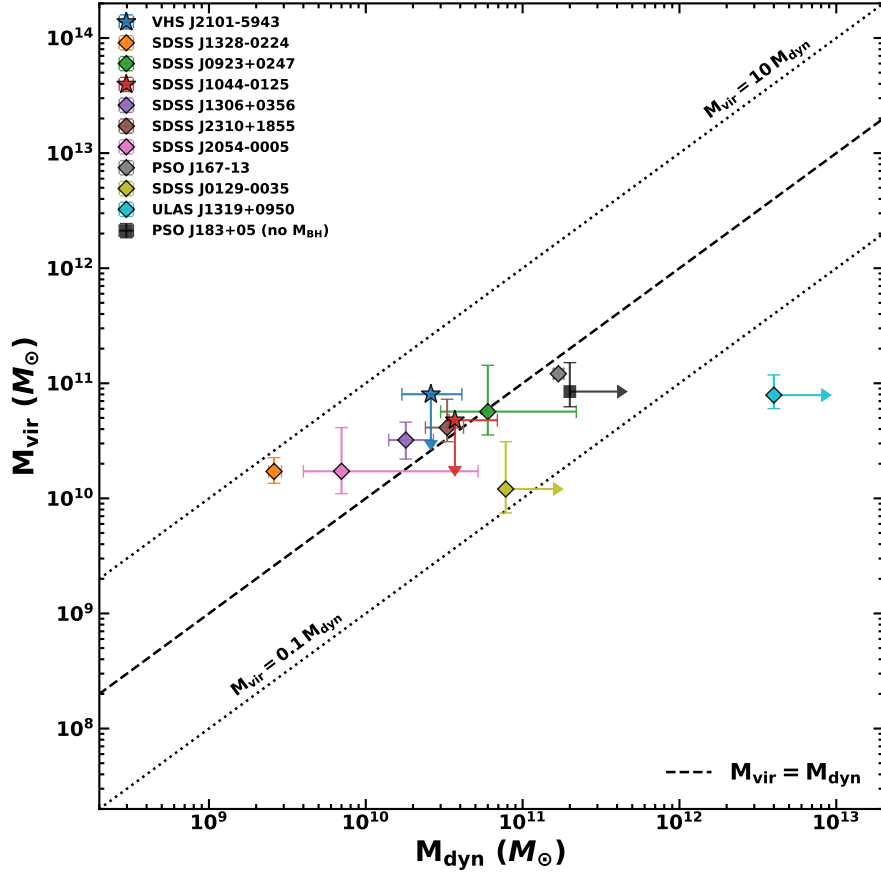


**Figure 4.12**

Comparison between dynamical virial mass ( $M_{\text{vir}}$ ) computed using flux map properties and dynamical mass ( $M_{\text{dyn}}$ ) obtained with the full kinematical model of the gas velocity field. The dashed line indicates the 1:1 relation, while dotted lines are 1 dex shifts. The objects represented with star symbols are upper limits on virial mass, since their emission appears consistent with a point-like source (as a result of 2D Gaussian fits within CASA). In these cases, following Willott et al. (2015b), we assume  $\beta = 55 \text{ deg}$  as disk inclination angle. The black square indicates PSO J183-05, for which we retrieved a lower limit on  $M_{\text{dyn}}$ , but for which  $M_{\text{BH}}$  is not available.

## 4.10 Conclusions

In this chapter, we investigated the relation between the supermassive BH mass ( $M_{\text{BH}}$ ) and the dynamical mass of the host galaxy ( $M_{\text{dyn}}$ ) of a sample of 10 quasars at  $2.3 \lesssim z \lesssim 6.5$  targeted in either  $[\text{CII}]_{158 \mu\text{m}}$  or CO rotational transitions by ALMA. We then studied the evolution of  $\Gamma = M_{\text{BH}}/M_{\text{dyn}}$  across cosmic time. Previous works exploiting ALMA observations attempted to trace the  $M_{\text{BH}} - M_{\text{dyn}}$  relation at high- $z$  by estimating the galaxy mass through virial

theorem and thus possibly introducing significant uncertainties and biases. To avoid such large uncertainties, we performed a kinematical modeling of the cold gas in the hosts taking into account the beam smearing effect.

In summary, we conclude that:

- The galaxy mass estimated using the virial theorem combining the axial ratio of flux map to estimate the disk inclination angle, and line FWHM as a proxy of circular velocity, suffers from large uncertainties and could underestimate the dynamical mass of the system (Lupi et al., 2019; Kohandel et al., 2019).
- The beam smearing effect strongly affects the observed velocity field in the host galaxy, making the disk inclination angle and galaxy dynamical mass almost degenerate parameters. The more the angular resolution decreases, the more significant this effect becomes, and it should be taken into account in kinematical modeling.
- The dynamical masses estimated from the kinematical modeling highlight evidence of the evolution of the  $M_{\text{BH}} - M_{\text{dyn}}$  relation consistently with previous works (e.g. Walter et al., 2004; McLure et al., 2006; Maiolino et al., 2009; Bennert et al., 2010, 2011b; Decarli et al., 2010, 2018; Merloni et al., 2010; Wang et al., 2010, 2013, 2016; Canalizo et al., 2012; Targett et al., 2012; Venemans et al., 2012, 2016, 2017c; Bongiorno et al., 2014; Trakhtenbrot et al., 2015). In particular, we conclude that, on average, our sample is placed above the reference relation found for galaxies in the local Universe. The normalization  $\alpha$  of the BH–galaxy relation is such that, on average, for a given value of  $M_{\text{dyn}}$ ,  $M_{\text{BH}}$  is  $\sim 10\times$  higher compared to that found by de Nicola et al. (2019), and  $\sim 150\times$  higher than what Reines & Volonteri (2015) found using the total stellar mass of local AGNs.
- The ratio  $\Gamma = M_{\text{BH}}/M_{\text{dyn}}$  at  $z \sim 4-6$  appears to be  $\sim 10\times$  higher than the local value, consistent with the result found by Decarli et al. (2010) extrapolated up to  $z = 7$ , except for four objects at  $z \sim 4-6$  that show  $\Gamma$  ratios consistent with the local one ( $\Gamma(z = 0)$ ). Despite the low statistics, this is the first evidence of a  $\Gamma$  value decreasing at  $z \sim 6$ . We are possibly witnessing the phase in which a BH rapidly grows with respect to the galaxy mass.

- The observed spread in  $M_{\text{BH}}/M_{\text{dyn}}$  values at  $z \sim 4 - 6$  is much greater compared to galaxies in the local Universe. Given the accurate galaxy dynamical mass estimates obtained in this work, the observed spread could be due to physical factors, and not associated with the large uncertainties affecting the galaxy virial mass estimates usually adopted in high- $z$  studies.
- The sources in our sample with  $M_{\text{BH}}$  to the order of  $10^8 M_{\odot}$  are close to the relation found for galaxies in the local Universe (Kormendy & Ho, 2013; de Nicola et al., 2019), while the most massive BHs ( $M_{\text{BH}} > 10^9 M_{\odot}$ ) lie above them, thus suggesting a faster evolution with respect to their host at  $z \sim 6$ .
- Most of our sample represents the bulk of the quasar population at  $z > 4$ ; thus, overall, the selection of our galaxy sample is not strongly affected by the 'Lauer' bias (Lauer et al., 2007; Schulze & Wisotzki, 2014). However, a wider range of BH masses and a larger sample are required in order to minimize the observational bias resulting from the intrinsic scatter in the  $M_{\text{BH}} - M_{\text{dyn}}$  relation.

Based on our blind search, we conclude that one third of high- $z$  quasar hosts have gas kinematics consistent with rotating disks (also confirmed by subsequent study at higher angular resolution; Neeleman et al. 2021), but it is still very challenging to infer the dynamical mass due to the poor angular resolution and sensitivity of current observations. The typical angular resolution of the observations ( $\sim 0.5''$ ) is frequently not good enough to constrain the dynamical parameters of the disks at  $z \gtrsim 5$ , and the fitting procedures cannot take into account possible distortions of the velocity field introduced by instrumental effects. As a result, we inferred the dynamical masses only for ten out of 72 quasars observed with ALMA so far. On the other hand, for those quasars with deep ALMA observations and high angular resolution, this work shows that dynamical mass estimations are also feasible at  $z \sim 6$ . Further ALMA high angular resolution observations of high- $z$  quasars are crucial to studying the evolution of the  $M_{\text{BH}}/M_{\text{dyn}}$  ratio and verifying whether  $\Gamma(z)$  decreases at  $z \gtrsim 6$  as suggested by our preliminary results.

# 5

## The interstellar medium of galaxies at high redshift

“ *If I have seen further it is by standing on the shoulders of Giants.* ”

— Isaac Newton

In **Chap. 3** we discussed feedback processes and their determinant role during the assembly of galaxies and BHs. Whatever is the nature of this feedback (i.e., star formation activity or BH accretion), it is able to act only on the gas content of galaxy by injecting energy into the ISM. Quasars at  $z > 6$  are fueled by copious amount of gas which also sustains episodes of intensive star formation. The host galaxies of high- $z$  quasars are therefore perfect laboratory to study the ISM under extreme conditions. Thanks to the advent of ALMA and the recently upgraded NOEMA, the last decade has witnessed an actual revolution for the study of high- $z$  quasar hosts at (sub-)mm wavelengths. At  $z \sim 6$  many important diagnostics of the ISM, including FIR-molecular and atomic fine-structure lines (FSLs), are redshifted in the (sub-)mm bands making them favorable targets for radio/mm interferometers. In addition, at  $z > 1$  the peak shift of the dust continuum emission (typically around rest-frame  $100 \mu\text{m}$ ) toward longer wavelengths, partially compensates the cosmological dimming (negative  $k$ -correction). As a result, the observed continuum flux density in the (sub-)mm bands remains roughly constant in the  $z \sim 1 - 10$  range.

In this chapter we introduce the basic concepts related to ISM observations, we briefly summarize the properties of the gas and dust emission in galaxies, and we discuss the main tracers of the ISM at high- $z$ .

## 5.1 Characteristics of the ISM

The ISM encompasses a small fraction of the total mass of a galaxy - typically few percents. However, it is a key component for fueling star formation and BH accretion, which in turn play a central role in determining the ISM physical and chemical properties via feedback processes. Due to its highly self-interacting and dissipating nature, ISM is essential in shaping the galaxies during their evolution. The ISM is mainly composed by hydrogen (H), and helium (He) as byproduct of the primordial nucleosynthesis by which deuterium and a small fraction of lithium have been also produced (e.g., Cyburt et al., 2016, for a review). The other elements are referred as *metals* (Z), and account for the remaining minority part of the galaxy mass. Metals are almost entirely produced by stellar nucleosynthesis and/or by explosive burning and photodisintegration during the late stages of stellar evolution (e.g., Maiolino & Mannucci, 2019, for a review). The ISM also contains  $\sim 1\%$  of dust that is intimately mixed with the gas, including most of the refractory elements (e.g., Fe and Si) in the form of grains with dimensions  $\sim 0.1 - 10 \mu\text{m}$ . Dust grains form via condensation of heavy elements in dense and cool regions such as SN remnants and the envelopes of evolved stars (asymptotic giant branch (AGB) stars), and they can further grow via aggregation in dense molecular clouds (Dwek, 1998; Dwek & Cherchneff, 2011; Zhukovska, 2014). The total dust mass in a galaxy is typically  $\simeq 100\times$  smaller than the gas mass.

The matter in the ISM is distributed in different thermal phases determined by the balance between radiative cooling and heating (e.g., Goldsmith & Langer, 1978). The ISM phases coexist in approximate pressure equilibrium and are divided according to the chemical state of the hydrogen (i.e., ionized, neutral, or molecular), and on the basis of their physical properties (i.e., temperature, density, and ionization state; see Draine 2011, and references therein). Atomic gas settles in two thermally stable phases, that are the *cold neutral medium* (CNM,  $T \sim 50 - 100 \text{K}$ ,  $n_{\text{H}} \sim 20 - 50 \text{cm}^{-3}$ ) distributed in compact clouds, and the more extended *warm neutral medium* (WNM,

$T \sim 5000 - 10000\text{K}$ ,  $n_{\text{H}} \sim 0.1 - 1\text{ cm}^{-3}$ ). The molecular gas is typically cold and dense ( $T \sim 10 - 50\text{K}$ ,  $n_{\text{H}} \sim 10^3 - 10^6\text{ cm}^{-3}$ ) due to the inefficient heating by UV radiation and cosmic rays, and it primarily resides in giant molecular clouds (GMCs) filling a small fraction ( $\sim 0.001\%$ ) of the total volume of the ISM. Within the dense molecular medium the formation of stars occurs from condensation and fragmentation of the GMCs. In star-forming regions, molecular clouds are invested by the intense FUV ( $6.0\text{ eV} < E < 13.6\text{ eV}$ ) radiation field of the O- and B-type stars. In these warm regions, the outskirts of GMCs are turned into photon-dominated regions (also dubbed as photo-dissociation regions (PDRs); Hollenbach & Tielens, 1999, see Figs. 5.1 and 5.3), where the heating and/or chemistry of the gas are significantly determined by the FUV radiation. In PDRs, the continuum flux from young stars is efficiently ( $\sim 0.1 - 1\%$ ) converted into atomic and molecular<sup>1</sup> line emission via gas heating by FUV-induced photoelectric ejection of energetic ( $\sim 1\text{ eV}$ ) electrons from dust grains (Tielens & Hollenbach, 1985a). Tielens & Hollenbach (1985a,b) pointed out that the emission from PDRs largely depends on the cloud density ( $n_{\text{H}}$ ), and the strength of the FUV radiation field ( $G_0$ ) illuminating the cloud (where  $G_0$  is in Habing flux units, i.e.,  $1.6 \times 10^{-3}\text{ erg s}^{-1}\text{ cm}^{-2}$ ; see Habing 1968). PDRs include a large fraction of the atomic neutral medium and most of the molecular clouds. PDRs are characterized by densities from  $n_{\text{H}} \approx 0.25\text{ cm}^{-3}$  to  $n_{\text{H}} \gtrsim 10^7\text{ cm}^{-3}$ , and FUV fluxes from  $G_0 \lesssim 1$  to  $G_0 \gtrsim 10^6$  (see, e.g., McKee & Ostriker, 1977; Hollenbach & Tielens, 1999; Kaufman et al., 1999; Meijerink et al., 2007). Molecular clouds can also be exposed to X-ray radiation, for example, near SN shocks or accreting BH in quasars (see, e.g., Langer, 1978; Krolik & Kallman, 1983; Krolik & Begelman, 1988; Lepp & McCray, 1983). X-ray photons are able to penetrate much deeper into the cloud (column densities of  $N_{\text{H}} \gtrsim 10^{22}\text{ cm}^{-2}$ ) affecting the chemical and thermal structure of the FUV-opaque molecular gas. Completely analogous to a PDR, an XDR is therefore defined as predominantly neutral gas in which X-rays dominate the gas heating and much of the chemistry through X-ray dissociation and ionization (e.g., Maloney et al. 1996; Hartquist & Williams 1998; Hollenbach & Tielens 1999; Meijerink et al. 2006). In XDRs, the incident radiation field is typically expressed in terms of X-ray flux,  $F_{\text{x}}(\text{erg s}^{-1}\text{ cm}^{-2})$ , over the range  $1 - 100\text{ keV}$ .

---

<sup>1</sup>Note that, further inside the clouds, the molecular phase persists thanks to dust- and molecular self-shielding.

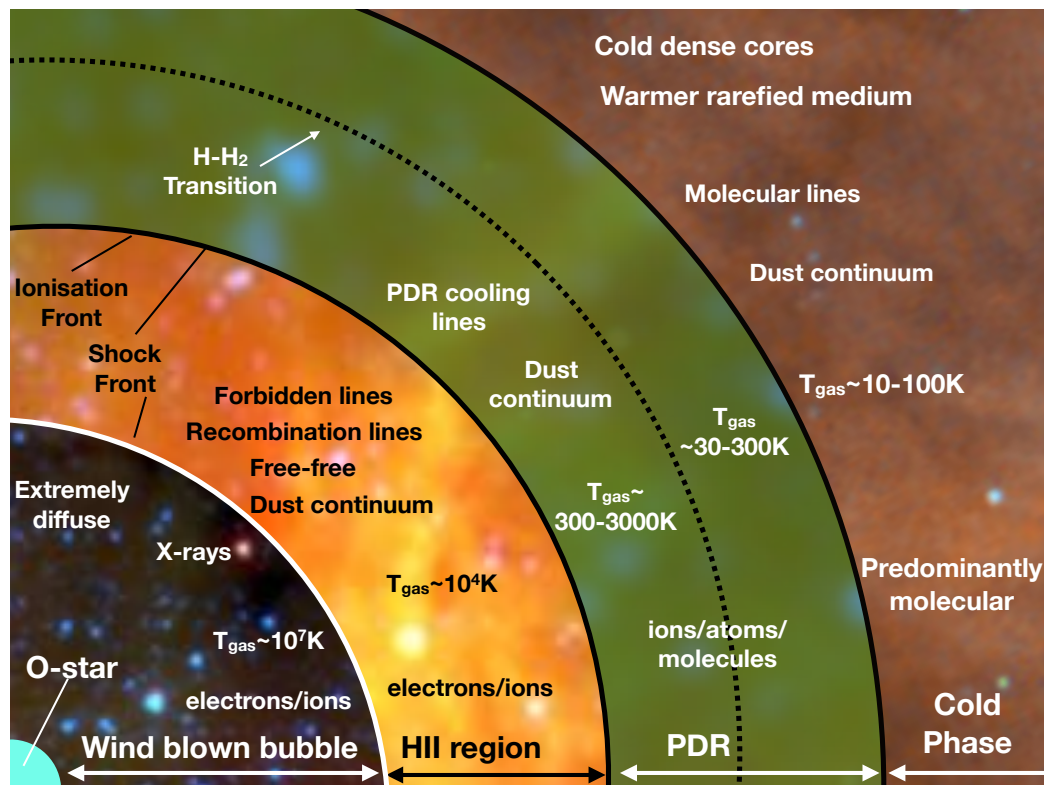


**Figure 5.1**

Schematic illustration of microphysical regimes in the ISM close to a young star. Energetic photon wind from the O star excavates an hot and very diffuse bubble in its surrounding medium. Beyond the bubble, the interstellar gas is predominantly photoionized by extreme-UV photons. The pressure in HII region makes it expanding producing a shock front. FUV radiation penetrates beyond the extent of the ionized phase producing the PDR. Further beyond, the shielding effects allow molecules to survive to the exciting radiation of the O star resulting in a cold dense molecular clumps, or warmer rarefied medium. The dominant emission is reported for each phase together with the typical gas temperature (dust temperature is generally decoupled from that of the gas). The diagram is not in scale. Figure from Haworth et al. (2018).

Molecular gas is also found outside GMCs, in a more extended and diffuse form similar to cool neutral clouds but with sufficiently high densities to prevent the photodissociation of  $H_2$  molecules ( $T \sim 50$  K,  $n_H \sim 100$  cm $^{-3}$ ). The atomic ISM together with the molecular gas account for the vast majority the gas mass of a galaxy. In terms of volume, a significant fraction of ISM is filled by ionized gas which however accounts for no more that 25% of the total gas mass. Part of this ISM phase is referred as *hot ionized medium* (HIM) or *coronal gas*. HIM is very hot and diffuse ( $T \gtrsim 10^6$  K,

$n_{\text{H}} \sim 10^{-3} \text{ cm}^{-3}$ ) and it is located in collisionally-ionized bubbles produced by blast waves from stellar winds and SN explosions. The ionized medium is also composed by radiatively-ionized gas in the surroundings of massive stars, the so-called HII regions. This phase is dubbed as *warm ionized medium* (WIM) and is characterized by temperature around  $T \sim 10^4 \text{ K}$ , and density range  $n_{\text{H}} \sim 0.3 - 10^4 \text{ cm}^{-3}$ .

The ISM is permeated by relativistic cosmic rays and photons that further contribute to the complex energy balance of the different gas phases. Cosmic rays are primarily constituted by protons and  $\alpha$  particles (i.e., He nuclei), with small fractions of electrons, nuclei of other light elements, neutrinos, and traces of antimatter. They are produced by SNe and stellar winds ejected by O- or B-type stars. Photons from all over the electromagnetic spectrum may originate via various phenomena, including the cosmic microwave background (CMB), emission from molecules, atoms, and ions, thermal emission from dust and massive stars, nuclear transitions, and free-free emission from hot gas.

The injection of energy into the ISM is mainly provided via photoelectric heating by dust grains and photoionization of atoms and molecules exposed to UV radiation from young stars and/or cosmic rays. Stellar winds and shocks, and radiation from AGN may also significantly contribute to the heating of the gas. On the other hand, cooling is primarily achieved via emission of spectral lines of atoms, ions, and molecules that represent the tracers of the ISM. However, within the interstellar gas only a small fraction of the energy generated by star-formation (and possibly AGN) is involved. The remaining large fraction is indeed channeled in FIR via dust reprocessing, or is radiated out to the Universe (depending on the geometry and dust content, Elbaz 2002). Atomic absorption in FUV and X-rays, together with emission from dust grain, completely reshape the galaxy SEDs.

## 5.2 Tracers of the ISM

The various ISM phases in galaxies are studied through the combination of atomic/molecular emission lines and dust continuum. In the following, we provide the basics of observing the ISM in high- $z$  galaxies.

## 5.2.1 Neutral-atomic and ionized gas tracers

One of the main tracers of the CNM is the radio HI 21-cm emission line. Unfortunately it cannot be studied at  $z > 0.5$  due to the limited sensitivity of the current facilities and artificial noise (i.e., telecommunications), and it will be eventually feasible with the forthcoming Square Kilometer Array (SKA; Carilli & Rawlings, 2004). For this reason, the atomic ISM phase has been widely studied via powerful FSLs, especially in high- $z$  galaxies and quasar hosts, for which these emission lines are conveniently shifted in FIR/(sub-)mm bands (see Fig. 5.2). Hydrogen recombination lines (e.g., Ly- $\alpha$ , H $\alpha$ ) together with some atomic FSLs such as the transitions of neutral and singly-ionized carbon ([CI], [CII]), singly-ionized nitrogen ([NII]), neutral and doubly-ionized oxygen ([OI], [OIII]), are recognized to be the dominant coolants of the atomic neutral or (warm) ionized ISM, depending on their ionization potential with respect to the hydrogen (13.6 eV; e.g., Spitzer, 1978). Hydrogen recombination lines are associated with the radiative deexcitation of an electron after it recombines with a proton. FIR FLSs on the other hand arise from the deexcitation of electrons in the shells of atoms and ions of metals that were excited by collisions with hydrogen atoms or electrons, depending on the gas phase. Since these lines are forbidden, they are typically optically thin, thus avoiding line trapping (i.e., resonant scattering) in the high column density media.

### **Singly-ionized carbon: [CII]<sub>158 $\mu$ m</sub>**

The fine-structure transition ( $^3P_{3/2} \rightarrow ^3P_{1/2}$ ) [CII]<sub>158 $\mu$ m</sub> is one of the brightest lines emitted from the cool gas ( $< 10^4$  K) in star-forming galaxies, and it is now routinely detected, and eventually spatially-resolved with ALMA even at  $z > 6$  (see, e.g., Decarli et al., 2018; Neeleman et al., 2019, 2021; Venemans et al., 2020; Walter et al., 2022). Thanks to its brightness, [CII]<sub>158 $\mu$ m</sub> is employed to map the cold gas kinematics in high- $z$  galaxies. Carbon has a lower ionization potential (11.3 eV) than hydrogen and therefore it originates both from the low-density ionized gas and the neutral medium, including clouds and PDRs. In the ionized medium, the C<sup>+</sup> ion is excited by collisions with electrons, and its 158- $\mu$ m transition has a critical density of  $n_e^{\text{crit}} \approx 46 \text{ cm}^{-3}$  (Oberst et al., 2006). On the other hand, in the neutral medium, most of the [CII]<sub>158 $\mu$ m</sub> arises from the PDRs where C<sup>+</sup> is collisionally excited by neutral and molecular hydrogen ( $n_{\text{H}}^{\text{crit}} \simeq 3.0 \times 10^3 \text{ cm}^{-3}$ ,  $n_{\text{H}_2}^{\text{crit}} \simeq 6.1 \times 10^3 \text{ cm}^{-3}$ ,

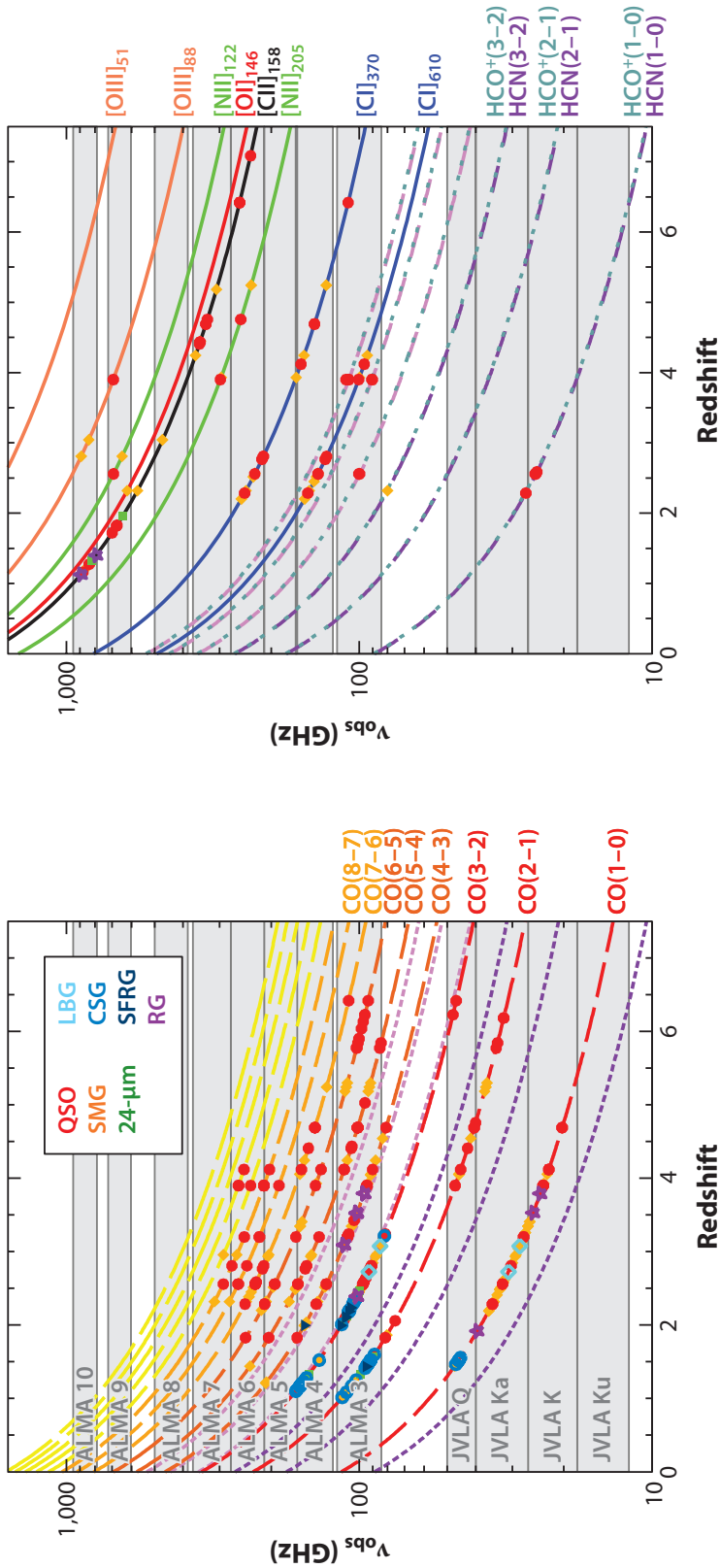


**Figure 5.2**

Observed frequency ( $\nu_{\text{obs}}$ ) of CO transitions (*left panel*), and other ISM tracers (*right panel*) as a function of redshift  $z$  following  $\nu_{\text{obs}} = \nu_{\text{rest}}/(1+z)$ , where  $\nu_{\text{rest}}$  is the rest frequency of the line. The horizontal bands are the frequency ranges covered by various telescopes. In particular, in the figure are reported the ALMA and the Jansky Very Large Array (JVLA) bands. The Green Bank Telescope (GBT) and the Australia Compact Array (ATCA) cover the JVLA bands. IRAM telescopes cover the lowest five ALMA bands. The circles are high-redshift ( $z > 1$ ) detections of the lines color-coded by source type as indicated on the upper right legend of the left panel (24- $\mu\text{m}$  = 24- $\mu\text{m}$  galaxy; CSG = color-selected star-forming galaxy, LBG = Lyman-break galaxy; QSO = quasar; RG = radio galaxy; SFRG = star-forming radio galaxy, SMG = submillimeter galaxy). Figure from Carilli & Walter (2013).

see, Goldsmith et al. 2012). Indeed, various works at low and high redshift, show that a large fraction ( $> 70\%$ ) of the total  $[\text{CII}]_{158\mu\text{m}}$  emission arises from PDRs in star-forming regions (see, e.g., Stacey et al. 1991; Carral et al. 1994; Lord et al. 1996; Colbert et al. 1999, for studies in nearby galaxies; and, e.g., Decarli et al. 2014; Pavesi et al. 2016; Novak et al. 2019, for high- $z$  galaxies and quasar hosts; see also **Chap. 6**).

### **Atomic carbon: [CI]**

Other important tracers of the atomic neutral medium are the  $[\text{CI}]_{369\mu\text{m}, 609\mu\text{m}}$  transitions. The simultaneous detection of these lines, allows to derive the excitation temperature<sup>2</sup>, neutral carbon column density, and mass (e.g., Ojha et al., 2001; Weiß et al., 2003; Walter et al., 2011). The ( $^3P_2 \rightarrow ^3P_1$ )  $[\text{CI}]_{369\mu\text{m}}$ , and the ( $^3P_1 \rightarrow ^3P_0$ )  $[\text{CI}]_{609\mu\text{m}}$  have critical density of  $1.2 \times 10^3 \text{ cm}^{-3}$ , and  $470 \text{ cm}^{-3}$ , respectively (see, e.g., Carilli & Walter, 2013, and references therein), which means that they trace the cold (dense) atomic neutral medium. Because the ionization potential of neutral carbon is close to the dissociation energy of the carbon monoxide (CO) molecule – the most abundant species in molecular gas after the molecular hydrogen ( $\text{H}_2$ ) –, C is expected to exist in a narrow range of physical conditions. The [CI] emission has been thought to emerge from a thin  $\text{C}^+/\text{C}/\text{CO}$  transition layer in the molecular clouds (Tielens & Hollenbach, 1985a,b; Hollenbach & Tielens, 1999; Kaufman et al., 1999, see **Fig. 5.3**). However, several lines of evidence highlight a close connection of [CI] emission and CO rotational transitions, suggesting that the [CI] line traces the bulk of molecular gas in galaxies (see, e.g., Ikeda et al., 2002; Papadopoulos et al., 2004; Walter et al., 2011; Alaghband-Zadeh et al., 2013; Israel et al., 2015; Bothwell et al., 2017; Valentino et al., 2018, 2020). This is also predicted by hydrodynamic simulations (e.g., Tomassetti et al., 2014) in which CO and [CI] are found to coexist throughout the bulk of the cold molecular component. A viable explanation is provided by clumpy, inhomogeneous PDR models (e.g., Meixner & Tielens, 1993; Spaans, 1996, see **Sect. 5.4**) in which the surface layers of [CI] are distributed across clumpy molecular clouds. The  $[\text{CI}]_{369\mu\text{m}, 609\mu\text{m}}$  transitions have been detected in several galaxies at high redshift (see, e.g., Walter et al., 2011, and references therein).

<sup>2</sup>The excitation temperature ( $T_{\text{exc}}$ ) is the equivalent temperature at which we would expect to find a system with the ratio of level population given by the Boltzmann distribution.

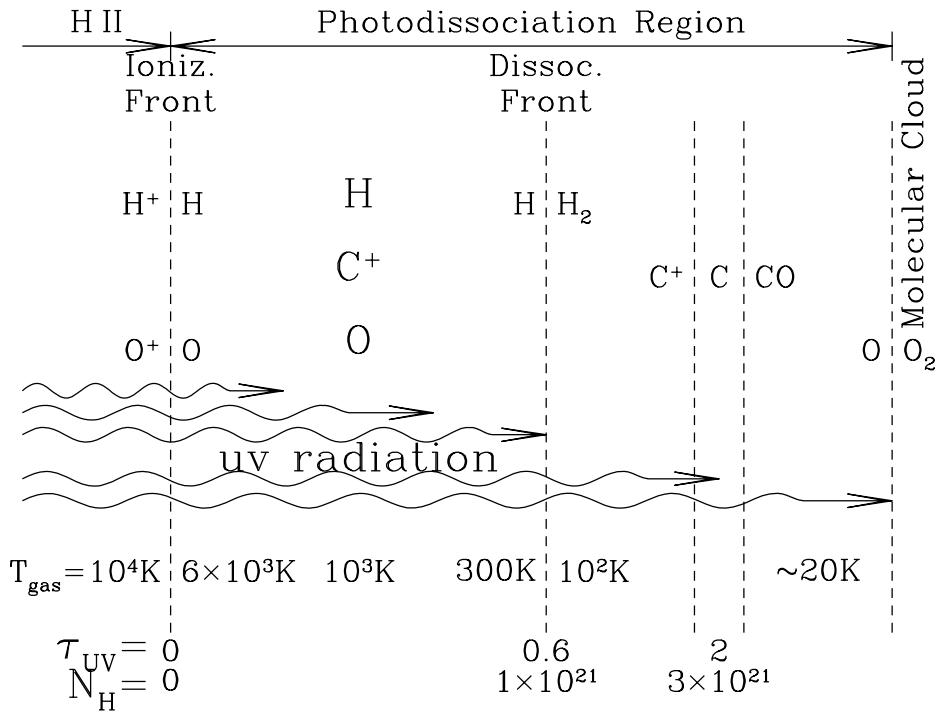


**Figure 5.3**

Structure of PDR at the interface between the HII region and the molecular gas. The figure reports the variation of continuum UV optical depth ( $\tau_{\text{UV}}$ ), hydrogen column density ( $N_{\text{H}}$ ), and gas temperature ( $T_{\text{gas}}$ ) as a function of the depth into the gas structure. The different gas species inside PDR are marked in the figure. Figure from Draine (2011).

### Other atomic FSLs

Other key diagnostics of the ISM which are ordinarily targeted in high-redshift galaxies in FIR/(sub-)mm bands are the FSLs  $[\text{NII}]_{122\mu\text{m}, 205\mu\text{m}}$ ,  $[\text{OI}]_{63\mu\text{m}}$ , and  $[\text{OIII}]_{52\mu\text{m}, 88\mu\text{m}}$ . Specifically, except  $[\text{OI}]$ , they trace the warm ionized medium. Thanks to their different ionization energies and atomic weights, the combination of these lines allows us to shed light on other ISM properties, such as the density of the ionized medium, the hardness of the radiation field, and even the ISM metallicity. In what follows, we briefly examine these latter emission lines.

The ionization potential of the nitrogen atom (14.5 eV) is greater than that of HI, therefore the  $\text{N}^+$  emission is due to radiative deexcitation of collisionally-excited electrons in the fully ionized medium. For an electron temperature of 8000 K, the critical density of the ( $^3P_1 \rightarrow ^3P_0$ )  $[\text{NII}]_{205\mu\text{m}}$  line is  $n_e^{\text{crit}} \approx 44 \text{ cm}^{-3}$

(Oberst et al., 2006). This means that this line traces the low-density diffuse medium ( $n_e \sim 0.1 - 1 \text{ cm}^{-3}$ ) rather than the dense (HII) regions ( $n_e \sim 0.5 - 1.0 \times 10^3 \text{ cm}^{-3}$ ), where it is rapidly thermalized and its emission is collisionally quenched (e.g., Herrera-Camus et al., 2016). The  $[\text{NII}]_{205 \mu\text{m}}$  line provides important clues for interpreting the observed  $[\text{CII}]_{158 \mu\text{m}}$  emission in galaxies.  $[\text{NII}]_{205 \mu\text{m}}$  has similar critical density than  $[\text{CII}]_{158 \mu\text{m}}$  for electron impact excitation in ionized medium. In addition,  $\text{N}^+$  and  $\text{C}^+$  have similar ionization potential, therefore their ratio principally depends on their relative abundance (e.g., Oberst et al., 2006). If one assumes the  $\text{C}^+/\text{N}^+$  abundance, the observed  $[\text{CII}]_{158 \mu\text{m}}$  luminosity can be written off as a contribution from the ionized medium, directly inferred from the  $[\text{NII}]_{205 \mu\text{m}}$  luminosity, and the  $[\text{CII}]_{158 \mu\text{m}}$  emission from PDRs. In addition, the different critical densities of  $[\text{NII}]_{122 \mu\text{m}}/[\text{NII}]_{205 \mu\text{m}}$  imply that this ratio can be used to measure the electron density, in analogy to the  $[\text{CI}]_{369 \mu\text{m}}/[\text{CI}]_{609 \mu\text{m}}$  ratio for the neutral medium (see, Oberst et al., 2006)

$[\text{NII}]_{122 \mu\text{m}}$  and  $[\text{OIII}]_{88 \mu\text{m}}$  have similar critical densities ( $\sim 300 - 500 \text{ cm}^{-3}$ ) but different ionization potentials (14.5 eV and 35 eV, for N and  $\text{O}^+$ , respectively), therefore their ratio is sensitive to the hardness of the radiation field. Remarkably, the  $[\text{OIII}]_{88 \mu\text{m}}$  line can be up to three times brighter than  $[\text{CII}]_{158 \mu\text{m}}$  line in galaxies with low-metallicity ( $Z < 1/3 Z_\odot$ , where  $Z_\odot$  is the solar metallicity) or with high-ionization state (Cormier et al., 2012; Harikane et al., 2018). This line has been revealed to be a powerful tool to study the ionized medium in primeval galaxies at  $z \sim 7 - 9$  (Inoue et al., 2016; Carniani et al., 2017b; Hashimoto et al., 2018, 2019a,b, see Fig. 5.4).

## 5.2.2 Molecular gas tracers

The molecular medium is entirely composed by hydrogen molecules  $\text{H}_2$ , while  $< 1\%$  of the mass consists mostly of CO, water vapor ( $\text{H}_2\text{O}$ ), and other molecules. However, the  $\text{H}_2$  molecule has high excitation requirements and it lacks of a permanent dipole moment (Dabrowski, 1984). This makes the cold molecular hydrogen invisible in emission for all the practical purposes.

Molecular excitation occurs via collisions or absorption of photons from the impinging radiation field. The rate of collisional excitations depends on the kinetic temperature of the gas via  $\gamma = \langle \sigma \times v \rangle$ , where  $\sigma$  is the collision cross

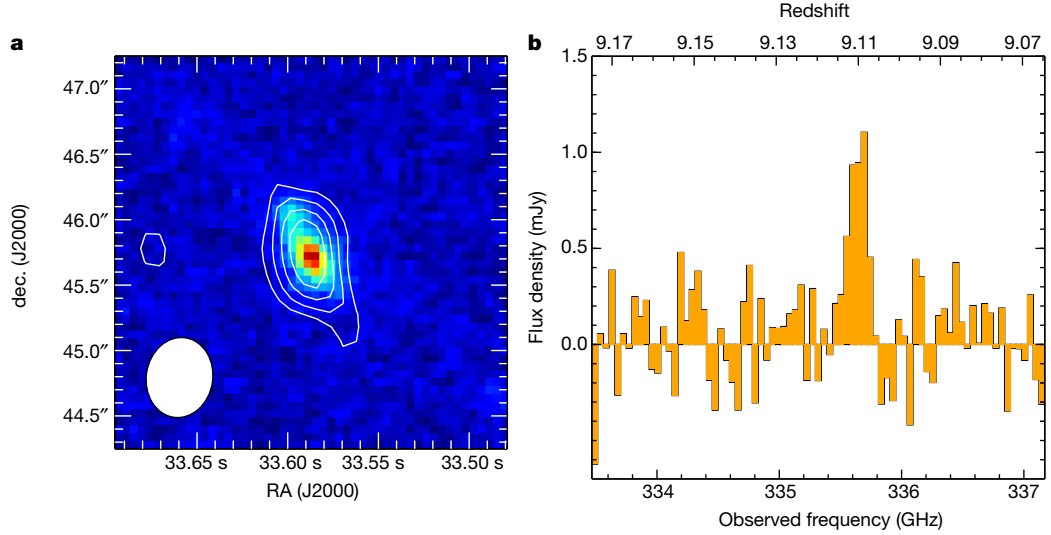


**Figure 5.4**

ALMA detection of  $[\text{OIII}]_{88\mu\text{m}}$  line in the gravitational lensed galaxy MACS1149-JD1 at  $z = 9.1$ . *Left panel*: HST image (F160W) with ALMA  $[\text{OIII}]$  contours overlaid at  $[3, 4, 5, 6]\sigma$ . The white ellipse is the ALMA synthesized beam. *Right panel*: ALMA  $[\text{OIII}]_{88\mu\text{m}}$  spectrum of the source. Top axis report the redshift values. Figure from Hashimoto et al. (2018).

section,  $v$  is the relative velocity of the colliders, and they are averaged over the gas velocity distribution. Typical values of  $\gamma$  for CO and  $\text{H}_2$  ranges from  $\sim 3$  to  $10^{-10} \text{ cm}^3 \text{ s}^{-1}$  (Flower & Launay, 1985; Yang et al., 2010). For a simple linear polar molecule as in the case of CO, quantum mechanics predict via Born-Oppenheimer approximation a rotational ladder of levels determined by the configuration of the nucleons. As a result, the energy of a rotational level is given by  $E_{\text{rot}} = J(J + 1)\hbar^2/2I$ ; where  $J$  is the angular momentum of the molecule, and  $I$  is the moment of inertia. Permitted rotational transitions can occur accordingly to the selection rules for magnetic dipole transitions,  $\Delta J = \pm 1$ . In this case the energy of the photon released from the level  $J$  to  $J - 1$  is  $h\nu_{\text{line}} = \Delta E_{\text{rot}} = \hbar^2 J/I$ . The rate of spontaneous emission depends exclusively on the physical properties of the molecule. The radiative de-excitation rates are determined by the Einstein A coefficient,  $A \propto \mu^2 \times \nu_{\text{line}}^3$ , where  $\mu$  is the molecular dipole moment in the  $J = 1$  state, so that high- $J$  transitions are significantly faster than those at low  $J$ . At the critical density  $n_{\text{crit}} = A/\gamma$ , collisional excitations equate the spontaneous radiative decay

rate<sup>3</sup>. In general, a collisionally-excited line make its greatest contribution to cooling around its critical density. Molecules with high dipole moment have also higher critical density. This means that high-density medium is required to significantly populate by collisions the upper levels of such molecules.

### **Carbon monoxide: CO rotational lines**

The most abundant molecule after H<sub>2</sub> is the carbon monoxide CO. Its rotational transitions are the primary coolants of the cold molecular gas, thus CO lines are used to infer the total molecular mass of galaxies (Bolatto et al., 2013, for a review). Low- $J$  ( $J_{\text{up}} < 6$ ) CO lines have relatively low critical density ( $\sim 10^3 - 10^4 \text{ cm}^{-3}$ , see the Leiden Atomic and Molecular Database<sup>4</sup>, Schöier et al. 2005) and excitation temperature, therefore they are associated with cold molecular gas in PDRs. In contrast, high- $J$  ( $J_{\text{up}} > 7$ ) transitions have a high critical density ( $n_{\text{crit}} \sim 10^5 \text{ cm}^{-3}$ ) and they mainly trace the high-density and/or high-temperature gas. The excitation of high- $J$  CO lines is typically explained by an intense X-ray radiation field impinging the molecular clouds in the central region of galaxies (XDRs), and/or by shocks produced by AGN-driven outflows (e.g., Meijerink et al., 2013; Gallerani et al., 2014; Mingozzi et al., 2018; Carniani et al., 2019). The combination of multiple CO line detections enables to study the CO spectral line energy distribution (SLED). The CO SLED is a powerful tool to distinguish the contribution of star formation and AGN (PDRs vs. XDRs) to the CO line emission and to constrain the properties of different gas phases, such as the density of the medium and the intensity of the radiation field (e.g., Riechers et al., 2009, 2013; Stefan et al., 2015; Yang et al., 2017; Cañameras et al., 2018; Carniani et al., 2019, see Fig. 5.5, and Chap. 6). CO emission has been ubiquitously detected in normal galaxies in the local Universe (see, e.g., Saintonge et al. 2017, 2018; and Tacconi et al. 2020 for a review) and in the highest-redshift quasars and SMGs (e.g., Riechers et al., 2013; Strandet et al., 2017; Venemans et al., 2017b; Novak et al., 2019; Li et al., 2020b), and it provides key information for characterizing the ISM (see, Carilli & Walter, 2013, for a review).

---

<sup>3</sup>We note that the definition adopted here is an approximation that does not properly take into account neither the summation over all levels that interact with the  $j^{\text{th}}$  state, nor the optical depth of the line. The effective critical density is actually lower by taking into account these factors.

<sup>4</sup><https://home.strw.leidenuniv.nl/~moldata/>

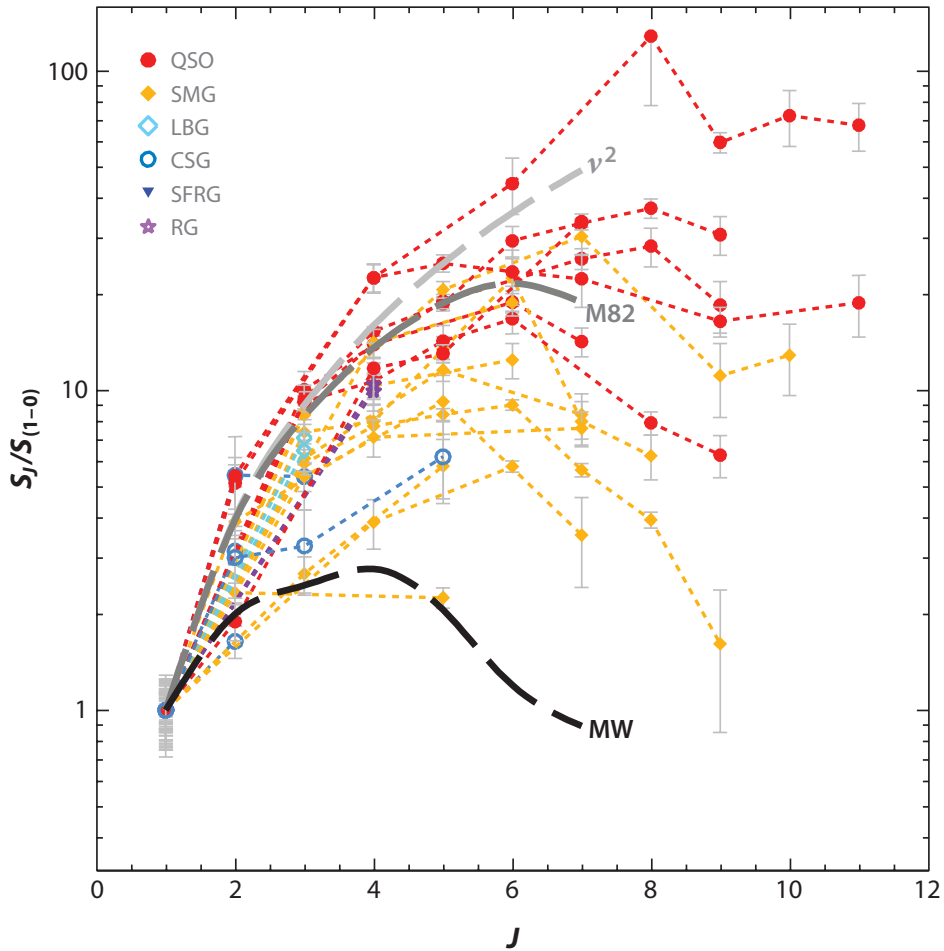


**Figure 5.5**

CO SLEDs color-coded by the source type for various objects for which CO(1–0) is available. CO fluxes are reported as a function of the rotational quantum number ( $J$ ), normalized to the CO(1–0) line. Quasars appear as the most excited sources which CO SLEDs peak around  $J \sim 6$ , consistent with the extreme conditions in which ISM is found. SMGs are slightly less excited on average, their CO SLEDs peak at  $J \sim 5$ . The dashed thick lines are the CO excitation ladders for the Milky Way (MW; black line), and M82 (dark gray line). The dashed gray line shows CO SLED trend for constant brightness temperature in the Rayleigh-Jeans regime, i.e.,  $S_J \propto \nu^2$  (this approximation is however not valid for high  $J$ ). Abbreviations: CSG (color-selected galaxies), LBG (Lyman-break galaxies), SFRG (star-forming radio galaxies), RG (radio galaxies). Figure from Carilli & Walter (2013).

Despite the low- $J$  CO lines are powerful diagnostics of the bulk of molecular gas, they cannot be used to investigate the dense cloud cores ( $n_{\text{H}_2} > 10^4 - 10^5 \text{ cm}^{-3}$ ) where star formation occurs. To map this gas phase, other tracers with higher critical density and lower optical depth are typically targeted such

as  $^{13}\text{CO}$ ,  $\text{C}^{18}\text{O}$ ,  $\text{CS}$ ,  $\text{CN}$ ,  $\text{HCO}^+$ ,  $\text{HCN}$ , and  $\text{HNC}$ . However, the low abundance of these molecules results in faint fluxes which make these transitions very hard to detect at high redshift. The observed frequency of CO lines and other important tracers as a function of the redshift are reported in **Fig. 5.2**.

### **Water vapor: $\text{H}_2\text{O}$ rotational lines**

Among dense gas tracers, water vapor ( $\text{H}_2\text{O}$ ) deserves particular attention. The  $\text{H}_2\text{O}$  molecule is an asymmetric rotor with a permanent electric dipole, its energy ladders are defined by three quantum numbers  $J_{K_{-1},K_{+1}}$ :  $K_{-1} + K_{+1} = \text{odd}$ , for para- $\text{H}_2\text{O}$ , and  $K_{-1} + K_{+1} = \text{even}$ , for ortho- $\text{H}_2\text{O}$ . The quantum selection rules for electric dipole radiative transitions are  $\Delta J = 0, \pm 1$ ;  $\Delta K_{-1} = \pm 1, \pm 3$ ; and  $\Delta K_{+1} = \pm 1, \pm 3$ , thus para- and ortho- $\text{H}_2\text{O}$  behave almost like separate species. Water vapor emission is a tracer of the warm dense molecular phase of the interstellar medium ( $n_{\text{H}_2} \gtrsim 10^5 - 10^6 \text{cm}^{-3}$ ,  $T \sim 50 - 100 \text{K}$ ; see, Liu et al., 2017), where UV/X-ray radiation from newly formed stars or powerful AGN increases the dust temperature above that of ice evaporation (e.g., Cernicharo et al., 2006). In these regions, the  $\text{H}_2\text{O}$  molecule can be unlocked from the icy mantle of the dust grains and released into the gas phase via photodesorption (see, e.g., Neufeld et al., 1995; Hollenbach et al., 2009), or by sputtering of grains in shocked-heated regions (e.g., Bergin et al., 2003; Flower & Pineau Des Forêts, 2010; González-Alfonso et al., 2012, 2013) where  $\text{H}_2\text{O}$  becomes the third most abundant species and the strongest molecular emitter after the high- $J$  ( $J_{\text{up}} > 7 - 8$ ) CO transitions. The  $\text{H}_2\text{O}$  molecule can also form in the gas phase through ion-neutral chemistry and neutral-neutral endothermic reactions (Graff & Dalgarno, 1987; Wagner & Graff, 1987; Hollenbach et al., 2009). Lower-level rotational transitions ( $E_{\text{up}} < 250 \text{K}$ ) arise in collisionally-excited gas with kinetic temperature of  $T_{\text{kin}} \sim 30 - 50 \text{K}$  and clump densities of about  $3 \times 10^5 \text{cm}^{-3}$ , where they may play an important role as a cooling agent (e.g., Neufeld & Kaufman, 1993; Neufeld et al., 1995; Bradford et al., 2011). The higher levels have very high critical density ( $> 10^8 \text{cm}^{-3}$ , e.g., Faure et al. 2007; Faure & Josselin 2008; Daniel et al. 2012), that is hardly reached even in the densest molecular cores. These lines require radiative excitation by an intense FIR radiation field from warm dust (Weiß et al., 2010; González-Alfonso et al., 2014), and therefore they do not contribute to the ISM cooling process. However, as revealed by the complex  $\text{H}_2\text{O}$  line profiles observed in the presence of outflows water

vapor lines can be also significantly excited by shocks (see, e.g., van der Tak et al., 2016). Because both collisions and IR pumping are responsible for populating the water vapor energy levels, H<sub>2</sub>O lines not only probe the physical conditions of the warm and dense molecular gas-phase ISM, but also provide important clues about the dust IR radiation density. Interestingly, the intensity of H<sub>2</sub>O lines is found to be nearly linearly proportional with the total IR luminosity of the galaxy (Omont et al., 2013; Yang et al., 2013, 2016a; Liu et al., 2017, see, Sects. 6.8.4 and 7.7.4).

Ground-based observations of water lines in nearby galaxies are limited by telluric atmospheric absorption and consequently have been restricted to radio maser transitions and a few transitions in IR-luminous galaxies (e.g., Combes & Wiklind, 1997; Menten et al., 2008). On the other hand, observational campaigns using space telescopes (e.g., Infrared Space Observatory (ISO), *Herschel*/PACS/SPIRE/HIFI) have been successful in detecting H<sub>2</sub>O features in local galaxies (mainly in absorption; Fischer et al., 1999, 2010; González-Alfonso et al., 2004, 2008, 2010, 2012; van der Werf et al., 2010; Weiß et al., 2010; Rangwala et al., 2011; Spinoglio et al., 2012; Pereira-Santaella et al., 2013; Liu et al., 2017). Furthermore, various H<sub>2</sub>O emission lines have been detected at higher redshifts ( $z > 1 - 2$ ) in starburst galaxies, Hy/ULIRGs (e.g., Bradford et al., 2011; Lis et al., 2011; Omont et al., 2011, 2013; van der Werf et al., 2011; Combes et al., 2012; Lupu et al., 2012; Bothwell et al., 2013; Yang et al., 2013, 2016a, 2019a, 2020a; Riechers et al., 2017, 2021), and also in a  $z > 6$  SMG (Riechers et al., 2013) and a lensed  $z > 6$  quasar host galaxy (Yang et al., 2019c).

### **Hydroxyl radical: OH rotational lines**

The hydroxyl radical (OH) is a key intermediary molecule that is formed in warm PDRs exposed to FUV radiation through the endothermic reaction between atomic oxygen and vibrationally excited H<sub>2</sub><sup>\*</sup>. Further reaction with H<sub>2</sub> leads to the formation of H<sub>2</sub>O. On the other hand, water vapor can photodissociate in gas unshielded from FUV radiation, producing OH. OH can also be formed in shocked gas where high gas temperatures can overcome the activation barrier of the O + H<sub>2</sub> reaction, or in quiescent obscured regions irradiated by cosmic rays or X-rays through ion-neutral reactions starting from H<sub>3</sub><sup>+</sup> (Hollenbach & Tielens, 1997; Agúndez et al., 2010). The OH molecule has a high dipole moment (1.668 Debye), therefore the radiative rates of

its rotational transitions are generally higher than those of CO. The critical densities of OH transitions are about  $10^9 - 10^{10} \text{ cm}^{-3}$  (Destombes et al., 1977; Dewangan et al., 1987), implying that OH excitation cannot be driven by collisions. Radiative pumping by IR photons is typically invoked to explain its emission. The electronic ground state has two fine-structure levels,  $^2\Pi_{3/2}$  (the ground state) and  $^2\Pi_{1/2}$ , each of which has two  $\Lambda$ -doubling levels (further split into two hyperfine sublevels). Furthermore, the OH molecule can also have a rotational angular momentum ( $J$ ), resulting in a ladder of rotational states with increasing  $J$ . The OH ground state  $^2\Pi_{3/2}$  ( $J = 3/2$ ) can absorb IR radiation near  $119 \mu\text{m}$ ,  $79 \mu\text{m}$ ,  $53 \mu\text{m}$ , and  $35 \mu\text{m}$ , followed by spontaneous radiative decay that repopulates the four ground sublevels, including the FIR OH cross-ladder transitions whose radiative rates are  $\sim 100\times$  weaker than the rotational transitions.

OH transitions, either in absorption or emission, were detected in local Seyfert galaxies, including M82 (Colbert et al., 1999), NGC 253 (Fischer et al., 1999; Bradford et al., 1999), IRAS 20100-4156 and 3Zw35 (Kegel et al., 1999), Arp 220 (González-Alfonso et al., 2004), NGC 1068 (Smith et al., 2004; Spinoglio et al., 2005), Mrk 231 (González-Alfonso et al., 2008), and NGC 4418 (González-Alfonso et al., 2014). Systematic searches for OH emission have revealed that some OH lines exhibit P-Cygni profiles, suggesting massive molecular outflows in samples of local (U)LIRGs and quasars (Fischer et al., 2010; González-Alfonso et al., 2010, 2012, 2013, 2017; Sturm et al., 2011; Spoon et al., 2013; Veilleux et al., 2013; Herrera-Camus et al., 2020b). OH emission has also been detected at  $z \gtrsim 6$  in the SMG HFLS 3 (Riechers et al., 2013), and in the quasar J1319+0950 (Herrera-Camus et al., 2020b, see, Fig. 5.6), demonstrating the feasibility of detecting these lines at very high- $z$  with ground-based observations.

### 5.2.3 Dust emission

Dust grains in star-forming regions of galaxies emit radiation due to the reprocessed-UV photons by young stars that are re-emitted in IR to mm wavelengths. The continuum emission in this wavelength range therefore encodes important information about the galaxy properties, such as the dust mass ( $M_{\text{dust}}$ ), IR luminosity, and the SFR. Because the dust grains are in local thermodynamic equilibrium (LTE), they emit thermal continuum

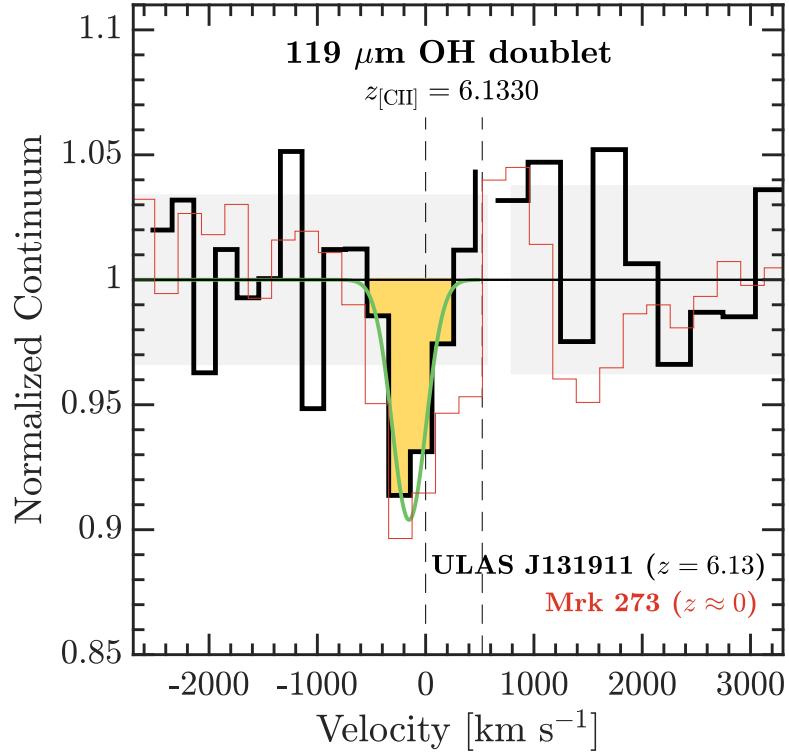


**Figure 5.6**

ALMA OH  $119\ \mu\text{m}$  spectrum of the  $z = 6.13$  quasar ULAS J1319+0950 (black line). The gray shaded area show the  $\pm 1\sigma$  noise level. The observed velocity is referred to the systemic [CII]-based redshift (Wang et al., 2013). The vertical dashed lines indicate the expected position of the OH  $119\ \mu\text{m}$  doublet. The green line is the best-fit single-component Gaussian model. The tentative absorption feature is blueshifted from the systemic redshift of  $\sim 150\ \text{km s}^{-1}$  suggesting the presence of molecular outflow. This outflow signature resembles in intensity and velocity structure the OH  $119\ \mu\text{m}$  absorption profile detected in the nearby Mrk 273 (red line Veilleux et al., 2013), here smoothed to match the ALMA spectrum velocity resolution. Figure from Herrera-Camus et al. (2020b).

radiation. However, dust grains are not ideal blackbodies. They absorb and emit radiation with an efficiency that depends by the wavelength of the incident photons (Draine & Lee, 1984). The observed flux density of thermal dust emission at the observed-frame frequency  $\nu/(1+z)$  from a source at redshift  $z$ , can be expressed by taking into account variation in opacity and source emissivity via the dubbed “graybody” law (e.g., Erickson et al., 1981; Schwartz, 1982; Hildebrand, 1983)

$$S_{\nu/(1+z)} = \frac{\Omega}{(1+z)^3} (1 - e^{-\tau(\nu)}) B_{\nu}(T_{\text{dust}}), \quad (5.1)$$

where  $\Omega$  is the solid angle subtended by the source,  $\tau(\nu)$  is the optical depth,  $B_\nu(T)$  is the Planck function  $B_\nu(T) = [2h\nu^3/c^2][\exp(h\nu/k_B T) - 1]^{-1}$ , and  $T_{\text{dust}}$  is the dust temperature. The dust optical depth is usually parametrized with a power law in terms of the dust opacity coefficients  $k_d(\nu)$  and the projected dust mass surface density  $\Sigma_d$  along the LOS as  $\tau(\nu) = \Sigma_d k_d(\nu) = (\nu/\nu_0)^\beta$ , with  $\beta$  being the dust emissivity index, and  $\nu_0$  is the frequency at which the dust optical depth reaches unity (Draine, 2006). The solid angle  $\Omega$  is related to the projected area of the source onto the sky plane  $A_{\text{source}}$ , via  $\Omega = A_{\text{source}}(1+z)^4 D_L^{-2}$ , where  $D_L$  is the luminosity distance at redshift  $z$ . For an unresolved source, to first approximation  $\tau(\nu) = M_{\text{dust}} k_d(\nu)/A_{\text{source}}$ . By inserting the latter expression into Eq. (5.1), the observed continuum flux can be directly related with the dust mass (see, e.g., Downes et al., 1992; Dunne et al., 2000):

$$S_{\nu/(1+z)} = \frac{1 - e^{-\tau(\nu)}}{\tau(\nu)} \frac{(1+z)}{D_L^2} k_d(\nu) M_{\text{dust}} B_\nu(T_{\text{dust}}). \quad (5.2)$$

In the case of a single-component optically-thin ( $\tau(\nu) \ll 1$ ) graybody model  $(1 - e^{-\tau(\nu)})/\tau(\nu) \approx 1$  and Eq. (5.2) can be approximated as:

$$S_{\nu/(1+z)} \approx \frac{(1+z)}{D_L^2} k_d(\nu) M_{\text{dust}} B_\nu(T_{\text{dust}}). \quad (5.3)$$

However, observational studies at low and high redshift (e.g., Blain et al., 2003; Conley et al., 2011; Rangwala et al., 2011; Casey, 2012; Riechers et al., 2013; Simpson et al., 2017; Faisst et al., 2020), highlighted that the optically-thin dust approximation may not be true at short wavelengths ( $\lambda < 100 \mu\text{m}$ ). However, the lack of multiband measurements, especially near the peak of the dust SED where the flux density is most sensitive to the dust temperature, results in large uncertainties in determining the dust parameters, and IR luminosity at high redshift.

## 5.3 The role of the CMB on high- $z$ ISM observations

The CMB temperature increases with the redshift as  $T_{\text{CMB}}(z) = 2.73 \times (1+z)$  as a consequence of the adiabatic expansion of the Universe. This means

that at  $z = 6$ , the CMB temperature is 19.1 K, thus comparable or even greater than the temperature of the dust and the cold ISM components that are found in galaxies and quasar hosts. For this reason, CMB can severely impact the (sub-)mm observations at high- $z$ . Specifically, CMB represents a strong background against which we measure the line and continuum emission and it provides an additional source of heating (da Cunha et al., 2013, see Fig. 5.7). As a result, both the dust temperature and line excitations increase at high redshifts (see, e.g., Obreschkow et al., 2009). These effects must be taken into account when gas and dust measurements are derived in (sub-)mm observations at high- $z$  (see Sect. 6.5). Specifically, da Cunha et al. (2013) show that in the optically-thin limit, the recoverable dust continuum against the CMB background is given by Eq. (5.3) via the substitution  $B_\nu(T_{\text{dust}}) \rightarrow \{B_\nu[T_{\text{dust}}(z)] - B_\nu[T_{\text{CMB}}(z)]\}$ , where  $T_{\text{dust}}(z)$  is the temperature of the dust including the heating provided by the CMB at redshift  $z$  via  $T_{\text{dust}}(z) = \left\{ (T_{\text{dust}}^{z=0})^{4+\beta} + (T_{\text{CMB}}^{z=0})^{4+\beta} [(1+z)^{4+\beta} - 1] \right\}^{\frac{1}{4+\beta}}$ . The latter implies that, for an intrinsic dust temperature of  $T_{\text{dust}} = 18$  K, the effect of the CMB becomes non-negligible at  $z \simeq 4$ ; the higher the redshift, the more the dust temperature approaches the temperature of the CMB. Moreover, in the LTE case, the fraction of intrinsic flux of CO lines that is recoverable against the cosmic background decreases monotonically with increasing redshift and decreasing  $J$  (see Fig. 5.7). However, the effect of the CMB on various transitions strongly depends on the detailed physical properties of the gas (e.g., the excitation temperature, density; see Combes et al. 1999; Obreschkow et al. 2009; da Cunha et al. 2013). Vallini et al. (2015) perform detailed calculation of the excitation temperature ( $T_{\text{exc}}$ ) of the  $[\text{CII}]_{158\mu\text{m}}$  emission in radiative transfer cosmological simulations at  $z \simeq 7$ . They obtain  $T_{\text{exc}}^{\text{PDR}}([\text{CII}]) \sim 30 - 120$  K in PDRs (with  $\text{SFR} \sim 0.1 - 100 M_\odot \text{yr}^{-1}$ ), and  $T_{\text{exc}}([\text{CII}]) \sim 22 - 23$  K in the CNM. This implies that, even at high- $z$ , the  $[\text{CII}]_{158\mu\text{m}}$  emission from star-forming regions is mostly robust against the CMB effects. However, we might lose the ability to detect an extended cooler gas component where the  $T_{\text{CMB}} \sim T_{\text{exc}}^{\text{CNM}}([\text{CII}])$ .

## 5.4 Modeling the line emission

Astronomers have developed sophisticated numerical codes to model and predict the emission of clouds of gas and dust subjected to various cooling

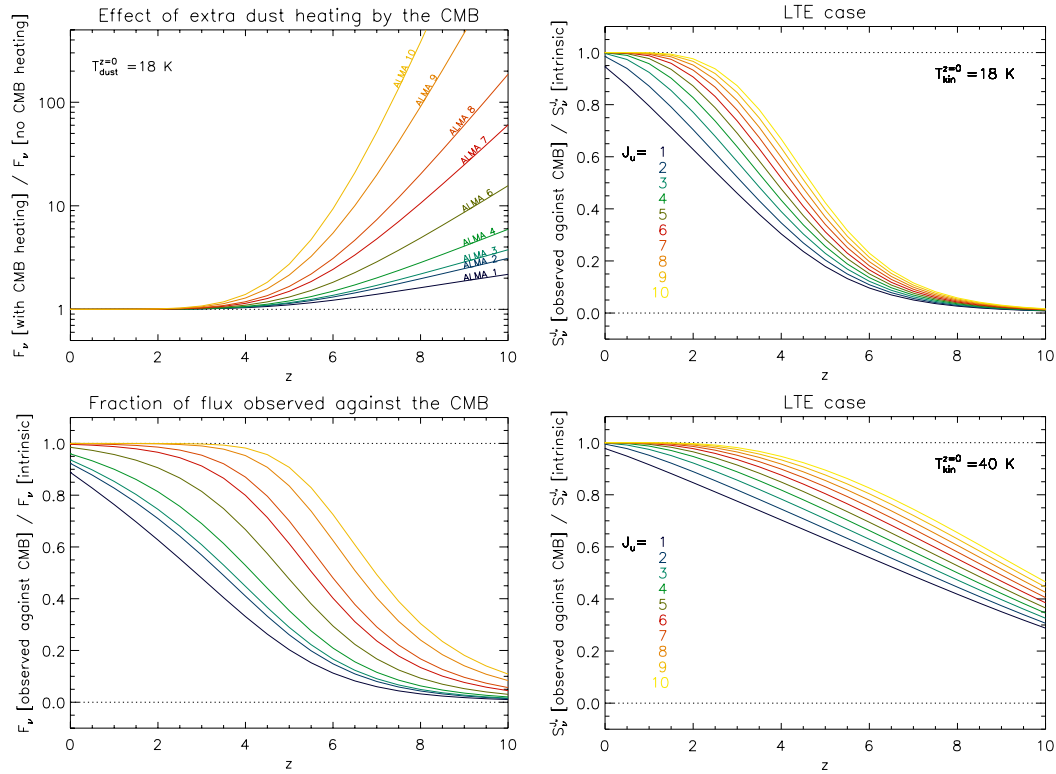


**Figure 5.7**

*Left panels:* effect of additional heating on the dust emission by increasing the CMB temperature with redshift (top). Here it is reported the relative increase of the predicted flux density in different ALMA bands due to the extra heating from the CMB. The dust temperature at  $z = 0$  is fixed at  $T_{\text{dust}}^{z=0} = 18$  K. In this panel the effect of contrast with the CMB background is not included. In the bottom panel it is reported the fraction of the intrinsic flux emitted by the galaxy recoverable against the CMB. The intrinsic flux includes the heating from the CMB. *Right panels:* ratio between the line (velocity-integrated) flux observed against the CMB background and the intrinsic line flux for different CO transitions at  $J_{\text{up}} = 1 - 10$  in LTE case. Top panel reports the case with gas kinetic temperature of  $T_{\text{kin}}^{z=0} = 18$  K, while in the bottom panel  $T_{\text{kin}}^{z=0} = 40$  K. LTE case implies that the excitation temperature of all the CO levels are equal to the gas kinetic temperature. The plots include both the heating and background effect due to the CMB. Figure from da Cunha et al. (2013).

and heating processes. A detailed discussion of the complex operations of these models is beyond the scope of this thesis. Here we just provide the reader with a brief description of the basic principles of the ISM modeling. Very generally, these numerical models are designed in order to predict the observed properties of the lines by starting from a set of input parameters (e.g., gas temperature and density, abundances, radiation field, velocity field, turbulence, source structure, geometry, etc.) from which they compute the

level population of the species by solving the statistical equilibrium equation. Then, the line intensities emerging from the gas cloud are derived by solving the radiative transfer equation across the structure (including internal and external radiation field) taking into account the geometry and kinematics of the gas. For practical purposes, such simulations are typically repeated by varying a number of parameters of interest. The results of these simulations are then compared with observations in order to put physical constraints on the targeted sources.

Substantial efforts have been invested over past years with the goal of designing increasingly accurate codes that can be able to deal with the diverse complex conditions found in the ISM of galaxies. One of the main complications in the treatment of the radiative transfer in gas is to the non-local coupling between the level population of the species and the radiation field. This coupling makes prohibitive any exact solution of the problem, especially for multi-level systems. In order to overcome such limitation, V. V. Sobolev in 1958 introduced an approximate but powerful method which greatly simplifies the solution of the radiative transfer problem. In this approximate treatment the absorption of photons by the species is assumed to be local. In other words, photons either are absorbed in the vicinity of the emitting region, or they escape the medium. This is the typical situation in which the gas has a large velocity gradient (LVG). In this situation, the motion of gas particles shifts by Doppler effect the frequency of the emitted photons outside the line profile of the (potentially) absorbing gas located in the surroundings. The medium is therefore “radiatively decoupled” and the level populations can be handled separately from the radiative transfer problem. Such approach is known as *escape probability* method and is currently implemented in the majority of the numerical codes in order to model a wide variety of astrophysical problems, especially for situations in which optically-thick lines are involved. Many different codes are available in the literature to simulate PDR/XDR conditions, each of which is based on different assumptions on the geometry, the thermal and chemical balance, and employ different implementations of the radiative transfer (e.g., Tielens & Hollenbach, 1985a; Meixner & Tielens, 1993; Maloney et al., 1996; Spaans, 1996; Kaufman et al., 1999, 2006; Elitzur & Asensio Ramos, 2006; Meijerink & Spaans, 2005; Meijerink et al., 2007; van der Tak et al., 2007; Pound & Wolfire, 2008; Bisbas et al., 2012; Ferland et al., 2017). However, due

to the huge complexity of the problem, the majority of the codes adopt very simplified assumptions based on (one-dimensional) infinite slab of gas impinged by an external radiation field. Such kind of models do not have a confined volume and no mass estimates can be retrieved from them. Undoubtedly, this simplification cannot provide a realistic picture of the ISM which is actually composed by ensembles of clouds and diffuse medium having a wide range of physical and geometrical properties. PDR/XDR codes are designed in order to simulate an archetypal cloud in galaxy. For these reasons, in order to mitigate large uncertainties due to unknown parameters, the quantitative comparison of data with the model predictions is typically assessed by employing the observed line ratios. This approach, when applied to high- $z$  galaxy observations – which are often spatially unresolved – yields estimates of ISM properties that have to be considered “averaged”, to some extent, on the overall galaxy.

# 6

## Characterizing the interstellar medium in $z > 6$ quasar host galaxies with a multiline survey

“Astronomy compels the soul to look upwards and leads us from this world to another.

— Plato

This chapter is drawn from “ALMA multiline survey of the ISM in two quasar host–companion galaxy pairs at  $z > 6$ ”, Pensabene A., Decarli R., Bañados E., Venemans B., Walter F., Bertoldi F., Fan X., Farina E. P., Li J., Mazzucchelli C., Novak M., Riechers D., Rix H.-W., Strauss M. A., Wang R., Weiß A., Yang J., Yang Y., *A&A*, 652, A66.

### 6.1 Introduction

Quasars at  $z > 6$  are thought to reside in the densest regions of the Universe. Indeed they are often found accompanied by or interacting with other galaxies (see, **Sect. 1.5**, and references therein). These quasar host–companion galaxy systems represent a unique testing ground to study star formation, AGN feedback, and structure growth in galaxies at  $z > 6$ . Multiline surveys of the ISM in these systems provide key diagnostics of the physical properties of the ISM, including densities, and the source of the powering radiation field (see, Carilli & Walter, 2013, for a review). Previous studies have detected galaxy dust continuum and gas emission lines even in highest redshift

quasars. These studies have mainly targeted the brightest emitters such as  $[\text{CII}]_{158\mu\text{m}}$ , and the low-/mid- $J$  CO rotational transitions (see, e.g., Walter et al., 2003, 2004, 2009; Maiolino et al., 2005, 2009, 2015; Wang et al., 2010, 2013; Gallerani et al., 2014; Willott et al., 2015b,a; Carniani et al., 2017a, 2019; Decarli et al., 2017, 2018; Venemans et al., 2017a,c,b, 2019; Feruglio et al., 2018), and have revealed the ubiquitous presence of massive cold-gas ( $M_{\text{gas}} \gtrsim 10^{10} M_{\odot}$ ) and dust ( $M_{\text{dust}} \gtrsim 10^9 M_{\odot}$ ) reservoirs in high- $z$  quasar host galaxies.

Multiple atomic FSLs and molecular transitions arising from different ISM phases provide direct and indirect information on the ionized phase in the proximity of young stars (e.g.,  $[\text{OIII}]_{88\mu\text{m}}$ ,  $[\text{NII}]_{122\mu\text{m}, 205\mu\text{m}}$ ) or the denser and warm phases buried in the cores of molecular clouds (e.g., high- $J$  CO,  $\text{H}_2\text{O}$ , hydroxyl OH and its anion (hydroxide)  $\text{OH}^-$ ; see Sect. 5.2). However, only recent studies have started to probe these diagnostics in a few  $z > 6$  systems (e.g., Riechers et al., 2009, 2013; Strandet et al., 2017; Venemans et al., 2017c,b; Walter et al., 2018; Hashimoto et al., 2019a,b; Novak et al., 2019; Wang et al., 2019b; Yang et al., 2019c; Li et al., 2020a,b).

This chapter is focused on the ISM characterization of two  $z > 6$  quasar host galaxies, PJ231-20 at  $z \sim 6.59$ , and PJ308-21 at  $z \sim 6.24$ , and the nearby companions that were serendipitously discovered with ALMA (Decarli et al., 2017; Neeleman et al., 2019). These companions are among the most star-forming galaxies known to date (with  $[\text{CII}]$ -based  $\text{SFR} \gtrsim 200 - 500 M_{\odot} \text{yr}^{-1}$ ) at  $z > 6$  that do not show evidence of AGN activity in the rest-frame optical/UV (Decarli et al., 2017; Mazzucchelli et al., 2019) and in the X-rays (Connor et al., 2019, 2020). For these objects, the  $[\text{CII}]_{158\mu\text{m}}$  line and dust continuum have clearly been detected with previous ALMA observations (Decarli et al., 2017), while higher-resolution  $[\text{CII}]_{158\mu\text{m}}$  follow-up observations have allowed us to study of their kinematics (see Decarli et al., 2019a; Neeleman et al., 2019). The companion galaxies in the two systems have a projected separation of  $\sim 8.5$  kpc and  $\sim 14$  kpc, with a velocity offset of  $+137 \text{ km s}^{-1}$  and  $+591 \text{ km s}^{-1}$  for PJ231-20 and PJ308-21, respectively. Remarkably, the  $[\text{CII}]_{158\mu\text{m}}$  emission of the companion galaxy in the PJ308-21 system stretches over about 25 kpc and  $> 1500 \text{ km s}^{-1}$  toward and beyond the quasar host, suggesting that the satellite galaxy is tidally stripped by the interaction with the central quasar host galaxy (Decarli et al.,

2017, 2019a). Furthermore, in the systems PJ231-20 and PJ308-21, Ly $\alpha$  nebular emission has recently been discovered (Farina et al., 2019). This might indicate that the PJ231-20 quasar also recently underwent a merger event with the close companion galaxy.

Here we present ALMA band 3–6 observations of the PJ231-20 and PJ308-21 systems, in which we sampled the FIR dust continuum and various emission lines probing different ISM phases and conditions. The lines include the [NII]<sub>205 $\mu$ m</sub> and neutral carbon [CI]<sub>369 $\mu$ m</sub>, tracers of the low-density fully ionized medium (electron density  $n_e \lesssim 1 \text{ cm}^{-3}$ ), and the cold dense atomic phase of the ISM ( $n_H \sim 10^3 \text{ cm}^{-3}$ ; see, Sect. 5.2.1). We also present observations of the molecular transitions of CO at intermediate and high- $J$  (7–6, 10–9, 15–14, 16–15), three water vapor (ortho-)H<sub>2</sub>O rotational transitions (3<sub>12</sub>–2<sub>21</sub>, 3<sub>21</sub>–3<sub>12</sub>, and 3<sub>03</sub>–2<sub>12</sub>), and the hydroxyl molecule OH<sub>163 $\mu$ m</sub> doublet, which are associated with the warm dense phase of the ISM ( $n_H \gtrsim 10^5 \text{ cm}^{-3}$ ,  $T > 100 \text{ K}$ ; see Sect. 5.2.2). Combining the different pieces of information and making use of CLOUDY radiative transfer models (Ferland et al., 2017), we study a variety of the physical properties of the dust and gas-phase ISM in the quasar hosts and companion galaxies. This allows us to distinguish line excitation by star formation and AGN processes. This study provides an overview of the complex conditions of the multiphase ISM in galaxies at  $z \sim 6$ .

The chapter is organized as follows: in Sect. 6.2 we present the ALMA observations, and we describe the reduction of the data. In Sect. 6.3 we outline the analysis we conducted on the calibrated data, and we report FIR line emission and continuum measurements in the sources of systems PJ231-20 and PJ308-21. In Sect. 6.4 we describe the setup and the outputs of our CLOUDY models. In Sect. 6.5 we present and discuss the results we obtained from the dust continuum. Then, we dedicate Sect. 6.6 to the tracers of the ionized medium and the results we obtained from them, and in Sect. 6.7 we focus on the atomic medium and place constraints on its physical properties. In Sect. 6.8 we study the molecular phase of the ISM by analyzing the CO, H<sub>2</sub>O and OH lines. In Sect. 6.9 we estimate the various mass budgets of the different gas components. Finally, in Sect. 6.10 we summarize our results and draw our conclusions.

Throughout this chapter, we assume a standard  $\Lambda$ CDM cosmology with  $H_0 = 69.3 \text{ km s}^{-1} \text{ Mpc}^{-1}$ ,  $\Omega_m = 0.287$ , and  $\Omega_\Lambda = 1 - \Omega_m$  from Hinshaw et al. (2013).

## 6.2 Observations and data reduction

We present the ALMA Cycle 5 datasets of quasar PJ231-20, quasar PJ308-21 (hereafter QSO PJ231-20 and QSO PJ308-21, respectively) and their companion galaxies (program ID: 2017.1.00139.S, PI: R. Decarli) located at redshift  $z \sim 6.59$  and  $z \sim 6.24$ , respectively. The observations were executed during April-August 2018 using 43-48 ALMA 12-m antennas in compact configurations (C43-2 and C43-3). The program comprised three frequency settings each in ALMA bands 4, 5, and 6 that covered nine atomic fine-structure and molecular lines:  $[\text{NII}]_{205 \mu\text{m}}$ , high- $J$  CO(10–9, 15–14, 16–15),  $\text{H}_2\text{O}$  ( $3_{03} - 2_{12}$ ,  $3_{12} - 2_{21}$ ,  $3_{21} - 3_{12}$ ), the OH doublet, and the dust continuum emission. However, for PJ308-21, only the band 6 setup was executed. It encompasses CO(15–14, 16–15),  $\text{H}_2\text{O}$   $3_{03} - 2_{12}$ , and the  $\text{OH}_{163 \mu\text{m}}$  doublet.

We also present follow-up ALMA Cycle 7 observations of the same objects (program ID: 2019.1.00147.S, PI: R. Decarli), in which we sampled the atomic FSL  $[\text{CI}]_{369 \mu\text{m}}$  and the molecular mid- $J$  CO(7–6) transition together with dust continuum emission in ALMA band 3. These observations were executed in October 2019 using 43-48 ALMA 12-m antennas in the C43-4 configuration. All the observations were designed not to spatially resolve the emission of each source, but have an angular resolution that was high enough to resolve the companions from the quasars. This allowed us to maximize the signal-to-noise ratio (S/N) within the beam. The angular resolution ranges between  $\sim 1''.00$  and  $\sim 1''.80$ . In **Tab. 6.1** we summarize the ALMA observations, and in **Tab. 6.2** we report the covered emission lines in each frequency setup together with their rest frequencies.

We performed data reduction using the default calibration pipeline with the CASA (v.5.1.1-5 and v.5.6.1-8 for Cycle 5 and Cycle 7 data, respectively) package (McMullin et al., 2007). Calibrated visibilities were imaged using the CASA task `tclean` with a “natural” weighting scheme in order to maximize the sensitivity of the resulting maps. Dirty images were cleaned by employing two circular masks that were superimposed to include continuum emission of the central quasar and the companion. In the cleaning run, we stopped the

**Table 6.1:** Information about targeted objects and characteristics of ALMA observations for each frequency setup.

| Object ID   | PJ231-20  |               |   |               | PJ308-21  |               |   |               |
|---|---|---------------|---|---------------|---|---------------|---|---------------|
|   | QSO   |               | companion (*)                                       |               | QSO   |               | companion   |               |
| R.A. (J2000.0)                                      | 15 <sup>h</sup> 26 <sup>m</sup> 37 <sup>s</sup> .84 |               | 15 <sup>h</sup> 26 <sup>m</sup> 37 <sup>s</sup> .87 |               | 20 <sup>h</sup> 32 <sup>m</sup> 10 <sup>s</sup> .00 |               | 20 <sup>h</sup> 32 <sup>m</sup> 10 <sup>s</sup> .17 |               |
| DEC. (J2000.0)                                      | -20°50'0".8   |               | -20°50'2".3   |               | -21°14'2".4   |               | -21°14'2".7   |               |
| redshift <sup>(1)</sup>                             | 6.58651 ± 0.00017                                   |               | 6.5900 ± 0.0008                                     |               | 6.2342 ± 0.0010                                     |               | 6.2485 ± 0.0005                                     |               |
| Frequency setup <sup>(2)</sup>                      | A   | B             | C   | D             | A   | B             | C   | D             |
| Band  | 3   | 4             | 5   | 6             | 3   | 3             | 6   | 6             |
| Central frequency (GHz) <sup>(3)</sup>              | 99.755  | 146.456       | 199.350   | 234.397       | 104.901   | 104.901       | 245.870   | 245.870       |
| Time on source (min)                                | 33.82   | 19.70         | 28.27   | 8.72          | 41.97   | 41.97         | 39.83   | 39.83         |
| Array configuration                                 | C43-4   | C43-2, C43-3  | C43-2   | C43-2         | C43-4   | C43-4         | C43-2   | C43-2         |
| Number of antennas                                  | 43  | 48            | 48  | 45            | 48  | 48            | 44  | 44            |
| Baselines (m)                                       | 15 – 1547   | 15 – 500      | 15 – 360  | 15 – 483      | 15 – 783  | 15 – 783      | 15 – 455  | 15 – 455      |
| Beam (arcsec <sup>2</sup> ) <sup>(4)</sup>          | 0".99 × 0".89                                       | 1".49 × 1".22 | 1".76 × 1".14                                       | 1".10 × 1".01 | 1".32 × 1".13                                       | 1".32 × 1".13 | 1".19 × 0".97                                       | 1".19 × 0".97 |
| RMS cont. (mJy beam <sup>-1</sup> )                 | 0.011   | 0.019         | 0.029   | 0.042         | 0.009   | 0.009         | 0.015   | 0.015         |
| (RMS) cube (mJy beam <sup>-1</sup> ) <sup>(5)</sup> | 0.24  | 0.27          | 0.47  | 0.48          | 0.19  | 0.19          | 0.20  | 0.20          |
| Observation date                                    | 2019 Oct 6  | 2018 Apr 23   | 2018 Jun 4  | 2018 Aug 21   | 2019 Oct 14   | 2019 Oct 14   | 2018 Aug 12   | 2018 Aug 12   |

**Notes.** <sup>(1)</sup>Redshift of [CII]<sub>158μm</sub> line from Decarli et al. (2017). <sup>(2)</sup>Setup A refers to ALMA Cycle 7 data, while setups C, B, and D refer to Cycle 5 data. <sup>(3)</sup>Central frequency of the entire frequency setup. <sup>(4)</sup>Beam sizes are those from the natural maps. <sup>(5)</sup>Averaged RMS sensitivity over the entire bandwidth of the cubes (channel width of 40 km s<sup>-1</sup>). (\*) We note that Neeleman et al. (2019) found two companions in the PJ231-20 ALMA field located south and southwest of the QSO. However, our observations do not allow us to spatially resolve the two sources. We assume that the bulk of the emission from companion galaxies arises from the source south of the central PJ231-20 QSO, which is reported in Decarli et al. (2017) and denoted “C” in Neeleman et al. (2019).

**Table 6.2:** Covered emission lines in each frequency setup with their rest frequency.

| Covered emission lines  | Rest frequency (GHz) <sup>(1)</sup> | setup ID <sup>(2)</sup> |
|---|-------------------------------------|-------------------------|
| CO(7–6)   | 806.652                             | A                       |
| [Cl] <sub>369μm</sub>   | 809.342                             |                         |
| CO(10–9)  | 1151.985                            | B                       |
| H <sub>2</sub> O 3 <sub>12</sub> –2 <sub>21</sub>   | 1153.127                            |                         |
| H <sub>2</sub> O 3 <sub>21</sub> –3 <sub>12</sub>   | 1162.912                            |                         |
| [NII] <sub>205μm</sub>  | 1461.131                            | C                       |
| H <sub>2</sub> O 3 <sub>03</sub> –2 <sub>12</sub>   | 1716.770                            | D                       |
| CO(15–14)   | 1726.603                            |                         |
| OH <sup>2</sup> Π <sub>1/2, 3/2</sub> <sup>+</sup> – <sup>1</sup> / <sub>2</sub> <sup>–</sup> (*) | 1834.744                            |                         |
| OH <sup>2</sup> Π <sub>1/2, 3/2</sub> <sup>–</sup> – <sup>1</sup> / <sub>2</sub> <sup>+</sup> (*) | 1837.800                            |                         |
| CO(16–15)   | 1841.346                            |                         |

**Notes.** <sup>(1)</sup>Rest frequency of the lines are taken from the "Splatalogue database for astronomical spectroscopy" available at <https://www.cv.nrao.edu/php/splat>, see references therein. <sup>(2)</sup>Setup IDs are listed in **Tab. 6.1**. (\*)The Λ-doubling transitions of the hydroxyl molecule listed here are two triplets produced by the hyperfine structure splitting of the upper and lower level that is not spectrally resolved in the observations. We report the average rest frequency of the triplets. The six transitions are OH <sup>2</sup>Π<sub>1/2, 3/2</sub><sup>+</sup>–<sup>1</sup>/<sub>2</sub><sup>–</sup>, 1–1; OH <sup>2</sup>Π<sub>1/2, 3/2</sub><sup>+</sup>–<sup>1</sup>/<sub>2</sub><sup>–</sup>, 2–1; OH <sup>2</sup>Π<sub>1/2, 3/2</sub><sup>+</sup>–<sup>1</sup>/<sub>2</sub><sup>–</sup>, 1–0 and OH <sup>2</sup>Π<sub>1/2, 3/2</sub><sup>–</sup>–<sup>1</sup>/<sub>2</sub><sup>+</sup>, 1–1; OH <sup>2</sup>Π<sub>1/2, 3/2</sub><sup>–</sup>–<sup>1</sup>/<sub>2</sub><sup>+</sup>, 2–1; and OH <sup>2</sup>Π<sub>1/2, 3/2</sub><sup>–</sup>–<sup>1</sup>/<sub>2</sub><sup>+</sup>, 1–0.

procedure when the peak flux in the residual image within the mask dropped close to the RMS noise of the image in regions without source emission (i.e.,  $\sim 1\sigma$  cleaning threshold). For each setup, we produced two image-frequency cubes for the lower side band (LSB) and the upper side band (USB), respectively, with a channel width of  $40 \text{ km s}^{-1}$ . We obtained continuum images by combining the line-free channels from all spectral windows in multifrequency synthesis mode. The line-free channels were determined by inspecting the visibilities in all the frequency sidebands. When no line was detected, we selected line-free channels by adopting a line width of  $300 \text{ km s}^{-1}$  and source redshift based on the [CII]<sub>158μm</sub> line observations published by Decarli et al. (2017). We used the CASA task `uvcontsub` to fit the continuum visibilities in the line-free channels, and we obtained continuum-subtracted cubes with  $40 \text{ km s}^{-1}$  of channel width. We fit the continuum emission in the LSB and USB separately (maximum bandwidth of  $\sim 4 \text{ GHz}$ ) as a constant with frequency. This gave us two continuum-subtracted cubes for each frequency setup. In order to achieve Nyquist-Shannon sampling, we set the cube pixel

sizes in the image plane to  $0''.1$ , equal to  $\sim 1/7$  of the FWHM of the minor axis of the ALMA-synthesized beam. In this way, we obtained cubes and continuum images with a pixel size of  $0''.1$ . Self-calibration was attempted but showed no additional improvement for any of the observations, so we did not use it for what follows. Finally, the continuum images and line cubes were corrected for the primary beam response. We supplemented our analysis with the ALMA Cycle 3  $[\text{CII}]_{158\mu\text{m}}$  observations of PJ231-20 and PJ308-21 presented in Decarli et al. 2017 (program ID: 2015.1.01115.S), which we analyzed in a consistent way.

## 6.3 Line and continuum measurements

To obtain information on the different ISM phases and dust, we measured lines and continuum properties. The observed emission in the ALMA cubes was integrated over the beam and projected along the line of sight. If the source emission is not spatially resolved in the observation, the spectrum measured in the brightest pixel corresponds to the integrated spectrum of the source over its whole extension. By inspecting the continuum and the velocity-integrated line maps, we verified that the flux peak (measured in  $\text{Jy beam}^{-1}$  and  $\text{Jy beam}^{-1} \text{ km s}^{-1}$ , respectively) was consistent with the integrated flux over an aperture containing the observed emission for each object, even for high S/N and high angular resolution (such as the CO(7–6) line in QSO PJ231-20 in setup A). Therefore the targeted sources are (at best) marginally resolved in the observations. This conclusion, at least for system PJ231-20, is supported by measurements of the size of the continuum and  $[\text{CII}]_{158\mu\text{m}}$  line emitting region obtained from ALMA high angular resolution observations (Neeleman et al., 2019). This allowed us to safely perform a single-pixel analysis of the data. The uncertainties introduced by ignoring the aperture correction are comparable to the typical uncertainties ( $> 10\%$ ) ascribed to the line and continuum flux measurements taking the ALMA visibility calibration errors ( $\sim 20\%$ ) into account. Furthermore, we took advantage of the single-pixel analysis to maximize the S/N in the extracted spectra and to simultaneously minimize biases on the flux measurements that might arise from the blending of quasar and companion galaxy in the frequency setups at low angular resolution. Finally, we assessed that the different beam sizes of the various data cubes in the different ALMA bands did not

significantly bias the flux estimates. To do so, we tapered the highest to the lowest spatial resolution data using the option `restoringbeam` within the CASA task `tclean`, and we verified that the flux measurements obtained from single-pixel analysis in the tapered data were consistent within the uncertainties with those estimated from the data cubes obtained by imaging all the calibrated visibilities. In particular, we obtained an additional data cube by imaging the calibrated visibilities of ALMA setup A of system PJ231-20 (which has the smallest restoring beam from the original data reduction) using a tapering scheme resulting in a restoring beam of  $1''.7 \times 1''.2$  (similar to that of setup C, which has the lower angular resolution). In the case of PJ308-21 data, the beam sizes are comparable.

In this way, we identified the brightest pixel in the continuum map of each ALMA band and extracted the (beam-)integrated spectra of the quasars and the companion galaxies from the full data cubes (i.e., with the continuum inside) in the selected pixel. We then fit each spectrum as a constant representing the continuum<sup>1</sup>, and a Gaussian for the line. In order to explore the parameter space, we used the MCMC ensemble sampler `emcee` (Foreman-Mackey et al., 2013), and we obtained the posterior probability distributions of the free parameters. Finally, we computed the best values and uncertainties from the 50th, 16th, and 84th percentile of the distributions. In addition, we derived line luminosities as (see, e.g., Carilli & Walter, 2013)

$$L_{\text{line}} [L_{\odot}] = 1.04 \times 10^{-3} S \Delta \nu \nu_{\text{obs}} D_L^2, \quad (6.1)$$

$$L'_{\text{line}} [\text{K km s}^{-1} \text{pc}^2] = 3.25 \times 10^7 S \Delta \nu \frac{D_L^2}{(1+z)^3 \nu_{\text{obs}}^2}, \quad (6.2)$$

where  $S \Delta \nu$  is the line velocity-integrated flux in  $\text{Jy beam}^{-1} \text{km s}^{-1}$ ,  $\nu_{\text{obs}}$  is the observed central frequency of the line in GHz, and  $D_L$  is the luminosity distance in Mpc. The relation between Eq. (6.1) and (6.2) is  $L_{\text{line}} = 3 \times 10^{-11} \nu_{\text{rest}}^3 L'_{\text{line}}$ .

In **Tab. 6.3** we report the measured and derived quantities for the observed lines and continuum emission in each frequency setup for the quasars and their companions. In order to confirm the robustness of the spectral fit results against spurious effects of the noise (especially in the very critical cases of

<sup>1</sup>For a typical S/N  $\sim 60$ – $100$  over a bandwidth of  $\sim 4$  GHz in ALMA band 3-6, the continuum emission is well described by a zeroth-order polynomial within the uncertainties.

low S/N, e.g., the lines in the spectra of QSO PJ308-21), we performed different spectral fits by accurately varying the imposing priors and starting points in the MCMC fitting procedure. We thus assessed that the line was detected (although at low significance) when the derived best-fit models in all the cases indicate a self-consistent solution. In addition, we performed all the fits to the data at a lower spectral resolution ( $80 \text{ km s}^{-1}$ ) and verified that all derived parameters were consistent within  $\sim 1\sigma$  with those reported in **Tab. 6.3**. In **Fig. 6.1** and **6.2** we report the observed spectra of systems PJ231-20 and PJ308-21, respectively, together with the line and continuum best-fit models. We also report the corresponding continuum-subtracted line velocity-integrated maps over  $360 \text{ km s}^{-1}$ . This value maximizes the S/N of the CO(10–9) velocity-integrated map of QSO PJ231-20. We used this as a reference value in order to obtain all the other line maps. In **Fig. 6.3** we show the line-free continuum maps in the various frequency bands. In some cases (see **Figs. 6.1, 6.2**) the peaks of the line velocity-integrated maps of systems PJ231-20 and PJ308-21 show a shift with respect to the reference position of the sources. However, in all the cases, the shift is well inside the beam of the observed map. This effect is probably ascribable to the continuum subtraction and/or the low S/N of the emission. Therefore we conclude that the line and the continuum peaks are spatially consistent at the available resolution.

Throughout this chapter, we report the significance on the measured flux of a line emission in units of  $\sigma = \sqrt{\Delta v \text{FWHM}} \times \langle \text{RMS} \rangle$ , where  $\Delta v$  is the channel width ( $40 \text{ km s}^{-1}$ ), FWHM is the full width at half maximum of the line best-fit Gaussian, and the  $\langle \text{RMS} \rangle$  is the average RMS noise in the line cube (see **Tab. 6.1**). When no line emission is detected in the observation, we report  $3\sigma$  upper limits assuming  $\text{FWHM} = 300 \text{ km s}^{-1}$ . Finally, for the nondetections of continuum emission we report the  $3\sigma$  upper limit, with  $\sigma$  equal to RMS noise of the continuum.

## 6.4 CLOUDY models of photo- and X-ray dissociation regions

PDRs/XDRs models are ordinarily used in order to model the observed continuum and line emission in galaxies (see **Sect. 5.4**). In this chapter, in

Table 6.3: Measurements and derived quantities from the ALMA spectra of the quasars and their companion galaxies.

|   |                              | QSO                            |   |   |                              |                                |   | companion                                 |  |  |
|---|------------------------------|--------------------------------|---|---|------------------------------|--------------------------------|---|---|--|--|
| Emission line   | $z_{\text{line}}$            | FWHM<br>( $\text{km s}^{-1}$ ) | $S\Delta\nu$<br>( $\text{Jy km s}^{-1}$ ) | $I_{\text{line}}$<br>( $10^9 L_{\odot}$ ) | $z_{\text{line}}$            | FWHM<br>( $\text{km s}^{-1}$ ) | $S\Delta\nu$<br>( $\text{Jy km s}^{-1}$ ) | $I_{\text{line}}$<br>( $10^9 L_{\odot}$ ) |  |  |
| [NII] $_{205\mu\text{m}}$                             | $6.5848^{+0.0012}_{-0.0012}$ | $276^{+199}_{-97}$             | $0.21^{+0.09}_{-0.07}$                    | $0.18^{+0.08}_{-0.06}$                    | $6.591^{+0.002}_{-0.002}$    | $229^{+252}_{-97}$             | $0.10^{+0.07}_{-0.06}$                    | $0.08^{+0.06}_{-0.05}$                    |  |  |
| [CII] $_{158\mu\text{m}}$                             | $6.5864^{+0.0003}_{-0.0003}$ | $372^{+23}_{-21}$              | $2.54^{+0.13}_{-0.13}$                    | $2.87^{+0.15}_{-0.15}$                    | $6.5897^{+0.0003}_{-0.0003}$ | $492^{+41}_{-39}$              | $2.36^{+0.16}_{-0.16}$                    | $2.68^{+0.18}_{-0.18}$                    |  |  |
| [Cl] $_{369\mu\text{m}}$                              | $6.5873^{+0.0014}_{-0.0014}$ | $243^{+97}_{-70}$              | $0.11^{+0.04}_{-0.04}$                    | $0.05^{+0.02}_{-0.02}$                    | —                            | —                              | $< 0.08$                                  | $< 0.04$                                  |  |  |
| CO(7–6)   | $6.5863^{+0.0007}_{-0.0007}$ | $335^{+39}_{-34}$              | $0.46^{+0.04}_{-0.04}$                    | $0.22^{+0.02}_{-0.02}$                    | $6.5870^{+0.0020}_{-0.0014}$ | $614^{+242}_{-184}$            | $0.24^{+0.07}_{-0.06}$                    | $0.12^{+0.03}_{-0.03}$                    |  |  |
| CO(10–9) (*)  | $6.5878^{+0.0005}_{-0.0005}$ | $293^{+53}_{-43}$              | $0.40^{+0.06}_{-0.06}$                    | $0.28^{+0.04}_{-0.05}$                    | $6.5873^{+0.0005}_{-0.0010}$ | $183^{+160}_{-67}$             | $0.11^{+0.04}_{-0.03}$                    | $0.08^{+0.03}_{-0.02}$                    |  |  |
| CO(15–14)   | $6.5851^{+0.0017}_{-0.0013}$ | $454^{+81}_{-128}$             | $0.33^{+0.10}_{-0.09}$                    | $0.34^{+0.10}_{-0.10}$                    | —                            | —                              | $< 0.16$                                  | $< 0.16$                                  |  |  |
| CO(16–15)   | $6.5857^{+0.0003}_{-0.0003}$ | $83^{+72}_{-24}$               | $0.15^{+0.05}_{-0.04}$                    | $0.16^{+0.06}_{-0.04}$                    | —                            | —                              | $< 0.16$                                  | $< 0.17$                                  |  |  |
| H <sub>2</sub> O 3 <sub>12</sub> –2 <sub>21</sub> (*) | $6.5874^{+0.0005}_{-0.0010}$ | $191^{+69}_{-49}$              | $0.18^{+0.06}_{-0.05}$                    | $0.12^{+0.04}_{-0.03}$                    | —                            | —                              | $< 0.09$                                  | $< 0.06$                                  |  |  |
| H <sub>2</sub> O 3 <sub>21</sub> –3 <sub>12</sub>     | $6.5859^{+0.0010}_{-0.0010}$ | $396^{+98}_{-75}$              | $0.33^{+0.07}_{-0.06}$                    | $0.23^{+0.05}_{-0.04}$                    | —                            | —                              | $< 0.09$                                  | $< 0.06$                                  |  |  |
| H <sub>2</sub> O 3 <sub>03</sub> –2 <sub>12</sub>     | $6.5853^{+0.0007}_{-0.0007}$ | $187^{+96}_{-66}$              | $0.18^{+0.07}_{-0.06}$                    | $0.18^{+0.07}_{-0.06}$                    | —                            | —                              | $< 0.16$                                  | $< 0.16$                                  |  |  |
| OH <sup>2</sup> $\Pi_{1/2,2}^{3+} - \frac{1}{2}^{-}$  | $6.5863^{+0.0006}_{-0.0006}$ | $322^{+70}_{-59}$              | $0.45^{+0.09}_{-0.08}$                    | $0.49^{+0.10}_{-0.09}$                    | $6.5879^{+0.0019}_{-0.0019}$ | $296^{+108}_{-118}$            | $0.19^{+0.09}_{-0.09}$                    | $0.21^{+0.10}_{-0.10}$                    |  |  |
| OH <sup>2</sup> $\Pi_{1/2,2}^{3-} - \frac{1}{2}^{+}$  | $6.5851^{+0.0006}_{-0.0009}$ | $230^{+91}_{-66}$              | $0.34^{+0.09}_{-0.09}$                    | $0.37^{+0.10}_{-0.10}$                    | $6.589^{+0.002}_{-0.002}$    | $414^{+113}_{-185}$            | $0.27^{+0.12}_{-0.12}$                    | $0.30^{+0.13}_{-0.13}$                    |  |  |
| Dust continuum <sup>(1)</sup>                         |                              | $F_{\nu}$ (mJy)                | $F_{\nu}$ (mJy)                           |   |                              | $F_{\nu}$ (mJy)                |   |   |  |  |
| 93.85 GHz   |                              | $0.22 \pm 0.01$                | $0.22 \pm 0.01$                           |   |                              | $< 0.033$                      |   |   |  |  |
| 105.72 GHz  |                              | $0.31 \pm 0.02$                | $0.31 \pm 0.02$                           |   |                              | $0.07 \pm 0.02$                |   |   |  |  |
| 140.34 GHz  |                              | $0.72 \pm 0.02$                | $0.72 \pm 0.02$                           |   |                              | $0.19 \pm 0.05$                |   |   |  |  |
| 152.57 GHz  |                              | $0.86 \pm 0.03$                | $0.86 \pm 0.03$                           |   |                              | $0.32 \pm 0.03$                |   |   |  |  |
| 193.41 GHz  |                              | $1.91 \pm 0.04$                | $1.91 \pm 0.04$                           |   |                              | $0.64 \pm 0.04$                |   |   |  |  |
| 205.31 GHz  |                              | $2.19 \pm 0.03$                | $2.19 \pm 0.03$                           |   |                              | $0.64 \pm 0.03$                |   |   |  |  |
| 226.79 GHz  |                              | $2.88 \pm 0.05$                | $2.88 \pm 0.05$                           |   |                              | $0.84 \pm 0.05$                |   |   |  |  |
| 234.13 GHz  |                              | $3.29 \pm 0.05$                | $3.29 \pm 0.05$                           |   |                              | $0.93 \pm 0.05$                |   |   |  |  |
| 241.94 GHz  |                              | $3.46 \pm 0.06$                | $3.46 \pm 0.06$                           |   |                              | $0.93 \pm 0.05$                |   |   |  |  |
| 250.08 GHz  |                              | $3.94 \pm 0.06$                | $3.94 \pm 0.06$                           |   |                              | $1.14 \pm 0.07$                |   |   |  |  |

Table 6.3: (continued)

|   |                              | QSO                            |   |   |                              |                                |   | companion                                 |  |  |
|---|------------------------------|--------------------------------|---|---|------------------------------|--------------------------------|---|---|--|--|
| Emission line                                     | $z_{\text{line}}$            | FWHM<br>( $\text{km s}^{-1}$ ) | $S\Delta\nu$<br>( $\text{Jy km s}^{-1}$ ) | $L_{\text{line}}$<br>( $10^9 L_{\odot}$ ) | $z_{\text{line}}$            | FWHM<br>( $\text{km s}^{-1}$ ) | $S\Delta\nu$<br>( $\text{Jy km s}^{-1}$ ) | $L_{\text{line}}$<br>( $10^9 L_{\odot}$ ) |  |  |
| [CII] $_{158\mu\text{m}}$                         | $6.2354^{+0.0003}_{-0.0002}$ | $533^{+47}_{-43}$              | $1.65^{+0.13}_{-0.12}$                    | $1.73^{+0.14}_{-0.13}$                    | $6.2495^{+0.0005}_{-0.0006}$ | $239^{+46}_{-40}$              | $0.43^{+0.07}_{-0.07}$                    | $0.46^{+0.08}_{-0.07}$                    |  |  |
| [Cl] $_{369\mu\text{m}}$                          | —                            | —                              | $<0.06$                                   | $<0.03$                                   | —                            | —                              | $<0.06$                                   | $<0.03$                                   |  |  |
| CO(7–6)   | —                            | —                              | $<0.06$                                   | $<0.03$                                   | —                            | —                              | $<0.06$                                   | $<0.03$                                   |  |  |
| CO(15–14)   | $6.2364^{+0.0020}_{-0.0018}$ | $498^{+49}_{-97}$              | $0.13^{+0.04}_{-0.04}$                    | $0.12^{+0.04}_{-0.04}$                    | —                            | —                              | $<0.07$                                   | $<0.06$                                   |  |  |
| CO(16–15)   | —                            | —                              | $<0.07$                                   | $<0.07$                                   | —                            | —                              | $<0.07$                                   | $<0.07$                                   |  |  |
| H <sub>2</sub> O 3 <sub>03</sub> –2 <sub>12</sub> | $6.234^{+0.003}_{-0.002}$    | $264^{+134}_{-120}$            | $0.03^{+0.03}_{-0.02}$                    | $0.03^{+0.03}_{-0.02}$                    | —                            | —                              | $<0.07$                                   | $<0.06$                                   |  |  |
| OH $^2\Pi_{1/2,2}^{3+} - ^1\Pi_{1/2}^-$           | $6.2348^{+0.0030}_{-0.0017}$ | $262^{+145}_{-137}$            | $0.04^{+0.03}_{-0.02}$                    | $0.04^{+0.03}_{-0.02}$                    | —                            | —                              | $<0.07$                                   | $<0.07$                                   |  |  |
| OH $^2\Pi_{1/2,2}^{3-} - ^1\Pi_{1/2}^+$           | $6.234^{+0.002}_{-0.002}$    | $400^{+113}_{-165}$            | $0.10^{+0.05}_{-0.05}$                    | $0.10^{+0.05}_{-0.05}$                    | —                            | —                              | $<0.07$                                   | $<0.07$                                   |  |  |
| Dust continuum <sup>(1)</sup>                     |                              | $F_{\nu}$ (mJy)                |   |   |                              | $F_{\nu}$ (mJy)                |   |   |  |  |
| 98.95 GHz   |                              | $0.03 \pm 0.01$                |   |   |                              | $<0.02$                        |   |   |  |  |
| 110.87 GHz  |                              | $0.04 \pm 0.01$                |   |   |                              | $<0.02$                        |   |   |  |  |
| 237.99 GHz  |                              | $0.45 \pm 0.02$                |   |   |                              | $0.08 \pm 0.02$                |   |   |  |  |
| 246.94 GHz  |                              | $0.55 \pm 0.04$                |   |   |                              | $<0.12$                        |   |   |  |  |
| 253.61 GHz  |                              | $0.59 \pm 0.02$                |   |   |                              | $0.06 \pm 0.02$                |   |   |  |  |
| 262.89 GHz  |                              | $0.59 \pm 0.06$                |   |   |                              | $<0.09$                        |   |   |  |  |

**Notes.** When the line emission is not detected, upper limits ( $3\sigma$ ) on continuum, line flux, and luminosity are reported. <sup>(1)</sup>We report the central frequency of the LSB and USB for each frequency setup in which we measured the continuum fluxes. <sup>(\*)</sup>The CO(10-9) and H<sub>2</sub>O 3<sub>1,2</sub>–2<sub>2,1</sub> lines are partially blended.

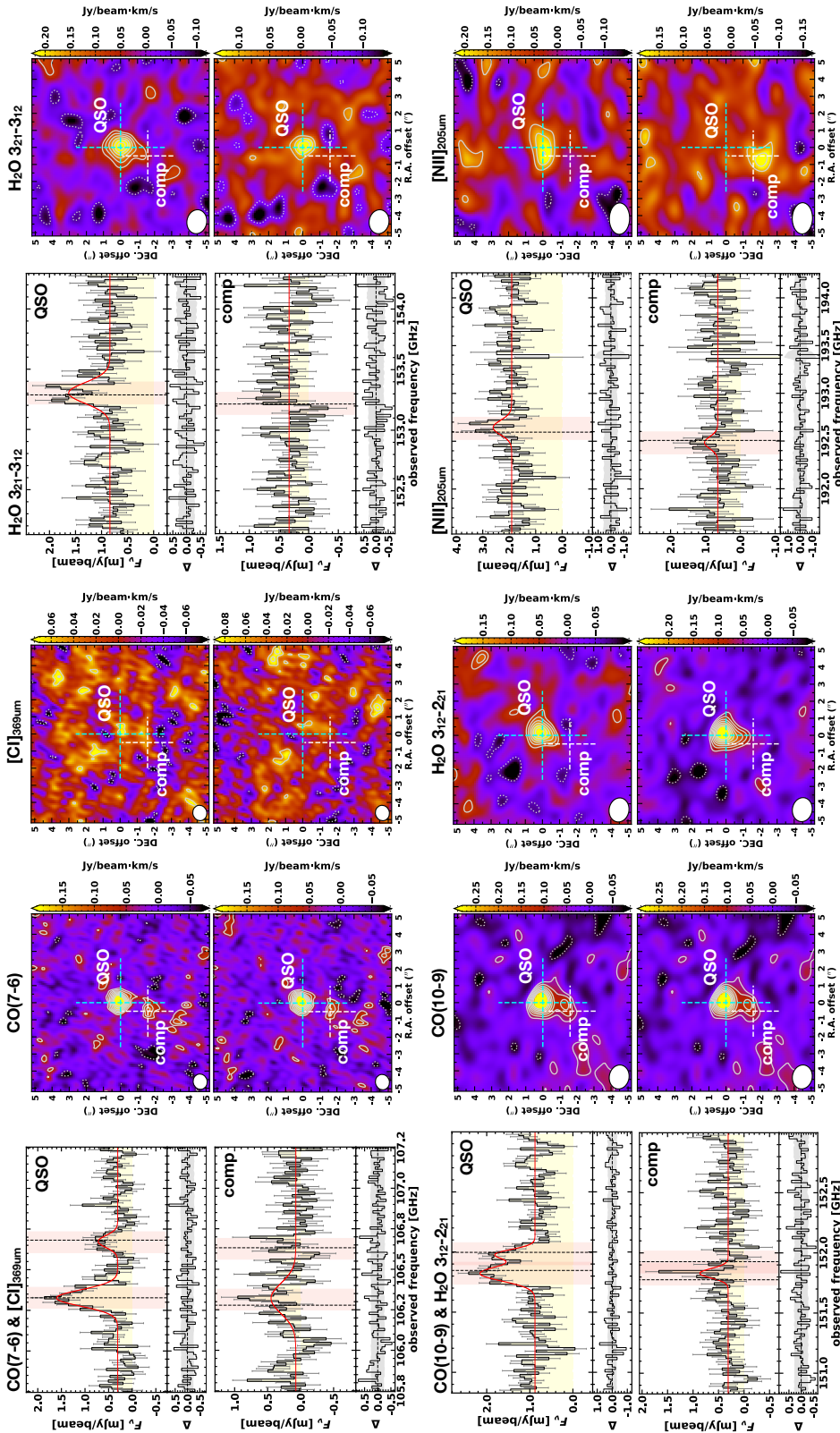
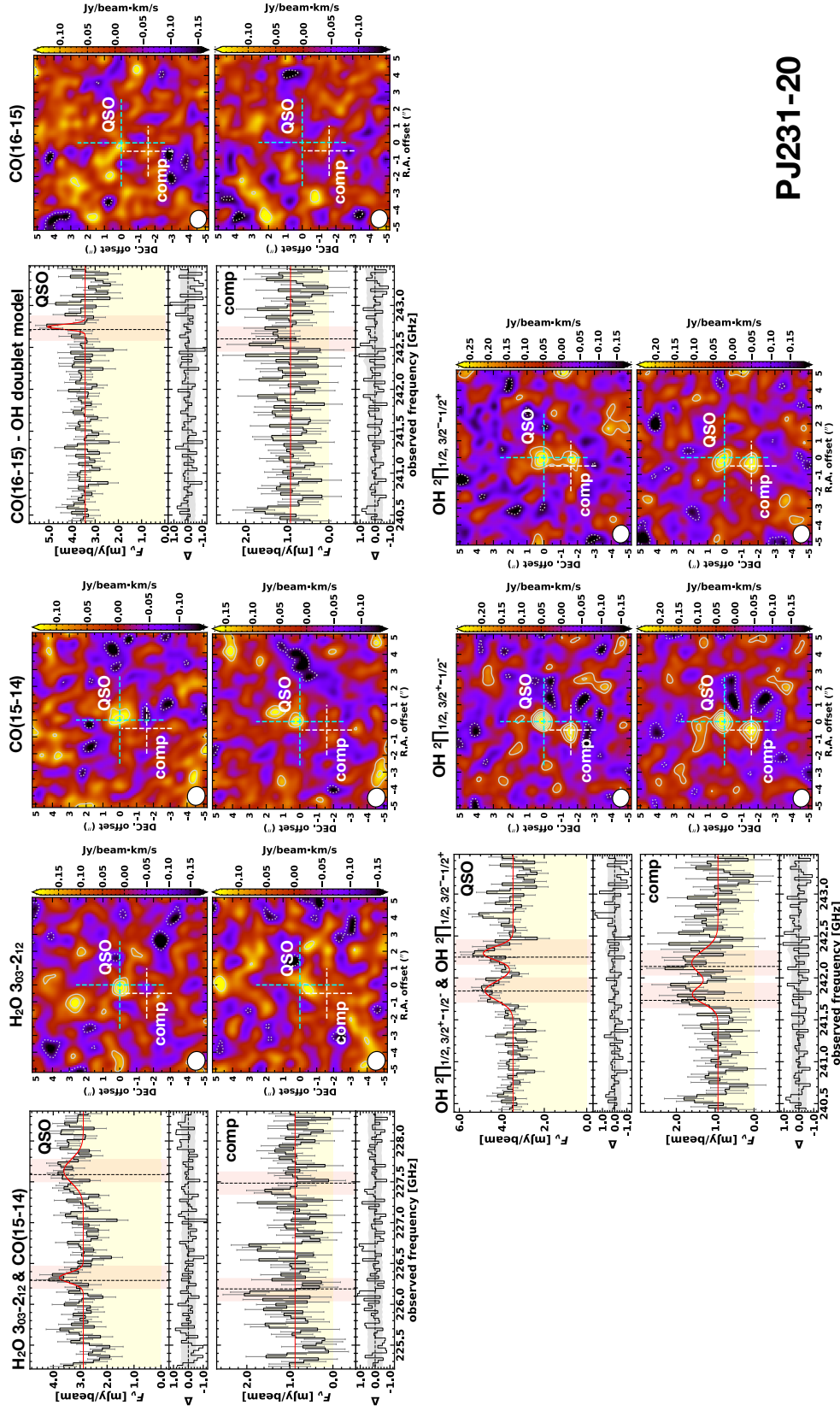


Figure 6.1

Detections and nondetections in system PJ231-20. We show the observed integrated spectra for the quasar and its companion galaxy in a frequency range around the targeted transition. In the panels showing the spectra, we show the best-fit model (red line), the fit residuals (at the bottom of each panel), the expected frequency of the line (vertical dashed black line) and the channels used to obtain the continuum-subtracted line velocity-integrated maps (over  $360 \text{ km s}^{-1}$ ) that are shown to the right of each spectrum (red shaded area). When the line is not detected, the best-fit model is a constant polynomial fitting the continuum emission alone. In the spectra covering the CO(16–15) line, we performed the fit after subtracting the best-fit model for the OH doublet (bottom panels). The spectra we show were extracted at the position of the quasar and companion galaxy. The positions of the sources are indicated in the line velocity-integrated maps with cyan and white crosses, respectively. The solid contours in the maps show the  $[2, 3, 4, 5, 6, 7, 8] \times \sigma$  levels, and dashed contours indicate the  $-2\sigma$  level.



PJ231-20

Figure 6.1  
(continued)

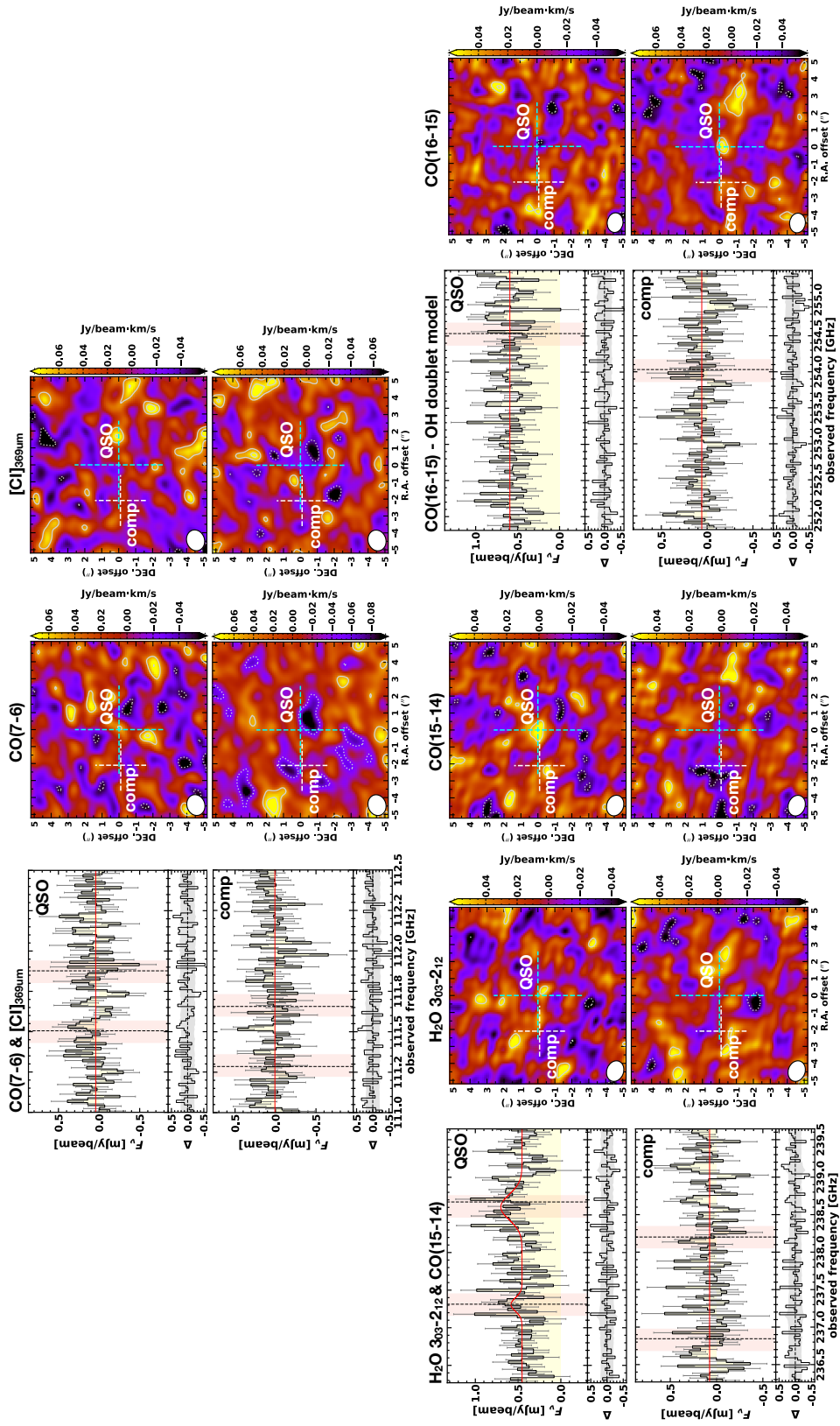


**Figure 6.2**

Detections and nondetections in system PJ308-21. See Fig. 6.1 for a description of the various panels.

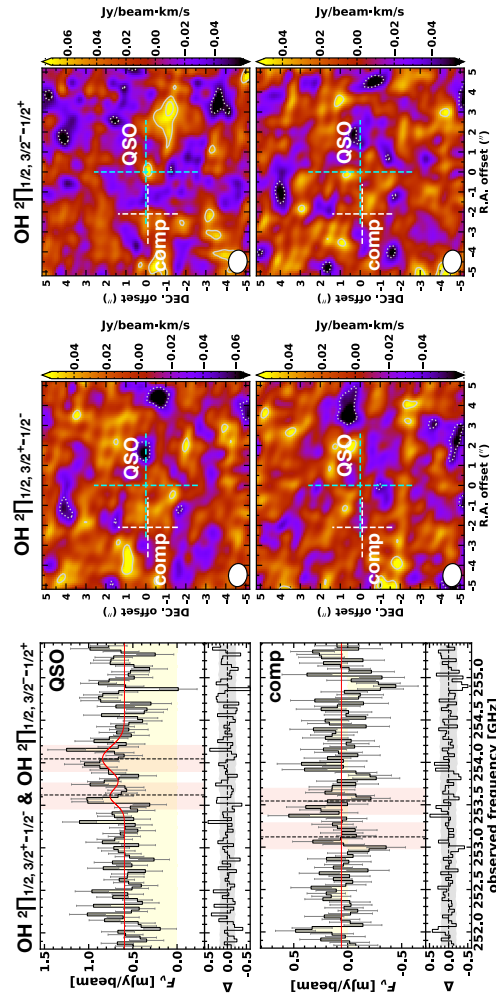
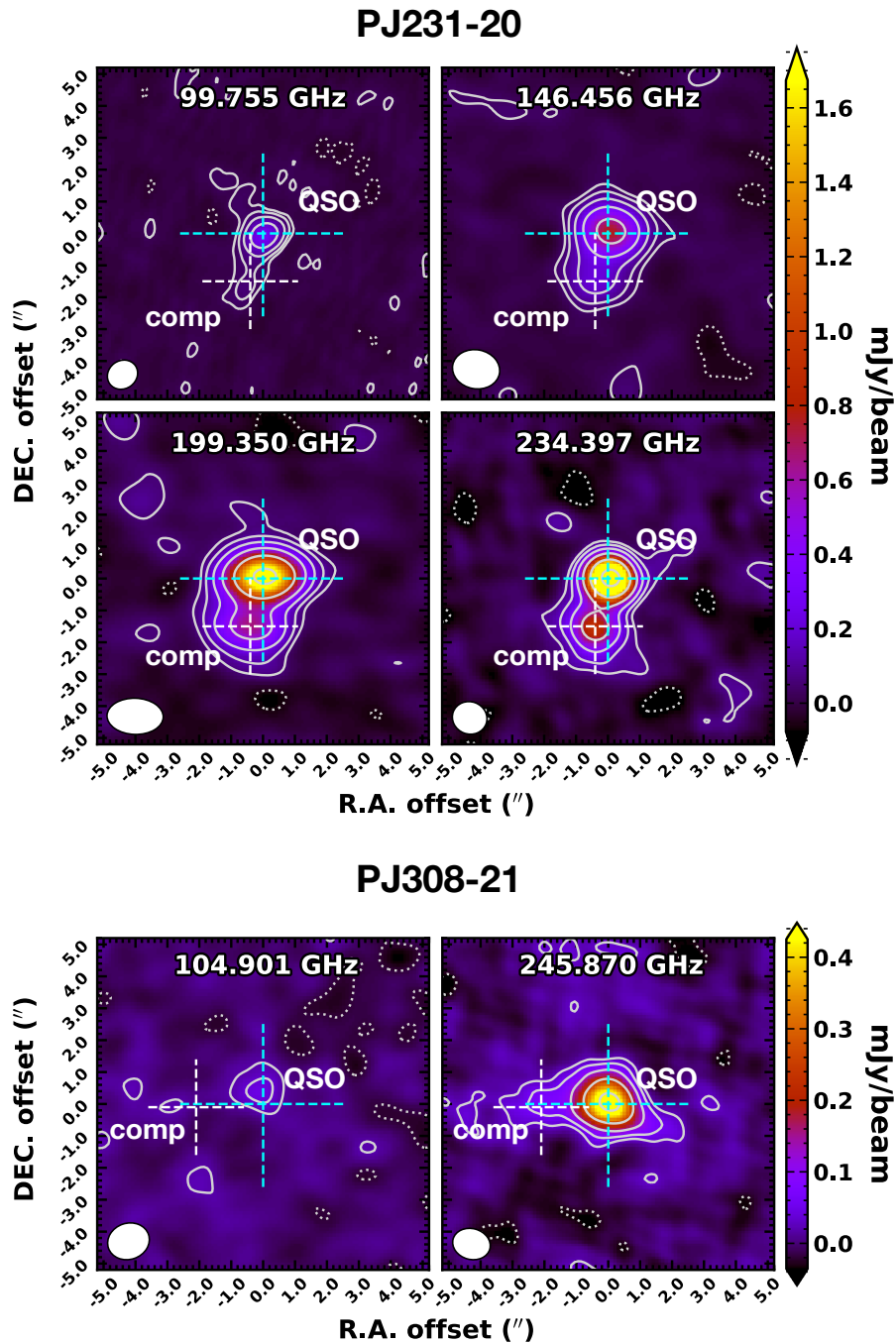


Figure 6.2  
(continued)



**Figure 6.3**

Continuum maps in the four frequency setups of PJ231-20 (*upper panels*), and the two setups of system PJ308-21 (*lower panels*). The central frequencies of each setup are reported at the top of each panel. The white ellipses indicate the ALMA FWHM synthesized beam. The positions of the quasars and the companions from which we extracted the spectra from line cubes are marked by cyan and white crosses, respectively. The solid contours indicate  $[2, 4, 8, 16, 32, 64]\sigma$ , and dashed contours are the  $-2\sigma$  value.

order to characterize the ISM in the quasar and companion galaxy in systems PJ231-20 and PJ308-21, we employed the CLOUDY radiative-transfer code (version c.17.01, Ferland et al. 2017). CLOUDY is highly customizable code and allows the simultaneous treatment of all the species we studied. With this code we obtained a suite of diagnostics to interpret the observed line ratios in our sources. In the following we describe how the models were set up.

Within CLOUDY, we ran a total of  $270 \times 2$  PDR/XDR models assuming a 1D gas slab of constant total hydrogen density in the range  $\log(n_{\text{H}}/\text{cm}^{-3}) = [2, 6]$  (15 models,  $\sim 0.29$  dex spacing), varying the strength of the radiation field (18 models), for two values of the total cloud hydrogen column density of  $N_{\text{H}} = 10^{23}, 10^{24} \text{ cm}^{-2}$ . In the case of PDR models, we defined the SED of the impinging radiation field as blackbody emission with a temperature of  $T = 5 \times 10^4 \text{ K}$  scaled to obtain Habing fluxes at the gas slab surface in the range  $\log G_0 = [1, 6]$  ( $\sim 0.29$  dex spacing). In the case of XDR, we chose a standard AGN template as the incident continuum SED,

$$f_{\nu} = \nu^{\alpha_{\text{UV}}} \exp(-h\nu/k_{\text{B}}T_{\text{BB}}) \exp(-k_{\text{B}}T_{\text{IR}}/h\nu) + a\nu^{\alpha_{\text{X}}}, \quad (6.3)$$

with parameters set in order to generate the continuum used in a large atlas of model broad-line region line intensities (Korista et al., 1997). We normalized this incident SED in order to have X-ray flux between 1 – 100 keV in the range  $\log[F_{\text{X}}/(\text{erg s}^{-1} \text{ cm}^{-2})] = [-2.0, 2.0]$  ( $\sim 0.24$  dex spacing) at the cloud surface. This range fully covers the X-ray radiation field strengths that are generally considered in standard XDR models (e.g., Maloney et al., 1996; Meijerink et al., 2007).

For the gas slab we assumed the default interstellar medium metal abundances (abundance ISM) stored in CLOUDY. We adopted dust ISM grains (grains ISM) stored in CLOUDY with the size distribution and abundance from Mathis (1997). In addition, we included polycyclic aromatic hydrocarbons (PAHs, grains PAH) with the distribution from Abel et al. (2008), which generally dominate the photoelectric heating of grains. We also included the CMB radiation at  $z = 6$  that affects the far-IR line luminosity of galaxies at high  $z$  (see Sect. 5.3). We adopted the default CLOUDY prescriptions for the cosmic-ray ionization rate background (cosmic rays background), which are an important source of heating deep into the molecular cloud. The mean H cosmic-ray ionization rate is  $2 \times 10^{-16} \text{ s}^{-1}$  (Indriolo

et al., 2007), and the  $\text{H}_2$  secondary ionization rate is  $4.6 \times 10^{-16} \text{ s}^{-1}$  (Glassgold & Langer, 1974). Finally, we added  $1.5 \text{ km s}^{-1}$  in quadrature to the thermal motions within the cloud to model the effect of line broadening that is produced by microturbulence.

In order to simulate the absorption of ionizing radiation caused by atomic hydrogen in front of PDRs, we modified the incident continuum in the PDR and XDR cases by extinction due to photoelectric absorption by a cold neutral slab with a column density of  $10^{24} \text{ cm}^{-2}$  (extinguish column 24, see Cruddace et al. 1974). The code computes the radiative transfer through the slab up to a total hydrogen column density of  $N_{\text{H}} = 10^{23}, 10^{24} \text{ cm}^{-2}$ . We chose this stopping criterion to fully sample the molecular component that is typically located at  $N_{\text{H}} > 10^{22} \text{ cm}^{-2}$ , which is observed in GMCs (e.g., McKee & Ostriker, 1977). However, a higher column density  $N_{\text{H}} \gtrsim 5 \times 10^{23} \text{ cm}^{-2}$  is required to properly model  $\text{H}_2\text{O}$  and OH emission (see, e.g., Goicoechea et al., 2005; González-Alfonso et al., 2014; Spinoglio et al., 2005; Liu et al., 2017).

With our PDR and XDR models we obtained grids of line intensities and emitted continuum emerging from the cloud surface (both in unit of  $\text{erg s}^{-1} \text{ cm}^{-2}$ ) as a function of the density of the medium (total hydrogen density,  $n_{\text{H}}$  ranges  $10^2 - 10^6 \text{ cm}^{-3}$ ) and the strength of the radiation field (parameterized by  $G_0 = 10^1 - 10^6$  or  $F_{\text{X}} (\text{erg s}^{-1} \text{ cm}^{-2}) = 10^{-2} - 10^2$  in the case of PDR and XDR, respectively) for two values of the total hydrogen column density  $N_{\text{H}} = 10^{23}, 10^{24} \text{ cm}^{-2}$ .

In the following sections, we present various results obtained from dust FIR continuum and line detections in the targeted sources. By comparing our model results with the observed emission, we then place constraints on the key parameters characterizing the ISM in the quasar hosts and companion galaxies.

## 6.5 Dust properties: FIR continuum

The continuum emission detected in the FIR and (sub-)mm bands is dominated by emission from dust distributed in the diffuse medium and star-forming regions of a galaxies (see Sect. 5.2.3). The typical dust temperature for quasar hosts lies in the range  $T_{\text{dust}} \sim 40 - 70 \text{ K}$  (e.g., Priddey & McMahon, 2001; Beelen et al., 2006; Wang et al., 2008; Leipski et al., 2013, 2014) and

increases to  $\gtrsim 100 - 500$  K in the proximity of the central BH accretion disk (Rowan-Robinson, 1995; Charmandaris et al., 2004; Beelen et al., 2006). In this chapter we assume optically thin dust emission (see, e.g., Beelen et al., 2006), therefore the continuum flux in the Rayleigh-Jeans limit is proportional to the dust mass,  $M_{\text{dust}}$ , and temperature,  $T_{\text{dust}}$  (see Eq. 5.3). The optically thin dust approximation may not be true at short wavelengths (see Sect. 5.2.3), but likely holds for our observations because most of the continuum data are at rest frame  $\lambda > 200 \mu\text{m}$ . In order to estimate  $M_{\text{dust}}$  and  $T_{\text{dust}}$  in the quasar host galaxies and their companions, we modeled the continuum data with a modified blackbody taking the effect of the CMB radiation into account (da Cunha et al., 2013, see,). As we discussed in Sect. 5.3, at the redshifts of the sources, the CMB represents an additional non-negligible source of heating and provides a strong background against which we measure line and continuum emission.

Following da Cunha et al. (2013), we therefore define the flux density in the optically thin limit as

$$F_{\nu/(1+z)}^{\text{intr}} = B_{\nu}[T_{\text{dust}}(z)]k_{\text{d}}(\nu)(1+z)M_{\text{dust}}D_L^{-2}, \quad (6.4)$$

$$F_{\nu/(1+z)}^{\text{obs}} = \left(1 - \frac{B_{\nu}[T_{\text{CMB}}(z)]}{B_{\nu}[T_{\text{dust}}(z)]}\right) F_{\nu/(1+z)}^{\text{intr}}, \quad (6.5)$$

where  $F_{\nu/(1+z)}^{\text{intr}}$  and  $F_{\nu/(1+z)}^{\text{obs}}$  are the intrinsic and observed flux density against the CMB, respectively,  $k_{\text{d}}(\nu) = k_0(\nu/\nu_0)^{\beta}$ , where  $\nu_0 = 352.7$  GHz (Dunne et al., 2000, see, Sect. 5.2.3). da Cunha et al. (2013) also showed that the observed galaxy dust temperature at certain redshift,  $T_{\text{dust}}(z)$ , is higher than the dust temperature that we would observe at  $z = 0$  because CMB photons are absorbed by the dust grains:  $T_{\text{dust}}(z) = \{(T_{\text{dust}}^{z=0})^{4+\beta} + (T_{\text{CMB}}^{z=0})^{4+\beta}[(1+z)^{4+\beta} - 1]\}^{1/(4+\beta)}$ . However, at  $z \approx 6.5$  and typical dust temperatures of  $T_{\text{dust}} > 35$  K, this correction is  $< 2\%$ , much less than the relative uncertainties we expect on dust temperature estimate. We therefore ignored this correction. Hence, we used the model defined in Eq. (6.5) to fit the quasar and companion continuum data reported in Tab. 6.3, together with ALMA band 6 data presented in Decarli et al. (2017), from which we obtained line and continuum measurements. In order to determine the best-fit model, we made use of the emcee code (Foreman-Mackey et al., 2013), allowing  $M_{\text{dust}}$ , and  $\beta$  to freely vary during the fitting procedure. We limited the parameter space by imposing box-like priors defined as  $\log M_{\text{dust}}[M_{\odot}] > 0$ , and  $\beta \in (1, 2.5)$ . In

addition, the sampled frequency range of the observations mostly covers the Rayleigh-Jeans tail of the dust thermal emission. The observed flux density in this regime is  $\propto T_{\text{dust}} M_{\text{dust}}$ , which makes these parameters degenerate. We therefore employed a relative tight Gaussian prior on  $T_{\text{dust}}$  with a mean and standard deviation equal to 47 K and 5 K, respectively. These choices are consistent with the typical measurements in quasar host galaxies reported in the literature (e.g., Priddey & McMahon, 2001; Beelen et al., 2006; Wang et al., 2008; Leipski et al., 2013, 2014) and are also validated by the results obtained below for the water vapor lines (see Sect. 6.8.4). On the other hand, if the companion galaxies do not host a quasar (as suggested by rest-frame UV and X-ray studies, see Decarli et al. 2017; Connor et al. 2019, 2020), we expect that the dust temperature may not be as high as that of the quasar host galaxies because the additional dust heating by an AGN is lacking. The nondetection of water lines in the companions also argues against a high  $T_{\text{dust}}$  (despite the detections of the OH<sub>163 $\mu$ m</sub> doublet, which likely traces similar regions as are traced by H<sub>2</sub>O lines, see Sects. 6.8.3, 6.8.7). In the case of the companion galaxies, we therefore also considered a lower-temperature scenario. To do so, we performed an additional fit centering the Gaussian dust temperature prior on  $T_{\text{dust}} = 35$  K, which is a representative value of the population of SMGs at  $z \sim 1 - 3$  (e.g., Chapman et al., 2005; Kovács et al., 2006). In the fits we also took the upper limit measurements on dust continuum into account by inserting a penalty term in the log-likelihood function in the form  $\mathcal{P} = -0.5[(\text{model} - \text{data})/\text{data}]^2$ , if model > data, otherwise,  $\mathcal{P} = 0$ . Finally, we assumed the source [CII]-based redshifts reported in Decarli et al. 2017 (see Tab. 6.3). In Fig. 6.4 we show the best-fit models of the continuum emission in systems PJ231-20 and PJ308-21, respectively, together with the posterior probability distributions of the parameters. From these results, we estimated the rest-frame IR and total IR (TIR, 8 – 1000  $\mu$ m, Sanders et al. 2003) and FIR (40 – 400  $\mu$ m, Helou et al. 1988, respectively) luminosities of the sources by integrating the best-fit models over the corresponding frequency ranges. Finally, we inferred the SFR using the local scaling relation from Murphy et al. (2011),  $\text{SFR}_{\text{IR}}/(M_{\odot} \text{ yr}^{-1}) = 1.49 \times 10^{-10} L_{\text{TIR}}/L_{\odot}$ , assuming that the IR-luminosity is dominated by star formation and under the hypothesis that the entire Balmer continuum (i.e., 912 <  $\lambda$  < 3646) is absorbed and re-irradiated by dust in the optically thin limit. Any contribution of the central AGN to the IR luminosity will therefore result in an overestimation

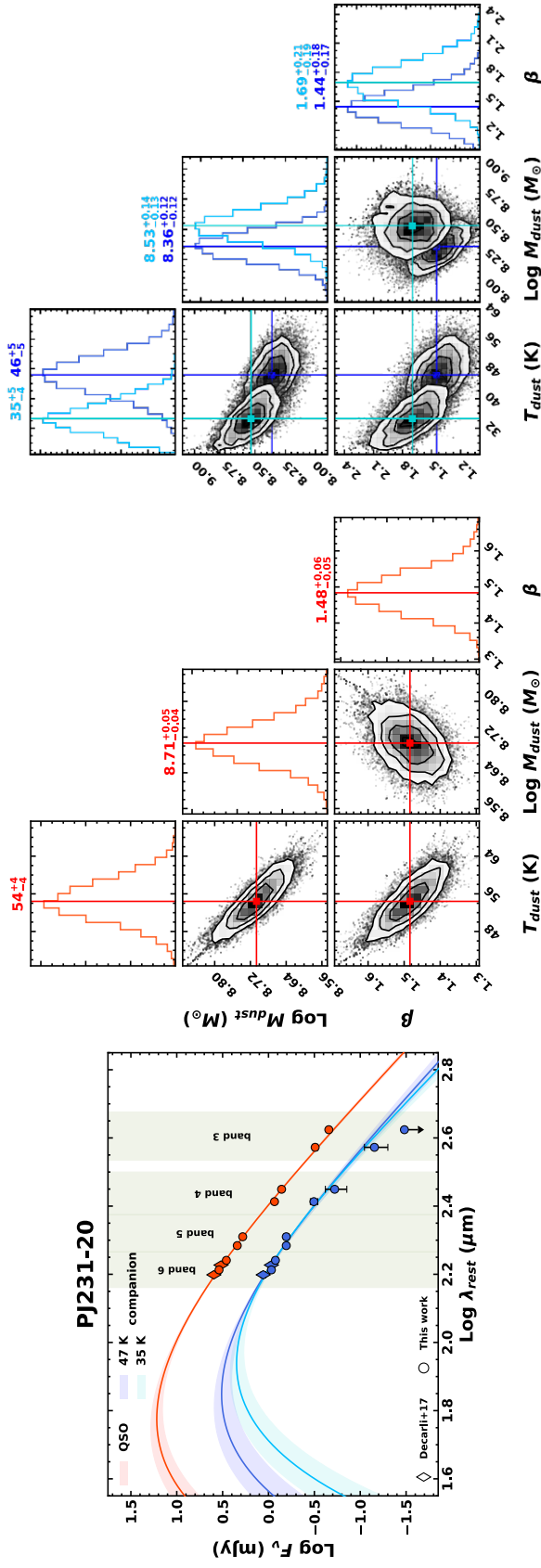


**Figure 6.4**

Models of the dust SEDs of sources PJ231-20 (*this page*) and PJ308-21 (*next page*). In the left panel, circles and diamonds indicate continuum data obtained in this work and those obtained from the ALMA Cycle 6 [CII]<sub>158 μm</sub> observations (Decarli et al., 2017), respectively. Downward arrows indicate 3σ upper limits. The best-fit modified blackbody model is indicated with a solid red line for the quasars, and blue and cyan lines for companion galaxies assuming  $T_{\text{dust}} = 47$  K and 35 K, respectively. The shaded areas show the 1σ confidence intervals. Green bands indicate the ALMA frequency bands redshifted to the quasar-companion pair rest frame ( $z_{\text{pair}} = [z_{\text{QSO}} + z_{\text{comp}}]/2$ ). The right panel shows the posterior probability distributions of the free parameters (red for quasars, blue and cyan for companions). The vertical lines indicate the best-fit values computed as 50th percentiles of the distributions. The best-fit values with their uncertainties are also reported.

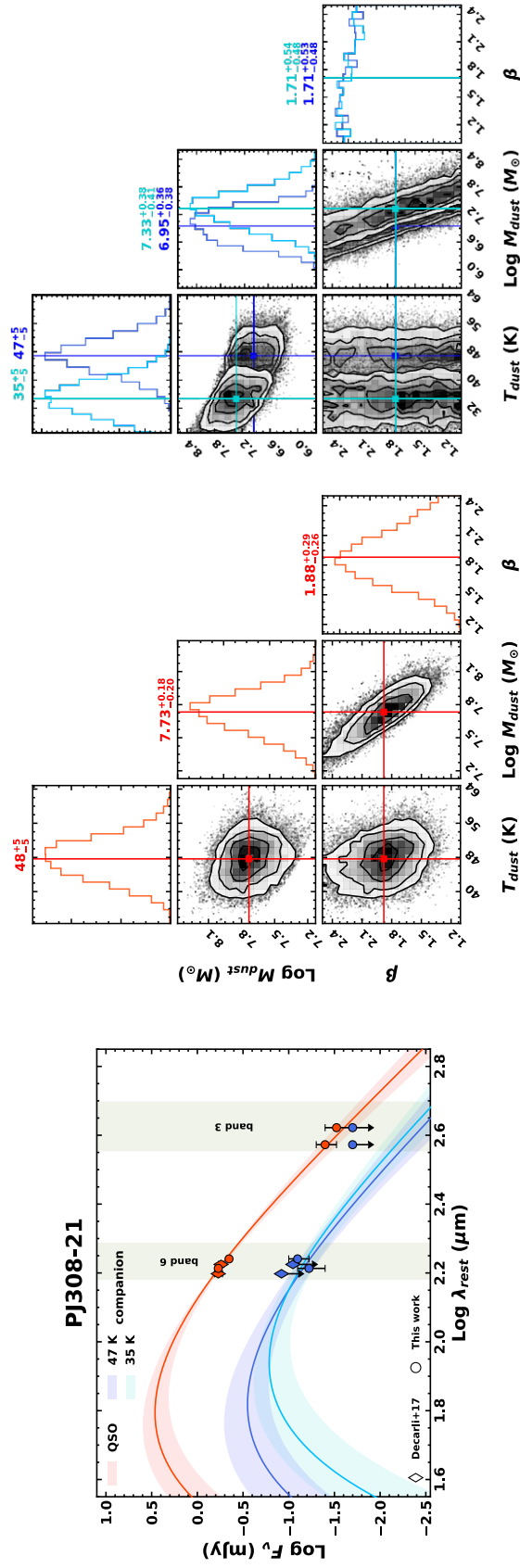


Figure 6.4 (continued)

of the  $\text{SFR}_{\text{IR}}$ . The initial mass function (IMF) implicitly assumed in this  $L_{\text{TIR}}$  to SFR conversion is a Kroupa IMF (Kroupa, 2001), with a slope of  $-1.3$  for stellar masses between  $0.1 - 0.5 M_{\odot}$ , and  $-2.3$  for stellar masses ranging between  $0.5$  and  $100 M_{\odot}$ . In **Tab. 6.4** we report all the derived quantities obtained with the dust continuum modeling.

In the case of the quasar and companion galaxy in system PJ231-20, we find good constraints on the dust mass ( $\lesssim 0.1$  dex) and the spectral emissivity index (relative error of  $\lesssim 10\%$ ). On the other hand, the dust temperature values obtained from the posterior probability distribution are consistent within  $1\sigma$  with the imposed prior, confirming that  $T_{\text{dust}}$  cannot be constrained with the fit. In the case of the quasar and companion in the system PJ308-21, we found only tentative constraints on  $M_{\text{dust}}$  and  $\beta$  because the coverage of the dust SEDs is poor. The best-fit values of  $\beta$  in the PJ231-20 and PJ308-21 quasars and companions range between  $\sim 1.5 - 1.9$  and are consistent with the values estimated in both low-redshift sources (e.g., Conley et al., 2011; Casey, 2012) and those at  $z > 5 - 6$  (e.g. Riechers et al., 2013; Carniani et al., 2019; Novak et al., 2019; Yang et al., 2019c; Faisst et al., 2020). We note that although we assumed different dust temperatures of 47 K and 35 K as priors in the dust SED fit of the companion galaxies, we obtained similar results that are consistent within  $1.5\sigma$ . As shown in **Fig. 6.4**, this is mainly due to the lack of high-frequency continuum measurements, where the peak of dust SED is placed. However, an additional large source of uncertainty in the dust fitting is the optically thin dust approximation. The shape of the dust SED may be altered by the dust opacity at short wavelengths, thus affecting the derived  $L_{\text{TIR}}$ . Furthermore, if a warmer dust component is present, it may significantly contribute to the IR luminosity.

## 6.6 Ionized medium

We detected the  $[\text{NII}]_{205\mu\text{m}}$  ( ${}^3P_1 \rightarrow {}^3P_0$ ) line in system PJ231-20 with a significance of  $\sim 4\sigma$  and  $\sim 2\sigma$  for the quasar and the companion galaxy, respectively (see **Figs. 6.1, 6.2**). The line measurements are reported in **Tab. 6.3**. In **Sect. 5.2.1** we discussed how the  $[\text{NII}]_{205\mu\text{m}}$  line can provide us with important clues for interpreting the observed  $[\text{CII}]_{158\mu\text{m}}$  emission (Decarli et al., 2017).

**Table 6.4:** Dust properties in sources PJ231-20 and PJ308-21.

|          |       | $T_{\text{dust}}$<br>(K) | $\text{Log } M_{\text{dust}}$<br>( $M_{\odot}$ ) | $\beta$                | $\text{Log } L_{\text{FIR}}^{(1)}$<br>( $L_{\odot}$ ) | $\text{Log } L_{\text{TIR}}^{(2)}$<br>( $L_{\odot}$ ) | $\text{SFR}_{\text{IR}}$<br>( $M_{\odot} \text{ yr}^{-1}$ ) |
|----------|-------|--------------------------|--|------------------------|---|---|---|
| PJ231-20 | QSO   | 54                       | $8.71^{+0.05}_{-0.04}$                           | $1.48^{+0.06}_{-0.05}$ | $13.13^{+0.06}_{-0.06}$                               | $13.28^{+0.09}_{-0.09}$                               | $2849^{+633}_{-533}$  |
|          | comp. | 46                       | $8.36^{+0.12}_{-0.12}$                           | $1.44^{+0.18}_{-0.17}$ | $12.40^{+0.09}_{-0.10}$                               | $12.47^{+0.12}_{-0.13}$                               | $442^{+140}_{-112}$   |
|          |       | 35                       | $8.53^{+0.14}_{-0.13}$                           | $1.69^{+0.21}_{-0.19}$ | $12.16^{+0.12}_{-0.10}$                               | $12.18^{+0.14}_{-0.11}$                               | $224^{+75}_{-55}$   |
| PJ308-21 | QSO   | 48                       | $7.73^{+0.18}_{-0.20}$                           | $1.9^{+0.3}_{-0.3}$    | $12.31^{+0.14}_{-0.13}$                               | $12.42^{+0.18}_{-0.17}$                               | $392^{+193}_{-128}$   |
|          | comp. | 47                       | $7.0^{+0.4}_{-0.4}$                              | $1.7^{+0.5}_{-0.5}$    | $11.28^{+0.25}_{-0.19}$                               | $11.4^{+0.3}_{-0.2}$                                  | $38^{+28}_{-16}$  |
|          |       | 35                       | $7.3^{+0.4}_{-0.4}$                              | $1.7^{+0.5}_{-0.5}$    | $11.0^{+0.2}_{-0.2}$                                  | $11.1^{+0.2}_{-0.3}$                                  | $19^{+14}_{-8}$   |

**Notes.** <sup>(1),(2)</sup>FIR and TIR luminosities obtained by integrating the best-fit modified blackbody model in the (rest-frame) wavelength range 40–400  $\mu\text{m}$  (Helou et al., 1988) and 8–1000  $\mu\text{m}$  (Sanders et al., 2003), respectively.

### 6.6.1 Fraction of $[\text{CII}]_{158\mu\text{m}}$ from PDRs

The observed  $[\text{NII}]_{205\mu\text{m}}$  line emission reveals the fraction of  $[\text{CII}]_{158\mu\text{m}}$  arising from neutral gas. Following Díaz-Santos et al. (2017), we estimated the fraction of  $[\text{CII}]_{158\mu\text{m}}$  emission arising from PDRs by assuming a typical  $[\text{CII}]_{158\mu\text{m}}^{\text{ion}}/[\text{NII}]_{205\mu\text{m}} \approx 3$  that is observed in HII regions (Oberst et al., 2006),

$$f([\text{CII}]^{\text{PDR}}) = \frac{[\text{CII}]_{158\mu\text{m}}^{\text{PDR}}}{[\text{CII}]_{158\mu\text{m}}} \approx 1 - 3 \frac{[\text{NII}]_{205\mu\text{m}}}{[\text{CII}]_{158\mu\text{m}}}. \quad (6.6)$$

We note that while the  $[\text{CII}]/[\text{NII}]$  ratio for HII regions assumes solar metallicities, the high dust content seen in  $z \gtrsim 6$  quasar host galaxies suggests that the metallicities are indeed high (see, e.g., Novak et al. 2019, furthermore, this is also supported, although indirectly, by studies of the metallicity of the broad-line region in  $z \sim 6$  quasars, see, e.g., Pentericci et al. 2002; Jiang et al. 2007a; Onoue et al. 2020). Combining our  $[\text{CII}]_{158\mu\text{m}}$  line luminosity measurements with those of the  $[\text{NII}]_{205\mu\text{m}}$  line (see Tab. 6.3), we conclude that PDRs account for  $\gtrsim 80\%$  of the  $[\text{CII}]_{158\mu\text{m}}$  emission in QSO PJ231-20 and its companion galaxy. This result is consistent with previous studies on local starburst galaxies showing that no more than  $\sim 30\%$  of the  $[\text{CII}]_{158\mu\text{m}}$  emission is emitted by the diffuse ionized medium (e.g., Stacey et al., 1991; Carral et al., 1994; Lord et al., 1996; Colbert et al., 1999). Studies of the  $[\text{CII}]\text{-to-}[\text{NII}]$  ratio in FIR bright galaxies at higher redshifts ( $z > 4 - 5$ ) have also concluded that only a small fraction of  $[\text{CII}]_{158\mu\text{m}}$  emission arises from

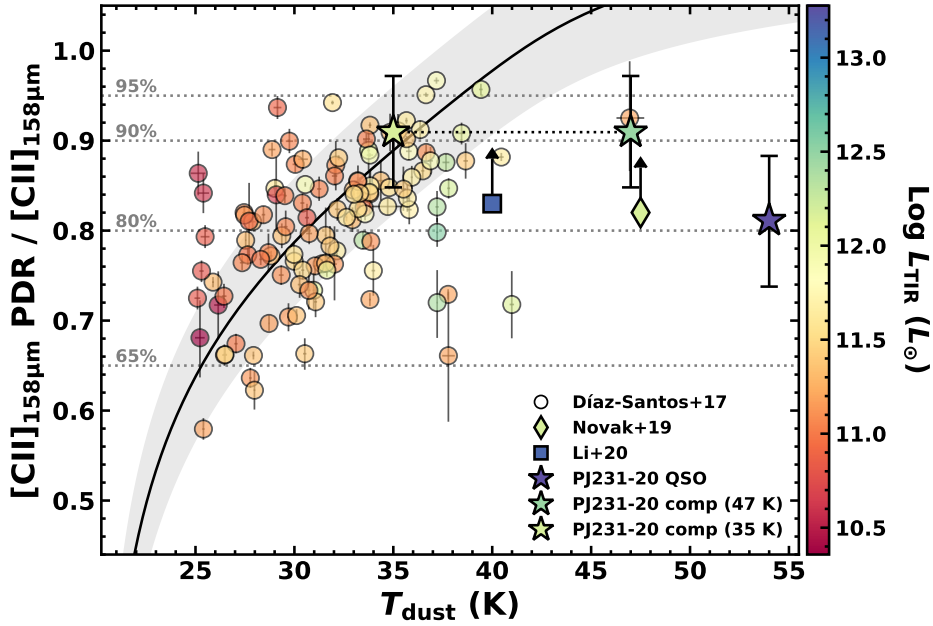


**Figure 6.5**

Fraction of  $[\text{CII}]_{158\mu\text{m}}$  arising from the PDR as a function of dust temperature, color-coded by the logarithm of the total IR luminosity. The QSO PJ231-20 and its companion galaxy are marked by stars. For the companion we report the cases with an assumed dust temperature of 47 K and 35 K. These points are connected by a dashed line. The diamond marks the  $3\sigma$  upper limit on quasar ULAS J1342+0928 at  $z = 7.54$  (Novak et al., 2019), while the square is the upper limit on SDSS J2310+1855 at  $z = 6.00$  (Li et al., 2020a,b). The latter limits are computed using the  $[\text{NII}]_{205\mu\text{m}}/[\text{NII}]_{122\mu\text{m}}$  line luminosity ratio to estimate the electron density and then the fraction of  $[\text{CII}]_{158\mu\text{m}}$  from the ionized gas from Oberst et al. (2006).  $T_{\text{dust}}$  and  $L_{\text{TIR}}$  for SDSS J2310+1855 are derived via a dust SED fitting by Shao et al. (2019), and for ULAS J1342+0928,  $L_{\text{TIR}}$  is estimated in Novak et al. (2019) by assuming  $T_{\text{dust}} = 47\text{ K}$  (here slightly shifted for better visualization). Circles represent the LIRG sample presented in Díaz-Santos et al. (2017). The solid black line shows the best-fit model  $f([\text{CII}]_{158\mu\text{m}}^{\text{PDR}}) = 0.82(\pm 0.01) + 0.41(\pm 0.04) \log(S_{63}/S_{158})$ , where  $S_{63}$  and  $S_{158}$  are the continuum flux density at  $63\mu\text{m}$  and  $158\mu\text{m}$ , respectively. The gray shaded area is the  $1\sigma$  confidence interval. The approximate relation between the flux density ratio and  $T_{\text{dust}}$  is provided by Díaz-Santos et al. (2017),  $T_{\text{dust}} = 20.24 + 14.54(S_{63}/S_{158}) - 3.75(S_{63}/S_{158})^2 + 0.46(S_{63}/S_{158})^3$ .

the ionized gas-phase ISM (see, e.g., Decarli et al., 2014; Pavesi et al., 2016; Novak et al., 2019).

In Fig. 6.5 we compare  $f([\text{CII}]^{\text{PDR}})$  and the dust temperature of QSO PJ231-20 and its companion with a sample of local luminous IR galaxies (LIRGs) reported in Díaz-Santos et al. (2017) and with the value of two high- $z$

quasars: SDSS J2310+1855 at  $z = 6.00$  (Li et al., 2020a,b) and the most distant quasar known so far, ULAS J1348+0928 at  $z = 7.54$  (Novak et al., 2019). Díaz-Santos et al. (2017) reported that galaxies with warmer  $T_{\text{dust}}$  show a higher  $f([\text{CII}]^{\text{PDR}})$ ; therefore the fraction of  $[\text{CII}]_{158\mu\text{m}}$  emitted from PDRs increases in highly star-forming systems. The authors also ruled out a significant role for AGN in increasing  $f([\text{CII}]^{\text{PDR}})$  in galaxies. A possible interpretation is that HII regions are more enshrouded by dust in high  $T_{\text{dust}}$  galaxies than those of more evolved systems with lower  $T_{\text{dust}}$ , in which stellar feedback processes have already cleared out most of the dust from the star-forming regions (Díaz-Santos et al., 2017, and references therein). That is, the fractions of  $[\text{CII}]_{158\mu\text{m}}$  arising from the ionized medium are associated with low-density fossil HII regions and diffuse ionized gas that is not associated with hot young stars. While the high dust temperatures (47 – 54K) of the high- $z$  galaxies presented in this work lie outside the range of the LIRG sample, the assumption of  $T_{\text{dust}} = 35\text{K}$  in the case of the companion to PJ231-20 means that this object agrees with the trend of local LIRGs shown in Fig. 6.5.

## 6.6.2 IR line deficits

The ratio of the luminosity of ISM cooling lines, such as  $L_{[\text{CII}]158\mu\text{m}}$ ,  $L_{[\text{NII}]205\mu\text{m}}$  to the total IR luminosity ( $L_{\text{TIR}}$ ) measures the ratio of the cooling of the gas to that of the dust. These ratios decrease by  $\sim 1 - 2$  orders of magnitude with increasing dust temperature and IR luminosity in local galaxies (e.g., Malhotra et al., 1997; Graciá-Carpio et al., 2011; Farrah et al., 2013; Díaz-Santos et al., 2013, 2017; Zhao et al., 2013, 2016; Herrera-Camus et al., 2018a) and those at high redshift (e.g., Decarli et al., 2012, 2014; Bañados et al., 2015a; Novak et al., 2019; Rybak et al., 2019). The underlying causes of the so-called line deficits are still debated. The physical arguments that are most often proposed include changes in ionization parameter that produce a high dust-to-gas opacity ratio, optically thick dust screening part of the line emission, and progressive thermalization of the lines with low critical densities. However, a possible explanation is that HII regions are dustier in IR-bright galaxies than in low-luminosity systems (e.g., Luhman et al., 2003; González-Alfonso et al., 2008; Abel et al., 2009; Graciá-Carpio et al., 2011; Farrah et al., 2013; Riechers et al., 2014; Díaz-Santos et al., 2017; Herrera-Camus et al., 2018b). In this scenario, a higher fraction of

UV photons produced by young stars is absorbed by dust, thus suppressing ionizing photons that would otherwise be absorbed by the neutral medium, thereby decreasing the photoionization heating efficiency, whose net effect is to decrease the line emission relative to the IR luminosity. On the other hand, if  $[\text{CII}]_{158\mu\text{m}}^{\text{ion}}$  and  $[\text{NII}]_{205\mu\text{m}}$  emission were to arise from different ISM phases (i.e., low-density regions and diffuse ionized gas that is not associated with hot young stars) than the IR continuum emission, then the line deficit could be driven by a boosting of the IR luminosity rather than by a deficit in the observed line flux. However, consistently with what we discussed in **Sect. 6.6.1**, a fraction of this excess energy can be transferred to the surrounding neutral or molecular medium, increasing the  $[\text{CII}]_{158\mu\text{m}}^{\text{PDR}}$  emission and therefore decreasing the deficit.

In **Fig. 6.6** we compare the  $[\text{CII}]_{158\mu\text{m}}$  and  $[\text{NII}]_{205\mu\text{m}}$  line deficits in the quasars and companion galaxies presented in this chapter with the local LIRG sample of Díaz-Santos et al. (2017) and quasar J1342+0928 at  $z = 7.54$  (Novak et al., 2019). Our findings are consistent within the scatter with the overall trends observed in LIRGs. In particular, the line deficit of the companion galaxy in the low dust temperature case ( $T_{\text{dust}} = 35\text{ K}$ ) in system PJ231-20 is typical of the bulk of the local LIRG population. Noticeably, while we find that the host and companion galaxy of QSO PJ231-20 shows  $[\text{NII}]_{205\mu\text{m}}$  line deficits that is consistent within the errors, the deficit in  $[\text{CII}]_{158\mu\text{m}}$  is significantly more pronounced in the quasar than in the companion galaxy. However, this is probably not evidence that a powerful AGN affects the  $[\text{CII}]_{158\mu\text{m}}$  line deficit (unless an AGN biases our  $L_{\text{TIR}}$  measurement): this scenario is excluded from the study of local ULIRGs sample (e.g., Díaz-Santos et al., 2013, 2017; Farrah et al., 2013) showing no strong dependence of line deficit and  $[\text{CII}]_{158\mu\text{m}}^{\text{PDR}}$  fraction with the AGN contribution. In this context, not even higher ionization lines such as  $[\text{OIII}]_{88\mu\text{m}}$  appear to be significantly affected by AGN (see, e.g., Walter et al., 2018). In system PJ308-21, the quasar shows a similar  $[\text{CII}]_{158\mu\text{m}}$  deficit to that of the companion galaxy, and both sources exhibit less extreme deficits than in QSO PJ231-20 and its companion. This suggests that the observed line deficit is only slightly affected by an AGN. The observed scatter in the  $L_{[\text{CII}]_{158\mu\text{m}}}/L_{\text{TIR}}$  ratio might be caused the variation in the PDR contribution to the total  $[\text{CII}]_{158\mu\text{m}}$  with increasing  $T_{\text{dust}}$  (Díaz-Santos et al., 2017, see **Fig. 6.5**).

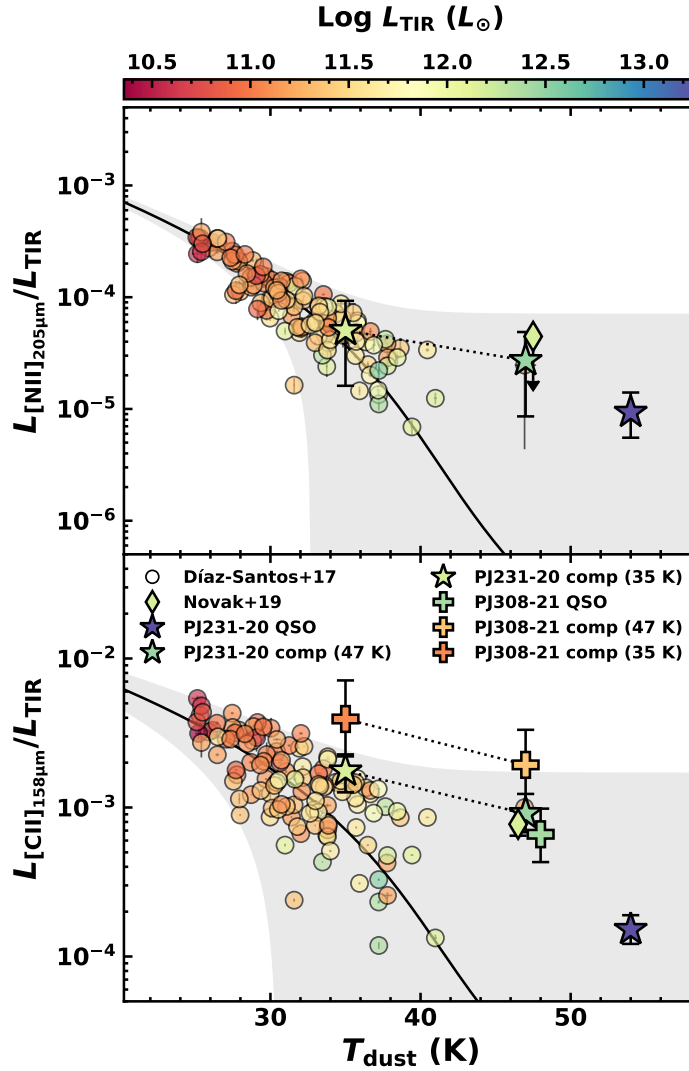


**Figure 6.6**

[NII] $_{205\mu\text{m}}$  and [CII] $_{158\mu\text{m}}$  line deficits (top and bottom panel, respectively) with respect to the total IR luminosity ( $L_{\text{TIR}}(8 - 1000\mu\text{m})$ ) for quasars PJ231-20 and PJ308-21 and the companion galaxies and the LIRG sample of Díaz-Santos et al. (2017) as a function of dust temperature and color-coded by  $\log L_{\text{TIR}}$ . We also report the measurements obtained for the  $z = 7.54$  quasar ULAS J1342+0928 (Novak et al., 2019). The sources in system PJ231-20 are indicated by stars, and those in system PJ308-21 are marked with crosses. For the companion galaxies we report the cases with assumed dust temperatures of 47K and 35K. These points are connected by a dashed line. The solid lines are the best fit to the LIRG sample performed in Díaz-Santos et al. (2017) using the model  $L_{\text{line}}/L_{\text{FIR}} = \epsilon_0 \exp[(-S_{63}/S_{158})/\delta]$  with  $(\epsilon_0, \delta) = ((1.26 \pm 0.16) \times 10^{-3}, 0.50 \pm 0.04)$  for the [NII] $_{205\mu\text{m}}$  line, and  $(\epsilon_0, \delta) = ((14.0 \pm 0.9) \times 10^{-3}, 0.68 \pm 0.04)$  for [CII] $_{158\mu\text{m}}$  line. We scaled the best fits by a constant factor because different FIR luminosity definitions were employed by Díaz-Santos et al. (2017). The best-fit scaling values are 0.56 for [NII] $_{205\mu\text{m}}$  line and 0.44 for [CII] $_{158\mu\text{m}}$  line. The gray shaded area represents the  $1\sigma$  scatter of the relation. The Novak et al. (2019) points were slightly shifted along the dust temperature axis (assumed to be 47K) for a better visualization of the data.

## 6.7 Atomic medium

We detected the atomic fine-structure line ( $^3P_2 \rightarrow ^3P_1$ )  $[\text{CI}]_{369\mu\text{m}}$  in QSO PJ231-20 with a significance of  $\sim 4.5\sigma$  while we derived upper limits for the companion and for objects in system PJ308-21.

### 6.7.1 $[\text{CI}]_{369\mu\text{m}}$ -to-TIR ratio

In **Fig. 6.7** we show the  $L_{[\text{CI}]_{369\mu\text{m}}}$ -to- $L_{\text{TIR}}$  ratio as a function of dust temperature for a variety of galaxies and AGN in the local and high- $z$  Universe (see Valentino et al., 2020, and references therein for full details). The observed average ratio is  $L_{[\text{CI}]_{369\mu\text{m}}}/L_{\text{TIR}} \sim 10^{-5}$ , but there is a negative correlation with  $T_{\text{dust}}$ . However, in contrast to the  $[\text{NII}]_{205\mu\text{m}}$  and  $[\text{CII}]_{158\mu\text{m}}$  line deficits (see **Fig. 6.6**), this trend is expected.  $[\text{CI}]$  in PDR models is predicted to arise in regions in which the gas kinetic temperature is similar to dust temperature  $T_{\text{dust}}$  (e.g., Tielens & Hollenbach, 1985a) and in which the IR luminosity rises with a high power of  $T_{\text{dust}}$  ( $L_{\text{TIR}} \propto T_{\text{dust}}^{4+\beta}$ ), while the line emission into the cloud is only proportional to the gas temperature. Then, the trend shown in **Fig. 6.7** is also driven by a redshift dependence. Valentino et al. (2018, 2020) found that the observed  $L_{[\text{CI}]_{369\mu\text{m}}}$ -to- $L_{\text{TIR}}$  ratios are, on average, lower in high- $z$  SMGs than in local star-forming and main sequence (MS) galaxies. The most plausible underlying reason of this trend therefore is a potential evolution in the dust temperature with redshift that enhances  $L_{\text{TIR}}$  (e.g., Schreiber et al., 2018; Liang et al., 2019; Ma et al., 2019; Faisst et al., 2020; Riechers et al., 2020). Furthermore, the IR luminosity measured in local AGN and high- $z$  quasars (which are also expected to have higher  $T_{\text{dust}}$  than a star-forming galaxy) might be affected by a substantial contribution from a dusty torus that boosts the observed  $L_{\text{TIR}}$ , thus driving the observed decrease of  $L_{[\text{CI}]_{369\mu\text{m}}}/L_{\text{TIR}}$  with  $T_{\text{dust}}$ . However,  $L_{[\text{CI}]_{369\mu\text{m}}}$  and  $L_{\text{TIR}}$  trace the neutral gas and the SFR, respectively, thus their ratio is a proxy of the gas depletion timescale  $\tau_{\text{dep}} = M_{\text{gas}}/\text{SFR}$ , representing the efficiency of the star formation. Therefore the observed trend of  $L_{[\text{CI}]_{369\mu\text{m}}}/L_{\text{TIR}}$  might be interpreted as due to a decrease in  $\tau_{\text{dep}}$  (or equivalently, a higher star-formation efficiency) in high- $z$  SMGs and quasar hosts than in MS and local star-forming galaxies. This result is consistent with several CO-based studies (e.g., Daddi et al., 2010; Genzel et al., 2015; Tacconi et al., 2018; Birkin et al., 2021).

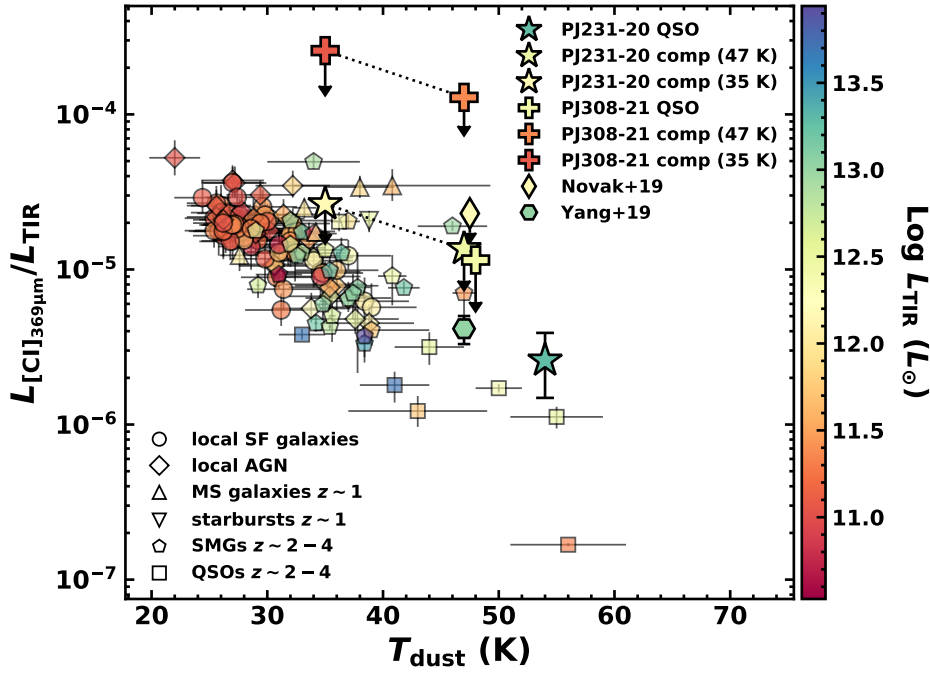


**Figure 6.7**

Comparison of  $L_{[\text{CI}]369\mu\text{m}}/L_{\text{TIR}}$  and dust temperature ( $T_{\text{dust}}$ ) observed in systems PJ231-20 and PJ308-21 with various local and high- $z$  galaxies. Data points are color-coded by  $\log L_{\text{TIR}}$ . The reported sample is taken from Valentino et al. (2020, and references therein) and comprises local star-forming (SF) galaxies (circles) and AGN (diamonds); main-sequence (MS) galaxies (upright triangles) and starburst galaxies (upside-down triangles) at  $z \sim 1$ ; and  $z \sim 2-4$  SMGs (pentagons) and QSOs (squares). The QSO PJ231-20 and its companion are indicated with stars, and the PJ308-21 sources are marked with crosses. For the companions we report the cases with an assumed dust temperature of 47 K and 35 K. These points are connected by a dashed line. The upper limit in our sources corresponds to  $3\sigma$ . We also report measurements in quasar ULAS J1342+0928 at  $z = 7.54$  (see Novak et al., 2019) and quasar J0439+1634 at  $z \simeq 6.5$  (Yang et al., 2019c).

We obtained  $3\sigma$  upper limits of the  $[\text{CI}]_{369\mu\text{m}}$  line for all sources in the systems we studied, except for QSO PJ231-20, for which we measure  $L_{[\text{CI}]369\mu\text{m}}/L_{\text{TIR}} = 2.6_{-1.1}^{+1.4} \times 10^{-6}$ . This value together with the assumed  $T_{\text{dust}}$  locate this source in the parameter ranges observed in other high- $z$  quasars. In particular, a similar  $L_{[\text{CI}]369\mu\text{m}}/L_{\text{TIR}}$  ratio ( $4.2_{-0.8}^{+0.8} \times 10^{-6}$ ) has been measured by Yang et al. (2019c) in the  $z \simeq 6.5$  quasar J0439+1634. This result suggests a high star-formation efficiency in these sources relative to their local counterparts. For the other sources we studied, we obtained  $L_{[\text{CI}]369\mu\text{m}}/L_{\text{TIR}} < 10^{-4} - 10^{-5}$  limits that are  $\sim 1-2$  orders of magnitude lower than  $L_{[\text{CII}]158\mu\text{m}}/L_{\text{TIR}}$ . We also

estimated an  $L_{[\text{CI}]_{369\mu\text{m}}}/L_{[\text{CII}]_{158\mu\text{m}}}$  of  $\sim 2\%$  in QSO PJ231-20 and  $< 2 - 6\%$  in all the other sources. These values are similar to the value measured in the quasar host galaxy J1148+5251 at  $z = 6.42$  by Riechers et al. (2009). These results support the assumption that  $[\text{CI}]_{369\mu\text{m}}$  is a weaker coolant than the dust continuum and  $[\text{CII}]_{158\mu\text{m}}$  at these high redshifts. In Sect. 6.9 we further exploit the  $[\text{CI}]_{369\mu\text{m}}$  detections in quasar hosts and companions to place constraints on the amount of neutral carbon and molecular gas in the ISM.

### 6.7.2 $[\text{CII}]_{158\mu\text{m}}$ -to- $[\text{CI}]_{369\mu\text{m}}$ ratio

The  $[\text{CII}]_{158\mu\text{m}}$ -to- $[\text{CI}]_{369\mu\text{m}}$  ratio is extremely useful to distinguish between PDR and XDR models, as other high- $z$  studies have shown (Venemans et al., 2017a,c; Novak et al., 2019). In Fig. 6.8 we show the  $[\text{CII}]$ -to- $[\text{CI}]$  intensity ratio obtained from our CLOUDY grids with  $N_{\text{H}} = 10^{23} \text{ cm}^{-2}$ . In the PDR case, the  $[\text{CII}]$ -to- $[\text{CI}]$  ratio ranges between  $\lesssim 2$  and  $\gtrsim 70$ , and in the XDR case it does not exceed a value of  $\sim 15$ . These ranges are consistent with those that are found in other models in the literature (e.g., Kaufman et al., 1999; Meijerink et al., 2007). The different values of the  $[\text{CII}]$ -to- $[\text{CI}]$  ratio predicted in PDR and XDR models arise because the CO-to-C abundance ratio produced in the XDR regime is lower (see, e.g., Maloney et al., 1996; Meijerink & Spaans, 2005). While PDRs have a sharp  $\text{C}^+/\text{C}/\text{CO}$  transition layer at a certain depth in the clouds (depending on the density and FUV field strength), X-ray photons can penetrate much deeper into the cloud, which affects its whole structure. As a result, both C and  $\text{C}^+$  are present in the XDR regime throughout most of the cloud, and their column density increases much more gradually as a function of cloud depth than in the PDR case.

Additional constraints on the radiation field in galaxies are provided by the  $[\text{CI}]_{369\mu\text{m}}$ -to-TIR and  $[\text{CII}]_{158\mu\text{m}}$ -to-TIR luminosity ratios. For high FUV fluxes ( $G_0 \gtrsim 10^2$ ) these ratios are expected to decrease as  $G_0$  increases in the PDR case, with almost no dependence on ISM density. By increasing  $G_0$ , the  $\text{C}^+/\text{C}/\text{CO}$  transition layer in which  $[\text{CI}]$  transitions take place is pushed deeper into the cloud, but the C column density remains substantially unaffected. The gas heating efficiency due to photoelectric effects on dust grains reaches its maximum values at  $G_0 \sim 10 - 100$  and becomes less efficient at higher fluxes, while the dust heating per UV photon remains at the same

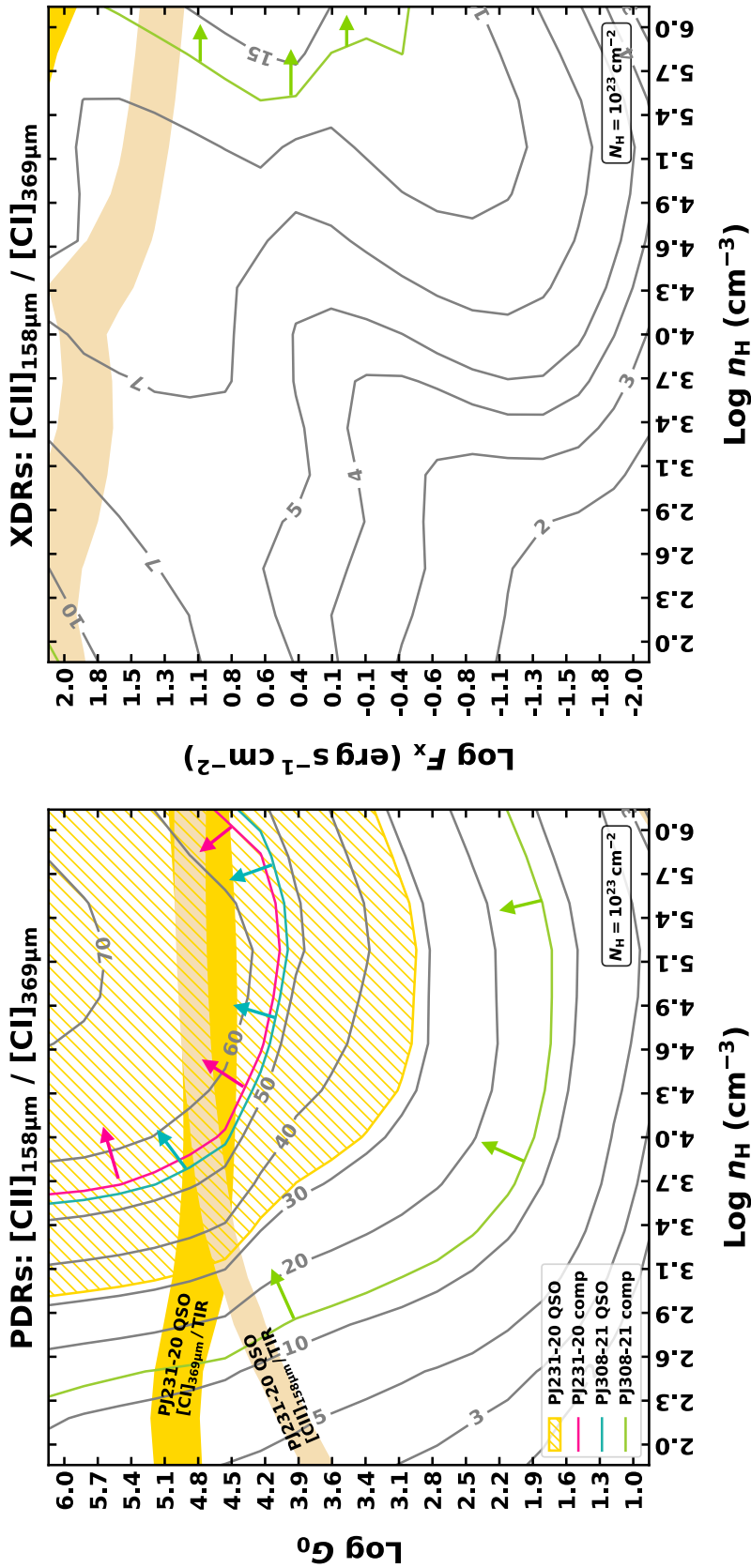


Figure 6.8

Grids of the  $[\text{CII}]_{158\mu\text{m}}/[\text{CI}]_{369\mu\text{m}}$  intensity line ratio as a function of the strength of the radiation field ( $G_0$  or  $F_X$ ) and total hydrogen density ( $n_{\text{H}}$ ) in the PDR (left panel) and XDR case (right panel). The adopted total hydrogen column density is  $N_{\text{H}} = 10^{23} \text{ cm}^{-2}$ . Model values are indicated by gray contours (linear scale), and constraints on the observed line ratios are superimposed. The dashed gold area indicates the  $[\text{CII}]_{158\mu\text{m}}\text{-to-}[\text{CI}]_{369\mu\text{m}}$  luminosity ratio measured in QSO PJ231-20 within its uncertainties, and  $3\sigma$  lower limits on the other sources are reported (see the legend in the bottom left corner of the left panel). The  $[\text{CII}]_{158\mu\text{m}}\text{-to-}[\text{CI}]_{369\mu\text{m}}$  ratios in QSO PJ231-20 and its companion are scaled according to the estimated fraction of  $[\text{CII}]_{158\mu\text{m}}$  arising from PDRs. The XDR case does not reproduce the observed ratios in any source, except for a small range of values corresponding to the lower limit measured in QSO PJ308-21. We also report the  $[\text{CI}]_{369\mu\text{m}}\text{-to-TIR}$  and  $[\text{CII}]_{158\mu\text{m}}\text{-to-TIR}$  luminosity ratio estimates in QSO PJ231-20 as filled gold and light brown areas, respectively. This provides additional constraints on the radiation field flux.

level (e.g., Kaufman et al., 1999). In this case, the  $[\text{CII}]_{158\mu\text{m}}$  line luminosity increases logarithmically, but the IR luminosity is linearly proportional to  $G_0$ . As a result, the  $[\text{CI}]_{369\mu\text{m}}$ -to-TIR and  $[\text{CII}]_{158\mu\text{m}}$ -to-TIR luminosity ratios mostly depend on  $G_0$  for high UV fluxes (see also, e.g., Tielens & Hollenbach, 1985a; Kaufman et al., 1999; Gerin & Phillips, 2000).

The observed luminosity ratios, corrected for the fraction of  $[\text{CII}]_{158\mu\text{m}}$  that actually arises from PDRs (see Sect. 6.6.1), are  $L_{[\text{CII}]158\mu\text{m}}/L_{[\text{CI}]369\mu\text{m}} = 46_{-14}^{+30}$  for the QSO PJ231-20, and  $3\sigma$  limits of  $> 55, 53,$  and  $13$  in its companion, the QSO PJ308-21, and the companion galaxy to QSO PJ308-21, respectively. For all the sources, the PDR scenario is therefore favored. In the case of QSO PJ231-20, this diagnostic indicates a density  $n_{\text{H}} > 10^3 \text{ cm}^{-3}$  and an FUV radiation field strength of  $> 10^3 G_0$ . Similar constraints are inferred for all the other sources (see Fig. 6.8). In addition, by combining the estimated values of the  $L_{[\text{CI}]369\mu\text{m}}$ -to- $L_{\text{TIR}}$  and  $L_{[\text{CII}]158\mu\text{m}}$ -to- $L_{\text{TIR}}$  ratios with the  $[\text{CII}]_{158\mu\text{m}}/[\text{CI}]_{369\mu\text{m}}$  CLOUDY models (see Fig. 6.8), we constrained the FUV flux to  $G_0 \simeq 3 \times 10^4 - 10^5$  in QSO PJ231-20. A similar value was reported for the J0439+1634 quasar at  $z \simeq 6.5$  by Yang et al. (2019c).

## 6.8 Molecular medium

We detected multiple CO lines (7–6, 10–9, 15–14, and 16–15) in QSO host PJ231-20 with various degrees of significance, but we detect only CO(7–6) and CO(10–9) in the companion galaxy. We also only have a marginal CO(15–14) detection in QSO PJ308-21. In this section, we also report three  $\text{H}_2\text{O}$  line detections in QSO PJ231-20 ( $3_{12} - 2_{21}$ ,  $3_{21} - 3_{12}$ , and  $3_{03} - 2_{12}$ ) and a tentative detection of  $\text{H}_2\text{O}$   $3_{03} - 2_{12}$  in QSO PJ308-21. For the companion galaxies, we only have upper limits on water lines. We also detected the  $\text{OH}_{163\mu\text{m}}$  doublet in QSO PJ231-20 and the companion galaxy together with a tentative detection in QSO PJ308-21. The measurements are reported in Tab. 6.3.

### 6.8.1 CO(1–0)-normalized SLEDs

The CO SLED shows the relative luminosity of various CO transitions in an astrophysical source. It is used to gauge the underlying physical conditions (density, intensity, and source of the radiation field) of the CO-emitting

gas. The intensity of the observed lines is usually normalized to the ground transition, CO(1–0), which cannot be observed with ALMA in the targeted sources. Nevertheless, we estimated its intensity following empirical relations of the CO(1–0) and the IR luminosity (see, e.g., Carilli & Walter, 2013, for a review). Alternatively, the dust masses estimated via the Rayleigh-Jeans dust continuum (see Sect. 6.5) can be converted into a CO(1–0) luminosity via a gas-to-dust mass ratio,  $\delta_{\text{gdr}}$ , and a CO-to-H<sub>2</sub> (light-to-mass) conversion factor,  $\alpha_{\text{CO}}$  (see Bolatto et al., 2013, for a review):  $L'_{\text{CO}(1-0)} = M_{\text{dust}} \delta_{\text{gdr}} / \alpha_{\text{CO}}$ .

By starting from the dust masses derived in Sect. 6.5, we therefore first estimated the molecular gas mass  $M_{\text{H}_2}$  of our sources by adopting  $\delta_{\text{gdr}} = 100$  (e.g., Genzel et al. 2015, see Sect. 6.9). By employing the typical value of  $\alpha_{\text{CO}} = 0.8 (\text{K km s}^{-1} \text{ pc}^2)^{-1}$  (Downes & Solomon, 1998) that was adopted in the literature for SMGs and quasar hosts (see Carilli & Walter 2013 for a comprehensive discussion) and assuming that 75% of the dust-derived gas mass is in molecular form (e.g., Riechers et al., 2013; Wang et al., 2016; Venemans et al., 2017b), we then find  $L_{\text{CO}(1-0)} \sim 2.4 \times 10^6 L_{\odot}$  for QSO PJ231-20 and  $L_{\text{CO}(1-0)} \sim 2.6 \times 10^5 L_{\odot}$  for QSO PJ308-21. On the other hand, in the case of companion galaxies, we assumed  $T_{\text{dust}} = 47 \text{ K}$  and found  $L_{\text{CO}(1-0)} \sim 1.1 \times 10^6 L_{\odot}$  and  $\sim 0.4 \times 10^5 L_{\odot}$  for the source in systems PJ231-20 and PJ308-21, respectively. These values increase by a factor of  $\sim 2\times$  when a dust temperature of 35 K is assumed. However, they are consistent within the uncertainties with the values obtained adopting a higher dust temperature. In Fig. 6.9 we compare the CO measurements of our sources, normalizing by CO(1–0) with the average CO(1–0)-normalized SLEDs of low- $z$  starburst galaxies and AGN, respectively (Mashian et al., 2015; Rosenberg et al., 2015), the Milky Way Galactic center (Fixsen et al., 1999), and various measurements of  $z > 6$  sources retrieved from the literature. The high- $z$  sources we show include the quasars J2310+1855 at  $z = 6.00$  (Carniani et al., 2019; Shao et al., 2019; Li et al., 2020b), J1319+0959 at  $z = 6.12$  (Wang et al., 2013; Carniani et al., 2019), J1148+5251 at  $z = 6.4$  (Walter et al., 2003; Riechers et al., 2009; Stefan et al., 2015; Gallerani et al., 2014), J0439+1634 at  $z = 6.52$  (Yang et al., 2019c), and J0305-3150, J0109-3047, and J2348-3054 at  $z = 6.61, 6.79,$  and  $6.90$ , respectively (Venemans et al., 2017b)<sup>2</sup>, and the  $z = 6.34$  SMG HFLS 3 (Riechers et al., 2013). For the

<sup>2</sup>See Table 2 in Carniani et al. (2019) and Table 1 in Venemans et al. (2017b) for the complete collection of measurements.

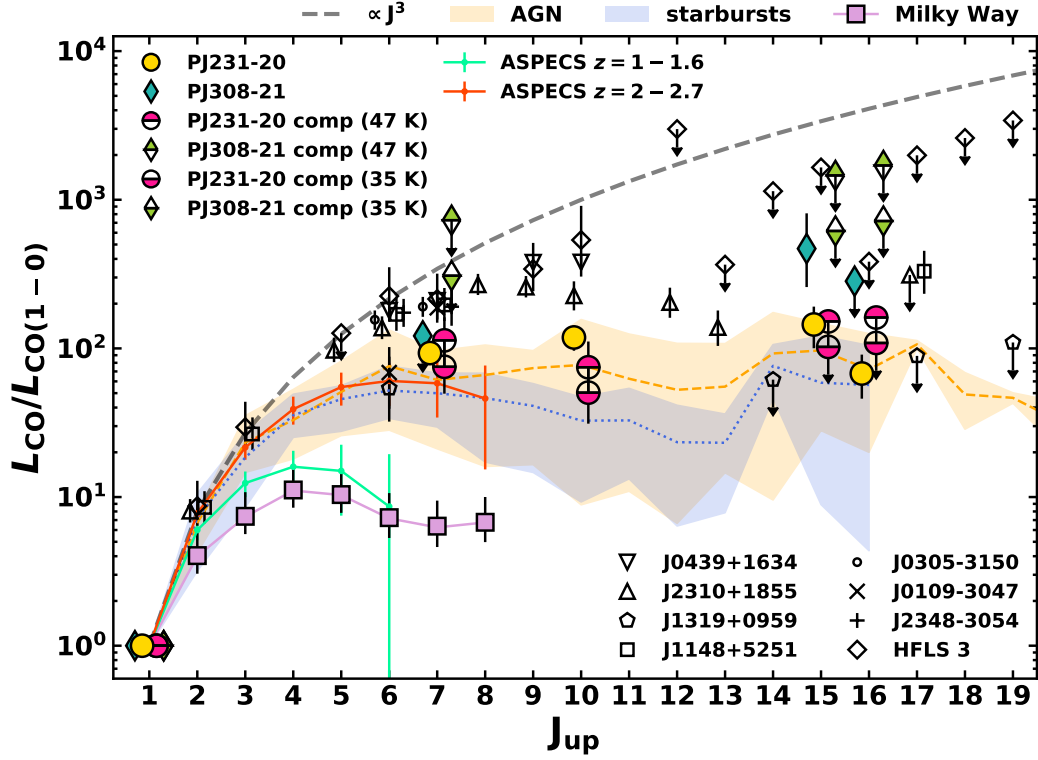


**Figure 6.9**

Average CO(1-0)-normalized SLEDs (in  $L_{\odot}$ ). Colored circles and diamonds are measurements obtained in this work for systems PJ231-20 and PJ308-21. For the companion galaxies we show the two SLEDs obtained assuming  $T_{\text{dust}} = 47\text{ K}$  (filled half-top symbols) and  $35\text{ K}$  (filled half-bottom symbols). Empty symbols refer to the CO ladders of other high- $z$  quasars and one SMG (HFLS 3) from the literature (see Riechers et al., 2013; Venemans et al., 2017b; Carniani et al., 2019; Yang et al., 2019c; Li et al., 2020b, and references therein). Average CO SLEDs of local AGN and starburst galaxies from the literature (Mashian et al., 2015; Rosenberg et al., 2015) are reported by the dashed orange and dotted blue lines, respectively. Shaded areas are the confidence limits (computed as the 16th and 85th percentile of the distribution, respectively). Violet squares are the Milky Way Galactic center CO-normalized ladders from Fixsen et al. (1999). Average CO SLEDs of starburst galaxies at  $z \sim 1-1.6$  and  $z \sim 2-2.6$  from ASPECS are shown as green and red lines, respectively. The dashed gray line is the expected thermalized CO SLED in the Rayleigh-Jeans limit.

quasars for which  $L_{\text{CO}(1-0)}$  was not available in the literature, we derived  $L_{\text{CO}(1-0)}$  from dust masses provided in Carniani et al. (2019) using the same assumptions as described above for systems PJ231-20 and PJ308-21. In addition, we report the CO SLED models obtained from the ASPECS ALMA large program for  $z \sim 1-2$  starburst galaxies (Boogaard et al., 2020). Despite

the large uncertainties, we can identify an overall trend for the low- $z$  starburst and AGN CO SLEDs. Starburst CO SLEDs typically reach a peak at  $J_{\text{up}} \simeq 6-7$  and show a steady decline afterward. The average CO SLED of local AGN is more excited at high- $J$  ( $J_{\text{up}} \gtrsim 9-10$ ) than is that of the starbursts, consistent with the scenario in which high- $J$  CO transitions are associated with a highly excited medium due to the strong radiation field or shocks produced by the AGN activity.

Here, the QSO PJ231-20 CO SLED is similar to those of local AGN. In particular, the observed CO(10-9)-to-CO(1-0) luminosity ratio can help us to distinguish between AGN and the starburst regime. On the other hand, the CO SLED of the PJ231-20 companion galaxy is consistent within  $\sim 1\sigma$  with both the starbursts and AGN population, even when the upper limits on the CO(15-14)-to-CO(1-0) and CO(16-15)-to-CO(1-0) luminosity ratios are taken into account. On the other hand, when we assume a dust temperature of 35 K, the CO SLED appears similar to the average CO SLED of starburst galaxies. However, Mazzucchelli et al. (2019) failed to detect the PJ231-20 companion in the rest-frame optical/UV wavelengths, revealing that this source is highly dust-enshrouded, with an SED similar to that of Arp 220, which is a highly star-forming and highly dust-obscured ULIRG in the local Universe. In addition, Connor et al. (2020) did not detect the PJ231-20 companion even in X-ray observations, which rules out the presence of an AGN in this source, at least with a luminosity similar to that of optically selected quasars. These previous studies suggest that star formation probably dominates the radiation field (and therefore the CO excitation) in this source. While little information is available for the PJ308-21 companion, we observe a high CO(15-14)-to-CO(1-0) luminosity ratio for the quasar host, possibly revealing the contribution of the AGN that excites this high- $J$  CO ladder (see, e.g., Schleicher et al., 2010; Gallerani et al., 2014; Carniani et al., 2019). Finally, the observed CO(7-6)-to-CO(1-0) luminosity ratios in the quasar host PJ231-20 and its companion, and the upper limit available for QSO PJ308-21, are lower than those of other  $z > 6$  quasars (e.g., Venemans et al., 2017b), but are consistent within the uncertainties with the average CO SLED model of the  $z \gtrsim 2$  starburst galaxies in the ASPECS field. Interestingly, the latter appears to be fairly similar to the average CO SLED of local starburst galaxies. However, we note that the CO luminosity ratios in high- $z$  sources have large uncertainties. In particular, the estimate of  $L_{\text{CO}(1-0)}$  is significantly

affected by the assumed gas-to-dust ratio and the uncertainties on dust mass obtained from the dust SED (see, e.g., **Sect. 6.5**).

## 6.8.2 CO SLED models

From the CLOUDY grids, we retrieved the CO line intensities and normalized them to the CO(1–0) line intensity, thus obtaining the normalized CO SLEDs as function of  $n_{\text{H}}$  and radiation field flux ( $G_0$  or  $F_X$  in the case of PDR and XDR models, respectively). In **Fig. 6.10** we show the CO SLED models in the PDR and XDR case for two values of cloud gas density,  $n_{\text{H}} \simeq 0.7 \times 10^3 \text{ cm}^{-3}$  and  $\simeq 1 \times 10^5 \text{ cm}^{-3}$ , for which we varied the radiation field strength at fixed hydrogen column density  $N_{\text{H}} = 10^{23} \text{ cm}^{-2}$ . The results show that in the PDR case, the CO SLED is almost independent of  $G_0$ , in contrast to the XDR case. These behaviors are the direct consequence of a completely different heating mechanism driven by absorption of UV and X-ray photons. X-rays have very low cross sections and therefore can penetrate much deeper into the cloud (at column densities  $> 10^{22} \text{ cm}^{-2}$ ). Furthermore, X-ray photons have a higher heating efficiency than UV photons, which maintains molecular clouds at a high temperature even at high column density (Lepp & Dalgarno, 1996; Maloney et al., 1996; Meijerink & Spaans, 2005). As expected, in the PDR and XDR cases, the peak of the CO SLED rises and shifts to higher  $J$  values as the density increases. The population of high- $J$  CO levels (set by the competition of collisional excitation and radiative de-excitation) increases with increasing cloud density due to the higher critical densities of these lines and progressively thermalizes, saturating at a certain value. In the optically thick and high-temperature (or low-frequency) limit, the luminosities (in  $L_{\odot}$  units) of the CO rotational lines are approximately proportional to  $J^3$  (see, e.g., Obreschkow et al., 2009; da Cunha et al., 2013; Narayanan & Krumholz, 2014). At higher- $J$  transitions, the PDR CO SLED drops considerably and flattens at a low level due to the small amount of hot gas in the outer layer of the molecular cloud. On the other hand, in XDRs, a much larger fraction of the gas is at higher temperature, thus the CO SLED does not drop as dramatically. For this reason, observations of high- $J$  CO lines are expected reveal an additional source of heating, for example, X-rays (see, e.g., Schleicher et al., 2010). We note that our CO SLED model predictions agree with other PDR/XDR CLOUDY models reported in the literature (e.g., Vallini et al., 2018, 2019).

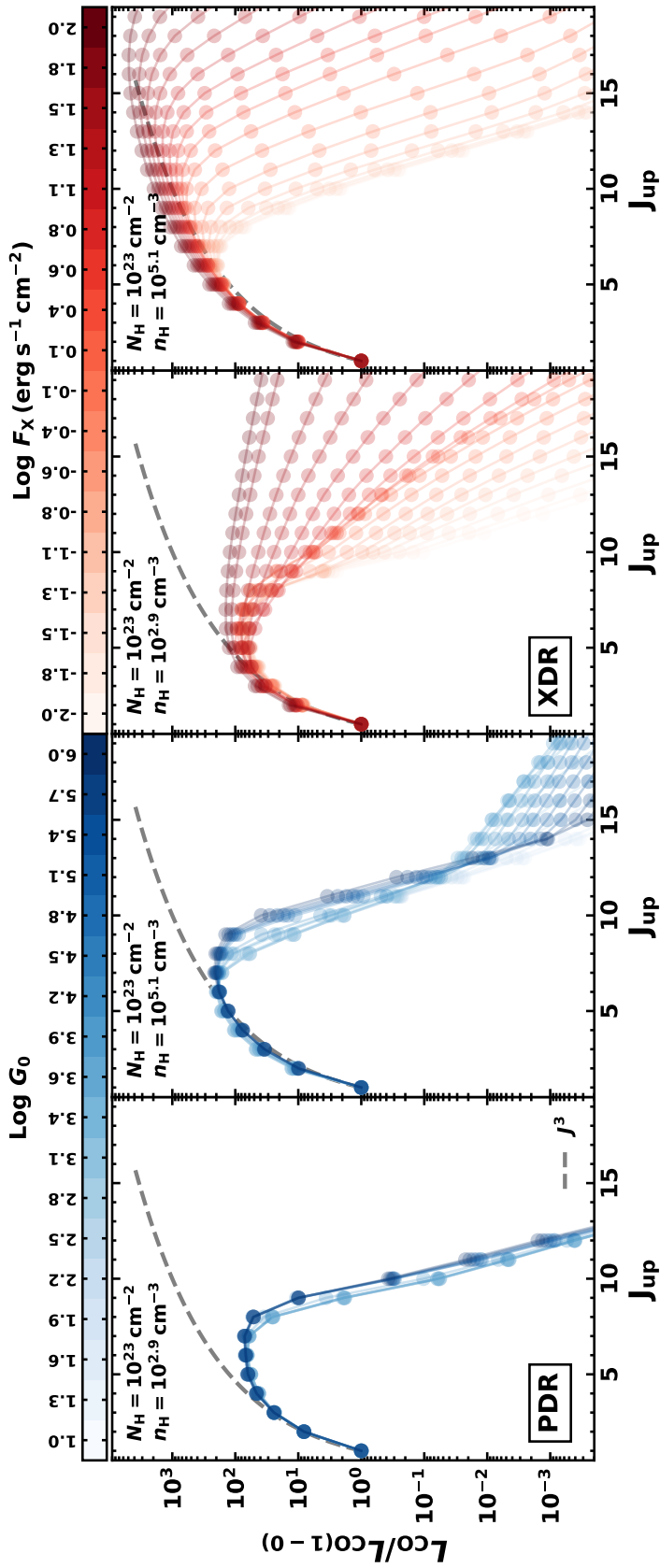
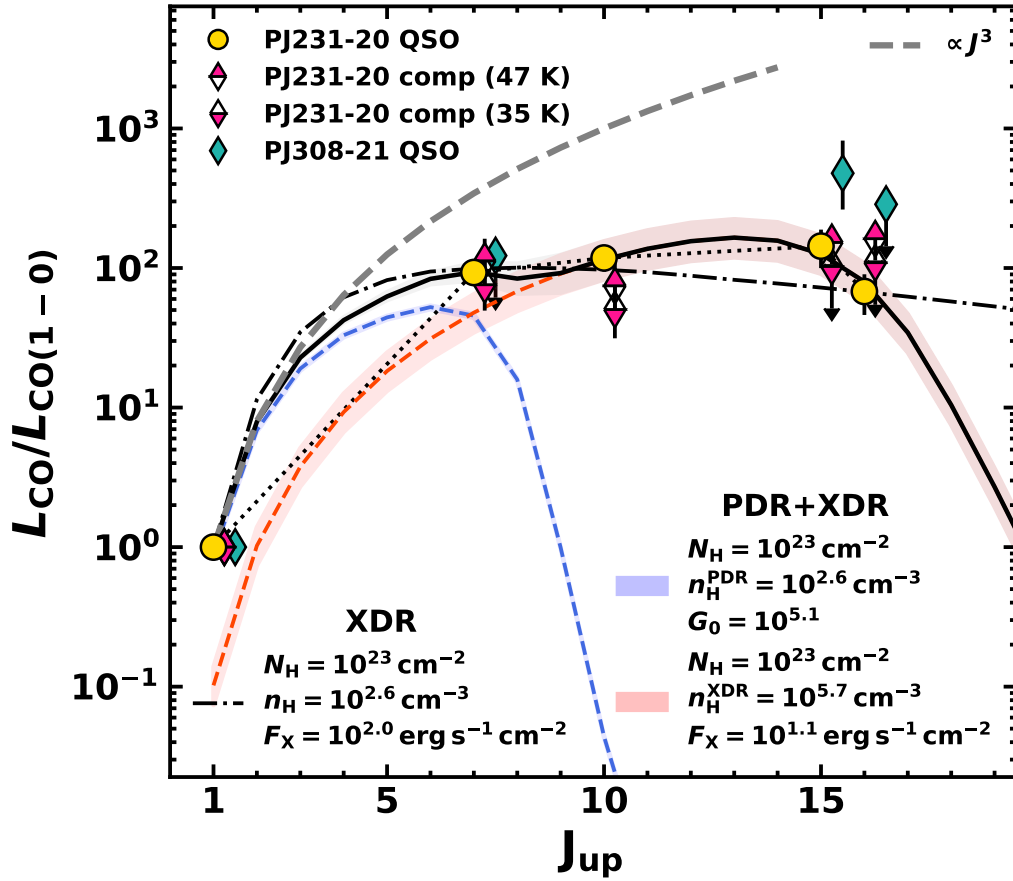


Figure 6.10

CLOUDY CO(1-0)-normalized SLED models in the PDR (left panels) and XDR regime (right panels) for which the intensity of the incident radiation field was varied over the entire parameter space and for two reference values of total hydrogen density ( $n_{\text{H}} = 10^{2.9}, 10^{5.1} \text{ cm}^{-3}$ ) and column density  $N_{\text{H}} = 10^{23} \text{ cm}^{-2}$ . PDR cases are shown in blue, and XDRs are in red. Both are color-coded according to the values of the radiation field flux. The dashed gray line indicates the  $J^3$  curve, which is the expected trend of the CO SLED in LTE (in the optically thick and high-temperature or low-frequency limit).

For QSO PJ231-20, the mere detection (although at modest significance) of very high- $J$  CO transitions, with estimated  $L_{\text{CO}(15-14)}/L_{\text{CO}(1-0)}$  and  $L_{\text{CO}(16-15)}/L_{\text{CO}(1-0)}$  ratios of  $\sim 100$ , immediately points to a significant XDR contribution. In **Fig. 6.11** we show our best-fit CLOUDY models of the CO SLED in QSO PJ231-20 obtained by minimizing  $\chi^2$ . The high- $J$  normalized CO fluxes ( $J_{\text{up}} = 15, 16$ ) in QSO PJ231-20 cannot be reproduced by a single PDR model. We obtained excellent agreement using a composite (PDR+XDR) model in the form  $W_{\text{PDR}}F_{\text{CO}}^{\text{PDR}}(n_{\text{H}}^{\text{PDR}}, G_0) + W_{\text{XDR}}F_{\text{CO}}^{\text{XDR}}(n_{\text{H}}^{\text{XDR}}, F_{\text{X}})$ , adopting  $N_{\text{H}} = 10^{23} \text{ cm}^{-2}$ . Here  $W_{\text{PDR}}$  and  $W_{\text{XDR}}$  are the relative contributions of the PDR ( $F_{\text{CO}}^{\text{PDR}}$ ) and XDR component ( $F_{\text{CO}}^{\text{XDR}}$ ) to the CO(1-0) emission, respectively. The best-fit model has  $W_{\text{PDR}} = 0.90 \pm 0.04$  and  $W_{\text{XDR}} = 0.10 \pm 0.04$ , a total hydrogen density  $n_{\text{H}}^{\text{PDR}} \sim 4 \times 10^2 \text{ cm}^{-3}$ ,  $n_{\text{H}}^{\text{XDR}} \sim 5 \times 10^5 \text{ cm}^{-3}$ , and a UV/X-ray radiation field strength of  $G_0 \sim 1 \times 10^5$  and  $F_{\text{X}} \sim 10 \text{ erg s}^{-1} \text{ cm}^{-2}$ , respectively. Because we considered the same column densities for PDR and XDR models,  $W_{\text{PDR}}$  and  $W_{\text{XDR}}$  are directly connected with the CO mass budget in the ISM. Therefore this result indicates that PDRs account for  $\sim 90\%$  of the molecular mass in the quasar host. However, while XDRs account for a small fraction of the molecular mass, they dominate the CO emission at  $J_{\text{up}} \geq 10$ . In QSO PJ231-20, we measured  $L_{\text{CO}(7-6)}/L_{\text{CO}(1-0)} = 93_{-12}^{+13}$ . This ratio is  $\sim 30\%$  with respect to the value expected for CO thermalized emission in the optically thick and Rayleigh-Jeans limit (described by the  $J^3$  curve in **Fig. 6.11**). However, although the composite model allows us to accurately reproduce the observed CO SLED in QSO PJ231-20, the number of free parameters is greater than the number of data points, which produces degeneracies in the best-fit parameters. In **Fig. 6.11** we also show the best-fit model obtained by employing a single XDR component. In this case, the best-fit model approximately agrees with the observed CO SLED in QSO PJ231-20, with a value  $n_{\text{H}} \sim 4 \times 10^2 \text{ cm}^{-3}$ , but it indicates an extreme value of the X-ray radiation field intensity of  $F_{\text{X}} \sim 10^2 \text{ erg s}^{-1} \text{ cm}^{-2}$ , corresponding to the upper boundary of the parameter space. Therefore this result should be taken into account with caution. In **Fig. 6.11** we also report the observed CO SLED in the PJ231-20 companion galaxy and QSO PJ308-21. Despite detecting  $L_{\text{CO}(7-6)}/L_{\text{CO}(1-0)}$  and  $L_{\text{CO}(10-9)}/L_{\text{CO}(1-0)}$  in the PJ231-20 companion, we cannot safely infer a significant XDR contribution in this source because we lack high- $J$  CO detections. On the other hand, the high  $L_{\text{CO}(15-14)}/L_{\text{CO}(1-0)} \sim 3 \times 10^2$  measured in QSO



**Figure 6.11**

CO(1–0)-normalized SLED fits of QSO PJ231-20. Gold circles indicate the CO luminosity ratios measured in the quasar. The dot-dashed black line is the best-fit model using a single XDR model. The composite (PDR+XDR) model described in the text is represented with the solid black line. The dashed blue and red lines show the PDR and XDR component, respectively. The shadowed area indicates the  $1\sigma$  uncertainties on the normalization values. Best-fit parameters are reported in the legends at the bottom of the figure. The dashed gray line is the theoretical trend ( $\propto J^3$ ) of the CO SLED in the LTE, optically thick, and high-temperature (or low frequency) limit. The red and blue diamonds (slightly shifted horizontally for clarity) are the CO(1–0)-normalized SLED in the PJ231-20 companion galaxy and QSO PJ308-21, respectively. For the PJ231-20 companion we report the CO SLEDs obtained assuming  $T_{\text{dust}} = 47\text{K}$  (half-top filled magenta diamonds) and  $35\text{K}$  (half-bottom filled magenta diamonds, see Sect. 6.8.1).

PJ308-21 (although with a low S/N) can only be reproduced with our models by adopting a strong XDR component.

Overall, our CO SLED modeling suggests that a significant contribution to CO emission arises from clouds that are exposed to X-ray radiation, at least in quasar hosts. This result appears to be in contrast with our  $[\text{CII}]_{158\mu\text{m}}/[\text{CI}]_{369\mu\text{m}}$  modeling discussed in **Sect. 6.7.2**. However, in our composite PDR+XDR model, we found that PDRs dominate the molecular mass budget and thus dominate the  $[\text{CII}]_{158\mu\text{m}}$  and  $[\text{CI}]_{369\mu\text{m}}$  emission. In this scenario, the high- $J$  CO lines mainly arise from the molecular medium in the central region of the quasar host galaxy, while emission from lower- $J$  CO lines and FSLs traces the ISM on larger scales. The good correlation of the  $[\text{CI}]$  and  $J \leq 7$  CO lines suggests that these lines trace the spatially extended gas reservoir associated with vigorous star formation rather than the denser and more concentrated gas that is traced by high- $J$  CO lines (see, e.g., Gerin & Phillips 2000; Engel et al. 2010; Ivison et al. 2011; Jiao et al. 2017 for studies of nearby sources, and, e.g., Weiß et al. 2005; Tacconi et al. 2008; Bothwell et al. 2010, 2013; Riechers et al. 2011; Walter et al. 2011; Yang et al. 2017; Valentino et al. 2018, 2020, for intermediate and high- $z$  works). Finally, we stress that the uncertainties reported in our CO(1–0)-normalized SLEDs are statistical errors that ignore any systematic uncertainties associated with the assumption of a gas-to-dust ratio by which we estimated the CO(1–0) luminosity in this chapter. Our results should therefore be considered tentative. In order to better constrain the relative contribution of PDRs and XDRs in these sources, we need observations of other CO lines over a wide range of values of  $J$ . We also point out that our analysis does not rule out the possibility that another source of heating such as cosmic rays, shocks, or mechanical heating from turbulence may contribute significantly to the mid- or high- $J$  CO excitation (see, e.g., Hollenbach & McKee, 1989; Flower & Pineau Des Forêts, 2010; Mingozzi et al., 2018; Godard et al., 2019; Vallini et al., 2019)

### 6.8.3 H<sub>2</sub>O rotational lines

We present submillimeter H<sub>2</sub>O emission in our two  $z > 6$  nonlensed quasar host galaxies. In particular, we report three H<sub>2</sub>O line detections in QSO PJ231-20 ( $3_{12} - 2_{21}$ ,  $3_{21} - 3_{12}$ , and  $3_{03} - 2_{12}$ ) and a tentative detection of H<sub>2</sub>O  $3_{03} - 2_{12}$  in QSO PJ308-21, but we only have upper limits on water lines from the companion galaxies. The water vapor energy levels and the targeted (ortho-)H<sub>2</sub>O transitions are reported in **Fig. 6.12**. The H<sub>2</sub>O  $3_{12} - 2_{21}$  and

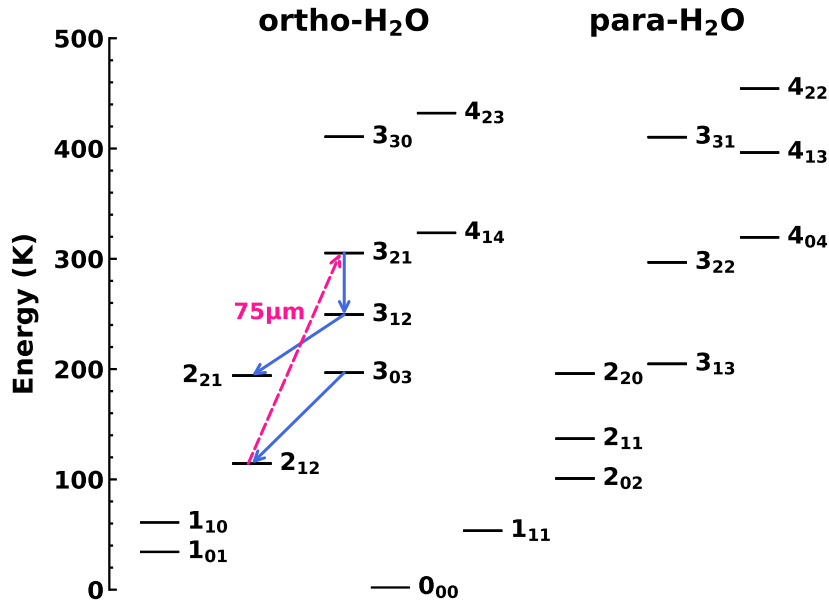


**Figure 6.12**

Part of the H<sub>2</sub>O energy level diagram. Para- and ortho-H<sub>2</sub>O ladders are shown together with the detected H<sub>2</sub>O line transitions (blue arrows). The magenta arrow indicates the IR radiative-pumped transition at 75 μm that populates the 3<sub>21</sub> level (see, González-Alfonso et al., 2014; Liu et al., 2017).

3<sub>21</sub> – 3<sub>12</sub> lines are likely mainly produced by the cascade process in response to absorption of IR photons at 75 μm, while the H<sub>2</sub>O 3<sub>03</sub> – 2<sub>12</sub> line is more sensitive to collisions and is enhanced in systems with a higher gas kinetic temperature (e.g., van der Werf et al., 2011; González-Alfonso et al., 2014; Liu et al., 2017).

#### 6.8.4 $L_{\text{H}_2\text{O}} - L_{\text{TIR}}$ relation

In the upper panel of **Fig. 6.13** we compare the H<sub>2</sub>O 3<sub>21</sub> – 3<sub>12</sub> line with the total IR luminosity obtained through the fit of the dust SED of QSO PJ231-20 and its companion (see **Tab. 6.4**) with a sample of nearby ULIRGs presented in Yang et al. (2013). For this comparison, we also included H<sub>2</sub>O detections of  $z \sim 2.5 - 3.5$  Hy/ULIRGs from Yang et al. (2016a), APM 08279+5255 at  $z \simeq 3.9$  (van der Werf et al., 2011), the  $z = 6.34$  SMG HFLS 3 (Riechers et al., 2013), and J0439+1634, a  $z \simeq 6.5$  quasar host galaxy (Yang et al., 2019c). Our data are consistent within the uncertainties with the almost linear relation found by Yang et al. (2013, 2016a),  $L_{\text{H}_2\text{O}} \propto L_{\text{TIR}}^{1.1-1.2}$ . This correlation appears to be the straightforward consequence of the IR-

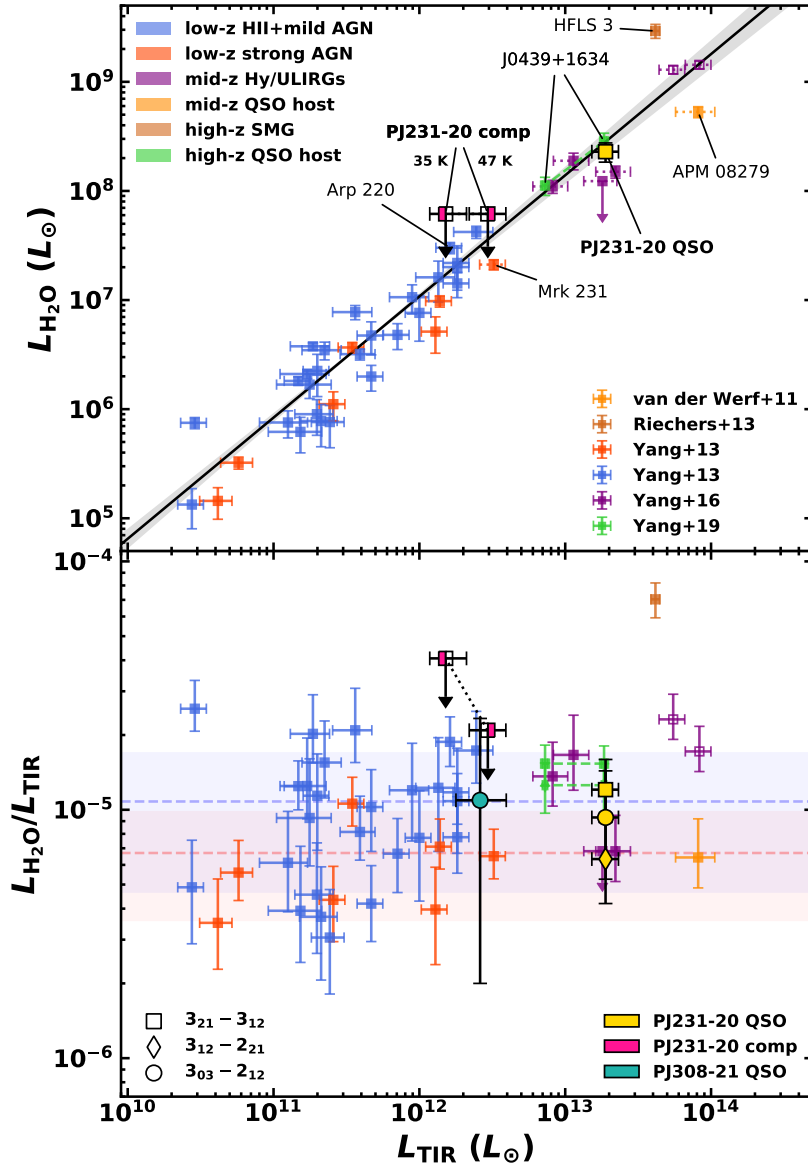


**Figure 6.13**

*Upper panel:*  $L_{\text{H}_2\text{O}(3_{21}-3_{12})} - L_{\text{TIR}}$  relation. The solid black line shows the best power-law fit from Yang et al. (2013) considering the low-z HII+mild and strong AGN sample (blue and red squares, respectively). The gray area is the  $1\sigma$  confidence limit. The gold and magenta squares indicate the quasar host PJ231-20 and its companion, respectively. In the case of the companion, we report the cases assuming  $T_{\text{dust}} = 47$  K (left half-filled magenta square) and 35 K (right half-filled magenta square). These points are connected by a dotted black line. Purple squares are the mid-z Hy/ULIRGs of Yang et al. (2016a). We also report measurements of APM 08279+5255 (van der Werf et al., 2011), the  $z \sim 6.3$  SMG HFLS 3 (Riechers et al., 2013), and the  $z \sim 6.5$  J0439+1634 quasar (Yang et al., 2019c). Empty squares indicate measurements that were not corrected for gravitational lensing. *Lower panel:*  $L_{\text{H}_2\text{O}}/L_{\text{TIR}}$  vs. total IR luminosity. Symbols are the same as in the upper panel. Together with  $L_{\text{H}_2\text{O}}/L_{\text{TIR}}$  for the  $3_{21} - 3_{12}$  transition, we also report those for  $3_{12} - 2_{21}$  and  $3_{03} - 2_{12}$  for QSO PJ231-20, the companion galaxy, QSO PJ308-21, and the quasar J0439+1634, as indicated in the legend.

pumping mechanism responsible for the population of the upper level ( $3_{21}$ ) of the  $\text{H}_2\text{O}$  molecules (Yang et al., 2013), which after absorption of far-IR photons, cascade via the lines we observe in an approximately constant fraction. However, Liu et al. (2017) emphasized that the medium-excitation  $\text{H}_2\text{O}$  transitions (such as  $3_{21} - 3_{12}$ ) probe the physical regions of galaxies in which a large fraction of FIR emission is generated. Therefore the observed  $L_{\text{H}_2\text{O}} - L_{\text{TIR}}$  correlation could be largely driven by the sizes of FIR- and water vapor-emitting regions. In the next chapter we will return on this point. The  $\text{H}_2\text{O}$  detections presented in this chapter together with those of Riechers et al. (2013) and Yang et al. (2019c) extend the redshift range explored in the previous works by Yang et al. (2013, 2016a), confirming that this relation also appears to hold at very high- $z$ .

Yang et al. (2013) found slightly different values of  $L_{\text{H}_2\text{O}}$ -to- $L_{\text{TIR}}$  ratios for the  $3_{21} - 3_{12}$  transition in local AGN and star-formation-dominated galaxies with possible mild AGN contribution. However, apart from individual studies (e.g., González-Alfonso et al. 2010 for Mrk 231, and van der Werf et al. 2011 for APM 08279) showing that AGN could be the main power source exciting the  $\text{H}_2\text{O}$  lines in this objects, it is still not clear how a strong AGN could affect the  $\text{H}_2\text{O}$  emission. One possibility is that the buried AGN results in a higher TIR-to- $75\mu\text{m}$  luminosity ratio than in starburst galaxies because the shape of the IR SED of these sources is different (e.g., Kirkpatrick et al., 2015; Yang et al., 2016a). In addition, high X-ray fluxes can photodissociate  $\text{H}_2\text{O}$  molecules. On the other hand, a high dust continuum opacity at  $100\mu\text{m}$  ( $\tau_{100}$ ) and/or large velocity dispersion can enhance the  $\text{H}_2\text{O}$  luminosity (e.g., Arp220, González-Alfonso et al., 2014; Yang et al., 2016a).

For the  $3_{21} - 3_{12}$  transition toward QSO PJ231-20, we find  $L_{\text{H}_2\text{O}}/L_{\text{TIR}} \sim 1.2 \times 10^{-5}$ , which is comparable with the ratio measured in the  $z \sim 6.5$  quasar J0439+1634 (Yang et al., 2019c). This value is higher than the average ratio measured by Yang et al. (2013) in local AGN-dominated sources ( $7 \pm 3 \times 10^{-6}$ ) and is consistent with that measured in star-forming galaxies ( $1.1 \pm 0.6 \times 10^{-5}$ ), suggesting a significant contribution of star formation to the IR radiation exciting the  $\text{H}_2\text{O}$  line. In Fig. 6.13 we also report the  $L_{\text{H}_2\text{O}}$ -to- $L_{\text{TIR}}$  ratios for the  $3_{12} - 2_{21}$  and  $3_{03} - 2_{12}$  transitions detected in QSO PJ231-20 and the tentative  $\text{H}_2\text{O}$   $3_{03} - 2_{12}$  detection in QSO PJ308-21. These values are in the range measured for the  $3_{21} - 3_{12}$  transition in local ULIRGs.

### 6.8.5 H<sub>2</sub>O(3<sub>21</sub> – 3<sub>12</sub>)-normalized SLED

By combining the three water vapor lines detected in QSO PJ231-20, we trace in **Fig. 6.14** the line flux ratios, that is, the normalized H<sub>2</sub>O SLED, and we compare them with the results for local and high-*z* sources found in the literature. The SLEDs were normalized to H<sub>2</sub>O 3<sub>21</sub> – 3<sub>12</sub>, a medium-excitation line that is predicted to be easily radiatively pumped in the warm dense medium (see Liu et al., 2017). Therefore the ratios with the other transitions directly reflect the effect of IR-pumping line excitation.

In **Fig. 6.14**, the average H<sub>2</sub>O SLED of the local ULIRG sample by Yang et al. (2013) shows two peaks at the energy of H<sub>2</sub>O 2<sub>02</sub> – 1<sub>11</sub> and 3<sub>21</sub> – 3<sub>12</sub> transitions, indicating a high IR pumping efficiency at 75 μm. This is consistent with the models of Liu et al. (2017), which show that these two lines are efficiently pumped in the warm ISM component at  $T_{\text{dust}} \gtrsim 40$  K. The bulk H<sub>2</sub>O emission observed in star-forming galaxies of Yang et al. (2013) is explained by González-Alfonso et al. (2014) by a model with  $T_{\text{dust}} = 55 - 75$  K,  $\tau_{100} \sim 0.1$  and H<sub>2</sub>O column density  $N_{\text{H}_2\text{O}} \sim (0.5 - 2) \times 10^{17} \text{ cm}^{-2}$ , including a significant contribution from collisional excitation and line radiative pumping. Despite significant uncertainties, the observed H<sub>2</sub>O line ratios in QSO PJ231-20 show a clear peak at the 3<sub>21</sub> – 3<sub>12</sub> transition. In particular, the line ratio 3<sub>12</sub> – 2<sub>21</sub>/3<sub>21</sub> – 3<sub>12</sub> is consistent with the value observed in  $z \sim 6.3$  SMG HFLS 3 (Riechers et al., 2013) and in the  $z \sim 6.5$  quasar J0439+1634 (Yang et al., 2019c), whose H<sub>2</sub>O SLEDs also peak at 3<sub>21</sub> – 3<sub>12</sub>. The stronger intensity of H<sub>2</sub>O 3<sub>21</sub> – 3<sub>12</sub> measured in QSO PJ231-20 than the other transitions lower in the cascade, in conjunction with the high critical density of the observed transitions ( $\gtrsim 10^8 \text{ cm}^{-3}$ ), suggests that the contribution from collisional excitation of the upper energy levels of the observed water vapor transitions is minor. Other factors that could contribute to the QSO PJ231-20 H<sub>2</sub>O SLED peak at 3<sub>21</sub> – 3<sub>12</sub> are the shape of the IR dust SED that peaks close to 75 μm, thus allowing high pumping efficiency, together with the large FWHM ( $\sim 400 \text{ km s}^{-1}$ ) of the H<sub>2</sub>O 3<sub>21</sub> – 3<sub>12</sub> line, which increases the cross sections for absorbing pumping photons (e.g., González-Alfonso et al., 2014).

### 6.8.6 H<sub>2</sub>O SLED models

In this section we retrieve quantitative information about the ISM that is associated with the H<sub>2</sub>O emission by modeling the water vapor SLED using

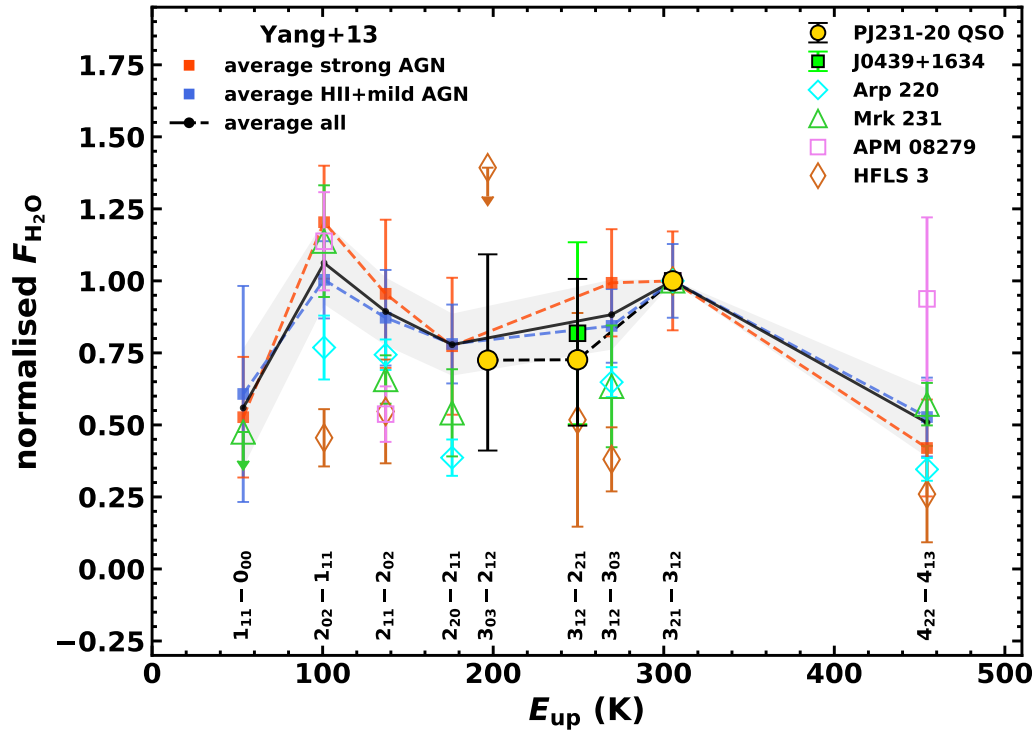


**Figure 6.14**

$\text{H}_2\text{O}(3_{21} - 3_{12})$ -normalized  $\text{H}_2\text{O}$  intensities (in  $\text{Jy km s}^{-1}$ ) as a function of the excitation temperature of the upper level. Gold circles are the  $\text{H}_2\text{O}$  ratios measured in the QSO PJ231-20. The solid black line reports the average  $\text{H}_2\text{O}$  SLED of the whole sample of Yang et al. (2013). The gray shadowed area represents the  $1\text{-}\sigma$  uncertainty. The dashed red and blue lines indicate the average values of strong-AGN- and HII+mild-AGN-dominated galaxies, respectively, as classified by Yang et al. (2013). We also report data retrieved from the literature for the two nearby sources Arp 220 (Rangwala et al., 2011) and the AGN-dominated Mrk 231 (González-Alfonso et al., 2010). For comparison, we also show the  $\text{H}_2\text{O}$  flux ratios observed in high- $z$  sources such as APM 08279+5255 (van der Werf et al., 2011), the lensed  $z > 6$  quasar J0439+1634 (Yang et al., 2019c), and the SMG HFLS3 (Riechers et al., 2013). The energy of the upper levels of the  $2_{20} - 2_{11}$  and  $3_{12} - 3_{03}$  transitions were shifted for clarity to  $-20$  and  $+20$  K, respectively.

our CLOUDY models. Our CLOUDY outputs predict emerging intensities of a large number of water vapor transitions. In Fig. 6.15 we report the  $\text{H}_2\text{O}$  SLED normalized to the  $\text{H}_2\text{O}$   $3_{21} - 3_{12}$  line in the PDR and XDR regimes. We do this for two representative values of the total hydrogen density  $n_{\text{H}} \simeq 2 \times 10^2 \text{ cm}^{-3}$  and  $\simeq 4 \times 10^4 \text{ cm}^{-3}$  for which we varied the radiation field strength with a fixed total hydrogen column density  $N_{\text{H}} = 10^{24} \text{ cm}^{-2}$ .

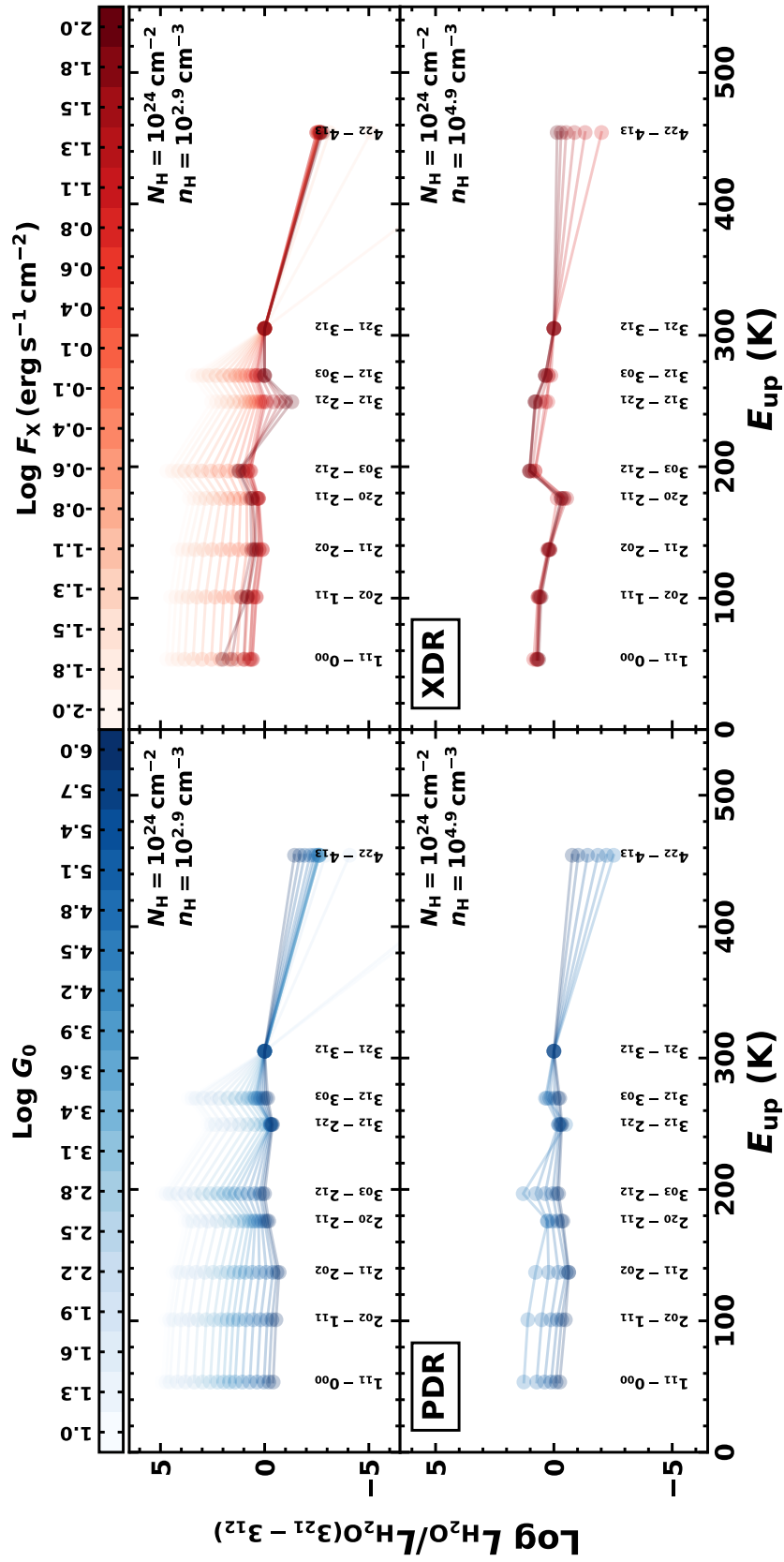


**Figure 6.15**

CLOUDY  $\text{H}_2\text{O}(3_{21} - 3_{12})$ -normalized SLED models in the PDR (left panels) and XDR regime (right panels), for which we varied the intensity of the incident radiation field over the entire parameter space and for two reference values of total hydrogen density ( $n_{\text{H}} = 10^{2.3}, 10^{4.6} \text{ cm}^{-3}$ ), and column density  $N_{\text{H}} = 10^{24} \text{ cm}^{-2}$ . PDR cases are shown in blue and XDRs are red. They are color-coded according to the values of the radiation field flux. The energy of the upper levels of the  $2_{20} - 2_{11}$  and  $3_{12} - 3_{03}$  transitions were shifted for clarity to  $-20$  and  $+20$  K, respectively. In order to exclude unphysical models, we report  $\text{H}_2\text{O}$  SLEDs in which the  $\text{H}_2\text{O } 3_{12} - 2_{21}$  intensity is  $> 10^{-2} \times$  that of the corresponding  $\text{CO}(10-9)$  line.

In the PDR and XDR cases, the H<sub>2</sub>O SLED flattens as the intensity of the radiation field increases. In particular, the  $L_{\text{H}_2\text{O}}/L_{\text{H}_2\text{O}(3_{21}-3_{12})}$  line ratios for transitions with energy upper level  $E_{\text{up}} < 300\text{ K}$  approach similar values that vary within a factor of  $\sim 4$ . Because the total hydrogen density of the cloud models spans a range that is well below the typical critical density of H<sub>2</sub>O lines ( $\sim 10^8 - 10^9\text{ cm}^{-3}$ ), this might be explained in terms of a progressively more efficient IR pumping of the high-lying H<sub>2</sub>O energy levels as the UV/X-ray photon flux increases, which subsequently cascade radiatively toward low-energy levels. This implies that these H<sub>2</sub>O lines tend to statistical equilibrium, in agreement with the analysis of González-Alfonso et al. (2014) and Liu et al. (2017), for instance. Furthermore, as also mentioned in Sect. 6.8.3, at a gas kinetic temperature  $\gtrsim 300\text{ K}$ , water molecules can form in the gas phase through the neutral-neutral endothermic reaction  $\text{OH} + \text{H}_2 \rightarrow \text{H}_2\text{O} + \text{H}$ . Therefore an increase in total hydrogen density ( $n_{\text{H}} > 10^4\text{ cm}^{-3}$ ) inside the cloud requires a higher radiation field flux ( $G_0 > 2 \times 10^4$ ,  $F_{\text{X}} > 0.05 - 0.1\text{ erg s}^{-1}\text{ cm}^{-2}$ ) to maintain the gas temperature above the reaction activation barrier in a large volume of the cloud in order to produce a significant H<sub>2</sub>O column density  $N_{\text{H}_2\text{O}} > 10^{15}\text{ cm}^{-2}$  (see also, e.g., Neufeld et al., 1995, 2002; Cernicharo et al., 2006; Meijerink et al., 2011). On the other hand, in XDRs, strong X-ray radiation can photodissociate a large fraction of the H<sub>2</sub>O molecules, thus quenching their line emission. However, because the H<sub>2</sub>O 3<sub>21</sub> – 3<sub>12</sub> transition is highly sensitive to the pumping by IR photons (e.g., Liu et al., 2017), low UV or X-ray fluxes cannot efficiently populate its upper level. This produces unphysical results in the predicted  $L_{\text{H}_2\text{O}}/L_{\text{H}_2\text{O}(3_{21}-3_{12})}$ . In Fig. 6.15, to exclude such non-physical results that clearly are at odds with observations, we report the H<sub>2</sub>O SLEDs for which the H<sub>2</sub>O 3<sub>12</sub> – 2<sub>21</sub> predicted intensity is at least  $10^{-2}\times$  that of the CO(10–9) line because these two lines have a similar frequency and are observed to have similar fluxes (see Fig. 6.1 of this chapter, but see also, e.g., Riechers et al. 2013; Yang et al. 2019c).

Using the H<sub>2</sub>O line ratios predicted by our CLOUDY models, we performed the H<sub>2</sub>O SLED fit of QSO PJ231-20. We report the results in Fig. 6.16. The observed H<sub>2</sub>O line ratios of QSO PJ231-20 cannot be satisfyingly reproduced by any models with  $N_{\text{H}} = 10^{23}\text{ cm}^{-2}$ , while the agreement between data and best-fit model significantly improves in a higher column density PDR model with  $N_{\text{H}} = 10^{24}\text{ cm}^{-2}$ . The resulting best-fit model indicates a high-

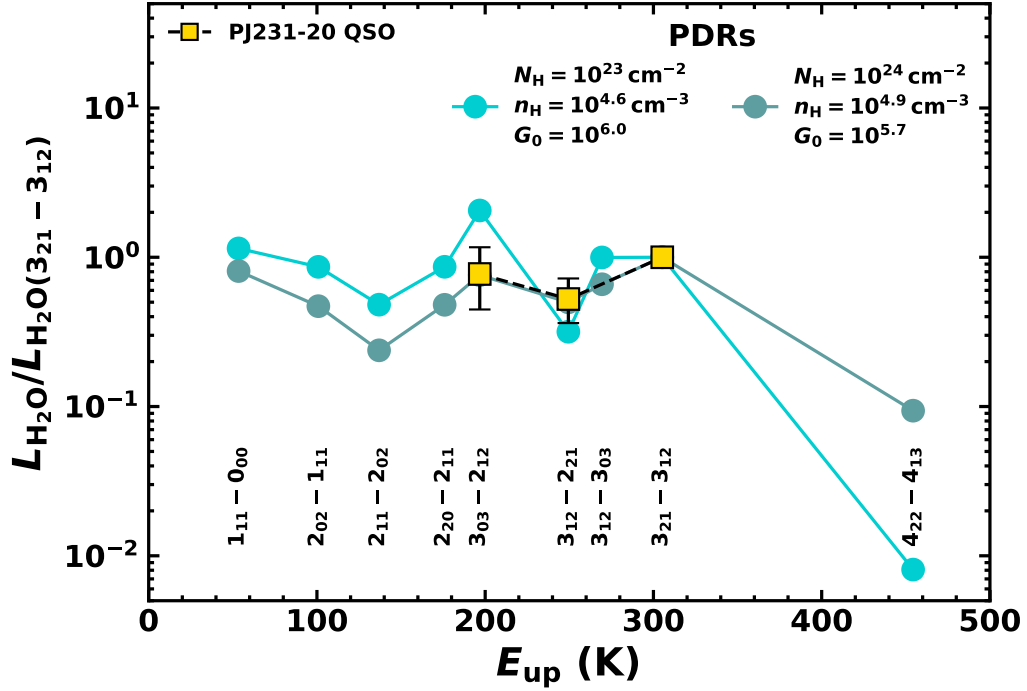


**Figure 6.16**

Best-fit models of the  $\text{H}_2\text{O}(3_{21} - 3_{12})$ -normalized SLED in QSO PJ231-20. Gold squares are the observed line ratios, and light and dark blue circles are the PDR best-fit models with  $N_{\text{H}} = 10^{23}$  and  $10^{24} \text{ cm}^{-2}$ , respectively. The best-fit parameters are indicated in the upper part of the panel.

density medium with  $n_{\text{H}} \sim 0.8 \times 10^5 \text{ cm}^{-3}$ , exposed to a strong FUV radiation field with  $G_0 \sim 5 \times 10^5$ . The mere requirement of a high cloud column density implies that the observed water vapor transitions arise deep in the cloud where the water vapor column density reaches  $N_{\text{H}_2\text{O}} \gtrsim 3 \times 10^{17} \text{ cm}^{-2}$ . Furthermore, because the  $\text{H}_2\text{O}$  line ratios observed in QSO PJ231-20 are similar and because the three  $\text{H}_2\text{O}$  transitions  $3_{21} - 3_{12}$ ,  $3_{12} - 2_{21}$ , and  $3_{03} - 2_{12}$  have similar frequencies and are connected by a cascade process, our result suggests that these lines are near statistical equilibrium. However, the low number of data points makes the result uncertain. In particular, the cloud density is poorly constrained with the fit. On the other hand, the high density value found for QSO PJ231-20  $\text{H}_2\text{O}$  lines is in the range that is typically inferred from  $\text{H}_2\text{O}$  SLED modeling in local sources (see, e.g., González-Alfonso et al., 2014; Liu et al., 2017) and in high- $z$  quasars (e.g., van der Werf et al., 2011)

## 6.8.7 OH transitions

We present detections of the  $\Lambda$ -doublet  $\text{OH}_{163\mu\text{m}}$  in QSO PJ231-20 and the companion galaxy together with a tentative detection in QSO PJ308-21. When this doublet was detected in other galaxies, it was mostly observed in emission. These lines are likely produced by a fluorescence-like mechanism through absorption of IR photons at  $35\mu\text{m}$  and  $75\mu\text{m}$  emitted by warm dust, and thus they trace the warm moderate-dense molecular medium ( $T \sim 150 - 300\text{K}$ ,  $n_{\text{H}_2} \lesssim 10^4 - 10^5\text{cm}^{-3}$ ) in star-forming regions (e.g., Goicoechea & Cernicharo, 2002; Goicoechea et al., 2005). The observed OH line fluxes in our systems are comparable with those of mid- $J$  CO and are greater than those of the  $\text{H}_2\text{O}$  lines, showing that OH can be a powerful tracer of the molecular medium at  $z \sim 6$ . We find similar  $L_{\text{OH-to-TIR}}$  ratios  $\sim 2 - 4 \times 10^{-5}$  in quasars PJ231-20 and PJ308-21, and we estimate a higher value  $\sim 10^{-4}$  in the PJ231-20 companion galaxy. A similar value is found in the SMG AzTEC-3 and HFSL 3 at  $z = 5.3$  and  $z = 6.34$ , respectively (Riechers et al., 2013, 2014).

In **Fig. 6.17** we compare the observed values of the  $\text{H}_2\text{O}$ -to- $\text{OH}_{163\mu\text{m}}$  line ratios with our CLOUDY predictions in a diagnostic plot. We considered  $\text{OH}_{163\mu\text{m}}$  as the sum of the luminosity of the two  $\Lambda$ -doubling transitions of  $\text{OH}_{163\mu\text{m}}$ , including the hyperfine structure lines. For QSO PJ231-20, the model predictions are fully consistent with what we found in **Sect. 6.8.6**. This indicates a high-density medium exposed to a strong FUV field. We also found similar constraints for the companion galaxy and QSO PJ308-21, with  $G_0 > 10^4$  and  $n_{\text{H}} < 1.5 \times 10^4 - 0.5 \times 10^6\text{cm}^{-3}$ , respectively. These findings, albeit for a lower column density, also broadly agree with the constraints obtained from  $[\text{CII}]_{158\mu\text{m}}$ -to- $[\text{CI}]_{369\mu\text{m}}$  ratios and the CO SLED modeling (see **Sects. 6.7.2** and **6.8.2**).

## 6.9 Mass budgets

Starting from the FSL luminosities obtained in this chapter (see **Tab. 6.3**) and adopting simplistic assumptions, we can estimate the mass contributions in our systems in the form of ionized, atomic, and molecular mediums. In the two-level approximation, assuming LTE and in the optically thin limit

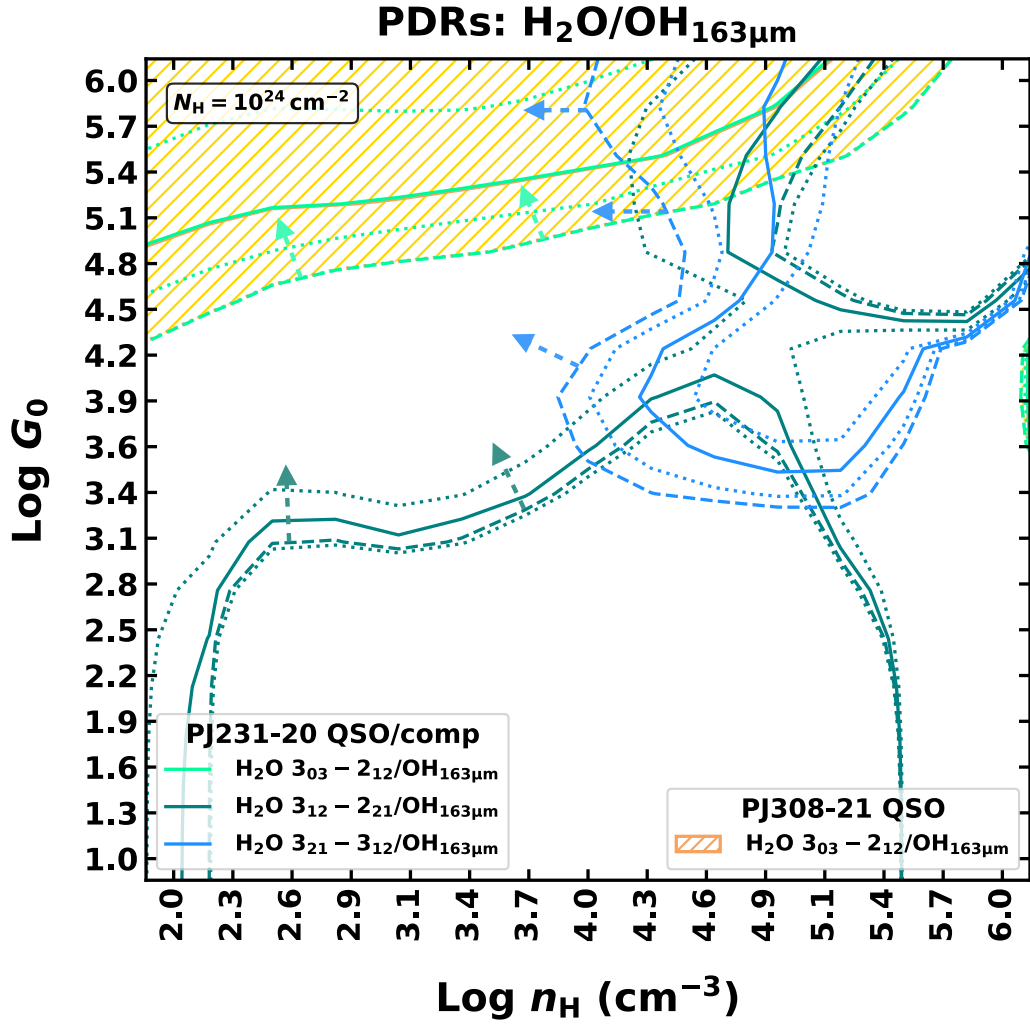


**Figure 6.17**

CLOUDY models of H<sub>2</sub>O/OH<sub>163μm</sub> luminosity ratios. Model predictions are reported for QSO PJ231-20 (solid and dotted lines indicate values and their uncertainties) and 3σ upper limits for its companion (dashed lines). The dashed gold area reports the constraints retrieved from QSO PJ308-21 detections. The clouds' column density of the models is  $N_H = 10^{24} \text{ cm}^{-2}$ .

and Rayleigh-Jeans regime, the beam-averaged column density of a species  $s$  in the upper level  $u$  is (see, e.g., Goldsmith & Langer, 1999)

$$N_s \approx \gamma_u \frac{c^2}{8\pi k_B} \nu_{\text{obs}}^{-2} S \Delta\nu (1+z)^{-1}, \quad (6.7)$$

with

$$\gamma_u = \frac{8\pi k_B \nu_{\text{ul}}^2}{hc^3 A_{\text{ul}}} \frac{Q(T_{\text{ex}})}{g_u} e^{E_u/k_B T_{\text{ex}}}. \quad (6.8)$$

Here,  $S\Delta\nu$  is the observed line velocity-integrated flux,  $A_{ul}$  is the Einstein coefficient,  $Q(T_{\text{ex}})$  is the partition function of the species  $s$  (depending on the excitation temperature  $T_{\text{ex}}$ ), and  $g_u$  and  $E_u$  are the statistical weight and the energy of the upper level, respectively. The total number of particles of species  $s$  is obtained by integrating over the size of the emitting region. Using the definition of line luminosity (Solomon et al., 1992), we can express the total mass of the species  $s$  as

$$M_s = C m_s \gamma_u L'_{\text{line}}, \quad (6.9)$$

where  $C = 9.52 \times 10^{41}$  is the conversion factor between  $\text{km pc}^2$  and  $\text{cm}^3$ , and  $m_s$  is the mass of the species  $s$ . Using Eq. (6.9), we derive the CI mass following Weiß et al. (2003) through

$$M_{\text{CI}}[M_{\odot}] = 4.566 \times 10^{-4} Q(T_{\text{ex}}) \frac{1}{5} e^{62.5/T_{\text{ex}}} L'_{[\text{CI}]_{369\mu\text{m}}}, \quad (6.10)$$

where  $Q(T_{\text{ex}}) = 1 + 3e^{-T_1/T_{\text{ex}}} + 5e^{-T_2/T_{\text{ex}}}$  is the CI partition function, and  $T_1 = 23.6\text{ K}$ ,  $T_2 = 62.5\text{ K}$  are the energies (per unit of  $k_B$ ) above the ground state of the two [CI] ( ${}^3P_1 \rightarrow {}^3P_0$ ) and ( ${}^3P_2 \rightarrow {}^3P_1$ ) transitions, respectively. Assuming an excitation temperature of  $T_{\text{ex}} = 30\text{ K}$  (see, e.g., Walter et al., 2011), we find for QSO PJ231-20 a neutral carbon mass of  $M_{\text{CI}} = (0.7 \pm 0.3) \times 10^7 M_{\odot}$ , and carbon mass limit of  $M_{\text{CI}} < 0.4 - 0.5 \times 10^7 M_{\odot}$  for its companion and the sources in system PJ308-21. We note that if we assumed a higher excitation temperature  $T_{\text{ex}} = 50\text{ K}$ , the derived  $M_{\text{CI}}$  would be  $\sim 40\%$  lower. Using these mass estimates, we can place constraints on the molecular gas mass ( $M_{\text{H}_2}$ ) using the atomic carbon-to-molecular hydrogen abundance ratio derived by Walter et al. (2011) for a sample of  $z = 2 - 3$  FIR-bright sources (SMGs and quasar host galaxies),  $X[\text{CI}]/X[\text{H}_2] = M_{\text{CI}}/(6M_{\text{H}_2}) = (8.4 \pm 3.5) \times 10^{-5}$ . Applying this abundance, we obtain a molecular gas mass of  $M_{\text{H}_2} = 1.3_{-0.6}^{+1.1} \times 10^{10} M_{\odot}$  for QSO PJ231-20 and  $M_{\text{H}_2} < 1.8 \times 10^{10} M_{\odot}$  for the companion galaxy and the other sources in system PJ308-21.

Following Ferkinhoff et al. (2011), in the high-temperature limit, we can also derive the minimum mass of ionized hydrogen ( $\text{H}^+$ ) assuming that all nitrogen in HII regions is singly ionized as

$$M_{\text{min}}(\text{H}^+) = \frac{L_{[\text{NII}]205\mu\text{m}} m_{\text{H}}}{(g_1/Q(T_{\text{ex}})) A_{10} h \nu_{10} \chi(\text{N}^+)} \approx 2.27 \frac{L_{[\text{NII}]205\mu\text{m}}}{L_{\odot}} M_{\odot}, \quad (6.11)$$

where  $A_{10}$  is the Einstein coefficient for spontaneous emission of the  $[\text{NII}]_{205\ \mu\text{m}}$  ( $^3P_1 \rightarrow ^3P_0$ ) transition ( $2.08 \times 10^{-6} \text{ s}^{-1}$ ),  $g_1 = 3$  is the statistical weight of the  $J = 1$  level,  $\nu_{10} = 1461.1318 \text{ GHz}$  is the rest-frame frequency of the transition,  $m_{\text{H}}$  is the mass of the hydrogen atom, and  $\chi(\text{N}^+)$  is the  $\text{N}^+$ -to- $\text{H}^+$  abundance ratio. For the minimum mass case, in our working assumption  $\chi(\text{N}^+) = \chi(\text{N})$ . When we assume solar metallicity, the HII-region gas-phase nitrogen abundance therefore is  $\chi(\text{N}) = 9.3 \times 10^{-5}$  (Savage & Sembach, 1996). This gives  $M_{\text{min}}(\text{H}^+) = (4.1 \pm 1.6) \times 10^8 M_{\odot}$ , and  $(1.8 \pm 1.2) \times 10^8 M_{\odot}$  for the PJ231-20 QSO host and companion galaxy, respectively.

Starting from the dust mass budgets derived in **Sect. 6.5**, we can also obtain independent measurements of the gas masses adopting the local gas-to-dust ratio of  $\delta_{\text{gdr}} \sim 70 - 100$  (see, e.g., Draine et al., 2007; Sandstrom et al., 2013; Genzel et al., 2015). A similar gas-to-dust ratio of  $\sim 70$  has also been found in high- $z$  starburst galaxies (e.g., Riechers et al., 2013; Wang et al., 2016). Adopting the local value, we obtain (atomic and molecular) gas masses of  $M_{\text{gas}} = (3.6 - 5.1) \times 10^{10} M_{\odot}$  and  $(1.6 - 3.4) \times 10^{10} M_{\odot}$  for the PJ231-20 QSO host and companion galaxy, respectively, and  $M_{\text{gas}} = (3.8 - 5.4) \times 10^9 M_{\odot}$  and  $(0.7 - 2.0) \times 10^9 M_{\odot}$  for the PJ308-20 QSO host and companion galaxy, respectively. When we further assume that  $\sim 75\%$  of the dust-derived gas mass is in molecular form (e.g., Riechers et al., 2013; Wang et al., 2016), these values are consistent with those derived above from  $M_{\text{Cl}}$  applying the  $\text{Cl}$ -to- $\text{H}_2$  abundance ratio.

Finally, from the gas mass values derived above, we obtain a lower limit on the gas ionization percentage of  $M_{\text{min}}(\text{H}^+)/M_{\text{H}_2} > 1 - 3\%$ . For comparison, Ferkinhoff et al. (2011) found values  $< 1\%$  for nearby galaxies (in the sample of Brauher et al. 2008), while high-ionization percentages suggest a high SFR density ( $> 10^2 - 10^3 M_{\odot} \text{ yr}^{-1} \text{ kpc}^{-2}$ , see Ferkinhoff et al. 2011).

## 6.10 Summary and conclusions

In this chapter we have presented ALMA observations of two quasar host-companion galaxy pairs PJ231-20 and PJ308-21 at  $z > 6$ , captured when the Universe is  $< 900 \text{ Myr}$  old. The companion galaxies were serendipitously discovered with previous ALMA observations in the field of known quasars, but they show no evidence of AGN activity. This multiline study investigated

the effect of the star formation and AGN activity on the ISM in massive galaxies at the cosmic dawn.

The lines covered in the ALMA observations include tracers of the atomic ionized or neutral and molecular medium, such as  $[\text{NII}]_{205\ \mu\text{m}}$ ,  $[\text{CI}]_{369\ \mu\text{m}}$ ,  $\text{CO}(7-6, 10-9, 15-14, 16-15)$ ,  $\text{H}_2\text{O } 3_{12}-2_{21}$ ,  $3_{21}-3_{12}$ ,  $3_{03}-2_{12}$ , and the  $\text{OH}_{163\ \mu\text{m}}$  doublet. However, for system PJ308-21, only half of the program was executed. This work was complemented with previously collected ALMA  $[\text{CII}]_{158\ \mu\text{m}}$  observations (Decarli et al., 2018) that were analyzed in a consistent way. In order to interpret our results and place quantitative constraints on the physical properties of the ISM in galaxies, we ran a set of PDR/XDR models by employing the CLOUDY radiative transfer code for which we varied the volume hydrogen density, radiation field strength, and total hydrogen column density. The main results obtained in this chapter are summarized below.

- We modeled the FIR dust continuum on all the four targeted galaxies. We modeled this emission as a modified blackbody and inferred dust masses, spectral indexes, total IR luminosities, and SFRs (see **Sect. 6.5** and **Tab. 6.4**).
- From the analysis of the  $[\text{CII}]_{158\ \mu\text{m}}$  and  $[\text{NII}]_{205\ \mu\text{m}}$  lines, we found that  $\gtrsim 80\%$  of  $[\text{CII}]_{158\ \mu\text{m}}$  emission in the quasar and companion galaxies of system PJ231-20 arises from neutral gas in the photodissociation regions rather from the fully (diffuse) ionized medium. Furthermore, the observed line deficits are comparable with those of local LIRGs.
- The  $[\text{CI}]_{369\ \mu\text{m}}/\text{TIR}$  luminosity ratios in the targeted systems are similar to those measured in  $z \sim 2-4$  SMGs and quasars, revealing a high star-formation efficiency in our galaxies.
- CLOUDY models suggest that  $[\text{CII}]_{158\ \mu\text{m}}$  and  $[\text{CI}]_{369\ \mu\text{m}}$  emission predominantly arises in PDRs illuminated by the FUV radiation field. In particular, constraints obtained from the  $[\text{CII}]_{158\ \mu\text{m}}$ -to-TIR and  $[\text{CI}]_{369\ \mu\text{m}}$ -to-TIR luminosity ratios for QSO PJ231-20 indicate a high FUV field intensity of  $G_0 \sim 10^5$  ( $\sim 1.6 \times 10^2 \text{ erg s}^{-1} \text{ cm}^{-2}$ ) and density of  $n_{\text{H}} > 10^3$ . We found similar constraints for the other sources.
- From the atomic fine-structure lines, we retrieved constraints on atomic carbon, ionized hydrogen, and molecular gas masses. The latter are

consistent with the dust-derived gas masses assuming the local gas-to-dust ratio and that  $\sim 75\%$  of the gas mass is in molecular form. For the quasar and companion in system PJ231-20, we also inferred gas ionization percentages of  $> 1 - 3\%$ , which is greater than the typical values observed in nearby galaxies, suggesting a high SFR density  $> 10^2 - 10^3 M_{\odot} \text{ yr}^{-1} \text{ kpc}^{-2}$ .

- The multiple mid- and high- $J$  CO line detections allowed us to study the CO SLEDs (see **Sect. 6.8.1**). Despite large uncertainties, the QSO PJ231-20 SLED resembles those of local AGN. A similar result is obtained for the companion galaxy. On the other hand, when we assumed a low dust temperature of 35 K, the CO SLED of the companion appears similar to the average SLED of local starburst galaxies. However, the mere detections of high- $J$  ( $J_{\text{up}} = 16, 15$ ) CO lines in the PJ231-20 and PJ308-21 quasars suggest an additional heating source that is not the PDRs. The CO SLED of QSO PJ231-20 is well reproduced by a CLOUDY PDR+XDR composite model. The result indicates that PDRs dominate the low- and mid- $J$  CO line luminosities and account for  $\sim 90\%$  of the CO mass, while XDRs, which may be the main drivers of high- $J$  CO emission lines, contribute to  $\sim 10\%$  of the mass. The latter likely resides in the central regions of the PJ231-20 QSO host galaxy, exposed to strong X-ray radiation due to the BH accretion. The best-fit PDR component indicates  $n_{\text{H}}^{\text{PDR}} \sim 4 \times 10^2 \text{ cm}^{-3}$  and  $G_0 \sim 1 \times 10^5$ , and the XDR component is determined by  $n_{\text{H}}^{\text{XDR}} \sim 5 \times 10^5 \text{ cm}^{-3}$  and  $F_{\text{X}} \sim 10 \text{ erg s}^{-1} \text{ cm}^{-2}$ . However, because we have only a few data points, these results are affected by degeneracies.
- We detected three H<sub>2</sub>O lines ( $3_{12} - 2_{21}$ ,  $3_{21} - 3_{12}$ , and  $3_{03} - 2_{12}$ ) in QSO PJ231-20, and H<sub>2</sub>O  $3_{03} - 2_{12}$  in QSO PJ308-21. The QSO PJ231-20 lies on the  $L_{\text{H}_2\text{O}} \propto L_{\text{TIR}}^{1.1-1.2}$  trend found for low- $z$  sources, suggesting that the H<sub>2</sub>O  $3_{21} - 3_{12}$  line is predominantly excited by pumping of IR photons of the dust UV-reprocessed radiation field. The  $L_{\text{H}_2\text{O}}$ -to- $L_{\text{TIR}}$  ratios in the PJ231-20 and PJ308-21 systems are  $\sim 10^{-5}$ , which is within the range observed in starburst galaxies at low  $z$ . The observed H<sub>2</sub>O SLED in QSO PJ231-20 indicates that collisional excitation of the upper energy levels of the observed water vapor transitions is likely minor. Furthermore, the SLED is similar to that of other high- $z$  sources.

CLOUDY best-fit models are obtained using a single PDR component with  $n_{\text{H}} \sim 0.8 \times 10^5 \text{ cm}^{-3}$ ,  $G_0 \sim 5 \times 10^5$  and a high hydrogen column density of  $N_{\text{H}} = 10^{24} \text{ cm}^{-2}$ , indicating that  $\text{H}_2\text{O}$  emission arises deeply in the molecular clouds with a high density, exposed to a strong radiation field.

- The  $\text{H}_2\text{O}$ -to- $\text{OH}_{163\mu\text{m}}$  ratios in QSO PJ231-20 predicted by CLOUDY are fully consistent with the results obtained from the  $\text{H}_2\text{O}$  SLED modeling, indicating that  $\text{OH}_{163\mu\text{m}}$  doublet emission likely arises from similar regions traced by water vapor. We found similar constraints, but with large uncertainties, for the PJ231-20 companion galaxy and QSO PJ308-21, indicating that the ISM is exposed to strong FUV radiation field with  $G_0 > 10^4$ . These results also broadly agree with the analysis of CO and atomic fine-structure lines.

In conclusion, in quasars PJ231-20 and PJ308-21, the AGN activity is mainly revealed through high- $J$  CO line emission, requiring an additional source of heating other than PDRs, which might be provided by a strong X-ray radiation field. The CO SLEDs in conjunction with the nondetections of high- $J$  CO lines in companions, at least for PJ231-20, suggest a less excited medium, possibly as a consequence of the lack of a strong AGN as suggested by previous optical/UV and X-rays observations. Then, the analysis of the atomic fine-structure and molecular lines, in conjunction with the analysis of  $\text{H}_2\text{O}$  and  $\text{OH}_{163\mu\text{m}}$  transitions, indicates a strong radiation field in the quasar host and companion galaxies associated with massive episodes of star formation, as reflected by the enormous amount of dust ( $M_{\text{dust}} \approx 0.5 \times 10^8 - 0.5 \times 10^9 M_{\odot}$ ) heated at relatively high temperature and huge gas reservoir ( $M_{\text{gas}} \gtrsim 10^{10} M_{\odot}$ ) and high star-formation efficiencies. However, although our analysis of the ISM properties highlights differences in the quasars and their companion galaxies, the current data do not allow us to definitively rule out the presence of an AGN in the companions, especially for the PJ308-21 companion galaxy, for which there is little information due to the lack of line detections.

This work demonstrates the power of mm-wavelength observations in dissecting ISM properties of quasar hosts and SMGs at cosmic dawn. Future deeper follow-up observations have to be conducted in order to achieve a higher S/N and sample additional FIR emission lines to further push our analysis.

Moreover, extending this line of research to larger samples of galaxies with and without AGN will provide us with a robust statistical framework to explore the interplay between AGN and star formation in extreme conditions at early cosmic epochs.



# 7

## Unveiling the warm dense gas in $z > 6$ quasars via water vapor emission

“It is not because things are difficult that we do not dare; it is because we do not dare that things are difficult.

— Lucius Annaeus Seneca

This chapter is taken from “*Unveiling the warm dense phase of the ISM in  $z > 6$  quasar host galaxies via  $H_2O$  emission*”, Pensabene A., van der Werf P., Decarli R., et al. (in prep.). This project was carried out in collaboration with P. van der Werf and his group at Leiden Observatory (Leiden University, The Netherlands).

### 7.1 Introduction

Water vapor is the strongest molecular emitter after high- $J$  CO transitions in the ISM of IR-bright galaxies (see, e.g., Omont et al., 2013; Yang et al., 2016a).  $H_2O$  lines are excited in shocked-heated regions, outflowing gas, and in the warm dense molecular gas (see, Sects. 3.5, 5.2.2; and references therein) where the star-formation ultimately occurs. Therefore, unlike other tracers traditionally used to study the dense gas (such as CO and HCN, see Sect. 5.2.2), water vapor probes star-forming regions deeply buried in dust or heated gas in extreme environments of AGN. On the down side, the

complexity of H<sub>2</sub>O radiative spectrum implies that the excitation mechanism and ISM physical conditions cannot be derived on the basis of the detection of a single line (see, e.g., González-Alfonso et al., 2014; Liu et al., 2017, and Sect. 5.2.2). Both collisions and absorption of resonant radiation contribute to the excitation of H<sub>2</sub>O levels. In particular, IR radiative pumping is the main excitation mechanism of the high-*J* H<sub>2</sub>O lines. This implies that water vapor emission not only provides us with insights on the physical properties of the warm dense medium, but also with key information on the local IR radiation field. Furthermore, water lines show P-Cygni profiles that are unambiguously associated with massive molecular outflows (see, e.g., Fischer et al., 2010; González-Alfonso et al., 2010, 2012; van der Werf et al., 2011; Liu et al., 2017). The flip side of the study of water lines in distant galaxies is that, due to its complex radiative properties a full suite of lines needs to be sampled in order to infer quantitative estimates of the various parameters at play. However, so far only sporadic H<sub>2</sub>O detections in some high-*z* sources are available thus far (Riechers et al., 2013; Yang et al., 2019c; Li et al., 2020b), thus leaving the warm and dense molecular phase at *z* > 6 largely uncharted.

The recently upgraded NOEMA telescope has marked a rapid change of gear for (sub-)mm observations of distant galaxies in the Northern sky. Thanks to the new wide-band high-performance correlator PolyFix, in synergy with the ten 15-m NOEMA antennas that have increased the sensitivity of the telescope, we are able to target simultaneously many different FIR diagnostics. In particular, at redshift *z* > 6, many interesting dipole transitions of H<sub>2</sub>O molecule are redshifted in the NOEMA bands.

This chapter is focused on the characterization of the warm dense ISM and the local IR radiation field in three *z* > 6 quasar host galaxies, J2310+1855, J1148+5251, and J0439+1634. For these objects, [CII]<sub>158μm</sub>, multiple CO lines, and other ISM probes (including sparse H<sub>2</sub>O lines), together with dust continuum, were previously detected (Bertoldi et al., 2003; Robson et al., 2004; Walter et al., 2004, 2009; Maiolino et al., 2005, 2012; Beelen et al., 2006; Riechers et al., 2009; Wang et al., 2011, 2013; Leipski et al., 2013; Gallerani et al., 2014; Ciccone et al., 2015; Feruglio et al., 2018; Carniani et al., 2019; Hashimoto et al., 2019b; Shao et al., 2019; Yang et al., 2019c; Li et al., 2020a,b; Yue et al., 2021). Here we present NOEMA 2-mm band

observations toward J2310+1855, J1148+5251, and J0439+1634, targeted in their four ortho-/para-H<sub>2</sub>O rotational lines ( $3_{12} - 3_{03}$ ,  $1_{11} - 0_{00}$ ,  $2_{20} - 2_{11}$ , and  $4_{22} - 4_{13}$ ), together with the underlying FIR dust continuum. The targeted lines cover a wide range in H<sub>2</sub>O energy levels. After combining information from such tracers, in conjunction with data retrieved from literature, we performed radiative transfer analysis by employing MOLPOP-CEP radiative transfer code (Asensio Ramos & Elitzur, 2018). This enabled us to study the H<sub>2</sub>O excitation mechanisms and to put constraints on the physical properties of the warm dense phase of the ISM and the local IR dust radiation field in quasar host galaxies at cosmic dawn. We also use our detections to study the H<sub>2</sub>O-IR luminosities relations.

This chapter is organized as follows: in **Sect. 7.2** we present our sample, the NOEMA observations, and we describe the data processing. In **Sect. 7.3** we outline the characteristics of H<sub>2</sub>O emission lines and their excitation mechanism. In **Sect. 7.4** we describe the analysis of the calibrated data, and we report the H<sub>2</sub>O line and FIR continuum measurements toward our three quasar host galaxies. In **Sect. 7.5** we focus on the dust properties inferred from the analysis of the FIR dust continuum. In **Sect. 7.6** we describe the setup of our radiative transfer models obtained with MOLPOP-CEP code. In **Sect. 7.7** we compare our measurements with other studies in the literature and we present and discuss our results obtained by modeling the H<sub>2</sub>O lines. Finally, in **Sect. 7.8** we summarize the results and we draw our conclusions.

Throughout this chapter we assume a standard  $\Lambda$ CDM cosmology with  $H_0 = 67.7 \text{ km s}^{-1} \text{ Mpc}^{-1}$ ,  $\Omega_m = 0.307$ ,  $\Omega_\Lambda = 1 - \Omega_m$  from Planck Collaboration et al. (2016).

## 7.2 Observations and data reduction

The goal of this work is to capitalize on multiple H<sub>2</sub>O lines in order to unveil their excitation mechanisms and to characterize the warm dense molecular ISM and the local dust IR radiation field in a sample of  $z > 6$  IR-bright quasar host galaxies. For these purposes, the quasars J2310+1855 ( $z = 6.00$ ), J1148+5251 ( $z = 6.42$ ) and J0439+1634 ( $z = 6.52$ ), are ideal targets visible from the NOEMA site. They are among the IR-brightest of all known quasars at  $z \lesssim 6$ . For this reason, on the basis of the observed (almost

**Table 7.1:** The sample of quasars studied in this work

| Object ID                | Short name | R.A.<br>(J2000.0) | DEC.<br>(J2000.0)                                    | $z_{[\text{CII}]}$ <sup>(1)</sup> |
|--------------------------|------------|-------------------|--|-----------------------------------|
| SDSS J231038.88+185519.7 | J2310+1855 | 23°10′38″.882     | 18 <sup>h</sup> 55 <sup>m</sup> 19 <sup>s</sup> .700 | 6.0031                            |
| SDSS J114816.64+525150.3 | J1148+5251 | 11°48′16″.652     | 52 <sup>h</sup> 51 <sup>m</sup> 50 <sup>s</sup> .440 | 6.4189                            |
| 2MASS J04394708+1634160  | J0439+1634 | 04°39′47″.110     | 16 <sup>h</sup> 34 <sup>m</sup> 15 <sup>s</sup> .820 | 6.5188                            |

**Notes.** <sup>(1)</sup>Redshift of the source estimated from  $[\text{CII}]_{158\mu\text{m}}$  line (see, Maiolino et al., 2005; Wang et al., 2013; Yang et al., 2019c).

linear) correlation between  $\text{H}_2\text{O}$  and IR luminosities (Yang et al., 2013; Liu et al., 2017), they are expected to have bright  $\text{H}_2\text{O}$  lines. In addition they are previously detected in some  $\text{H}_2\text{O}$  lines (Yang et al. 2019c; Li et al. 2020a, and Riechers et al. in prep.; see **Tab. 7.3**) that we use here to complement our analysis. We note that the J0439+1634 is a lensed source with a host galaxy magnification factor in the range 2.6-6.6 (95% confidence interval; see, Fan et al. 2019; Yang et al. 2019c). All the quantities reported in this chapter for J0439+1634 have to be intended as purely observed quantities (unless differently specified). In **Tab. 7.1** we summarize the properties of our sample.

We observed the targeted quasars using the IRAM/NOEMA interferometer in compact (C or D) array configuration (project ID: S19DL). The PolyFix band 2 receiver was tuned to secure the 1080 – 1130 GHz and 1190 – 1245 GHz rest-frame frequency windows in the LSB and USB respectively.

The quasar J2310+1855 was observed on October 12 and November 10, 2019. The blazar 3C454.3 was observed as phase and amplitude calibrator, while absolute flux scale and the bandpass were set by observing the MWC349 calibrator. The precipitable water vapor (PWV) column density was 8-10 mm in the October track, and 4-6 mm in the November one. The quasar J1148+5251 was observed on September 09, 2019. We observed the sources 3C84 and LKHA101 as flux and bandpass calibrators. The PWV during the observations was 2-6 mm. Finally, J0439+1634 was observed on August 09, 13, and 14, 2019. The sources 3C84, 3C454.3, MWC349, and LKHA101 were used as flux and bandpass calibrators, while the radio-loud quasar 0446+112 acted as phase and amplitude calibrator. The PWV was 8–12 mm in the first visit, and 2–4 mm in the other tracks.

We used the CLIC software in the GILDAS suite (February 2020 version) to reduce and calibrate the data. The high PWV and consequently high system temperature ( $> 200$  K at the tuning frequencies) led to poor phase RMS residuals in the August 09, 13 and October 12 tracks, which were thus flagged out. The calibrated cubes have 8726, 9090, and 6690 visibilities for J2310+1855, J1148+5251 and J0439+1634 respectively, corresponding to 3.0, 3.2, and 2.3 hr on source (9 antennas equivalent).

We adopted the MAPPING software in the GILDAS suite to invert the visibilities and image the cube. The half power primary beam width is  $29.2''$ ,  $31.0''$ , and  $31.4''$  at the tuning frequencies of the three quasars (172.443 GHz, 162.776 GHz, and 160.612 GHz for J2310+1855, J1148+5251, and J0439+1634, respectively). Using natural weighting of the visibilities, we obtain synthesized beams of  $1.47'' \times 0.79''$ ,  $2.45'' \times 2.13''$ , and  $2.81'' \times 2.51''$ . We resampled the cubes adopting a channel width of  $50 \text{ km s}^{-1}$ . The achieved median RMS per channel in the LSB and USB respectively are  $0.61 \text{ mJy beam}^{-1}$  and  $1.50 \text{ mJy beam}^{-1}$  for J2310+1855,  $0.42 \text{ mJy beam}^{-1}$  and  $0.60 \text{ mJy beam}^{-1}$  for J1148+5251, and  $0.52 \text{ mJy beam}^{-1}$ ,  $0.66 \text{ mJy beam}^{-1}$  in the case of J0439+1634 observations.

## 7.3 Overview on the H<sub>2</sub>O emission lines

In **Fig. 7.1** we show the ladder structure of H<sub>2</sub>O molecule (limited to energy levels  $< 500$  K). In the figure we indicate the H<sub>2</sub>O transitions targeted in our NOEMA program together with the additional lines reported in literature for our three targeted quasars. The properties of the transitions such as the energy of the upper levels ( $E_{\text{up}}$ ), the rest frequencies ( $\nu_{\text{rest}}$ ), and the Einstein A coefficients for spontaneous emission, are summarized in **Tab. 7.2**.

As we discussed in **Sect. 5.2.2**, the excitation of water vapor molecule is very sensitive to the physical conditions of the line emitting region. As revealed by previous studies (e.g., González-Alfonso et al., 2012, 2014; Liu et al., 2017), low-level transitions ( $E_{\text{up}} < 250$  K) arise in warm collisionally-excited gas ( $T_{\text{kin}} \sim 30 - 50$  K,  $n_{\text{H}} \sim 10^5 \text{ cm}^{-3}$ ) that drives the low level populations toward the Boltzmann distribution with excitation temperature ( $T_{\text{ex}}$ ) equal to the gas kinetic temperature ( $T_{\text{kin}}$ ). This may occur even in environments with density well below the critical one ( $n_{\text{crit}} \sim 10^7 - 10^9 \text{ cm}^{-3}$ ; see e.g., Faure et al. 2007)

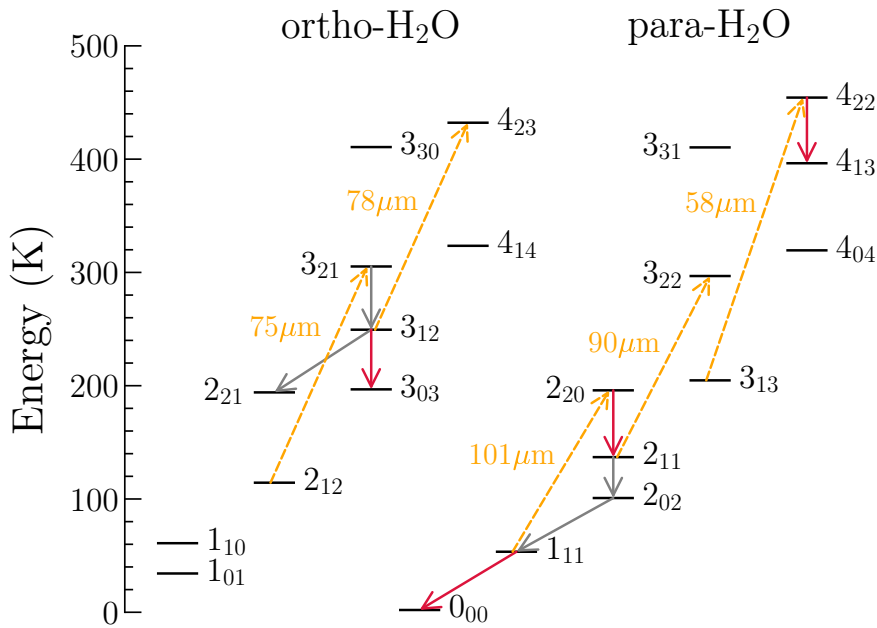


**Figure 7.1**

Energy level diagram of  $\text{H}_2\text{O}$ . Downward solid red and gray arrows are the transitions reported in this chapter and those available in the literature (see Yang et al. 2019c, Li et al. 2020b, Riechers et al., in prep.). The upward dashed orange arrows indicate the FIR  $\text{H}_2\text{O}$  pumping (absorption) lines. The respective wavelengths are also reported.

due to the large optical depth of such  $\text{H}_2\text{O}$  lines and radiative trapping effect that lowers the effective density at which the lines appear to be thermalized (see, e.g., Poelman et al., 2007). The high-lying  $\text{H}_2\text{O}$  lines require instead radiative excitation by far-IR photons from warm dust ( $T_{\text{dust}} \sim 70 - 100\text{K}$ ) that are then re-emitted through a fluorescence process. This is illustrated in **Fig. 7.1**, where three far-IR pumping lines ( $58\ \mu\text{m}$ ,  $75\ \mu\text{m}$ ,  $101\ \mu\text{m}$ ) account for the radiative excitation of sub-mm lines. Interestingly, the low-excitation lines ( $E_{\text{up}} < 150\text{K}$ ) are predicted to become weaker or completely disappear under the continuum level for increasing the dust temperature (e.g., Liu et al., 2017). In particular, the para- $\text{H}_2\text{O}$  ground state transition  $1_{11} - 0_{00}$  is not involved in any IR-pumping cycle and its flux is predicted to be negligible in regions where the IR pumping dominates. Indeed, the upper level  $1_{11}$  can be populated only by absorption of line photons at  $269\ \mu\text{m}$ , or by a collisional event. This implies that, in absence of significant collisional excitation (i.e. high gas density and gas temperature), the  $\text{H}_2\text{O}$   $1_{11} - 0_{00}$  line will be mainly detected in absorption in case of significant  $269\ \mu\text{m}$  continuum opacity (e.g.,

**Table 7.2:** List of targeted H<sub>2</sub>O emission lines in the quasars.

| Transition   | $\nu_{\text{rest}}^{(1)}$<br>(GHz) | $E_{\text{up}}^{(2)}$<br>(K) | $\text{Log}A_{ij}^{(3)}$<br>(s <sup>-1</sup> ) |
|--|------------------------------------|------------------------------|--|
| H <sub>2</sub> O 1 <sub>11</sub> – 0 <sub>00</sub> | 1113.343                           | 60.963                       | –1.73  |
| H <sub>2</sub> O 2 <sub>02</sub> – 1 <sub>11</sub> | 987.927                            | 100.845                      | –2.23  |
| H <sub>2</sub> O 2 <sub>11</sub> – 2 <sub>02</sub> | 752.033                            | 136.937                      | –2.15  |
| H <sub>2</sub> O 2 <sub>20</sub> – 2 <sub>11</sub> | 1228.789                           | 195.909                      | –0.58  |
| H <sub>2</sub> O 3 <sub>12</sub> – 3 <sub>03</sub> | 1097.365                           | 249.435                      | –1.78  |
| H <sub>2</sub> O 3 <sub>12</sub> – 2 <sub>21</sub> | 1153.127                           | 249.435                      | –2.57  |
| H <sub>2</sub> O 3 <sub>21</sub> – 3 <sub>12</sub> | 1162.912                           | 305.247                      | –1.64  |
| H <sub>2</sub> O 4 <sub>22</sub> – 4 <sub>13</sub> | 1207.639                           | 454.337                      | –1.55  |

**Notes.** <sup>(1)</sup>Rest frequency. <sup>(2)</sup>Energy of the upper level of the transition in units of Boltzmann constant. <sup>(3)</sup>Base-10 logarithm of the Einstein A coefficient for spontaneous emission. Data are taken from the "Splatalogue database for astronomical spectroscopy" available at <https://www.cv.nrao.edu/php/splat>, see references therein.

González-Alfonso et al., 2004; Rangwala et al., 2011). On the other hand, in warm gas region with low continuum opacity, the ground state transition is expected to be detected in emission. In this case, the 1<sub>11</sub> level will be significantly populated by collisions thus enhancing the IR pumping cycle by absorption of 101  $\mu\text{m}$  photons and boosting the  $J = 2$  para-H<sub>2</sub>O lines.

In our NOEMA program we detected up to three para-/ortho-H<sub>2</sub>O lines in each quasars that we complemented with other  $J = 2$ , and  $J = 3$  H<sub>2</sub>O lines from literature (Yang et al., 2019c; Li et al., 2020b, Riechers et al. in prep.; see **Tab. 7.3**). This dataset allows us to cover a wide range of energy of H<sub>2</sub>O levels ( $50\text{ K} < E_{\text{up}} < 500\text{ K}$ ), thus enabling for the first time a comprehensive analysis of the H<sub>2</sub>O energetics in these high- $z$  quasars.

## 7.4 Line and continuum measurements

Since our sources are not spatially resolved in the observations, we obtained the beam-integrated spectra by performing single-pixel extraction at the nominal coordinates of the targets from the data-cubes including the continuum emission. We then performed spectral fitting with a composite model including a single Gaussian component for the line and a constant for the continuum. We sampled the parameter space by using the MCMC ensemble

sampler python package `emcee` (Foreman-Mackey et al., 2013). This procedure allows us to effectively sample the posterior probability space. As data uncertainties in the likelihood estimates, we assume the  $1\text{-}\sigma$  Gaussian RMS of each imaged channel, and we neglected any systematic term. We therefore obtained the posterior probability distributions of the free parameters from which we derived the line and continuum measurements by computing the 50th percentile as the nominal values, and the 16th, 84th percentile as  $1\text{-}\sigma$  statistical uncertainties. We then derived the line luminosities as (see, e.g., Carilli & Walter, 2013) using Eqs. (6.1) and (6.2). We show the spectra of the sources with the best-fit models in Fig. 7.2 and we report the derived quantities in Tab. 7.3. In the table we also list for convenience the additional  $\text{H}_2\text{O}$  line detections retrieved from the literature. We note that, as also reported by Yang et al. (2019c), all our observed  $\text{H}_2\text{O}$  lines in J0439+1634 are well fitted by a single Gaussian profile thus suggesting that a contribution from differential lensing affecting the kinematics structure of this source could be likely minor (see, e.g., Rivera et al., 2019; Yang et al., 2019a). However, only with future (sub-)mm high-resolution observations, the details of the differential lensing effect will be quantified.

Throughout this chapter, we report the significance on the measured line fluxes in unit of  $\sigma = \sqrt{\Delta\nu \text{FWHM}} \times \langle \text{RMS} \rangle$ , where  $\Delta\nu$  is the channel width ( $50 \text{ km s}^{-1}$ ), FWHM is the full width at half maximum of the line best-fit Gaussian (in  $\text{km s}^{-1}$ ), and the  $\langle \text{RMS} \rangle$  is the median RMS noise of the line cube (see Sect. 7.2). In the cases in which a line emission is not detected in the spectra, we report  $3\sigma$  upper limits assuming  $\text{FWHM} = 300 \text{ km s}^{-1}$ .

## 7.5 Dust properties from FIR continuum

The FIR continuum flux densities are key measurements to constrain the dust physical properties of galaxies. As we discussed Sect. 5.2.3, the observed dust continuum can be expressed in terms of the dust mass ( $M_{\text{dust}}$ ) and the dust opacity  $\tau(\nu)$  via Eq. (5.2). The latter equation provides us with a useful formula to estimate the dust mass and temperature from the observed (sub-)mm continuum flux densities. However, it depends on largely unknown parameters such as the  $\tau(\nu)$ , and the dust mass absorption coefficient  $k_{\text{d}}(\nu)$  which are difficult to be determined. For our quasars, only detections at rest-frame  $\lambda > 40 \mu\text{m}$  are available from literature. This limitation prevents

**Table 7.3:** Measurements and derived quantities of the NOEMA spectra of the quasars.

| J2310+1855                            |                              |                                |  |   |  |                               |                        |                     |
|---------------------------------------|------------------------------|--------------------------------|--|---|--|-------------------------------|------------------------|---------------------|
| Emission line                         | $z_{\text{line}}$            | FWHM<br>( $\text{km s}^{-1}$ ) | $S\Delta v$<br>( $\text{Jy km s}^{-1}$ ) | $L_{\text{line}}$<br>( $10^9 L_{\odot}$ ) | $L'_{\text{line}}$<br>( $10^{10} \text{K km s}^{-1} \text{pc}^2$ ) | Dust continuum <sup>(1)</sup> | $S_{\nu}$<br>(mJy)     | Ref. <sup>(2)</sup> |
| $\text{H}_2\text{O } 3_{12} - 3_{03}$ | $6.0037^{+0.0018}_{-0.0017}$ | $494^{+140}_{-128}$            | $0.61^{+0.16}_{-0.15}$                   | $0.35^{+0.09}_{-0.09}$                    | $0.8^{+0.2}_{-0.2}$  | 158.207 GHz                   | $1.77^{+0.04}_{-0.04}$ | This work           |
| $\text{H}_2\text{O } 1_{11} - 0_{00}$ | —                            | —                              | $< 0.23$                                 | $< 0.13$                                  | $< 0.30$   |                               |                        |                     |
| $\text{H}_2\text{O } 4_{22} - 4_{13}$ | $6.0047^{+0.0013}_{-0.0022}$ | $314^{+328}_{-132}$            | $0.6^{+0.3}_{-0.2}$                      | $0.35^{+0.16}_{-0.13}$                    | $0.6^{+0.3}_{-0.2}$  | 173.738 GHz                   | $2.27^{+0.08}_{-0.08}$ |                     |
| $\text{H}_2\text{O } 2_{20} - 2_{11}$ | —                            | —                              | $< 0.55$                                 | $< 0.35$                                  | $< 0.59$   |                               |                        |                     |
| $\text{H}_2\text{O } 2_{02} - 1_{11}$ |                              |                                | $0.70 \pm 0.05$                          | $0.36 \pm 0.03$                           | $1.16 \pm 0.08$  | 141.070 GHz                   | $1.42 \pm 0.03$        | Li+20               |
| $\text{H}_2\text{O } 3_{12} - 2_{21}$ |                              |                                | $0.53 \pm 0.17$                          | $0.32 \pm 0.10$                           | $0.7 \pm 0.2$  | 164.496 GHz                   | $2.33 \pm 0.11$        | Riechers+           |
| $\text{H}_2\text{O } 3_{21} - 3_{12}$ |                              |                                | $1.25 \pm 0.17$                          | $0.76 \pm 0.10$                           | $1.5 \pm 0.2$  |                               |                        |                     |
| J1148+5251                            |                              |                                |  |   |  |                               |                        |                     |
| $\text{H}_2\text{O } 3_{12} - 3_{03}$ | $6.4192^{+0.0007}_{-0.0009}$ | $337^{+110}_{-77}$             | $0.47^{+0.10}_{-0.09}$                   | $0.30^{+0.06}_{-0.06}$                    | $0.70^{+0.15}_{-0.13}$   | 148.510 GHz                   | $0.50^{+0.03}_{-0.03}$ | This work           |
| $\text{H}_2\text{O } 1_{11} - 0_{00}$ | $6.415^{+0.003}_{-0.004}$    | $789^{+261}_{-256}$            | $0.36^{+0.14}_{-0.13}$                   | $0.23^{+0.09}_{-0.09}$                    | $0.52^{+0.20}_{-0.19}$   |                               |                        |                     |
| $\text{H}_2\text{O } 4_{22} - 4_{13}$ | —                            | —                              | $< 0.21$                                 | $< 0.15$                                  | $< 0.25$   | 164.202 GHz                   | $0.70^{+0.03}_{-0.03}$ | This work           |
| $\text{H}_2\text{O } 2_{20} - 2_{11}$ | $6.416^{+0.003}_{-0.003}$    | $790^{+214}_{-223}$            | $0.64^{+0.20}_{-0.19}$                   | $0.45^{+0.14}_{-0.14}$                    | $0.8^{+0.2}_{-0.2}$  |                               |                        |                     |
| $\text{H}_2\text{O } 2_{11} - 2_{02}$ |                              |                                | $0.37 \pm 0.13$                          | $0.16 \pm 0.06$                           | $1.2 \pm 0.4$  | 101.367 GHz                   | $0.22 \pm 0.06$        | Riechers+           |
| $\text{H}_2\text{O } 2_{02} - 1_{11}$ |                              |                                | $0.24 \pm 0.10$                          | $0.14 \pm 0.06$                           | $0.44 \pm 0.18$  | 133.164 GHz                   | $0.48 \pm 0.05$        |                     |
| $\text{H}_2\text{O } 3_{12} - 2_{21}$ |                              |                                | $0.33 \pm 0.11$                          | $0.22 \pm 0.07$                           | $0.44 \pm 0.15$  | 155.277 GHz                   | $0.84 \pm 0.04$        |                     |
| $\text{H}_2\text{O } 3_{21} - 3_{12}$ |                              |                                | $0.63 \pm 0.07$                          | $0.42 \pm 0.05$                           | $0.83 \pm 0.09$  |                               |                        |                     |
| J0439+1634                            |                              |                                |  |   |  |                               |                        |                     |
| $\text{H}_2\text{O } 3_{12} - 3_{03}$ | $6.5195^{+0.0004}_{-0.0004}$ | $372^{+44}_{-39}$              | $1.27^{+0.13}_{-0.12}$                   | $0.82^{+0.08}_{-0.08}$                    | $1.93^{+0.19}_{-0.19}$   | 146.535 GHz                   | $3.28^{+0.03}_{-0.03}$ | This work           |
| $\text{H}_2\text{O } 1_{11} - 0_{00}$ | —                            | —                              | $< 0.19$                                 | $< 0.12$                                  | $< 0.29$   |                               |                        |                     |
| $\text{H}_2\text{O } 4_{22} - 4_{13}$ | $6.5195^{+0.0010}_{-0.0010}$ | $321^{+169}_{-100}$            | $0.46^{+0.14}_{-0.12}$                   | $0.32^{+0.10}_{-0.09}$                    | $0.57^{+0.17}_{-0.15}$   | 162.286 GHz                   | $4.27^{+0.04}_{-0.04}$ |                     |
| $\text{H}_2\text{O } 2_{20} - 2_{11}$ | $6.5185^{+0.0006}_{-0.0006}$ | $382^{+82}_{-61}$              | $1.12^{+0.16}_{-0.15}$                   | $0.81^{+0.12}_{-0.11}$                    | $1.36^{+0.20}_{-0.18}$   |                               |                        |                     |
| $\text{H}_2\text{O } 3_{12} - 2_{21}$ |                              |                                | $0.9 \pm 0.2$                            | $0.61 \pm 0.13$                           | $1.2 \pm 0.3$  | 154.667 GHz                   | $3.50 \pm 0.04$        | Yang+19             |
| $\text{H}_2\text{O } 3_{21} - 3_{12}$ |                              |                                | $1.1 \pm 0.2$                            | $0.75 \pm 0.14$                           | $1.5 \pm 0.3$  |                               |                        |                     |

**Notes.** <sup>(1)</sup>Here we report the central frequency of the LSB and USB of each frequency setup of this work. For the literature data, the dust continuum reference frequency is set to one of  $\text{H}_2\text{O}$  line expected frequency (based on the redshift measurement from [CII]<sub>158 $\mu\text{m}$</sub>  line, see Decarli et al. 2018; Yang et al. 2019c, and references therein) encompassed in the continuum frequency bandwidth. <sup>(2)</sup>References: Yang+19 (Yang et al., 2019c), Li+20 (Li et al., 2020b), Riechers+ (Riechers et al., in prep.).

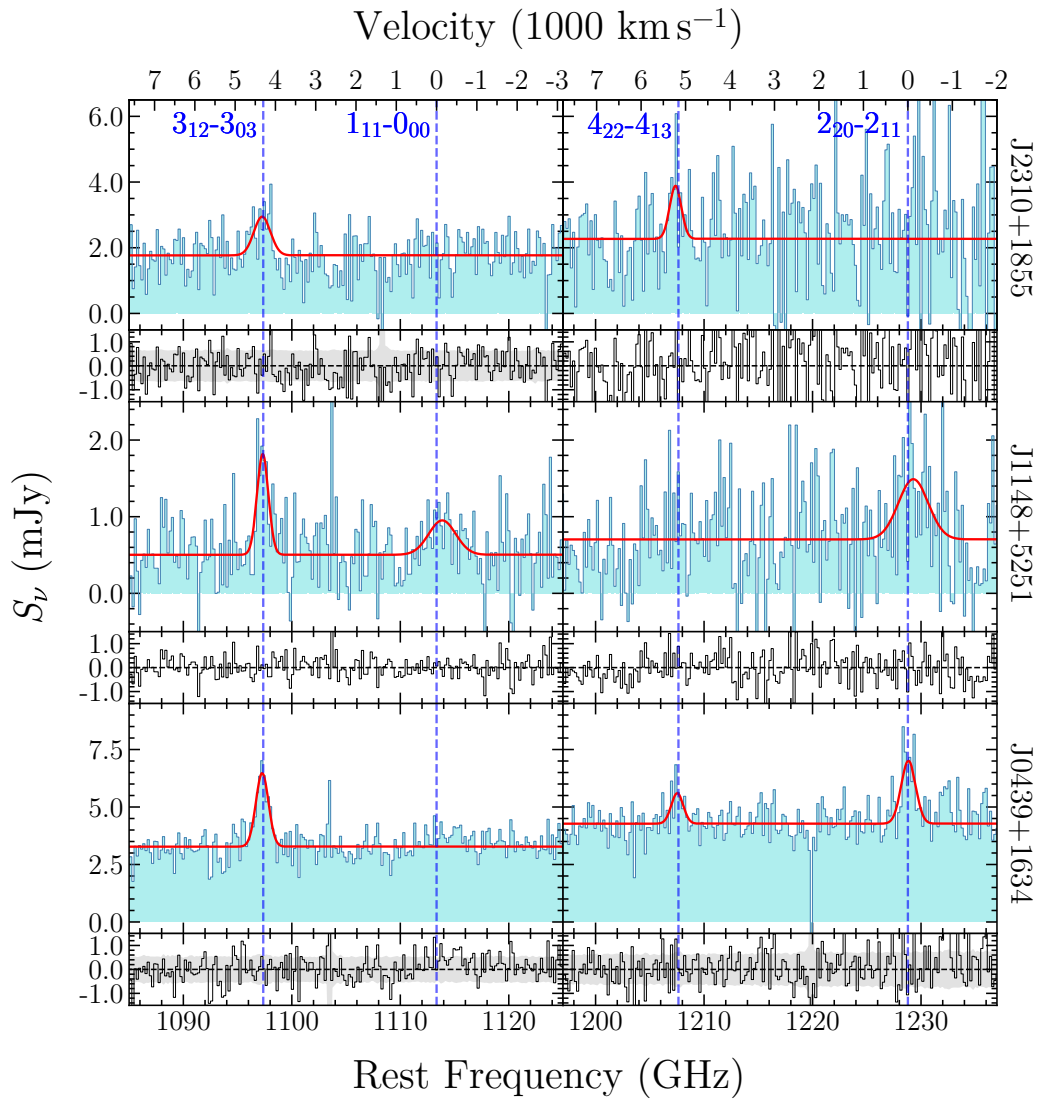


**Figure 7.2**

NOEMA spectra of  $z > 6$  quasars J2310+1855, J1148+5251 and J0439+1634 (from the top to the bottom). We report the observed data in light blue and the best fit model in red. The blue dashed lines indicate the rest frequencies of the targeted  $\text{H}_2\text{O}$  transitions which quantum numbers are also reported. At the bottom of each spectra we report the residuals (data-model) and the grey area showing the noise RMS in each channel.

us from reliably sampling the Wien’s tail of the dust SEDs (see, e.g., Leipski et al., 2014; Shao et al., 2019). Therefore, for sake of simplicity here we assume that the dust emission is optically thin, and we parametrize  $k_d(\nu) = k_0(\nu/\nu_0)^\beta$ , with  $k_{850\mu\text{m}} = 0.77 \text{ cm}^2 \text{ g}^{-1}$  and  $\beta$  is the spectral emissivity index taken as the average values for graphite and silicates given by Draine & Lee (1984) and

by Hughes et al. (1993) (see, Dunne et al., 2000). Under these assumptions Eq. (5.2) reduces to

$$S_{\nu/(1+z)} \approx \frac{(1+z)}{D_L^2} k_{850\mu\text{m}} M_{\text{dust}} \left( \frac{\nu}{352.7 \text{ GHz}} \right)^\beta B_\nu(T_{\text{dust}}). \quad (7.1)$$

However, we verified that the results that follow, are consistently obtained adopting a general graybody model. On the other hand, Eq. (7.1) allows us to reduce the number of free parameters in the fit.

Since our sources are located at relatively high- $z$ , the observed flux densities must be corrected for the effect of the CMB (see Eq. 6.5, Sects. 5.3, and 6.5). Throughout the rest of the chapter we indicate with  $T_{\text{dust}}$  the *actual* dust temperature (i.e.  $T_{\text{dust}}(z)$ ) including the contribution from the CMB to the dust heating.

The quasars J2310+1855 and J1148+5251 are widely studied in literature. For these sources, dust physical properties are constrained using different SED decomposition methods (see, e.g., Leipski et al., 2013, 2014; Shao et al., 2019). However, here we aim to obtain quasar dust properties by adopting a unique method for all the sources. Therefore, we combine our continuum measurements in J2310+1855, J1148+5251, and J0439+1634 (see Tab. 7.3), with the available continuum flux density measurements from the literature in the range  $\lambda_{\text{rest}} \approx 50 - 1000 \mu\text{m}$ , where the dust emission is expected to be powered primarily by the re-processed optical/UV radiation of young stars in star-forming regions thus avoiding MIR excess due to AGN torus contribution and/or very hot dust components (Casey, 2012; Leipski et al., 2013, 2014; Casey et al., 2014). We therefore use Eqs. (6.5), and (7.1) to fit the dust SEDs of our quasars by using  $T_{\text{dust}}$ ,  $M_{\text{dust}}$  and  $\beta$  as free parameters. We explore the parameter space by adopting a Bayesian approach via the MCMC ensemble sampler emcee (Foreman-Mackey et al., 2013). In this procedure, we treated continuum data as independent measurements with Gaussian statistical uncertainties ignoring any systematics. For the free parameters we first adopted box-like priors as follows:  $T_{\text{CMB}}(z) \leq T_{\text{dust}} \leq 100 \text{ K}$ ;  $6.0 \leq \log M_{\text{dust}} \leq 10.0$  and typical values of  $1.0 \leq \beta \leq 2.5$  observed in star-forming galaxies and quasars (e.g., Beelen et al., 2006; Leipski et al., 2013, 2014). In the case of J0439+1634, the available data are limited to the Rayleigh-Jeans tail of the dust SED, where the observed flux density is  $\propto T_{\text{dust}} M_{\text{dust}}$  thus making these parameters degenerate. In this case, we

include a Gaussian prior on  $T_{\text{dust}}$  in the log-likelihood function of the form  $-0.5\{(T_{\text{dust}} - 47\text{K})/(5\text{K})\}^2$ , with 47K being the typical dust temperature measured in high- $z$  quasar hosts (e.g., Beelen et al., 2006; Wang et al., 2007, 2008; Leipski et al., 2013, 2014). We show the fit results in Fig. 7.3. Then, by integrating the best-fit models, we derived rest-frame IR (42.5–122.5  $\mu\text{m}$ ; Helou et al. 1985), FIR (40–400  $\mu\text{m}$ ; Helou et al. 1988), and TIR (8–1000  $\mu\text{m}$ ; Sanders et al. 2003) luminosities of the sources. Finally, we inferred the SFR using the local scaling relation from Murphy et al. (2011);  $\text{SFR}_{\text{IR}}(M_{\odot} \text{yr}^{-1}) = 1.49 \times 10^{-10} L_{\text{TIR}}/L_{\odot}$ , under the hypothesis that the entire Balmer continuum (i.e.  $912 < \lambda < 3646$ ) is absorbed and re-irradiated by the dust in the optically thin limit. Here, a Kroupa initial mass function (IMF; Kroupa 2001) is implicitly assumed, having a slope of  $-1.3$  for stellar masses between  $0.1 - 0.5 M_{\odot}$ , and  $-2.3$  for stellar masses ranging between  $0.5 - 100 M_{\odot}$ . In Tab. 7.4 we report all the derived quantities obtained with our dust continuum modeling. We note that, under our working assumptions, any possible contribution of the central AGN to the IR luminosity will result in biases on derived quantities, and, in particular, an overestimation of  $L_{\text{IR}}$  and  $\text{SFR}_{\text{IR}}$ .

The estimated dust temperature of J2310+1855 is consistent within uncertainties with that derived from Shao et al. (2019) who performed a more sophisticated SED decomposition in UV/optical-FIR range, by adopting a spectral emissivity index of  $\beta = 1.6$ . We also found consistent result for our derived dust temperature of J1148+5251 and the value reported in Beelen et al. (2006), while a slightly higher value of  $T_{\text{dust}} \approx 60\text{K}$  is measured by Leipski et al. (2013, 2014), all assuming  $\beta = 1.6$ . However, we note that the derived dust parameters from SED fitting depend on the adopted functional form as well as the broad-band photometry used in the fit. Indeed, a single-temperature modified blackbody model cannot account for the superimposed emission from multiple dust components in galaxy. In general, the contribution to the IR-luminosity on the Rayleigh-Jeans side of the dust SED is expected to be dominated by the vast cold dust reservoir ( $T \sim 20\text{K}$ ), while warmer dust components ( $T \gtrsim 50 - 60\text{K}$ ) boost the IR-luminosity at shorter wavelengths (e.g., Dunne & Eales, 2001; Farrah et al., 2003; Casey, 2012; Galametz et al., 2012; Kirkpatrick et al., 2012, 2015). However, the luminosity on Rayleigh-Jeans regime is only linearly proportional to the dust temperature, while  $L_{\text{IR}} \propto M_{\text{dust}} T_{\text{dust}}^{4+\beta}$  near to the peak of the dust SED.

### Figure 7.3

Infrared dust continuum SED modeling of J2310+1855 (yellow), J1148+5251 (blue), and J0439+1634 (red). The upper-right panel shows continuum data retrieved from literature in the wavelengths range  $\lambda_{\text{rest}} \approx 50 - 1000 \mu\text{m}$  together with our NOEMA 2-mm continuum measurements as reported in the legend. The solid curves are the best-fit model results with shaded areas indicating the 1- $\sigma$  confidence interval. The adjacent panels show the posterior probability distribution of free parameters. The best-fit values and uncertainties reported at the top of each distribution are computed by 50th, 16th, and 84th percentiles. The 2D contours show the  $[1, 2, 3]\sigma$  confidence intervals that are also highlighted in the marginalized distributions. The vertical green area is the 2-mm wide-band of the NOEMA PolyFix correlator, centered on the average redshift of the quasars. References: Bertoldi+03 (Bertoldi et al., 2003); Robson+04 (Robson et al., 2004); Beelen+06 (Beelen et al., 2006), Riechers+09, + (Riechers et al., 2009, Riechers et al. in prep.); Wang+11, +13 (Wang et al., 2011, 2013); Walter+09 (Walter et al., 2009); Leipski+13 (Leipski et al., 2013); Gallerani+14 (Gallerani et al., 2014); Cicone+15 (Cicone et al., 2015); Feruglio+18 (Feruglio et al., 2018); Carniani+19 (Carniani et al., 2019); Hashimoto+19 (Hashimoto et al., 2019b); Shao+19 (Shao et al., 2019); Yang+19 (Yang et al., 2019c); Li+20a, +20b (Li et al., 2020a, b).

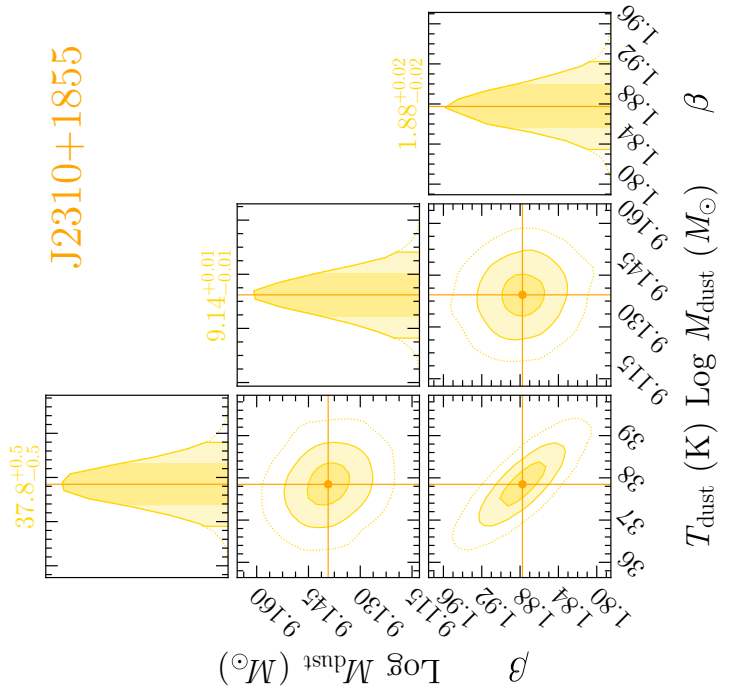
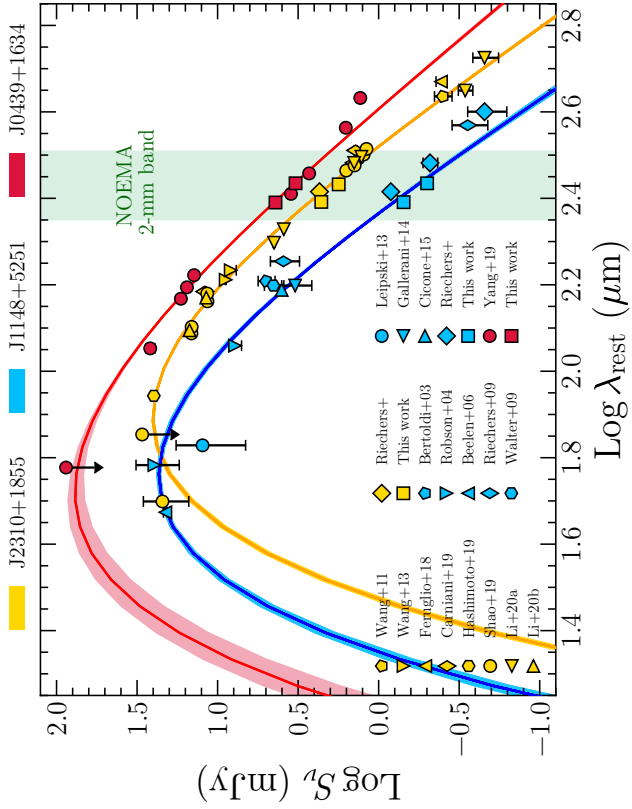
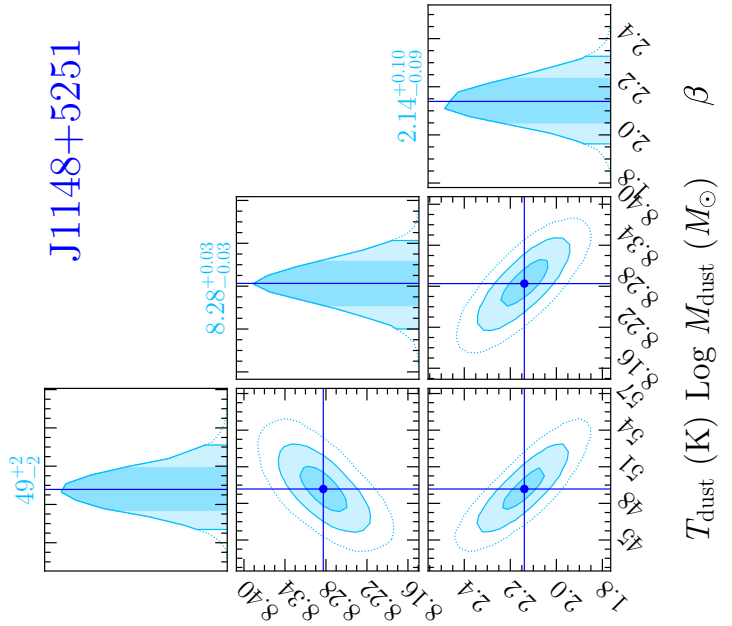
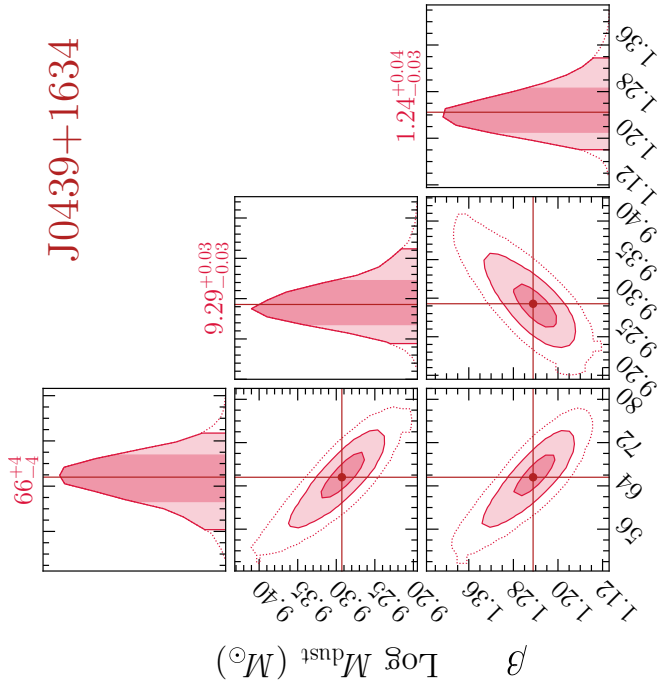


**Table 7.4:** Dust properties in quasar host galaxies.

| Object ID   | J2310+1855             | J1148+5251             | J0439+1634              |
|---|------------------------|------------------------|-------------------------|
| $T_{\text{dust}}$ (K)                                 | $37.8^{+0.5}_{-0.5}$   | $49^{+2}_{-2}$         | $65^{+4}_{-4}$ (*)      |
| $\text{Log } M_{\text{dust}}/M_{\odot}$               | $9.14^{+0.01}_{-0.01}$ | $8.28^{+0.03}_{-0.03}$ | $9.29^{+0.03}_{-0.03}$  |
| $\beta$   | $1.88^{+0.02}_{-0.02}$ | $2.14^{+0.10}_{-0.09}$ | $1.24^{+0.04}_{-0.03}$  |
| $L_{\text{IR}} (10^{13} L_{\odot})$ <sup>(1)</sup>    | $1.43^{+0.03}_{-0.03}$ | $1.61^{+0.04}_{-0.04}$ | $5.5^{+0.5}_{-0.5}$     |
| $L_{\text{FIR}} (10^{13} L_{\odot})$ <sup>(2)</sup>   | $1.59^{+0.03}_{-0.03}$ | $1.68^{+0.04}_{-0.04}$ | $5.8^{+0.5}_{-0.5}$     |
| $L_{\text{TIR}} (10^{13} L_{\odot})$ <sup>(3)</sup>   | $1.75^{+0.04}_{-0.04}$ | $2.38^{+0.07}_{-0.07}$ | $9.8^{+1.7}_{-1.6}$     |
| $\text{SFR}_{\text{TIR}} (M_{\odot} \text{ yr}^{-1})$ | $2592^{+56}_{-57}$     | $3534^{+108}_{-98}$    | $14581^{+2461}_{-2357}$ |

**Notes.** <sup>(1),(2),(3)</sup>The infrared (IR), far-infrared (FIR), and total infrared (TIR) luminosities obtained by integrating the best-fit modified blackbody model in the (rest-frame) wavelength range 42.5–122.5  $\mu\text{m}$  (Helou et al., 1985), 40–400  $\mu\text{m}$  (Helou et al., 1988), and 8–1000  $\mu\text{m}$  (Sanders et al., 2003), respectively. (\*)For this parameter we employed a Gaussian prior in the fitting procedure.

For this reason, the warmer component may significantly bias our single-component blackbody dust SED fit result toward higher dust temperatures, even if it represents a small fraction of the total dust mass. For this reason, our dust temperature estimates should be considered as *luminosity-weighted*, in contrast to the *mass-weighted* dust temperature physically associated to the bulk of the cold dust emission in galaxies (see, e.g., Scoville et al., 2016; Liang et al., 2019; Faisst et al., 2020; Sommovigo et al., 2021). Indeed, the available data do not allow us to measure the small secondary peak due to the cold dust on the Rayleigh-Jeans tail of the SED, making impossible to constrain the temperature of the cold dust component from the SED.

## 7.6 Radiative transfer analysis

The observed line and continuum luminosities incorporate key information on the physical properties of the emitting regions. Such information can be extracted by a forward modeling of the observed quantities under a number of simplified assumptions on the geometry of the emitting region and on the atomic/molecular excitations and radiative transfer processes. In this chapter we adopt the publicly-available radiative transfer code MOLPOP-CEP (Asensio Ramos & Elitzur, 2018) in order to simulate the emission of  $\text{H}_2\text{O}$  lines from a molecular cloud under the effect of a dust radiation field. Compared to other methods, MOLPOP-CEP solves "exactly" (i.e. in principle, at any level

level of accuracy) the radiative transfer equations for a multiline problem through the coupled escape probability approach (CEP, Elitzur & Asensio Ramos, 2006) for a one-dimensional plane-parallel slab that can present arbitrary spatial variations of the physical conditions. This code divides the source in a set of zones in which the level population equations are derived from first principles and solved self-consistently including interactions with the transferred radiation and possibly an external radiation field. Therefore, the emergent line fluxes are predicted as a function of the depth into the line-emitting region and can be directly compared with the observations. This level of sophistication is necessary since we are dealing with radiative transfer under potentially very optically thick conditions, both in the continuum and in the lines.

Within MOLPOP-CEP we studied the water vapor emission by setting up uniform slab models of molecular cloud impinged by an external radiation field produced by the dust. The parameters of interest for the molecular system are the density of molecular hydrogen  $n_{\text{H}_2}$ , the kinetic temperature of the gas  $T_{\text{kin}}$ , the water abundance  $X_{\text{H}_2\text{O}}$ , and the  $\text{H}_2\text{O}$  column density  $N_{\text{H}_2\text{O}}$ . Then, we characterized the external dust radiation field by adopting a single modified blackbody model in the form  $(1 - e^{-\tau(\nu)})B_\nu(T_{\text{dust}})$ . The radiation field is therefore determined by the dust temperature  $T_{\text{dust}}$ , and the continuum optical depth  $\tau(\nu)$  at each frequency  $\nu$ .

In order to model the  $\text{H}_2\text{O}$  emission in our quasar host galaxies, we assumed fiducial values of  $\text{Log } n_{\text{H}_2} (\text{cm}^{-3}) = 4.5$ ,  $T_{\text{kin}} = 50 \text{ K}$ , and  $X_{\text{H}_2\text{O}} = 2 \times 10^{-6}$  (see, e.g., Meijerink & Spaans, 2005; González-Alfonso et al., 2010; Liu et al., 2017; van Dishoeck et al., 2021). We therefore generated a  $16 \times 25$  grid of models with different dust radiation field by varying the dust temperature in the range  $T_{\text{dust}} = [45, 195] \text{ K}$  (with 10 K linear spacing), and continuum optical depth at  $100 \mu\text{m}$  in the range  $\tau_{100} = [0.01, 1.5 \times 10^2]$  ( $\sim 0.17$  dex spacing). The functional form of the optical depth at every wavelength is then determined by a tabulation available within the code, on the base of the properties of the standard ISM dust (see, Asensio Ramos & Elitzur, 2018). The dust radiation field impinges the molecular system from a side and the code computes the radiation transfer all the way into the cloud until the water vapor column density reaches the value  $N_{\text{H}_2\text{O}} = 1 \times 10^{19} \text{ cm}^{-2}$  ( $N_{\text{H}_2} = 5 \times 10^{24} \text{ cm}^{-2}$ ). The ranges of variation of the parameters are set in

order to encompass the typical values observed in local and high- $z$  galaxies (see, e.g., van der Werf et al., 2011; González-Alfonso et al., 2014; Yang et al., 2016a, 2020a; Liu et al., 2017), and in line with what we found in **Chap. 6**. In addition, we took into account the effect of CMB radiation background at  $z = 6$  by inserting a perfect blackbody radiation field with a temperature of  $T_{\text{CMB}} = 19.08 \text{ K}$  illuminating the molecular slab from both sides. Following the prescriptions reported in Asensio Ramos & Elitzur (2018), we set up the calculation by dividing the molecular cloud into 20 zones, achieving a relative accuracy in the solution of  $< 0.01$  with the accelerated  $\Lambda$ -iteration method (ALI). For para- and ortho- $\text{H}_2\text{O}$  collisional excitations we assume  $\text{H}_2$  molecules as unique collisional partners by adopting collisional rate coefficients from Green et al. (1993).

The models adopted in this chapter are suitable in order to simulate the emission of a typical molecular cloud in galaxy. However, as discussed in **Sects. 5.4** and **6.4**, such kind of modeling suffers from limitations due to the simplified assumptions. For these reasons, in this chapter we employ line ratios in order to compare the model predictions with the observations.

As discussed in **Sects. 5.2.2** and **7.3**, collisions can be the dominant mechanism of the excitation of low- $J$   $\text{H}_2\text{O}$  lines. This conclusion is indeed supported by various results reported in literature for local and high- $z$  star-forming galaxies, SMGs, and AGN (see, e.g., González-Alfonso et al., 2010; van der Werf et al., 2011; Liu et al., 2017; Yang et al., 2020a). The effect of collisions on  $\text{H}_2\text{O}$  excitation is expected to be driven mainly by the gas density and temperature.

A comprehensive modeling of water vapor emission should include the contribution of multiple gas components in order to well reproduce the collisionally-excited low- $J$  and radiatively-excited high- $J$   $\text{H}_2\text{O}$  lines simultaneously (see, e.g., González-Alfonso et al., 2010; Liu et al., 2017; Yang et al., 2020a). However, we verified that our current data do not allow us to constrain gas temperature and density such that any multicomponent approach would be inconclusive. We therefore employed a simple single gas component modeling with fixed gas density, temperature and water vapor abundance as discussed above.

## 7.7 Results and discussion

### 7.7.1 H<sub>2</sub>O spectral line energy distributions

A powerful tool to investigate the excitation of water vapor lines is the H<sub>2</sub>O SLED, that is the water vapor line ratios as function of the energy of the upper level of transitions. In **Fig. 7.4** we compare the H<sub>2</sub>O (3<sub>12</sub> – 3<sub>03</sub>)-normalized SLEDs (using line velocity-integrated fluxes in unit of Jy km s<sup>-1</sup>) in our quasars, with the average SLEDs of local ULIRGs, including cases with mild AGN contribution ("HII+mild AGN"), and AGN-dominated galaxies ("strong-AGN") as reported by Yang et al. (2013). In order to extend the comparison, in **Fig. 7.4** we also report three detailed H<sub>2</sub>O SLED available in the literature, for the local type-1 Seyfert galaxy Mrk 231 (González-Alfonso et al., 2010), the local ULIRG Arp 220 (Rangwala et al., 2011), and the SMG HFLS 3 at  $z = 6.34$  (Riechers et al., 2013). To first order, our quasars show H<sub>2</sub>O SLEDs that resemble the ones of other high- $z$  galaxies (with or without prominent AGN). This confirms earlier results (see, e.g., Yang et al., 2013, 2016a; Riechers et al., 2013; González-Alfonso et al., 2014, and **Chap. 6**) suggesting that the H<sub>2</sub>O IR pumping strongly depends on the local dust IR radiation field properties rather than the kind of source responsible of the dust heating.

More specifically, Yang et al. (2013) report a higher detection rate of H<sub>2</sub>O 1<sub>11</sub> – 0<sub>00</sub> in strong AGN possibly indicating strong H<sub>2</sub>O collisional excitation due to high density in AGN circumnuclear region (see discussion in **Sect. 7.3**). However, we detected the para-H<sub>2</sub>O ground state transition only in the quasar J1148+5251. In accordance with the discussion in **Sect. 7.3**, this may suggest that the bulk of H<sub>2</sub>O emission in this source arises from a warm ISM with low continuum opacity. At the same time, J1148+5251 is the only one source in our sample that is not detected in its H<sub>2</sub>O 4<sub>22</sub> – 4<sub>13</sub> transition. This might point to a lack of very warm dust in J1148+5251 compared to the other two sources. All the sources show a peak in the H<sub>2</sub>O 3<sub>21</sub> – 3<sub>12</sub> line (although less prominent for J0439+1634) as in the average local SLED of ULIRGs and AGN, thus unveiling the efficient mechanism of the IR pumping excitation by absorption of 75  $\mu$ m photons in the warm medium in conjunction with gas collisions that are able to approximately thermalize the 3<sub>21</sub> upper level (e.g., Liu et al., 2017). In addition, every de-excitation in the H<sub>2</sub>O 3<sub>21</sub> – 3<sub>12</sub> line will be followed by a cascade in the H<sub>2</sub>O 3<sub>12</sub> – 3<sub>03</sub>

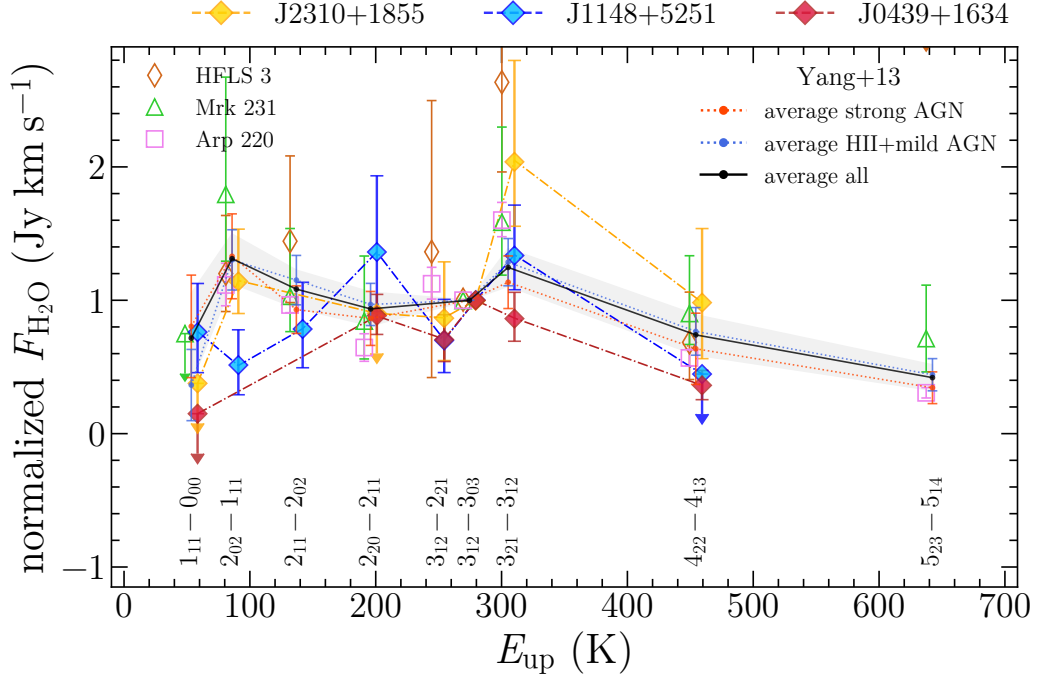


**Figure 7.4**

$\text{H}_2\text{O}$  ( $3_{12} - 3_{03}$ )-normalized intensities (in  $\text{Jy km s}^{-1}$ ) as a function of the energy of the upper levels. Colored diamonds are the  $\text{H}_2\text{O}$  line ratios of our three quasars as indicated in the legend at the top of the panel. The red and blue dotted lines are, respectively, the average  $\text{H}_2\text{O}$  SLED of local strong-AGN- and HII+mild-AGN-dominated galaxies reported in Yang et al. (2013). The solid black line is the average SLED of the whole sample with the grey shadowed area representing the  $1\sigma$  uncertainty. We also report data retrieved from the literature for nearby sources Arp 220 (Rangwala et al., 2011) and the AGN-dominated Mrk 231 (González-Alfonso et al., 2010), and the SMG HFLS 3 at  $z = 6.34$  (Riechers et al., 2013). The energy of upper levels of  $2_{02} - 2_{11}$  and  $3_{12} - 3_{03}$  transitions were shifted for clarity to  $-15\text{ K}$  and  $+25\text{ K}$ , respectively. We also slightly shifted the SLEDs of Arp 220, Mrk 231, HFLS 3 horizontally to  $-5\text{ K}$ , and those of our quasars to  $+5\text{ K}$  for clarity.

and  $3_{12} - 2_{21}$  transitions (see Fig. 7.4), with relative intensities determined by the A-Einstein coefficient of spontaneous emission (see Tab. 7.2). In these optically thin conditions, González-Alfonso et al. (2014) predicted a  $3_{21} - 3_{12}$ -to- $3_{12} - 3_{03}$  flux ratio of 1.16, well consistent with what we measure in J1148+5251 and J0439+1634. On the other hand, the higher value of this ratio in J2310+1855 suggests that higher line and/or continuum optical depth possibly decreases the strength of the  $3_{12} - 3_{03}$  line relative to  $3_{21} - 3_{12}$  via absorption of the  $3_{12} - 3_{03}$  photons re-emitted in the  $3_{21} - 2_{21}$  line, or significant IR-pumping of the  $\text{H}_2\text{O}$   $4_{23} - 3_{12}$  transition due to

absorption of continuum photons at  $78\ \mu\text{m}$ . In optically thin conditions the  $\text{H}_2\text{O}$   $2_{20} - 2_{11}$ ,  $2_{11} - 2_{02}$ , and  $2_{02} - 1_{11}$  lines powered via pumping by  $101\ \mu\text{m}$  photons form a closed loop and are expected to have equal fluxes due to the statistical equilibrium (see, e.g., González-Alfonso et al., 2014; Liu et al., 2017). However, high dust temperature and continuum optical depth increase the efficiency in the  $3_{22} - 2_{11}$   $90\ \mu\text{m}$  radiatively-pumped transition thus decreasing the  $2_{11} - 2_{02}$  line relative to the other lines within the loop. In particular since the  $\text{H}_2\text{O}$   $2_{02} - 1_{11}$  transition is predicted to be easily excited by collisions in the warm medium (Liu et al., 2017), the  $2_{02} - 1_{11}$ -to- $2_{11} - 2_{02}$  flux ratio is expected to be  $\gtrsim 1$  for optical thick continuum and high  $\text{H}_2\text{O}$  column density ( $N_{\text{H}_2\text{O}} > 10^{17}\ \text{cm}^{-2}$ , see, e.g., González-Alfonso et al. 2014; Liu et al. 2017). In J1148+5251 we found that the  $2_{20} - 2_{11}$ ,  $2_{11} - 2_{02}$ , and  $2_{02} - 1_{11}$  exhibit consistent fluxes, with  $2_{02} - 1_{11}$ -to- $2_{11} - 2_{02}$  flux ratio  $\sim 1$  thus suggesting optically thin conditions. Similarly, J2310+1855 shows a  $2_{02} - 1_{11}$ -to- $2_{20} - 2_{11}$  flux ratio lower limit  $> 1$  possibly indicating very warm dust and optically thick continuum making an efficient radiative pumping of the  $3_{31} - 2_{20}$  line due to absorption of  $67\ \mu\text{m}$  photons (see, e.g. Liu et al., 2017). We also note that the  $\text{H}_2\text{O}$   $2_{02} - 1_{11}$  can be boosted relative to the  $2_{20} - 2_{11}$  due to the efficient collisional excitation of the lower line; however, the non-detection of the  $\text{H}_2\text{O}$   $1_{11} - 0_{00}$  line in J2310+1855, the prominent peak in  $3_{21} - 3_{12}$ , and the relatively high flux in  $4_{22} - 4_{13}$  line point to a minor contribution of this effect in this source.

## 7.7.2 Modeling water vapor SLEDs

In Fig. 7.5 we show our MOLPOP-CEP predictions of the  $\text{H}_2\text{O}$  fluxes for different values of  $N_{\text{H}_2\text{O}}$ ,  $\tau_{100}$  and  $T_{\text{dust}}$ . Our model predictions clearly reveal the effect of the IR-pumping of  $J = 3$ , and  $J = 4$  lines. Indeed, for each couple ( $N_{\text{H}_2\text{O}}$ ,  $\tau_{100}$ ), the fluxes of high-energy  $\text{H}_2\text{O}$  lines, display a larger variation by increasing  $T_{\text{dust}}$ , relatively to low-lying lines. Additionally, we found that  $\text{H}_2\text{O}$  fluxes at  $E_{\text{up}} > 250\ \text{K}$  systematically increase at high values of continuum optical depth, with the largest absolute variations occurring at high  $T_{\text{dust}}$  values. This is not surprising as higher dust temperatures and continuum optical depths significantly boost the amount of IR photons that can be absorbed by  $\text{H}_2\text{O}$  molecules. This increases the fluxes of high- $J$   $\text{H}_2\text{O}$  lines the level populations of which are exclusively determined by radiative pumping toward a Boltzmann distribution close to the dust temperature

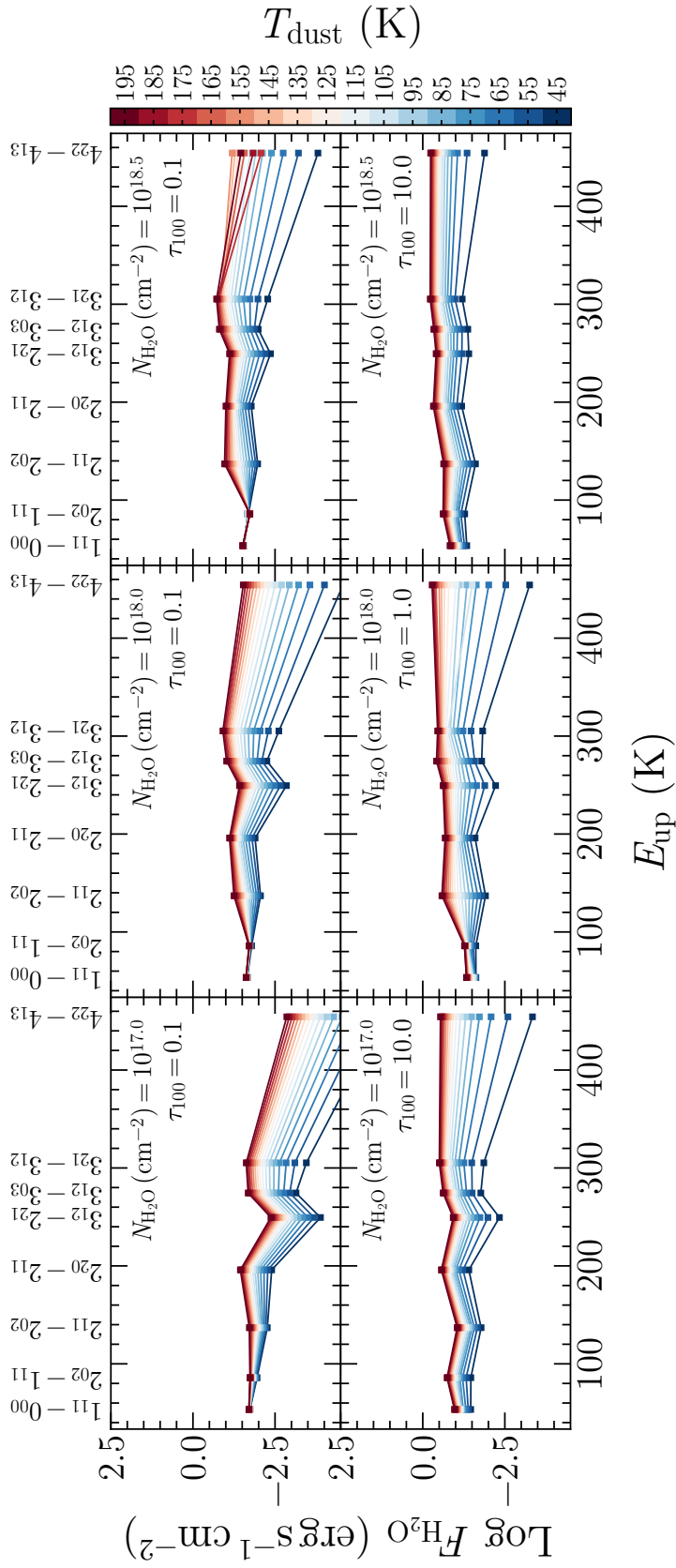


**Figure 7.5**

H<sub>2</sub>O line fluxes as a function of the energy of the upper levels obtained from our MOLPOP-CEP runs. Here we report output predictions with different value of water vapor column density (from left to right  $N_{\text{H}_2\text{O}} = 10^{17}, 10^{18}, 10^{18.5}$  cm<sup>-2</sup>) and continuum optical depth ( $\tau_{100} = 0.1, 1.0, 10$ ) as reported at the upper right corner of each panel. The H<sub>2</sub>O fluxes in each panel are color-coded with dust temperature value.

(see, e.g., Liu et al., 2017). In order to infer the ISM conditions in our quasar host galaxies, we employed our MOLPOP-CEP model grids in order to perform fits of the quasar H<sub>2</sub>O SLEDs. By assuming a single component model, we explored the (discrete) parameter space ( $T_{\text{dust}}$ ,  $\tau_{100}$ ,  $N_{\text{H}_2\text{O}}$ ) by using a Bayesian approach with the MCMC ensemble sampler emcee python package (Foreman-Mackey et al., 2013). We adopted uniform priors for all the three free parameters within the ranges of the model grid. We therefore retrieved the posterior probability distributions by maximizing the log-likelihood function by assuming that each data point follows an independent Gaussian distribution. In this procedure, we also took into account the measurement upper limits by assuming one third of their  $3\sigma$  limits as nominal values and uncertainties, respectively. In **Tab. 7.5** we report the best-fit parameters for each source and in **Fig. 7.6** we show the best-fit H<sub>2</sub>O SLED models and the posterior probability distributions of the free parameters.

In general, our best-fit models reproduce well the observed H<sub>2</sub>O SLEDs. All the modeled H<sub>2</sub>O line luminosity ratios are consistent within the uncertainties with the measured data, except for a few line ratios in the SLEDs of J2310+1855 and J0439+1634 quasars. The worst case is that of J2310+1855 SLED where the best-fit model underestimates the H<sub>2</sub>O  $2_{02}-1_{11}$ - and  $3_{21}-3_{12}$ -to- $3_{12}-3_{03}$  ratios, which however are consistent within  $\sim 2\sigma$  with the observations. However, we note that deviations in ratios involving low- $J$  lines may be expected if there is an additional low-excitation ISM component (see, e.g., González-Alfonso et al., 2010; Liu et al., 2017; Yang et al., 2020a)

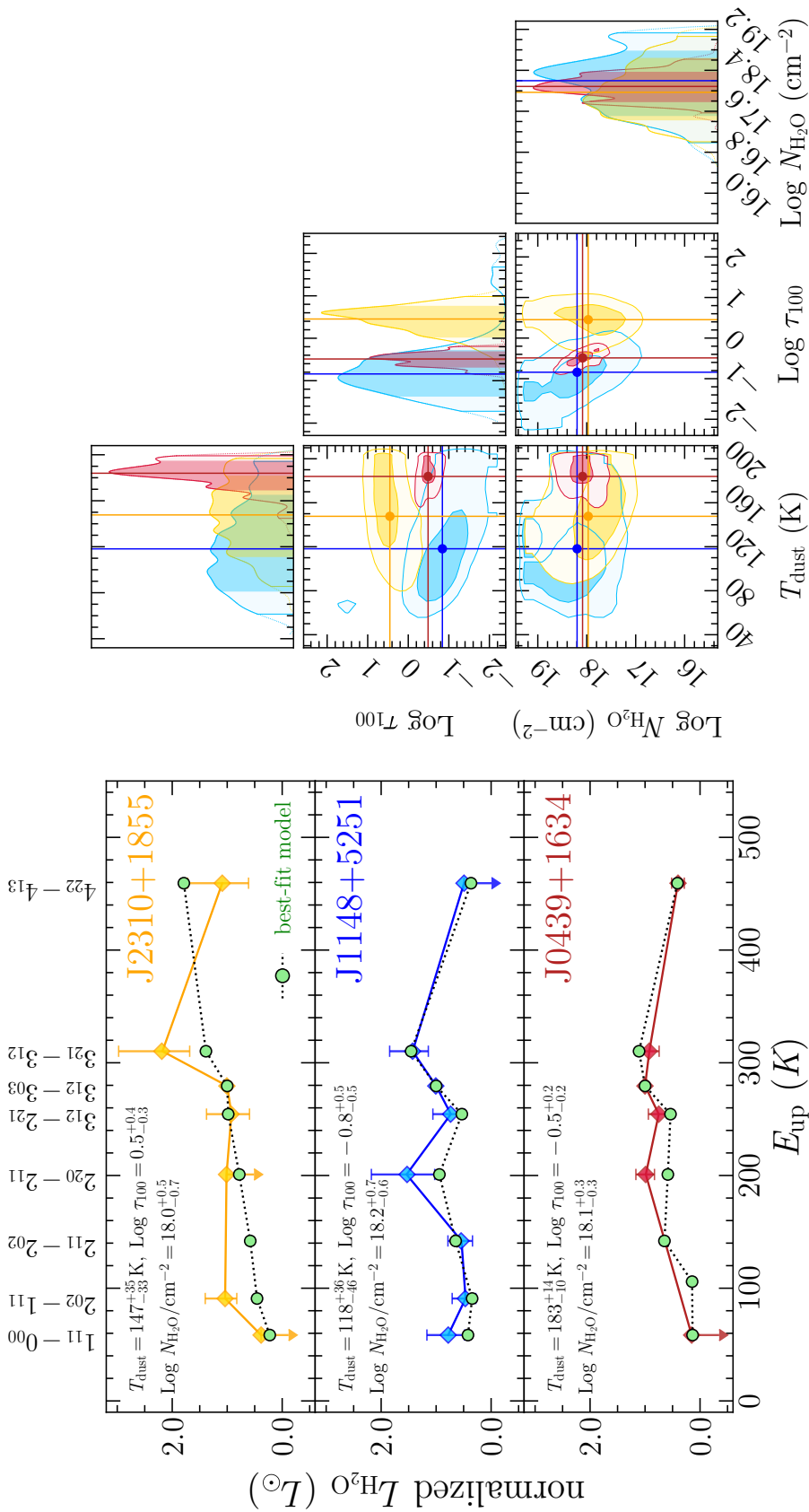
The posterior probability distributions of free parameters in **Fig. 7.6** point to very high dust temperature ranging in  $T_{\text{dust}} \sim 80 - 190$  K with the highest values found in those sources in which the high- $J$  H<sub>2</sub>O  $4_{22}-4_{13}$  line is detected in accordance with the discussion of **Sect. 7.7.1**. The best-fit models predict optically thin continuum conditions at  $100 \mu\text{m}$  (i.e.,  $\tau_{100} < 1$ ), except in the case of J2310+1855 quasar for which  $\tau_{100} \sim 1.5 - 8$  is favored. Finally, high H<sub>2</sub>O column density  $N_{\text{H}_2\text{O}} \sim 2 \times 10^{17} - 8 \times 10^{18} \text{ cm}^{-2}$  is needed in order to match observations, which corresponds to a molecular hydrogen column density  $N_{\text{H}_2} \sim 1 \times 10^{23} - 4 \times 10^{24} \text{ cm}^{-2}$  given the assumed the H<sub>2</sub>O abundance. This result is in line with what we found in the previous **Chap. 6**. However,

**Table 7.5:** Best-fit dust and gas properties of quasar host galaxies retrieved from the H<sub>2</sub>O SLED modeling.

| Object ID  | J2310+1855           | J1148+5251           | J0439+1634           |
|--|----------------------|----------------------|----------------------|
| $T_{\text{dust}}$ (K)                                    | $147^{+35}_{-33}$    | $118^{+36}_{-46}$    | $183^{+14}_{-46}$    |
| $\text{Log } \tau_{100}$                                 | $0.5^{+0.4}_{-0.3}$  | $-0.8^{+0.5}_{-0.5}$ | $-0.5^{+0.2}_{-0.2}$ |
| $\text{Log } N_{\text{H}_2\text{O}}$ (cm <sup>-2</sup> ) | $18.0^{+0.5}_{-0.7}$ | $18.2^{+0.7}_{-0.6}$ | $18.1^{+0.3}_{-0.3}$ |
| $T_{\text{kin}}$ (K)                                     |                      | 50                   |                      |
| $\text{Log } n_{\text{H}_2}$ (cm <sup>-3</sup> )         |                      | 4.5                  |                      |
| $X_{\text{H}_2\text{O}}$                                 |                      | $2 \times 10^{-6}$   |                      |

the best-fit results are affected by large uncertainties reflecting the spread of the parameter distributions in Fig. 7.6. The most accurate predictions are obtained for J0439+1634 source, which is not surprising given the achieved high S/N of these observations.

Our simple analysis reveals the presence of an intense warm dust component that can be responsible for the water vapor excitation and emission in molecular clumps with high molecular column density. In particular, for the quasar J2310+1855 we estimated a dust temperature of the optically-thick warm component of  $T_{\text{dust}} \sim 150$  K, which yields a blackbody SED peak at around rest-frame  $\approx 20 \mu\text{m}$ . Interestingly, this value resembles the wavelength peak of the dusty torus components found by Shao et al. (2019) who performed a dust SED decomposition of J2310+1855 continuum emission over a wide wavelength range. This result could indicate a significant MIR contribution of the dusty torus in triggering the water vapor emission, at least in the quasar nuclear region. However, with the current analysis and data it is not possible to infer geometrical properties (e.g., extension) of the bulk of the hot/warm dust component and the warm line-emitting region. We estimate a similar high dust temperature of  $T_{\text{dust}} \sim 180$  K in J0439+1634 indicating the presence of a hot dust component in this quasar. Future MIR studies will possibly reveal if this component could be associated to a central dusty torus as in the case of J2310+1855. We do not reach a similar conclusion for the quasar J1148+5251, when comparing the best-fit dust radiation field temperature with the dusty-torus component inferred by Leipski et al. (2013, 2014). Our results are in line with similar analysis conducted in other sources at low and high redshifts (e.g., González-Alfonso et al., 2010; van der Werf et al.,


**Figure 7.6**

Modeling of H<sub>2</sub>O SLEDs of quasar host galaxies. *Left panels:* The colored diamonds are the observed line luminosities normalized to the H<sub>2</sub>O 3<sub>12</sub> – 3<sub>03</sub> luminosity as a function of the energy of the upper level. The filled green circles are the best-fit models obtained with our MOLPOP-CEP grids. The best-fit parameters are reported at the top left corner of each panel. The reported uncertainties take into account only statistical errors ignoring any systematics. *Right panels:* The MCMC output posterior probability distributions of free parameters. Contour plots show 1 $\sigma$ , and 2 $\sigma$  confident interval, with the correspondent interval that is also indicated with the same color in the marginalized distributions.

2011; Liu et al., 2017; Jarugula et al., 2019; Yang et al., 2020a), predicting hot/warm dust component in the core regions of quasars, ULIRGs, SMGs and normal star-forming galaxies, albeit the different modeling details.

### 7.7.3 Boltzmann diagrams of H<sub>2</sub>O levels

In **Fig. 7.7** we present the level population diagrams predicted by our MOLPOP-CEP models, namely the density of the H<sub>2</sub>O levels ( $n_i$ ), normalized by their quantum degeneracy ( $g_i$ ), as function of the energy of the levels ( $E$ ). Boltzmann statistics predicts that, in LTE condition, the level population of a specie obeys to  $n_i/n_{\text{tot}} = g_i/Q(T) \exp(-E/k_B T)$ , where  $n_{\text{tot}}$  is the total density of the species, and  $Q(T)$  is the partition function. Therefore a thermalized level population is represented by a straight line in a  $\ln(n_i/g_i) - E/k_B$  diagram, the intercept and slope of which are determined by  $n_{\text{tot}}/Q(T)$ , and  $1/T$ , respectively. Our predictions reveal that low energy levels ( $E < 200$  K) are nearly thermalized (i.e. the population is determined by an excitation temperature equal to the gas kinetic temperature,  $T_{\text{ex}} = T_{\text{kin}}$ ), while high energy levels are sub-thermally populated. In these conditions the level populations cannot be characterized by a single  $T_{\text{ex}}$ . Since the high energy levels are populated by absorption of IR photons, the density of such levels is boosted by increasing the dust temperature, as expected as soon as  $T_{\text{dust}} > T_{\text{kin}}$ . This effect is further enhanced in optically thick case, in which high energy levels start to be overpopulated above the thermal values due to the radiative pumping mechanism. These results are in agreement with previous studies reported in literature (e.g., Liu et al., 2017). We note that, the H<sub>2</sub>O SLED, despite it is a powerful diagnostic tool, remains quite elusive in intuitively understanding the ISM excitation conditions without a detailed investigation of the various line ratios. This is mainly due to the interplay of collisions and radiative pumping mechanism in exciting the water vapor lines. This is not the case, for example, for the CO rotational lines, in which transitions toward upper levels are primarily driven by collisions. Indeed, the CO SLED reports the line luminosities as a function of the upper level rotational quantum number  $J_{\text{up}}$ , that, differently from the H<sub>2</sub>O, is linearly proportional to the energy of the transitions ( $\Delta E \propto J + 1$ ) thus providing a direct tool to investigate the excitation conditions of molecular medium (see **Sect. 6.8**). In **Fig. 7.8** we show the best-fit population level diagrams for our three quasars as predicted by the MOLPOP-CEP H<sub>2</sub>O SLED modeling

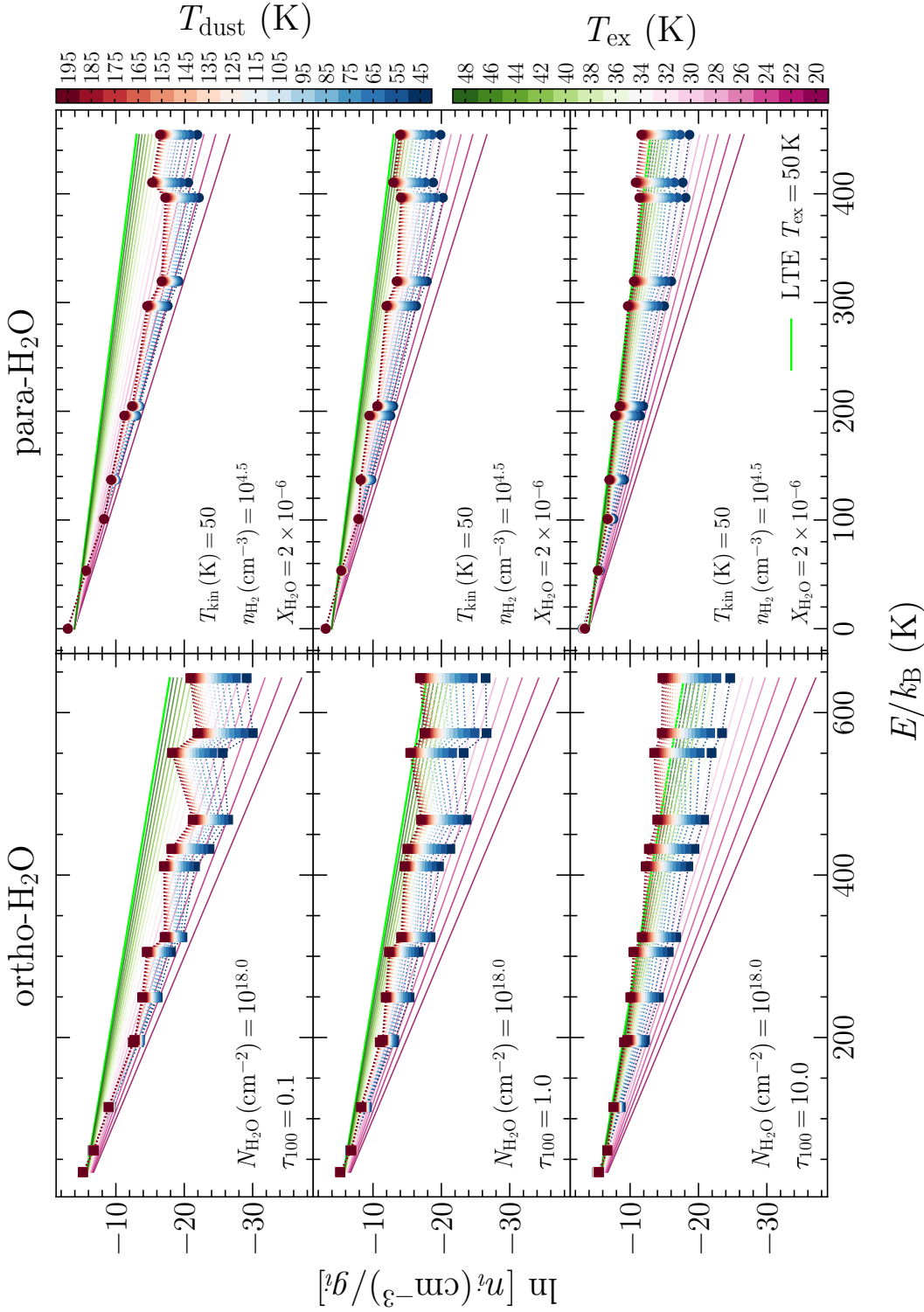


**Figure 7.7**

MOLPOP-CEP predictions of the level population diagrams for ortho-H<sub>2</sub>O (squares, left panels) and para-H<sub>2</sub>O levels (circles, right panels). In each row of this plot the densities of the H<sub>2</sub>O levels ( $n_i$ ) divided by the level degeneracies ( $g_i$ ) are plotted against the energy of the levels ( $E/k_B$ ) with different set of parameters as reported in the lower right corner of the panels. The different colors are different values of the dust temperature. Straight solid lines are theoretical prediction of Boltzmann population colored according to their excitation temperature ( $T_{\text{ex}}$ ). The lime solid line indicates the LTE case in which the excitation temperature equates the gas kinetic temperature ( $T_{\text{kin}} = T_{\text{ex}} = 50\text{K}$ ).

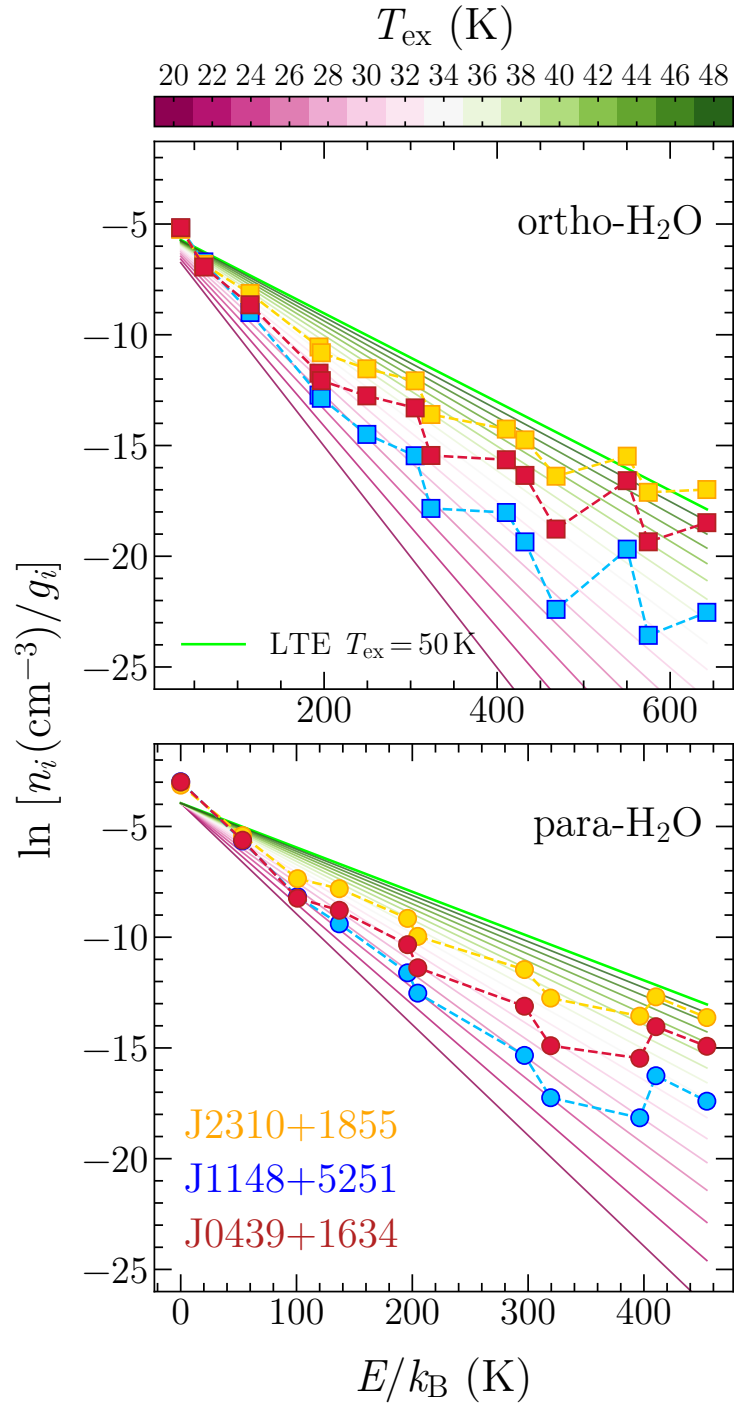


**Figure 7.8**

Models of ortho- and para-H<sub>2</sub>O population level diagrams (upper and lower panel, respectively) for our three quasar host galaxies color-coded according to the legend in the lower left corner. The reported model corresponds to the best-fit MOLPOP-CEP model obtained through the H<sub>2</sub>O SLED fittings (see Sect. 7.7.2). Straight lines are the analytical population diagrams assuming Boltzmann distribution at different excitation temperatures according to the color bar at the top of the panels. The lime green line corresponds to the LTE case ( $T_{\text{kin}} = T_{\text{ex}}$ ).

discussed in the previous sections. The results show a significant contribution of the dust radiation field in exciting the high- $J$  H<sub>2</sub>O lines in J2310+1855 compared to the other quasars. This is in line with the prominent peak of the H<sub>2</sub>O SLED in the  $3_{21} - 3_{12}$  transition, and the mere detection of the H<sub>2</sub>O  $4_{22} - 4_{13}$ . Indeed, significantly higher  $T_{\text{dust}}$  and  $\tau_{100}$  values are inferred for this source. Contrary, J1148+5251 appear much less excited in the high energy H<sub>2</sub>O levels consistently with the lack of H<sub>2</sub>O  $4_{22} - 4_{13}$  emission and the detection of the ground state line  $1_{11} - 0_{00}$  indicating a minor contribution of the radiative pumping in populating higher energy levels.

### 7.7.4 $L_{\text{H}_2\text{O}} - L_{\text{TIR}}$ correlations

Previous studies revealed the existence of nearly linear correlations between  $L_{\text{H}_2\text{O}}$  and  $L_{\text{TIR}}(8 - 1000 \mu\text{m})$  extending over  $\sim 12$  orders of magnitudes from the young stellar objects (YSOs, San José-García, 2015; San José-García et al., 2016), where H<sub>2</sub>O molecules are collisionally excited in shocked gas (e.g., Mottram et al., 2014), to high- $z$  galaxies (Omont et al., 2013; Yang et al., 2013, 2016a; Liu et al., 2017), in which radiative pumping plays an important role in exciting the water vapor emission. However, these correlations have been interpreted differently in the Galactic and extragalactic context. In protostellar environments the H<sub>2</sub>O emission is spatially compact and located in the very proximity of the protostar and it is not associated to the entire molecular cloud (see, e.g., van Dishoeck et al., 2021). In this context, the FIR luminosity, that traces the protostellar envelopes in which the stars are forming, is not directly related to the water vapor emission. On the other hand, in the extragalactic context the  $L_{\text{H}_2\text{O}} - L_{\text{TIR}}$  correlations is thought to be the direct consequence of the FIR pumping. In this sense, the water vapor emission arises in molecular clouds that are not necessarily co-spatial with the star-formation activity. However, recent studies (see, e.g., van Dishoeck et al., 2021, and references therein) showed that low- and mid- $J$  H<sub>2</sub>O ( $E_{\text{up}} < 300\text{K}$ ) line ratios do not significantly differ in the Galactic and extragalactic environments. This evidence suggests that a common mechanism is at the base of water vapor excitation extending from high- $z$  sources to individual Galactic YSOs. That is, the H<sub>2</sub>O emission is likely a good tracer of star formation activity buried in the protostellar envelopes. Therefore, H<sub>2</sub>O traces proportionally the SFR as in the case of other dense gas tracers (e.g., HCN; Gao & Solomon, 2004a,b). In particular, if a large

fraction of the mass of the warm molecular ISM, where the bulk of the  $\text{H}_2\text{O}$  emission arises, is merely spatially-correlated with the physical regions where most of the FIR is generated, the nature of such correlations could be easily explained as driven by the size of the emitting region (see, e.g., González-Alfonso et al., 2014; Liu et al., 2017). Indeed, similar linear correlations are found for CO, where transitions of which are collisionally excited in the molecular gas (see, e.g., Greve et al., 2014; Lu et al., 2014; Liu et al., 2015; Kamenetzky et al., 2016; Yang et al., 2017). These correlations can be viewed as proxies of a galaxy-integrated Schmidt-Kennicutt relation (Kennicutt, 1998) reflecting the well-established fact that the star-formation (traced by  $L_{\text{TIR}}$ ) occurs within the molecular ISM (which mass is traced by the CO lines). On the other hand, if the radiative pumping drives the excitation of  $\text{H}_2\text{O}$  emission in high- $z$  galaxies, then one might expect that this affects to some extent the  $L_{\text{H}_2\text{O}} - L_{\text{TIR}}$  relation. González-Alfonso et al. (2014) show that steeper than linear  $L_{\text{H}_2\text{O}} - L_{\text{TIR}}$  relation is expected if, on average,  $\tau_{100}$  is an increasing function of  $L_{\text{TIR}}$ . By using FIR pumping model, they predicted a  $L_{\text{H}_2\text{O}} \propto L_{\text{TIR}}^{1.3}$  for the  $\text{H}_2\text{O } 2_{02} - 1_{11}$  line and similar supralinear relation for the other  $\text{H}_2\text{O}$  transitions. On the other hand, Liu et al. (2017) show that collisions significantly contribute to the excitation of the mid- $J$   $\text{H}_2\text{O}$  lines, thus suggesting that the correlations are not the mere consequence of the radiative pumping effect.

In **Fig. 7.9** we report  $L_{\text{H}_2\text{O}} - L_{\text{TIR}}$  correlations and the  $L_{\text{H}_2\text{O}}$ -to- $L_{\text{TIR}}$  ratios of the available lines in our quasar host galaxies. In order to study these correlations over the widest dynamical range, we complement our data with previous observations from the literature. In particular, we retrieved measurements of the local and high- $z$  Hy/ULIRGs samples from Omont et al. (2013) and Yang et al. (2013, 2016a). We also include additional individual measurements of the quasar host galaxies APM 08279 at  $z = 3.9$  (van der Werf et al., 2011), and PJ231-20 (PSO J231.6576-20.8335) at  $z = 6.59$  from Pensabene et al. (2021, see, **Chap. 6**); the Hy/ULIRGs/SMGs HLSJ0918 (HLSJ091828.6+514223, Combes et al., 2012; Rawle et al., 2014) at  $z = 5.2$ , and HFLS 3 at  $z = 6.34$  (Riechers et al., 2013); the dusty star-forming galaxies (DSFGs) SPT 0538 (SPT-S J0538165030.8, Bothwell et al., 2013), and MAMBO-9 at  $z = 5.85$  (MM J100026.36+021527.9, Casey et al., 2019); and the hot dust-obscured galaxy (Hot DOG) W0410-0913 from Stanley et al. (2021) (with  $L_{\text{TIR}}$  taken from Fan et al. 2016). When possible, we report the

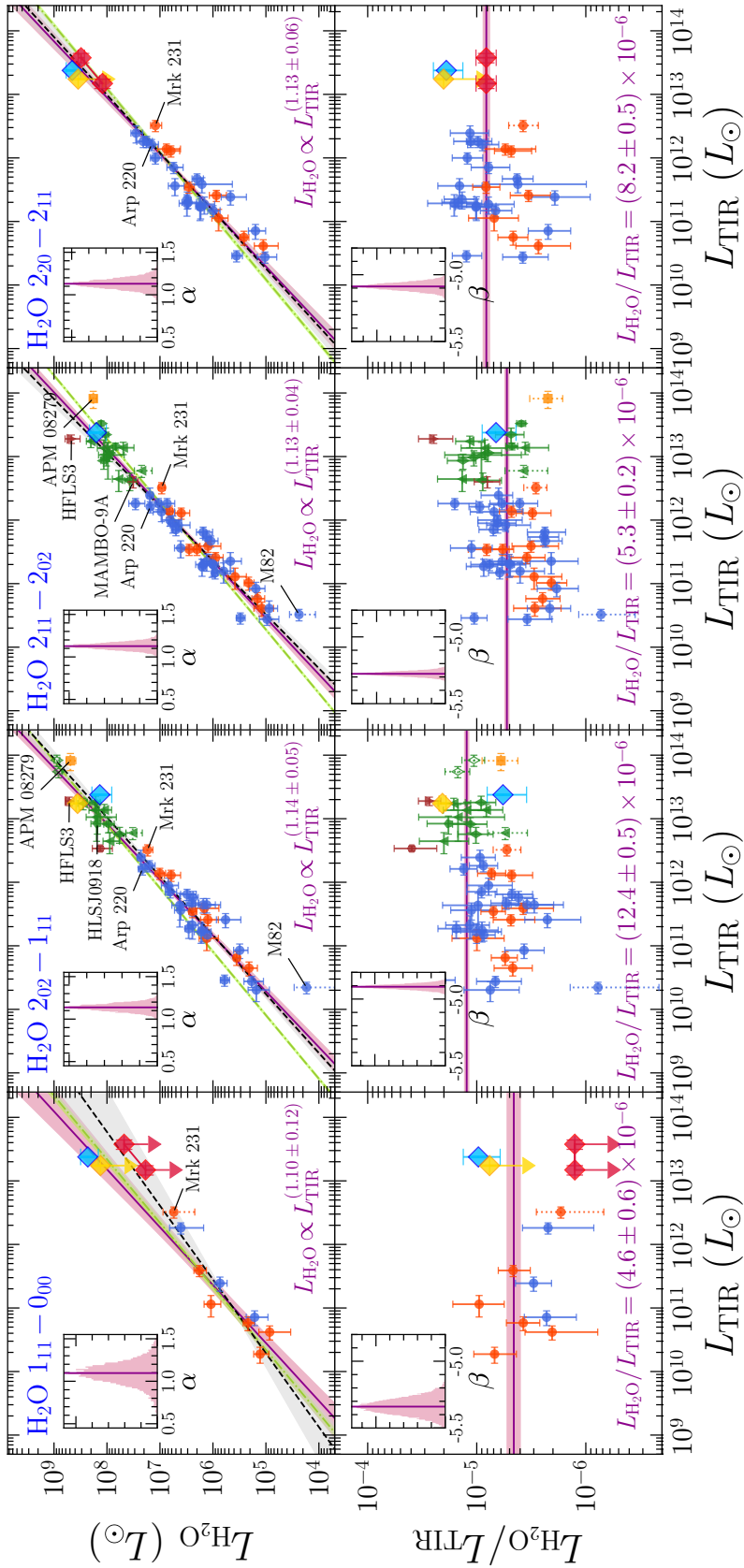


**Figure 7.9**

Correlations between H<sub>2</sub>O line luminosity and the total IR luminosity. Lower panels report the correspondent  $L_{\text{H}_2\text{O}}/L_{\text{TIR}}$  as a function of  $L_{\text{TIR}}$ . Data points show measurements of local and high- $z$  Hy/ULIRGs, SMGs, DSFGs/Hot DOGs and QSO hosts retrieved from the literature. They are color-coded by their type, while different symbols indicate the literature references according to the legend (see next figure). Our three quasar host galaxies are reported with colored diamonds. For the lensed quasar J0439+1634 (red diamonds connected by a line), we report the 95% confidence interval of intrinsic luminosities by adopting the magnification factor as reported in Yang et al. (2019c, see also Sect. 7.4). We adopted the average magnification factor as fiducial value in the fit. Data points with empty symbols are not corrected for gravitational lensing and were excluded from the fit. We also excluded those data points reported with dotted error bars as explained in the text. Downward arrows are  $3\sigma$  upper limits that we also ignored in the fit. The solid purple lines show our best-fit models. The inset panels show the posterior probability distribution of the slope of H<sub>2</sub>O–TIR luminosity correlations, and  $\beta$  in the case of  $L_{\text{H}_2\text{O}}/L_{\text{TIR}}$ . The best fit values are reported at the bottom of each panel. For comparison, we also show the results obtained by assuming an exact linear relation ( $\alpha = 1$ , dot-dashed green lines) and the best-fit model by Yang et al. (2013, dashed black lines). The shaded areas indicate the  $1-\sigma$  confidence intervals.

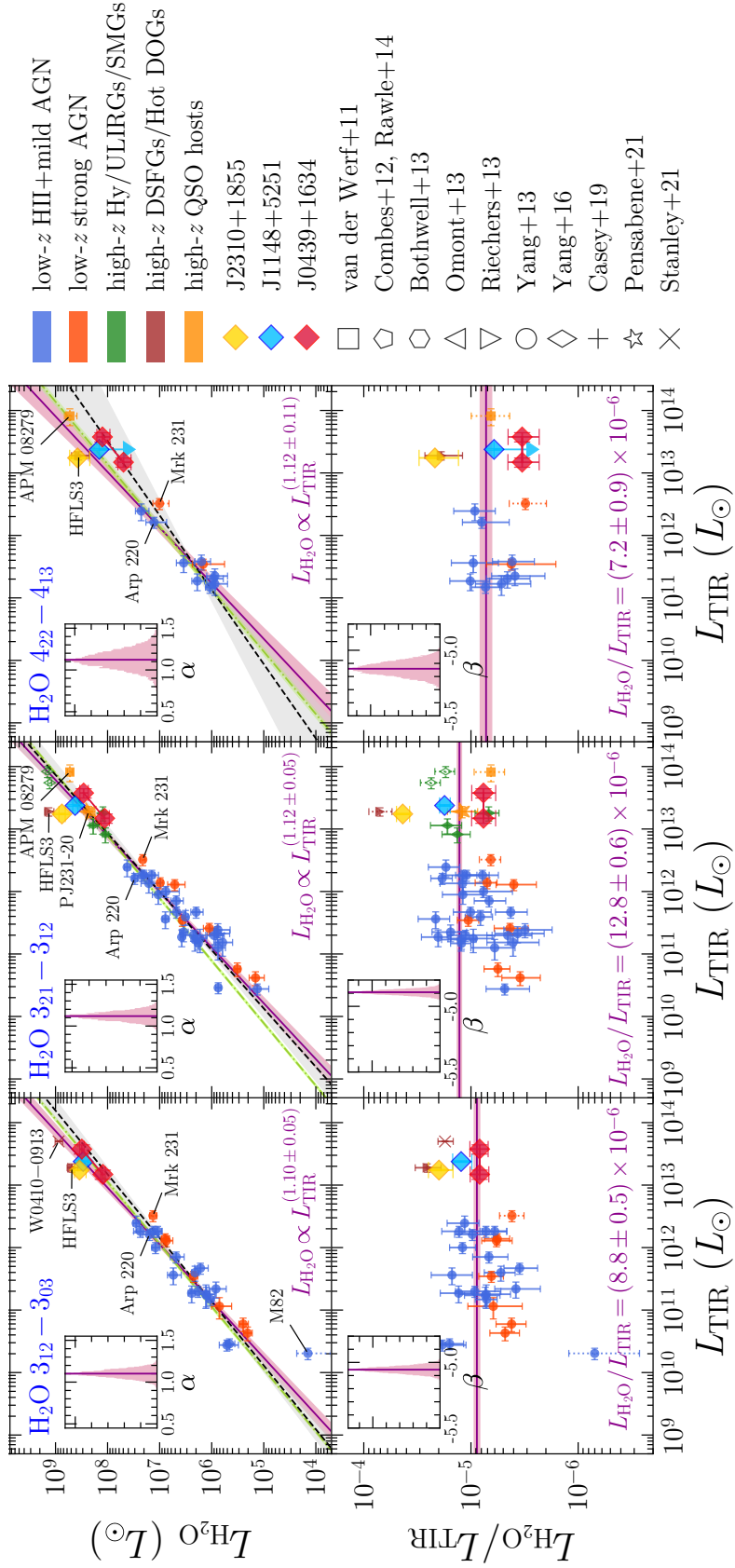


Figure 7.9  
(continued)

**Table 7.6:** Best-fit slopes of  $L_{\text{H}_2\text{O}} - L_{\text{TIR}}$  relations and averaged  $L_{\text{H}_2\text{O}}/L_{\text{TIR}}$  values

| H <sub>2</sub> O line             | $\alpha$    | $\langle L_{\text{H}_2\text{O}}/L_{\text{TIR}} \rangle \times 10^{-6}$ |
|-----------------------------------|-------------|--|
| 1 <sub>11</sub> – 0 <sub>00</sub> | 1.10 ± 0.12 | 4.6 ± 0.6  |
| 2 <sub>02</sub> – 1 <sub>11</sub> | 1.14 ± 0.05 | 12.4 ± 0.5   |
| 2 <sub>11</sub> – 2 <sub>02</sub> | 1.13 ± 0.04 | 5.3 ± 0.2  |
| 2 <sub>20</sub> – 2 <sub>11</sub> | 1.13 ± 0.06 | 8.2 ± 0.5  |
| 3 <sub>12</sub> – 3 <sub>03</sub> | 1.10 ± 0.05 | 8.8 ± 0.5  |
| 3 <sub>21</sub> – 3 <sub>12</sub> | 1.12 ± 0.05 | 12.8 ± 0.6   |
| 4 <sub>22</sub> – 4 <sub>13</sub> | 1.12 ± 0.11 | 7.2 ± 0.9  |

values corrected for the gravitational lensing. We note that our data provide new constraints to the H<sub>2</sub>O–TIR luminosity relations at  $L_{\text{TIR}} \gtrsim 10^{13} L_{\odot}$  and  $L_{\text{H}_2\text{O}} \gtrsim 10^8 L_{\odot}$  where only sparse detections are available in the literature thus far.

By assuming linear functional form of the type  $\text{Log } L_{\text{H}_2\text{O}} = \alpha \text{Log } L_{\text{TIR}} + \beta$ , we performed linear regressions in log-log space through a hierarchical Bayesian approach using the `linmix` python package (Kelly, 2007). In order to reduce possible biases of the fitting results, following Yang et al. (2013, 2016a) we excluded M82 due to its peculiar very low values of its H<sub>2</sub>O lines (see, Weiß et al., 2010; Yang et al., 2013, for a discussion). We also excluded SDP 81 due to missing flux filtered out by interferometer (Omont et al., 2013), and the H<sub>2</sub>O 3<sub>21</sub> – 3<sub>12</sub> transition of HFLS 3 due to its unusual high  $L_{\text{H}_2\text{O}}$ -to- $L_{\text{TIR}}$  ratio. Finally, we excluded all the sources not corrected for the gravitational lensing and all measurements for which we obtained an upper limit on H<sub>2</sub>O luminosity. In the case of the lensed quasar J0439+1634, we derived the intrinsic luminosities by adopting a mean magnification factor of 4.6 (see, Sect. 7.4, Yang et al. 2019c) and we used them as fiducial values in the fit. In Fig. 7.9 we report the best-fit results. For comparison we report the relation found by Yang et al. (2013) and the best-fit models obtained assuming an exact linear relation (i.e.,  $\alpha = 1$ ). Finally, we fit the  $L_{\text{H}_2\text{O}}/L_{\text{TIR}}$  ratios by adopting the same aforementioned assumptions.

Our results are reported in Tab. 7.6. All the best-fit slopes are consistent with slightly supralinear relations except for the ground transition H<sub>2</sub>O 1<sub>11</sub>–0<sub>00</sub>, for which the fit result points to a linear relation within the uncertainty. We also

obtained a similar result in the case of the  $\text{H}_2\text{O } 4_{22} - 4_{13}$  line. However, the latter results could suffer from large uncertainties due to the low number of available data points. The slopes of the correlations are all consistent within the uncertainties with those found by Yang et al. (2013, 2016a), however we found that the nominal values of  $\alpha$  are higher than those previously reported. This is valid for all the correlations except that involving the  $\text{H}_2\text{O } 2_{11} - 2_{02}$  line. Overall, the supralinear trend of  $L_{\text{H}_2\text{O}} - L_{\text{TIR}}$  correlations support the idea that, at least for mid- and high- $J$   $\text{H}_2\text{O}$  lines, the correlations are likely driven by the IR pumping effect rather than the mere cospatiality of the line- and IR-continuum-emitting region (see, González-Alfonso et al., 2014). Our analysis of the  $L_{\text{H}_2\text{O}}/L_{\text{TIR}}$  values leads to average higher values than reported by Yang et al. (2013, 2016a). We do not find any substantial difference in the  $\text{H}_2\text{O}$ -TIR luminosity ratios measured in our high- $z$  quasars than those of local AGN and star-forming galaxies as expected if  $\text{H}_2\text{O}$  is a pure tracer of the buried star-formation activity. Interestingly, by inspecting the results on  $\text{H}_2\text{O}$ -to-TIR luminosity ratios, we found that J2310+1855 shows systematically higher values with respect to the average ratios, consistent with the measurements obtained in HFLS 3 (Riechers et al., 2013). In optically thick systems, large velocity dispersion can increase the number of absorbed photons by  $\text{H}_2\text{O}$  molecules thus enhancing the  $L_{\text{H}_2\text{O}}/L_{\text{TIR}}$  values (González-Alfonso et al., 2014; Yang et al., 2016a). Both J2310+1855 and HFLS 3 are predicted to be optically thick at  $100 \mu\text{m}$  (see, Sect. 7.7.2 and Riechers et al. 2013), however the FWHM of  $\text{H}_2\text{O}$  lines in J2310+1855 are measured to be within the typical range of  $300 - 500 \text{ km s}^{-1}$  (see also Li et al. 2020b), while broader  $\text{H}_2\text{O}$  lines (FWHM  $\sim 900 \text{ km s}^{-1}$ ) are found in HFLS 3. These measurements possibly support radiative transfer models showing that supralinear  $\text{H}_2\text{O}$ -TIR correlations can be produced by an increased continuum opacity in systems with high  $L_{\text{TIR}}$  (González-Alfonso et al., 2014).

## 7.8 Summary and conclusions

We have presented NOEMA observations toward three IR-bright quasars (J2310+1855, J1148+5251, J0439+1634) at  $z > 6$ , targeted in multiple water vapor lines as well as FIR continuum. These quasars were previously detected in multiple ISM probes including some  $\text{H}_2\text{O}$  lines. The covered lines of our observations are the para-/ortho- $\text{H}_2\text{O } 3_{12} - 3_{03}$ ,  $1_{11} - 0_{00}$ ,  $2_{20} - 2_{11}$ , and

$4_{22} - 4_{13}$ . The combination of our new H<sub>2</sub>O detections, in conjunction with those from literature, allowed us to investigate the warm dense phase of the ISM, and the local IR dust radiation field at cosmic dawn. Our detection allowed us to pose new constraints on the H<sub>2</sub>O-IR luminosity relations which enclose key information on H<sub>2</sub>O excitations mechanism. In order to interpret our results and place quantitative constraints on the physical parameters of the ISM and local dust radiation field in galaxies, we employed MOLPOP-CEP radiative transfer code. The main results obtained in this chapter are summarized below.

- We modeled FIR dust continuum in all three quasar host galaxies by assuming a single-component modified blackbody. With this approach we inferred dust masses, temperature, emissivity indexes, the IR luminosities and the SFRs (see, **Sect. 7.5**, and **Tab. 7.4**). Our estimates are consistent with previous results reported in literature.
- By combining our multiple H<sub>2</sub>O lines we studied the H<sub>2</sub>O SLEDs of quasar host galaxies. Our H<sub>2</sub>O SLEDs do not show obvious imprinting of powerful AGN activity characterizing our sources when compared to the SLEDs of local ULIRGs, AGN, and as well as other high-*z* sources. However, on the base of the H<sub>2</sub>O excitation physics, a detailed qualitative analysis of the individual line ratios suggests that the bulk of H<sub>2</sub>O emission in J1148+5251 arises from warm ISM with low continuum opacity. Similar analysis point to the presence of relatively warmer dust in J2310+1855, and J0439+1634 that boosts the excitation of high-*J* H<sub>2</sub>O lines with respect to J1148+5251.
- By using our MOLPOP-CEP predictions, we modeled the observed H<sub>2</sub>O SLEDs of the quasar host galaxies. Our results reproduce well the observed data. The best-fit models reveal the presence of an intense warm dust component the temperature of which ranges in  $T_{\text{dust}} \sim 80 - 190$  K, with the highest values found in those sources detected in their high-lying  $J = 4$  H<sub>2</sub>O transition. The molecular hydrogen column densities of the bulk of H<sub>2</sub>O emitting medium in our quasar host galaxies are predicted to be within the range  $N_{\text{H}_2} \sim 10^{23} - 4 \times 10^{24} \text{ cm}^{-2}$ , in line with what we found in the previous **Chap. 6**. Finally, continuum optical thin conditions ( $\tau_{100} < 1$ ) are predicted in all sources except

in J2310+1855, consistently with the qualitative analysis of the H<sub>2</sub>O SLEDs.

- A detailed analysis of MOLPOP-CEP model predictions highlights the effect of the simultaneous contribution of collisions and radiative pumping in exciting the H<sub>2</sub>O lines. In particular, within our working assumptions, the low- $J$  H<sub>2</sub>O lines are nearly thermalized while at high- $J$ , the population of H<sub>2</sub>O levels are mainly driven by the dust radiation field. This combination results in a H<sub>2</sub>O level population that cannot be characterized by a single excitation temperature. We use our best parameters inferred from the modeling of the H<sub>2</sub>O SLEDs to retrieve the level population of water vapor in our quasar host galaxies. This analysis led to a more direct comparison of ISM excitation in quasars compared to the qualitative study of the H<sub>2</sub>O SLEDs. We found a significant contribution in populating the high- $J$  H<sub>2</sub>O lines in J2310+1855 compare to the other quasars. The excitation temperatures of  $E > 200$  K H<sub>2</sub>O levels are roughly  $T_{\text{ex}} \sim 40 - 50$  K, while are around  $T_{\text{ex}} \sim 25 - 30$  K in J1148+5251.
- We study the correlations between H<sub>2</sub>O and TIR luminosity and the H<sub>2</sub>O-to-TIR luminosity ratios. Our new detections, in combination with data from the literature, allowed us to put constraints on the  $L_{\text{TIR}} \gtrsim 10^{13} L_{\odot}$  and  $L_{\text{H}_2\text{O}} \gtrsim 10^8 L_{\odot}$  part of the correlations. The fit of the correlations point to supralinear trend in all the cases except for H<sub>2</sub>O 2<sub>11</sub> – 2<sub>02</sub> line which correlation with  $L_{\text{TIR}}$  is consistent with a linear dependence. Overall, our results support the idea that, at least for mid- and high- $J$  H<sub>2</sub>O transitions, the  $L_{\text{H}_2\text{O}} - L_{\text{TIR}}$  correlations are driven by the radiation pumping of the lines rather than the co-spatiality of the H<sub>2</sub>O-line- and IR-continuum-emitting regions. The analysis of the  $L_{\text{H}_2\text{O}}/L_{\text{TIR}}$  ratios leads to higher average values than those reported in Yang et al. (2013, 2016a), and did not highlight any significant evidence in the values measured in high- $z$ , local AGN, and local star-forming galaxies. This result suggests that H<sub>2</sub>O could be used as a proxy of star-formation also in high- $z$  quasar host galaxies.

In conclusion, in this chapter we show how the combination of multiple H<sub>2</sub>O lines enable to shed light on the properties of the warm molecular medium in massive galaxies emerging from the EoR. Water vapor lines are also powerful

diagnostics of the warm dust component that is difficult to unveil through a simple analysis of the dust continuum SED of high- $z$  quasar host galaxies. However, our investigations were limited to the poor S/N of the current data. Further investigations on a larger sample of sources targeting multiple H<sub>2</sub>O lines with deeper observations are required in order to determine if our results are (or not) typical characteristics of the  $z > 6$  quasar population. The brightness of H<sub>2</sub>O lines compared to other typically used molecular tracers, makes them ideal probes of shocked medium by AGN-driven outflow. Future deeper observations could expose the characteristic P-Cygni profiles in the spectra of such powerful primordial quasars. For these reasons we started an observational campaign with ALMA aiming to double the sample of quasars targeted in multiple H<sub>2</sub>O lines. This project is approved and it is currently in the queue of ALMA Cycle 8 scheduled observations. The forthcoming analysis of these observations will be presented in a future work.

# 8

## Summary & Concluding remarks

” *Here, on the edge of what we know, in contact with the ocean of the unknown, shines the mystery and beauty of the world. And it’s breathtaking.*

— Carlo Rovelli

This Ph.D. thesis was devoted to the study of quasar host galaxies in the early Universe ( $z > 6$ , age of the Universe  $< 1$  Gyr). For this purpose we adopted a multifaceted approach. First, we reviewed the main techniques aimed to unveil the population of  $z > 6$  quasars to which we contributed with the identification and characterization of new  $z > 6$  quasars. Our discoveries allowed us to shed light on the properties of the surrounding IGM at the end of the EoR, and to put constraints on the formation of the very first supermassive BHs. We then used high- $z$  quasars as probes of the onset of the BH–galaxy relation at the earliest epochs. This allowed us to investigate the competitive process between BH growth and galaxy assembly across cosmic time, and to get insights on the general properties of the cold gas kinematics in the high- $z$  quasars.

The second part of this thesis was focused on the characterization of the most distant  $z > 6$  quasar host galaxies by the study of their ISM. This is crucial for our understanding of how galaxies are shaped during their formation and their early evolution. In this context, multiline surveys with extremely sensitive telescopes such as ALMA and NOEMA, allowed us the dissect the

different gas phases and probes the extreme conditions at which the ISM is exposed in these highly star-forming galaxies with and without luminous quasars at the cosmic dawn. We finally put constraints on the embedded warm dense star-forming medium and the local IR radiation field of the warm dust in  $z > 6$  quasar hosts, for which little information were available until recently.

In the following, we summarize the main results obtained in this thesis, we draw our conclusions, and we discuss the future perspectives.

### **The rise of the giants: quasars at the dawn of cosmic time**

The discovery of luminous quasars at  $z > 7$ , with the most distant placed at  $z = 7.64$  (Wang et al., 2021a), revealed that supermassive BHs with  $M_{\text{BH}} \sim 10^9 M_{\odot}$  must be already in place less than 1 Gyr after the Big Bang. This fact challenges our understanding of how black holes formed in the first place. Various scenarios have been proposed in order to explain the rapid build-up of massive black holes in the young Universe. These include (super-)Eddington accretion of Pop III remnants, DCBH, or runaway mergers in dense star clusters. The increasingly sensitive optical/NIR wide-field surveys, in conjunction with the refinement of the selection techniques, opened a powerful window for the study of the formation and evolution of the first BHs. Thanks to the efforts of various groups, to date, more than  $\sim 200$  quasars have been identified at  $z > 6$ .

In this context, I performed optical/NIR photometric observations with ESO/NTT at La Silla Observatory (Chile), and with NOT at Roque the Los Muchachos Observatory (La Palma, Canary Islands) during 2018-2019. These activities led to the discovery of three new  $z > 6$  quasars: PJ344-02, at  $z \approx 6.5$ ; PJ083+11, a new WLQ at  $z = 6.3401$ ; and PJ172+18 at  $z = 6.82$ , the most distant radio-loud quasar known so far. In **Chap. 2** we reported our contribution to these results which are published in Andika et al. (2020), and Bañados et al. (2021) (both including Pensabene, A.). The newly discovered quasars were selected starting from optical/NIR survey catalogs, and then were unambiguously identified through various spectroscopic follow-up campaigns. By using NIR spectra, we inferred MgII-based BH masses, and Eddington ratios of  $M_{\text{BH}} \approx 2 \times 10^9 M_{\odot}$ ,  $L_{\text{bol}}/L_{\text{Edd}} \approx 0.5$ , for PJ083+11; and  $M_{\text{BH}} \approx 3 \times 10^8 M_{\odot}$ ,  $L_{\text{bol}}/L_{\text{Edd}} \approx 2.2$ , in the case of PJ172+18. The spectrum of PJ083+11 shows a proximity zone size of  $R_p \approx 1.2 \text{ pMpc}$ , which suggests a

quasar lifetime of only  $t_Q \sim 10^3 - 10^{4.5}$  yr consistent with the BLR formation time predicted by simulations. The observed short  $t_Q$  is at variance with the BH mass having formed with the observed instantaneous accretion rate. This evidence suggests that this WLQ is a young quasar in an early phase of moderate accretion which BLR is not fully form yet.

The high Eddington ratio of PJ172+18 places this object among the fastest accreting quasars at any redshift. The properties of the strong Ly- $\alpha$  emission line in this quasar suggest a high ionized fraction ( $> 90\%$ ) of the surrounding IGM. The observed proximity zone size,  $R_p \approx 6$  pMpc, is among the largest measured at these redshifts, such that the quasar lifetime exceeds the average  $t_Q$  of the  $z \gtrsim 6$  quasar population. The extrapolation of observed steep radio spectrum implies a radio loudness parameter of  $R_{4400} \approx 70$ , which classifies PJ172+18 as a RL quasar. Our radio VLA band-L follow up revealed PJ172+18 a factor  $\sim 2$  fainter than expected based on FIRST observations taken two decades previously. This fact together with the large observed proximity zone size, suggests that we are witnessing the turning-off phase of PJ172+18 quasar.

### **The onset of the black hole–galaxy relation at early epochs**

The existence of tight correlations between supermassive BHs and the properties of their host galaxies in the contemporary Universe is a key building block for our understanding of galaxy formation and evolution. These relations are thought to be the result of the complex interplay between the assembling of galaxy stellar mass, and the AGN feedback which injects energy into the ISM. Indeed, AGN feedback is able to quench the star formation and expels gas from the galaxy gravitational potential through galactic-scale outflows. These tight BH-galaxy correlations are one of the main lines of observational evidence supporting the coevolution paradigm. Investigating the onset of such relations at early epochs ( $z > 6$ ) is therefore crucial in order to put constraints on galaxy formation and evolution models.

In **Chap. 4**, we focused on the relation between BH mass ( $M_{\text{BH}}$ ) and the dynamical mass ( $M_{\text{dyn}}$ ) of the host galaxy. Previous works suggest an evolution of the  $M_{\text{BH}} - M_{\text{dyn}}$  relation with redshift, indicating that the BH growth precedes the galaxy mass assembly during their coevolution at  $z > 3$ . However, dynamical masses at high redshift are often estimated through the virial theorem, thus introducing significant uncertainties. Within the scope of this

work, we studied the  $M_{\text{BH}} - M_{\text{dyn}}$  relation of a sample of  $2 < z < 7$  quasars by constraining their galaxy masses through a full kinematical modeling of the cold gas kinematics, thus avoiding all possible biases and effects introduced by the rough estimates usually adopted so far. For this purpose, we retrieved public observations of 72 quasar hosts observed with ALMA either in  $[\text{CII}]_{158\mu\text{m}}$ , or CO lines. We then selected those quasars whose line emission is spatially resolved, and we performed a kinematic analysis on ALMA observations. We estimated the dynamical masses of the systems by modeling the gas kinematics with a rotating disk, taking into account geometrical and instrumental effects. Our dynamical mass estimates, combined with  $M_{\text{BH}}$  obtained from the literature, and our new CIV 1550 Å observations allowed us to investigate the  $M_{\text{BH}}/M_{\text{dyn}}$  in the early Universe. Overall, we obtained a sample of ten quasars at  $z \sim 2 - 7$ , in which line emission is detected with high S/N ( $\gtrsim 5 - 10$ ), and the gas kinematics are spatially resolved and dominated by ordered rotations. The estimated dynamical masses place six out of ten quasars above the local relation yielding to  $M_{\text{BH}}/M_{\text{dyn}}$  ratio  $\sim 10 \times$  higher than those estimated in low- $z$  galaxies. On the other hand, we found that four quasars at  $z \sim 4 - 6$  have dynamical-to-BH-mass ratios consistent with what is observed in early-type galaxies in the local Universe. This work is published in Pensabene et al. (2020).

### **The multiphase ISM in $z > 6$ quasar host galaxies**

The study of the physical properties of the ISM in primordial galaxies is fundamental in order to shed light on how galaxies have been shaped during its formation and evolution from the cosmic reionization to the present epoch. Due to the huge luminosity of the AGN paired with the rapid consumption of huge gas reservoirs,  $z > 6$  quasars are excellent laboratory to study the ISM in the violent environment of the first massive galaxies.

In **Chap. 6**, we presented a multiline survey of the ISM in two  $z > 6$  quasar host galaxies, PJ231-20 ( $z = 6.59$ ), PJ308-21 ( $z = 6.23$ ), and their two companion galaxies. In this chapter we capitalized on observations carried out using ALMA by which we targeted 11 main tracers of the ISM including atomic FSLs and molecular lines:  $[\text{NII}]_{205\mu\text{m}}$ ,  $[\text{CI}]_{369\mu\text{m}}$ , CO ( $J_{\text{up}} = 7, 10, 15, 16$ ),  $\text{H}_2\text{O}$   $3_{12} - 2_{21}$ ,  $3_{21} - 3_{12}$ ,  $3_{03} - 2_{12}$ , and the  $\text{OH}_{163\mu\text{m}}$  doublet. The underlying FIR continuum samples the Rayleigh-Jeans tail of the respective dust emission. By combining this information with our earlier ALMA  $[\text{CII}]_{158\mu\text{m}}$  observations,

we explored the effects of star formation and BH feedback on the ISM of galaxies using the CLOUDY radiative transfer models. We estimated dust masses, spectral indexes, IR luminosities, and SFRs from the FIR continuum. The analysis of the FSLs indicated that the  $[\text{CII}]_{158\mu\text{m}}$  and  $[\text{CI}]_{369\mu\text{m}}$  emission arises predominantly from the neutral medium in PDRs. We found that line deficits agree with those of local LIRGs. The CO SLEDs revealed significant high- $J$  CO excitation in both quasar hosts. Our CO SLED modeling of the quasar PJ231-20 showed that PDRs dominate the molecular mass and CO luminosities for  $J_{\text{up}} \leq 7$ , while the  $J_{\text{up}} \geq 10$  CO emission is likely driven by XDRs produced by the AGN at the very center of the quasar host galaxy. The  $J_{\text{up}} > 10$  lines are undetected in the other galaxies in our study. The  $\text{H}_2\text{O}$  line detection in quasar PJ231-20 placed this object on the  $L_{\text{H}_2\text{O}} - L_{\text{TIR}}$  relation found for low- $z$  sources, thus suggesting that this water vapor transition is predominantly excited by the IR pumping. Models of  $\text{H}_2\text{O}$  SLED and of the  $\text{H}_2\text{O}$ -to- $\text{OH}_{163\mu\text{m}}$  ratio pointed to PDR contributions with high volume and column density ( $n_{\text{H}} \sim 0.8 \times 10^5 \text{ cm}^{-3}$ ,  $N_{\text{H}} = 10^{24} \text{ cm}^{-2}$ ) in an intense radiation field. Our analysis suggested a less highly excited medium in the companion galaxies. However, current data did not allow us to definitely rule out an AGN in these sources, as suggested by previous studies of the same objects. This work demonstrates the power of multiline studies of FIR diagnostic in order to dissect the physical conditions in galaxies emerging from cosmic dawn. This study is reported in Pensabene et al. (2021).

### **Unraveling the warm and dense gas in dusty $z > 6$ quasars**

Water vapor is one of the brightest molecular emitters after CO in IR-bright galaxies and it allows us to investigate an ISM phase that cannot be probed with other tracers.  $\text{H}_2\text{O}$  has a complex spectrum and it is excited both by collisions in the warm and dense gas, and by radiative pumping in regions with intense IR dust radiation field. Water vapor emission also traces shock-heated regions by outflowing gas revealed by high-velocity broad line components and the typical P-Cygni line profile. Therefore, by surveying  $\text{H}_2\text{O}$  in galaxies we can probe the embedded medium where star formation ultimately occurs and search for molecular outflows driven by AGN feedback. However, despite the sporadic  $\text{H}_2\text{O}$  detections in some high- $z$  sources,  $\text{H}_2\text{O}$  is rarely exploited as a tracers of ISM in distant galaxies because observations of several transitions are required in order to infer quantitative constraints on the line-emitting

region. Thus the warm and dense gas at  $z > 6$  remains largely unexplored. In **Chap. 7** we reported a systematic survey of H<sub>2</sub>O emission in three  $z > 6$  IR-bright quasars. In this chapter we capitalized on NOEMA observations toward J2310+1855, J1148+5251, and J0439+1634 targeted in their multiple para-/ortho-H<sub>2</sub>O transitions ( $3_{12} - 3_{03}$ ,  $1_{11} - 0_{00}$ ,  $2_{20} - 2_{11}$ , and  $4_{22} - 4_{13}$ ), as well as FIR continuum. By combining our data with previous detections reported in the literature, we studied the physical properties of both the warm dense phase of the ISM, and the warm component of the dust content. In addition, we explored the H<sub>2</sub>O excitation mechanisms in our quasar host galaxies. We estimated dust masses and temperatures, spectral indexes, IR luminosities, and the SFRs from the modeling of the FIR continuum using a single modified blackbody. We modeled the H<sub>2</sub>O lines using MOLPOP-CEP radiative transfer model and we put constraints on the column density of the medium where the bulk of water vapor emission arises. We also retrieved estimates of the continuum optical depth and dust temperature of the local IR radiation field responsible for the radiatively-pumped excitation of high-lying H<sub>2</sub>O lines. We found that, water vapor lines in our quasar host galaxies are primarily excited in dense ( $n_{\text{H}_2} \sim 10^4 - 10^5 \text{ cm}^{-3}$ ) molecular medium with a column density of  $N_{\text{H}_2} \sim 10^{23} - 4 \times 10^{24} \text{ cm}^{-2}$ . High- $J$  H<sub>2</sub>O lines are mainly radiatively pumped by intense optically-thin IR radiation field associated to a warm dust component the temperature of which ranges in  $T_{\text{dust}} \sim 80 - 190 \text{ K}$ . However, in the case of J2310+1855, our analysis points to a higher value of the continuum optical depth at  $100 \mu\text{m}$  ( $\tau_{100} > 1$ ). Our quantitative results are in agreement with expectations based on the H<sub>2</sub>O SLEDs of local and high- $z$  ULIRGs and AGN. Boltzmann diagram highlighted the significant role of IR pumping to populate high H<sub>2</sub>O energy levels. This analysis allowed us to directly compare the excitation conditions in our quasar host galaxies. Our observations enabled us to sample the high-luminosity part of the  $L_{\text{H}_2\text{O}} - L_{\text{TIR}}$  relations and to put new constraints on their trends. Overall, our results point to superlinear trends indicating that H<sub>2</sub>O–TIR relations are likely driven by the effect of the IR pumping rather than the mere cospatiality between the FIR-continuum- and the line-emitting regions. The observed  $L_{\text{H}_2\text{O}}/L_{\text{TIR}}$  ratios in our  $z > 6$  quasars did not show any strong deviation with respect to those measured in star-forming galaxies and AGN at lower redshift. This supports the idea that H<sub>2</sub>O can be likely used to trace the star-formation buried into the depths of dense molecular clouds. This work was conducted

in collaboration with Prof. Dr. Paul van der Werf and his group at Leiden Observatory (Leiden University), and will be reported in a forthcoming paper (Pensabene A., van der Werf P., Decarli R., et al., in prep.).

## Closing statements & Future perspectives

The last decades have witnessed an enormous progress in pushing forward the redshift frontier which allowed to unveil and characterize ever larger samples of galaxies emerging from the cosmic dawn. The advent of extremely sensitive telescopes such as ALMA and NOEMA has revolutionized the study of high- $z$  quasar host galaxies at the (sub-)mm wavelengths. The unprecedented details of the new data have enabled us to carry out exquisite analysis that were restricted to the local Universe until recently. Such studies are fundamental for our understanding of the formation of the first galaxies and black holes. This thesis aimed to contribute to these efforts. This work demonstrates that FIR/(sub-)mm studies are a powerful tool to dissect the complex conditions of the interstellar medium in  $z > 6$  quasar host galaxies and to investigate the interplay between AGN activity and star formation in galaxies across the cosmic time. The results of this thesis can be used as a benchmark for future high-redshift studies. Future (sub-)mm observations with superior sensitivity and higher angular resolution will secure spatially-resolved diagnostics of the ISM within galaxies. This will allow us to study the spatial distribution of the different gas tracers and dust components, and to quantitatively assess the impact of the most powerful AGN and the intense star formation on the assembly of galaxies at the end of the Epoch of Reionization. Larger quasar samples targeted in multiple tracers will allow us to perform statistical studies and to reduce the uncertainties on the predictions obtained with radiative transfer models. The forthcoming launch of the JWST on December 18th, 2021, will allow us to unravel the stellar population of  $z > 6$  quasars for the very first time, thus significantly contribute at completing our picture of these primordial galaxies. Finally, ambitious projects such as the *Vera C. Rubin Observatory* and *Euclid Space Telescope* promise to broaden our current view on the Universe by revealing galaxies and quasars at the earliest epochs. The next decade will witness a real revolution for the extragalactic astronomy at high redshift.



# References

- Abbott, B. P., Abbott, R., Abbott, T. D., et al. (2016). *Phys. Rev. Lett.*, **116**, 061102.
- Abbott, B. P., Abbott, R., Abbott, T. D., et al. (2019). *Physical Review X*, **9**, 031040.
- Abel, N. P., van Hoof, P. A. M., Shaw, G., et al. (2008). *ApJ*, **686**, 1125–1136.
- Abel, N. P., Dudley, C., Fischer, J., et al. (2009). *ApJ*, **701**, 1147–1160.
- Abel, T., Bryan, G. L. & Norman, M. L. (2000). *ApJ*, **540**, 39–44.
- Agarwal, B., Khochfar, S., Johnson, J. L., et al. (2012). *MNRAS*, **425**, 2854–2871.
- Agúndez, M., Goicoechea, J. R., Cernicharo, J., et al. (2010). *ApJ*, **713**, 662–670.
- Aihara, H., Arimoto, N., Armstrong, R., et al. (2018). *PASJ*, **70**, S4.
- Aird, J., Nandra, K., Laird, E. S., et al. (2010). *MNRAS*, **401**, 2531–2551.
- Aird, J., Coil, A. L., Moustakas, J., et al. (2012). *ApJ*, **746**, 90.
- Aird, J., Comastri, A., Brusa, M., et al. (2013). *arXiv e-prints*, arXiv:1306.2325.
- Akiyama, M., He, W., Ikeda, H., et al. (2018). *PASJ*, **70**, S34.
- Alaghband-Zadeh, S., Chapman, S. C., Swinbank, A. M., et al. (2013). *MNRAS*, **435**, 1493–1510.
- Alexander, D. M. & Hickox, R. C. (2012). *New A Rev.*, **56**, 93–121.
- Alexander, D. M., Brandt, W. N., Smail, I., et al. (2008). *AJ*, **135**, 1968–1981.
- Andika, I. T., Jahnke, K., Onoue, M., et al. (2020). *ApJ*, **903**, 34.
- Angulo, R. E., Springel, V., White, S. D. M., et al. (2012). *MNRAS*, **426**, 2046–2062.
- Antonucci, R. R. J. & Miller, J. S. (1985). *ApJ*, **297**, 621–632.
- Antonucci, R. (1993). *ARA&A*, **31**, 473–521.
- Asensio Ramos, A. & Elitzur, M. (2018). *A&A*, **616**, A131.
- Asplund, M., Grevesse, N., Sauval, A. J. & Scott, P. (2009). *ARA&A*, **47**, 481–522.
- Astropy Collaboration, Robitaille, T. P., Tollerud, E. J., et al. (2013). *A&A*, **558**, A33.
- Astropy Collaboration, Price-Whelan, A. M., Sipőcz, B. M., et al. (2018). *AJ*, **156**, 123.
- Bañados, E., Venemans, B. P., Morganson, E., et al. (2014). *AJ*, **148**, 14.
- Bañados, E., Decarli, R., Walter, F., et al. (2015a). *ApJ*, **805**, L8.
- Bañados, E., Venemans, B. P., Morganson, E., et al. (2015b). *ApJ*, **804**, 118.
- Bañados, E., Venemans, B. P., Decarli, R., et al. (2016). *ApJS*, **227**, 11.
- Bañados, E., Venemans, B. P., Mazzucchelli, C., et al. (2018). *Nature*, **553**, 473–476.
- Bañados, E., Mazzucchelli, C., Momjian, E., et al. (2021). *ApJ*, **909**, 80.
- Bahcall, J. N., Kozlovsky, B.-Z. & Salpeter, E. E. (1972). *ApJ*, **171**, 467.
- Baldry, I. K., Driver, S. P., Loveday, J., et al. (2012). *MNRAS*, **421**, 621–634.
- Baldry, I. K., Glazebrook, K., Brinkmann, J., et al. (2004). *ApJ*, **600**, 681–694.
- Baldwin, J. A., Phillips, M. M. & Terlevich, R. (1981a). *PASP*, **93**, 5–19.
- Baldwin, J. A., Phillips, M. M. & Terlevich, R. (1981b). *PASP*, **93**, 817.
- Balmaverde, B., Gilli, R., Mignoli, M., et al. (2017). *A&A*, **606**, A23.
- Banerji, M., Carilli, C. L., Jones, G., et al. (2017). *MNRAS*, **465**, 4390–4405.
- Banerji, M., McMahon, R. G., Hewett, P. C., et al. (2012). *MNRAS*, **427**, 2275–2291.
- Banerji, M., Alaghband-Zadeh, S., Hewett, P. C. & McMahon, R. G. (2015). *MNRAS*, **447**, 3368–3389.
- Barai, P., Gallerani, S., Pallottini, A., et al. (2018). *MNRAS*, **473**, 4003–4020.
- Bardeen, J. M. (1970). *Nature*, **226**, 64–65.
- Baron, D. & Ménard, B. (2019). *MNRAS*, **487**, 3404–3418.

- Baumgartner, W. H., Tueller, J., Markwardt, C. B., et al. (2013). *ApJS*, **207**, 19.
- Becker, G. D., Bolton, J. S. & Lidz, A. (2015). *PASA*, **32**, e045.
- Becker, R. H., White, R. L. & Helfand, D. J. (1995). *ApJ*, **450**, 559.
- Beelen, A., Cox, P., Benford, D. J., et al. (2006). *ApJ*, **642**, 694–701.
- Begelman, M. C., Volonteri, M. & Rees, M. J. (2006). *MNRAS*, **370**, 289–298.
- Begelman, M. C., Rossi, E. M. & Armitage, P. J. (2008). *MNRAS*, **387**, 1649–1659.
- Begeman, K. G. (1987). PhD thesis. -.
- Behroozi, P. S., Wechsler, R. H. & Conroy, C. (2013). *ApJ*, **770**, 57.
- Beifiori, A., Courteau, S., Corsini, E. M. & Zhu, Y. (2012). *MNRAS*, **419**, 2497–2528.
- Bell, E. F., Papovich, C., Wolf, C., et al. (2005). *ApJ*, **625**, 23–36.
- Belladitta, S., Moretti, A., Caccianiga, A., et al. (2020). *A&A*, **635**, L7.
- Bennert, N., Falcke, H., Schulz, H., et al. (2002). *ApJ*, **574**, L105–L109.
- Bennert, V. N., Treu, T., Woo, J.-H., et al. (2010). *ApJ*, **708**, 1507–1527.
- Bennert, V. N., Auger, M. W., Treu, T., et al. (2011a). *ApJ*, **726**, 59.
- Bennert, V. N., Auger, M. W., Treu, T., et al. (2011b). *ApJ*, **742**, 107.
- Bennert, V. N., Treu, T., Auger, M. W., et al. (2015). *ApJ*, **809**, 20.
- Benson, A. J., Lacey, C. G., Baugh, C. M., et al. (2002a). *MNRAS*, **333**, 156–176.
- Benson, A. J., Frenk, C. S., Lacey, C. G., et al. (2002b). *MNRAS*, **333**, 177–190.
- Bentz, M. C. & Manne-Nicholas, E. (2018). *ApJ*, **864**, 146.
- Bentz, M. C., Peterson, B. M., Pogge, R. W., et al. (2006). *ApJ*, **644**, 133–142.
- Bentz, M. C., Peterson, B. M., Netzer, H., et al. (2009). *ApJ*, **697**, 160–181.
- Bergin, E. A., Kaufman, M. J., Melnick, G. J., et al. (2003). *ApJ*, **582**, 830–845.
- Bertola, E., Dadina, M., Cappi, M., et al. (2020). *A&A*, **638**, A136.
- Bertoldi, F., Carilli, C. L., Cox, P., et al. (2003). *A&A*, **406**, L55–L58.
- Bessell, M. S. (2005). *ARA&A*, **43**, 293–336.
- Bianchi, S., Maiolino, R. & Risaliti, G. (2012). *Advances in Astronomy*, **2012**, 782030.
- Bieri, R., Dubois, Y., Silk, J., et al. (2016). *MNRAS*, **455**, 4166–4182.
- Binggeli, B., Sandage, A. & Tammann, G. A. (1988). *ARA&A*, **26**, 509–560.
- Binney, J. & Tremaine, S. (2008). *Galactic Dynamics: Second Edition*.
- Birkin, J. E., Weiss, A., Wardlow, J. L., et al. (2021). *MNRAS*, **501**, 3926–3950.
- Bisbas, T. G., Bell, T. A., Viti, S., et al. (2012). *MNRAS*, **427**, 2100–2118.
- Bischetti, M., Piconcelli, E., Vietri, G., et al. (2017). *A&A*, **598**, A122.
- Bischetti, M., Piconcelli, E., Feruglio, C., et al. (2019a). *A&A*, **628**, A118.
- Bischetti, M., Maiolino, R., Carniani, S., et al. (2019b). *A&A*, **630**, A59.
- Blain, A. W., Barnard, V. E. & Chapman, S. C. (2003). *MNRAS*, **338**, 733–744.
- Blandford, R. D. & McKee, C. F. (1982). *ApJ*, **255**, 419–439.
- Blanton, M. R., Hogg, D. W., Bahcall, N. A., et al. (2003). *ApJ*, **594**, 186–207.
- Bochkarev, N. G. & Gaskell, C. M. (2009). *Astronomy Letters*, **35**, 287–293.
- Bock, D. C. J., Large, M. I. & Sadler, E. M. (1999). *AJ*, **117**, 1578–1593.
- Böhm, A., Wisotzki, L., Bell, E. F., et al. (2013). *A&A*, **549**, A46.
- Boissay, R., Ricci, C. & Paltani, S. (2016). *A&A*, **588**, A70.
- Bolatto, A. D., Wolfire, M. & Leroy, A. K. (2013). *ARA&A*, **51**, 207–268.
- Bolton, J. S., Haehnelt, M. G., Warren, S. J., et al. (2011). *MNRAS*, **416**, L70–L74.
- Bolton, J. S. & Haehnelt, M. G. (2007a). *MNRAS*, **381**, L35–L39.
- Bolton, J. S. & Haehnelt, M. G. (2007b). *MNRAS*, **374**, 493–514.
- Bongiorno, A., Maiolino, R., Brusa, M., et al. (2014). *MNRAS*, **443**, 2077–2091.

- Bonoli, S., Marulli, F., Springel, V., et al. (2009). *MNRAS*, **396**, 423–438.
- Bonoli, S., Mayer, L. & Callegari, S. (2014). *MNRAS*, **437**, 1576–1592.
- Boogaard, L. A., van der Werf, P., Weiss, A., et al. (2020). *ApJ*, **902**, 109.
- Borys, C., Smail, I., Chapman, S. C., et al. (2005). *ApJ*, **635**, 853–863.
- Bosma, A. (1978). PhD thesis. -.
- Bothwell, M. S., Chapman, S. C., Tacconi, L., et al. (2010). *MNRAS*, **405**, 219–233.
- Bothwell, M. S., Aguirre, J. E., Chapman, S. C., et al. (2013). *ApJ*, **779**, 67.
- Bothwell, M. S., Aguirre, J. E., Aravena, M., et al. (2017). *MNRAS*, **466**, 2825–2841.
- Bouwens, R. J., Illingworth, G. D., Oesch, P. A., et al. (2012). *ApJ*, **754**, 83.
- Bouwens, R. J., Illingworth, G. D., Oesch, P. A., et al. (2015). *ApJ*, **803**, 34.
- Boyle, B. J., Shanks, T., Croom, S. M., et al. (2000). *MNRAS*, **317**, 1014–1022.
- Bradford, C. M., Stacey, G. J., Fischer, J., et al. (1999). *The Universe as Seen by ISO*. Ed. by Cox, P. & Kessler, M. Vol. 427. ESA Special Publication, 861.
- Bradford, C. M., Bolatto, A. D., Maloney, P. R., et al. (2011). *ApJ*, **741**, L37.
- Brandt, W. N. & Alexander, D. M. (2015). *A&A Rev.*, **23**, 1.
- Brauher, J. R., Dale, D. A. & Helou, G. (2008). *ApJS*, **178**, 280–301.
- Brinchmann, J., Charlot, S., White, S. D. M., et al. (2004). *MNRAS*, **351**, 1151–1179.
- Brinchmann, J. & Ellis, R. S. (2000). *ApJ*, **536**, L77–L80.
- Brusa, M., Civano, F., Comastri, A., et al. (2010). *ApJ*, **716**, 348–369.
- Brusa, M., Feruglio, C., Cresci, G., et al. (2015a). *A&A*, **578**, A11.
- Brusa, M., Bongiorno, A., Cresci, G., et al. (2015b). *MNRAS*, **446**, 2394–2417.
- Brusa, M., Perna, M., Cresci, G., et al. (2016). *A&A*, **588**, A58.
- Brusa, M., Cresci, G., Daddi, E., et al. (2018). *A&A*, **612**, A29.
- Buchner, J. & Bauer, F. E. (2017). *MNRAS*, **465**, 4348–4362.
- Buzzoni, B., Delabre, B., Dekker, H., et al. (1984). *The Messenger*, **38**, 9.
- Cañameras, R., Yang, C., Nesvadba, N. P. H., et al. (2018). *A&A*, **620**, A61.
- Canalizo, G., Wold, M., Hiner, K. D., et al. (2012). *ApJ*, **760**, 38.
- Cano-Díaz, M., Maiolino, R., Marconi, A., et al. (2012). *A&A*, **537**, L8.
- Cappellari, M. & Emsellem, E. (2004). *PASP*, **116**, 138–147.
- Cappelluti, N., Hasinger, G. & Natarajan, P. (2021). *arXiv e-prints*, arXiv:2109.08701.
- Carilli, C. L. & Rawlings, S. (2004). *New A Rev.*, **48**, 979–984.
- Carilli, C. L. & Walter, F. (2013). *ARA&A*, **51**, 105–161.
- Carnall, A. C., Shanks, T., Chehade, B., et al. (2015). *MNRAS*, **451**, L16–L20.
- Carniani, S., Marconi, A., Biggs, A., et al. (2013). *A&A*, **559**, A29.
- Carniani, S., Marconi, A., Maiolino, R., et al. (2016). *A&A*, **591**, A28.
- Carniani, S., Marconi, A., Maiolino, R., et al. (2017a). *A&A*, **605**, A105.
- Carniani, S., Maiolino, R., Pallottini, A., et al. (2017b). *A&A*, **605**, A42.
- Carniani, S., Gallerani, S., Vallini, L., et al. (2019). *MNRAS*, **489**, 3939–3952.
- Carr, B. J. (2003). *Quantum Gravity: From Theory to Experimental Search*. Ed. by Giulini, D., Kiefer, C. & Laemmerzahl, C. Vol. 631, 301–321.
- Carral, P., Hollenbach, D. J., Lord, S. D., et al. (1994). *ApJ*, **423**, 223.
- Carrera, F. J., Page, M. J., Stevens, J. A., et al. (2011). *MNRAS*, **413**, 2791–2807.
- Casey, C. M. (2012). *MNRAS*, **425**, 3094–3103.
- Casey, C. M., Narayanan, D. & Cooray, A. (2014). *Phys. Rep.*, **541**, 45–161.
- Casey, C. M., Zavala, J. A., Aravena, M., et al. (2019). *ApJ*, **887**, 55.
- Cattaneo, A., Dekel, A., Faber, S. M. & Guiderdoni, B. (2008). *MNRAS*, **389**, 567–584.

- Cattaneo, A., Faber, S. M., Binney, J., et al. (2009). *Nature*, **460**, 213–219.
- Cattaneo, A., Mamon, G. A., Warnick, K. & Knebe, A. (2011). *A&A*, **533**, A5.
- Gen, R. & Haiman, Z. (2000). *ApJ*, **542**, L75–L78.
- Cernicharo, J., Goicoechea, J. R., Pardo, J. R. & Asensio-Ramos, A. (2006). *ApJ*, **642**, 940–953.
- Chambers, K. C., Magnier, E. A., Metcalfe, N., et al. (2016). *arXiv e-prints*, arXiv:1612.05560.
- Chapman, S. C., Blain, A. W., Smail, I. & Ivison, R. J. (2005). *ApJ*, **622**, 772–796.
- Charmandaris, V., Uchida, K. I., Weedman, D., et al. (2004). *ApJS*, **154**, 142–146.
- Chartas, G., Cappi, M., Vignali, C., et al. (2021). *arXiv e-prints*, arXiv:2106.14907.
- Chehade, B., Carnall, A. C., Shanks, T., et al. (2018). *MNRAS*, **478**, 1649–1659.
- Cherepashchuk, A. M. & Lyutyi, V. M. (1973). *Astrophys. Lett.*, **13**, 165.
- Cicone, C., Maiolino, R., Gallerani, S., et al. (2015). *A&A*, **574**, A14.
- Ciotti, L. & Ostriker, J. P. (1997). *ApJ*, **487**, L105–L108.
- Ciotti, L., Ostriker, J. P. & Proga, D. (2010). *ApJ*, **717**, 708–723.
- Cisternas, M., Jahnke, K., Bongiorno, A., et al. (2011a). *ApJ*, **741**, L11.
- Cisternas, M., Jahnke, K., Inskip, K. J., et al. (2011b). *ApJ*, **726**, 57.
- Coatman, L., Hewett, P. C., Banerji, M., et al. (2017). *MNRAS*, **465**, 2120–2142.
- Colbert, J. W., Malkan, M. A., Clegg, P. E., et al. (1999). *ApJ*, **511**, 721–729.
- Cole, S. (1991). *ApJ*, **367**, 45.
- Colless, M., Dalton, G., Maddox, S., et al. (2001). *MNRAS*, **328**, 1039–1063.
- Combes, F., Maoli, R. & Omont, A. (1999). *A&A*, **345**, 369–379.
- Combes, F., Rex, M., Rawle, T. D., et al. (2012). *A&A*, **538**, L4.
- Combes, F. & Wiklind, T. (1997). *ApJ*, **486**, L79–L82.
- Comerford, J. M., Gerke, B. F., Newman, J. A., et al. (2009). *ApJ*, **698**, 956–965.
- Condon, J. J., Cotton, W. D., Greisen, E. W., et al. (1998). *AJ*, **115**, 1693–1716.
- Conley, A., Cooray, A., Vieira, J. D., et al. (2011). *ApJ*, **732**, L35.
- Connor, T., Bañados, E., Stern, D., et al. (2019). *ApJ*, **887**, 171.
- Connor, T., Bañados, E., Mazzucchelli, C., et al. (2020). *ApJ*, **900**, 189.
- Coppin, K. E. K., Swinbank, A. M., Neri, R., et al. (2008). *MNRAS*, **389**, 45–62.
- Cormier, D., Lebouteiller, V., Madden, S. C., et al. (2012). *A&A*, **548**, A20.
- Costa, T., Sijacki, D. & Haehnelt, M. G. (2014a). *MNRAS*, **444**, 2355–2376.
- Costa, T., Sijacki, D., Trenti, M. & Haehnelt, M. G. (2014b). *MNRAS*, **439**, 2146–2174.
- Cowie, L. L., Songaila, A., Hu, E. M. & Cohen, J. G. (1996). *AJ*, **112**, 839.
- Cresci, G., Hicks, E. K. S., Genzel, R., et al. (2009). *ApJ*, **697**, 115–132.
- Cresci, G., Mainieri, V., Brusa, M., et al. (2015). *ApJ*, **799**, 82.
- Croton, D. J. (2006). *MNRAS*, **369**, 1808–1812.
- Croton, D. J. (2009). *MNRAS*, **394**, 1109–1119.
- Croton, D. J., Springel, V., White, S. D. M., et al. (2006a). *MNRAS*, **367**, 864–864.
- Croton, D. J., Springel, V., White, S. D. M., et al. (2006b). *MNRAS*, **365**, 11–28.
- Cruddace, R., Paresce, F., Bowyer, S. & Lampton, M. (1974). *ApJ*, **187**, 497–504.
- Crummy, J., Fabian, A. C., Gallo, L. & Ross, R. R. (2006). *MNRAS*, **365**, 1067–1081.
- Cucciati, O., Tresse, L., Ilbert, O., et al. (2012). *A&A*, **539**, A31.
- Cybert, R. H., Fields, B. D., Olive, K. A. & Yeh, T.-H. (2016). *Reviews of Modern Physics*, **88**, 015004.
- da Cunha, E., Groves, B., Walter, F., et al. (2013). *ApJ*, **766**, 13.

- Dabrowski, I. (1984). *Canadian Journal of Physics*, **62**, 1639.
- Daddi, E., Dickinson, M., Morrison, G., et al. (2007). *ApJ*, **670**, 156–172.
- Daddi, E., Bournaud, F., Walter, F., et al. (2010). *ApJ*, **713**, 686–707.
- Daniel, F., Goicoechea, J. R., Cernicharo, J., et al. (2012). *A&A*, **547**, A81.
- Davies, F. B., Furlanetto, S. R. & McQuinn, M. (2016). *MNRAS*, **457**, 3006–3023.
- de Blok, W. J. G. & McGaugh, S. S. (1997). *MNRAS*, **290**, 533–552.
- De Looze, I., Cormier, D., Lebouteiller, V., et al. (2014). *A&A*, **568**, A62.
- de Nicola, S., Marconi, A. & Longo, G. (2019). *MNRAS*, **490**, 600–612.
- De Rosa, G., Decarli, R., Walter, F., et al. (2011). *ApJ*, **739**, 56.
- De Rosa, G., Venemans, B. P., Decarli, R., et al. (2014). *ApJ*, **790**, 145.
- Decarli, R., Falomo, R., Treves, A., et al. (2010). *MNRAS*, **402**, 2453–2461.
- Decarli, R., Walter, F., Neri, R., et al. (2012). *ApJ*, **752**, 2.
- Decarli, R., Walter, F., Carilli, C., et al. (2014). *ApJ*, **782**, L17.
- Decarli, R., Walter, F., Venemans, B. P., et al. (2017). *Nature*, **545**, 457–461.
- Decarli, R., Walter, F., Venemans, B. P., et al. (2018). *ApJ*, **854**, 97.
- Decarli, R., Dotti, M., Bañados, E., et al. (2019a). *ApJ*, **880**, 157.
- Decarli, R., Mignoli, M., Gilli, R., et al. (2019b). *A&A*, **631**, L10.
- Dekel, A. & Silk, J. (1986). *ApJ*, **303**, 39.
- Dekel, A. & Birnboim, Y. (2006). *MNRAS*, **368**, 2–20.
- Dekel, A., Sari, R. & Ceverino, D. (2009). *ApJ*, **703**, 785–801.
- Denney, K. D. (2012). *ApJ*, **759**, 44.
- Destombes, J. L., Marliere, C., Baudry, A. & Brillet, J. (1977). *A&A*, **61**, 769.
- Devecchi, B. & Volonteri, M. (2009). *ApJ*, **694**, 302–313.
- Dewangan, D. P., Flower, D. R. & Alexander, M. H. (1987). *MNRAS*, **226**, 505–512.
- Dey, A., Schlegel, D. J., Lang, D., et al. (2019). *AJ*, **157**, 168.
- Di Matteo, T., Springel, V. & Hernquist, L. (2005). *Nature*, **433**, 604–607.
- Diamond-Stanic, A. M., Fan, X., Brandt, W. N., et al. (2009). *ApJ*, **699**, 782–799.
- Díaz-Santos, T., Armus, L., Charmandaris, V., et al. (2013). *ApJ*, **774**, 68.
- Díaz-Santos, T., Armus, L., Charmandaris, V., et al. (2017). *ApJ*, **846**, 32.
- Dibai, E. A. (1977). *Soviet Astronomy Letters*, **3**, 1–3.
- Dibai, E. A. (1987). *Soviet Ast.*, **31**, 117.
- Dicken, D., Tadhunter, C., Axon, D., et al. (2009). *ApJ*, **694**, 268–285.
- Dicken, D., Tadhunter, C., Axon, D., et al. (2010). *ApJ*, **722**, 1333–1341.
- DiPompeo, M. A., Hickox, R. C., Myers, A. D. & Geach, J. E. (2017). *MNRAS*, **464**, 3526–3535.
- Djupvik, A. A. & Andersen, J. (2010). *Highlights of Spanish Astrophysics V*. Vol. 14. Astrophysics and Space Science Proceedings, 211.
- Doeleman, S. S., Weintroub, J., Rogers, A. E. E., et al. (2008). *Nature*, **455**, 78–80.
- Donley, J. L., Rieke, G. H., Pérez-González, P. G. & Barro, G. (2008). *ApJ*, **687**, 111–132.
- Donoso, E., Yan, L., Tsai, C., et al. (2012). *ApJ*, **748**, 80.
- Downes, D. & Solomon, P. M. (1998). *ApJ*, **507**, 615–654.
- Downes, D., Radford, J. E., Greve, A., et al. (1992). *ApJ*, **398**, L25.
- Draine, B. T. (2006). *ApJ*, **636**, 1114–1120.
- Draine, B. T. & Lee, H. M. (1984). *ApJ*, **285**, 89.
- Draine, B. T., Dale, D. A., Bendo, G., et al. (2007). *ApJ*, **663**, 866–894.

- Draine, B. T. (2011). *Physics of the Interstellar and Intergalactic Medium*.
- Dressler, A. (1989). *Active Galactic Nuclei*. Ed. by Osterbrock, D. E. & Miller, J. S. Vol. 134, 217.
- Dugan, Z., Bryan, S., Gaibler, V., et al. (2014). *ApJ*, **796**, 113.
- Dunlop, J. S. (2013). *The First Galaxies*. Ed. by Wiklind, T., Mobasher, B. & Bromm, V. Vol. 396, 223.
- Dunne, L. & Eales, S. A. (2001). *MNRAS*, **327**, 697–714.
- Dunne, L., Eales, S., Edmunds, M., et al. (2000). *MNRAS*, **315**, 115–139.
- Dwek, E. (1998). *ApJ*, **501**, 643.
- Dwek, E. & Cherchneff, I. (2011). *ApJ*, **727**, 63.
- Edge, A., Sutherland, W., Kuijken, K., et al. (2013). *The Messenger*, **154**, 32–34.
- Eilers, A.-C., Davies, F. B., Hennawi, J. F., et al. (2017). *ApJ*, **840**, 24.
- Eilers, A.-C., Hennawi, J. F. & Davies, F. B. (2018a). *ApJ*, **867**, 30.
- Eilers, A.-C., Davies, F. B. & Hennawi, J. F. (2018b). *ApJ*, **864**, 53.
- Eilers, A.-C., Hennawi, J. F., Decarli, R., et al. (2020). *ApJ*, **900**, 37.
- Elbaz, D. (2002). *Ap&SS*, **281**, 449–452.
- Elbaz, D., Dickinson, M., Hwang, H. S., et al. (2011). *A&A*, **533**, A119.
- Elitzur, M. & Asensio Ramos, A. (2006). *MNRAS*, **365**, 779–791.
- Elvis, M., Wilkes, B. J., McDowell, J. C., et al. (1994). *ApJS*, **95**, 1.
- Engel, H., Tacconi, L. J., Davies, R. I., et al. (2010). *ApJ*, **724**, 233–243.
- Epinat, B., Contini, T., Le Fèvre, O., et al. (2009). *A&A*, **504**, 789–805.
- Epinat, B., Amram, P., Balkowski, C. & Marcelin, M. (2010). *MNRAS*, **401**, 2113–2147.
- Erickson, E. F., Knacke, R. F., Tokunaga, A. T. & Haas, M. R. (1981). *ApJ*, **245**, 148–153.
- Event Horizon Telescope Collaboration (2019). *ApJ*, **875**, L1.
- Faber, S. M., Willmer, C. N. A., Wolf, C., et al. (2007). *ApJ*, **665**, 265–294.
- Fabian, A. C. (2012). *ARA&A*, **50**, 455–489.
- Faisst, A. L., Fudamoto, Y., Oesch, P. A., et al. (2020). *MNRAS*, **498**, 4192–4204.
- Fan, L., Han, Y., Nikutta, R., et al. (2016). *ApJ*, **823**, 107.
- Fan, X., White, R. L., Davis, M., et al. (2000). *AJ*, **120**, 1167–1174.
- Fan, X., Narayanan, V. K., Lupton, R. H., et al. (2001a). *AJ*, **122**, 2833–2849.
- Fan, X., Strauss, M. A., Schneider, D. P., et al. (2001b). *AJ*, **121**, 54–65.
- Fan, X., Hennawi, J. F., Richards, G. T., et al. (2004). *AJ*, **128**, 515–522.
- Fan, X., Carilli, C. L. & Keating, B. (2006). *ARA&A*, **44**, 415–462.
- Fan, X., Wang, F., Yang, J., et al. (2019). *ApJ*, **870**, L11.
- Farina, E. P., Venemans, B. P., Decarli, R., et al. (2017). *ApJ*, **848**, 78.
- Farina, E. P., Arrigoni-Battaia, F., Costa, T., et al. (2019). *ApJ*, **887**, 196.
- Farrar, D., Afonso, J., Efstathiou, A., et al. (2003). *MNRAS*, **343**, 585–607.
- Farrar, D., Leboutteiller, V., Spoon, H. W. W., et al. (2013). *ApJ*, **776**, 38.
- Faure, A. & Josselin, E. (2008). *A&A*, **492**, 257–264.
- Faure, A., Crimier, N., Ceccarelli, C., et al. (2007). *A&A*, **472**, 1029–1035.
- Ferkinhoff, C., Brisbin, D., Nikola, T., et al. (2011). *ApJ*, **740**, L29.
- Ferland, G. J., Chatzikos, M., Guzmán, F., et al. (2017). *Rev. Mexicana Astron. Astrofis.*, **53**, 385–438.
- Ferrarese, L. & Ford, H. (2005). *Space Sci. Rev.*, **116**, 523–624.

- Ferrarese, L. & Merritt, D. (2000). *ApJ*, **539**, L9–L12.
- Ferrarese, L., Ford, H. C. & Jaffe, W. (1996). *ApJ*, **470**, 444.
- Feruglio, C., Ferrara, A., Bischetti, M., et al. (2017). *A&A*, **608**, A30.
- Feruglio, C., Fiore, F., Carniani, S., et al. (2018). *A&A*, **619**, A39.
- Fischer, J., Luhman, M. L., Satyapal, S., et al. (1999). *Ap&SS*, **266**, 91–98.
- Fischer, J., Sturm, E., González-Alfonso, E., et al. (2010). *A&A*, **518**, L41.
- Fixsen, D. J., Bennett, C. L. & Mather, J. C. (1999). *ApJ*, **526**, 207–214.
- Flores, H., Hammer, F., Puech, M., et al. (2006). *A&A*, **455**, 107–118.
- Flower, D. R. & Launay, J. M. (1985). *MNRAS*, **214**, 271–277.
- Flower, D. R. & Pineau Des Forêts, G. (2010). *MNRAS*, **406**, 1745–1758.
- Foreman-Mackey, D., Hogg, D. W., Lang, D. & Goodman, J. (2013). *Publications of the Astronomical Society of the Pacific*, **125**, 306.
- Freeman, K. C. (1970). *ApJ*, **160**, 811.
- Freese, K., Bodenheimer, P., Spolyar, D. & Gondolo, P. (2008). *ApJ*, **685**, L101.
- Gaibler, V., Khochfar, S., Krause, M. & Silk, J. (2012). *MNRAS*, **425**, 438–449.
- Galametz, M., Kennicutt, R. C., Albrecht, M., et al. (2012). *MNRAS*, **425**, 763–787.
- Gallerani, S., Ferrara, A., Neri, R. & Maiolino, R. (2014). *MNRAS*, **445**, 2848–2853.
- Gao, L., Yoshida, N., Abel, T., et al. (2007). *MNRAS*, **378**, 449–468.
- Gao, Y. & Solomon, P. M. (2004a). *ApJS*, **152**, 63–80.
- Gao, Y. & Solomon, P. M. (2004b). *ApJ*, **606**, 271–290.
- Gaskell, C. M. (2010). *First Stars and Galaxies: Challenges for the Next Decade*. Ed. by Whalen, D. J., Bromm, V. & Yoshida, N. Vol. 1294. American Institute of Physics Conference Series, 261–261.
- Gaskell, C. M. (2011). *SF2A-2011: Proceedings of the Annual meeting of the French Society of Astronomy and Astrophysics*. Ed. by Alecian, G., Belkacem, K., Samadi, R. & Valls-Gabaud, D., 577–582.
- Gaskell, C. M. (2009). *New A Rev.*, **53**, 140–148.
- Gebhardt, K., Bender, R., Bower, G., et al. (2000). *ApJ*, **539**, L13–L16.
- Gelbord, J. M. (2003). PhD thesis. THE JOHNS HOPKINS UNIVERSITY.
- Genzel, R., Newman, S., Jones, T., et al. (2011). *ApJ*, **733**, 101.
- Genzel, R., Tacconi, L. J., Lutz, D., et al. (2015). *ApJ*, **800**, 20.
- Gerin, M. & Phillips, T. G. (2000). *ApJ*, **537**, 644–653.
- Ghez, A. M., Klein, B. L., Morris, M. & Becklin, E. E. (1998). *ApJ*, **509**, 678–686.
- Gillessen, S., Eisenhauer, F., Trippe, S., et al. (2009). *ApJ*, **692**, 1075–1109.
- Glassgold, A. E. & Langer, W. D. (1974). *ApJ*, **193**, 73–91.
- Gnerucci, A., Marconi, A., Cresci, G., et al. (2011). *A&A*, **533**, A124.
- Godard, B., Pineau des Forêts, G., Lesaffre, P., et al. (2019). *A&A*, **622**, A100.
- Goicoechea, J. R. & Cernicharo, J. (2002). *ApJ*, **576**, L77–L81.
- Goicoechea, J. R., Martín-Pintado, J. & Cernicharo, J. (2005). *ApJ*, **619**, 291–296.
- Goldsmith, P. F. & Langer, W. D. (1978). *ApJ*, **222**, 881–895.
- Goldsmith, P. F. & Langer, W. D. (1999). *ApJ*, **517**, 209–225.
- Goldsmith, P. F., Langer, W. D., Pineda, J. L. & Velusamy, T. (2012). *ApJS*, **203**, 13.
- Gonçalves, T. S., Martin, D. C., Menéndez-Delmestre, K., et al. (2012). *ApJ*, **759**, 67.
- González-Alfonso, E., Smith, H. A., Fischer, J. & Cernicharo, J. (2004). *ApJ*, **613**, 247–261.
- González-Alfonso, E., Smith, H. A., Ashby, M. L. N., et al. (2008). *ApJ*, **675**, 303–315.

- González-Alfonso, E., Fischer, J., Isaak, K., et al. (2010). *A&A*, **518**, L43.
- González-Alfonso, E., Fischer, J., Graciá-Carpio, J., et al. (2012). *A&A*, **541**, A4.
- González-Alfonso, E., Fischer, J., Bruderer, S., et al. (2013). *A&A*, **550**, A25.
- González-Alfonso, E., Fischer, J., Aalto, S. & Falstad, N. (2014). *A&A*, **567**, A91.
- González-Alfonso, E., Fischer, J., Spoon, H. W. W., et al. (2017). *ApJ*, **836**, 11.
- Graciá-Carpio, J., Sturm, E., Hailey-Dunsh Heath, S., et al. (2011). *ApJ*, **728**, L7.
- Graff, M. M. & Dalgarno, A. (1987). *ApJ*, **317**, 432.
- Graham, A. W. (2007). *MNRAS*, **379**, 711–722.
- Graham, A. W. & Scott, N. (2013). *ApJ*, **764**, 151.
- Granato, G. L., De Zotti, G., Silva, L., et al. (2004). *ApJ*, **600**, 580–594.
- Grazian, A., Fontana, A., Santini, P., et al. (2015). *A&A*, **575**, A96.
- Green, S., Maluendes, S. & McLean, A. D. (1993). *ApJS*, **85**, 181.
- Greene, J. E. & Ho, L. C. (2005). *ApJ*, **630**, 122–129.
- Greene, J. E., Peng, C. Y., Kim, M., et al. (2010). *ApJ*, **721**, 26–45.
- Gregg, M. D., Lacy, M., White, R. L., et al. (2002). *ApJ*, **564**, 133–142.
- Greve, T. R., Leonidaki, I., Xilouris, E. M., et al. (2014). *ApJ*, **794**, 142.
- Grier, C. J., Shen, Y., Horne, K., et al. (2019). *ApJ*, **887**, 38.
- Gruppioni, C., Pozzi, F., Rodighiero, G., et al. (2013). *MNRAS*, **432**, 23–52.
- Gültekin, K., Richstone, D. O., Gebhardt, K., et al. (2009). *ApJ*, **698**, 198–221.
- Gunn, J. E. & Peterson, B. A. (1965). *ApJ*, **142**, 1633–1636.
- Habing, H. J. (1968). *Bull. Astron. Inst. Netherlands*, **19**, 421.
- Haiman, Z. & Cen, R. (2001). *The Physics of Galaxy Formation*. Ed. by Umemura, M. & Susa, H. Vol. 222. Astronomical Society of the Pacific Conference Series, 101.
- Harikane, Y., Ouchi, M., Shibuya, T., et al. (2018). *ApJ*, **859**, 84.
- Häring, N. & Rix, H.-W. (2004). *ApJ*, **604**, L89–L92.
- Harris, C. R., Millman, K. J., van der Walt, S. J., et al. (2020). *Nature*, **585**, 357–362.
- Harrison, C. M. (2017). *Nature Astronomy*, **1**, 0165.
- Harrison, C. (2014). PhD thesis. Durham University.
- Hartquist, T. W. & Williams, D. A. (1998). *The molecular astrophysics of stars and galaxies*, **4**.
- Hashimoto, T., Laporte, N., Mawatari, K., et al. (2018). *Nature*, **557**, 392–395.
- Hashimoto, T., Inoue, A. K., Mawatari, K., et al. (2019a). *PASJ*, **71**, 71.
- Hashimoto, T., Inoue, A. K., Tamura, Y., et al. (2019b). *PASJ*, **71**, 109.
- Haworth, T. J., Glover, S. C. O., Koepferl, C. M., et al. (2018). *New A Rev.*, **82**, 1–58.
- Heckman, T. M. & Best, P. N. (2014). *ARA&A*, **52**, 589–660.
- Helou, G., Soifer, B. T. & Rowan-Robinson, M. (1985). *ApJ*, **298**, L7–L11.
- Helou, G., Khan, I. R., Malek, L. & Boehmer, L. (1988). *ApJS*, **68**, 151.
- Herrera-Camus, R., Bolatto, A., Smith, J. D., et al. (2016). *ApJ*, **826**, 175.
- Herrera-Camus, R., Sturm, E., Graciá-Carpio, J., et al. (2018a). *ApJ*, **861**, 94.
- Herrera-Camus, R., Sturm, E., Graciá-Carpio, J., et al. (2018b). *ApJ*, **861**, 95.
- Herrera-Camus, R., Tacconi, L., Genzel, R., et al. (2019). *ApJ*, **871**, 37.
- Herrera-Camus, R., Janssen, A., Sturm, E., et al. (2020a). *A&A*, **635**, A47.
- Herrera-Camus, R., Sturm, E., Graciá-Carpio, J., et al. (2020b). *A&A*, **633**, L4.
- Herrera-Camus, R., Förster Schreiber, N., Genzel, R., et al. (2021). *A&A*, **649**, A31.
- Hildebrand, R. H. (1983). *QJRAS*, **24**, 267–282.
- Hill, M. D. & Shanks, T. (2011). *MNRAS*, **410**, 762–774.

- Hinshaw, G., Larson, D., Komatsu, E., et al. (2013). *The Astrophysical Journal Supplement Series*, **208**, 19.
- Hirschmann, M., Khochfar, S., Burkert, A., et al. (2010). *MNRAS*, **407**, 1016–1032.
- Ho, L. C. (2008). *ARA&A*, **46**, 475–539.
- Ho, L. (1999). *Observational Evidence for the Black Holes in the Universe*. Ed. by Chakrabarti, S. K. Vol. 234, 157.
- Ho, L. C. (2007). *ApJ*, **669**, 821–829.
- Ho, L. C. & Kim, M. (2014). *ApJ*, **789**, 17.
- Hollenbach, D. J. & Tielens, A. G. G. M. (1997). *ARA&A*, **35**, 179–216.
- Hollenbach, D. J. & Tielens, A. G. G. M. (1999). *Reviews of Modern Physics*, **71**, 173–230.
- Hollenbach, D. & McKee, C. F. (1989). *ApJ*, **342**, 306.
- Hollenbach, D., Kaufman, M. J., Bergin, E. A. & Melnick, G. J. (2009). *ApJ*, **690**, 1497–1521.
- Hopkins, A. M. (2004). *ApJ*, **615**, 209–221.
- Hopkins, P. F., Strauss, M. A., Hall, P. B., et al. (2004). *AJ*, **128**, 1112–1123.
- Hopkins, P. F., Hernquist, L., Cox, T. J., et al. (2005). *ApJ*, **630**, 705–715.
- Hopkins, P. F., Somerville, R. S., Hernquist, L., et al. (2006). *ApJ*, **652**, 864–888.
- Hopkins, P. F., Hernquist, L., Cox, T. J. & Kereš, D. (2008). *The Astrophysical Journal Supplement Series*, **175**, 356–389.
- Hopkins, P. F., Murray, N. & Thompson, T. A. (2009). *MNRAS*, **398**, 303–311.
- Hryniewicz, K., Czerny, B., Nikolajuk, M. & Kuraszkiewicz, J. (2010). *MNRAS*, **404**, 2028–2036.
- Hu, J. (2008). *MNRAS*, **386**, 2242–2252.
- Hughes, D. H., Robson, E. I., Dunlop, J. S. & Gear, W. K. (1993). *MNRAS*, **263**, 607–618.
- Hunter, J. D. (2007). *Computing in Science Engineering*, **9**, 90–95.
- Ikeda, M., Oka, T., Tatematsu, K., et al. (2002). *ApJS*, **139**, 467–485.
- Ilbert, O., Salvato, M., Le Floch, E., et al. (2010). *ApJ*, **709**, 644–663.
- Ilbert, O., McCracken, H. J., Le Fèvre, O., et al. (2013). *A&A*, **556**, A55.
- Imanishi, M. (2002). *ApJ*, **569**, 44–53.
- Imanishi, M. & Wada, K. (2004). *ApJ*, **617**, 214–231.
- Imanishi, M., Ichikawa, K., Takeuchi, T., et al. (2011). *PASJ*, **63**, 447.
- Inayoshi, K., Visbal, E. & Haiman, Z. (2020). *ARA&A*, **58**, 27–97.
- Indriolo, N., Geballe, T. R., Oka, T. & McCall, B. J. (2007). *ApJ*, **671**, 1736–1747.
- Inoue, A. K., Tamura, Y., Matsuo, H., et al. (2016). *Science*, **352**, 1559–1562.
- Ishibashi, W. & Fabian, A. C. (2012). *MNRAS*, **427**, 2998–3005.
- Ishibashi, W. & Fabian, A. C. (2014). *MNRAS*, **441**, 1474–1478.
- Ishibashi, W., Fabian, A. C. & Canning, R. E. A. (2013). *MNRAS*, **431**, 2350–2355.
- Israel, F. P., Rosenberg, M. J. F. & van der Werf, P. (2015). *A&A*, **578**, A95.
- Iverson, R. J., Papadopoulos, P. P., Smail, I., et al. (2011). *MNRAS*, **412**, 1913–1925.
- Izumi, T., Onoue, M., Shirakata, H., et al. (2018). *PASJ*, **70**, 36.
- Izumi, T., Onoue, M., Matsuoka, Y., et al. (2019). *PASJ*, **71**, 111.
- Jaffe, W., Ford, H., Ferrarese, L., et al. (1996). *ApJ*, **460**, 214.
- Jahnke, K. & Macciò, A. V. (2011). *ApJ*, **734**, 92.
- Jahnke, K., Bongiorno, A., Brusa, M., et al. (2009). *ApJ*, **706**, L215–L220.

- Jarugula, S., Vieira, J. D., Spilker, J. S., et al. (2019). *ApJ*, **880**, 92.
- Jiang, L., Fan, X., Vestergaard, M., et al. (2007a). *AJ*, **134**, 1150.
- Jiang, L., Fan, X., Ivezić, Ž., et al. (2007b). *ApJ*, **656**, 680–690.
- Jiang, L., McGreer, I. D., Fan, X., et al. (2016). *ApJ*, **833**, 222.
- Jiao, Q., Zhao, Y., Zhu, M., et al. (2017). *ApJ*, **840**, L18.
- Johnson, J. L., Whalen, D. J., Fryer, C. L. & Li, H. (2012). *ApJ*, **750**, 66.
- Jones, G. C., Carilli, C. L., Shao, Y., et al. (2017). *ApJ*, **850**, 180.
- Juneau, S., Glazebrook, K., Crampton, D., et al. (2005). *ApJ*, **619**, L135–L138.
- Kamenetzky, J., Rangwala, N., Glenn, J., et al. (2016). *ApJ*, **829**, 93.
- Kamphuis, P., Józsa, G. I. G., Oh, S. H., et al. (2015). *MNRAS*, **452**, 3139–3158.
- Kashikawa, N., Ishizaki, Y., Willott, C. J., et al. (2015). *ApJ*, **798**, 28.
- Kaspi, S., Smith, P. S., Netzer, H., et al. (2000). *ApJ*, **533**, 631–649.
- Kaspi, S., Maoz, D., Netzer, H., et al. (2005). *ApJ*, **629**, 61–71.
- Kaspi, S., Brandt, W. N., Maoz, D., et al. (2007). *ApJ*, **659**, 997–1007.
- Kauffmann, G., White, S. D. M. & Guiderdoni, B. (1993). *MNRAS*, **264**, 201–218.
- Kauffmann, G., Heckman, T. M., White, S. D. M., et al. (2003a). *MNRAS*, **341**, 33–53.
- Kauffmann, G., Heckman, T. M., Tremonti, C., et al. (2003b). *MNRAS*, **346**, 1055–1077.
- Kaufman, M. J., Wolfire, M. G., Hollenbach, D. J. & Luhman, M. L. (1999). *ApJ*, **527**, 795–813.
- Kaufman, M. J., Wolfire, M. G. & Hollenbach, D. J. (2006). *ApJ*, **644**, 283–299.
- Keating, L. C., Haehnelt, M. G., Cantalupo, S. & Puchwein, E. (2015). *MNRAS*, **454**, 681–697.
- Kegel, W. H., Hertenstein, T. & Quirrenbach, A. (1999). *A&A*, **351**, 472–476.
- Kellermann, K. I., Sramek, R., Schmidt, M., et al. (1989). *AJ*, **98**, 1195.
- Kelly, B. C. (2007). *ApJ*, **665**, 1489–1506.
- Kennicutt Robert C., J. (1998). *ApJ*, **498**, 541–552.
- Kereš, D., Katz, N., Weinberg, D. H. & Davé, R. (2005). *MNRAS*, **363**, 2–28.
- Kerr, R. P. (1963). *Phys. Rev. Lett.*, **11**, 237–238.
- Kim, M., Ho, L. C., Peng, C. Y., et al. (2008). *ApJS*, **179**, 283–305.
- King, A. R. (2010). *Accretion and Ejection in AGN: a Global View*. Ed. by Maraschi, L., Ghisellini, G., Della Ceca, R. & Tavecchio, F. Vol. 427. Astronomical Society of the Pacific Conference Series, 315.
- King, A. & Pounds, K. (2015). *ARA&A*, **53**, 115–154.
- Kirkpatrick, A., Pope, A., Alexander, D. M., et al. (2012). *ApJ*, **759**, 139.
- Kirkpatrick, A., Pope, A., Sajina, A., et al. (2015). *ApJ*, **814**, 9.
- Klypin, A., Kravtsov, A. V., Valenzuela, O. & Prada, F. (1999). *ApJ*, **522**, 82–92.
- Kocevski, D. D., Faber, S. M., Mozena, M., et al. (2012). *ApJ*, **744**, 148.
- Kohandel, M., Pallottini, A., Ferrara, A., et al. (2019). *MNRAS*, 1423.
- Koptelova, E., Hwang, C.-Y., Yu, P.-C., et al. (2017). *Scientific Reports*, **7**, 41617.
- Korista, K., Baldwin, J., Ferland, G. & Verner, D. (1997). *ApJS*, **108**, 401–415.
- Kormendy, J. (1993). *The Nearest Active Galaxies*. Ed. by Beckman, J., Colina, L. & Netzer, H., 197–218.
- Kormendy, J. & Ho, L. C. (2013). *ARA&A*, **51**, 511–653.
- Kormendy, J. & Richstone, D. (1995). *ARA&A*, **33**, 581.
- Koss, M., Mushotzky, R., Veilleux, S. & Winter, L. (2010). *ApJ*, **716**, L125–L130.

- Kovács, A., Chapman, S. C., Dowell, C. D., et al. (2006). *ApJ*, **650**, 592–603.
- Kratzer, R. M. & Richards, G. T. (2015). *AJ*, **149**, 61.
- Krolik, J. H. & Kallman, T. R. (1983). *ApJ*, **267**, 610–624.
- Krolik, J. H. & Begelman, M. C. (1988). *ApJ*, **329**, 702.
- Kroupa, P. (2001). *MNRAS*, **322**, 231–246.
- Kroupa, P., Subr, L., Jerabkova, T. & Wang, L. (2020). *MNRAS*, **498**, 5652–5683.
- Kukula, M. J., Dunlop, J. S., McLure, R. J., et al. (2001). *MNRAS*, **326**, 1533–1546.
- Labita, M., Decarli, R., Treves, A. & Falomo, R. (2009a). *MNRAS*, **396**, 1537–1544.
- Labita, M., Decarli, R., Treves, A. & Falomo, R. (2009b). *MNRAS*, **399**, 2099–2106.
- Lagos, C. D. P., Lacey, C. G., Baugh, C. M., et al. (2011). *MNRAS*, **416**, 1566–1584.
- Lamastra, A., Menci, N., Maiolino, R., et al. (2010). *MNRAS*, **405**, 29–40.
- Langer, W. D. (1978). *ApJ*, **225**, 860–868.
- Laor, A. (2001). *ApJ*, **553**, 677–682.
- Laor, A. & Davis, S. W. (2011). *MNRAS*, **417**, 681–688.
- Läscher, R., Greene, J. E., Seth, A., et al. (2016). *ApJ*, **825**, 3.
- Lauer, T. R., Tremaine, S., Richstone, D. & Faber, S. M. (2007). *ApJ*, **670**, 249–260.
- Lawrence, A., Warren, S. J., Almaini, O., et al. (2007). *MNRAS*, **379**, 1599–1617.
- Leighly, K. M., Halpern, J. P., Jenkins, E. B., et al. (2007a). *ApJ*, **663**, 103–117.
- Leighly, K. M., Halpern, J. P., Jenkins, E. B. & Casebeer, D. (2007b). *ApJS*, **173**, 1–36.
- Leipski, C., Meisenheimer, K., Walter, F., et al. (2013). *ApJ*, **772**, 103.
- Leipski, C., Meisenheimer, K., Walter, F., et al. (2014). *ApJ*, **785**, 154.
- Lepp, S. & Dalgarno, A. (1996). *A&A*, **306**, L21–L24.
- Lepp, S. & McCray, R. (1983). *ApJ*, **269**, 560–567.
- Li, J., Wang, R., Cox, P., et al. (2020a). *ApJ*, **900**, 131.
- Li, J., Wang, R., Riechers, D., et al. (2020b). *ApJ*, **889**, 162.
- Liang, L., Feldmann, R., Kereš, D., et al. (2019). *MNRAS*, **489**, 1397–1422.
- Lidz, A., McQuinn, M., Zaldarriaga, M., et al. (2007). *ApJ*, **670**, 39–59.
- Lilly, S. J., Carollo, C. M., Pipino, A., et al. (2013). *ApJ*, **772**, 119.
- Lis, D. C., Neufeld, D. A., Phillips, T. G., et al. (2011). *ApJ*, **738**, L6.
- Liu, D., Gao, Y., Isaak, K., et al. (2015). *ApJ*, **810**, L14.
- Liu, L., Weiß, A., Perez-Beaupuits, J. P., et al. (2017). *ApJ*, **846**, 5.
- Loeb, A. & Rybicki, G. B. (1999). *ApJ*, **524**, 527–535.
- Lord, S. D., Hollenbach, D. J., Haas, M. R., et al. (1996). *ApJ*, **465**, 703.
- Lu, N., Zhao, Y., Xu, C. K., et al. (2014). *ApJ*, **787**, L23.
- Luhman, M. L., Satyapal, S., Fischer, J., et al. (2003). *ApJ*, **594**, 758–775.
- Luo, B., Brandt, W. N., Hall, P. B., et al. (2015). *ApJ*, **805**, 122.
- Lupi, A., Volonteri, M., Decarli, R., et al. (2019). *MNRAS*, **488**, 4004–4022.
- Lupu, R. E., Scott, K. S., Aguirre, J. E., et al. (2012). *ApJ*, **757**, 135.
- Lutz, D. (2014). *ARA&A*, **52**, 373–414.
- Lyutyi, V. M. & Cherepashchuk, A. M. (1972). *Astronomicheskij Tsirkulyar*, **688**, 1.
- Ma, X., Hayward, C. C., Casey, C. M., et al. (2019). *MNRAS*, **487**, 1844–1864.
- Madau, P. & Dickinson, M. (2014). *ARA&A*, **52**, 415–486.
- Madau, P. & Rees, M. J. (2000). *ApJ*, **542**, L69–L73.
- Madau, P. & Rees, M. J. (2001). *ApJ*, **551**, L27–L30.
- Magorrian, J., Tremaine, S., Richstone, D., et al. (1998). *AJ*, **115**, 2285–2305.
- Mainieri, V., Bongiorno, A., Merloni, A., et al. (2011). *A&A*, **535**, A80.

- Maiolino, R. & Mannucci, F. (2019). *A&A Rev.*, **27**, 3.
- Maiolino, R., Cox, P., Caselli, P., et al. (2005). *A&A*, **440**, L51–L54.
- Maiolino, R., Caselli, P., Nagao, T., et al. (2009). *A&A*, **500**, L1–L4.
- Maiolino, R., Gallerani, S., Neri, R., et al. (2012). *MNRAS*, **425**, L66–L70.
- Maiolino, R., Carniani, S., Fontana, A., et al. (2015). *MNRAS*, **452**, 54–68.
- Maiolino, R., Russell, H. R., Fabian, A. C., et al. (2017). *Nature*, **544**, 202–206.
- Malhotra, S., Helou, G., Stacey, G., et al. (1997). *ApJ*, **491**, L27–L30.
- Maloney, P. R., Hollenbach, D. J. & Tielens, A. G. G. M. (1996). *ApJ*, **466**, 561.
- Mannucci, F., Cresci, G., Maiolino, R., et al. (2009). *MNRAS*, **398**, 1915–1931.
- Marconi, A. & Hunt, L. K. (2003). *ApJ*, **589**, L21–L24.
- Marconi, A., Axon, D. J., Maiolino, R., et al. (2008). *ApJ*, **678**, 693–700.
- Marshall, M. A., Mechtley, M., Windhorst, R. A., et al. (2020a). *ApJ*, **900**, 21.
- Marshall, M. A., Ni, Y., Di Matteo, T., et al. (2020b). *MNRAS*, **499**, 3819–3836.
- Marshall, M. A., Wyithe, J. S. B., Windhorst, R. A., et al. (2021). *MNRAS*, **506**, 1209–1228.
- Mashian, N., Sturm, E., Sternberg, A., et al. (2015). *ApJ*, **802**, 81.
- Mathis, J. S. (1997). *From Stardust to Planetesimals*. Ed. by Pendleton, Y. J. Vol. 122. Astronomical Society of the Pacific Conference Series, 87.
- Matsuoka, Y., Onoue, M., Kashikawa, N., et al. (2016). *ApJ*, **828**, 26.
- Matsuoka, Y., Onoue, M., Kashikawa, N., et al. (2018a). *PASJ*, **70**, S35.
- Matsuoka, Y., Iwasawa, K., Onoue, M., et al. (2018b). *ApJS*, **237**, 5.
- Matsuoka, Y., Strauss, M. A., Kashikawa, N., et al. (2018c). *ApJ*, **869**, 150.
- Matsuoka, Y., Onoue, M., Kashikawa, N., et al. (2019a). *ApJ*, **872**, L2.
- Matsuoka, Y., Iwasawa, K., Onoue, M., et al. (2019b). *ApJ*, **883**, 183.
- Mazzucchelli, C., Bañados, E., Decarli, R., et al. (2017a). *ApJ*, **834**, 83.
- Mazzucchelli, C., Bañados, E., Venemans, B. P., et al. (2017b). *ApJ*, **849**, 91.
- Mazzucchelli, C., Decarli, R., Farina, E. P., et al. (2019). *ApJ*, **881**, 163.
- McClintock, J. E. & Remillard, R. A. (2006). *Compact stellar X-ray sources*. Vol. 39, 157–213.
- McConnell, N. J. & Ma, C.-P. (2013). *ApJ*, **764**, 184.
- McGill, K. L., Woo, J.-H., Treu, T. & Malkan, M. A. (2008). *ApJ*, **673**, 703–714.
- McGreer, I. D., Becker, R. H., Helfand, D. J. & White, R. L. (2006). *ApJ*, **652**, 157–162.
- McGreer, I. D., Fan, X., Jiang, L. & Cai, Z. (2018). *AJ*, **155**, 131.
- McKee, C. F. & Ostriker, J. P. (1977). *ApJ*, **218**, 148–169.
- McLeod, K. K. & Bechtold, J. (2009). *ApJ*, **704**, 415–438.
- McLure, R. J. & Jarvis, M. J. (2002). *MNRAS*, **337**, 109–116.
- McLure, R. J., Jarvis, M. J., Targett, T. A., et al. (2006). *MNRAS*, **368**, 1395–1403.
- McLure, R. J. & Dunlop, J. S. (2004). *MNRAS*, **352**, 1390–1404.
- McMahon, R. G., Banerji, M., Gonzalez, E., et al. (2013). *The Messenger*, **154**, 35–37.
- McMullin, J. P., Waters, B., Schiebel, D., et al. (2007). *Astronomical Data Analysis Software and Systems XVI*. Vol. 376, 127.
- McNamara, B. R. & Nulsen, P. E. J. (2007). *ARA&A*, **45**, 117–175.
- McNamara, B. R. & Nulsen, P. E. J. (2012). *New Journal of Physics*, **14**, 055023.
- Mechtley, M., Windhorst, R. A., Ryan, R. E., et al. (2012). *ApJ*, **756**, L38.
- Meier, D. L. (1976a). *ApJ*, **203**, L103–L105.

- Meier, D. L. (1976b). *ApJ*, **207**, 343–350.
- Meijerink, R. & Spaans, M. (2005). *A&A*, **436**, 397–409.
- Meijerink, R., Spaans, M. & Israel, F. P. (2006). *ApJ*, **650**, L103–L106.
- Meijerink, R., Spaans, M. & Israel, F. P. (2007). *A&A*, **461**, 793–811.
- Meijerink, R., Spaans, M., Loenen, A. F. & van der Werf, P. P. (2011). *A&A*, **525**, A119.
- Meijerink, R., Kristensen, L. E., Weiß, A., et al. (2013). *ApJ*, **762**, L16.
- Meixner, M. & Tielens, A. G. G. M. (1993). *ApJ*, **405**, 216.
- Menci, N., Fiore, F., Puccetti, S. & Cavaliere, A. (2008). *ApJ*, **686**, 219–229.
- Mendez, A. J., Coil, A. L., Lotz, J., et al. (2011). *ApJ*, **736**, 110.
- Menten, K. M., Lundgren, A., Belloche, A., et al. (2008). *A&A*, **477**, 185–192.
- Merloni, A., Bongiorno, A., Bolzonella, M., et al. (2010). *ApJ*, **708**, 137–157.
- Merritt, D. & Ferrarese, L. (2001). *MNRAS*, **320**, L30–L34.
- Meusinger, H. & Balafkan, N. (2014). *A&A*, **568**, A114.
- Miley, G. K., Neugebauer, G. & Soifer, B. T. (1985). *ApJ*, **293**, L11–L14.
- Mingozi, M., Vallini, L., Pozzi, F., et al. (2018). *MNRAS*, **474**, 3640–3648.
- Miralda-Escudé, J. (1998). *ApJ*, **501**, 15–22.
- Mitra, K., Chatterjee, S., DiPompeo, M. A., et al. (2018). *MNRAS*, **477**, 45–55.
- Momjian, E., Carilli, C. L., Walter, F. & Venemans, B. (2014). *AJ*, **147**, 6.
- Moorwood, A., Cuby, J. G. & Lidman, C. (1998). *The Messenger*, **91**, 9–13.
- Moré, J. J., Garbow, B. S. & Hillstrom, K. E. (1980). Tech. rep. Argonne, IL: Argonne Nat. Lab.
- Morganson, E., De Rosa, G., Decarli, R., et al. (2012). *AJ*, **143**, 142.
- Morganti, R. (2017). *Frontiers in Astronomy and Space Sciences*, **4**, 42.
- Morselli, L., Mignoli, M., Gilli, R., et al. (2014). *A&A*, **568**, A1.
- Mortlock, D. J., Warren, S. J., Venemans, B. P., et al. (2011). *Nature*, **474**, 616–619.
- Mottram, J. C., Kristensen, L. E., van Dishoeck, E. F., et al. (2014). *A&A*, **572**, A21.
- Mukherjee, D., Bicknell, G. V., Wagner, A. Y., et al. (2018). *MNRAS*, **479**, 5544–5566.
- Mullaney, J. R., Alexander, D. M., Goulding, A. D. & Hickox, R. C. (2011). *MNRAS*, **414**, 1082–1110.
- Murphy, E. J., Condon, J. J., Schinnerer, E., et al. (2011). *ApJ*, **737**, 67.
- Narayanan, D. & Krumholz, M. R. (2014). *MNRAS*, **442**, 1411–1428.
- Nayakshin, S. (2014). *MNRAS*, **437**, 2404–2411.
- Nayakshin, S. & Zubovas, K. (2012). *MNRAS*, **427**, 372–378.
- Neeleman, M., Bañados, E., Walter, F., et al. (2019). *ApJ*, **882**, 10.
- Neeleman, M., Novak, M., Venemans, B. P., et al. (2021). *ApJ*, **911**, 141.
- Nesvadba, N. P. H., Lehnert, M. D., Eisenhauer, F., et al. (2006). *ApJ*, **650**, 693–705.
- Nesvadba, N. P. H., Lehnert, M. D., De Breuck, C., et al. (2008). *A&A*, **491**, 407–424.
- Nesvadba, N. P. H., Boulanger, F., Salomé, P., et al. (2010). *A&A*, **521**, A65.
- Netzer, H. (1990). *Active Galactic Nuclei*. Ed. by Blandford, R. D., Netzer, H., Woltjer, L., et al., 57–160.
- Netzer, H. (2015). *ARA&A*, **53**, 365–408.
- Netzer, H. & Peterson, B. M. (1997). *Astronomical Time Series*. Ed. by Maoz, D., Sternberg, A. & Leibowitz, E. M. Vol. 218, 85.
- Neufeld, D. A. & Kaufman, M. J. (1993). *ApJ*, **418**, 263.
- Neufeld, D. A., Lepp, S. & Melnick, G. J. (1995). *ApJS*, **100**, 132.

- Neufeld, D. A., Kaufman, M. J., Goldsmith, P. F., et al. (2002). *ApJ*, **580**, 278–284.
- Newman, S. F., Genzel, R., Förster-Schreiber, N. M., et al. (2012). *ApJ*, **761**, 43.
- Ni, Q., Brandt, W. N., Luo, B., et al. (2018). *MNRAS*, **480**, 5184–5202.
- Nikołajuk, M. & Walter, R. (2012). *MNRAS*, **420**, 2518–2525.
- Novak, M., Bañados, E., Decarli, R., et al. (2019). *ApJ*, **881**, 63.
- Nyland, K., Dong, D. Z., Patil, P., et al. (2020). *ApJ*, **905**, 74.
- Oberst, T. E., Parshley, S. C., Stacey, G. J., et al. (2006). *ApJ*, **652**, L125–L128.
- Obreschkow, D., Heywood, I., Klöckner, H. R. & Rawlings, S. (2009). *ApJ*, **702**, 1321–1335.
- O’Brien, J. C., Freeman, K. C. & van der Kruit, P. C. (2010). *A&A*, **515**, A61.
- Ojha, R., Stark, A. A., Hsieh, H. H., et al. (2001). *ApJ*, **548**, 253–257.
- Omont, A., Neri, R., Cox, P., et al. (2011). *A&A*, **530**, L3.
- Omont, A., Yang, C., Cox, P., et al. (2013). *A&A*, **551**, A115.
- Onken, C. A., Ferrarese, L., Merritt, D., et al. (2004). *ApJ*, **615**, 645–651.
- Onoue, M., Bañados, E., Mazzucchelli, C., et al. (2020). *ApJ*, **898**, 105.
- Osterbrock, D. E. & Ferland, G. J. (2006). *Astrophysics of gaseous nebulae and active galactic nuclei*.
- Ostriker, J. P. & Ciotti, L. (2005). *Philosophical Transactions of the Royal Society of London Series A*, **363**, 667.
- Overzier, R. A., Guo, Q., Kauffmann, G., et al. (2009). *MNRAS*, **394**, 577–594.
- Padovani, P. (2016). *A&A Rev.*, **24**, 13.
- Padovani, P. (2017). *Nature Astronomy*, **1**, 0194.
- Pancoast, A., Brewer, B. J., Treu, T., et al. (2014). *MNRAS*, **445**, 3073–3091.
- Papadopoulos, P. P., Thi, W. F. & Viti, S. (2004). *MNRAS*, **351**, 147–160.
- Park, D., Woo, J.-H., Denney, K. D. & Shin, J. (2013). *ApJ*, **770**, 87.
- Park, D., Barth, A. J., Woo, J.-H., et al. (2017). *ApJ*, **839**, 93.
- Pavesi, R., Riechers, D. A., Capak, P. L., et al. (2016). *ApJ*, **832**, 151.
- Peng, C. Y. (2007). *ApJ*, **671**, 1098–1107.
- Peng, C. Y., Impey, C. D., Rix, H.-W., et al. (2006a). *ApJ*, **649**, 616–634.
- Peng, C. Y., Impey, C. D., Ho, L. C., et al. (2006b). *ApJ*, **640**, 114–125.
- Pensabene, A., Carniani, S., Perna, M., et al. (2020). *A&A*, **637**, A84.
- Pensabene, A., Decarli, R., Bañados, E., et al. (2021). *A&A*, **652**, A66.
- Pentericci, L., Fan, X., Rix, H.-W., et al. (2002). *AJ*, **123**, 2151–2158.
- Pereira-Santaella, M., Spinoglio, L., Busquet, G., et al. (2013). *ApJ*, **768**, 55.
- Peterson, B. M., Ferrarese, L., Gilbert, K. M., et al. (2004). *ApJ*, **613**, 682–699.
- Planck Collaboration, Ade, P. A. R., Aghanim, N., et al. (2016). *A&A*, **594**, A13.
- Plotkin, R. M., Shemmer, O., Trakhtenbrot, B., et al. (2015). *ApJ*, **805**, 123.
- Poelman, D. R., Spaans, M. & Tielens, A. G. G. M. (2007). *A&A*, **464**, 1023–1027.
- Pogge, R. W., Atwood, B., Brewer, D. F., et al. (2010). *Ground-based and Airborne Instrumentation for Astronomy III*. Ed. by McLean, I. S., Ramsay, S. K. & Takami, H. Vol. 7735. Society of Photo-Optical Instrumentation Engineers (SPIE) Conference Series, 77350A.
- Polletta, M., Courvoisier, T. J. L., Hooper, E. J. & Wilkes, B. J. (2000). *A&A*, **362**, 75–96.
- Pons, E., McMahon, R. G., Simcoe, R. A., et al. (2019). *MNRAS*, **484**, 5142–5154.
- Popping, G., Decarli, R., Man, A. W. S., et al. (2017). *A&A*, **602**, A11.

- Portinari, L., Kotilainen, J., Falomo, R. & Decarli, R. (2012). *MNRAS*, **420**, 732–744.
- Pound, M. W. & Wolfire, M. G. (2008). *Astronomical Data Analysis Software and Systems XVII*. Ed. by Argyle, R. W., Bunclark, P. S. & Lewis, J. R. Vol. 394. Astronomical Society of the Pacific Conference Series, 654.
- Pounds, K. A. & Page, K. L. (2006). *MNRAS*, **372**, 1275–1278.
- Press, W. H. & Schechter, P. (1974). *ApJ*, **187**, 425–438.
- Priddey, R. S. & McMahon, R. G. (2001). *MNRAS*, **324**, L17–L22.
- Rangwala, N., Maloney, P. R., Glenn, J., et al. (2011). *ApJ*, **743**, 94.
- Rawle, T. D., Egami, E., Bussmann, R. S., et al. (2014). *ApJ*, **783**, 59.
- Read, J. I. & Trentham, N. (2005). *Philosophical Transactions of the Royal Society of London Series A*, **363**, 2693.
- Reddy, N. A. & Steidel, C. C. (2009). *ApJ*, **692**, 778–803.
- Reed, S. L., McMahon, R. G., Banerji, M., et al. (2015). *MNRAS*, **454**, 3952–3961.
- Reed, S. L., McMahon, R. G., Martini, P., et al. (2017). *MNRAS*, **468**, 4702–4718.
- Reed, S. L., Banerji, M., Becker, G. D., et al. (2019). *MNRAS*, **487**, 1874–1885.
- Rees, M. J. & Ostriker, J. P. (1977). *MNRAS*, **179**, 541–559.
- Rees, M. J. (1984). *ARA&A*, **22**, 471–506.
- Rees, M. J. (1989). *MNRAS*, **239**, 1P–4.
- Reeves, J. N., O’Brien, P. T., Braito, V., et al. (2009). *ApJ*, **701**, 493–507.
- Reines, A. E. & Volonteri, M. (2015). *ApJ*, **813**, 82.
- Rengelink, R. B., Tang, Y., de Bruyn, A. G., et al. (1997). *A&AS*, **124**, 259–280.
- Richards, G. T., Hall, P. B., Vanden Berk, D. E., et al. (2003). *AJ*, **126**, 1131–1147.
- Richards, G. T., Lacy, M., Storrie-Lombardi, L. J., et al. (2006). *ApJS*, **166**, 470–497.
- Richards, G. T., Kruczek, N. E., Gallagher, S. C., et al. (2011). *AJ*, **141**, 167.
- Ridgway, S. E., Heckman, T. M., Calzetti, D. & Lehnert, M. (2001). *ApJ*, **550**, 122–141.
- Riechers, D. A., Walter, F., Bertoldi, F., et al. (2009). *ApJ*, **703**, 1338–1345.
- Riechers, D. A., Carilli, L. C., Walter, F., et al. (2011). *ApJ*, **733**, L11.
- Riechers, D. A., Bradford, C. M., Clements, D. L., et al. (2013). *Nature*, **496**, 329–333.
- Riechers, D. A., Carilli, C. L., Capak, P. L., et al. (2014). *ApJ*, **796**, 84.
- Riechers, D. A., Leung, T. K. D., Ivison, R. J., et al. (2017). *ApJ*, **850**, 1.
- Riechers, D. A., Hodge, J. A., Pavesi, R., et al. (2020). *ApJ*, **895**, 81.
- Riechers, D. A., Nayyeri, H., Burgarella, D., et al. (2021). *ApJ*, **907**, 62.
- Rivera, J., Baker, A. J., Gallardo, P. A., et al. (2019). *ApJ*, **879**, 95.
- Robson, I., Priddey, R. S., Isaak, K. G. & McMahon, R. G. (2004). *MNRAS*, **351**, L29–L33.
- Rodighiero, G., Cimatti, A., Gruppioni, C., et al. (2010). *A&A*, **518**, L25.
- Rodighiero, G., Daddi, E., Baronchelli, I., et al. (2011). *ApJ*, **739**, L40.
- Rodríguez-Ardila, A. & Viegas, S. M. (2003). *MNRAS*, **340**, L33–L37.
- Rosenberg, M. J. F., van der Werf, P. P., Aalto, S., et al. (2015). *ApJ*, **801**, 72.
- Ross, N. P., Hamann, F., Zakamska, N. L., et al. (2015). *MNRAS*, **453**, 3932–3952.
- Rowan-Robinson, M. (1995). *MNRAS*, **272**, 737–748.
- Rupke, D. S. N. & Veilleux, S. (2011). *ApJ*, **729**, L27.
- Rybak, M., Calistro Rivera, G., Hodge, J. A., et al. (2019). *ApJ*, **876**, 112.
- Saintonge, A., Catinella, B., Tacconi, L. J., et al. (2017). *ApJS*, **233**, 22.

- Saintonge, A., Wilson, C. D., Xiao, T., et al. (2018). *MNRAS*, **481**, 3497–3519.
- San José-García, I., Mottram, J. C., van Dishoeck, E. F., et al. (2016). *A&A*, **585**, A103.
- San José-García, I. (2015). PhD thesis. Leiden University.
- Sandage, A. (1965). *ApJ*, **141**, 1560.
- Sanders, D. B., Soifer, B. T., Elias, J. H., et al. (1988). *ApJ*, **325**, 74.
- Sanders, D. B., Mazzarella, J. M., Kim, D. C., et al. (2003). *AJ*, **126**, 1607–1664.
- Sandstrom, K. M., Leroy, A. K., Walter, F., et al. (2013). *ApJ*, **777**, 5.
- Sani, E., Marconi, A., Hunt, L. K. & Risaliti, G. (2011). *MNRAS*, **413**, 1479–1494.
- Sargent, M. T., Béthermin, M., Daddi, E. & Elbaz, D. (2012). *ApJ*, **747**, L31.
- Sarria, J. E., Maiolino, R., La Franca, F., et al. (2010). *A&A*, **522**, L3.
- Saturni, F. G., Trevese, D., Vagnetti, F., et al. (2016). *A&A*, **587**, A43.
- Savage, B. D. & Sembach, K. R. (1996). *ARA&A*, **34**, 279–330.
- Saxena, A., Marinello, M., Overzier, R. A., et al. (2018). *MNRAS*, **480**, 2733–2742.
- Schartmann, M., Meisenheimer, K., Camenzind, M., et al. (2008). *A&A*, **482**, 67–80.
- Schawinski, K., Urry, C. M., Virani, S., et al. (2010). *ApJ*, **711**, 284–302.
- Schawinski, K., Treister, E., Urry, C. M., et al. (2011). *ApJ*, **727**, L31.
- Schawinski, K., Simmons, B. D., Urry, C. M., et al. (2012). *MNRAS*, **425**, L61–L65.
- Schaye, J., Crain, R. A., Bower, R. G., et al. (2015). *MNRAS*, **446**, 521–554.
- Schechter, P. (1976). *ApJ*, **203**, 297–306.
- Schiminovich, D., Wyder, T. K., Martin, D. C., et al. (2007). *ApJS*, **173**, 315–341.
- Schlafly, E. F., Meisner, A. M. & Green, G. M. (2019). *ApJS*, **240**, 30.
- Schleicher, D. R. G., Spaans, M. & Klessen, R. S. (2010). *A&A*, **513**, A7.
- Schmidt, M. (1963). *Nature*, **197**, 1040.
- Schmidt, M., Schneider, D. P. & Gunn, J. E. (1995). *AJ*, **110**, 68.
- Schneider, P. (2006). *Extragalactic Astronomy and Cosmology*.
- Schöier, F. L., van der Tak, F. F. S., van Dishoeck, E. F. & Black, J. H. (2005). *A&A*, **432**, 369–379.
- Schramm, M. & Silverman, J. D. (2013). *ApJ*, **767**, 13.
- Schreiber, C., Elbaz, D., Pannella, M., et al. (2018). *A&A*, **609**, A30.
- Schulze, A. & Wisotzki, L. (2014). *MNRAS*, **438**, 3422–3433.
- Schutte, Z., Reines, A. E. & Greene, J. E. (2019). *ApJ*, **887**, 245.
- Schwartz, P. R. (1982). *ApJ*, **252**, 589–593.
- Scoville, N., Sheth, K., Aussel, H., et al. (2016). *ApJ*, **820**, 83.
- Seyfert, C. K. (1943). *ApJ*, **97**, 28.
- Shakura, N. I. & Sunyaev, R. A. (1973). *A&A*, **500**, 33–51.
- Shao, L., Kauffmann, G., Li, C., et al. (2013). *MNRAS*, **436**, 3451–3463.
- Shao, Y., Wang, R., Jones, G. C., et al. (2017). *ApJ*, **845**, 138.
- Shao, Y., Wang, R., Carilli, C. L., et al. (2019). *ApJ*, **876**, 99.
- Shemmer, O., Trakhtenbrot, B., Anderson, S. F., et al. (2010). *ApJ*, **722**, L152–L156.
- Shen, Y. (2013). *Bulletin of the Astronomical Society of India*, **41**, 61–115.
- Shen, Y., Greene, J. E., Strauss, M. A., et al. (2008). *ApJ*, **680**, 169–190.
- Shen, Y., Richards, G. T., Strauss, M. A., et al. (2011). *ApJS*, **194**, 45.
- Shen, Y., Wu, J., Jiang, L., et al. (2019a). *ApJ*, **873**, 35.
- Shen, Y., Grier, C. J., Horne, K., et al. (2019b). *ApJ*, **883**, L14.
- Shen, Y., Hall, P. B., Horne, K., et al. (2019c). *ApJS*, **241**, 34.

- Sheth, R. K. & Tormen, G. (1999). *MNRAS*, **308**, 119–126.
- Shibata, M. & Shapiro, S. L. (2002). *ApJ*, **572**, L39–L43.
- Shields, G. A., Menezes, K. L., Massart, C. A. & Vand en Bout, P. (2006). *ApJ*, **641**, 683–688.
- Sijacki, D., Springel, V., Di Matteo, T. & Hernquist, L. (2007). *MNRAS*, **380**, 877–900.
- Sijacki, D., Vogelsberger, M., Genel, S., et al. (2015). *MNRAS*, **452**, 575–596.
- Silk, J. (2013). *ApJ*, **772**, 112.
- Silk, J. & Mamon, G. A. (2012). *Research in Astronomy and Astrophysics*, **12**, 917–946.
- Silk, J. & Rees, M. J. (1998). *A&A*, **331**, L1–L4.
- Silva, L., Granato, G. L., Bressan, A. & Danese, L. (1998). *ApJ*, **509**, 103–117.
- Simcoe, R. A., Burgasser, A. J., Schechter, P. L., et al. (2013). *PASP*, **125**, 270.
- Simpson, J. M., Smail, I., Swinbank, A. M., et al. (2017). *ApJ*, **839**, 58.
- Smith, H., Gonzalez-Alfonso, E., Fischer, J., et al. (2004). *The Neutral ISM in Starburst Galaxies*. Ed. by Aalto, S., Huttemeister, S. & Pedlar, A. Vol. 320. Astronomical Society of the Pacific Conference Series, 49.
- Sobolewska, M. A. & Done, C. (2007). *MNRAS*, **374**, 150–158.
- Solomon, P. M. & Vanden Bout, P. A. (2005). *ARA&A*, **43**, 677–725.
- Solomon, P. M., Radford, S. J. E. & Downes, D. (1992). *Nature*, **356**, 318–319.
- Soltan, A. (1982). *MNRAS*, **200**, 115–122.
- Somerville, R. S. & Davé, R. (2015). *ARA&A*, **53**, 51–113.
- Sommovigo, L., Ferrara, A., Carniani, S., et al. (2021). *MNRAS*, **503**, 4878–4891.
- Song, M., Finkelstein, S. L., Ashby, M. L. N., et al. (2016). *ApJ*, **825**, 5.
- Spaans, M. (1996). *A&A*, **307**, 271.
- Spilker, J. S., Aravena, M., Phadke, K. A., et al. (2020). *ApJ*, **905**, 86.
- Spinoglio, L. & Fernández-Ontiveros, J. A. (2021). *IAU Symposium*, **356**, 29–43.
- Spinoglio, L. & Malkan, M. A. (1989). *ApJ*, **342**, 83.
- Spinoglio, L., Malkan, M. A., Smith, H. A., et al. (2005). *ApJ*, **623**, 123–136.
- Spinoglio, L., Pereira-Santaella, M., Busquet, G., et al. (2012). *ApJ*, **758**, 108.
- Spitzer Lyman, J. (1978). *JRASC*, **72**, 349.
- Spoon, H. W. W., Farrah, D., Lebouteiller, V., et al. (2013). *ApJ*, **775**, 127.
- Stacey, G. J., Geis, N., Genzel, R., et al. (1991). *ApJ*, **373**, 423.
- Stanley, F., Knudsen, K. K., Aalto, S., et al. (2021). *A&A*, **646**, A178.
- Stefan, I. I., Carilli, C. L., Wagg, J., et al. (2015). *MNRAS*, **451**, 1713–1718.
- Stern, D., Kirkpatrick, J. D., Allen, L. E., et al. (2007). *ApJ*, **663**, 677–685.
- Strandet, M. L., Weiss, A., De Breuck, C., et al. (2017). *ApJ*, **842**, L15.
- Strateva, I., Ivezić, Ž., Knapp, G. R., et al. (2001). *AJ*, **122**, 1861–1874.
- Strauss, M. A., Weinberg, D. H., Lupton, R. H., et al. (2002). *AJ*, **124**, 1810–1824.
- Sturm, E., González-Alfonso, E., Veilleux, S., et al. (2011). *ApJ*, **733**, L16.
- Swaters, R. A., Madore, B. F. & Trewhella, M. (2000). *ApJ*, **531**, L107–L110.
- Swaters, R. A., Sancisi, R., van Albada, T. S. & van der Hulst, J. M. (2009). *A&A*, **493**, 871–892.
- Symeonidis, M. (2017). *MNRAS*, **465**, 1401–1408.
- Symeonidis, M., Giblin, B. M., Page, M. J., et al. (2016). *MNRAS*, **459**, 257–276.
- Tacconi, L. J., Genzel, R., Smail, I., et al. (2008). *ApJ*, **680**, 246–262.
- Tacconi, L. J., Genzel, R., Saintonge, A., et al. (2018). *ApJ*, **853**, 179.

- Tacconi, L. J., Genzel, R. & Sternberg, A. (2020). *ARA&A*, **58**, 157–203.
- Tadhunter, C., Dicken, D., Holt, J., et al. (2007). *ApJ*, **661**, L13–L16.
- Tang, J.-J., Goto, T., Ohyama, Y., et al. (2017). *MNRAS*, **466**, 4568–4572.
- Targett, T. A., Dunlop, J. S. & McLure, R. J. (2012). *MNRAS*, **420**, 3621–3631.
- Taylor, E. N., Franx, M., Brinchmann, J., et al. (2010). *ApJ*, **722**, 1–19.
- Thomas, D., Maraston, C., Bender, R. & Mendes de Oliveira, C. (2005). *ApJ*, **621**, 673–694.
- Thomas, D., Maraston, C., Schawinski, K., et al. (2010). *MNRAS*, **404**, 1775–1789.
- Tielens, A. G. G. M. & Hollenbach, D. (1985a). *ApJ*, **291**, 722–746.
- Tielens, A. G. G. M. & Hollenbach, D. (1985b). *ApJ*, **291**, 747–754.
- Tomassetti, M., Porciani, C., Romano-Diaz, E., et al. (2014). *MNRAS*, **445**, L124–L128.
- Tombesi, F., Sambruna, R. M., Reeves, J. N., et al. (2010a). *ApJ*, **719**, 700–715.
- Tombesi, F., Cappi, M., Reeves, J. N., et al. (2010b). *A&A*, **521**, A57.
- Tombesi, F., Cappi, M., Reeves, J. N. & Braito, V. (2012). *MNRAS*, **422**, L1–L5.
- Tomczak, A. R., Quadri, R. F., Tran, K.-V. H., et al. (2014). *ApJ*, **783**, 85.
- Trakhtenbrot, B., Netzer, H., Lira, P. & Shemmer, O. (2011). *ApJ*, **730**, 7.
- Trakhtenbrot, B., Urry, C. M., Civano, F., et al. (2015). *Science*, **349**, 168–171.
- Trakhtenbrot, B., Lira, P., Netzer, H., et al. (2017). *ApJ*, **836**, 8.
- Treister, E., Schawinski, K., Urry, C. M. & Simmons, B. D. (2012). *ApJ*, **758**, L39.
- Treister, E., Natarajan, P., Sanders, D. B., et al. (2010). *Science*, **328**, 600.
- Tremaine, S., Gebhardt, K., Bender, R., et al. (2002). *ApJ*, **574**, 740–753.
- Trentham, N. & Hodgkin, S. (2002). *MNRAS*, **333**, 423–442.
- Trentham, N. & Tully, R. B. (2002). *MNRAS*, **335**, 712–732.
- Trentham, N., Sampson, L. & Banerji, M. (2005). *MNRAS*, **357**, 783–792.
- Treu, T., Malkan, M. A. & Blandford, R. D. (2004). *ApJ*, **615**, L97–L100.
- Treu, T., Woo, J.-H., Malkan, M. A. & Blandford, R. D. (2007). *ApJ*, **667**, 117–130.
- Trevese, D., Perna, M., Vagnetti, F., et al. (2014). *ApJ*, **795**, 164.
- Urrutia, T., Lacy, M. & Becker, R. H. (2008). *ApJ*, **674**, 80–96.
- Urrutia, T., Becker, R. H., White, R. L., et al. (2009). *ApJ*, **698**, 1095–1109.
- Urry, C. M. & Padovani, P. (1995). *PASP*, **107**, 803.
- Valentino, F., Magdis, G. E., Daddi, E., et al. (2018). *ApJ*, **869**, 27.
- Valentino, F., Magdis, G. E., Daddi, E., et al. (2020). *ApJ*, **890**, 24.
- Vallini, L., Gallerani, S., Ferrara, A., et al. (2015). *ApJ*, **813**, 36.
- Vallini, L., Pallottini, A., Ferrara, A., et al. (2018). *MNRAS*, **473**, 271–285.
- Vallini, L., Tielens, A. G. G. M., Pallottini, A., et al. (2019). *MNRAS*, **490**, 4502–4514.
- van Breugel, W., De Breuck, C., Stanford, S. A., et al. (1999). *ApJ*, **518**, L61–L64.
- van der Tak, F. F. S., Black, J. H., Schöier, F. L., et al. (2007). *A&A*, **468**, 627–635.
- van der Tak, F. F. S., Weiß, A., Liu, L. & Güsten, R. (2016). *A&A*, **593**, A43.
- van der Werf, P. P., Isaak, K. G., Meijerink, R., et al. (2010). *A&A*, **518**, L42.
- van der Werf, P. P., Berciano Alba, A., Spaans, M., et al. (2011). *ApJ*, **741**, L38.
- van Dishoeck, E. F., Kristensen, L. E., Mottram, J. C., et al. (2021). *A&A*, **648**, A24.
- Veilleux, S., Shopbell, P. L., Rupke, D. S., et al. (2003). *AJ*, **126**, 2185–2208.
- Veilleux, S., Meléndez, M., Sturm, E., et al. (2013). *ApJ*, **776**, 27.
- Veilleux, S. & Osterbrock, D. E. (1987). *ApJS*, **63**, 295.
- Venemans, B. P., Findlay, J. R., Sutherland, W. J., et al. (2013). *ApJ*, **779**, 24.

- Venemans, B. P., Bañados, E., Decarli, R., et al. (2015). *ApJ*, **801**, L11.
- Venemans, B. P., McMahon, R. G., Walter, F., et al. (2012). *ApJ*, **751**, L25.
- Venemans, B. P., Walter, F., Zschaechner, L., et al. (2016). *ApJ*, **816**, 37.
- Venemans, B. P., Walter, F., Decarli, R., et al. (2017a). *ApJ*, **851**, L8.
- Venemans, B. P., Walter, F., Decarli, R., et al. (2017b). *ApJ*, **845**, 154.
- Venemans, B. P., Walter, F., Decarli, R., et al. (2017c). *ApJ*, **837**, 146.
- Venemans, B. P., Decarli, R., Walter, F., et al. (2018). *ApJ*, **866**, 159.
- Venemans, B. P., Neeleman, M., Walter, F., et al. (2019). *ApJ*, **874**, L30.
- Venemans, B. P., Walter, F., Neeleman, M., et al. (2020). *ApJ*, **904**, 130.
- Vernet, J., Dekker, H., D’Odorico, S., et al. (2011). *A&A*, **536**, A105.
- Vestergaard, M. & Osmer, P. S. (2009). *ApJ*, **699**, 800–816.
- Vestergaard, M., Fan, X., Tremonti, C. A., et al. (2008). *ApJ*, **674**, L1.
- Vestergaard, M. & Peterson, B. M. (2006). *ApJ*, **641**, 689–709.
- Vietri, G., Piconcelli, E., Bischetti, M., et al. (2018). *A&A*, **617**, A81.
- Vignali, C., Piconcelli, E., Perna, M., et al. (2018). *MNRAS*, **477**, 780–790.
- Virtanen, P., Gommers, R., Oliphant, T. E., et al. (2020). *Nature Methods*, **17**, 261–272.
- Vito, F., Brandt, W. N., Yang, G., et al. (2018). *MNRAS*, **473**, 2378–2406.
- Vito, F., Brandt, W. N., Bauer, F. E., et al. (2019). *A&A*, **628**, L6.
- Voges, W., Aschenbach, B., Boller, T., et al. (1999). *A&A*, **349**, 389–405.
- Volonteri, M. & Stark, D. P. (2011). *MNRAS*, **417**, 2085–2093.
- Volonteri, M. (2010). *A&A Rev.*, **18**, 279–315.
- Volonteri, M. & Rees, M. J. (2005). *ApJ*, **633**, 624–629.
- Volonteri, M. & Reines, A. E. (2016). *ApJ*, **820**, L6.
- Wagner, A. F. & Graff, M. M. (1987). *ApJ*, **317**, 423.
- Walter, F., Weiß, A., Downes, D., et al. (2011). *ApJ*, **730**, 18.
- Walter, F., Bertoldi, F., Carilli, C., et al. (2003). *Nature*, **424**, 406–408.
- Walter, F., Carilli, C., Bertoldi, F., et al. (2004). *ApJ*, **615**, L17–L20.
- Walter, F., Riechers, D., Cox, P., et al. (2009). *Nature*, **457**, 699–701.
- Walter, F., Riechers, D., Novak, M., et al. (2018). *ApJ*, **869**, L22.
- Walter, F., Neeleman, M., Decarli, R., et al. (2022). *arXiv e-prints*, arXiv:2201.06396.
- Wandel, A., Peterson, B. M. & Malkan, M. A. (1999). *ApJ*, **526**, 579–591.
- Wang, F., Yang, J., Fan, X., et al. (2018a). *ApJ*, **869**, L9.
- Wang, F., Yang, J., Fan, X., et al. (2018b). *ApJ*, **869**, L9.
- Wang, F., Yang, J., Fan, X., et al. (2019a). *ApJ*, **884**, 30.
- Wang, F., Wang, R., Fan, X., et al. (2019b). *ApJ*, **880**, 2.
- Wang, F., Davies, F. B., Yang, J., et al. (2020). *ApJ*, **896**, 23.
- Wang, F., Yang, J., Fan, X., et al. (2021a). *ApJ*, **907**, L1.
- Wang, F., Fan, X., Yang, J., et al. (2021b). *ApJ*, **908**, 53.
- Wang, J.-G., Dong, X.-B., Wang, T.-G., et al. (2009). *ApJ*, **707**, 1334–1346.
- Wang, R., Carilli, C. L., Beelen, A., et al. (2007). *AJ*, **134**, 617–627.
- Wang, R., Wagg, J., Carilli, C. L., et al. (2008). *AJ*, **135**, 1201–1206.
- Wang, R., Carilli, C. L., Neri, R., et al. (2010). *ApJ*, **714**, 699–712.
- Wang, R., Wagg, J., Carilli, C. L., et al. (2011). *AJ*, **142**, 101.
- Wang, R., Wagg, J., Carilli, C. L., et al. (2013). *ApJ*, **773**, 44.
- Wang, R., Wu, X.-B., Neri, R., et al. (2016). *ApJ*, **830**, 53.

- Wang, R., Shao, Y., Carilli, C. L., et al. (2019c). *ApJ*, **887**, 40.
- Warren, S. J., Hewett, P. C., Osmer, P. S. & Irwin, M. J. (1987). *Nature*, **330**, 453–455.
- Weigel, A. K., Schawinski, K. & Bruderer, C. (2016). *MNRAS*, **459**, 2150–2187.
- Weiner, B. J., Willmer, C. N. A., Faber, S. M., et al. (2006). *ApJ*, **653**, 1027–1048.
- Weiner, B. J., Coil, A. L., Prochaska, J. X., et al. (2009). *ApJ*, **692**, 187–211.
- Weiß, A., Henkel, C., Downes, D. & Walter, F. (2003). *A&A*, **409**, L41–L45.
- Weiß, A., Downes, D., Henkel, C. & Walter, F. (2005). *A&A*, **429**, L25–L28.
- Weiß, A., Requena-Torres, M. A., Güsten, R., et al. (2010). *A&A*, **521**, L1.
- Weller, J., Ostriker, J. P., Bode, P. & Shaw, L. (2005). *MNRAS*, **364**, 823–832.
- Whitaker, K. E., van Dokkum, P. G., Brammer, G. & Franx, M. (2012). *ApJ*, **754**, L29.
- Willott, C. J., Delorme, P., Omont, A., et al. (2007). *AJ*, **134**, 2435–2450.
- Willott, C. J., Albert, L., Arzoumanian, D., et al. (2010a). *AJ*, **140**, 546–560.
- Willott, C. J., Delorme, P., Reylé, C., et al. (2010b). *AJ*, **139**, 906–918.
- Willott, C. J., Omont, A. & Bergeron, J. (2013). *ApJ*, **770**, 13.
- Willott, C. J., Carilli, C. L., Wagg, J. & Wang, R. (2015a). *ApJ*, **807**, 180.
- Willott, C. J., Bergeron, J. & Omont, A. (2015b). *ApJ*, **801**, 123.
- Willott, C. J., Bergeron, J. & Omont, A. (2017). *ApJ*, **850**, 108.
- Wilson, J. C., Henderson, C. P., Herter, T. L., et al. (2004). *Ground-based Instrumentation for Astronomy*. Ed. by Moorwood, A. F. M. & Iye, M. Vol. 5492. Society of Photo-Optical Instrumentation Engineers (SPIE) Conference Series, 1295–1305.
- Wolfe, A. M., Gawiser, E. & Prochaska, J. X. (2005). *ARA&A*, **43**, 861–918.
- Woo, J.-H., Treu, T., Malkan, M. A. & Blandford, R. D. (2006). *ApJ*, **645**, 900–919.
- Woo, J.-H., Treu, T., Malkan, M. A. & Blandford, R. D. (2008). *ApJ*, **681**, 925–930.
- Woo, J.-H., Treu, T., Barth, A. J., et al. (2010). *ApJ*, **716**, 269–280.
- Woo, J.-H., Schulze, A., Park, D., et al. (2013). *ApJ*, **772**, 49.
- Woo, J.-H., Yoon, Y., Park, S., et al. (2015). *ApJ*, **801**, 38.
- Wright, E. L., Eisenhardt, P. R. M., Mainzer, A. K., et al. (2010). *AJ*, **140**, 1868–1881.
- Wu, J., Brandt, W. N., Hall, P. B., et al. (2011). *ApJ*, **736**, 28.
- Wu, J., Brandt, W. N., Anderson, S. F., et al. (2012). *ApJ*, **747**, 10.
- Wyithe, J. S. B. (2006a). *MNRAS*, **365**, 1082–1098.
- Wyithe, J. S. B. (2006b). *MNRAS*, **371**, 1536–1536.
- Wyithe, J. S. B. & Loeb, A. (2012). *MNRAS*, **425**, 2892–2902.
- Wyithe, J. S. B., Loeb, A. & Carilli, C. (2005). *ApJ*, **628**, 575–582.
- Yang, B., Stancil, P. C., Balakrishnan, N. & Forrey, R. C. (2010). *ApJ*, **718**, 1062–1069.
- Yang, C., Gao, Y., Omont, A., et al. (2013). *ApJ*, **771**, L24.
- Yang, C., Omont, A., Beelen, A., et al. (2016a). *A&A*, **595**, A80.
- Yang, C., Omont, A., Beelen, A., et al. (2017). *A&A*, **608**, A144.
- Yang, C., Gavazzi, R., Beelen, A., et al. (2019a). *A&A*, **624**, A138.
- Yang, C., González-Alfonso, E., Omont, A., et al. (2020a). *A&A*, **634**, L3.
- Yang, J., Wang, F., Wu, X.-B., et al. (2016b). *ApJ*, **829**, 33.
- Yang, J., Wang, F., Fan, X., et al. (2019b). *AJ*, **157**, 236.
- Yang, J., Venemans, B., Wang, F., et al. (2019c). *ApJ*, **880**, 153.
- Yang, J., Wang, F., Fan, X., et al. (2020b). *ApJ*, **897**, L14.
- York, D. G., Adelman, J., Anderson John E., J., et al. (2000). *AJ*, **120**, 1579–1587.

- Yoshida, N., Omukai, K., Hernquist, L. & Abel, T. (2006). *ApJ*, **652**, 6–25.
- Yue, M., Yang, J., Fan, X., et al. (2021). *ApJ*, **917**, 99.
- Zakamska, N. L., Hamann, F., Pâris, I., et al. (2016). *MNRAS*, **459**, 3144–3160.
- Zhao, Y., Lu, N., Xu, C. K., et al. (2013). *ApJ*, **765**, L13.
- Zhao, Y., Lu, N., Xu, C. K., et al. (2016). *ApJ*, **819**, 69.
- Zhukovska, S. (2014). *A&A*, **562**, A76.
- Zubovas, K. & King, A. (2012). *ApJ*, **745**, L34.
- Zubovas, K. & King, A. (2016). *MNRAS*, **462**, 4055–4066.
- Zubovas, K. & King, A. R. (2014). *MNRAS*, **439**, 400–406.
- Zubovas, K., Nayakshin, S., Sazonov, S. & Sunyaev, R. (2013). *MNRAS*, **431**, 793–798.



# Appendix

In the following sections we report the additional contents of **Chap. 4**. This appendix are taken from Pensabene et al. (2020).

## A.1 Integrated spectra: line properties and derived quantities

From the best-fit of the integrated spectra of **Sect. 4.3.1**, we directly retrieved the line FWHM, and the velocity-integrated flux of the line ( $F_{\text{line}}$ ). Then, we also inferred line luminosity ( $L_{\text{line}}$ ), [CII] mass ( $M_{[\text{CII}]}$ ), total gas mass ( $M_{\text{gas}}$ ), and the [CII]-based star formation rate ( $\text{SFR}_{[\text{CII}]}$ ). The line luminosities were computed following Solomon & Vanden Bout (2005):

$$L_{\text{line}} [L_{\odot}] = 1.04 \times 10^{-3} F_{\text{line}} \nu_{\text{rest}} (1+z)^{-1} D_L^2, \quad (\text{A.1})$$

where  $F_{\text{line}}$  is in unit of  $\text{Jy km s}^{-1}$ ;  $\nu_{\text{rest}}$  in GHz, and  $D_L$  in Mpc.

Then, by analogy with Venemans et al. (2017a), assuming optically thin [CII] emission and local thermodynamical equilibrium (LTE) of the carbon line, we estimated the mass of singly ionized carbon in galaxies as:

$$\begin{aligned} M_{[\text{CII}]} [M_{\odot}] &= C m_C \frac{8\pi k_B \nu_{\text{rest}}^2}{hc^3 A_{\text{ul}}} Q(T_{\text{ex}}) \frac{1}{4} e^{91.2/T_{\text{ex}}} L'_{[\text{CII}]} \\ &= 2.92 \times 10^{-4} Q(T_{\text{ex}}) \frac{1}{4} e^{91.2/T_{\text{ex}}} L'_{[\text{CII}]}, \end{aligned} \quad (\text{A.2})$$

where  $C$  is the conversion factor between  $\text{pc}^2$  and  $\text{cm}^2$ ,  $m_C$  the mass of a carbon atom,  $A_{\text{ul}} = 2.29 \times 10^{-6} \text{s}^{-1}$  the Einstein coefficient,  $Q(T_{\text{ex}}) = 2 + 4e^{-91.2/T_{\text{ex}}}$  the CII partition function, and  $T_{\text{ex}}$  the excitation temperature<sup>1</sup> that we set equal to  $T_{\text{ex}} = 100 \text{K}$  (see Venemans et al., 2017a). Then, assuming

<sup>1</sup>This is the temperature of the equivalent Boltzmann distribution assuming LTE.

**Table A.1:** Key parameters and derived quantities estimated from the fits of integrated spectra.

| No. <sup>(1)</sup> | Object ID                     | $\text{FWHM}_{[\text{CII}]}$<br>( $\text{km s}^{-1}$ ) | $F_{[\text{CII}]}$<br>( $\text{Jy km s}^{-1}$ ) | $L_{[\text{CII}]}$<br>( $10^9 L_{\odot}$ ) | $M_{[\text{CII}]}$<br>( $10^6 M_{\odot}$ ) | $M_{\text{gas}}$<br>( $10^9 M_{\odot}$ ) | $\text{SFR}_{[\text{CII}]}$<br>( $M_{\odot} \text{ yr}^{-1}$ ) |
|--------------------|-------------------------------|--|---|--|--|--|--|
| 2                  | VHS J2101-5943 <sup>(†)</sup> | $222^{+19}_{-17}$                                      | $0.48^{+0.04}_{-0.04}$                          | $0.019^{+0.020}_{-0.017}$                  |  |  |  |
| 6                  | SDSS J1328-0224               | $277^{+22}_{-24}$                                      | $2.43^{+0.16}_{-0.17}$                          | $1.63^{+0.11}_{-0.11}$                     | $4.3^{+0.3}_{-0.3}$                        | $1.22^{+0.08}_{-0.08}$                   | $223^{+18}_{-17}$  |
| 7                  | SDSS J0923+0247               | $328^{+13}_{-12}$                                      | $5.10^{+0.18}_{-0.18}$                          | $3.44^{+0.12}_{-0.12}$                     | $9.1^{+0.3}_{-0.3}$                        | $2.58^{+0.09}_{-0.09}$                   | $537^{+22}_{-22}$  |
| 9                  | SDSS J0129-0035               | $189^{+9}_{-9}$  | $2.14^{+0.08}_{-0.08}$                          | $2.01^{+0.08}_{-0.08}$                     | $5.3^{+0.2}_{-0.2}$                        | $1.50^{+0.06}_{-0.06}$                   | $284^{+13}_{-13}$  |
| 10                 | SDSS J1044-0125               | $422^{+69}_{-28}$                                      | $1.31^{+0.19}_{-0.19}$                          | $1.23^{+0.18}_{-0.18}$                     | $3.3^{+0.5}_{-0.5}$                        | $0.92^{+0.14}_{-0.13}$                   | $159^{+28}_{-27}$  |
| 11                 | SDSS J1306+0356               | $232^{+28}_{-24}$                                      | $2.4^{+0.2}_{-0.2}$                             | $2.4^{+0.2}_{-0.2}$                        | $6.3^{+0.6}_{-0.6}$                        | $1.77^{+0.16}_{-0.16}$                   | $346^{+36}_{-36}$  |
| 12                 | SDSS J2310+1855               | $381^{+13}_{-13}$                                      | $8.0^{+0.2}_{-0.2}$                             | $7.9^{+0.2}_{-0.2}$                        | $21.0^{+0.6}_{-0.6}$                       | $5.92^{+0.18}_{-0.18}$                   | $1434^{+52}_{-50}$   |
| 14                 | SDSS J2054-0005               | $243^{+10}_{-10}$                                      | $3.36^{+0.12}_{-0.12}$                          | $3.36^{+0.12}_{-0.12}$                     | $8.9^{+0.3}_{-0.3}$                        | $2.51^{+0.09}_{-0.09}$                   | $522^{+23}_{-22}$  |
| 19                 | ULAS J1319+0950               | $484^{+33}_{-33}$                                      | $2.60^{+0.16}_{-0.15}$                          | $2.65^{+0.16}_{-0.16}$                     | $7.0^{+0.4}_{-0.4}$                        | $1.99^{+0.12}_{-0.12}$                   | $395^{+29}_{-28}$  |
| 22                 | PSO J308-21                   | $403^{+35}_{-33}$                                      | $1.03^{+0.08}_{-0.08}$                          | $1.08^{+0.08}_{-0.08}$                     | $2.7^{+0.2}_{-0.2}$                        | $0.81^{+0.06}_{-0.06}$                   | $137^{+13}_{-13}$  |
| 25                 | PSO J183+05                   | $382^{+19}_{-17}$                                      | $5.1^{+0.2}_{-0.2}$                             | $5.6^{+0.2}_{-0.2}$                        | $14.8^{+0.6}_{-0.6}$                       | $4.19^{+0.17}_{-0.17}$                   | $954^{+47}_{-44}$  |
| 26                 | PSO J167-13                   | $499^{+17}_{-17}$                                      | $3.20^{+0.10}_{-0.10}$                          | $3.57^{+0.11}_{-0.11}$                     | $9.5^{+0.3}_{-0.3}$                        | $2.68^{+0.08}_{-0.08}$                   | $562^{+20}_{-20}$  |
| 28                 | VIKING J0305-3150             | $245^{+15}_{-14}$                                      | $3.69^{+0.19}_{-0.18}$                          | $4.2^{+0.2}_{-0.2}$                        | $11.2^{+0.6}_{-0.5}$                       | $3.15^{+0.16}_{-0.15}$                   | $682^{+41}_{-38}$  |

**Notes.** <sup>(1)</sup>Source identification numbers in agreement with those listed in the first column of **Tab. 4.1**. <sup>(†)</sup>This source is observed in CO(3–2). In this case, FWHM and flux refer to this line. We thus do not derive the [CII]-based quantities for that.

that all carbon atoms are singly ionized, we also derived a lower limit on the total gas mass ( $M_{\text{gas}}$ ) using the carbon abundance relative to hydrogen atom (Asplund et al., 2009)  $M_{\text{C}}/M_{\text{H}} = 3.54 \times 10^{-3}$ . Finally, we estimated the SFRs using the  $\text{SFR} - L_{[\text{CII}]}$  relation for high-redshift ( $z > 0.5$ ) galaxies from De Looze et al. (2014):

$$\text{SFR}_{[\text{CII}]} [M_{\odot} \text{ yr}^{-1}] = 3.0 \times 10^{-9} (L_{[\text{CII}]} / L_{\odot})^{1.18}, \quad (\text{A.3})$$

with a systematic uncertainty of a factor of  $\sim 2.5$ . In **Tab. A.1**, we listed the results of spectral fits and the derived quantities for those sources with dynamical mass constrained. The reported quantities are consistent within  $\sim 2\sigma$  to the estimates published in other works (e.g. Banerji et al., 2017; Wang et al., 2013; Decarli et al., 2017, 2018; Trakhtenbrot et al., 2017; Venemans et al., 2017b).

## A.2 Mass support from random motions

We investigate here the turbulent pressure support term, which arises from non-rotational motions, on the total dynamical mass of our quasar host galaxies (see, e.g., Epinat et al., 2009; Taylor et al., 2010). This term is not

taken into account in our disk model since the gas is circularly rotating in a thin disc.

Following Epinat et al. (2009), we quantify the mass supported by random motions inside the galaxy through the virial theorem:

$$M_\sigma = C \frac{\sigma_0^2 R_D}{G}, \quad (\text{A.4})$$

where  $R_D$  is the scale radius of the exponential brightness profile (see **Sect. 4.4**);  $\sigma_0$  an estimate of constant velocity dispersion throughout the whole galaxy, and  $C$  is a parameter depending on the mass distribution and geometry. Here, we assume  $C = 2.25$ , which is the average value of known galactic mass distribution models (Binney & Tremaine, 2008).

The intrinsic velocity dispersion can be estimated from the observed velocity-dispersion map after taking into account the angular and spectral resolution of observations. As a representative example, we choose SDSS J0923+0247. The velocity field of the latter shows a clear velocity gradient, and we estimated the disk inclination of  $\sim 29$  deg and dynamical mass of  $\sim 6.0 \times 10^{11} M_\odot$  (see **Fig. 4.6**). Although our rotating thin disk model reproduces the observed velocity map very well, the observed velocity dispersion is slightly ( $\sim 1.4\times$ ) higher than what was expected by our best-fit (see **Fig. A.1**). Indeed, the best-fitting velocity-dispersion field includes only the effect of the unresolved velocity gradients and enlargement of the emission line profile due to the beam smearing and the instrumental line-spread function (set to  $\sigma_{\text{LSF}} = 15 \text{ km s}^{-1}$ ). As previously mentioned, our model does not include random motions due to the physics of the gas. The intrinsic velocity dispersion of the gas can be estimated by quadratically subtracting the model from the measured velocity-dispersion map. The model and quadratic residuals are shown in **Fig. A.1**. Then, we computed the “1/errors”-weighted mean velocity dispersion ( $\sigma_0$ ), where the aforementioned errors are associated with the observed velocity-dispersion values that are estimated from the spaxel-by-spaxel line fit of the datacube. The resulting value is  $\sigma_0 \sim 54 \text{ km s}^{-1}$ . Using this value in **Eq. (A.4)**, we obtain  $M_\sigma \sim 1.3 \times 10^9 M_\odot$ . This mass budget accounts for only  $\sim 2\%$  of the estimated dynamical mass obtained with kinematical modeling assuming rotating thin disk geometry. By comparing this value with the uncertainties of the dynamical mass estimate ( $\sim 0.5$  dex), we conclude that the mass support from random motions is negligible in

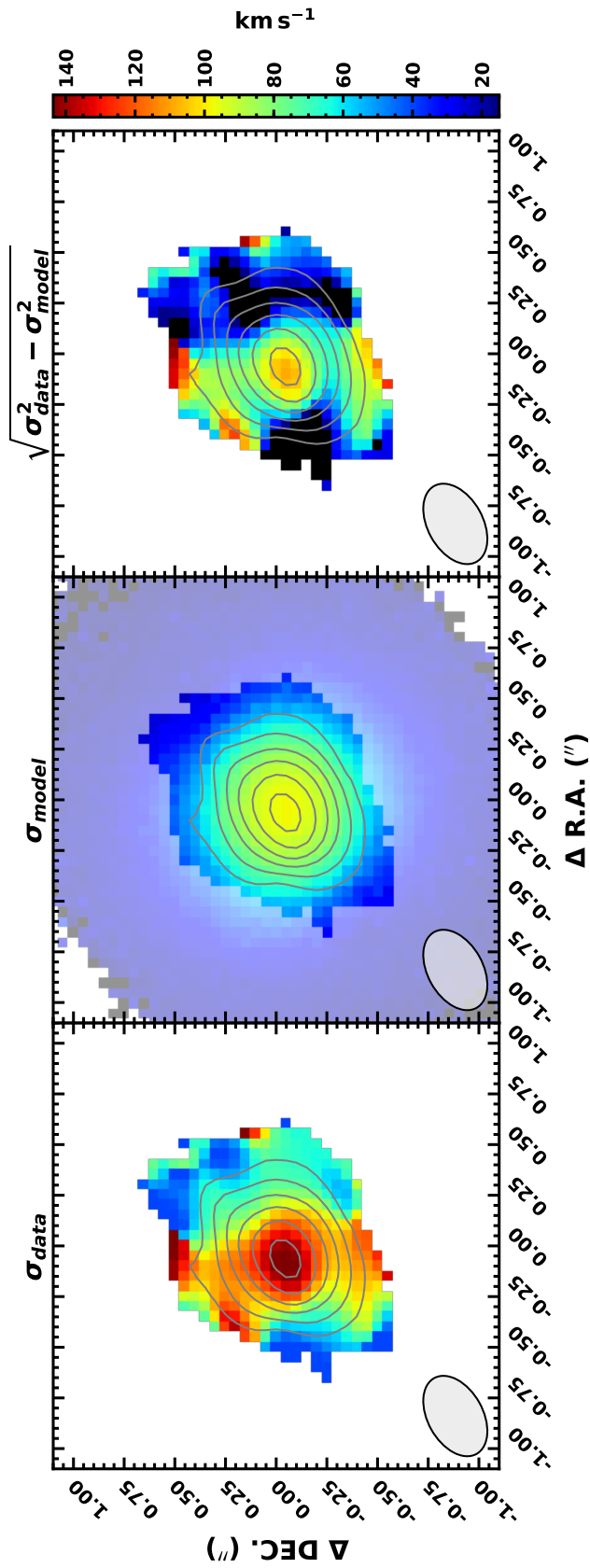


**Figure A.1**

Estimation of local velocity dispersion in J0923+0247. *Left panel:* observed velocity-dispersion field. *Central panel:* simulated flux-weighted velocity-dispersion map along the LOS, corresponding to the best-fit model of the velocity field. *Right panel:* quadratic residuals representing the local velocity dispersion along the LOS. The contours show the line-velocity integrated map. The contours correspond to  $[0.25I_0, 0.5I_0, 0.68I_0, 0.9I_0]$ , where  $I_0$  is the maximum value of the observed flux. In the bottom-left corner of each panel, the FWHM of the synthesized beam is shown.

this system. We adopted the same technique for all the sources for which we obtained a dynamical mass estimate and verified that the eventual mass budget arising from random motions is always included within the dynamical mass uncertainties. Therefore, we conclude that the rotating gas disk model provides a good description for the gas kinematics of our quasar host galaxies. We stress that, for systems that show complex or perturbed kinematics (e.g., due to the presence of outflow or a companion in the close environment of quasar; see, **Sect. 4.7**), the assumption of rotating disk geometry is undoubtedly less meaningful than for relaxed systems. This is the case of, for example, SDSS J0129-0356 and ULAS J1319+0950, for which the best fits are consistent with face-on disks. On the other hand, the observed velocity dispersion is still high ( $\sim 100 - 200 \text{ km s}^{-1}$ , but consistent within  $2 - 3\sigma$  to the model), which is not expected for a face-on disk. Although this evidence supports the fact that, at least in these extreme cases, the hypothesis of a thin rotating disk is too simplified, and the dynamical mass estimates should be considered tentative; deeper observations are needed in order to properly describe the kinematics in these complex systems, rather than a more accurate kinematical modeling of the current observations. However, our fitting method enables us to homogeneously study the whole sample.

## A.3 Comparison between dynamical masses and the spectroastrometric mass estimates

Since the dynamical masses estimated in this work are measured through a full kinematical modeling of the velocity field, they can be considered reliable mass estimates. Comparing them with mass measurements obtained with other methods enables us to test the consistency of the results. In this section, we compare the host galaxy's dynamical mass measurements listed in **Tab. 4.2** with the mass estimates obtained through the spectroastrometry method by Gnerucci et al. [2011](#) and the virial mass estimates obtained in **Sect. 4.9.3**.

Spectroastrometry is a technique that combines spatial and spectral resolution to probe spatial scales smaller than the angular resolution of the observations.

**Table A.2:** Parameters estimated from a 2D Gaussian fit of the flux maps, virial mass estimates, and the results of the spectroastrometry method.

| No. <sup>(1)</sup> | Object ID       | FWHM <sub>maj</sub> <sup>(2)</sup><br>(mas) | FWHM <sub>min</sub> <sup>(3)</sup><br>(mas) | $R_{\text{em}}$<br>(kpc) | $M_{\text{vir}}$<br>( $10^{10} M_{\odot}$ ) | $r_{\text{spec}}$<br>(kpc) | $\mu_{\text{spec}}$<br>( $10^{10} M_{\odot}$ ) |
|--------------------|-----------------|---|---|--------------------------|---|----------------------------|--|
| 2                  | VHS J2101-5943  | point-like source                           |   | $< 8.34$                 | $< 8.0$                                     | $< 2.3$                    | $< 2.6$  |
| 6                  | SDSS J1328-0224 | $339 \pm 50$                                | $189 \pm 35$                                | $1.13^{+0.17}_{-0.17}$   | $1.7^{+0.5}_{-0.4}$                         | $0.3 \pm 0.2$              | $0.5 \pm 0.3$                                  |
| 7                  | SDSS J0923+0247 | $385 \pm 50$                                | $340 \pm 58$                                | $1.28^{+0.17}_{-0.17}$   | $5.7^{+8.7}_{-2.1}$                         | $0.7 \pm 0.1$              | $1.8 \pm 0.4$                                  |
| 9                  | SDSS J0129-0035 | $303 \pm 51$                                | $271 \pm 59$                                | $0.91^{+0.15}_{-0.15}$   | $1.2^{+1.9}_{-0.5}$                         | $0.37 \pm 0.06$            | $0.30 \pm 0.06$                                |
| 10                 | SDSS J1044-0125 | point-like source                           |   | $< 1.38$                 | $< 4.8$                                     | $0.4 \pm 0.3$              | $1.8 \pm 1.5$                                  |
| 11                 | SDSS J1306+0356 | $1290 \pm 430$                              | $410 \pm 240$                               | $3.8^{+1.3}_{-1.2}$      | $3.2^{+1.4}_{-1.0}$                         | $1.1 \pm 0.7$              | $1.4 \pm 0.9$                                  |
| 12                 | SDSS J2310+1855 | $512 \pm 61$                                | $287 \pm 135$                               | $1.50^{+0.18}_{-0.18}$   | $4.1^{+3.1}_{-1.0}$                         | $0.41 \pm 0.07$            | $1.4 \pm 0.3$                                  |
| 14                 | SDSS J2054-0005 | $352 \pm 72$                                | $293 \pm 97$                                | $1.0^{+0.2}_{-0.2}$      | $1.7^{+2.4}_{-0.6}$                         | $0.33 \pm 0.08$            | $0.45 \pm 0.12$                                |
| 19                 | ULAS J1319+0950 | $536 \pm 95$                                | $328 \pm 78$                                | $1.6^{+0.3}_{-0.3}$      | $7.9^{+3.9}_{-1.9}$                         | $0.64 \pm 0.12$            | $3.5 \pm 1.0$                                  |
| 25                 | PSO J183+05     | $604 \pm 63$                                | $477 \pm 52$                                | $1.70^{+0.18}_{-0.18}$   | $8.5^{+6.6}_{-2.2}$                         | $0.44 \pm 0.12$            | $1.5 \pm 0.5$                                  |
| 26                 | PSO J167-13     | $1068 \pm 74$                               | $467 \pm 53$                                | $3.0^{+0.2}_{-0.2}$      | $12.1^{+1.2}_{-1.1}$                        | $1.16 \pm 0.12$            | $6.7 \pm 1.0$                                  |

**Notes.** <sup>(1)</sup>Source identification numbers in agreement with those listed in the first column of **Tab. 4.1**. <sup>(2),(3)</sup>Major and minor FWHM of the 2D best-fit Gaussian of the flux maps deconvolved from the beam. Point-like sources are explicitly indicated. In these cases, minor FWHM of the synthesized beam is taken as upper limit on the angular dimension of the emitting region. Uncertainties on quantities are statistical errors ignoring any possible systematic biases.

We applied it to the case of our high- $z$  quasar sample to estimate the product  $\mu = M_{\text{dyn}} \sin^2 \beta$ . Following Gnerucci et al. (2011), we measured the FWHM and the central frequency of the line from the integrated spectra, (e.g., see **Fig. 4.2**), then we collapsed the redshifted and blueshifted channels obtaining “red” and “blue” maps, respectively (see **Fig. A.2**). If the galaxy disk is at least marginally resolved, the latter two maps are spatially shifted due to the rotation of the gas. Then, we performed a 2D fit of collapsed maps using an elliptical Gaussian function, and we determined the position of the two centroids. Thus, we computed the spectroastrometric radius ( $r_{\text{spec}}$ ), as the half distance between “red” and “blue” centroids. Finally, we used the FWHM and  $r_{\text{spec}}$  measurements, and we estimated the spectroastrometric mass (see, Eq. 2 in Gnerucci et al. 2011):

$$M_{\text{spec}} \sin^2 \beta = f_{\text{spec}} \mu_{\text{spec}} = f_{\text{spec}} \frac{\text{FWHM}_{\text{line}}^2 r_{\text{spec}}}{G}, \quad (\text{A.5})$$

where  $f_{\text{spec}}$  is the calibrator factor. Here, we used the value of Gnerucci et al. (2011);  $f_{\text{spec}} = 1.0 \pm 0.1$ . The  $r_{\text{spec}}$  values and  $\mu_{\text{spec}}$  are listed in **Tab. A.2**. In **Fig. A.3** (upper panel), we compare  $\mu_{\text{spec}}$  from spectroastrometry with  $M_{\text{dyn}} \sin^2 \beta$  measured from the full kinematical modeling (see **Tab. 4.2**). We conclude that the two estimators are consistent within uncertainties. We also compare  $\mu_{\text{vir}} = M_{\text{vir}} \sin^2 \beta$  from virial estimates (see **Sect. 4.9.3**) with

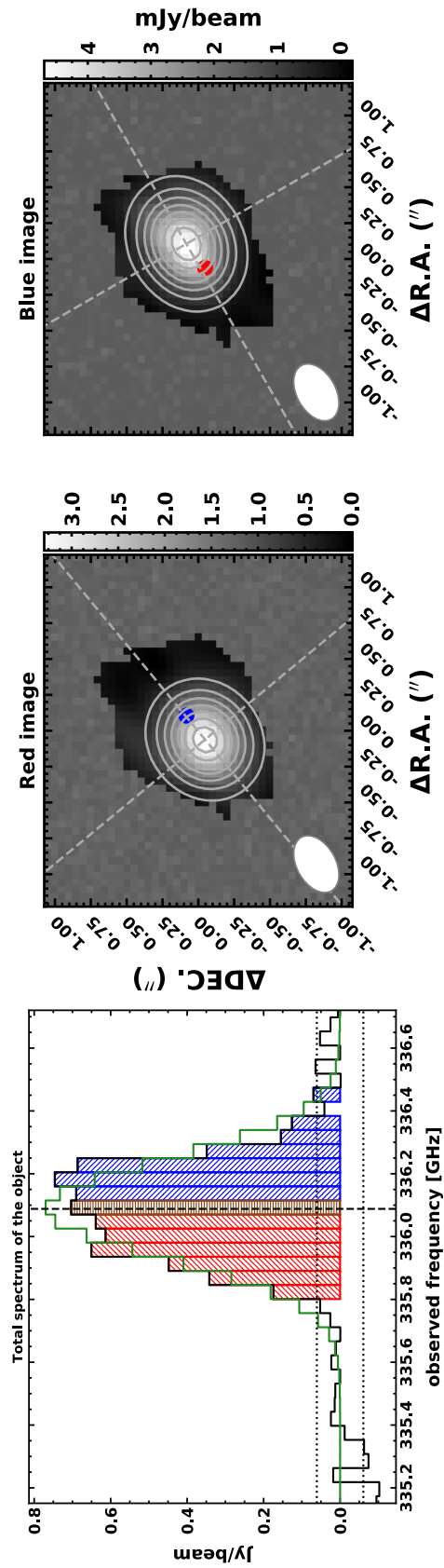


**Figure A.2**

Integrated spectrum and red/blue maps of SDSS J0923+0247. *Left panel:* the data and the best-fit model is shown with black and green lines, respectively. The red dashed vertical line indicates the central frequency; the RMS of the residuals is indicated by the dotted horizontal lines. Channels used to create the red and blue maps (show on the right panels) are filled with their respective colors. The central brown bin is added to the red and blue side of the collapsed images with a weight given by the fraction of red and blue bins. *Right panels:* the best 2D Gaussian model is shown with white contours. The blue and red circles indicate the centroid positions of the counterpart map. Here, pixels not defined in the maps are replaced with simulated noise in order to avoid numerical drawbacks in the fitting process.

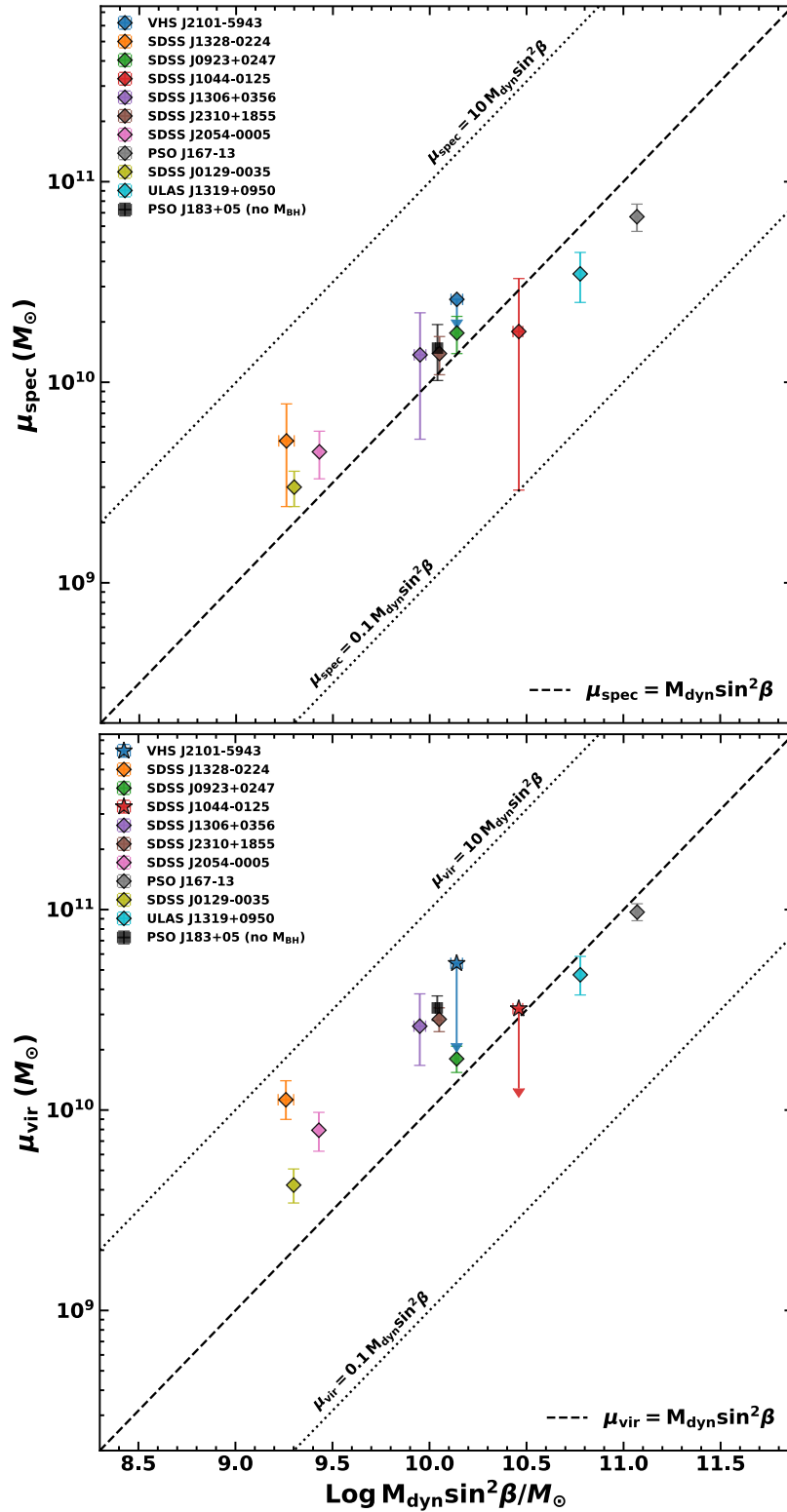


**Figure A.3**

Comparison of galaxy mass factors obtained with spectroastrometry (*upper panel*) and virial estimates (*bottom panel*) with  $M_{\text{dyn}} \sin^2 \beta$  from full kinematical modeling of the host galaxy's gas velocity field. The dashed black line represents the 1:1 relation. The object symbols are the same as in Fig. 4.12.

$M_{\text{dyn}} \sin^2 \beta$  (bottom panel of **Fig. A.3**). The results show that the virial mass factor  $\mu_{\text{vir}}$  and  $M_{\text{dyn}} \sin^2 \beta$  have a non-linear relation with large dispersion. Therefore, we conclude that the classical virial method does not provide a reliable prediction of  $M_{\text{dyn}} \sin^2 \beta$ . On the other hand, although the spectroastrometry method also suffers from large uncertainties and biases, we conclude that  $\mu_{\text{spec}}$  are in better agreement with dynamical mass factor obtained with the full kinematical modeling of galaxy discs presented in this work. In fact, as discussed by Gnerucci et al. (2011), the classical virial mass estimate can be biased by systematic errors mostly associated with the measurement of galaxy dimensions. This result confirms the reliability and usefulness of the spectroastrometry method, especially in the typical case of both poor spatial resolution and S/N ratio of the majority of the current available observations of high- $z$  galaxies.

## A.4 LBT observations and NIR spectra

The observations of the five quasars (SDSS J0129-0035, SDSS J2054-0005 and SDSS J2310+1855, PSO J308-21, and PSO J138+05) were executed between 2018 September and 2019 June (PI: G. Cresci) with LUCI in seeing-limited conditions using the standard strategy for near-infrared long-slit spectroscopic observations: we dithered the objects along the  $1''$  slit following an ABAB cycle in order to subtract the sky. We made use of the low-resolution grating (G200,  $\lambda/\Delta\lambda \approx 2000$ ) and the N1.8 camera (pixel size  $\sim 0.25''/\text{pix}$ ) to maximize the S/N. In order to obtain an accurate flux calibration of the spectra, that is required to estimate  $L_{\lambda}$ , we also obtained images of the quasars with the  $J$  or  $K$  filter using the N3.75 camera (pixel size  $\sim 0.12''/\text{pix}$ ). The total exposure time for spectroscopy is  $\sim 2$  hours per target, and  $\sim 100, 200$  or  $800$  seconds for the imaging of the targets, depending on their apparent magnitude. The data were reduced and delivered by the LBT Imaging Data Center using the dedicated pipelines.

The requested time was derived assuming for the MgII line flux a typical value of  $5 \times 10^{-16} \text{ erg}^{-1} \text{ s}^{-1} \text{ cm}^{-2}$  at  $z \sim 6$  (Mazzucchelli et al., 2017b), and for the CIV line a flux  $F_{\text{CIV}} \sim 3 \times F_{\text{MgII}}$  (Shen et al., 2011), and a line width of  $4000 \text{ km s}^{-1}$ . Unfortunately, we did not achieve the requested sensitivities due to bad weather conditions, and we detected BLR emission only in J2310+1855. We therefore present here the  $M_{\text{BH}}$  mass of J2310+1855 de-

rived from the observations of CIV BLR line. We also note that both Feruglio et al. (2018) and Shen et al. (2019a) obtained independent NIR spectra of this target with different facilities. In particular, Shen et al. (2019a) published NIR spectra of a large sample  $z \sim 5.7$  quasars, also providing an  $M_{\text{BH}}$  measurement for the J2310+1855 through virial relations based on CIV and MgII broad emission line. Before modeling the CIV line in our LBT spectrum, we subtracted the continuum emission, fitting a power law at both sides of the ionized carbon line (in the two windows at 1450 Å and 1700 Å). Then, we used a single Gaussian model to reproduce the CIV BLR emission profile. In fact, the low S/N does not allow us to constrain the possible contribution from iron emission in the region around the CIV, which is expected to be negligible (see, e.g., Shen et al., 2008, 2011), nor the possible emission from the CIV NLR line (e.g., Shen et al., 2011).

From the best fit of the CIV line, we derived a FWHM  $\sim 12500 \text{ km s}^{-1}$ , and from the extrapolated continuum at 1350 Å, a flux of  $F_{1350} \sim 1.1 \times 10^{-17} \text{ erg s}^{-1} \text{ cm}^{-2}$ , and a luminosity of  $\sim 10^{45.8} \text{ erg s}^{-1}$ . Using the Vestergaard & Peterson (2006) relation, we obtained  $\log M_{\text{BH}} \sim 9.8$ , consistent with Shen et al. (2019a). The CIV line is blueshifted with respect to the  $[\text{CII}]_{158 \mu\text{m}}$  systemic of  $\Delta v \sim -7200 \text{ km s}^{-1}$ , strongly suggesting the presence of outflows in this source. We note that the values of FWHM and  $\Delta v$  of CIV broad line in the J2310+1855 spectrum are consistent with the typical values estimated in high- $z$  quasars (see, e.g., Vietri et al., 2018). The CIV-based  $M_{\text{BH}}$  estimate can be therefore strongly biased; by adopting the different calibrations introduced to correct for the outflow contribution in CIV lines (see, e.g., Vignali et al., 2018, and references therein), we obtained mass estimates in the range  $\log M_{\text{BH}} = 8.9 - 9.4$ , which is in agreement with the estimate by Feruglio et al. (2018). The uncertainties on these measurements are dominated by the intrinsic scatter ( $\approx 0.3$  dex; see, e.g., Vestergaard & Peterson 2006; Denney 2012; Park et al. 2017) in the single-epoch calibrations, which are much larger than the typical uncertainties ascribed to the measurements of the line widths and fluxes.

The latter values are consistent with the MgII-based  $M_{\text{BH}}$  reported in Shen et al. (2019a), which is used in this work to study the  $M_{\text{BH}} - M_{\text{dyn}}$  relation. In Fig. A.4, we show the NIR spectrum of J2310+1855 with the best fit of the CIV broad line.

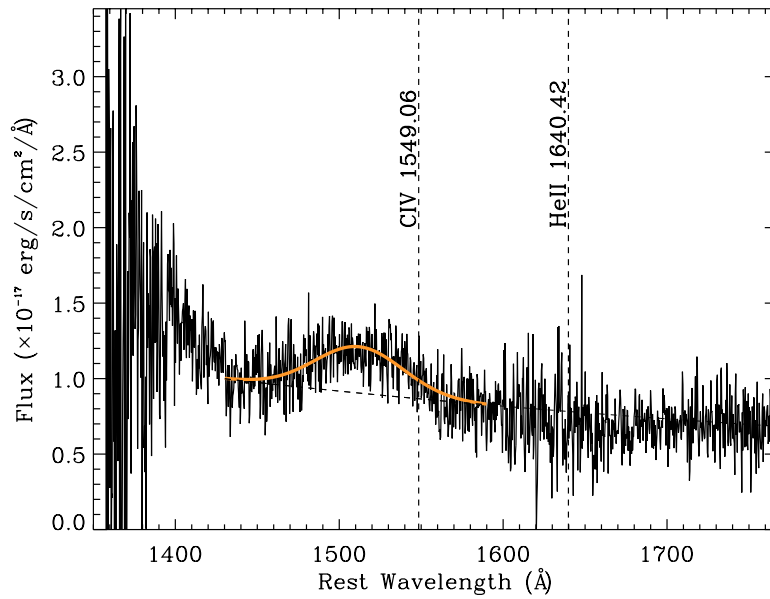


**Figure A.4**

Portion of LBT/LUCI  $zJ$  spectrum of SDSS J2310+1855 around CIV line for which the expected wavelength is indicated in the figure according to [CII]-based redshift. The orange and black dashed curves indicate the spectrum's best fit (line + continuum and continuum, respectively).

## A.5 Maps, integrated spectra, and the results of the kinematical modelling

Here, we report the integrated spectra, flux, velocity, and velocity-dispersion maps for objects in **Tab. 4.2** in **Fig. A.5**. See **Fig. 4.2** and **Fig. 4.3** for the descriptions of each panel. We also report the 2D best fit of the flux and velocity maps in **Fig. A.6**. The different panels are labeled as they are in **Fig. 4.6**; we refer to the latter for a description of the figures.

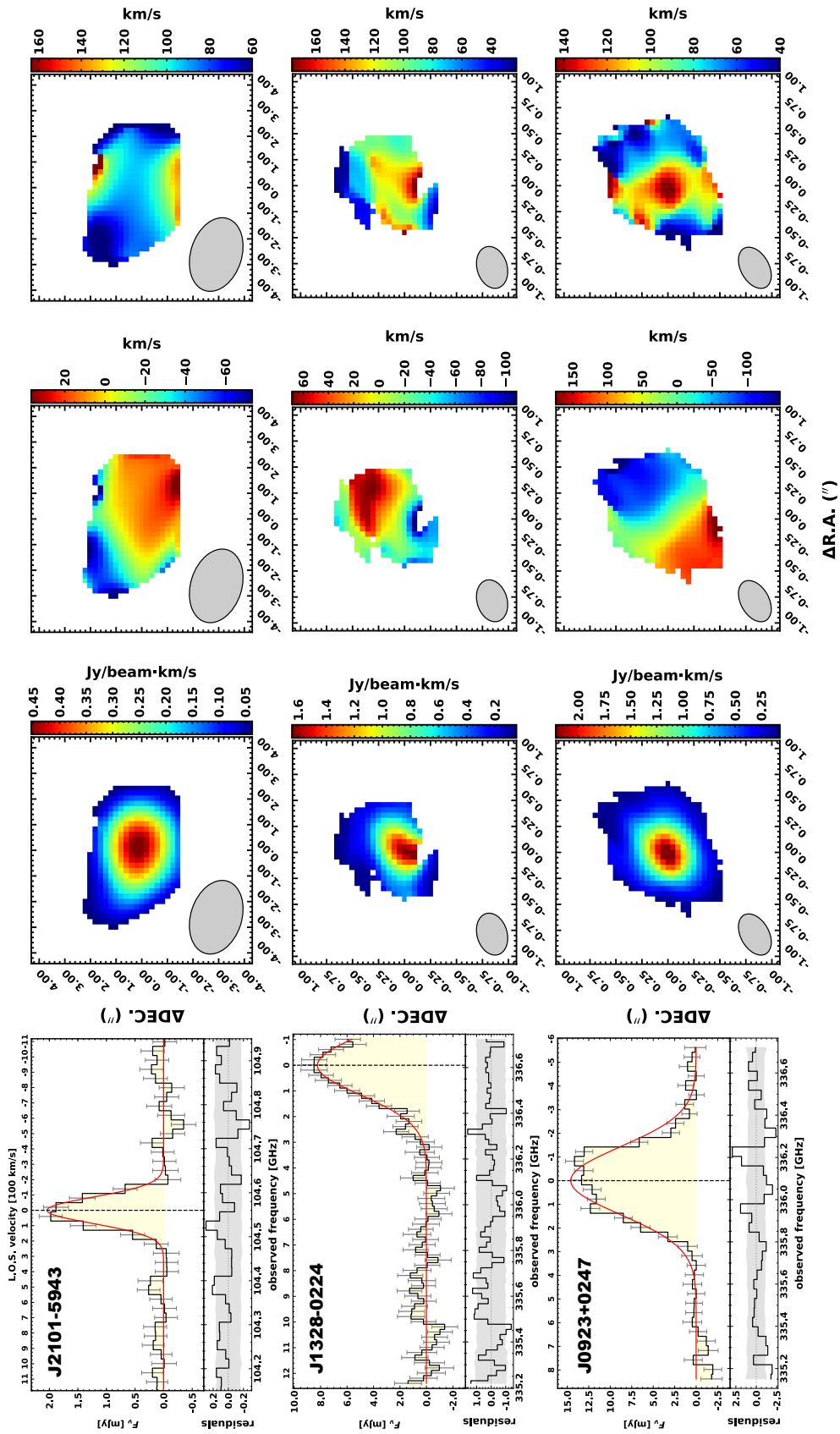


Figure A.5

Line integrated spectra, flux, velocity, and velocity-dispersion maps along the line of sight for objects listed in Tab. 4.2. See Fig. 4.2 and Fig. 4.3 for the description of each panel.

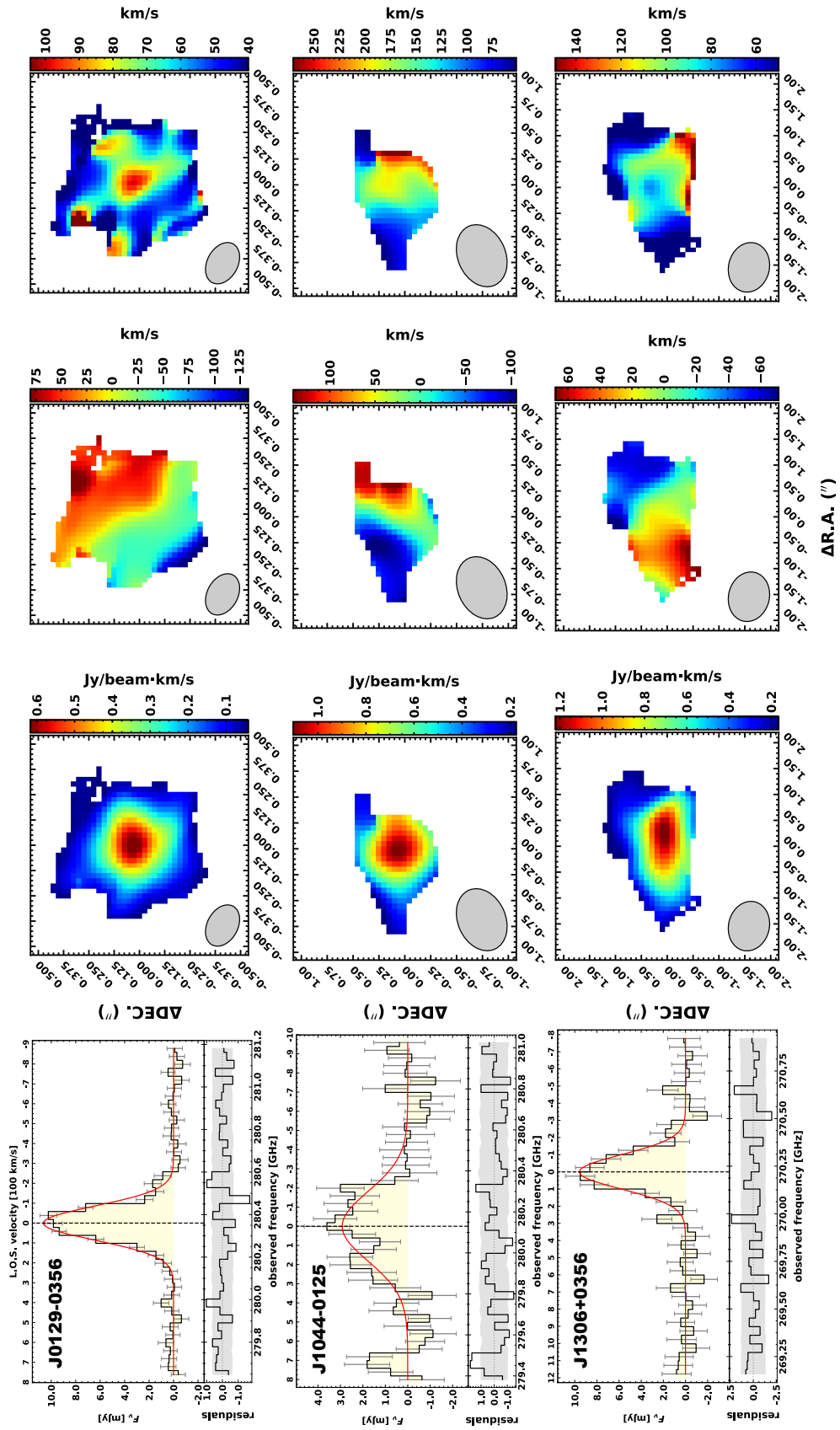


Figure A.5  
(continued)

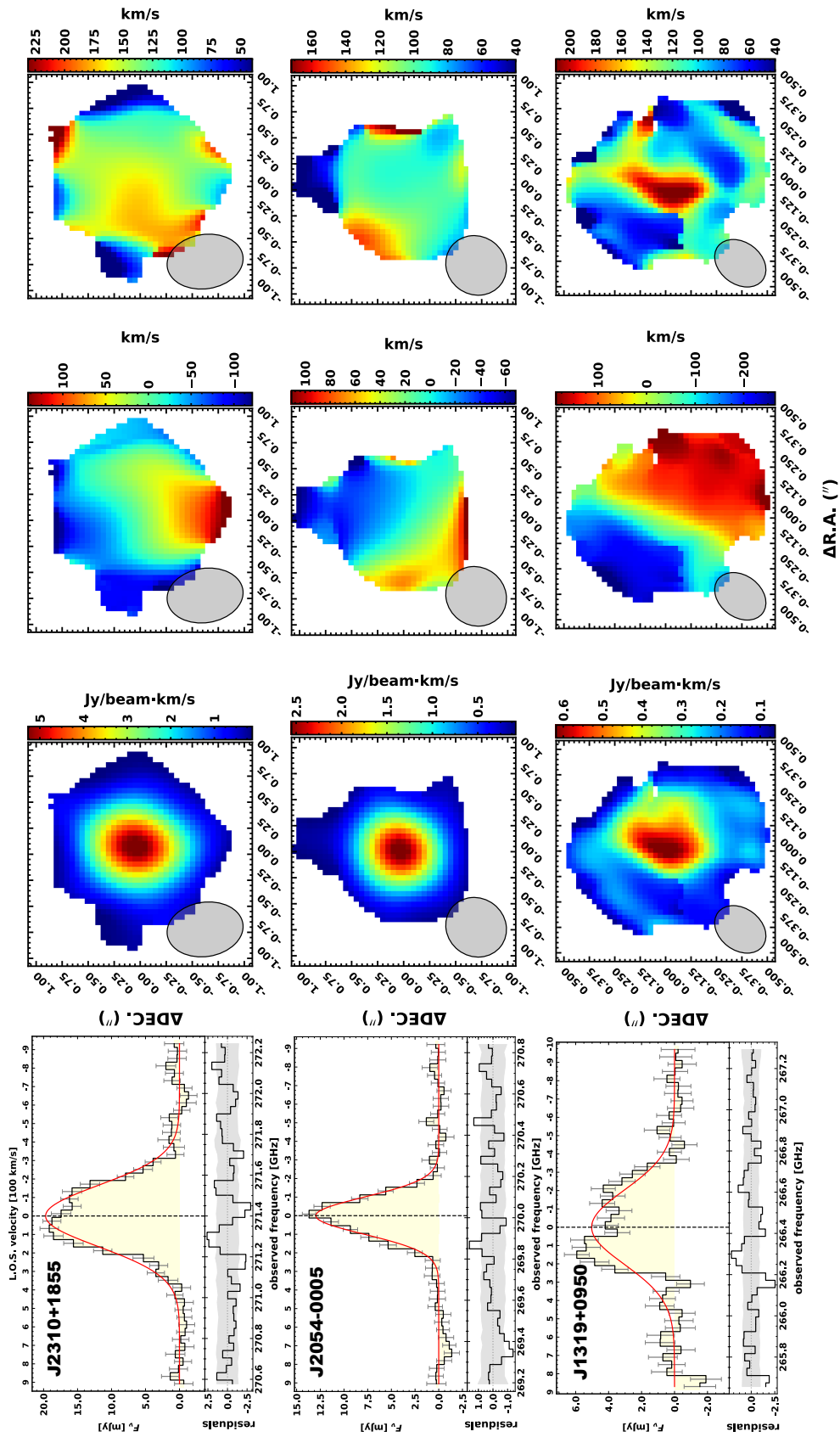


Figure A.5  
(continued)

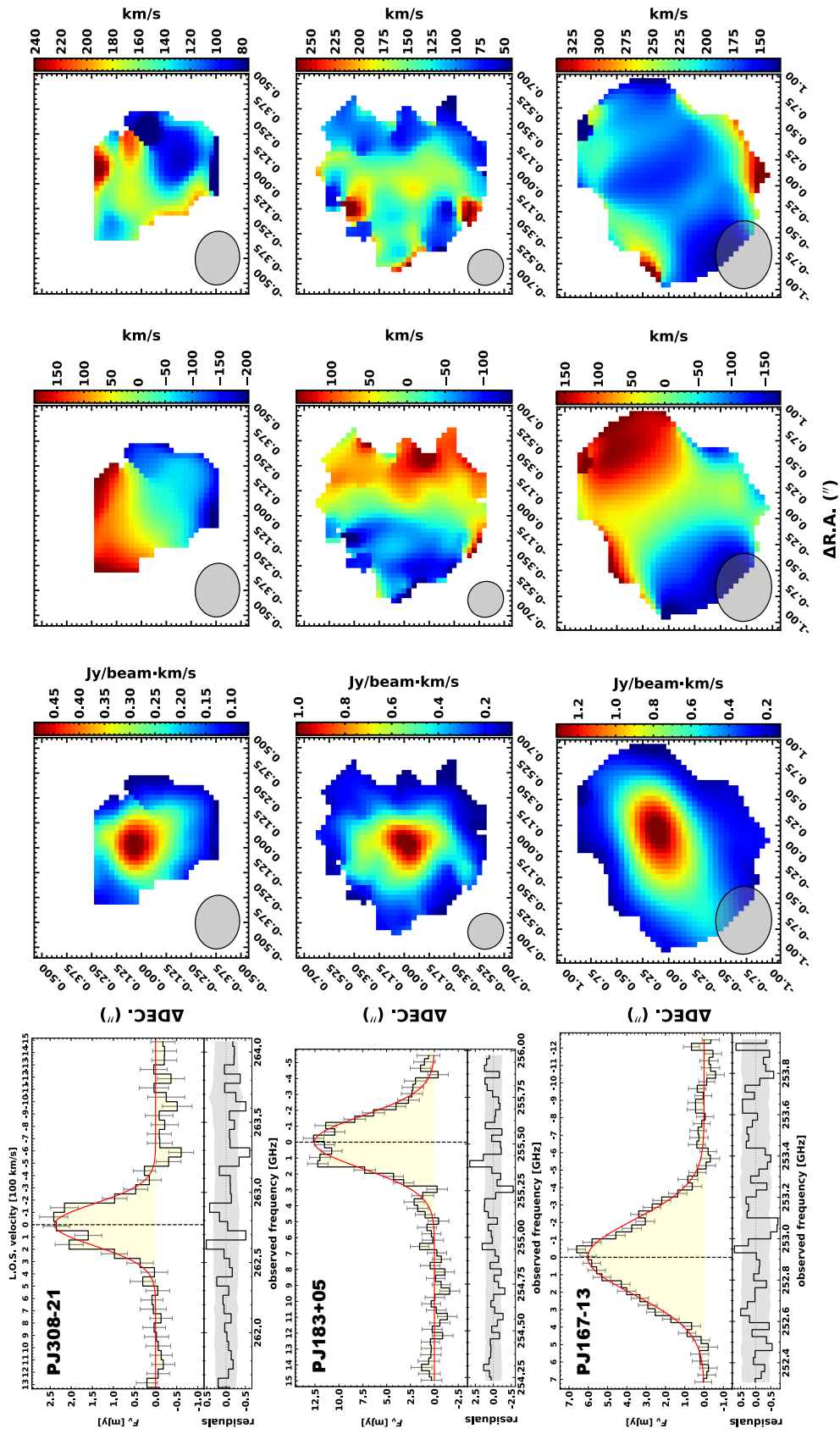


Figure A.5

(continued)

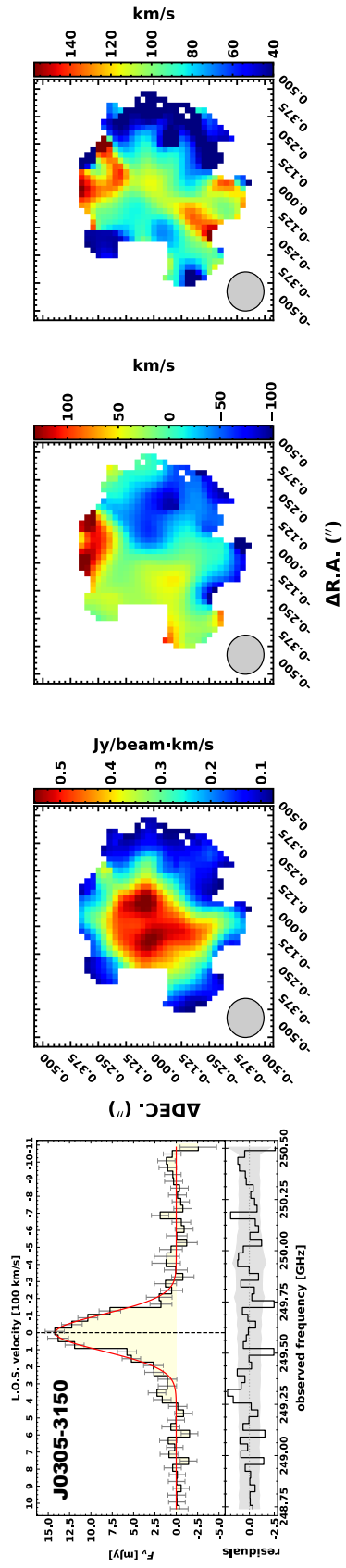
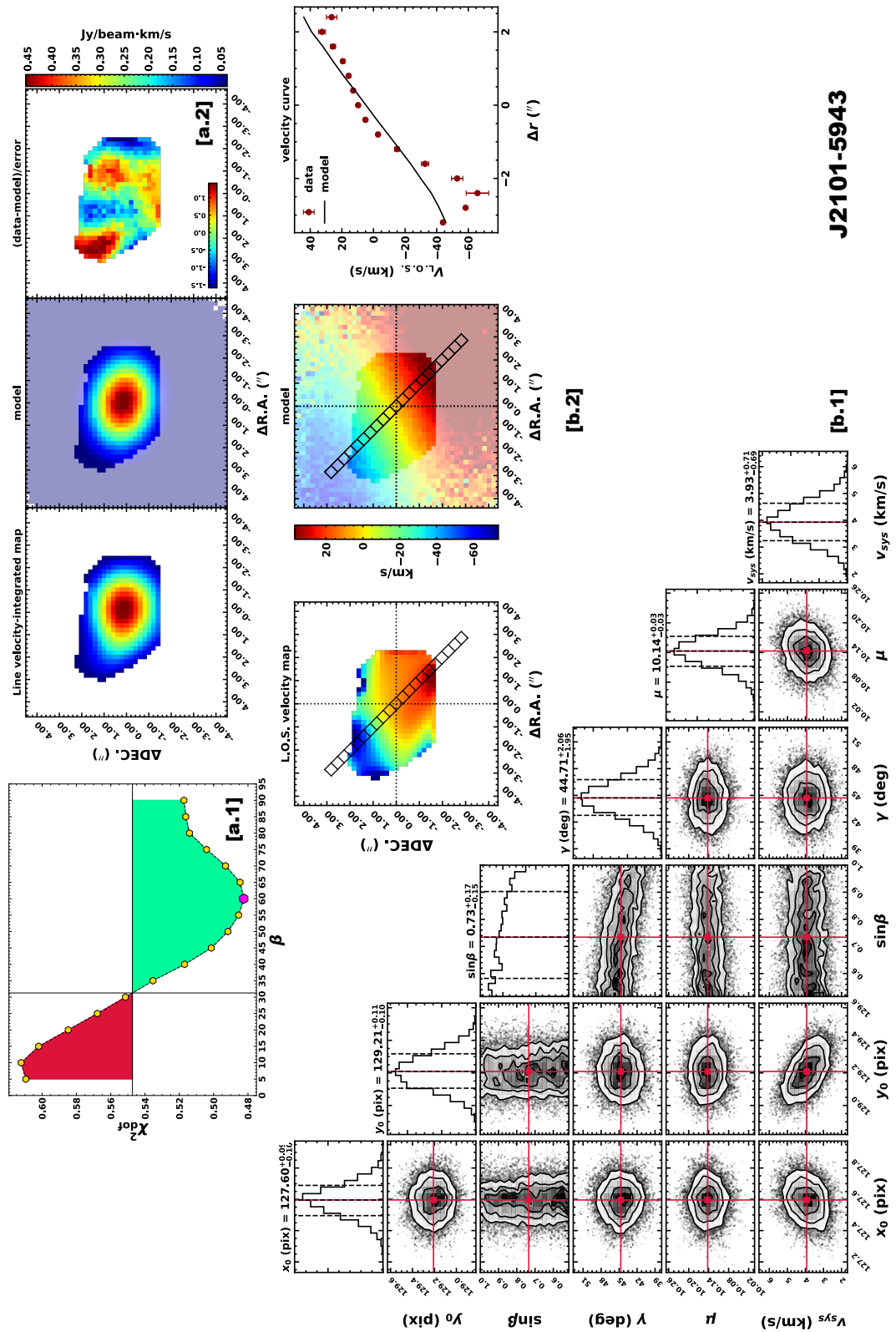


Figure A.5

(continued)



**J2101-5943**

**Figure A.6**

Results of 2D kinematical modelling for objects listed in Tab. 4.2. We refer to Fig. 4.6 for descriptions of individual panels.

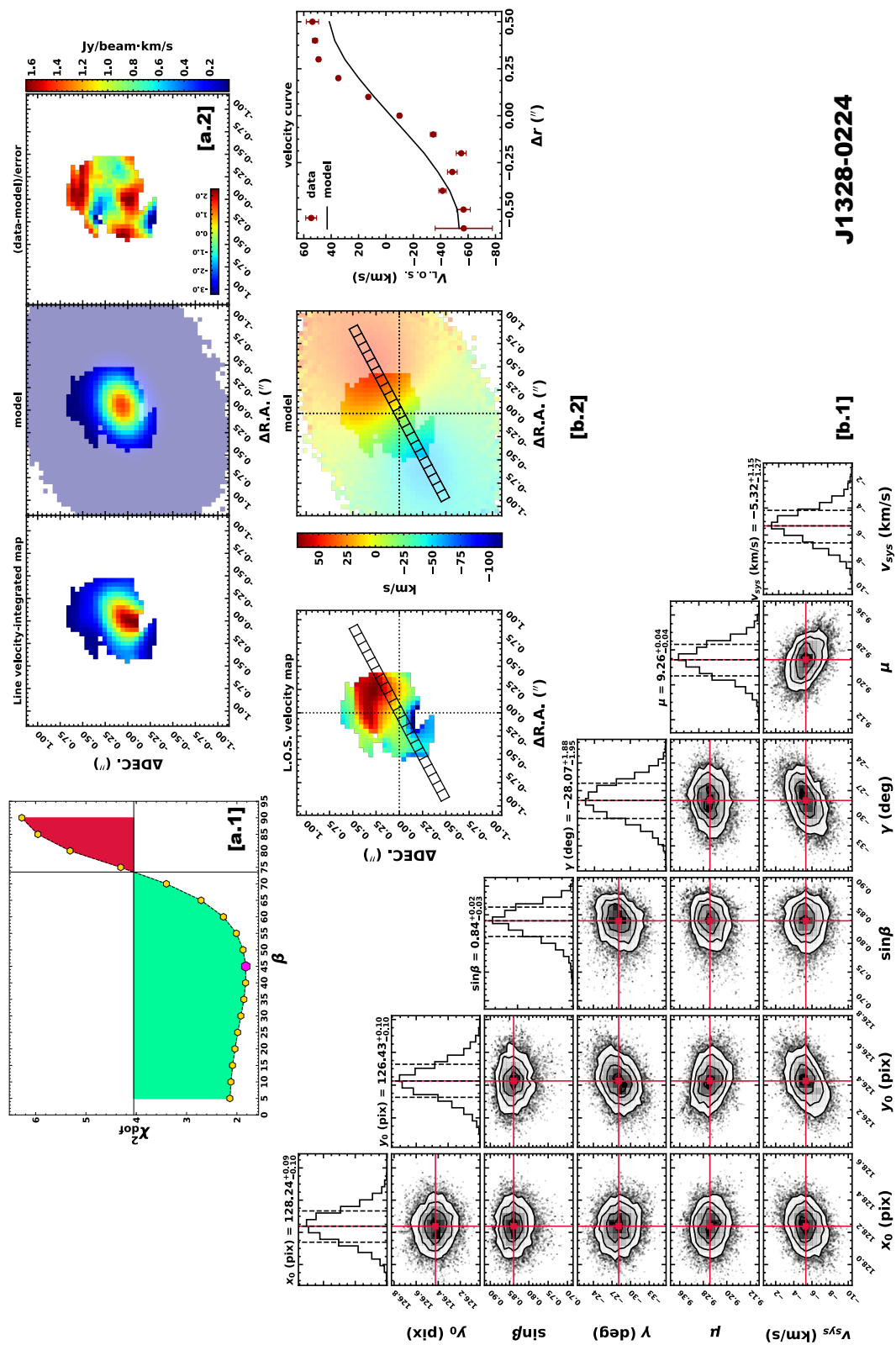


Figure A.6

(continued)

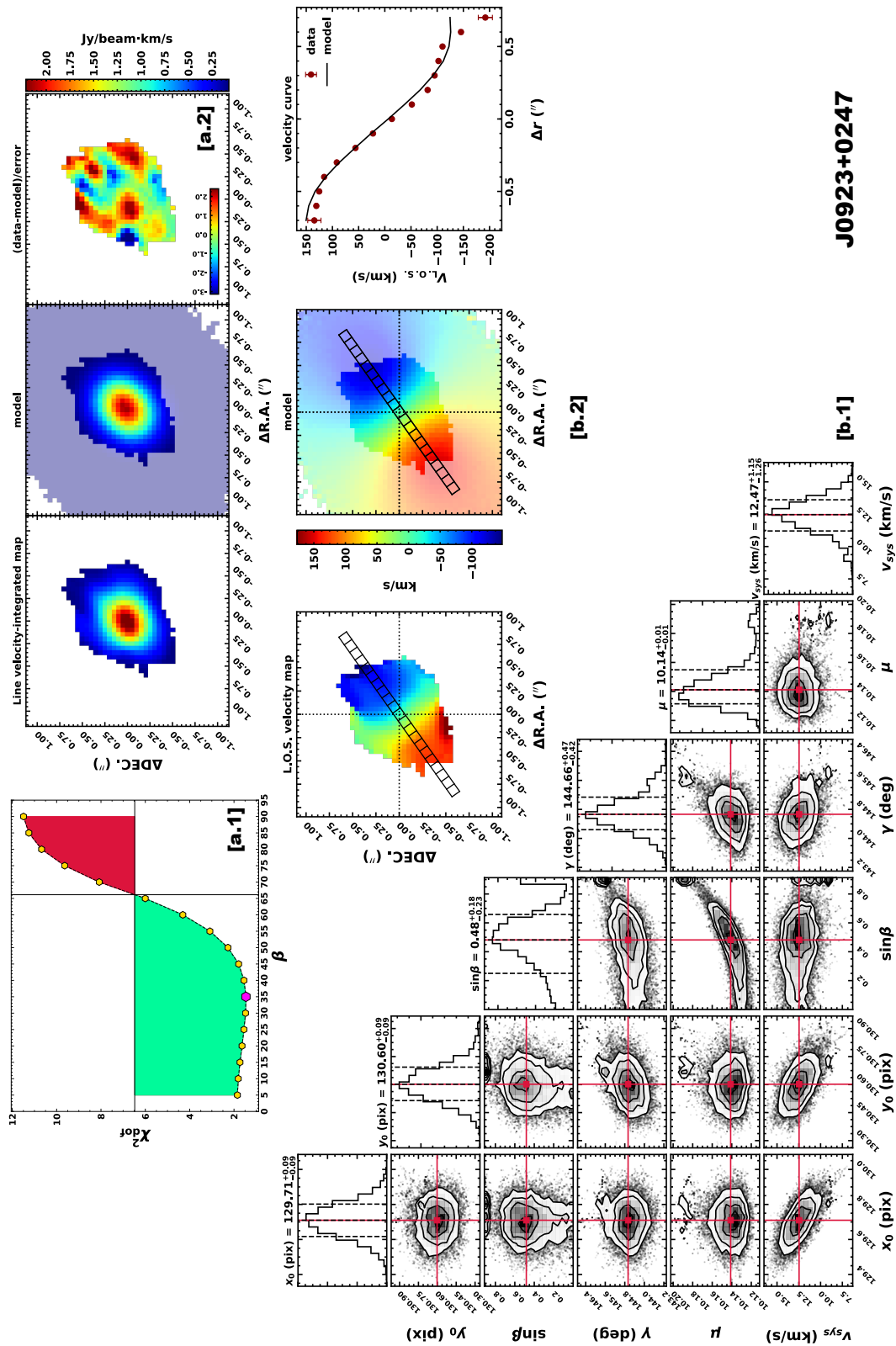
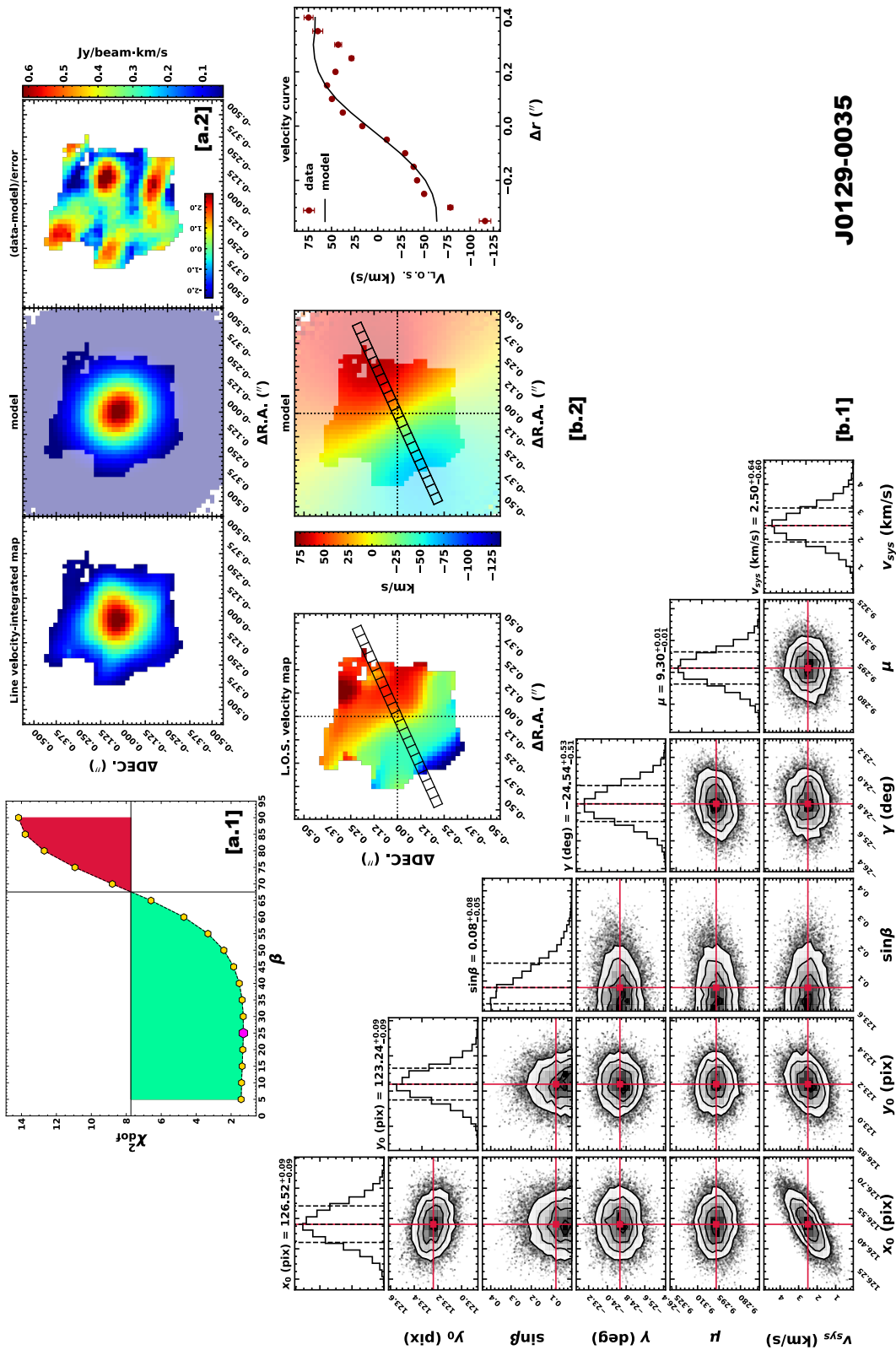


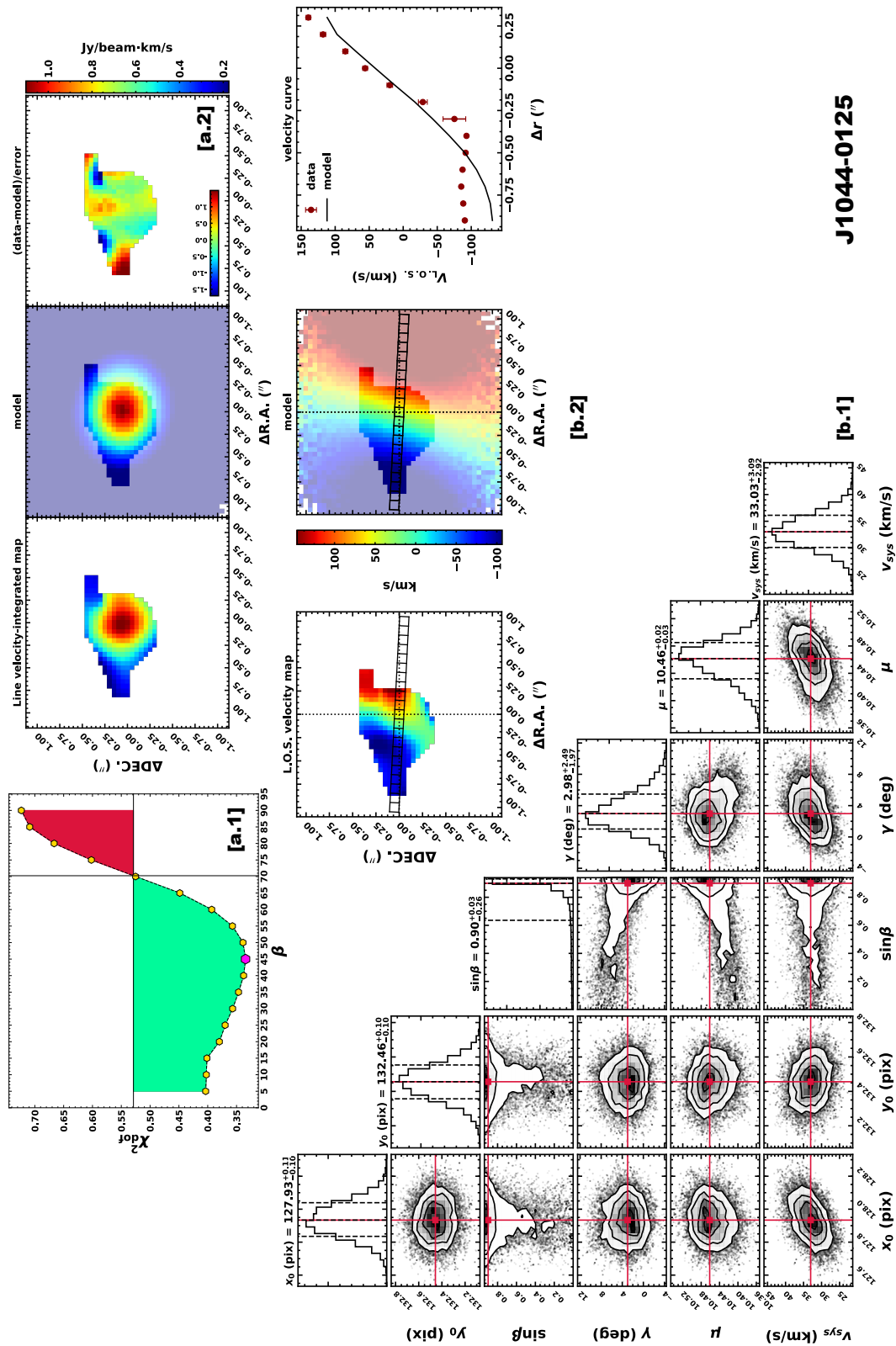
Figure A.6  
(continued)



J0129-0035

Figure A.6

(continued)



**J1044-0125**

**Figure A.6**  
(continued)

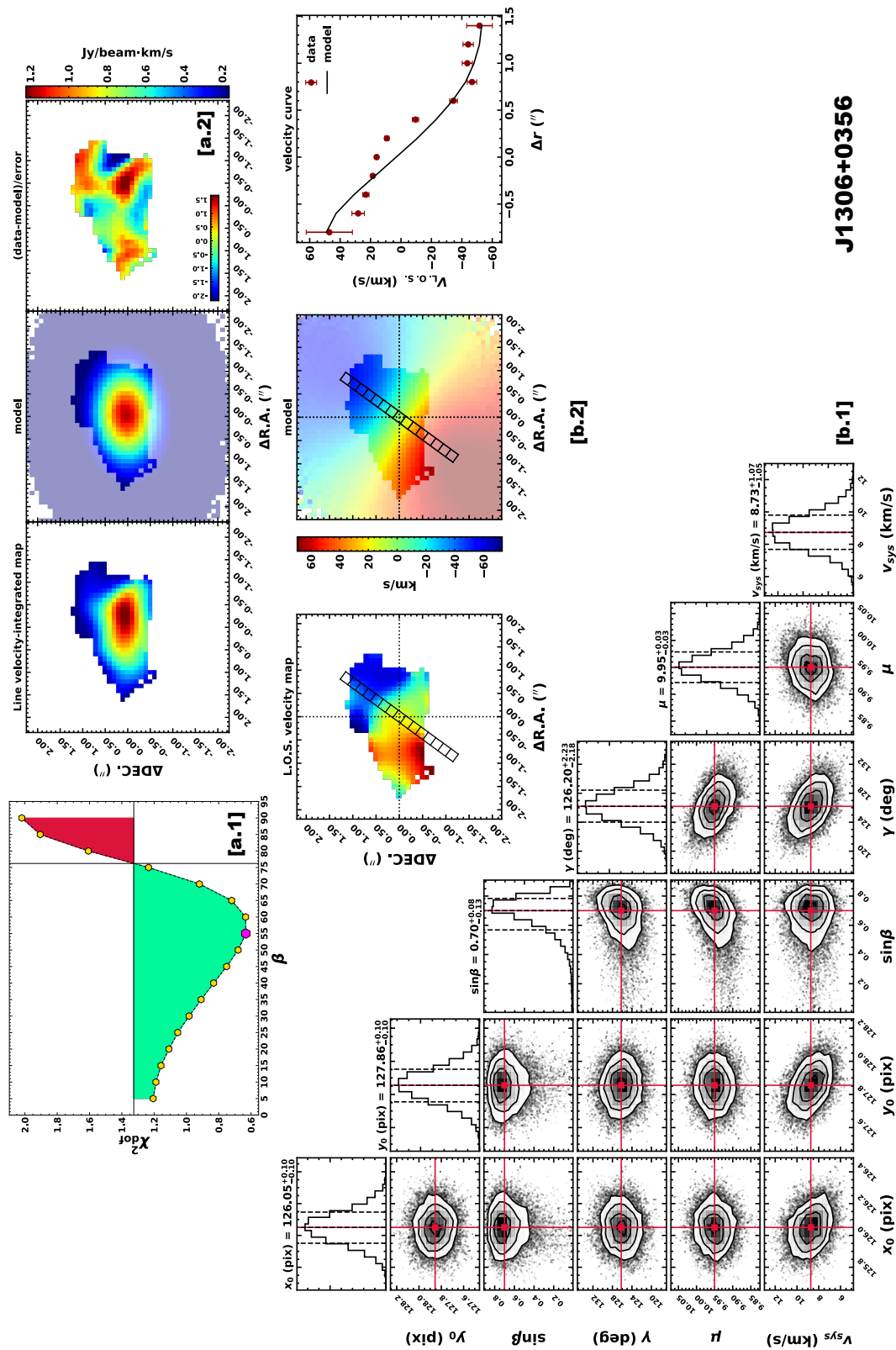
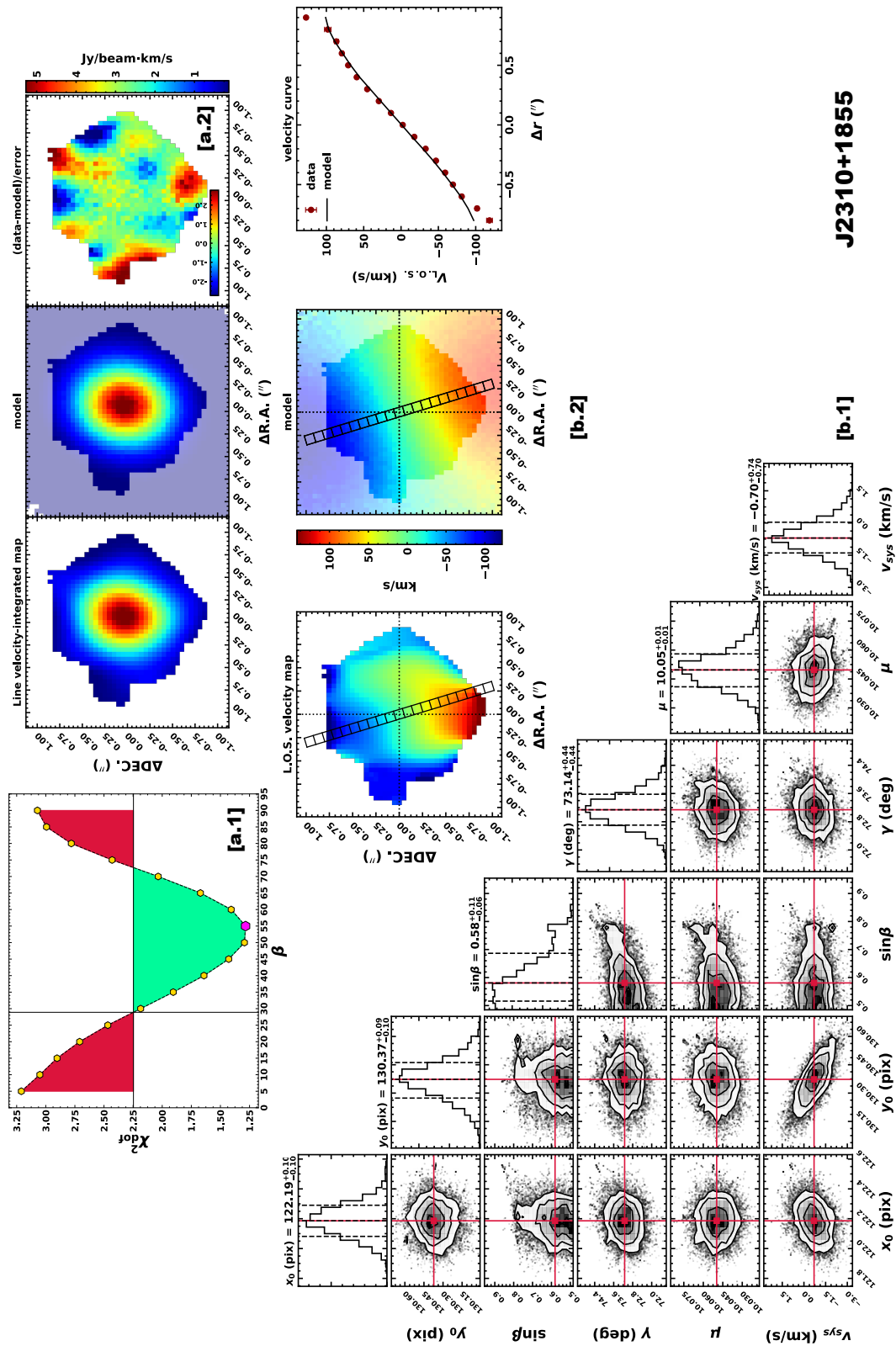


Figure A.6

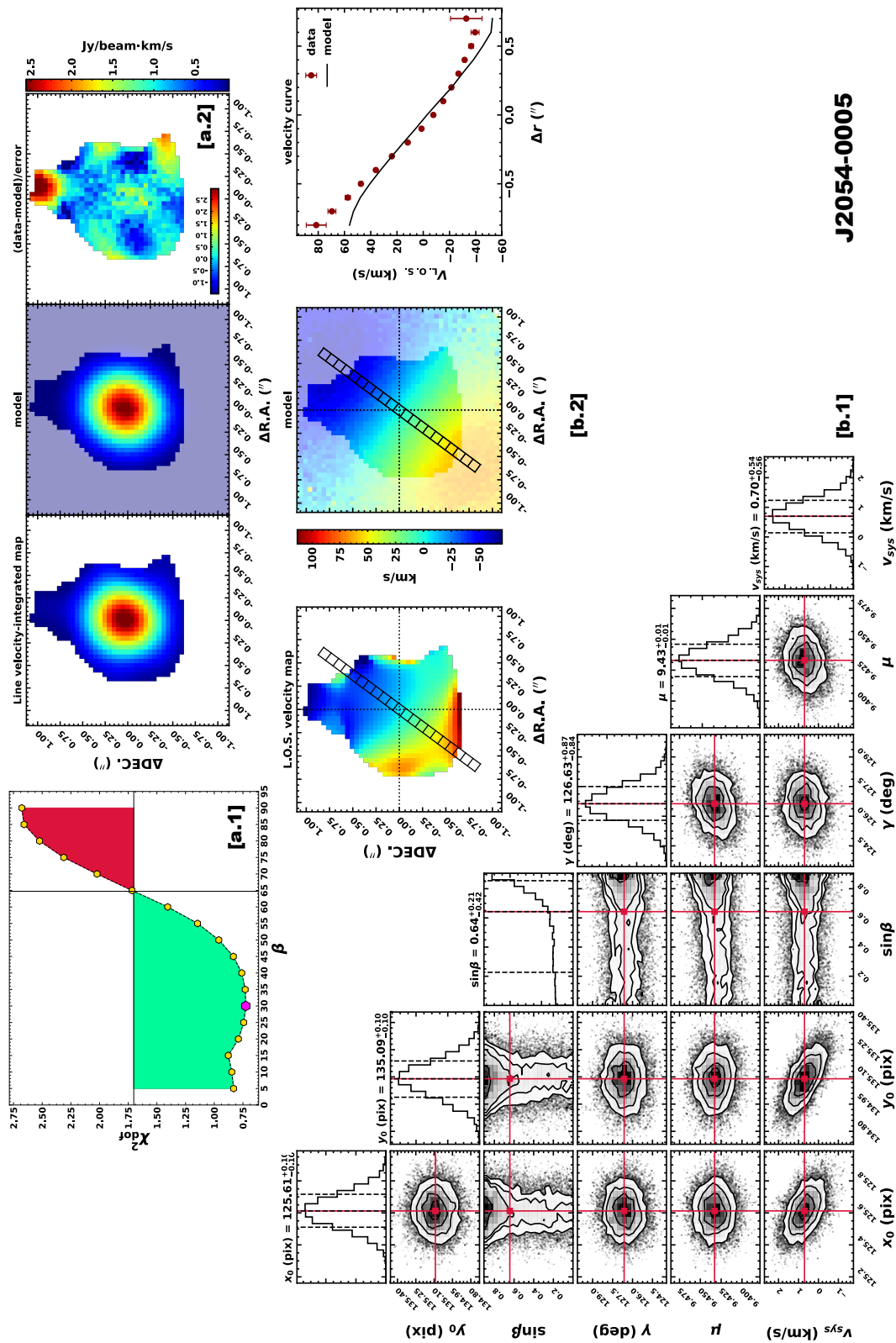
(continued)



**J2310+1855**

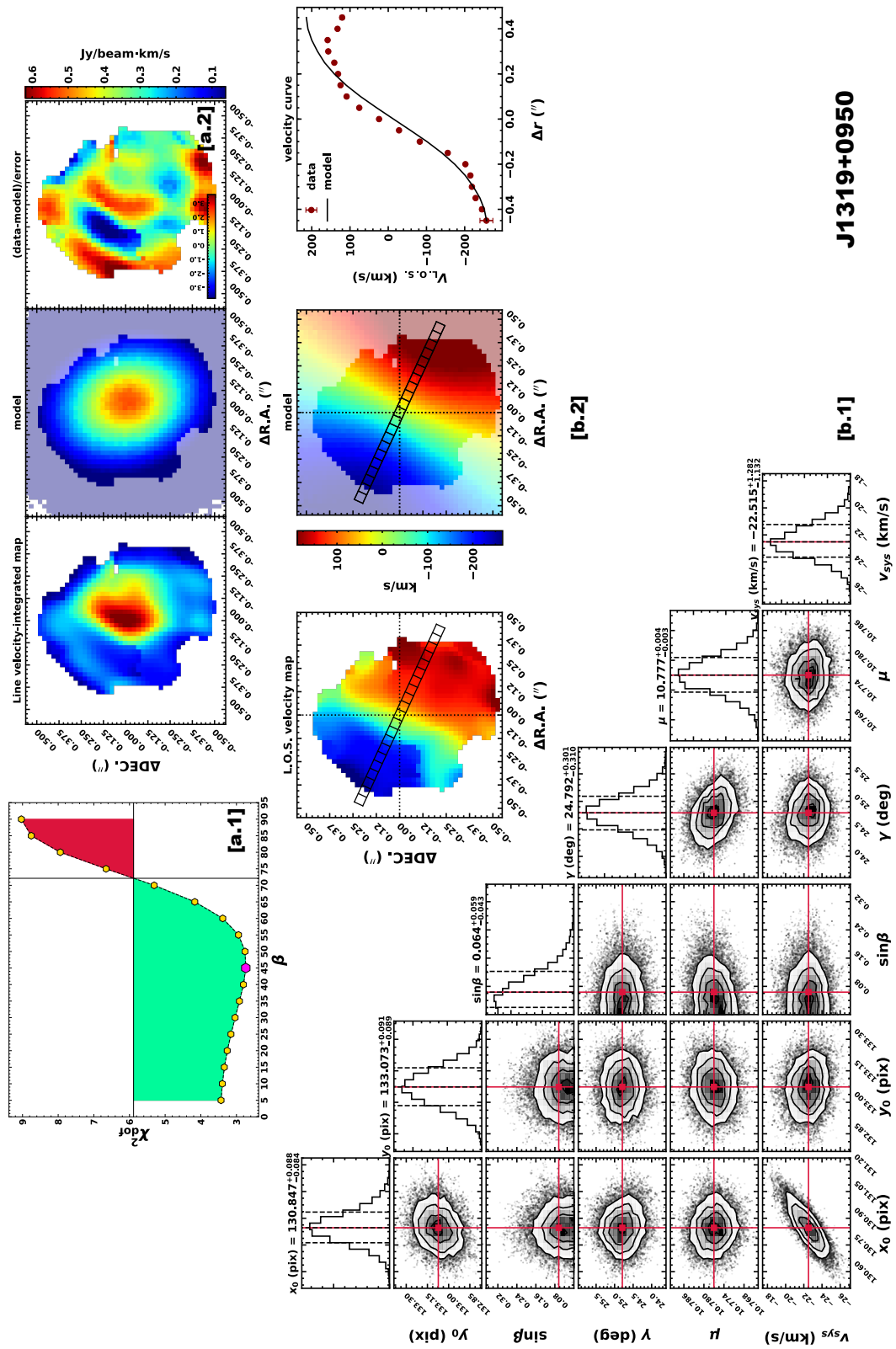
**Figure A.6**

(continued)



J2054-0005

Figure A.6  
(continued)

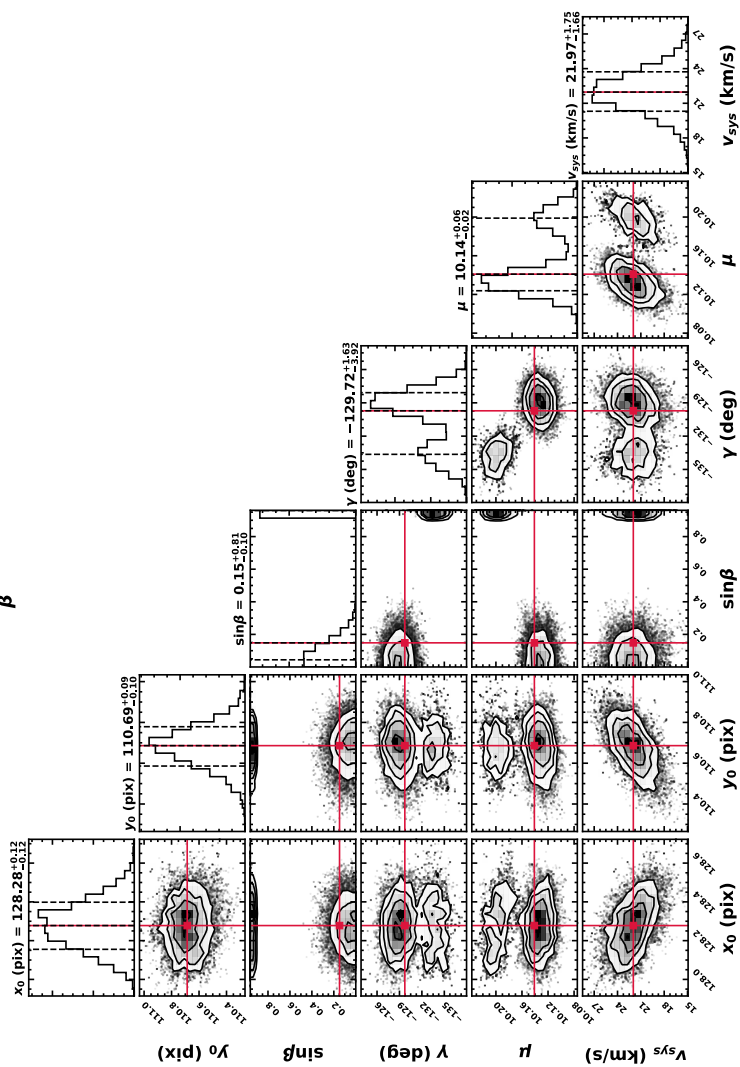
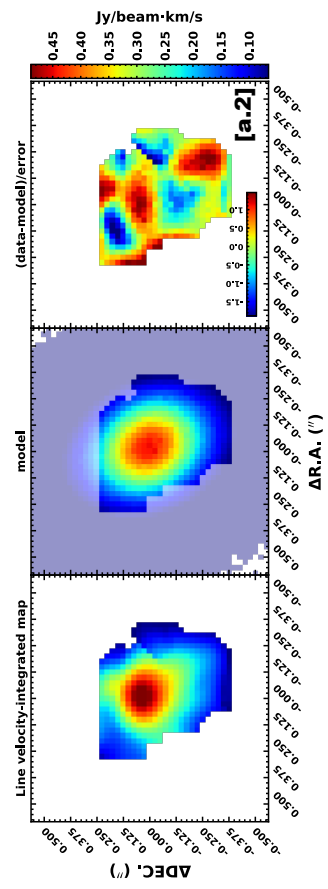
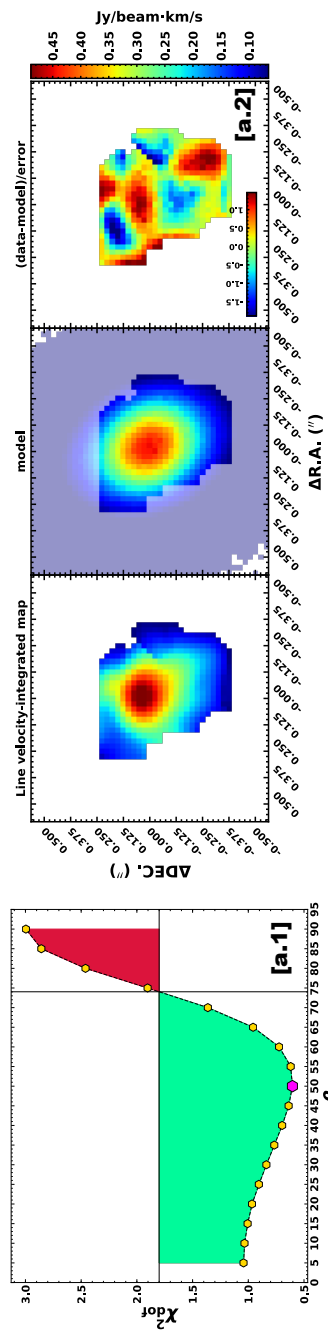


**J1319+0950**

**A.5** Maps, integrated spectra, and the results of the kinematical modelling

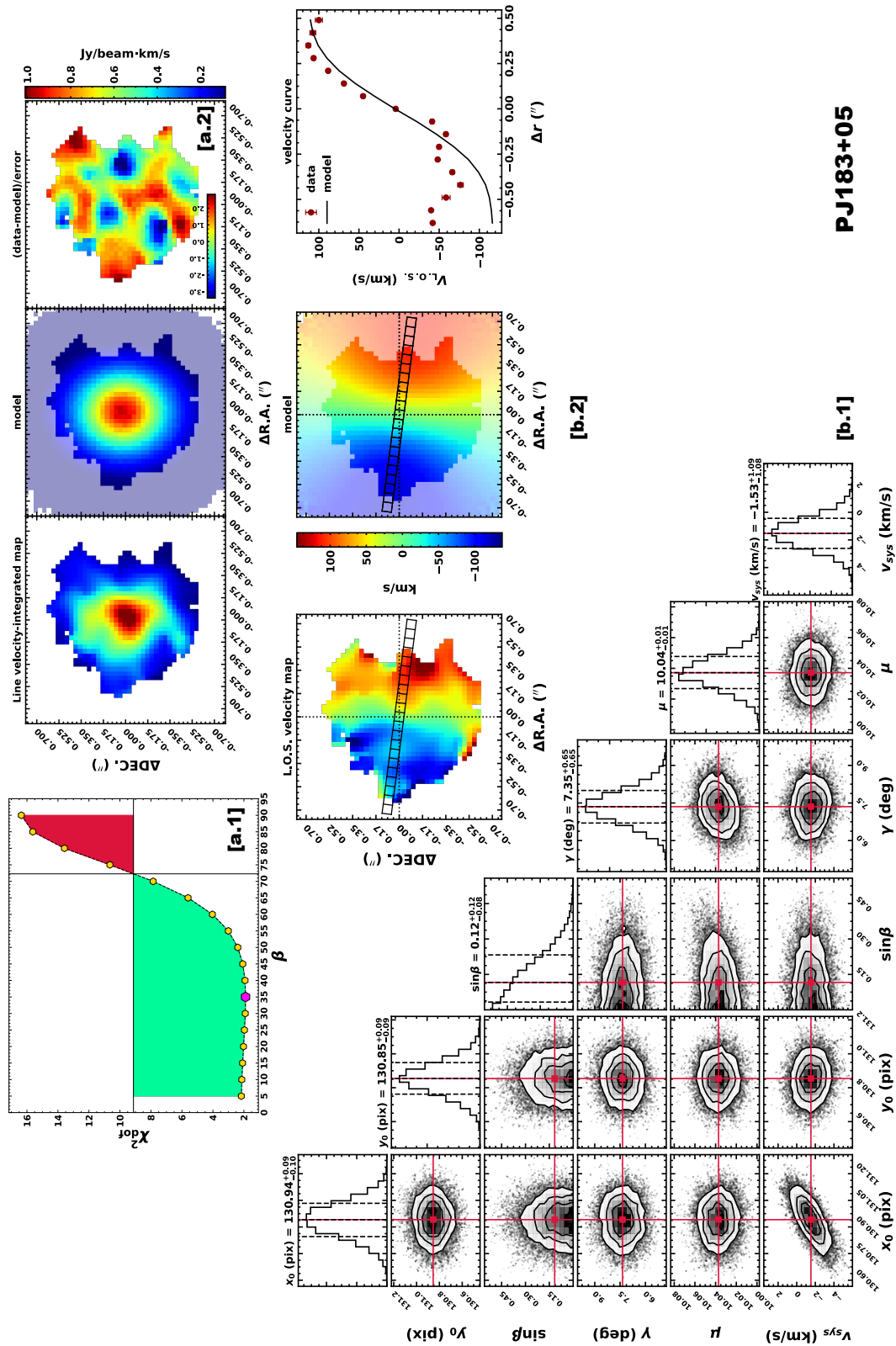
**Figure A.6**

(continued)



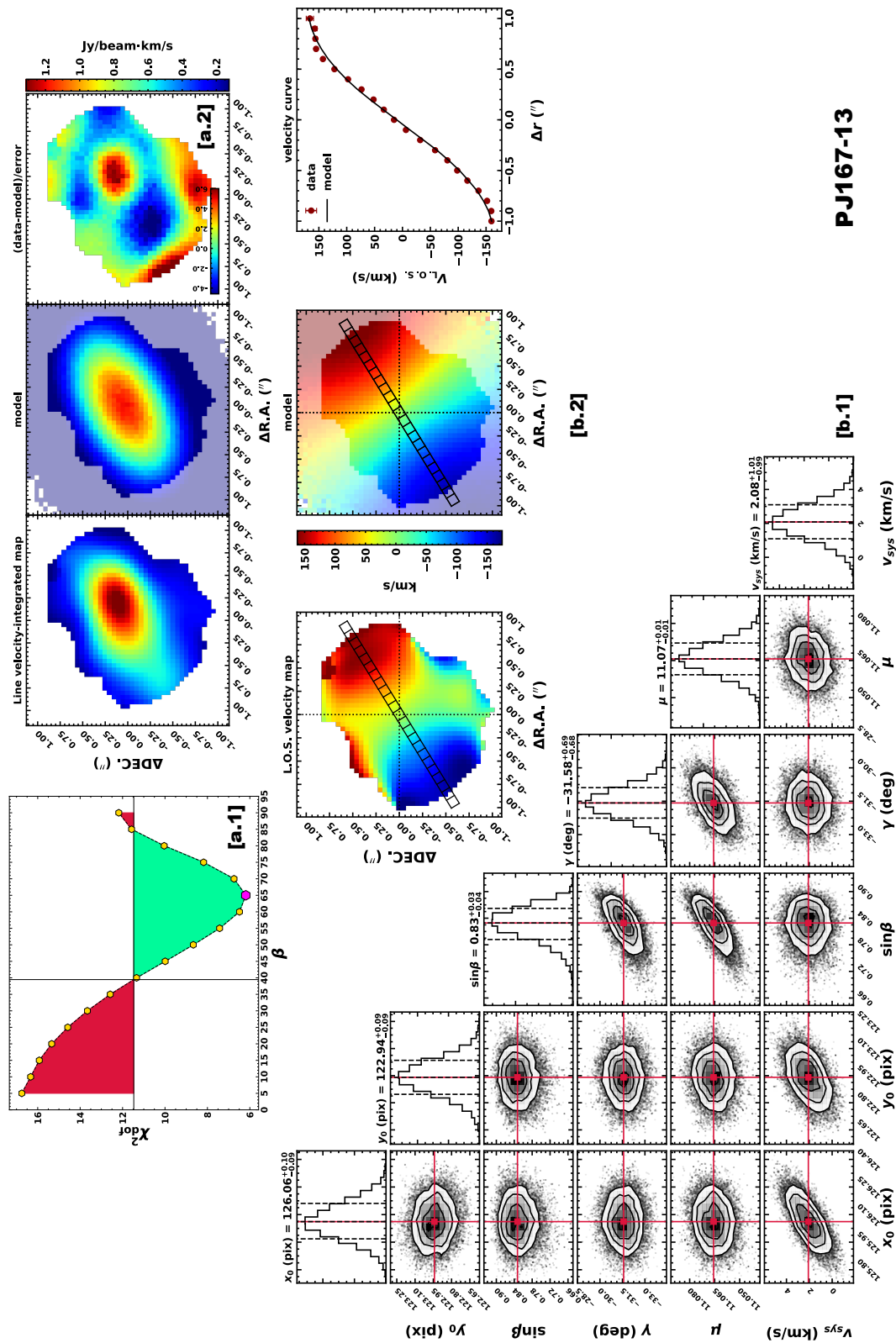
PJ308-21

Figure A.6  
(continued)



PJ183+05

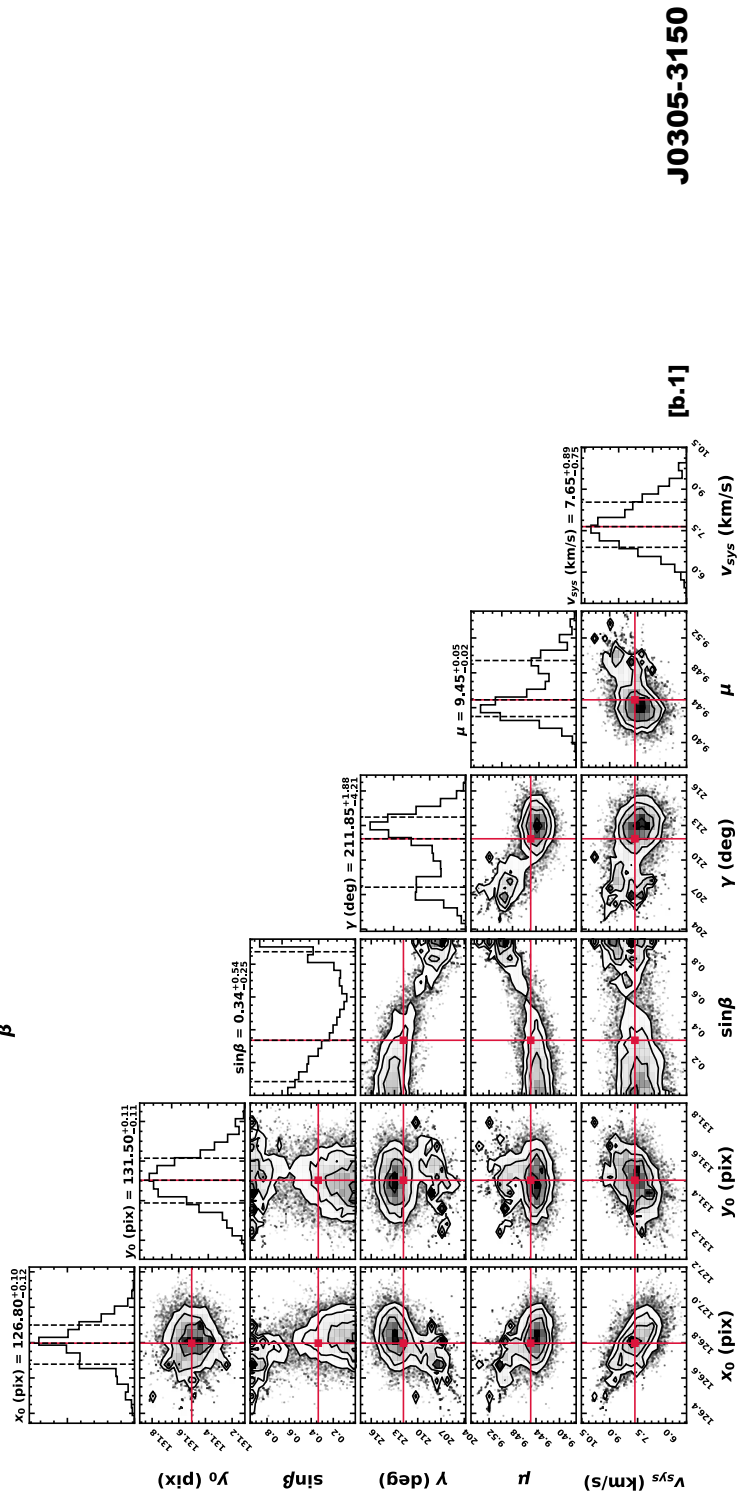
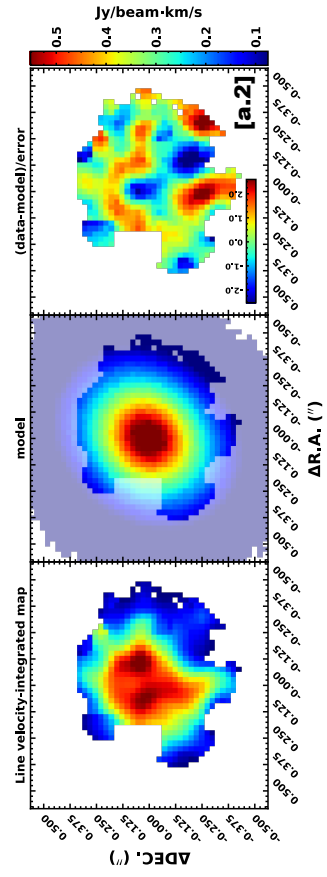
Figure A.6  
(continued)



PJ167-13

Figure A.6

(continued)



**J0305-3150**

**Figure A.6**

(continued)



## Colophon

This thesis was typeset with  $\text{\LaTeX}$ . I used an adaptation of the *Clean Thesis* style (<http://cleanthesis.der-ric.de/>) developed by Ricardo Langner. This research made use of Astropy (<http://www.astropy.org>), a community-developed core Python package for Astronomy (Astropy Collaboration et al., 2013, 2018), NumPy (Harris et al., 2020), SciPy (Virtanen et al., 2020), and Matplotlib (Hunter, 2007).

